frontiers | Research Topics

Sichuan-tibet traffic corridor: Fundamental geological investigations and resource endowment

Edited by
Qiuming Pei, Bin Lin, Venkatramanan Senapathi and Hu Wang

Published in
Frontiers in Earth Science

ISSN 1664-8714
ISBN 978-2-8325-2519-7
DOI 10.3389/978-2-8325-2519-7

About Frontiers

Frontiers is more than just an open access publisher of scholarly articles: it is a pioneering approach to the world of academia, radically improving the way scholarly research is managed. The grand vision of Frontiers is a world where all people have an equal opportunity to seek, share and generate knowledge. Frontiers provides immediate and permanent online open access to all its publications, but this alone is not enough to realize our grand goals.

Frontiers journal series

The Frontiers journal series is a multi-tier and interdisciplinary set of open-access, online journals, promising a paradigm shift from the current review, selection and dissemination processes in academic publishing. All Frontiers journals are driven by researchers for researchers; therefore, they constitute a service to the scholarly community. At the same time, the *Frontiers journal series* operates on a revolutionary invention, the tiered publishing system, initially addressing specific communities of scholars, and gradually climbing up to broader public understanding, thus serving the interests of the lay society, too.

Dedication to quality

Each Frontiers article is a landmark of the highest quality, thanks to genuinely collaborative interactions between authors and review editors, who include some of the world's best academicians. Research must be certified by peers before entering a stream of knowledge that may eventually reach the public - and shape society; therefore, Frontiers only applies the most rigorous and unbiased reviews. Frontiers revolutionizes research publishing by freely delivering the most outstanding research, evaluated with no bias from both the academic and social point of view. By applying the most advanced information technologies, Frontiers is catapulting scholarly publishing into a new generation.

What are Frontiers Research Topics?

Frontiers Research Topics are very popular trademarks of the *Frontiers journals series*: they are collections of at least ten articles, all centered on a particular subject. With their unique mix of varied contributions from Original Research to Review Articles, Frontiers Research Topics unify the most influential researchers, the latest key findings and historical advances in a hot research area.

Find out more on how to host your own Frontiers Research Topic or contribute to one as an author by contacting the Frontiers editorial office: frontiersin.org/about/contact

Sichuan-tibet traffic corridor: Fundamental geological investigations and resource endowment

Topic editors

Qiuming Pei — Southwest Jiaotong University, China

Bin Lin — Institute of Mineral Resources, Chinese Academy of Geological Sciences, China

Venkatramanan Senapathi — Alagappa University, India

Hu Wang — Southwest Jiaotong University, China

Topic coordinator

Dian Li — Chengdu University of Technology, China

Citation

Pei, Q., Lin, B., Senapathi, V., Wang, H., eds. (2023). *Sichuan-tibet traffic corridor: Fundamental geological investigations and resource endowment*. Lausanne: Frontiers Media SA. doi: 10.3389/978-2-8325-2519-7

Table of contents

frontiers | Frontiers in Earth Science

TYPE Editorial
PUBLISHED 09 May 2023
DOI 10.3389/feart.2023.1204067

OPEN ACCESS

EDITED AND REVIEWED BY
Derek Keir,
University of Southampton,
United Kingdom

*CORRESPONDENCE
Qiuming Pei,
pqm@swjtu.edu.cn
Hu Wang,
wanghu9905@126.com

RECEIVED 11 April 2023
ACCEPTED 03 May 2023
PUBLISHED 09 May 2023

CITATION
Pei Q, Wang H, Lin B, Senapathi V and Li D (2023), Editorial: Sichuan-Tibet traffic corridor: fundamental geological investigations and resource endowment. *Front. Earth Sci.* 11:1204067. doi: 10.3389/feart.2023.1204067

Editorial: Sichuan-Tibet traffic corridor: fundamental geological investigations and resource endowment

Qiuming Pei[1]*, Hu Wang[1]*, Bin Lin[2], Venkatramanan Senapathi[3] and Dian Li[4]

[1]Faculty of Geosciences and Environmental Engineering, Southwest Jiaotong University, Chengdu, China, [2]Institute of Mineral Resources, Chinese Academy of Geological Sciences, Beijing, China, [3]Department of Disaster Management, Alagappa University, Karaikudi, Tamilnadu, India, [4]College of Earth Sciences, Chengdu University of Technology, Chengdu, China

KEYWORDS

geological investigations, tectonic-thermal evolution, active tectonics, remote sensing, mineral deposits, Sichuan-Tibet traffic corridor, Himalaya

Editorial on the Research Topic
Sichuan-Tibet traffic corridor: fundamental geological investigations and resource endowment

The Sichuan-Tibet traffic corridor (STTC), which extends across the western Sichuan Basin on the Yangtze block and the Tibetan Plateau (also called the Qinghai-Tibetan Plateau), acts as one of the most important external transport conduits in China (Lu and Cai, 2019). Specifically, the STTC has experienced a prolonged and complex tectonic history involving ocean spreading, subduction, accretion and continental collision events, and finally generated the broadest and highest elevation collisional system on Earth (Yin and Harrison, 2000; Ding et al., 2022). Its unique geological and geomorphic environment (e.g., high seismic intensity, high tectonic strain rates, elevated geothermal activity and extremely high elevation) makes the engineering construction along the STTC face unprecedented challenges (Peng et al., 2020; Cui et al., 2022). Over the past decades, progress regarding the primary geological problems of the STTC has been made to aid development of high-speed railways, hydropower stations, tunnels, urban planning projects, especially in the formation mechanisms of geological hazards and corresponding prevention and control technologies (e.g., Wang et al., 2020; Ma and Yao, 2023; Yang et al., 2023), which provides valuable guidance and scientific support for safe construction and operation in this area. However, the geology and surface processes in the STTC are still relatively poorly understood and require further investigation. Some key geological information such as tectonic evolution, lithological sequence, sedimentary environment, behaviour of active faults, magmatic-hydrothermal activities and associated resources needs to be further documented. Here, we have briefly summarized the key findings of ten original research articles on this Research Topic.

Revealing the tectonic evolution and structural deformation of the major faults in the Tibetan Plateau is of crucial importance to understanding the uplift mechanisms of the Tibetan Plateau and the related geologic hazards and resource exploitation (Wang and Shen, 2020; Spicer et al., 2021; Zhang et al., 2022a). The article by Shailendra et al. reports the first record of

granitoid magmatism (tonalite gneiss) in the eastern Karakoram terrane. Based on the identical geochronological and geochemical records, they conclude that the south-central Pamir, Karakoram and central Tibet microcontinents were a single continental block during the Neoproterozoic. Along the eastern margin of the Tibetan Plateau, Wang et al. provide new multi-proxy provenance data using U-Pb dating of detrital zircons, paleocurrent data, and detrital garnet geochemistry, and suggest that significant surface uplift and rapid denudation of the Longmen Shan Fault were probably initiated in the mid-Cretaceous (~120 Ma). Moreover, Feng et al. conduct multiple trenches and use radiocarbon dating to show paleoseismic history along the Xianshuihe Fault, which indicates a multi-fault seismic rupture behaviour. When it comes to the south Tibet, Wan and Wang utilize the broad magnetotelluric and audio magnetotelluric method to reveal three-dimensional electrical structure of the Gulu Fault, which is helpful in constraining the middle and upper crust conductors that could be used for geothermal exploitation. Also in South Tibet, Li et al. investigate two large-scale antimony deposits within the Abunabu mining area of the Tethys Himalayan metallogenic belt by field geological and mineralogical studies and He-Ar-S isotopic geochemical analyses.

Along the STTC, leucogranitic rocks, also known as Himalayan leucogranites, are widely distributed, which could be used as a "probe" to explore the deep Earth and are critical for understanding the tectonic-magmatic-metamorphic evolution and related economic mineralization of the Himalayan orogeny (Cao et al., 2022). Based on zircon and monazite U(-Th)-Pb ages, Sr-Nd-Pb-Hf isotopes and whole-rock major and trace element compositions for the Liemai two-mica granite in the Yardoi area of eastern Himalaya, together with previously published data, Dai et al. propose that underplating of mafic magmas following slab breakoff of the Neo-Tethys oceanic lithosphere, causing partial melting of the thickened (~50 km) amphibolitic lower crust in Himalaya and thus generate granites with adakitic signatures in the Yardoi area. Another case study from the Gyirong area of the central Himalayan orogenic belt by Pei et al. focuses on the Himalayan pegmatite. From the perspective of tourmalines, the authors document the geochemical behavior of tourmaline precipitation and its origin in the Gyirong pegmatite through *in situ* major and trace element and boron isotope studies. The results demonstrate that the Gyirong pegmatite was the product of crustal anatexis and that the crustal metapelitic rocks within the Greater Himalayan Crystalline Complex were the most likely source components. Notably, this leucogranite belt has world-class metallogenic potential for rare metal deposits.

With the rapid increase in data volume (big data) and the improvement of computing power, emerging technologies such as machine learning (ML), deep learning (DL) and optimization algorithms (OA) have significantly changed ways to solve specific problems in geoscience and geoengineering (Zhang et al., 2022b). Zeng et al. make an attempt at lithology identification by using three supervised-classification algorithms, namely, the k-nearest neighbors (KNN), maximum likelihood classification (MLC) and support vertical machine (SVM). Making use of Landsat-5 TM and ASTER data, this work establishes six methods to identify basalts in the famous Emeishan Large Igneous Province (LIP), which is of great significance for mapping the distribution of flood basalts and exploring the world-class Fe-Ti-V deposits and Ni-Cu-(OGE) sulfide deposits throughout the Emeishan LIP. The article by Dai et al. performs inversions of water depth, salinity, and lithium concentrations in the Zabuye Salt Lake of Tibet by using Landsat-8 remote sensing data and the Light Gradient Boosting Machine (LightGBM) algorithm. Compared with traditional station observations, it can overcome many disadvantages such as spatial discontinuity, long time consumption, and high labor costs. This study achieves high prediction accuracy of the LightGBM machine learning algorithm and could provide technical insight for remote sensing inversion of Salt Lake resources in the future. Furthermore, Guo et al. introduce an intelligent prediction model to estimate the Li, B, and TDS contents of two typical salt lakes (Bieruoze Co and Guopu Co lakes) on the Tibetan Plateau. Their model combines a feature selection algorithm with a machine learning algorithm using Sentinel-2 satellite data. The combined strategy of the genetic algorithm (GA)-based feature selection method and the random forest (RF) shows excellent performance and applicability in mineral content prediction of salt lakes.

The articles collected in this Research Topic undoubtely contribute to fundamental geological investigations and resource endowment within the STTC. We hope that some of the methods proposed and the findings obtained could help inspire future research in geosciences. We also need to recognize that the STTC represents a collage formed by multiphase subduction-collision processes and is one of the most tectonically active regions. This area is characterized by extremely complex geological-geomorphological attributes, which require long-term interdisciplinary research and integrated interpretations in the future.

Author contributions

All authors listed have made a substantial, direct, and intellectual contribution to the work and approved it for publication.

Funding

This Research Topic was supported by the Sichuan Natural Science Foundation (2022NSFSC0410), the second Tibetan Plateau Scientific Expedition and Research (STEP) program (2019QZKK0603) and the National Natural Science Foundation of China (42072244).

Acknowledgments

We greatly appreciate the time and effort of the reviewers, editors, and authors who contributed valuable insights and suggestions to these papers in this Research Topic. Our special thanks go to the Chief Editor Prof. Derek Keir and Associate Editor Prof. Stanislaw Mazur. The first author would also like to thank Prof. Inna Safonova for a helpful discussion.

Conflict of interest

The authors declare that the research was conducted in the absence of any commercial or financial relationships that could be construed as a potential conflict of interest.

Publisher's note

References

Cao, H.-W., Pei, Q.-M., Santosh, M., Li, G.-M., Zhang, L.-K., Zhang, X.-F., et al. (2022). Himalayan leucogranites: A review of geochemical and isotopic characteristics, timing of formation, Genesis, and rare metal mineralization. *Earth-Science Rev.* 234, 104229. doi:10.1016/j.earscirev.2022.104229

Cui, P., Ge, Y., Li, S., Li, Z., Xu, X., Zhou, G. G. D., et al. (2022). Scientific challenges in disaster risk reduction for the Sichuan–Tibet Railway. *Eng. Geol.* 309, 106837. doi:10.1016/j.enggeo.2022.106837

Ding, L., Kapp, P., Cai, F., Garzione, C. N., Xiong, Z., Wang, H., et al. (2022). Timing and mechanisms of Tibetan Plateau uplift. *Nat. Rev. Earth Environ.* 3 (10), 652–667. doi:10.1038/s43017-022-00318-4

Lu, C., and Cai, C. (2019). Challenges and countermeasures for construction safety during the sichuan–tibet railway project. *Engineering* 5 (5), 833–838. doi:10.1016/j.eng.2019.06.007

Ma, J., and Yao, X. (2023). Summer extreme precipitation in the key region of the sichuan-tibet railway. *Adv. Atmos. Sci.* 40 (5), 843–855. doi:10.1007/s00376-022-2133-z

Peng, J., Cui, P., and Zhuang, J. (2020). Challenges to engineering geology of SichuanTibet railway. *Chin. J. Rock Mech. Eng.* 39 (12), 2377–2389. (in Chinese with English abstract). doi:10.13722/j.cnki.jrme.2020.0446

Spicer, R. A., Su, T., Valdes, P. J., Farnsworth, A., Wu, F. X., Shi, G., et al. (2021). Why 'the uplift of the Tibetan Plateau' is a myth. *Natl. Sci. Rev.* 8 (1), nwaa091. doi:10.1093/nsr/nwaa091

Wang, M., and Shen, Z. K. (2020). Present-day crustal deformation of continental China derived from GPS and its tectonic implications. *J. Geophys. Res. Solid Earth* 125 (2). doi:10.1029/2019jb018774

Wang, W.-D., Li, J., and Han, Z. (2020). Comprehensive assessment of geological hazard safety along railway engineering using a novel method: A case study of the sichuan-tibet railway, China. *Geomatics, Nat. Hazards Risk* 11 (1), 1–21. doi:10.1080/19475705.2019.1699606

Yang, H., Cheng, Q., He, J., Xing, B., and Xiao, S. (2023). First insights into a debris avalanche blocking the Tonghua No. 1 tunnel in China's Sichuan–Tibet traffic corridor on 5 July 2022. *Landslides* 20 (4), 865–870. doi:10.1007/s10346-022-02018-y

Yin, A., and Harrison, T. M. (2000). Geologic evolution of the Himalayan-Tibetan orogen. *Annu. Rev. earth Planet. Sci.* 28 (1), 211–280. doi:10.1146/annurev.earth.28.1.211

Zhang, G., Tian, Y., Li, R., Shen, X., Zhang, Z., Sun, X., et al. (2022a). Progressive tectonic evolution from crustal shortening to mid-lower crustal expansion in the southeast Tibetan plateau: A synthesis of structural and thermochronological insights. *Earth-Science Rev.* 226, 103951. doi:10.1016/j.earscirev.2022.103951

Zhang, W., Gu, X., Tang, L., Yin, Y., Liu, D., and Zhang, Y. (2022b). Application of machine learning, deep learning and optimization algorithms in geoengineering and geoscience: Comprehensive review and future challenge. *Gondwana Res.* 109, 1–17. doi:10.1016/j.gr.2022.03.015

frontiers | Frontiers in Earth Science

TYPE Original Research
PUBLISHED 08 December 2022
DOI 10.3389/feart.2022.1027801

OPEN ACCESS

EDITED BY
Venkatramanan Senapathi,
Alagappa University, India

REVIEWED BY
Hadi Shafaii Moghadam,
Damghan University, Iran
Mustafa Açlan,
Yüzüncü Yıl University, Turkey

*CORRESPONDENCE
Vikas Adlakha,
vikas.himg@gmail.com

SPECIALTY SECTION
This article was submitted to Structural Geology and Tectonics, a section of the journal Frontiers in Earth Science

RECEIVED 25 August 2022
ACCEPTED 28 November 2022
PUBLISHED 08 December 2022

CITATION
Pundir S, Adlakha V, Kumar S, Singhal S and Das S (2022), A newly identified cryogenian (ca. 806 ma) basement tonalite gneiss from the Eastern Karakoram, NW India: Constraints from geochemistry and zircon U-Pb geochronology.
Front. Earth Sci. 10:1027801.
doi: 10.3389/feart.2022.1027801

A newly identified cryogenian (ca. 806 ma) basement tonalite gneiss from the Eastern Karakoram, NW India: Constraints from geochemistry and zircon U-Pb geochronology

Shailendra Pundir[1], Vikas Adlakha[1]*, Santosh Kumar[2], Saurabh Singhal[1] and Satyabrata Das[1]

[1]Wadia Institute of Himalayan Geology, Dehradun, Uttarakhand, India, [2]Department of Geology, Centre of Advanced Study, Kumaun University, Nainital, Uttarakhand, India

The Karakoram Terrane (KT) represents the southern margin of the Eurasian Plate, mainly consisting of Late Jurassic-Early Cretaceous subduction-related granites and post-collisional Miocene leucogranites, which intrude the Late Neo-Proterozoic basement. We report for the first time the existence of the Cryogenian KT basement as recorded from the geochemistry and geochronology of tonalite gneiss (ca. 806 Ma) in the southeastern Karakoram terrane, NW India. Geochemically, the studied tonalite gneiss is slightly peraluminous (Molar $Al_2O_3/CaO+Na_2O+K_2O=1.1$), calc-alkaline volcanic-arc granitoid, strongly fractionated REE ($La_N/Yb_N=33.99$), and high Sr/Y =19.75, more akin to its affinity with Tonalite–trondhjemite–granodiorite (TTG)/adakite. The whole-rock elemental data suggest that tonalite gneiss is more likely sourced from ancient mafic lower crust where garnet remained in the residue. The petrogenetic modeling of REE suggests that the melt similar to the observed tonalite gneiss can be generated through ~50% partial melting of a mafic lower crust with garnet, clinopyroxene, and amphibole assemblage. The synthesis and comparison of present and published Proterozoic magmatic records on the rocks from KT strongly dictate that the produced partial melt similar to observed tonalite gneiss most likely served as the parental melt for the development of TTGs in the Southern Pamir and more evolved granitoid in the Central Tibetan terrane. We propose that the studied tonalite gneiss from the southeast Karakoram is a product of Neoproterozoic Andean-type orogeny formed on the northwestern margin of the Rodinia supercontinent. Thus, our study favors the first time, the position of KT within the Cimmerian belt along with other East Asian continental blocks.

KEYWORDS

cryogenian magmatism, geochronology, geodynamics, karakoram, trans-himalaya

1 Introduction

The supercontinent Rodinia is considered to have assembled during Mesoproterozoic to Neoproterozoic (~1300 to 900 Ma), which fragmented later during late Neoproterozoic (Meert and Torsvik, 2003; Li et al., 2008; Cawood et al., 2016). The timing and origin of spatially distributed felsic magmatic rocks of Neoproterozoic time from the Asian terranes provide evidence on the assembly, growth and break-up of the Rodinia supercontinent (e.g., Zhao et al., 2018). Various studies on the paleogeographic reconstruction of Pamir, Tarim, Qiangtang, and Lhasa Terranes from East-Asia suggest the location of these continental blocks on the northwestern margin of the Rodinia supercontinent (eg., Condie, 2001; Li et al., 2008; Dong et al., 2011; Cawood et al., 2013; Cawood et al., 2016; Merdith et al., 2017; Zhao et al., 2018; Hu et al., 2018a; Hu et al., 2018b; Zhou et al., 2019; Kang et al., 2019). Later, these East Asian terranes formed the part of Gondwanaland during the Paleozoic hence all belong to Gondwanan ancestry (Crawford, 1974; Şengör 1984; Yeh and Shellnutt, 2016). The Karakoram Terrane (KT), southern Pamir, Tarim, Qiangtang, and Lhasa broke from the Gondwanan margin in the Early Permian and moved in the north which then collided with Eurasian margin in Middle Triassic that formed the Cimmerian orogen (Yeh and Shellnutt, 2016).

The KT represents the southern margin of the Eurasian Plate and is considered geologically equivalent to the southeast and central Pamir Terranes in the west and Qiangtang Terrane in the east (Figure 1A; Robinson, 2015; Villarreal et al., 2020). Geologically, the KT mainly consists of the Late-Jurassic to Early Cretaceous Karakoram Batholith (KB) which mainly consist of pre-collisional calc-alkaline I-type granitoids as the main magmatic event that formed due to subduction of Neo-Tethys oceanic lithosphere beneath south Eurasian plate margin (e.g., Fraser et al., 2001; Heuberger et al., 2007; Jain and Singh, 2009; Boutonnet et al., 2012; Phillips et al., 2013; Sen et al., 2014; Pundir et al., 2020a; Pundir et al., 2020b), and the Early Cretaceous to Late-Miocene Karakoram Metamorphic complex which mainly consists of regional Barrovian facies kyanite- and sillimanite-grade metamorphic rocks and leucogranites (e.g., Fraser et al., 2001; Rolland et al., 2009; Streule et al., 2009; Wallis et al., 2014). Similar to the KT, the southern Pamir records Late Jurassic-Late Cretaceous calc-alkaline subduction related I-type granitoids (Liu et al., 2020 and references therein) and Qiangtang terrane from central Tibet records Late Triassic to Late Cretaceous subduction-related I-type granites (e.g., Kapp et al., 2003; Peng et al., 2015; He et al., 2019). The Late Neo-Proterozoic terrane granitoids along the southern margin of the Eurasian Plate is exposed sporadically (e.g., the western Karakoram, the southeast Pamir, and the southern Qiangtang and Northern Lhasa region (central Tibet)) (Rolland et al., 2002; Dan et al., 2020; Liu et al., 2020). In the KT the record of crystalline Late Neo-Proterozoic basement occurs only in a few regions of the western Karakoram where the metadiorite (ca. 651 Ma; $^{40}Ar/^{39}Ar$) outcrops to the north of the Shyok Suture zone (SSZ) (Rolland et al., 2002). A record of pre-Ordovician granitic intrusion to the north of the Karakoram Batholith is also reported (Fort et al., 1994). However, no shreds of evidence on Late Neo-Proterozoic crystalline basement rocks are available from southeastern KT, India, unlike the Lhasa, Qiangtang, southeast Pamir, and western KT. Thus, the non-availability of such Late Neo-Proterozoic magmatism records in SE Karakoram limits our understanding of Late Neo-Proterozoic evolution and Paleogeographic reconstruction of the Karakoram and western Tibet. The geological, geographical, and geochronological correlation of the KT to the Pamir range to the NW, and central Tibet to the SE is important to understand the origin and position of the KT in the Cimmerian belt (e.g., Afghanistan, Pamir, Tarim, Qiangtang, and Lhasa terranes) that formed the northern margin of the Gondwanaland during the Paleozoic (e.g., Şengör, 1984).

This study presents the first whole-rock geochemical and zircon U-Pb geochronology of a sample of Neo-Proterozoic granite gneiss from the KT. We analyze the present set of new data in combination with the published geochemical record on similar Neoproterozoic granites of the Pamir Terrane and central Tibet to constrain the petrogenesis of the KT basement during the Neoproterozoic supercontinent cycle. Our study provides significant evidence to reveal the Paleogeography of the SE Karakoram in the context of Rodinia and Cimmerian terrane, which existed in the geological past.

2 Regional geology

The India-Asia collision zone or Trans-Himalaya and KT litho-tectonic units represent the southern margin of the Eurasian Plate (e.g., Searle et al., 1998; Jain and Singh, 2008; Searle and Hacker, 2019). The KT lies to the northwest of the Himalayan Mountains and extends from the Afghan block in the west to southwest Tibet in the east (Figure 1). The Rushan-Pshart Suture zone forms the northern boundary of the KT, where it abuts against the southern Pamir mountains, and the Shyok Suture Zone (SSZ) forms its southern boundary, which separates it from the Ladakh Batholith (Figure 1A; e.g., Schwab et al., 2004; Searle and Hacker, 2019).

The study area forms the part of NW India where the KT can be divided into three main geological units, namely 1) Karakoram Fault (KF) zone, 2) Karakoram Metamorphic Complex (KMC), and 3) Karakoram Batholith (KB) (e.g., Jain and Singh, 2008) (Figure 1B).

The southern margin of KT bounds the ~1000 km long lithospheric scale dextral strike-slip KF to the south (Searle

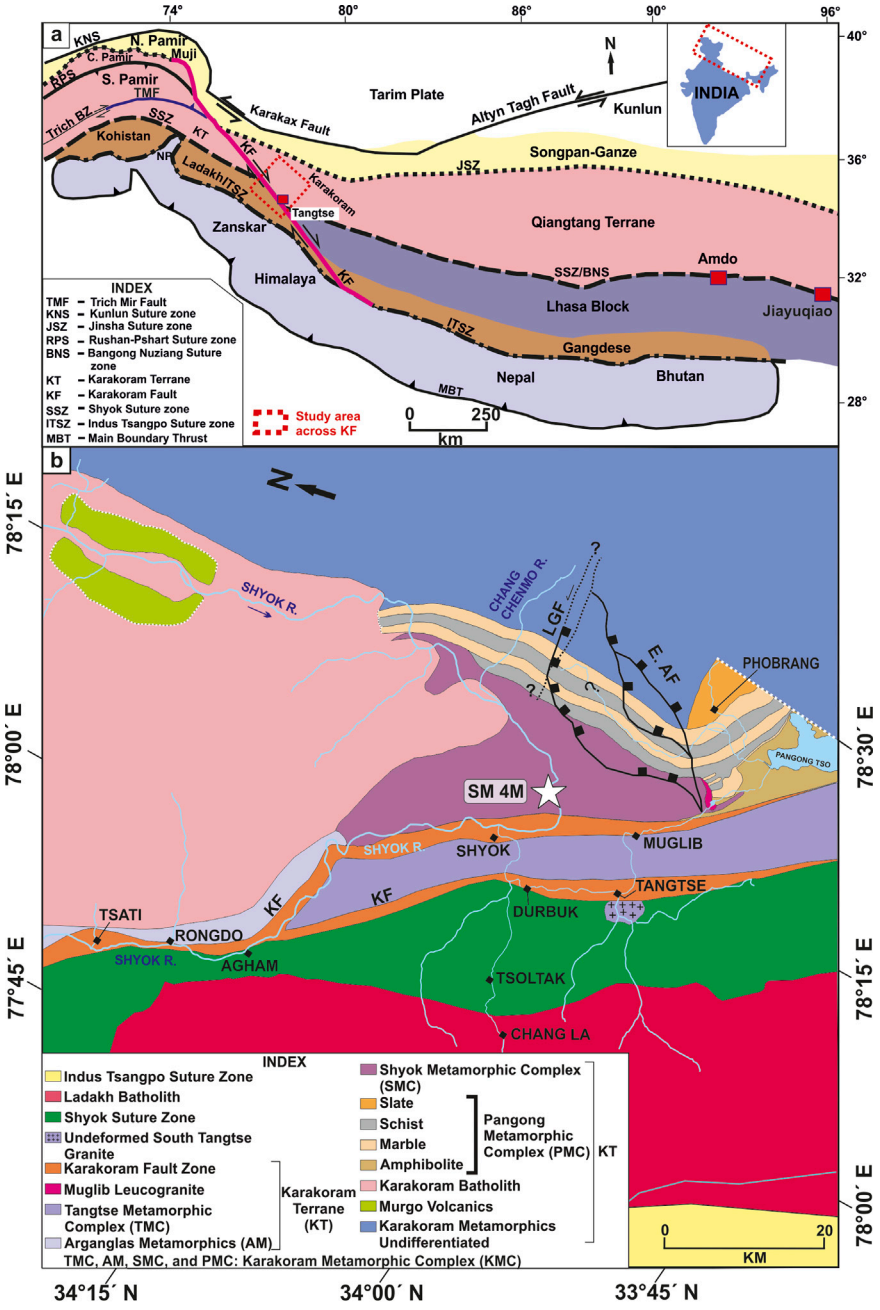

FIGURE 1
(A) Map showing the main tectonic structures and sutures in the Himalaya and Tibet (modified after Searle, 2011). The red dashed rectangle indicates the map area in Figure 1B. **(B)** Geological map of the study region (modified after Jain 2014; Pundir et al., 2020a). LGF: Longmu-Ghoza Co fault; E. AF: East Angmong Fault.

et al., 1998) (Figure 1A). In the SE Karakoram, the KF splays into two strands named the Tangtse strand in the SW and the Muglib strand in the NE, which forms a zone consisting of mylonite, granite gneiss, amphibolites, and leucogranites (e.g., Srimal, 1986; Searle et al., 1998; Weinberg and Mark, 2008). Locally, this zone is known as Tangtse Metamorphic Complex (TMC) or Pangong Injection Complex (PIC), and in the NW of Muglib strand, it is known as Shyok Metamorphic Complex (SMC) (Figure 1B; Searle et al., 1998; Pundir et al., 2020a). An undeformed porphyritic granite body of KB is exposed to the

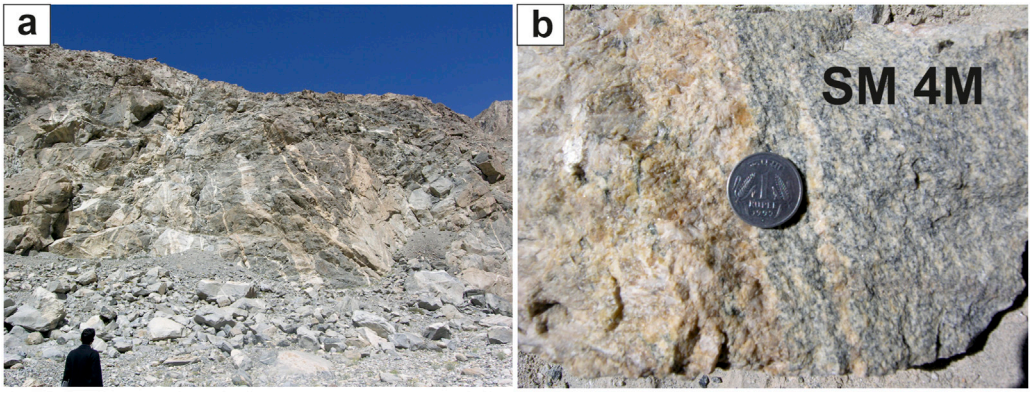

FIGURE 2
(A) High-grade metamorphic rocks and zone of partial melting observed to the north of the Shyok-Muglib strand of the KF known as SMC. **(B)** Collected sample of tonalite gneiss SM 4 M from the SMC zone of KB.

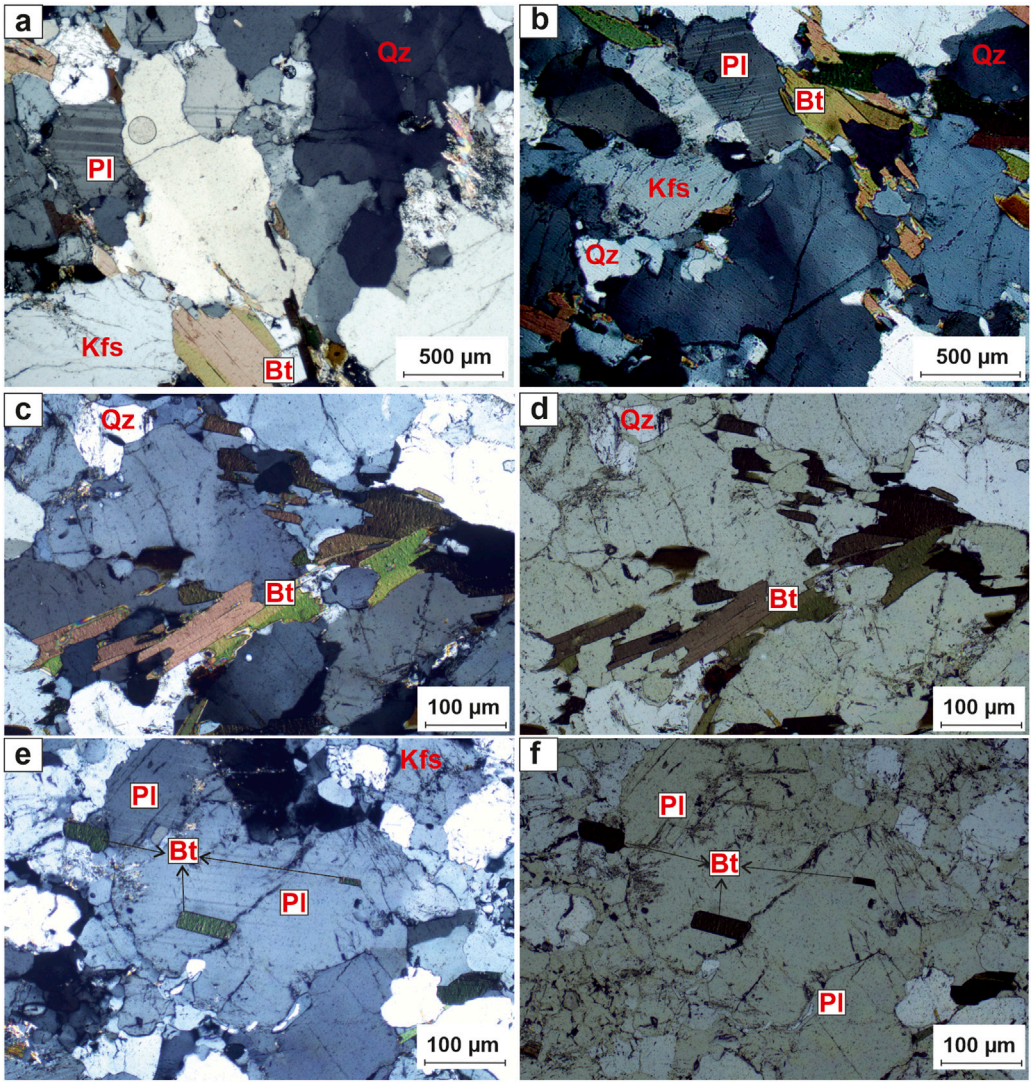

FIGURE 3
(A–F) Microphotograph of the tonalite gneiss SM 4 M mainly consists of quartz (Qz), K-feldspar (Kfs), plagioclase (Pl), and biotite (Bt).

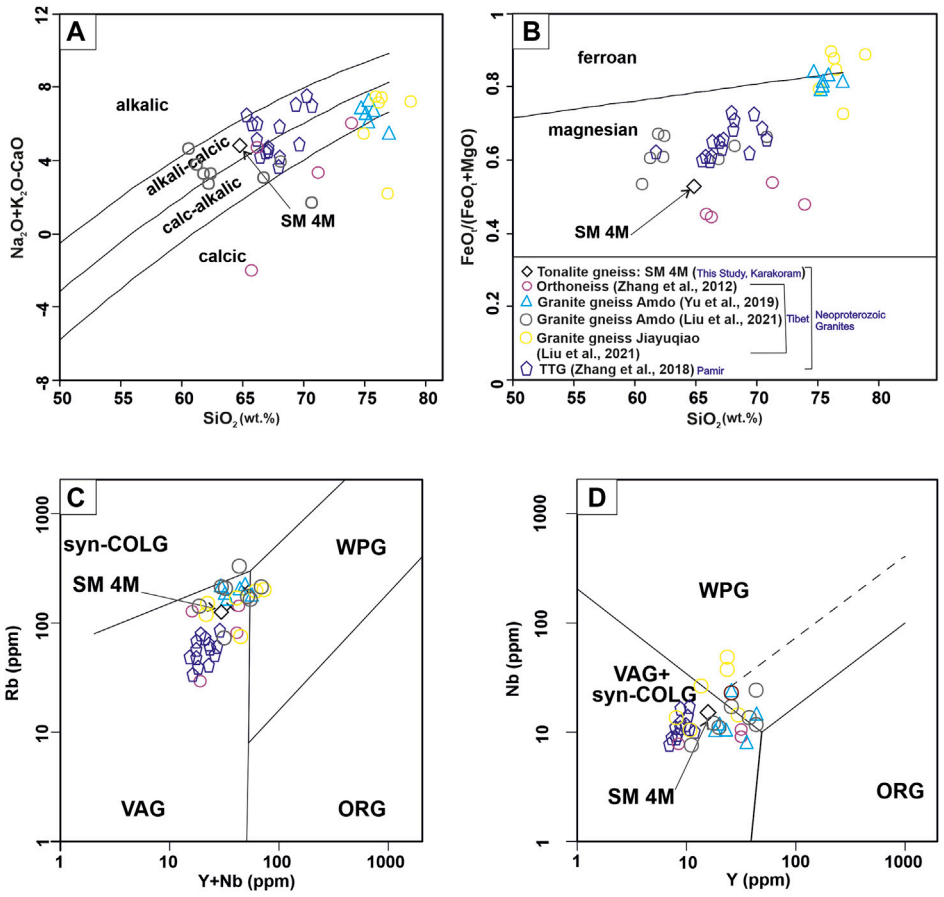

FIGURE 4
(A) Plot of Na_2O/K_2O-CaO against SiO_2 showing the approximate ranges for the alkalic, alkali–calcic, calc-alkalic, and calcic rock series (after Frost et al., 2001). **(B)** $FeO_t/(FeO_t/MgO)$ versus SiO_2 (wt%) diagram showing the boundary between ferroan plutons and magnesian plutons (after Frost et al., 2001). **(C)** Rb versus Y + Nb tectonic discrimination diagram (Pearce et al., 1984). **(D)** Nb versus Y tectonic discrimination diagram (Pearce et al., 1984), plotted to identify the tectonic setting of the analyzed samples.

north of KMC (Pundir et al., 2020a; Pundir et al., 2020b). The KB is mainly composed of hornblende-biotite and biotite bearing subduction-related magmatic rock suites, which are considered to be emplaced prior to the India-Asia collision (e.g., Jain and Singh, 2008), which later suffered submagmatic to solid state ductile deformation during Late-Cretaceous (Bose et al., 2022). The granites are porphyritic, consisting of randomly oriented ~2–5 cm long plagioclase and K-feldspar phenocrysts embedded in a fine-grained felsic groundmass (Pundir et al., 2020a). However, the TMC/PIC and SMC mainly consists of mylonite granite, foliation-parallel leucosome, i.e., deformed leucogranite as well as undeformed leucogranites, granite gneisses, amphibolites, bt-sammites and calc-silicate rocks (e.g., Reichardt et al., 2010; Boutonnet et al., 2012; Pundir et al., 2020a; Pundir et al., 2020b). In this study, the granite gneiss is exposed in the SMC (Figures 2A,B). This is biotite plagioclase bearing granitoid and is found in association with subduction-related Late-Jurassic Early- Cretaceous granitoids.

3 Sample selection and analytical methods

The sample of granite gneiss (SM 4 M) was collected from the SMC of the KT zone (Location: N 34.151128°; E 78.225104°) (Figure 1A and Figures 2A,B) and treated for whole-rock major and trace element analyses, and zircon U-Pb geochronology.

The whole-rock major and trace element compositions were analyzed using a wavelength dispersive X-Ray Fluorescence (Bruker Tiger S-8) on pressed-powder pellets at Wadia Institute of Himalayan Geology (WIHG), Dehradun, India. XRF technique analytical precision for both major and trace elements lie within ±2%–3% and ±5%–6%, respectively (Saini et al., 2007; Khanna, 2009). The rare Earth elements (REEs) were determined from the digested solution of rock powder using a Perkin-Elmer SCIEX-ICP Mass Spectrometer model ELAN-DRC-e. Rock standards (JG-2, GH, and MB-H) were used for calibration. The

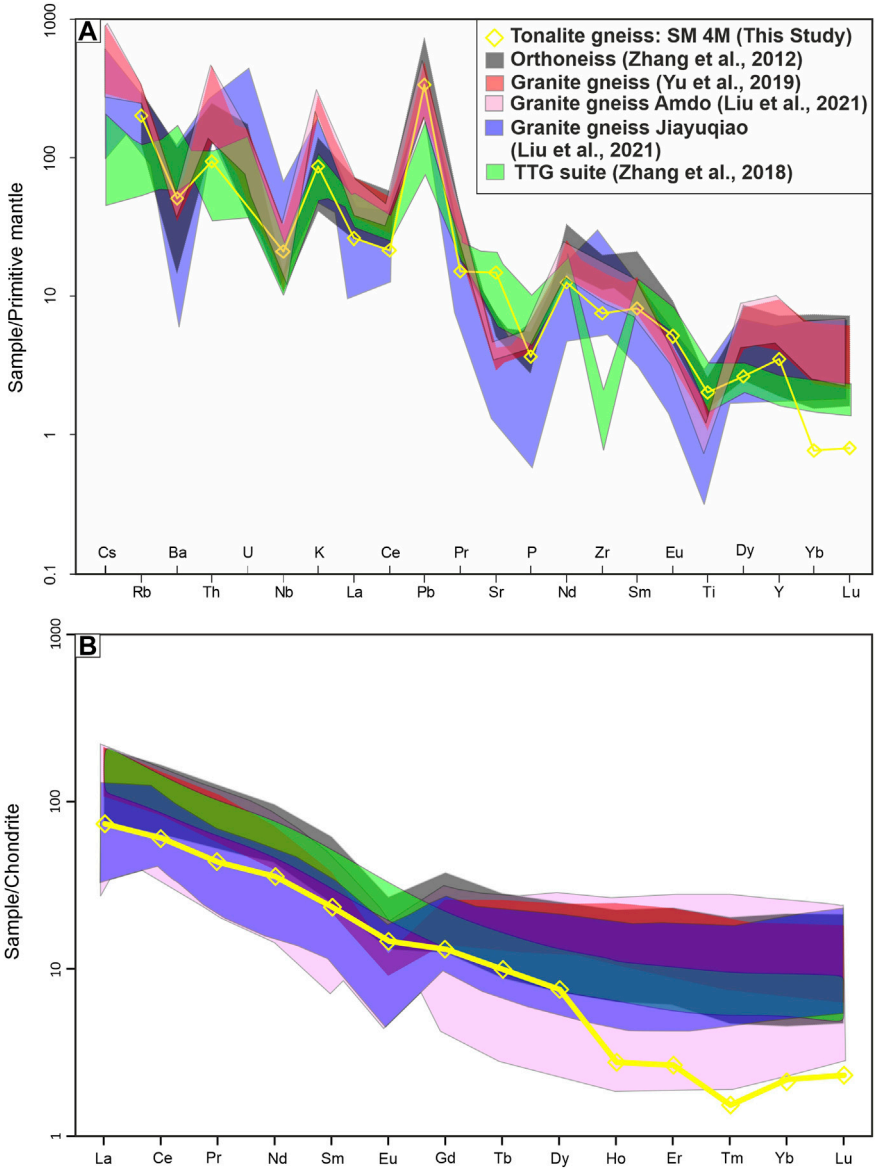

FIGURE 5
(A) Primitive mantle normalized spider diagram (after Sun and McDonough, 1989). **(B)** Chondrite-normalized REE patterns (after Sun and McDonough, 1989).

geochemical data processing and plotting were done using Geochemical Data Toolkit software (GCDkit, Janoušek et al., 2006).

Zircon U–Pb dating was performed using LA-MC-ICPMS (Neptune-plus, ThermoFisher Scientific Inc) fitted with a 193 nm excimer laser (UV Laser, Model Analyte G2, Cetec-Photon machine Inc.), equipped with high-performance HelEx-II sample chamber installed at WIHG, Dehradun. About 4 kg of the sample was crushed, powdered, and processed for zircon separation using jaw crusher, disk mill, gravity separation using Holman-Wilfley shaking table, magnetic separation using magnetic barrier separator, and heavy liquids separation using Bromoform ($CHBr_3$) and Diiodomethane (CH_2I_2). Euhedral to subhedral zircon grains were hand-picked up using a stereo zoom microscope, and zircons were mounted using PFA Teflon film at a temperature of ~275 °C. The internal zircon surfaces were exposed by means of 2400 grit sandpaper, and polished by 1- and 0.25-micron diamond paste. The zircon mounts were gold-coated for cathode-luminescence (CL) imaging using a Gatan Chroma CL UV attached to a Carl-Zeiss EVO 40 EP scanning electron microscope. The probe current varies from 10 to 20 nA. A zircon spot diameter of 20 μm was preferred to carry out U-Pb *in-situ* analysis. The standard 91500 zircon [(TIMS normalization

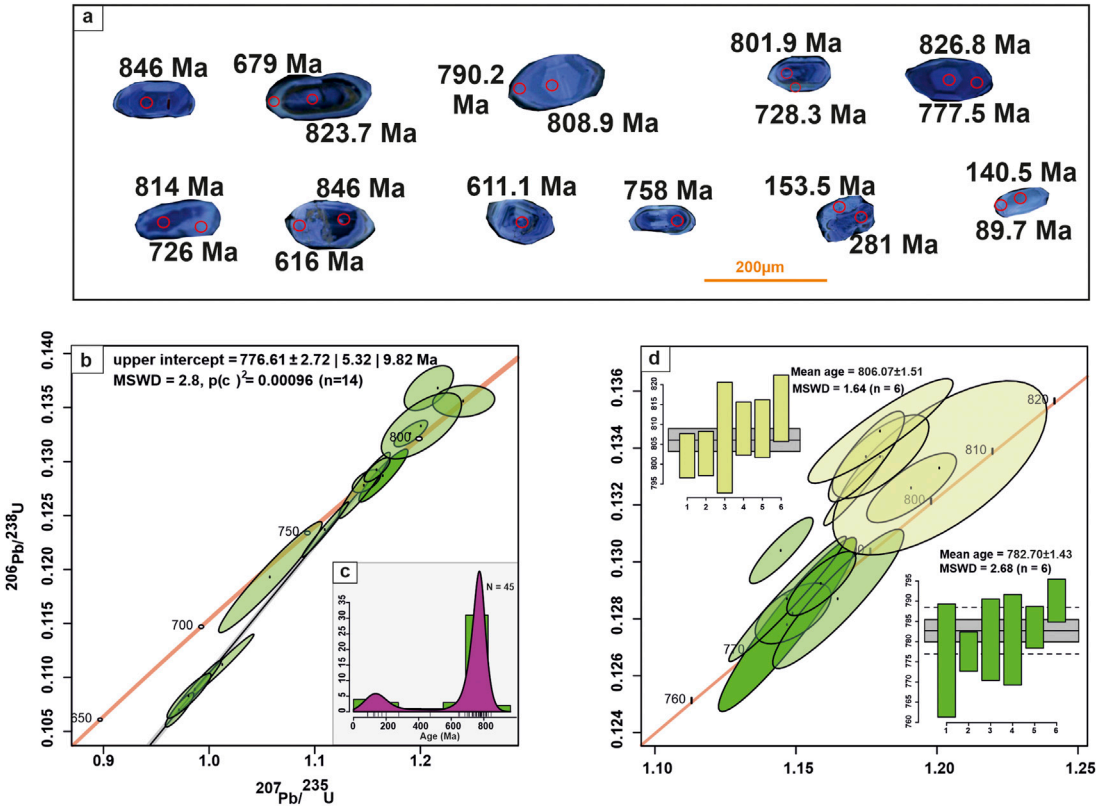

FIGURE 6
(A) Representative CL images of the studied tonalite gneiss, **(B)** $^{206}Pb-^{238}U$ ages and Concordia diagrams for LA-MC-ICP-MS zircon data plots, **(C)** Kernel density plot showing the distribution of $^{206}Pb-^{238}U$ ages. **(D)** Weighted mean ages for the most concordant $^{206}Pb-^{238}U$ ages.

data $^{206}Pb/^{238}U$ = 1062.32 ± 2.22 Ma; 2 sigma) (Wiedenbeck et al., 1995) and Plešovice zircon standard ID TIMS $^{206}Pb/^{238}U$ age = 337.13 ± 0.37 Ma (Sláma et al., 2008)] were used for correction of U-Pb downhole fractionation, accuracy assessment and data reduction (Paton et al., 2011), for detailed methodology see Mukherjee et al., 2017. Isoplot R was used for processing and plotting the U-Pb isotopic data (Vermeesch, 2018).

4 Petrography

The granite gneiss (SM 4 M) is a medium to coarse-grained rock mainly consisting of quartz (Qz), plagioclase (Pl), K-feldspar (Kfs), biotite (Bt), zircon (Zrn), and apatite (Ap) (mineral's symbols after Whitney and Evans, 2010) (Figure 3). Biotite is the only ferromagnesian phase present in the sample which are subhedral to euhedral mainly consisting of one set of basal cleavage showing its primary nature (Figures 3A–F). The quartz is showing slight undulose extinction and is devoid of any sub-solidus deformation e.g., sub-grain rotation and grain boundary migration. Plagioclase crystals are subhedral to euhedral and display polysynthetic twinning (Figures 3B,C). The K-feldspar is present in the form of orthoclase. As per the International Union of Geological Sciences (IUGS) recommended modal Q-A-P parameters (Supplementary Figure S1; Streckeisen 1976; Le Maitre 2002), the granite gneiss (SM 4 M) corresponds to tonalite.

5 Results

5.1 Whole-rock geochemistry, and zircon U–Pb geochronology results of the tonalite gneiss (SM 4 M)

Whole-rock major and trace-element geochemical data for the tonalite gneiss is given in Supplementary Table S1. The SiO_2 content of the tonalite gneiss is 64.85 wt% with 2.63 wt% K_2O and 4.65 wt% Na_2O. Molar A/CNK [Al_2O_3/($CaO+Na_2O+K_2O$=1.1)] ratio suggests a slightly peraluminous nature of the tonalite gneiss (Supplementary Table S1). The tonalite gneiss is alkali-calcic and magnesian in nature and belongs to the subduction-related volcanic arc granitoid (VAG), and VAG+syn-collisional granitoid (syn-COLG) fields (Figures 4A–D). The tonalite gneiss shows negative

TABLE 1 U-Pb LA-MC-ICPMS isotopic data of analyzed tonalite gneiss from Karakoram Terrane, NW India.

Spot	U (ppm)	Th (ppm)	Th/U	$^{207}Pb/^{235}U$	±%	$^{206}Pb/^{238}U$	±%	$^{207}Pb/^{235}U$ (Ma)	±Ma	$^{206}Pb/^{238}U$ (Ma)	±Ma
SM 4 M (tonalite gneiss)											
1_C	284	335	1.18	1.25	0.02	0.140	0.003	823	11	846	15
1_R	304	161.1	0.53	0.90	0.02	0.100	0.002	651.6	9.9	616	12
2_C	375	84.9	0.23	0.38	0.03	0.045	0.003	327	21	281	20
2_R	406	12.2	0.03	0.16	0.00	0.024	0.001	152.8	3.6	153.5	3.8
2_C	197	164	0.83	0.92	0.02	0.104	0.002	663.5	8.1	637	10
3_C	475	325	0.68	0.88	0.01	0.099	0.001	641	4.5	611.1	5
4_C	298	325	1.09	1.11	0.01	0.125	0.001	757.8	4.9	758	6.9
5_C	201	115	0.57	0.66	0.05	0.067	0.005	507	28	416	30
5_CR	172	133	0.77	1.30	0.02	0.140	0.002	846.9	9.8	846	13
5_CR2	169.6	157	0.93	1.15	0.02	0.128	0.003	775.5	9.7	775	14
6_C1	47.4	34.5	0.73	1.15	0.01	0.128	0.001	776.8	5.1	777.5	5
6_C2	39.9	32.5	0.81	1.21	0.02	0.137	0.002	804.2	8.8	826.8	9.5
6_CR	40.8	25.1	0.62	1.18	0.01	0.134	0.001	791.2	6.5	808.8	6.6
7_C	296	288	0.97	1.20	0.03	0.133	0.003	805	13	806	14
8_C	120.5	135.6	1.13	1.18	0.01	0.134	0.001	788.7	5.3	808.9	7.2
8_CR	164.9	169.1	1.03	1.14	0.01	0.130	0.001	774.7	4.4	790.2	5.4
9_C	430	350	0.81	1.17	0.01	0.133	0.001	786.7	4	801.9	5.9
9_R	313	344	1.10	1.06	0.01	0.120	0.001	731.6	3.2	728.3	4.6
10_C1	117.6	64.7	0.55	1.06	0.04	0.119	0.004	730	20	726	24
10_C2	107.6	58.2	0.54	1.18	0.02	0.135	0.002	791.1	9.9	814	8.7
11_R1	620	2.44	0.00	0.09	0.00	0.014	0.000	88.1	2.6	89.7	2.6
11_C2	352	15	0.04	0.16	0.01	0.022	0.001	149.8	4.7	140.5	4.1
11_R2	524	3.11	0.01	0.09	0.00	0.014	0.000	86.49	0.96	87.52	0.65
12_C	628	760	1.21	0.88	0.01	0.097	0.002	641.5	7.2	595.9	9.8
12_R	466	38.43	0.08	0.13	0.00	0.019	0.000	125.2	2.3	123.6	1.9
13_R	224	63.5	0.28	0.44	0.01	0.049	0.002	370	11	306.7	9.5
13_C	186.3	150	0.81	1.19	0.01	0.133	0.001	796.1	6.2	802.6	5.7
14_C1	181	110	0.61	1.03	0.05	0.116	0.005	717	23	705	30
14_C2	200	152	0.76	1.15	0.02	0.129	0.002	775.4	8	780	10
15_C	353	381	1.08	1.04	0.01	0.117	0.001	724.7	4.4	712.2	5.3
15_R	109.7	41.25	0.38	0.98	0.02	0.108	0.002	694.1	8.8	662.7	9.8
16_C1	284	236	0.83	1.11	0.02	0.124	0.002	759.3	9	752	12
16C2	49	28.2	0.58	1.24	0.02	0.136	0.001	819	10	819.4	6.9
17_C	234.4	230.1	0.98	1.06	0.01	0.116	0.001	733.2	6.4	709.2	7.8
17_R	314.1	29.2	0.09	0.19	0.00	0.028	0.000	176.3	2.8	175.6	2.1
18_C	76.8	72.4	0.94	1.09	0.02	0.116	0.002	746	9.6	707	10
18_C2	172	46.1	0.27	1.13	0.02	0.121	0.002	769.4	7.1	738	9.2
19_C	142	54.4	0.38	1.27	0.02	0.136	0.002	830.3	8.6	823.7	9.7
19_R	233	79.5	0.34	1.01	0.02	0.111	0.002	710	12	679	13
20_C	262	213	0.81	1.17	0.02	0.129	0.002	783.8	8.8	781	11
20_C2	123.3	110.2	0.89	1.16	0.01	0.129	0.001	781.6	4.7	783.5	5.3
21_C	228	158.7	0.70	0.99	0.02	0.109	0.002	698	11	666	13
21_C2	263	154	0.59	1.13	0.02	0.118	0.001	767	11	716.7	6.6
22_C	196.8	152.5	0.77	0.83	0.01	0.094	0.002	616.8	7.1	579	9.1
22_C2	206.7	174	0.84	0.97	0.01	0.107	0.001	689.2	5.6	655.2	7.6

anomalies for Nb and Ti (Figure 5A), along with light REEs (LREEs) enrichment relative to heavy REEs (HREEs) (La_N/Yb_N = 33.99; Ce_N/Yb_N = 27.76) (Figure 5B).

Zircon grains from tonalite gneiss are long prismatic and euhedral to subhedral in shape (Figure 6A). The CL images shows the oscillatory growth zoning in the cores while the rims are mostly homogeneous in nature (Figure 6A). Forty-five spot analyses were carried out on 22 zircon grains. Rims with Late Jurassic-Early Cretaceous have low Th/U values of 0.004–0.093, typical of metamorphic origin (e.g., Rubatto 2002) (Table 1). In contrast, the zircon cores from Neoproterozoic ages have high Th/U values of 0.27–1.21 typical of magmatic origin (Table 1). The Late Jurassic-Early Cretaceous zones in zircons are homogenous indicating late-stage recrystallization, while the older Late-Neoproterozoic zircons preserves oscillatory zoning (Figure 6). The oscillatory zoned cores along with high Th/U ratios suggest that the zircons are crystallized from silicate melts, and the obtained ages from these can be considered as crystallization age. There are four rims of Late-Neoproterozoic age which have high Th/U ratio and are discordant. Considering these ages geologically insignificant, we have not considered these points in our weighted mean age calculations. We use the ±3% discordant filter to get the geologically meaningful age. The cluster of data we have considered in age calculation are concordant and is used in weighted mean age calculations.

The zircon grains yielded $^{206}Pb/^{238}U$ ages ranging from ~700 to 846 (n=29) Ma with major magmatic pulses between ~700 and 809 Ma (n=21) (Figures 6B,C). Fourteen analyses provide an upper intercept age of 776.61 ± 2.72 with a MSWD = 2.8 (Figures 6B,C). The sample bears two different ^{206}Pb-^{238}U age groups; one with weighted mean age of 806.07 ± 1.51 Ma (MSWD = 1.64; n = 6) which we consider as the zircon crystallization age in the tonalite gneiss whereas another age group with weighted mean age of 782.70 ± 1.43 Ma (MSWD = 2.68; n = 6; inset of Figure 6D). These two mean ages represent two closely related felsic magmatic pulses at a short time interval.

6 Discussion

6.1 Source characterization and likely tectonic setting of neoproterozoic magmatism in the KT

The studied tonalite gneiss sample is intermediate in composition with SiO_2=64.85 wt%, and MgO=2.88 wt% and is slightly peraluminous in nature with A/CNK values of 1.1. The high Sr/Y ratio=19.75, La_N/Yb_N=33.99 ratio point to its similarity with the adakitic rocks (Defant et al., 2002). The Chondrite-normalized spidergram (Figure 5B) shows a steeply inclined REE pattern (high LREE/HREE ratios) similar to the Neoproterozoic granites of Tibet, and TTG suite (800 Ma) of southern Pamir (e.g., Zhang et al., 2018). The observed features suggest a mafic lower crustal source (e.g., granulite-facies) for the tonalite gneiss. We compared the tonalite gneiss with the granites of similar age from the adjacent terranes of central Tibet to assess their comparative petrogenesis and likely tectonic setting (Table 2; Figure 4). These Neoproterozoic granites are magnesian, calcic to alkali calcic in nature and show affinity with VAG (Figure 4) and follow the calc-alkaline trend (Figure 4). Hence, they bear geochemical features similar to granites formed in the subduction-related tectonic regimes.

6.2 A viable petrogenetic model linking the neoproterozoic magmatism in the KT, Southern Pamir, and Central Tibet

The qualitative analysis of whole-rock elemental data demonstrates that the tonalite gneiss (SiO_2=64.85, MgO=2.88wt%, with High LREE/HREE and Sr/Y ratio), might have formed through the melting of a mafic lower crust as noted for the Neoproterozoic TTG suite of the southern Pamir (Zhang et al., 2018), and for fractionated granitoid suite from the Central Tibet (e.g., Amdo and Jiayuqiao) (e.g., Liu et al., 2021). It is therefore imperative to test the hypothesis quantitatively using trace and REE modeling of mafic lower crustal composition (Weaver and Tarney, 1980), which probably formed the Neoproterozoic granitoid of these terranes. In the present study the analyzed sample is from the metamorphic terrane, therefore it is important to decipher the any metamorphic and other alteration effects on the sample. The petrographic features of the tonalite gneiss e.g., 1) primary euhedral crystals of biotite having cleavage in the basal section 2) the absence of sub-solidus deformation in the quartz grains e.g., sub-grain rotation and grain boundary migration etc. suggest that the rock preserved the magmatic texture and has not suffered any alteration and high-grade metamorphism. There are no evidences in this sample for alteration of biotite to chlorite. Any low-grade metamorphism only can affect the alkali element concentrations (e.g., K and Na) and LILE concentrations (e.g., Rb, Ba, Sr, Pb, and Cs). In contrast, these low-grade metamorphic activities have negligible impact on the abundances of immobile elements (e.g., Hu et al., 2018a), therefore, we carried out the REEs modeling in our study.

The melts with a high Sr/Y ratio can be generated at a depth of ~>30–40 km (>1.2 GPa) where garnet remains stable with residues of garnet-amphibolite, or eclogite and plagioclase remain unstable (Petford and Gallagher, 2001). The mineral modes (Gt=0.30, Amp=0.10, Cpx=0.20) of a mafic source for

TABLE 2 Compiled Sr-Nd and $\varepsilon Hf_{(i)}$ isotope data from Early-Neoproterozoic magmatic rocks from Northern Lhasa, Qiangtang terrane, Pamir and KT.

	Northern Lhasa (Central Tibet)	Amdo & Jiayuqiao Microcontinent Qiangtang terrane (Central Tibet)	Pamir Plateau	Karakoram Terrane (This Study)
Age (Ma)	856 to ~748	920-767	840-835	800
I_{Sr}	0.708 to 0.711	–	**Tonalite, Trondhjemite:** 0.705572-0.708341 **Granodiorite:** 0.700794-701938	–
$\varepsilon Nd_{(t)}$	−2.4 to +10.4	–	**Tonalite, Trondhjemite:** -9.71 to -8.23 **Granodiorite:** -4.43 to -5.45	–
$\varepsilon Hf_{(t)}$	-2 to +12.4	-8.9 to +4.0	**Tonalite, Trondhjemite:** -14 to -10 **Granodiorite:** -10 to -7	–
Inferences	Derivation from the depleted mantle (juvenile) with the older continental crustal component assimilation (arc and back-arc type)	**Protolith derived from partial melting of ancient crustal source**	**TTG suite derivation from partial melting of a mafic lower crust (≥30) km with a garnet amphibolite residue and granodiorite derivation from partial melting of a mafic crust at a shallower level**	**Derivation from partial melting of a lower crust where garnet remained residue during partial melting**
References	Hu et al. (2005); Dong et al. (2011); Hu et al. (2018a); Hu et al. (2018b)	Liu et al. (2021); Guynn et al. (2012); Yu et al. (2021); Zhang et al. (2012)	Zhang et al. (2018)	**This Study**

TABLE 3 Trace and rare Earth elements (REEs) modeling results for the studied tonalite gneiss (SM 4 M), TTGs of the South Pamir terrane, and Central Tibet.

	Parent (Lower crust, Weaver and Tarney, (1980))	Observed results (SM 4 M (This Study)	Calculated Partial Melting results (F=0.5)	Observed results (Average of TTGs, Zhang et al. (2018), Southern Pamir)	Calculated FC results (F=0.58)(Average of TTGs	Observed results (Average of Granitoids Liu et al. (2021); Yu et al. (2021)Central Tibet)	Calculated FC results (F=0.53)
La	9.5	18.01	18.40	28.12	28.70	30.33	30.90
Ce	17	37.98	31.89	51.67	53.82	64.71	57.42
Pr	2	4.23	3.71	5.80	6.40	6.77	7.00
Nd	8	17.11	13.02	20.91	21.51	23.33	23.38
Sm	2.75	3.67	2.96	4.69	4.86	4.42	5.27
Eu	1.1	0.87	0.98	1.15	1.15	0.71	1.18
Gd	3.95	2.76	2.22	2.86	3.73	4.00	4.06
Tb	0.58	0.38	---	0.35	---	0.62	----
Dy	3.35	1.96	1.59	1.82	2.57	3.85	2.78
Ho	0.73	0.16	---	0.35	---	0.81	----
Er	2	0.45	1.11	0.94	1.86	2.30	2.02
Tm	0.35	0.04	---	0.14	---	0.34	----
Yb	1.9	0.38	0.66	0.90	1.10	2.20	1.20
Lu	0.3	0.06	0.12	0.13	0.20	0.32	0.21

Note: For less fractionated SM, 4 M (SiO2=64.85, MgO=2.88wt%) the parent is Lower crust (Weaver and Tarney, 1980), while the calculated partial melting results at (F=0.5) were used as the parent for the highly fractionated TTGs (SiO2=67 wt%; MgO=1.61; Zhang et al., 2018) and Granitoids (SiO2=71.38 wt%; MgO=1.30; Liu et al., 2021; Yu et al., 2021).

the partial melting model were therefore chosen reasonably at ~900°C and at ~12–15 kbar (Qian and Hermann, 2013). The mineral/liquid partition coefficients (Kds) were taken from Qian and Hermann. (2013), Rollinson. (1993), and from GERM Partition Coefficient (Kds) Database as given in Supplementary Table S2.

The equilibrium batch melting was performed using the equation (Schilling and Winchester, 1967):

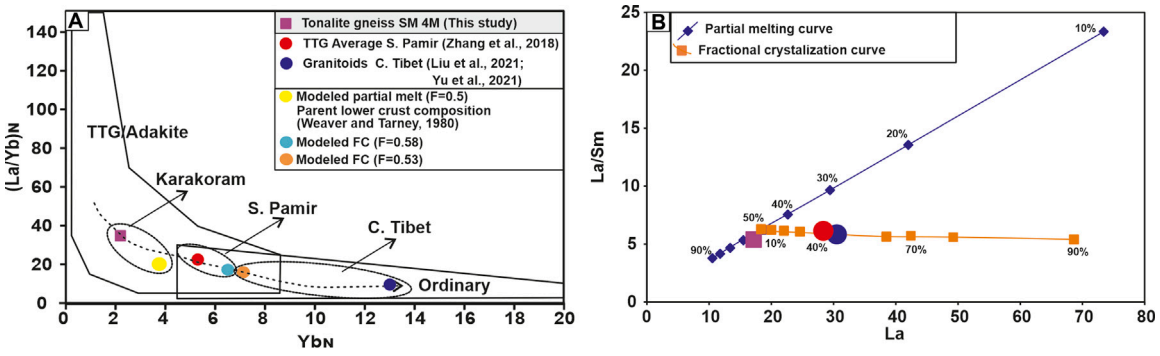

FIGURE 7
Calculated trends obtained from geochemical modeling of partial melting (PM) of a mafic lower crust (Weaver and Tarney, 1980), and fractional crystallization (FC) of the melt produced (50%) shown in terms of: **(A)** $(La/Yb)_N$ versus Yb_N **(B)** La/Sm versus La.

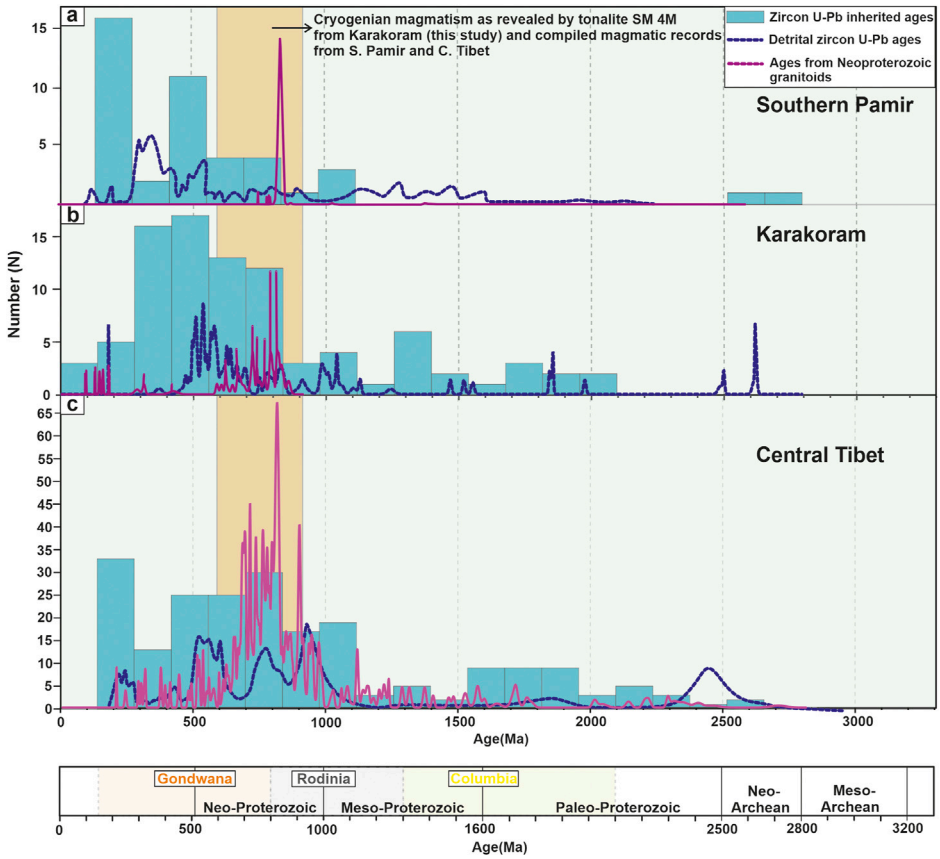

FIGURE 8
Probability density plot for the inherited zircon ages from the Triassic to Miocene granitoid, U–Pb detrital ages, and Neoproterozoic U–Pb ages from **(A)** the Karakoram, **(B)** Southern Pamir, and **(C)** Central Tibet (Data source-Karakoram: Boutonnet et al., 2012; Fraser et al., 2001; Heuberger et al., 2007; Kumar et al., 2017; Parrish and Tirrul, 1989; Pundir et al., 2020a; Pundir et al., 2020b; Ravikant et al., 2009; Schwab et al., 2004; Searle et al., 1998; Sen et al., 2014; Van buer et al., 2015; Weinberg et al., 2000; Southern Pamir: Chapman et al., 2018; Liu et al., 2020; Schwab et al., 2004; Central Tibet: Hao et al., 2016; Ou et al., 2017; Schwab et al., 2004; Sui et al., 2013; Wang et al., 2020; Wu et al., 2016; Zhai et al., 2013). Density plots of U–Pb detrital ages are taken from previous studies. Tibet: Gehrels et al., 2011; He et al., 2019; Song et al., 2017; Pamir: Chapman et al., 2018; Karakoram: Borneman et al., 2015. Density plots of Neoproterozoic U–Pb ages. Data Source: Tibet: Hu et al., 2005; Dong et al., 2011; Liu et al., 2021; Yu et al., 2021 (n=290), Karakoram: This study (n=45), Pamir: Zhang et al., 2018 (*n*=199).

$$\frac{C_l}{C_0} = \frac{1}{F + D - FD} \quad (1)$$

where, C_L and C_0 are the concentrations of an element in the melt and source respectively, F is the weight fraction of melt, and D is the bulk distribution coefficient.

For fractional crystallization we used the Rayleigh fractionation equation (Rayleigh, 1896):

$$\frac{C_l}{C_0} = F^{D-1} \quad (2)$$

where, C_L and C_0 are the concentrations of an element in the residual melt and parent magma respectively, F is the weight fraction of residual melt, and D is the bulk distribution coefficient. We consider the proportions (Bt=0.20, Plg=0.45, Kfs=0.05, Qz=0.30) of mineral mode present in the studied tonalite gneiss as fractionating phases.

The calculated results are summarized in Table 3 and trends of partial melting and fractional crystallization are shown on $(La/Yb)_N$ vs. Yb_N (Martin, 1986) (Figure 7A) on La/Sm vs. La (Figure 7B). The calculated results suggest that about 50% melting of a mafic lower crustal source can generate a composition similar to the tonalite gneiss SM 4 M (SiO_2=64.85, MgO=2.88wt%). Further fractional crystallization (FC) (~42%) of generated melt can produce rock members similar to the Tonalite–trondhjemite suite (SiO_2=67 wt%; MgO=1.61: average of Zhang et al., 2018 geochemical data) from the Southern Pamir, and about 47% FC can produce rock members similar to the granitoid suite (SiO_2=71.4 wt%; MgO=1.3; average of Liu et al., 2021; Yu et al., 2021) from the Central Tibet (Table 3). The generation of the SM 4 M at a high degree of partial melting (40%–60%) also supports its affinity toward the tonalitic nature of the melt (Arndt, 2013). It is therefore likely that melt similar to the low SiO_2 and high MgO tonalite gneiss SM 4 M served as parental magma which evolved through fractional differentiation forming the high SiO_2 and low MgO rock members of the TTG suites of southern Pamir and granitoid from Central Tibet. Based on geochemical and zircon Lu-Hf isotope data Liu et al., 2021 also suggested that the granodiorites and tonalites as the protolith of the central Tibet granitic gneisses. However, the likely genetic connotation between KT tonalite gneiss and rocks of TTG from Pamir needs to be tested further using a large database.

6.3 Pamir-karakoram-Tibet as fragments of rodinia supercontinent

We compile zircon U-Pb inherited ages from the Triassic to Miocene granitoid and detrital zircon U-Pb geochronological records from southern Pamir, Karakoram, and central Tibet, and compare them with Neoproterozoic magmatism of these terranes to decipher the geological magmatic history of these blocks during the Rodinia supercontinent cycle (Figure 8). The data compilation suggests that the terranes witnessed intense magmatism during Neoproterozoic and Cambrian times (Figure 8). We also compile the Sr-Nd and zircon Lu-Hf isotope values of the granitoids of ~920–748 Ma from these terranes to assess their comparative petrogenesis and the likely source of their formation (Table 2). The negative to positive $\varepsilon Nd_{(t)}$ and $\varepsilon Hf_{(t)}$ isotope values from the Early-Middle Neoproterozoic sedimentary deposits, as well as bedrock granite gneisses from Tibet along with high $(^{87}Sr/^{86}Sr)_I$ values of 0.708–0.711 (Table 2), suggest the origin of the granitoids from depleted mantle with the older continental crustal component assimilation (Table 2; Yu et al., 2021). However, the Neoproterozoic (857–767 Ma) granite gneiss from the Amdo & Jiayuqiao microcontinents from the Qiangtang terrane, Central Tibet have highly negative to positive values (−8.9 to 4.0), and geochemically the granite gneiss bears calc-alkaline nature, with the protolith derived from partial melting of ancient crustal source (e.g., tonalites and granodiorites) (Table 2; Liu et a., 2021). Similarly, the middle Neoproterozoic (~840 Ma) TTG suite from the central Pamir also have $\varepsilon Nd_{(i)}$ (−14 to −10) and zircon $\varepsilon Hf_{(i)}$ (−9.5 to −8.7) and geochemically the granitoids belong to TTG/adakites suites having enriched LILE, and LREEs as compared to HFSEs and HREEs with high Sr/Y and $(La/Yb)_N$ ratios suggesting its origin from partial melting of a mafic lower crust (Zhang et al., 2018). Our observed geochemical results from the present study also suggest that the tonalite gneiss (SM 4 M) from the eastern Karakoram melt might have derived from partial melting of the mafic lower continental crust (Figure 5B). Therefore, we argue that these continents might have experienced a similar geotectonic evolution during Neoproterozoic time. Considering limitations of interpretation based on only one sample of tonalite gneiss, it cannot be argued firmly the exact position of the KT within the Rodinia supercontinent but the theory of plate tectonics suggests that no rock is accidental (Fichter and Whitmeyer, 2019). The reason we got only one tonalite sample of Cryogenian age in this zone might be that partial migmatization have annealed and recrystallized the zircons of the Late Neo-Proterozoic terrane. Therefore, we argue that this sample bears significance in the Rodinia supercontinent reconstruction. Based on identical geochemical and geochronological records from the Karakoram and south-central Pamir, we propose the Karakoram, south-central Pamir and central Tibet microcontinents as a single continental block during Neoproterozoic. The Late Jurassic-Early Cretaceous rims from the zircons are homogenous indicating the tonalite gneiss have recorded thermal imprints during the subduction of Neo-Tethys Oceanic lithosphere along the Eurasian Plate margin.

7 Conclusions

The elemental data suggest that the studied tonalite gneiss is more likely sourced from the mafic lower crust where garnet remained in the residue. Petrogenetic modeling suggests that the parental melt similar to the tonalite gneiss can be generated by ~50% partial melting of the mafic lower crust which might have served as the parent to the TTGs and the more evolved granitoid suite from the Southern Pamir and Central Tibet during Neoproterozoic. The middle-Neoproterozoic tonalite gneiss, recorded for the first time from the KT, suggests Karakoram, south-central Pamir and central Tibet microcontinents as a single continental block during Neoproterozoic.

Data availability statement

The original contributions presented in the study are included in the article/Supplementary Material, further inquiries can be directed to the corresponding author.

Author contributions

SP wrote the manuscript with inputs from VA and SK. VA acquired funding for the research and did project administration. SS and SD produced the zircon U-Pb geochronological results.

Funding

This work was supported by Science and Engineering Research Board grant EMR/2014/000555 and Activity 7 of the WIHG CAP Himalaya awarded to VA.

Acknowledgments

Director, Wadia Institute of Himalayan Geology, Dehradun, is thanked for motivation and generous support during the research work. Manoranjan Mohanty and Rajwant, Department of Science and Technology (DST) and Science and Engineering Research Board (SERB), New Delhi, are thanked for their continuous support and encouragement. Naresh Kumar Juyal helped during CL imaging, and Chandra Shekhar helped while ICPMS and XRF analyses. Chhutapa Phuntsog Dorjay, Skalzang Namgyal, and Thinless Gyachho are thanked for field assistance. The Indo-Tibetan Border Police is highly acknowledged for help during fieldwork in Ladakh, NW India.

Conflict of interest

The authors declare that the research was conducted in the absence of any commercial or financial relationships that could be construed as a potential conflict of interest.

Publisher's note

Supplementary material

The Supplementary Material for this article can be found online at: https://www.frontiersin.org/articles/10.3389/feart.2022.1027801/full#supplementary-material

References

Arndt, N. T. (2013). Formation and evolution of the continental crust. *Geochem. Perspect.* 2 (3), 405–533. doi:10.7185/geochempersp.2.3

Borneman, N. L., Hodges, K. V., Van Soest, M. C., Bohon, W., Wartho, J. A., Cronk, S. S., et al. (2015). Age and structure of the Shyok suture in the Ladakh region of northwestern India: Implications for slip on the Karakoram fault system. *Tectonics* 34 (10), 2011–2033. doi:10.1002/2015TC003933

Bose, S., Adlakha, V., and Pundir, S. (2022). Submagmatic flow to solid-state ductile deformation of the Karakoram Batholith, India: Insights into syn-tectonic cooling and exhumation. *Int. J. Earth Sci.* 1-16, 2337–2352. doi:10.1007/s00531-022-02236-8

Boutonnet, E., Leloup, P. H., Arnaud, N., Paquette, J. L., Davis, W. J., and Hattori, K. (2012). Synkinematic magmatism, heterogeneous deformation, and progressive strain localization in a strike-slip shear zone: The case of the right-lateral Karakorum fault. *Tectonics* 31 (4), 3049. doi:10.1029/2011TC003049

Cawood, P. A., Strachan, R. A., Pisarevsky, S. A., Gladkochub, D. P., and Murphy, J. B. (2016). Linking collisional and accretionary orogens during Rodinia assembly and breakup: Implications for models of supercontinent cycles. *Earth Planet. Sci. Lett.* 449, 118–126. doi:10.1016/j.epsl.2016.05.049

Cawood, P. A., Wang, Y., Xu, Y., and Zhao, G. (2013). Locating South China in Rodinia and gondwana: A fragment of greater India lithosphere? *Geology* 41 (8), 903–906. doi:10.1130/G34395.1

Chapman, J. B., Scoggin, S. H., Kapp, P., Carrapa, B., Ducea, M. N., Worthington, J., et al. (2018). Mesozoic to cenozoic magmatic history of the Pamir. *Earth Planet. Sci. Lett.* 482, 181–192. doi:10.1016/j.epsl.2017.10.041

Condie, K. C. (2001). Continental growth during formation of Rodinia at 1.35-0.9 Ga. *Gondwana Res.* 4, 5–16. doi:10.1016/s1342-937x(05)70650-x

Crawford, A. R. (1974). The indus suture line, the Himalaya, Tibet and Gondwanaland. *Geol. Mag.* 111 (5), 369–383. doi:10.1017/S0016756800039935

Dan, W., Wang, Q., Zhang, X. Z., and Tang, G. J. (2020). Early paleozoic S-type granites as the basement of southern qiantang terrane, Tibet. *Lithos* 356, 105395. doi:10.1016/j.lithos.2020.105395

Defant, M. J., Xu, J. F., Kepezhinskas, P., Wang, Q., Zhang, Q., and Xiao, L. (2002). Adakites: Some variations on a theme. *Acta Pet. Sin.* 18, 129–142.

Dong, X., Zhang, Z., Santosh, M., Wang, W., Yu, F., and Liu, F. (2011). Late Neoproterozoic thermal events in the northern Lhasa terrane, south Tibet: Zircon

chronology and tectonic implications. *J. Geodyn.* 52 (5), 389–405. doi:10.1016/j.jog.2011.05.002

Fichter, L. S., and Whitmeyer, S. J. (2019). No rock is accidental! Stratigraphy, structure, and tectonics in the wilson cycle. *Dev. Struct. Geol. Tect.* 5, 145–160. doi:10.1016/b978-0-12-814048-2.00012-0

Fort, P. L., Tongiorgi, M., and Gaetani, M. (1994). Discovery of a crystalline basement and Early Ordovician marine transgression in the Karakorum mountain range, Pakistan. *Geol.* 22 (10), 941–944. doi:10.1130/0091-7613(1994)022<0941:doacba>2.3.co;2

Fraser, J. E., Searle, M. P., Parrish, R. R., and Noble, S. R. (2001). Chronology of deformation, metamorphism, and magmatism in the southern Karakoram Mountains. *Geol. Soc. Am. Bull.* 113 (11), 1443–1455. doi:10.1130/0016-7606(2001)113<1443:codmam>2.0.co;2

Frost, B. R., Barnes, C. G., Collins, W. J., Arculus, R. J., Ellis, D. J., and Frost, C. D. (2001). A geochemical classification for granitic rocks. *J. Petrology* 42 (11), 2033–2048. doi:10.1093/petrology/42.11.2033

Gehrels, G., Kapp, P., DeCelles, P., Pullen, A., Blakey, R., Weislogel, A., et al. (2011). Detrital zircon geochronology of pre-Tertiary strata in the Tibetan-Himalayan orogen. *Tectonics* 30 (5). doi:10.1029/2011TC002868

Guynn, J., Kapp, P., Gehrels, G. E., and Ding, L. (2012). U–Pb geochronology of basement rocks in central Tibet and paleogeographic implications. *J. Asian Earth Sci.* 43 (1), 23–50. doi:10.1016/j.jseaes.2011.09.003

Hao, L. L., Wang, Q., Wyman, D. A., Ou, Q., Dan, W., Jiang, Z. Q., et al. (2016). Underplating of basaltic magmas and crustal growth in a continental arc: Evidence from Late Mesozoic intermediate–felsic intrusive rocks in southern Qiangtang, central Tibet. *Lithos* 245, 223–242. doi:10.1016/j.lithos.2015.09.015

He, J., Kapp, P., Chapman, J. B., DeCelles, P. G., and Carrapa, B. (2019). A history of the Asian monsoon and its interactions with solid Earth tectonics in Cenozoic South Asia. *Geol. Soc. Spec. Publ.* 483 (1), 631–652. doi:10.1144/SP483.1

Heuberger, S., Schaltegger, U., Burg, J. P., Villa, I. M., Frank, M., Dawood, H., et al. (2007). Age and isotopic constraints on magmatism along the karakoram-kohistan suture zone, NW Pakistan: Evidence for subduction and continued convergence after India-asia collision. *Swiss J. geosci.* 100 (1), 85–107. doi:10.1007/s00015-007-1203-7

Hu, D., Wu, Z., Jiang, W., Shi, Y., Ye, P., and Liu, Q. (2005). SHRIMP zircon U-Pb age and Nd isotopic study on the Nyainqêntanglha Group in Tibet. *Sci. China Ser. D-Earth. Sci.* 48 (9), 1377–1386. doi:10.1360/04yd0183

Hu, P. Y., Zhai, Q. G., Wang, J., Tang, Y., Wang, H. T., and Hou, K. J. (2018a). Precambrian origin of the north Lhasa terrane, Tibetan plateau: Constraint from early cryogenian back-arc magmatism. *Precambrian Res.* 313, 51–67. doi:10.1016/j.precamres.2018.05.014

Hu, P. Y., Zhai, Q. G., Wang, J., Tang, Y., Wang, H. T., Zhu, Z. C., et al. (2018b). Middle Neoproterozoic (ca. 760 Ma) arc and back-arc system in the North Lhasa terrane, Tibet, inferred from coeval N-MORB-and arc-type gabbros. *Precambrian Res.* 316, 275–290. doi:10.1016/j.precamres.2018.08.022

Jain, A. K., and Singh, S. (2009). Geology and tectonics of the southeastern Ladakh and Karakoram. Bangalore: Geological society of India City.

Jain, A. K., and Singh, S. (2008). Tectonics of the southern asian Plate margin along the Karakoram shear zone: Constraints from field observations and U–Pb SHRIMP ages. *Tectonophysics* 451 (1-4), 186–205. doi:10.1016/j.tecto.2007.11.048

Jain, A. K. (2014). When did India–Asia collide and make the Himalaya? *Curr. Sci.* 106 (2), 254–266.

Janoušek, V., Farrow, C. M., and Erban, V. (2006). Interpretation of whole-rock geochemical data in igneous geochemistry: Introducing geochemical data Toolkit (GCDkit). *J. Pet.* 47 (6), 1255–1259. doi:10.1093/petrology/egl013

Kang, H., Li, D., Chen, Y., Song, L., Xue, G., Geng, J., et al. (2019). Micro-continental blocks in Gondwana assembly: Geological and geochemical evidence of the Indochina block, SE Tibetan Plateau. *Lithos* 326, 460–475. doi:10.1016/j.lithos.2019.01.002

Kapp, P., Murphy, M. A., Yin, A., Harrison, T. M., Ding, L., and Guo, J. (2003). Mesozoic and cenozoic tectonic evolution of the shiquanhe area of Western Tibet. *Tectonics* 22 (4), 1332. doi:10.1029/2001tc001332

Khanna, P. P. (2009). An appraisal of ICP-ms technique for determination of REEs: Long term QC assessment of silicate rock analysis. *Him. Geol.* 30, 95–99.

Kumar, S., Bora, S., Sharma, U. K., Yi, K., and Kim, N. (2017). Early cretaceous subvolcanic calc-alkaline granitoid magmatism in the nubra-shyok valley of the Shyok suture zone, Ladakh Himalaya, India: Evidence from geochemistry and U–Pb SHRIMP zircon geochronology. *Lithos* 277, 33–50. doi:10.1016/j.lithos.2016.11.019

Le Maitre, R. W. (2002). *A classification of igneous rocks: A classification and glossary of terms: Recommendations of the international union of geological sciences subcommission of the systematic of igneous rocks*. Cambridge, New York, Melbourne, VIC: Cambridge University Press.

Li, Z. X., Bogdanova, S., Collins, A. S., Davidson, A., De Waele, B., Ernst, R. E., et al. (2008). Assembly, configuration, and break-up history of Rodinia: A synthesis. *Precambrian Res.* 160 (1-2), 179–210. doi:10.1016/j.precamres.2007.04.021

Liu, X. Q., Zhang, C. L., Hao, X. S., Zou, H., Zhao, H. X., and Ye, X. T. (2020). Early cretaceous granitoids in the southern Pamir: Implications for the meso-tethys evolution of the Pamir plateau. *Lithos* 362, 105492. doi:10.1016/j.lithos.2020.105492

Liu, Y., Wang, Y., Li, S., Santosh, M., Guo, R., and Yu, S. (2021). Neoproterozoic Amdo and Jiayuqiao microblocks in the Tibetan plateau: Implications for Rodinia reconstruction. *Bulletin* 133 (3-4), 663–678. doi:10.1130/B35632.1

Martin, H. (1986). Effect of steeper Archean geothermal gradient on geochemistry of subduction-zone magmas. *Geol.* 14 (9), 753–756. doi:10.1130/0091-7613(1986)14<753:eosagg>2.0.co;2

Meert, J. G., and Torsvik, T. H. (2003). The making and unmaking of a supercontinent: Rodinia revisited. *Tectonophysics* 375 (1-4), 261–288. doi:10.1016/s0040-1951(03)00342-1

Merdith, A. S., Williams, S. E., Müller, R. D., and Collins, A. S. (2017). Kinematic constraints on the Rodinia to gondwana transition. *Precambrian Res.* 299, 132–150. doi:10.1016/j.precamres.2017.07.013

Mukherjee, P. K., Singhal, S., Adlakha, V., Rai, S. K., Dutt, S., Kharya, A., et al. (2017). <i>*in situ*</i> U-Pb zircon micro-geochronology of MCT zone rocks in the lesser Himalaya using LA–MC–ICPMS technique. *Curr. Sci.* 112, 802–810. doi:10.18520/cs/v112/i04/802-810

Ou, Q., Wang, Q., Wyman, D. A., Zhang, H. X., Yang, J. H., Zeng, J. P., et al. (2017). Eocene adakitic porphyries in the central-northern Qiangtang Block, central Tibet: Partial melting of thickened lower crust and implications for initial surface uplifting of the plateau. *J. Geophys. Res. Solid Earth* 122 (2), 1025–1053. doi:10.1002/2016JB013259

Parrish, R. R., and Tirrul, R. (1989). U-Pb age of the Baltoro granite, northwest Himalaya, and implications for monazite U-Pb systematics. *Geol.* 17 (12), 1076–1079. doi:10.1130/0091-7613(1989)017<1076:upaotb>2.3.co;2

Paton, C., Hellstrom, J., Paul, B., Woodhead, J., and Hergt, J. (2011). Iolite: Freeware for the visualisation and processing of mass spectrometric data. *J. Anal. At. Spectrom.* 26 (12), 2508–2518. doi:10.1039/C1JA10172B

Pearce, J. A., Harris, N. B., and Tindle, A. G. (1984). Trace element discrimination diagrams for the tectonic interpretation of granitic rocks. *J. Petrology* 25 (4), 956–983. doi:10.1093/petrology/25.4.956

Peng, T., Zhao, G., Fan, W., Peng, B., and Mao, Y. (2015). Late triassic granitic magmatism in the eastern Qiangtang, eastern Tibetan plateau: Geochronology, petrogenesis and implications for the tectonic evolution of the paleo-tethys. *Gondwana Res.* 27 (4), 1494–1508. doi:10.1016/j.gr.2014.01.009

Petford, N., and Gallagher, K. (2001). Partial melting of mafic (amphibolitic) lower crust by periodic influx of basaltic magma. *Earth Planet. Sci. Lett.* 193 (3-4), 483–499. doi:10.1016/s0012-821x(01)00481-2

Phillips, R. J., Searle, M. P., and Parrish, R. R. (2013). The geochemical and temporal evolution of the continental lithosphere and its relationship to continental-scale faulting: The Karakoram Fault, eastern Karakoram, NW Himalayas. *Geochem. Geophys. Geosyst.* 14 (3), 583–603. doi:10.1002/ggge.20061

Pundir, S., Adlakha, V., Kumar, S., and Singhal, S. (2020a). Closure of India–asia collision margin along the Shyok suture zone in the eastern Karakoram: New geochemical and zircon U–Pb geochronological observations. *Geol. Mag.* 157 (9), 1451–1472. doi:10.1017/S0016756819001547

Pundir, S., Adlakha, V., Kumar, S., Singhal, S., and Sen, K. (2020b). Petrology, geochemistry and geochronology of granites and granite gneisses in the SE Karakoram, India: Record of subduction-related and pre-to syn-kinematic magmatism in the Karakoram Fault zone. *Mineral. Pet.* 114 (5), 413–434. doi:10.1007/s00710-020-00706-y

Qian, Q., and Hermann, J. (2013). Partial melting of lower crust at 10–15 kbar: Constraints on adakite and TTG formation. *Contrib. Mineral. Pet.* 165 (6), 1195–1224. doi:10.1007/s00410-013-0854-9

Ravikant, V., Wu, F. Y., and Ji, W. Q. (2009). Zircon U–Pb and Hf isotopic constraints on petrogenesis of the Cretaceous–Tertiary granites in eastern Karakoram and Ladakh, India. *Lithos* 110 (1-4), 153–166. doi:10.1016/j.lithos.2008.12.013

Rayleigh, L. (1896). L. *Theoretical considerations respecting the separation of gases by diffusion and similar processes. Lond. Edinb. Dublin Philosophical Mag. J. Sci.* 42 (259), 493–498. doi:10.1080/14786449608620944

Reichardt, H., Weinberg, R. F., Andersson, U. B., and Fanning, C. M. (2010). Hybridization of granitic magmas in the source: The origin of the Karakoram Batholith, Ladakh, NW India. *Lithos* 116 (3–4), 249–272. doi:10.1016/j.lithos.2009.11.013

Robinson, A. C. (2015). Mesozoic tectonics of the Gondwanan terranes of the Pamir plateau. *J. Asian Earth Sci.* 102, 170–179. doi:10.1016/j.jseaes.2014.09.012

Rolland, Y., Mahéo, G., Pecher, A., and Villa, I. M. (2009). Syn-kinematic emplacement of the Pangong metamorphic and magmatic complex along the karakorum fault (N Ladakh). *J. Asian Earth Sci.* 34 (1), 10–25. doi:10.1016/j.jseaes.2008.03.009

Rolland, Y., Picard, C., Pêcher, A., Carrio, E., Sheppard, S. M., Oddone, M., et al. (2002). Presence and geodynamic significance of Cambro-Ordovician series of SE Karakoram (N Pakistan). *Geodin. Acta* 15 (1), 1–21. doi:10.1080/09853111.2002.10510736

Rollinson, H. (1993). Using geochemical data. *Eval. Present. Interpret.* 1993, 1.

Rubatto, D. (2002). Zircon trace element geochemistry: Partitioning with garnet and the link between U–Pb ages and metamorphism. *Chem. Geol.* 184 (1-2), 123–138. doi:10.1016/S0009-2541(01)00355-2

Saini, N. K., Mukherjee, P. K., Khanna, P. P., and Purohit, K. K. (2007). A proposed amphibolite reference rock sample (AM-H) from Himachal Pradesh. *J. Geol. Soc. India* 69 (4), 799.

Schilling, J. G., and Winchester, J. W. (1967). "Rare-Earth fractionation and magmatic processes," in *Mantles of earth and terrestrial planets*. Editor S. K. Runcorn (New York: Interscience), 267–283.

Schwab, M., Ratschbacher, L., Siebel, W., McWilliams, M., Minaev, V., Lutkov, V., et al. (2004). Assembly of the Pamirs: Age and origin of magmatic belts from the southern Tien Shan to the southern Pamirs and their relation to Tibet. *Tectonics* 23 (4), 1583. doi:10.1029/2003tc001583

Searle, M. P. (2011). Geological evolution of the Karakoram ranges. *Ital. J. Geosci.* 130 (2), 147–159. doi:10.3301/IJG.2011.08

Searle, M. P., and Hacker, B. R. (2019). Structural and metamorphic evolution of the Karakoram and Pamir following India–Kohistan–Asia collision. *Geol. Soc. Spec. Publ.* 483 (1), 555–582. doi:10.1144/sp483.6

Searle, M. P., Weinberg, R. F., and Dunlap, W. J. (1998). Transpressional tectonics along the Karakoram Fault zone, northern Ladakh: Constraints on Tibetan extrusion. *Geol. Soc. Spec. Publ.* 135 (1), 307–326. doi:10.1144/gsl.sp.1998.135.01.20

Sen, K., Mukherjee, B. K., and Collins, A. S. (2014). Interplay of deformation and magmatism in the Pangong Transpression Zone, eastern Ladakh, India: Implications for remobilization of the trans-Himalayan magmatic arc and initiation of the Karakoram Fault. *J. Struct. Geol.* 62, 13–24. doi:10.1016/j.jsg.2014.01.009

Sengör, A. C. (1984). The Cimmeride orogenic system and the tectonics of Eurasia. *Geol. Soc. Am. Spec. Pap.* 195, 82.

Sláma, J., Košler, J., Condon, D. J., Crowley, J. L., Gerdes, A., Hanchar, J. M., et al. (2008). Plešovice zircon—A new natural reference material for U–Pb and Hf isotopic microanalysis. *Chem. Geol.* 249 (1-2), 1–35. doi:10.1016/j.chemgeo.2007.11.005

Song, P., Ding, L., Li, Z., Lippert, P. C., and Yue, Y. (2017). An early bird from gondwana: Paleomagnetism of lower permian lavas from northern Qiangtang (Tibet) and the geography of the paleo-tethys. *Earth Planet. Sci. Lett.* 475, 119–133. doi:10.1016/j.epsl.2017.07.023

Srimal, N. (1986). India-Asia collision: Implications from the geology of the eastern Karakoram. *Geol.* 14 (6), 523–527. doi:10.1130/0091-7613(1986)14<523:iciftg>2.0.co;2

Streckeisen, A. (1976). To each plutonic rock its proper name. *Earth-science Rev.* 12 (1), 1–33. doi:10.1016/0012-8252(76)90052-0

Streule, M. J., Phillips, R. J., Searle, M. P., Waters, D. J., and Horstwood, M. S. A. (2009). Evolution and chronology of the Pangong metamorphic complex adjacent to the Karakoram Fault, Ladakh: Constraints from thermobarometry, metamorphic modelling and U–Pb geochronology. *J. Geol. Soc. Lond.* 166 (5), 919–932. doi:10.1144/0016-76492008-117

Sui, Q. L., Wang, Q., Zhu, D. C., Zhao, Z. D., Chen, Y., Santosh, M., et al. (2013). Compositional diversity of ca. 110 Ma magmatism in the northern Lhasa terrane, Tibet: Implications for the magmatic origin and crustal growth in a continent–continent collision zone. *Lithos* 168, 144–159. doi:10.1016/j.lithos.2013.01.012

Sun, S. S., and McDonough, W. F. (1989). Chemical and isotopic systematics of oceanic basalts: Implications for mantle composition and processes. *Geol. Soc. Spec. Publ.* 42 (1), 313–345. doi:10.1144/GSL.SP.1989.042.01.19

Van Buer, N. J., Jagoutz, O., Upadhyay, R., and Guillong, M. (2015). Mid-crustal detachment beneath Western Tibet exhumed where conjugate Karakoram and Longmu–Gozha Co faults intersect. *Earth Planet. Sci. Lett.* 413, 144–157. doi:10.1016/j.epsl.2014.12.053

Vermeesch, P. (2018). IsoplotR: A free and open toolbox for geochronology. *Geosci. Front.* 9 (5), 1479–1493. doi:10.1016/j.gsf.2018.04.001

Villarreal, D. P., Robinson, A. C., Carrapa, B., Worthington, J., Chapman, J. B., Oimahmadov, I., et al. (2020). Evidence for late triassic crustal suturing of the central and southern Pamir. *J. Asian Earth Sci. X* 3, 100024. doi:10.1016/j.jaesx.2019.100024

Wallis, D., Phillips, R. J., and Lloyd, G. E. (2014). Evolution of the eastern Karakoram metamorphic complex, Ladakh, NW India, and its relationship to magmatism and regional tectonics. *Tectonophysics* 626, 41–52. doi:10.1016/j.tecto.2014.03.023

Wang, H., Zhai, Q., Hu, P., Zeng, L., Tang, Y., and Zhu, Z. (2020). Early paleozoic granitic rocks of the South Qiangtang terrane, northern Tibetan plateau: Implications for subduction of the proto-(paleo-) tethys ocean. *J. Asian Earth Sci.* 204, 104579. doi:10.1016/j.jseaes.2020.104579

Weaver, B. L., and Tarney, J. (1980). Continental crust composition and nature of the lower crust: Constraints from mantle Nd–Sr isotope correlation. *Nature* 286 (5771), 342–346. doi:10.1038/286342a0

Weinberg, R. F., Dunlap, W. J., and Whitehouse, M. (2000). New field, structural and geochronological data from the Shyok and nubra valleys, northern Ladakh: Linking kohistan to Tibet. *Geol. Soc. Spec. Publ.* 170 (1), 253–275. doi:10.1144/gsl.sp.2000.170.01.14

Weinberg, R. F., and Mark, G. (2008). Magma migration, folding, and disaggregation of migmatites in the Karakoram shear zone, Ladakh, NW India. *Geol. Soc. Am. Bull.* 120 (7-8), 994–1009. doi:10.1130/b26227.1

Whitney, D. L., and Evans, B. W. (2010). Abbreviations for names of rock-forming minerals. *Am. Mineral.* 95 (1), 185–187. doi:10.2138/am.2010.3371

Wiedenbeck, M. A. P. C., Alle, P., Corfu, F. Y., Griffin, W. L., Meier, M., Oberli, F. V., et al. (1995). Three natural zircon standards for U-Th-Pb, Lu-Hf, trace element and REE analyses. *Geostand. Geoanal. Res.* 19 (1), 1–23. doi:10.1111/j.1751-908x.1995.tb00147.x

Wu, H., Xie, C., Li, C., Wang, M., Fan, J., and Xu, W. (2016). Tectonic shortening and crustal thickening in subduction zones: Evidence from middle–late jurassic magmatism in southern Qiangtang, China. *Gondwana Res.* 39, 1–13. doi:10.1016/j.gr.2016.06.009

Yeh, M. W., and Shellnutt, J. G. (2016). The initial break-up of Pangæa elicited by Late Palæozoic deglaciation. *Sci. Rep.* 6 (1), 31442–31449. doi:10.1038/srep31442

Yu, Y. P., Xie, C. M., Dong, Y. S., Dong, Y. C., Wang, B., Duan, M. L., et al. (2021). Early Neoproterozoic granitic gneisses in the Amdo micro-continent, Tibet: Petrogenesis and geodynamic implications. *Int. Geol. Rev.* 63 (3), 342–356. doi:10.1080/00206814.2019.1710866

Zhai, Q. G., Jahn, B. M., Su, L., Wang, J., Mo, X. X., Lee, H. Y., et al. (2013). Triassic arc magmatism in the Qiangtang area, northern Tibet: Zircon U–Pb ages, geochemical and Sr–Nd–Hf isotopic characteristics, and tectonic implications. *J. Asian Earth Sci.* 63, 162–178. doi:10.1016/j.jseaes.2012.08.025

Zhang, C. L., Zou, H. B., Ye, X. T., and Chen, X. Y. (2018). A newly identified Precambrian terrane at the Pamir Plateau: The Archean basement and Neoproterozoic granitic intrusions. *Precambrian Res.* 304, 73–87. doi:10.1016/j.precamres.2017.11.006

Zhang, Z. M., Dong, X., Liu, F., Lin, Y. H., Yan, R., and Santosh, M. (2012). Tectonic evolution of the Amdo terrane, central Tibet: Petrochemistry and zircon U-Pb geochronology. *J. Geol.* 120 (4), 431–451. doi:10.1086/665799

Zhao, G., Wang, Y., Huang, B., Dong, Y., Li, S., Zhang, G., et al. (2018). Geological reconstructions of the east Asian blocks: From the breakup of Rodinia to the assembly of pangea. *Earth. Sci. Rev.* 186, 262–286. doi:10.1016/j.earscirev.2018.10.003

Zhou, X., Zheng, J., Li, Y., Griffin, W. L., Xiong, Q., Moghadam, H. S., et al. (2019). Neoproterozoic sedimentary rocks track the location of the Lhasa Block during the Rodinia breakup. *Precambrian Res.* 320, 63–77. doi:10.1016/j.precamres.2018.10.005

frontiers | Frontiers in Earth Science

TYPE Original Research
PUBLISHED 05 January 2023
DOI 10.3389/feart.2022.1022280

OPEN ACCESS

EDITED BY
Qiuming Pei,
Southwest Jiaotong University, China

REVIEWED BY
Hengkai Li,
Jiangxi University of Science and Technology, China
Shaohua Zhao,
Ministry of Ecology and Environment Center for Satellite Application on Ecology and Environment, China
Nickolai Shadrin,
A.O. Kovalevsky Institute of Biology of the Southern Seas, Ukraine

*CORRESPONDENCE
Jingjing Dai,
daijingjing863@sina.com

SPECIALTY SECTION
This article was submitted to Structural Geology and Tectonics, a section of the journal Frontiers in Earth Science

RECEIVED 18 August 2022
ACCEPTED 14 September 2022
PUBLISHED 05 January 2023

CITATION
Dai J, Liu T, Zhao Y, Tian S, Ye C and Nie Z (2023), Remote sensing inversion of the Zabuye Salt Lake in Tibet, China using LightGBM algorithm.
Front. Earth Sci. 10:1022280.
doi: 10.3389/feart.2022.1022280

Remote sensing inversion of the Zabuye Salt Lake in Tibet, China using LightGBM algorithm

Jingjing Dai*[1], Tingyue Liu[2], Yuanyi Zhao[3], Shufang Tian[2], Chuanyong Ye[3] and Zhen Nie[3]

[1]MNR Key Laboratory of Metallogeny and Mineral Assessment, Institute of Mineral Resources, Chinese Academy of Geological Sciences, Beijing, China, [2]School of Earth Sciences and Resources, China University of Geosciences, Beijing, China, [3]MNR Key Laboratory of Saline Lake Resources and Environments, Institute of Mineral Resources, Chinese Academy of Geological Sciences, Beijing, China

The Zabuye Salt Lake in Tibet, China is the only salt lake in the world that contains natural crystalline lithium carbonate. The grade and spatial distribution of mineral resources are of great importance to the development and utilization of salt lake mineral resources. The use of remote sensing technology for salt lakes observations can overcome the disadvantages of traditional station observations, such as spatial discontinuity, high time consumption, and high labor costs. In addition, machine learning algorithms can efficiently analyze the information from remote sensing data. In this study, Landsat-8 remote sensing image data and the Light Gradient Boosting Machine (LightGBM) algorithm were used to perform inversions of the depth, salinity, and lithium concentration of the Zabuye Salt Lake. Moreover, the water volume, total salinity, and total lithium content of Zabuye Salt Lake in 2000 and 2017 were estimated, and the distribution of mineral resources and changes during the study period were analyzed. The results show that the water depth and volume of the entire lake increased sharply in 2017, resulting in a decrease in salinity and lithium concentration in the lake. Due to the inflow from the surrounding dry salterns, the South Lake experienced a relatively small change. Furthermore, the amount of lithium resources in North Lake decreased significantly in 2017 compared to 2000, possibly due to higher temperatures during the month of observation, which led to precipitation of lithium carbonate. Our study proves the feasibility and accuracy of the LightGBM machine learning algorithm for rapid inversion of salt lakes, which provides technical insight into remote sensing inversion of other mineral resources in salt lakes. Thus, the development of remote sensing technology in recent years can provide increasingly detailed assessments of salt lake resources in the future.

KEYWORDS

Zabuye Salt Lake, remote sensing, LightGBM algorithm, lithium, Tibetan Plateau

1 Introduction

The Tibetan Plateau is one of the four concentrated distribution areas of salt lakes in China. The salt lakes on the Tibetan Plateau are rich in potassium salt, lithium chloride, boron, and other mineral resources, and have high economic value (Lu et al., 2016; Yang et al., 2017; Lei, 2019). The Zabuye Salt Lake in Tibet has the second highest lithium grade followed Chile's Atacama Salt Lake in the world (Zheng et al., 2004). In particular, it is the only salt lake in the world with naturally occurring crystalline lithium carbonate (Zheng and Liu., 1987). With a high lithium to magnesium ratio, it is easy to form natural lithium carbonate deposits with high purity (Luo and Zheng, 2004). In recent years, the Zabuye Salt Lake Company has mainly mined and developed lithium resources, with an annual production capacity of about 5,000 tons and a gross profit margin of about 29%.

Since 1990, the Zabuye Salt Lake has shown a dramatic expansion trend, and this change will not only have an impact on the surrounding grasslands and salt pans, but also affect the salinity and lithium concentration in the brine during the salt lake development. However, the degree and scale of the impact is still unclear. Continuous observation of the Zabuye Salt Lake has been conducted by the Salt Lake Research Team of the Chinese Academy of Geological Sciences during the past 40 years, which has provided a large amount of meteorological, hydrological, and hydrochemical data (Qi and Zheng, 2006a, 2006b; Kong et al., 2017). However, there are some limitations to the observational data. While temporal continuity can be easily achieved, it is difficult to achieve spatial continuity of the data.

Remote sensing technology can be used to observe salt lakes from a macro perspective. It not only provides the spatial distribution of objects at different times, but also can reduce the required labor, material, and financial resources (Letey et al., 2011; Zhang et al., 2013; Pan et al., 2015; Liu et al., 2018; Fan et al., 2021). Therefore, remote sensing technology is an important tool for monitoring salt lakes. The most important parameters for remote sensing monitoring are chlorophyll concentration, suspended solids content, dissolved organic matter, water temperature, and water depth (Forget et al., 1999; Zhang et al., 2009; Zhang et al., 2010; Shi et al., 2011; Siswanto et al., 2011; Xi and Zhang, 2011; Zhu et al., 2011; Figueiredo et al., 2016; Cao et al., 2021), but there are relatively few studies on remote sensing inversion of mineral resources in salt lakes. Because the composition of the water of salt lakes is quite different from that of conventional freshwater lakes, it is difficult to transfer existing remote sensing results from freshwater lakes to salt lakes. Similarly, there are few studies on the spectra of the various mineral concentrations of brines in salt lakes (Yan and Zheng, 2015).

In addition, existing remote sensing inversion methods for salinity and lithium concentration in salt lakes generally use empirical inversion methods, such as principal component analysis, linear regression models, and multiple linear regression models (Su et al., 2008). However, the applied models usually have simple calculations and low inversion accuracy (Lyzenga, 1978). In recent years, machine learning algorithms have been increasingly used for inversion in remote sensing. Numerous studies have shown that machine learning algorithms have higher accuracy than traditional linear regression methods (Rogan et al., 2003; Larya et al., 2016; Rouet-Leduc et al., 2017; Maxwell et al., 2018). Machine learning algorithms currently used in salt lake research primarily include Back Propagation (BP) neural networks and Random Forest (RF) (Zhou et al., 2016; Wang, 2019). Light Gradient Boosting Machine (LightGBM) is an improved product based on RF, Extreme Gradient Boosting (XGBoost) and other algorithms. It is a new decision tree method proposed by Google in recent years (Xie et al., 2019; Pan et al., 2021). So far, it has not been used in salt lake research. However, in a few applications in other fields (Zhou et al., 2016; Xie et al., 2019; Song, 2021; Pan et al., 2021), its application results are better than those of traditional BP neural network, RF, Support Vector Machine (SVM) algorithms and other methods, with higher accuracy and running speed.

In this study, we used the LightGBM algorithm to perform an inversion of the depth, salinity, and lithium concentration of Zabuye Salt Lake from 2000 to 2017, to estimate the water volume, total salinity, and total lithium content. Based on these results, we analyzed the spatial distribution and changes of the mineral resources in the salt lake, which provided technical support for remote sensing inversion of other mineral resources in the salt lakes.

2 Materials and methods

2.1 Study area

Zabuye Salt Lake is located in the hinterland of the Tibetan Plateau at the northern foot of the western Gangdise Mountains. Its geographical coordinates are 83°57′10″–84°15′08″ E and 31°27′10″– 31°34′30″ N. The salt lake is divided into the South lake and the North lake. The South Lake is a solid-liquid lake with a depth of less than 1 m, while the North Lake is a brine lake with a depth of about 2 m. The South Lake has been under industrial development for the production of lithium carbonate since 2003.

The climate is characterized by low temperatures, large temperature differences, strong radiation, low precipitation, and high evaporation (Qi and Zheng, 2006b). Moreover, the annual precipitation is only 192 mm, but the annual evaporation can reach 2,269 mm. The lake is replenished by river water, atmospheric precipitation, and groundwater (Tian et al., 2005; Qi and Zheng, 2006a; Xu et al., 2017), and the water system around the lake is relatively well developed. The LangmeGaqu,

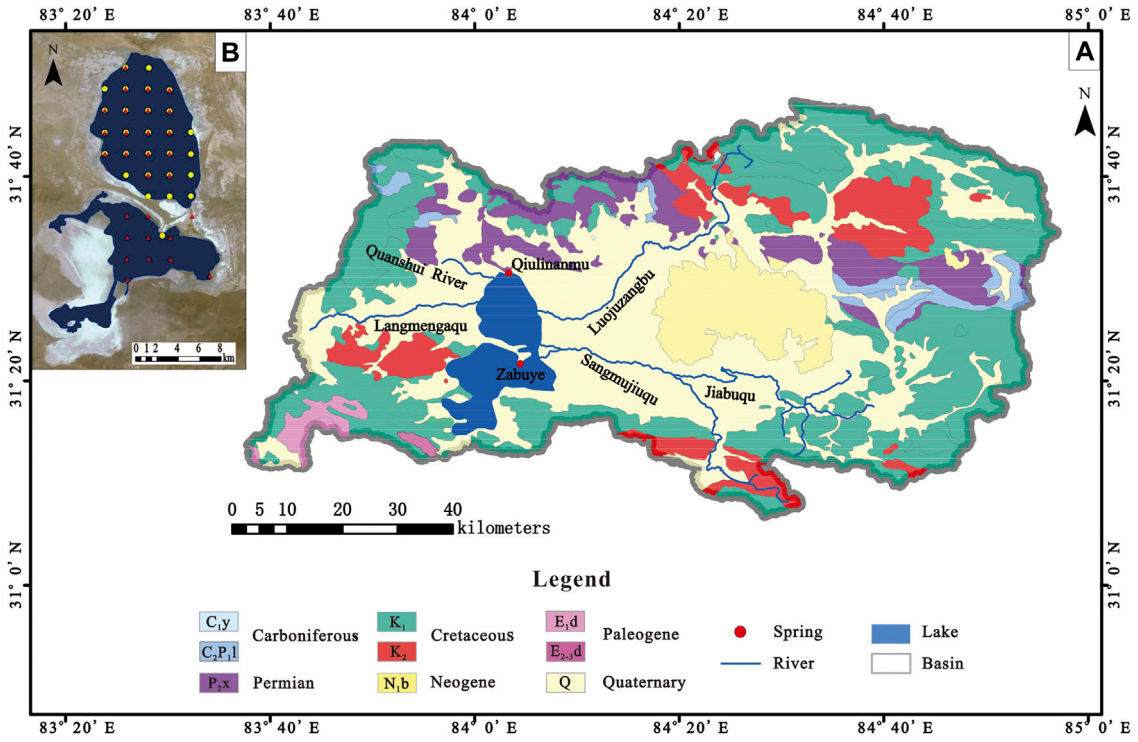

FIGURE 1
(A) Geological map of the Zabuye watershed. **(B)** Distribution map of sampling points (The red points are in 2000, and the yellow points are in 2017).

Luojuzangbo, Sangmujiuqu, Jiabuqu, and Quanshui rivers are the main rivers in this region. Other springs are mainly located on the travertine island in the middle of the lake and on the Qiulinanmu in the northern part of the lake. These rivers and springs contain various mineral resources, such as lithium and boron. The main exposed strata in this area are Carboniferous, Permian, Cretaceous, Paleogene, Neogene, and Quaternary (Figure 1A). Lithium and boron in river water are mainly derived from Quaternary sediments, surface weathering, and subsurface rocks. Lithium in spring water is mainly from surrounding rocks in contact with deep circulating groundwater (Liu et al., 2007). Due to the strong evaporation, the lithium concentration of Zabuye Salt Lake, which is greater than 1 g/L, can form a natural lithium carbonate deposit favourable for lithium extraction.

2.2 Datasets and preprocessing

2.2.1 Measurement data

In our study, there are two periods with measurement data: January 2000 and August 2017. The 2017 measurement data were provided by the Zabuye Salt Lake Field Observatory of the Chinese Academy of Geological Sciences, and the 2000 data were obtained from the literature (Tian et al., 2005; Tian et al., 2006). These data include the latitude and longitude coordinates, water depth, salinity, and lithium concentration of each sampling site. A distribution map of the sampling sites is shown in Figure 1B. Sampling sites were selected according to the Geological Exploration Standard of Saline Lake and Salt Minerals, and arranged in a 2 km × 2 km grid. However, the sampling data for the different study periods were slightly different. The 2000 data were relatively complete and covered the entire lake, while most of the 2017 data were from the North Lake, and only one measured data was from the South Lake. Then the data of the North and South Lake in 2000, the North Lake in 2017 were used as model training data in the inversion, and the data of the South Lake in 2017 were used for validation.

2.2.2 Landsat remote sensing data

The image data in the study are Landsat data with a medium resolution of 30 m. The Landsat data provide data in the spectral range from visible near infrared to thermal infrared (Yagmur et al., 2021) (Table 1). In this study, Landsat seven and eight data from visible to shortwave infrared were used to perform the remote sensing inversion, including bule, green, red, near-infrared (NIR), short-wave infrared1 (SWIR1), short-wave infrared2

TABLE 1 Landsat 7/8 image data band setting.

Sensor	Band number	Band name	Wavelength (μm)	Sensor	Band number	Band name	Wavelength (μm)
Landsat 7 ETM+	1	Blue	0.45–0.52	Landsat8 OLI	1	Coastal	0.43–0.45
	2	Green	0.52–0.60		2	Blue	0.45–0.52
	3	Red	0.63–0.69		3	Green	0.53–0.60
	4	NIR	0.77–0.90		4	Red	0.63–0.68
	5	SWIR1	1.55–1.75		5	NIR	0.85–0.89
	7	SWIR2	2.08–2.35		6	SWIR1	1.56–1.67
	8	Pan	0.52–0.90		7	SWIR2	2.10–2.30
	6	TIR	10.40–12.50		8	Pan	0.50–0.68
					9	Cirrus	1.36–1.39
				TIRS	10	TIR1	10.60–11.19
					11	TIR2	11.50–12.51

(SWIR2) and panchromatic bands. Landsat 7 data with the scene-number LE07_L1TP_142038_20000215_20170213_01_T1 in 2000 and Landsat 8 data with the scene-number LC08_L1TP_143038_20170823_20170912_01_T1 in 2017 were selected. The acquisition times of these images were found to be essentially the same as the sampling time of the measured data.

Radiometric calibration and atmospheric correction were performed prior to remote sensing inversion to correct for radiation distortion during image acquisition and to obtain the reflectance from remote sensing imagery (Lu et al., 2019).

2.3 Methods

In this study, we examined the spectra of different water depths, salinity, and lithium concentration, trained a LightGBM regression model, and determined the relationship between radiation data and measured values to predict and retrieve the water depth, salinity, and lithium concentration of the Zabuye Salt Lake. Since no records were abalibale for South Lake in 2017, two data periods were used to train the LightGBM model to improve its generalizability and obtain accurate water depth, salinity, and lithium concentration data for South Lake in 2017. Finally, using the area volume formul, and mass density volume formula, the total water volume, total salinity and total lithium content of the lake were calculated for each observation period.

2.3.1 Spectral measurements and analysis

Few studies have been made about the spectral measurements of water depth and salinity of salt lakes; therefore, the spectral responses are unclear. For this reason, spectral measurements and analyzes of the salt lake water samples were performed using Analyical Spectral Device (ASD) FieldSpec4 spectrum analyzer. The detection range of the FieldSpec4 covers the visible, near-infrared, and shortwave infrared regions (350–2,500 nm), and the spectral resolution is 3 nm in the near-inferred wavelength region and 8 nm in short wave-inferred wavelength region (MinJee et al., 2022). RS3 software was used to optimize the instrument and analyze the reflectance data.

Water depth measurements were performed as follows: 1) The instrument was set up and the illumination was adjusted to an angle of 45–60° between the light source and the water surface (Tang et al., 2004). The positions of the instrument and the sample remained unchanged during the measurements. 2) We standardized and calibrated the reflectance curve of the sample using a whiteboard. 3) We filled 50, 100, 150, and 200 ml of the salt lake water samples into the beakers. The temperature, light source, and salinity level remained the same, only the water depth was changed. 4) We recorded the reflectance curves of the samples with the ASD spectrum analyzer and performed a comparative analysis. The measurement procedure was similar for different salinity. The water depth and water volume remained the same, and only the salinity was changed.

2.3.2 Image fusion

Landsat satellite imagery has a panchromatic band with higher spatial resolution at a wavelength of 0.52–0.90 μm. Image fusion allows the use of spatial and spectral information, improves the correlation between spectral values and water depth, enhances texture and detail of ground objects, and reduces spatial information redundancy between image components (Dionisio et al., 2017; Vivone et al., 2020). Image fusion was then performed to obtain a high-resolution multispectral image. Research in recent years has shown that the wavelet transform, High Pass Filter (HPF) transform, Gram-Schmidt (GS) transform, and Nearst Neighbor Diffusion (NNDiffuse) transform provide the best results. In this study, these methods were compared and a correlation analysis of the transformed spectral values with water depth, salinity, and lithium content was performed.

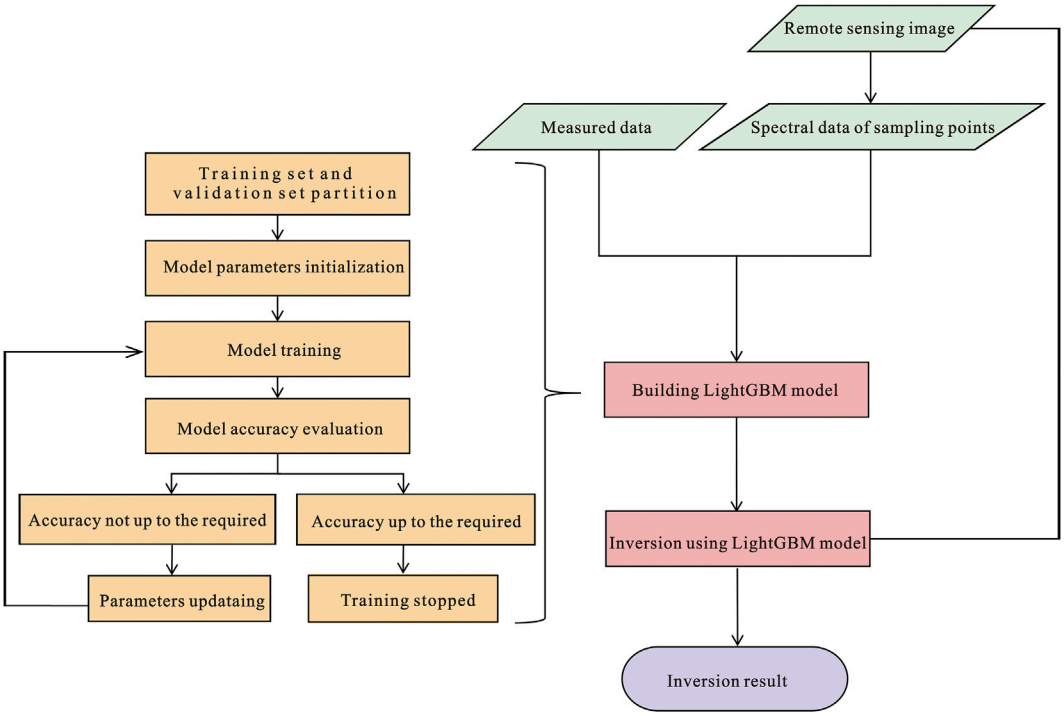

FIGURE 2
Technical flow chart of this study.

2.3.3 Inversion band selection

Direct sunlight and scattered light received from a body of water is strongly reflected in the red, green, and blue bands, while bodies of water absorb light in the near-infrared (NIR) wavelength. That is, the red, green, and blue bands reflect more solar radiation and contain more information about the water body. Waters with different depths, salinity, and lithium content have differences in the reflectance and absorption characteristics. Correlation analyses and regression fits were performed between the spectral values of the remote sensing images and water depth, salinity, and lithium concentration to determine the optimal inversion band (Li et al., 2013).

2.3.4 Inversion using LightGBM algorithm

The technical route of a salt lake inversion based on LightGBM is shown in Figure 2. It mainly includes three steps: the acquisition of spectral data from the sampling sites, the construction of LightGBM regression model, and the inversion of water depth, salinity, and lithium concentration. The whole experimental process is performed in ArcGIS and JupterNotebook, and the model accuracy is evaluated by the average relative error, root mean square error, and chi-square (R^2) (Nhu et al., 2020).

2.3.4.1 Spectral data acquisition of the sampling sites

The spectral data used in this study were obtained from remote sensing imagery. A mineral spectrum usually contains a set of characteristic absorption bands that were interpreted for each mineral. The vector data of the sample sites were generated according to the latitude and longitude, and the spectrum values of all remote sensing image bands in the same period were extracted into the vector of sampling sies that attributes to form the model training data according to the spatial location (Chen et al., 1995).

2.3.4.2 LightGBM regression model construction

LightGBM is a gradient boosting decision tree that widely used for various regression predictions (Duba et al., 2021; Gábor et al., 2022). Multiple decision trees are integrated in LightGBM, which can synthesize the decision results of multiple decision trees and avoid the low accuracy of a single learner. In addition, a histogram-based segmentation algorithm, a leaf growth strategy with depth constraint, a Goss sampling method, and a unique feature binding are used in LightGBM to improve the accuracy and training speed and filter effective data features (Zhang et al., 2019; Li et al., 2021; Song et al., 2021). Therefore, this algorithm is suitable for solving problems related to the complex mapping relationship between the radiation value and lithium

concentration caused by the limited number of Landsat remote sensing bands.

The LightGBM regression model is constructed as follows: 1) First, the measured data and spectral data were divided into a training set and a verification set; 2) The parameters of the LightGBM regression model were initialized; 3) The training set was used to train the LightGBM regression model. 4) The verification set was used to evaluate the accuracy of the training model. If the accuracy was not acceptable, the parameters were updated and re-trained. 5) The training was repeated until the accuracy was acceptable or could not be improved, and the regression model was built.

2.3.4.3 Water depth, salinity and lithium concentration inversion

Pixel, the basic unit of a remote sensing image, provides the spectral properties of the brine. Therefore, the basic unit of inversion of water depth, salinity, and lithium concentration is also the pixel. First, the remote sensing image is read in and a format conversion and rearrangement of the data is performed. Each pixel of the remote sensing data is converted into training data and input into the model, i.e., the pixel value of each band is used as a set of spectral data, and the pixel value of each band is used as an inversion feature. Second, the spectral data obtained in the first step are input to the trained LightGBM regression model to invert the value of each pixel point. According to the distribution of the previous spectral data in the spatial dimension of the remote sensing image, the obtained array of values is then inverted and merged into a single band image. Finally, the basic information such as the image coordinate system and the number of rows and columns are specified, and the image in TIFF format is output to obtain the inversion result.

2.3.5 The total salinity and lithium content assessment

When the water depth, salinity, and lithium concentration data are inverted at each pixel, integrals can be used to calculate the total water volume, salinity, and lithium of the entire lake area, where the entire lake is regarded as a collection of n (n = lake area/pixel area) times of water columns. The height of the water column is the water depth at that point, and the length and width of the water column are equal to the length and width of the pixel. Since the pixel resolution of the Landsat image is 30 m, the length and width of the water column are both 30 m, and the bottom area of the water column is 900 m^2.

According to the volume equation, the water depth retrieved by each pixel multiplied by the pixel area is the water volume corresponding to 900 m^2 of water. Similarly, the mass of the lake corresponding to each pixel can be determined by the product of water volume and density. Then, the volume of the entire lake area can be determined by a cumulative calculation. Salinity is calculated by the ratio of the mass of salt dissolved in the water to the mass of water, while lithium concentration refers to the mass of lithium ions dissolved in a unit volume of water. Therefore, the salinity of each pixel is the product of the salinity retrieved by the LightGBM and the volume of water in the area, while the lithium content is the product of the lithium concentration retrieved by the LightGBM and the volume of water in the area. The total salinity and lithium content can also be calculated using an accumulation calculation.

3 Results

3.1 Spectral measurement results

The spectra of waters with different depths and salinity shared the water characteristic of high spectral reflctance in blue, green, red, NIR bands and low reflectance in SWIR bands. The most significant difference in the spectra of waters with different depths is their reflectance (Figures 3A,B). As water depth increases, reflectance decreases in all bands. The most significant difference in the spectra of water with different salinity is also the reflectivity, and the regions at 440–1,000 nm are suitable for distinguishing them (Figures 3C,D). The reflectivity increases with increasing salinity. Thus, all bands in the visible light range up to the SWIR can be used to retrieve the water depth.

3.2 Image fusion results

The images were fused using the wavelet transform, HPF transform, and NNDiffuse transform and GS transform. The correlation results show that the correlation between the spectral value and the water depth improved significantly after the GS transformation. The highest correlation coefficient (0.956) occurs in the red band (Table 2). These results show that the GS fusion improves the correlation between the spectral value of the image and the water depth, and the fused image data is more suitable for determining the water depth than the original data.

The results of the correlation analysis (Table 2) show weak correlations between the reflectance values of different Landsat bands and salinity, especially in the red and SWIR bands. The panchromatic band show no correlation with salinity, for most of the correlation coefficients are less than 0.1. The GS transformation does not substantially improve the correlation, so the image fusion result was not suitable for salinity inversion, so as for the lithium concentration inversion.

3.3 Band selection results

In water depth inversion studies, blue, green, and red bands have been widely used for distinguishing water depth, but the accuracy of using one or two bands is not as high as using

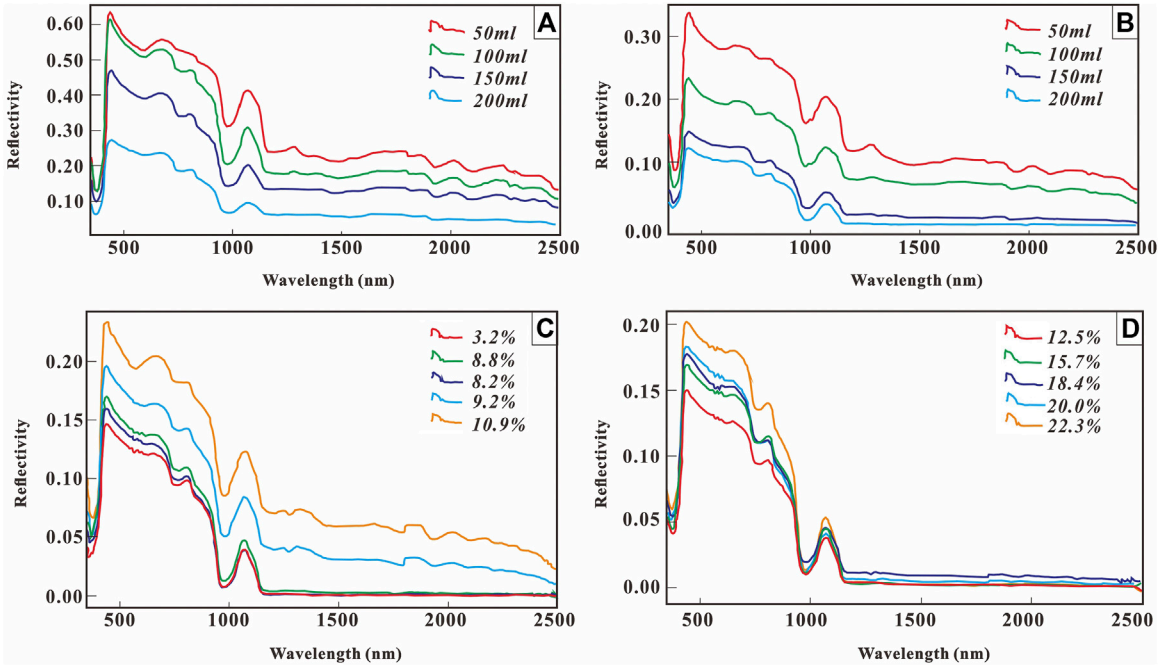

FIGURE 3
Spectral measurement results of the water with different depths and salinities. **(A)** Measured spectra of water at different depths in the North Lake; **(B)** Measured spectra of water at different depths in the South Lake; **(C)** Measured spectra of water at different salinities in the North Lake; **(D)** Measured spectra of water at different salinities in the South Lake.

TABLE 2 The correlation between the spectral value and the water depth, salinity and lithium concentration before and after image fusion.

Water parameters	Image processing	Blue	Green	Red	NIR	SWIR1	SWIR2
Water Depth	Before Fusion	0.72	0.53	−0.76	−0.71	−0.16	−0.11
	After Fusion	−0.61	−0.89	−0.956	−0.86	−0.77	−0.79
Salinity	Before Fusion	0.88	0.81	−0.34	−0.54	0.01	0.01
	After Fusion	−0.08	−0.32	−0.60	−0.59	−0.63	−0.66
Lithium concentration	Before Fusion	0.91	0.81	0.44	0.54	0.05	0.03
	After Fusion	0.16	0.67	0.86	0.86	0.78	0.79

TABLE 3 The correlation between the reflectance of Landsat imagery and the measured spectral value in single band and all bands.

R^2	Blue	Green	Red	NIR	SWIR1	SWIR2	All bands
Water Depth	−0.61	−0.89	−0.96	−0.86	−0.77	−0.79	0.98
Salinity	0.88	0.81	−0.34	−0.54	0.01	0.01	0.90
Lithium Concentration	0.91	0.81	0.44	0.54	0.05	0.03	0.95

multiple bands (Mao et al., 2012). Based on the correlation between salinity and reflectance of individual band, the correlation coefficient between the blue band and salinity is the highest with R^2 of 0.88. However, the correlation coefficient between all bands and salinity is 0.90, which is higher than that of the individual bands (Table 3).

Lithium chloride and lithium carbonate are part of the total salt mineral resources, and their concentrations are closely

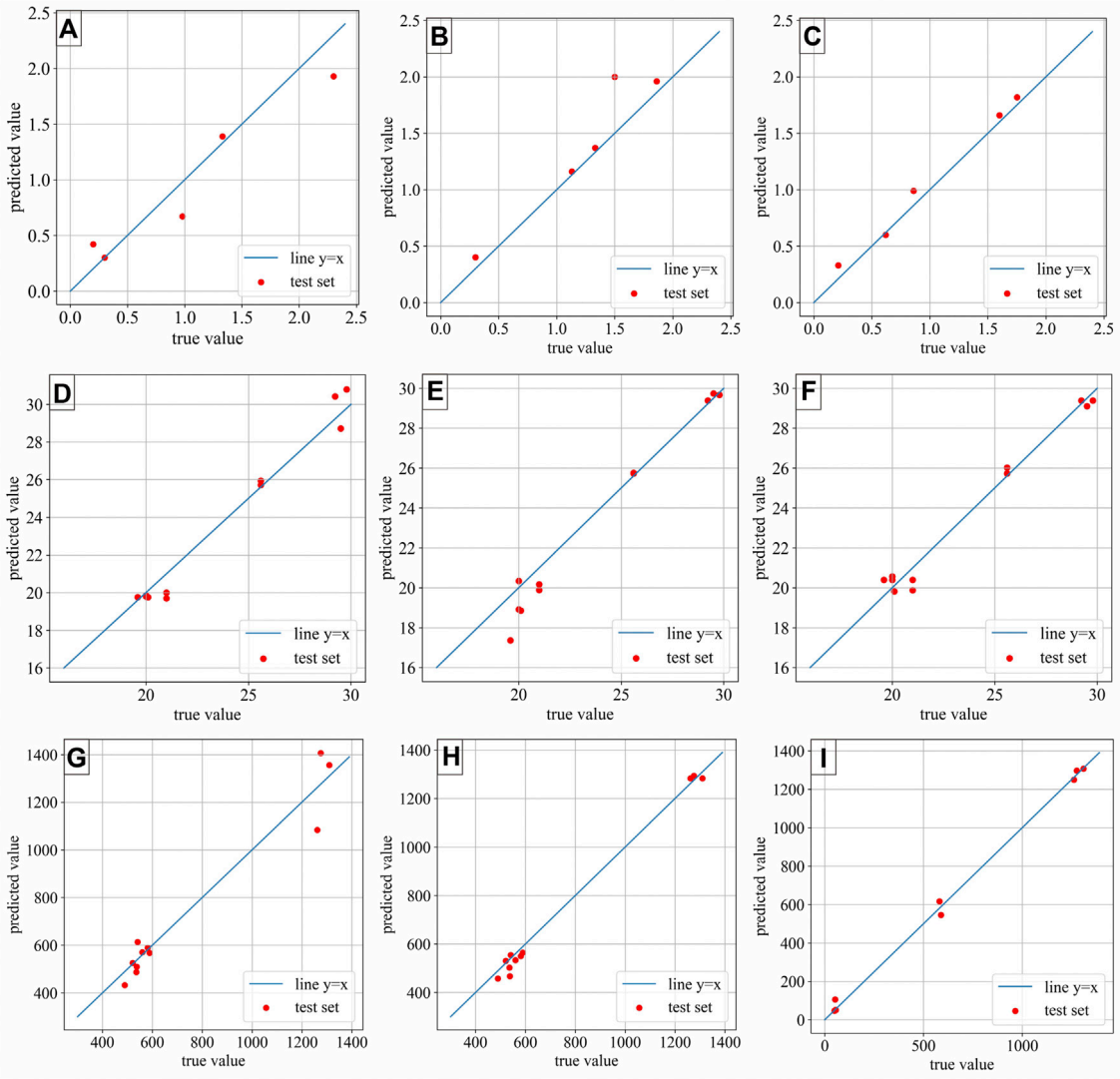

FIGURE 4
Comparison of true and predicted values in the test data set with different machine learning algorithms. **(A)** Water depth inversion based on BP neural network; **(B)** Water depth inversion based on Random Forest; **(C)** Water depth inversion based on LightGBM; **(D)** Salinity inversion based on BP neural network; **(E)** Salinity inversion based on Random Forest; **(F)** Salinity inversion based on LightGBM; **(G)** Lithium concentration inversion based on BP neural network; **(H)** Lithium concentration inversion based on Random Forest; **(I)** Lithium concentration inversion based on LightGBM.

related to salinity. Based on the correlation between lithium concentration and reflectance at the measured points, the correlation coefficient between all bands and lithium concentration is the highest, with R^2 of 0.95 (Table 3).

Due to the time interval between the two image dates is long, the lake and the surrounding environment have changed significantly. Therefore, the spectral values are likely to be very different. It is feasible to use one or two bands to fit the water depth value at one time point, but there are limitations to fitting the measured value at multiple time. The best result of fitting between reflectance and measured water depth is 0.96 for the red band and 0.98 for all bands (Table 3). Using all bands reduces the noise and highlights the effective information. Therefore, it is best to use all bands for inversion.

3.4 Water depth, salinity and lithium concentration inversion results

Linear fitting and three machine learning algorithms including BP neural network, RF, and LightGBM, were compared to determine the water depth, salinity, and lithium concentration. The results are shown in Figure 4 and Table 4. Machine learning algorithms have advantages over linear

TABLE 4 Fitting results for different methods.

Fitting method	Water depth		Salinity		Lithium concentration	
	MSE	R^2	MSE	R^2	MSE	R^2
Linear Fitting	0.071	0.837	1.371	0.942	9,318.04	0.934
BP Network	0.057	0.908	0.554	0.966	5,726.205	0.947
Random Forest	0.055	0.902	0.900	0.945	1,006.985	0.991
LightGBM	0.008	0.92	0.305	0.98	382.642	0.996

fitting. All three machine learning methods provide good fitting accuracy, and all points of the test set are close to a straight line, and the true value is close to the predicted value (Figure 4). Moreover, the LightGBM algorithm has the highest accuracy (Table 4). Therefore, the LightGBM algorithm was selected to retrieve the water depth, salinity, and lithium concentration.

In 2017, the water depth at the South Lake verification point was about 0.3 m. LightGBM predicted a water depth of 0.32 m at this point without the training data of South Lake, which is a good match. The water depth inversion result is shown in Figures 5A,B. This result shows that the machine learning algorithm can accurately predict the water depth using images with different dates. The water depth changes of the North and South Lakes are completely opposite. The water depth of the North Lake in 2017 was more than 1.5 m, which was much higher than in 2000, while the water depth of the South Lake in 2017 was lower than in 2000.

The salinity at the South Lake verification point was 23%, and the predicted value was 22.5% in 2017. The salinity predicted by LightGBM agreed well with the measurements, indicating the machine learning algorithm can accurately predict the salinity of lake water. The salinity inversion results are shown in Figures 5C,D. Salinity ranged from 21 to 29% in 2000 and from 19 to 21% in 2017, indicating a downward trend in salinity in the South Lake.

Figures 5E,F show the result of the inversion of lithium concentration in lake water. It was above 530 mg/L in 2000 and below 530 mg/L in 2017, which shows a significant downward trend in the last 20 years. The lithium concentration at the South Lake verification point was 372 mg/L, and the predicted value was 527 mg/L in 2017. The actual value is lower than the inversion result, indicating that the actual downward trend of lithium concentration is more significant than the inversion result.

After inversion and calculation, the total lithium content was determined (Figure 6). In the North Lake, the total water volume in 2000 was 1,037.22 × 10^5 m^3, resulting in a total salt content of 35.94 million tons. The total water volume in 2017 was 1,667.19 × 10^5 m^3, with a total salt content of 39.83 million tons. In the South Lake, the total water volume in 2000 was 269.36 × 10^5 m^3, and the total salt content was 7.734 million tons. After the development and exploitation of South lake, the water volume and salt content have decreased by about 27% and about 30%, respectively. In the last 20 years, the water volume of the North Lake has increased significantly, with a growth rate of 60.73%. In 2000, there were 653,700 tons of lithium carbonate in the North Lake and 81,800 tons in the South Lake; in 2017, there were 462,500 tons in the North Lake and 53,000 tons in the South Lake. The lithium resources decreased by 29.2% in the North Lake and 35.2% in the South Lake.

4 Discussion

4.1 The changes of Zabuye Salt Lake from 2000 to 2017

In this study, Landsat remote sensing imagery is used to determine the salinity and lithium concentration of the Zabuye Salt Lake, and the influence of salt lake expansion on salt and lithium content from 2000 to 2017 is analyzed. The Zabuye Salt Lake is recharged by atmospheric precipitation, alpine ice and snowmelt water, and spring water. Annual precipitation and evaporation obtained from field observation stations (Figure 7A) show no significant changes in precipitation and evaporation, so atmospheric precipitation is not the major reason for those changes in Zabuye Salt Lake.

Meteorological data from the Zabuye Salt Lake Observatory show that the temperature in the area has increased over the past 20 years (Figure 7B). Under the influence of climate change, the surrounding glaciers have melted, and river discharge in the Zabuye area has increased significantly, resulting in an increase in water volume and depth in the North Lake. The water depth in South Lake has decreased over the past 20 years due to the extensive development and utilization of lithium-bearing brine.

The expansion of the Zabuye Salt Lake will have a series of impacts on the quality of mineral resources. The most important impact on the lake water is the decrease in salinity and lithium concentration. From 2000 to 2017, the salinity of the North Lake shows a significant downward trend, while the salinity of the South Lake decreased slightly. The main reason for this is the difference

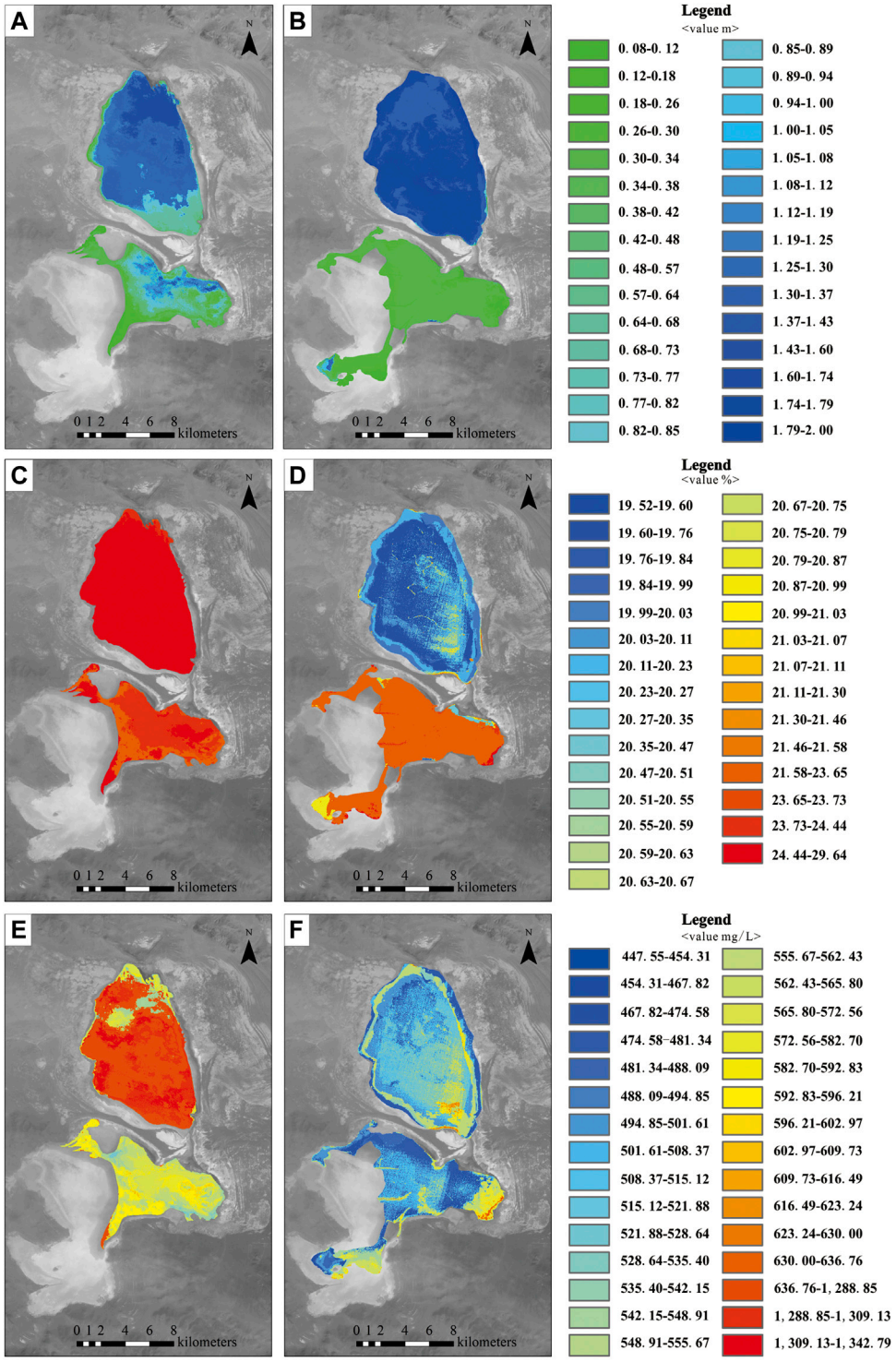

FIGURE 5
Water depth, salinity and lithium concentration inversion results. Water depth in **(A)** 2000 and **(B)** 2017; Salinity in **(C)** 2000 and **(D)** 2017; Lithium concentration in **(E)** 2000 and **(F)** 2017.

of replenishment between the two lakes. Another reason is the dry salt flats replenish South Lake time to time. The difference in recharge between the two lakes is due to surface runoff and subsurface runoff. In addition to the spring water from Qiulinanmu, the North Lake is recharged by four large surface runoffs and several subsurface drains, while the South Lake is

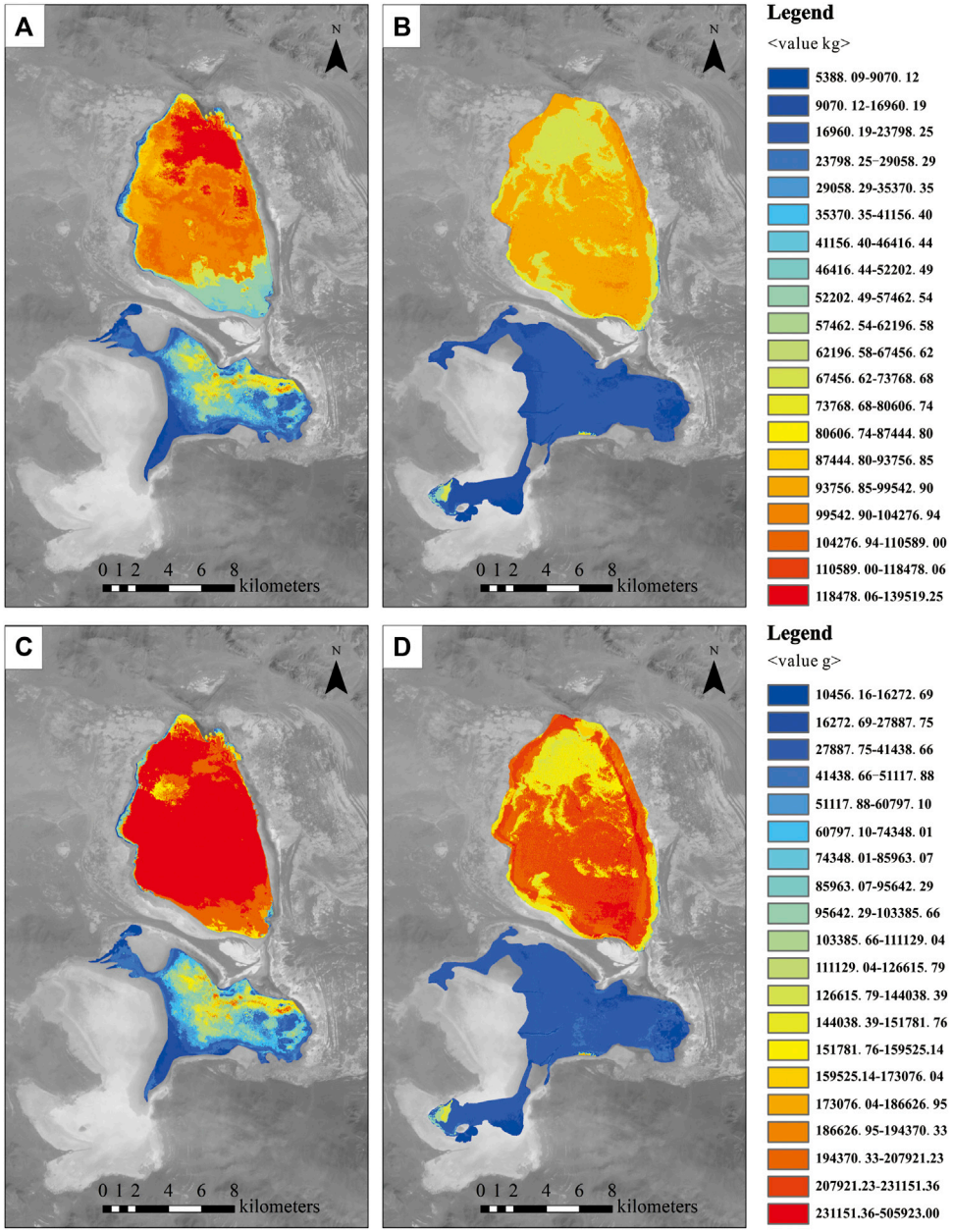

FIGURE 6
The total salinity and lithium content assessment results. Total salt content in **(A)** 2000 and **(B)** 2017; Total lithium content in **(C)** 2000 and **(D)** 2017.

mainly recharged by spring water from Zabuye Island. In addition, the dry salt flats around the South Lake can replenish the salt in the South Lake, so the salinity decrease is less than in the North Lake.

The downward trend of lithium concentration is also obvious. In 2000, the lithium concentration in salt lakes was above 530 mg/L, and after 2017, most of them were below 530 mg/L. The distribution of lithium concentration shows a certain regularity that gradually increase from north to south. Because the spring water is mainly distributed in the north of the lake and flows into the lake from north to the south. Normally, the lithium concentration of the spring water is lower than lake water, so the lithium concentration tends to increase from north to south.

The North Lake is an undeveloped lake, and the inversion results show that the lithium resources of the North Lake have decreased which may be related to the increasing temperature.

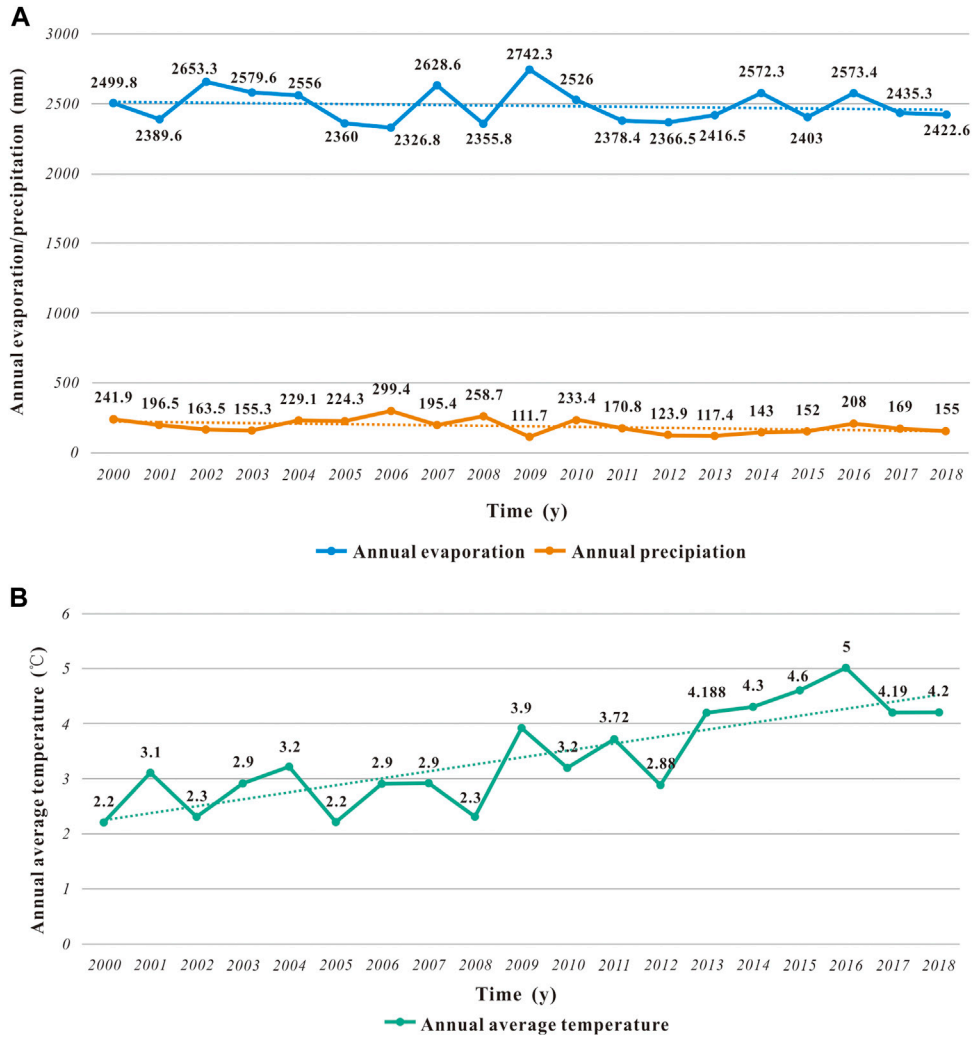

FIGURE 7
Evaporation, precipitation and temperature changes in Zabuye Salt Lake from 2000 to 2018. **(A)** Evaporation and precipitation trends from 2000 to 2018; **(B)** Temperature trend from 2000 to 2018.

The increase in temperature in the lake catchment cause the precipitation of lithium carbonate and then dissolved lithium resources in lake waters decrease accordingly. One reason for the decrease of lithium resources in the South Lake is the precipitation of lithium carbonate, and another reason is the development and utilization of the South Lake. In 2000, there were 653,700 tons of lithium carbonate in North Lake and 81,800 tons in the South Lake; in 2017, there were 462,500 tons in North Lake and 53,000 tons in South Lake. The lithium resources decreased by 29.2% in North Lake and 35.2% in South Lake. Based on the precipitation of lithium carbonate in the North Lake which was 29.2% from 2000 to 2017, we suggested the decrease of 4,900 tons in the South Lake is most likely attributed to the development and utilization. However, the mining volume of lithium in South Lake has far exceeded 4,900 tons in the past 20 years. Therefore, the spring water and dry salt flats of South Lake have provided large quantities of lithium for the South Lake.

4.2 Remote sensing inversion technology

Landsat satellite imagery has recorded global changes over the past 50 years, and provides important historical data for studying areas that have only recently been developed and exploited, such as the Tibetan Plateau. Satellite imagery and image processing can be used to monitor resources and environmental changes

comprehensively and accurately, providing scientific support for resource development and environmental protection. In this study, the machine learning algorithms were used for inversion and information extraction in areas with incomplete data. The result shows that machine learning algorithms can provide accurate predictions using limited training data, and enable multi-dimensional feature analysis. Existing inversion studies for the salt lake generally use combination of one or more bands. While it is feasible to fit the value of water parameters at a given time point, scalability at multiple time points is limited. This study uses the effective information of the whole band, while using the automatic screening feature of the LightGBM algorithm to reduce the data dimension and significantly improve the inversion accuracy.

The idea of using Big Data is contribute to realize the inversion and extraction of salt lake information. The accumulation of measured data is of great significance. When the amount of measured data is relatively large, machine learning between different lakes in different time periods can also make more accurate predictions. If the measured data of multiple salt lakes in multiple time periods are combined into a large data set, the mineral concentrations of salt lakes can be predicted without observation stations or measured data, which will save a lot of manpower and material resources for managing the development and utilization of salt lakes.

The inversion of mineral concentration in salt lakes also depends on the quality of remote sensing images. In the future, we can also strengthen the spectral exploration of minerals, improve the ability of remote sensing satellites to acquire information, and comprehensively improve the spatial and spectral resolution. Thus, we can obtain relatively accurate information about lake water without the support of measurement data, and make better use of remote sensing technology.

5 Conclusion

In this study, the Landsat remote sensing data and a high-precision LightGBM algorithm were used for the inversion of water depth, salinity, and lithium concentration. To improve the generalizability of the model and overcome the shortcomings of incomplete measured data, data in Zabuye Lake from 2000 to 2017 were selected for training the model. After a series of image processing, data statistics, and analysis, we came to the following conclusions:

Compared to 2000, the water depth of the lake increased in 2017, as did the water volume. The expansion of the Zabuye Salt Lake led to the decrease in salinity and lithium concentration. After the extensive development and exploitation of the South lake, the total amount of salt and lithium resources decreased from 2000 to 2017, with more dramatical trend in South Lake.

The salt lake inversion method in this study proved that the LightGBM algorithm has higher prediction accuracy than conventional analysis methods. Machine learning algorithms are feasible and superior in remote sensing inversion research. In addition, the accumulation of measurement data is of great significance to the analysis and prediction of salt lakes.

Remote sensing images contain important spectral information that can be used in inversion studies for salt lakes. With the development of remote sensing technology in recent years, the spatial and spectral resolutions of remote sensing images have greatly improved, which is important for more detailed assessment of salt lake resources in the future.

Data availability statement

The original contributions presented in the study are included in the article/supplementary material, further inquiries can be directed to the corresponding author.

Author contributions

JD wrote the manuscript, designed the study and provided guidance and funds; TL and YZ collected the material and performed the investigation; ST, CY, and ZN provided the geological information and guidance. All authors contributed to manuscript revision, read, and approved the submitted version.

Funding

This research was supported by the Academician Workstation Projects (HE2205 and HE2206), the National Natural Science Foundation of China (42172332), the China geological survey project (DD20221684), and the Basic Research Projects of the Institute of Mineral Resources, Chinese Academy of Geological Sciences (KK2102).

Acknowledgments

We would like to acknowledge assistance from the Institute of Mineral Resources of the Chinese Academy of Geological Sciences, the Zabuye Salt Lake field observation station of the Chinese Academy of Geological Science and China University of Geosciences (Beijing) for providing us with the field measured data. We are also grateful to Yongjie Lin, Andong Chen and Fanjing Kong from the Institute of Mineral Resources,

Chinese Academy of Geological Sciences for their constructive comments, which improved the paper significantly.

Conflict of interest

The authors declare that the research was conducted in the absence of any commercial or financial relationships that could be construed as a potential conflict of interest.

Publisher's note

All claims expressed in this article are solely those of the authors and do not necessarily represent those of their affiliated organizations, or those of the publisher, the editors and the reviewers. Any product that may be evaluated in this article, or claim that may be made by its manufacturer, is not guaranteed or endorsed by the publisher.

References

Cao, H., Han, L., Li, W., Liu, Z., and Li, L. (2021). Inversion and distribution of total suspended matter in water based on remote sensing images-A case study on yuqiao reservoir, China. *Water Environ. Res.* 93 (4), 582–595. doi:10.1002/wer.1460

Chen, K., Kao, W., and Tzeng, Y. (1995). Retrieval of surface parameters using dynamic learning neural network. *Int. J. Remote Sens.* 16 (5), 801–809. doi:10.1080/01431169508954444

Dionisio, R. E., Marcello, J., Eugenio, F., Angel, G. R., and Consuelo, G. M. (2017). Object-based quality evaluation procedure for fused remote sensing imagery. *Neurocomputing* 255, 40–51. doi:10.1016/j.neucom.2016.06.091

Duba, R. D., Girma, D. T., Achim, I., and Gachena, N. W. (2021). Diagnosis of diabetes mellitus using gradient boosting machine (LightGBM). *Diagnostics* 11 (9), 1714. doi:10.3390/diagnostics11091714

Fan, J., Luo, Y., Tan, S., Ma, W., Zhang, H., and Liu, F. (2021). Accuracy evaluation of the FY-3C/MWRI land surface temperature product in Hunan Province. *Remote Sens. Land & Resour.* 33 (1), 249–255. doi:10.6046/gtzyyg.2020066

Figueiredo, I. N., Pinto, L., and Gonçalves, G. (2016). A modified lyzenga's model for multispectral bathymetry using tikhonov regularization. *IEEE Geosci. Remote Sens. Lett.* 13 (1), 53–57. doi:10.1109/lgrs.2015.2496401

Forget, P., Ouillon, S., Lahet, F., and Broche, P. (1999). Inversion of reflectance spectra of nonchlorophyllous turbid coastal waters. *Remote Sens. Environ.* 68, 264–272. doi:10.1016/S0034-4257(98)00117-5

Gábor, C., Krisztina, L. P., Bence, F., Ádám, M., and Veronika, K. (2022). Human activity recognition of children with wearable devices using LightGBM machine learning. *Sci. Rep.* 12 (1), 5472. doi:10.1038/s41598-022-09521-1

Kong, W., Bu, L., Zheng, M., and Nie, Z. (2017). Overview of salt lake stations on Tibetan Plateau. *Sci. Technol. Rev.* 35 (6), 103–107. doi:10.3981/j.issn.1000-7857.2017.06.013

Larya, D. J., Alavib, A. H., Gandomic, A. H., and Walker, A. L. (2016). Machine learning in geosciences and remote sensing. *Geosci. Front.* 7, 3–10. doi:10.1016/j.gsf.2015.07.003

Lei, L. (2019). *Study on changes of lake areas since 2000 and it response to the climatic factors in Tibetan Plateau*. Chengdu, China: Chengdu University of Technology.

Letey, J., Hoffman, G. J., Hopmans, J. W., Grattan, S. R., Suarez, D., Corwin, D. L., et al. (2011). Evaluation of soil salinity leaching requirement guidelines. *Agric. Water Manag.* 98, 502–506. doi:10.1016/j.agwat.2010.08.009

Li, L., Li, Y., Yu, D., Liu, Z., Gao, Ya., and Qian, J. (2021). A multi-organ fusion and LightGBM based radiomics algorithm for high-risk esophageal varices prediction in cirrhotic patients. *IEEE Access* 9, 15041–15052. doi:10.1109/ACCESS.2021.3052776

Li, Y., Li, Y., Shi, K., Lv, H., Guo, Y., Zhou, L., et al. (2013). Evaluation of total suspended matter based on spectral classification. *Spectrosc. Spect. Anal.* 3 (10), 2721–2726. doi:10.3964/j.issn.1000-0593(2013)10-2721-06

Liu, F., Wang, C., and Wang, X. (2018). Application of near-surface remote sensing in monitoring the dynamics of forest canopy phenology. *J. Appl. Ecol.* 29 (6), 1768–1778. doi:10.13287/j.1001-9332.201806.016

Liu, X., Zheng, M., and Qi, Wen. (2007). Sources of ore-forming materials of the superlarge B and Li deposit in Zabuye salt lake, Tibet, China. *Acta Geol. Sin.* 81 (12), 1709–1715. doi:10.3321/j.issn:0001-5717.2007.12.011

Lu, S., Xiao, G., Jia, L., Zhang, W., and Luo, H. (2016). Extraction of the spatial-temporal lake water surface dataset in the Tibetan Plateau over the past 10 years. *Remote Sens. Land. Resour.* 28 (3), 181–187. doi:10.6046/gtzzyg.2016.03.28

Lu, T., Chen, S., Tu, Y., Yu, Y., Cao, Y., and Jiang, D. (2019). Comparative study on coastal depth inversion based on multi-source remote sensing data. *Chin. Geogr. Sci.* 29 (2), 192–201. doi:10.1007/s11769-018-1013-z

Luo, S. S., and Zheng, M. P. (2004). Exploitation actuality of saline lake lithium resources in Tibet. *Geol. Prospect.* 40 (3), 11–14. doi:10.3969/j.issn.0495-5331.2004.03.003

Lyzenga, D. R. (1978). Passive remote sensing techniques for map-ping water depth and bottom features. *Appl. Opt.* 17 (3), 379–383. doi:10.1364/AO.17.000379

Mao, Z., Chen, J., Pan, D., Tao, B., and Zhu, Q. (2012). A regional remote sensing algorithm for total suspended matter in the east China sea. *Remote Sens. Environ.* 124, 819–831. doi:10.1016/j.rse.2012.06.014

Maxwell, A. E., Warner, T. A., and Fang, F. (2018). Implementation of machine-learning classification in remote sensing: An applied review. *Int. J. Remote Sens.* 39 (9), 2784–2817. doi:10.1080/01431161.2018.1433343

MinJee, K., HyeIn, L., JaeHyun, C., Jae, L. K., and Changyeun, M. (2022). Development of a soil organic matter content prediction model based on supervised learning using vis-NIR/SWIR spectroscopy. *Sensors* 22 (14), 5129. doi:10.3390/s22145129

Nhu, V. H., Mohammadi, A., Shahabi, H., Shirzadi, A., Al-Ansari, N., Ahmad, B. B., et al. (2020). Monitoring and assessment of water level fluctuations of The lake Urmia and its environmental consequences using multitemporal Landsat 7 ETM+Images. *Int. J. Environ. Res. Public Health* 17, 4210–4216. doi:10.3390/ijerph17124210

Pan, X., Li, G., Liu, F., Wu, X., Kondoh, A., and Shen, Y. (2015). Using remote sensing to determine spatio-temporal variations in winter wheat growing area in the North China Plain. *Chin. J. Eco-Agriculture* 23 (4), 497–505. doi:10.13930/j.cnki.cjea.141505

Pan, Z., Fang, S., and Wang, H. (2021). LightGBM technique and differential evolution algorithm-based multi-objective optimization design of DS-APMM. *IEEE Trans. Energy Convers.* 36 (1), 441–455. doi:10.1109/TEC.2020.3009480

Qi, W., and Zheng, M. (2006b). Time-serial analyses of water level fluctuation of Zabuye salt lake, Tibet. *Sci. Geogr. Sin.* 26 (6), 693–700. doi:10.3969/j.issn.1000-0690.2006.06.009

Qi, W., and Zheng, M. (2006a). Winters and ARIMA model analysis of The lake ievel of salt lake Zabuye, tibeatan plateau. *J. Lake Sci.* 18 (1), 21–28. doi:10.3321/j.issn:1003-5427.2006.01.003

Rogan, J., Miller, J., Stow, D., Franklin, J., Levien, L., and Fischer, C. (2003). Land-cover change monitoring with classification trees using Landsat TM and ancillary data. *Photogramm. Eng. remote Sens.* 69 (7), 793–804. doi:10.14358/PERS.69.7.793

Rouet-Leduc, B., Hulbert, C., Lubbers, N., Barros, K., Humphreys, C. J., and Johnson, P. A. (2017). Machine learning predicts laboratory earthquakes. *Geophys. Res. Lett.* 44, 9276–9282. doi:10.1002/2017GL074677

Shi, K., Li, Y., Liu, Z., Xu, Y., Xu, X., Ma, W., et al. (2011). Estimation of total suspended matter concentration based on semi-analysis algorithm in inland turbid waters. *Environ. Sci.* 32 (6), 1571–1580. doi:10.13227/j.hjkx.2011.06.016

Siswanto, E., Tang, J., i Yamaguchi, H., Ahn, Y., Ishizaka, J., Yoo, S., et al. (2011). Empirical ocean-color algorithms to retrieve chlorophyll-a, total suspended matter, and colored dissolved organic matter absorption coefficient in the Yellow and East China Seas. *J. Oceanogr.* 67, 627–650. doi:10.1007/s10872-011-0062-z

Song, J., Liu, G., Jiang, J., Zhang, P., and Liang, Y. (2021). Prediction of protein–ATP binding residues based on ensemble of deep convolutional neural networks and LightGBM algorithm. *Int. J. Mol. Sci.* 22 (2), 939. doi:10.3390/ijms22020939

Su, H., Liu, H., and Heyman, W. (2008). Automated derivation of bathymetric information from multi-spectral satellite imagery using a non-linear inversion model. *Mar. Geod.* 31 (4), 281–298. doi:10.1080/01490410802466652

Tang, J. W., Tian, G., Wang, X., Wang, X., and Song, Q. (2004). The methods of water spectra measurement and analysis Ⅰ: Above-water method. *J. Remote Sens.* 9 (1), 37.

Tian, S., Hong, Y., and Qin, X. (2006). A remote sensing approach to the depth of the highly concentrated salt lake. *Remote Sens. Land. Resources* 1, 26.

Tian, S., Qin, X., Zheng, M., Hong, Y., and Kuang, S. (2005). Quantitative analysis of remote sensing on the total salinity of Zabuye salt lake in Tibet. *Geoscience* 19 (4), 506.

Vivone, G., Mura, M. D., Garzelli, A., Restaino, R., Scarpa, G., Ulfarsson, M. O., et al. (2020). A new benchmark based on recent advances in multispectral pansharpening: Revisiting pansharpening with classical and emerging pansharpening methods. *IEEE Geosci. Remote Sens. Mag.* 9 (1), 53–81. doi:10.1109/mgrs.2020.3019315

Wang, D. (2019). *Models for predicting the Li content in salt lake based on remote sensing: A case study of Argentina's arzaro salt lake*. Jilin, China: Jilin University.

Xi, H., and Zhang, Y. (2011). Total suspended matter observation in the Pearl River estuary from *in situ* and MERIS data. *Environ. Monit. Assess.* 177, 563–574. doi:10.1007/s10661-010-1657-3

Xie, Y., Xiang, W., Ji, M., Peng, J., and Huang, Y. (2019). An application and analysis of forecast housing rental based on xgboost and lightgbm algorithms. *Comput. Appl. Softw.* 36 (9), 152–155. doi:10.3969/j.issn.1000-386x.2019.09.027

Xu, W., Bu, L., Kong, W., Zheng, M., and Nie, Z. (2017). Monitoring of the dynamic change of Zabuye salt lake: A remote sensing approach. *Sci. Technol. Rev.* 35 (6), 89–96. doi:10.3981/j.issn.1000-7857.2017.06.011

Yagmur, N., Bilgilioglu, B. B., Dervisoglu, A., Musaoglu, N., and Tanik, A. (2021). Long and short-term assessment of surface area changes in saline and freshwater lakes via remote sensing. *Water Environ. J.* 35, 107–122. doi:10.1111/wej.12608

Yan, L., and Zheng, M. (2015). Influence of climate change on saline lakes of the Tibet Plateau, 1973-2010. *Geomorphology* 246, 68–78. doi:10.1016/j.geomorph.2015.06.006

Yang, K., Yao, F., Dong, D., Dong, W., and Luo, J. (2017). Spatiotemporal monitoring of lake area dynamics on the Tibetan plateau. *J. Geo-information Sci.* 19 (7), 972–982. doi:10.3724/SP.J.1047.2017.00972

Zhang, C., He, J., and Ma, Z. (2013). Remote sensing monitor of sea fog in fujian coastal region. *Chin. J. Agrometeorology* 34 (3), 366–373. doi:10.3969/j.issn.1000-6362.2013.03.018

Zhang, M., Tang, J., Dong, Q., Song, Q., and Ding, J. (2010). Retrieval of total suspended matter concentration in the Yellow and East China Seas from MODIS imagery. *Remote Sens. Environ.* 114 (2), 392–403. doi:10.1016/j.rse.2009.09.016

Zhang, Y., Liu, M., Wang, X., Zhu, G., and Chen, W. (2009). Bio-optical properties and estimation of the optically active substances in Lake Tianmuhu in summer. *Int. J. Remote Sens.* 30 (11), 2837–2857. doi:10.1080/01431160802558592

Zhang, Y., Wang, Y., Gao, M., Ma, Q., Zhao, J., Zhang, R., et al. (2019). A predictive data feature exploration-based air quality prediction approach. *IEEE Access* 7, 30732–30743. doi:10.1109/ACCESS.2019.2897754

Zheng, M., and Liu, W. (1987). New lithium mineral-zabuyeite. *Acta Mineral. Sin.* (03), 221.

Zheng, M. P., Xiang, R. J., and Ge, Z. H. (2004). Exploitation actuality and prospect of saline lake resources in Western China. *Land Resour. Inf.* (2), 21–25.

Zhou, Y., Zhang, R., Ma, H., Zhang, J., and Zhang, X. (2016). Retrieving of salt lake mineral ions salinity from hyper - spectral data based on BP neural network. *Remote Sens. Land. Resour.* 28 (2), 34–40. doi:10.6046/gtzyyg.2016.02.06

Zhu, W., Yu, Q., Tian, Y., Chen, R., and Gardner, G. B. (2011). Estimation of chromophoric dissolved organic matter in the Mississippi and Atchafalaya river plume regions using above-surface hyperspectral remote sensing. *J. Geophys. Res.* 116 (C2), C02011. doi:10.1029/2010JC006523

frontiers | Frontiers in Earth Science

TYPE Original Research
PUBLISHED 06 January 2023
DOI 10.3389/feart.2022.1033124

OPEN ACCESS

EDITED BY
Qiuming Pei,
Southwest Jiaotong University, China

REVIEWED BY
Hua-Wen Cao,
China Geological Survey, China
Kit Lai,
Fortescue Metals Group, Australia
Huan Li,
Central South University, China

*CORRESPONDENCE
Chenghui Wang,
wangchenghui@mail.cgs.gov.cn
Yubin Li,
liyb73@163.com

SPECIALTY SECTION
This article was submitted to Structural Geology and Tectonics, a section of the journal Frontiers in Earth Science

RECEIVED 31 August 2022
ACCEPTED 20 December 2022
PUBLISHED 06 January 2023

CITATION
Li Y, Wang C, Li Y, Sun Y, Puchi M, Zhang X, Lamu G and Yang Z (2023), Genesis of the Abunabu antimony deposits in the Tethys Himalayan metallogenic belt: Evidence from He–Ar and S isotopes of stibnite. *Front. Earth Sci.* 10:1033124. doi: 10.3389/feart.2022.1033124

Genesis of the Abunabu antimony deposits in the Tethys Himalayan metallogenic belt: Evidence from He–Ar and S isotopes of stibnite

Yang Li[1,2], Chenghui Wang[2]*, Yubin Li[3]*, Yan Sun[2], Mima Puchi[4], Xudong Zhang[5], Gesang Lamu[6] and Zong Yang[7]

[1]College of Earth Sciences, Chengdu University of Technology, Chengdu, Sichuan, China, [2]Institute of Mineral Resources, Chinese Academy of Geological Sciences, Beijing, China, [3]College of Engineering, Tibet University, Lhasa, Tibet, China, [4]Regional Geological Survey Team, Tibet Bureau of Geological Exploration and Development, Lhasa, Tibet, China, [5]No.5 Geological Brigade, Tibet Bureau of Geological Exploration and Development, Golmud, Qinghai, China, [6]No.6 Geological Brigade, Tibet Bureau of Geological Exploration and Development, Lhasa, Tibet, China, [7]Geological Survey Institute of Tibet Autonomous Region, Lhasa, Tibet, China

Introduction: The Abunabu antimony mining area is located between the Indus–Yarlung Tsangpo suture and the southern Tibetan detachment system. Ore deposits in the mining area provide an excellent opportunity to understand the nature and genesis of antimony mineralisation in the Tethys Himalayan metallogenic belt.

Methods: In this study, we analysed the He–Ar and S isotopic compositions of stibnite-hosted fluid inclusions as a basis for investigating the sources of ore-forming fluids in the Abunabu mining area and the Tethys Himalayan metallogenic belt.

Results: The analysed stibnites have ^{4}He contents of 0.016×10^{-7}–1.584×10^{-7} cm^3 STP/g, ^{40}Ar contents of 1.37×10^{-7}–2.94×10^{-7} cm^3 STP/g, $^{40}Ar/^{36}Ar$ ratios of 303.8–320.7, and $^{3}He/^{4}He$ (Ra) ratios of 0.021–0.351. These isotopic features indicate that the ore-forming fluids were primarily metamorphic fluids of crustal origin, with small amounts of magmatic-derived materials and modified air-saturated water with low $^{40}Ar^*/^{4}He$ ratios. The $\delta^{34}S$ values of stibnite vary within a narrow range of −4.9‰ to −3.5‰, with a mean value of −4.31‰, indicating a deep magmatic origin.

Discussion: On the basis of these results and a compilation of data for sulphide deposits in the metallogenic belt, we infer that compositional variations in the He and Ar isotopes of the ore-forming fluids of each antimony deposit in the Tethys Himalayan metallogenic belt are independent of each other. This suggests that antimony deposits in the belt had similar ore-forming fluid sources and mixing processes and that differences in the metallogenic tectonic setting within the belt emerged only in the later stages of deposit evolution. Our new results and compiled data also show that antimony–gold deposits and lead–zinc–antimony polymetallic deposits in the Tethys Himalayan metallogenic belt differ in their sulphur isotopic compositions and that multiple sulphur sources were involved in each of these types of deposit.

KEYWORDS

source of ore-forming fluid, metallogenic phase, Tethys Himalaya, Abunabu antimony mining area, He-Ar-S isotopes

1 Introduction

The Tethys Himalayan lead–zinc–antimony polymetallic metallogenic belt is located in southern Tibet and consists of various types of Cenozoic polymetallic deposit, such as antimony, antimony–gold, gold, lead–zinc, and lead–zinc–antimony deposits. Major deposits include the Cheqiongzhuobu antimony, Abunabu antimony, Mazhala antimony–gold, Chapula gold, Jisong lead–zinc, and Zhaxikang lead–zinc–antimony polymetallic deposits (Yang et al., 2006; 2009; Zheng et al., 2014; Sun et al., 2016; Sun et al., 2018; Zhai et al., 2018; Cao et al., 2019; Wang et al., 2020; Zhang et al., 2021). Although no copper or molybdenum deposits have been discovered in this metallogenic belt, rare-metal (such as tungsten, tin, beryllium, and rubidium) ore deposits have been discovered (Li et al., 2017; Liang et al., 2018; Cao et al., 2021). The Tethys Himalayan metallogenic belt has attracted broad scientific interest, and numerous studies have focused on the ore-forming geological features, ore-controlling factors, metallogenic material sources, metallogenic epochs, and ore-forming processes of antimony–(gold) and lead–zinc deposits (Nie et al., 2005; Hou et al., 2006; Yang et al., 2006; Qi et al., 2008; Zheng et al., 2012; Zhai et al., 2014; Duan et al., 2016; Wang et al., 2017; Xie et al., 2017; Liang et al., 2018; Sun et al., 2018). Some previous studies have established the properties and sources of ore-forming fluids in the antimony deposits (Meng et al., 2008; Yang et al., 2009; Zhu et al., 2012; Xie et al., 2017). Investigation of ore-forming fluids is crucial to the study of hydrothermal ore deposits because these fluids can be used to determine the type of ore deposit, establish the genesis of ore deposits, and guide exploration (Guo et al., 2011). Previous studies have investigated ore deposits in the Longzi–Cuona–Cuomei–Jiangzi area in the eastern Tethys Himalayan metallogenic belt (Wen et al., 2006; Yang et al., 2006; Zhu et al., 2012; Xie et al., 2017; Wang, 2019a; Wang, 2019b; Liang, 2019; Wang et al., 2021). However, the genesis of the antimony, gold, antimony–gold, and lead–zinc–antimony polymetallic deposits in the central and western parts of this metallogenic belt remains poorly understood and continues to be debated (Nie et al., 2005; Yang et al., 2006; Yang et al., 2009; Kali et al., 2010; Hou and Zhang, 2015; Xie et al., 2017). One of the major topics of debate is the classification of the genetic type of the antimony–gold deposits in the belt, with proposals including hydrothermal-vein (Duan et al., 2016), exhalation sedimentation–hydrothermal reformation (Zheng et al., 2014), epithermal cryogenic hydrothermal (Qi et al., 2008) and orogenic (Zhai et al., 2014; Zhai et al., 2018) types.

The Abunabu antimony mining area is located in the western Tethys Himalayan metallogenic belt, approximately 164 km southeast of Shiquanhe Town, Gar County, in the Ali area of Tibet Autonomous Region. Earlier exploration campaigns have revealed that this is a large-scale antimony mining area, with a resource of more than 100,000 t at 4.93% antimony (Fang et al., 2006; Chen et al., 2011). Hence, studying the genesis of the ore deposits in the Abunabu mining area is of significance for revealing the nature and evolution of antimony mineralisation in the Tethys Himalayan metallogenic belt. In this paper, we report the results of detailed field geological and microscope mineralogical investigations and He–Ar–S isotopic geochemical analyses of the Hamuqu and Quzhen antimony deposits in the Abunabu mining area. In addition, we conduct a comparison with the He–Ar–S isotopic compositions of typical antimony deposits in the Tethys Himalayan metallogenic belt to clarify the sources of ore-forming fluids and metals.

2 Regional geological setting

The Himalaya–Tibetan orogen is a tectonic assemblage of five W–E-trending terranes: (from north to south), the Songpan–Ganzi, North Qiangtang, South Qiangtang, Lhasa, and Himalayan terranes. The Himalayan terrane is separated from the Lhasa Block by the Indus–Yarlung Tsangpo suture (IYTS) and from the Indian plate by the Main Frontal Thrust (Figure 1A; e.g.; Yin and Harrison, 2000; Zhang et al., 2004; 2007; Zhang, Zhang, et al., 2012; Cao et al., 2018; Dai et al., 2020; Pan et al., 2022; Ma et al., 2022). The Himalayan terrane is divided (from north to south) into the Tethys Himalayan sequence (THS), the Greater Himalayan Crystalline Complex (GHC), the Lesser Himalayan sequence (LHS), and the sub-Himalayan sequence (SHS), which are separated by the southern Tibet detachment system (STDS), the Main Central Thrust fault (MCT), and the Main Boundary Thrust fault (MBT), respectively (Burchfiel et al., 1992; Yin, 2006; Martin, 2017). Phanerozoic strata exposed in the THS have been deposited on the Indian passive continental margin (Cao et al., 2018; Cao et al., 2020) and comprise mainly Palaeozoic to Palaeogene, low-grade-metamorphic, siliceous clastic and carbonate rocks (Myrow et al., 2019). A series of north Himalayan gneiss domes are developed in the centre of the THS (Cao et al., 2021). Previous studies have suggested that the Neo-Tethyan Ocean opened before the Late Triassic (ca. 230 Ma; Cao et al., 2018) and that oceanic crust began to subduct north-eastward beneath the Lhasa terrane during the Triassic (Wang et al., 2016; Cao et al., 2018; Cao et al., 2020). Rift-related basalts and turbidites of the Langjiexue Group are exposed in the Himalayan region (Cao et al., 2018; 2021; Huang et al., 2018). During the Late Jurassic to Early Cretaceous, the Cuomei igneous province formed, and the Indian plate started to drift northwards from the Australian plate (Zhu et al., 2009; Olierook et al., 2019). During the Jurassic–Cretaceous, numerous marine clastic and carbonate rocks were deposited in the passive continental margin of India. These strata are important host rocks of Pb–Zn–Ag–Sb–Au deposits in the Himalayan region (Yang et al., 2009). Neo-Tethyan oceanic crust was completely subducted beneath the Lhasa plate, and intercontinental collision occurred between the Indian and Lhasa plates during the Cenozoic (55 ± 5 Ma; Hu et al., 2016; Searle, 2019), followed by the subduction of the Indian continental crust (Cao et al., 2021).

In detail, the Himalayan terrane is divided into four major tectonic units (Cao et al., 2018; Figure 1B), which (from north to south) are as follows: (1) The THS, consisting of lower Palaeozoic to Eocene clastic and carbonate rocks deposited on the northern Indian passive margin; (2) the GHC, composed of a Proterozoic to Palaeozoic upper-amphibolite- to granulite-facies metasedimentary sequence (Kohn, 2014); (3) the LHS, including a Proterozoic greenschist-to amphibolite-facies metasedimentary sequence (Richards et al., 2005; Kohn, 2014); and (4) the SHS (Neogene Siwalik Formation), comprising Miocene–Pliocene foreland basin deposits. These four tectonic domains are separated by five boundary systems; i.e., the IYTS, STDS, MCT, MBT, and MFT (Figure 1B; Guillot et al., 2008; Cao et al., 2018). Within the Himalayan terrane, two sub-parallel belts of Cenozoic leucogranites have been identified: the Tethys Himalayan leucogranite belt (also termed the north Himalayan granite) to the north and the High Himalayan leucogranite belt to the south (Figure 1B; Wu et al., 2015; Cao et al., 2022). Intrusions with evident silicification, sericitisation, and carbonatisation have a close

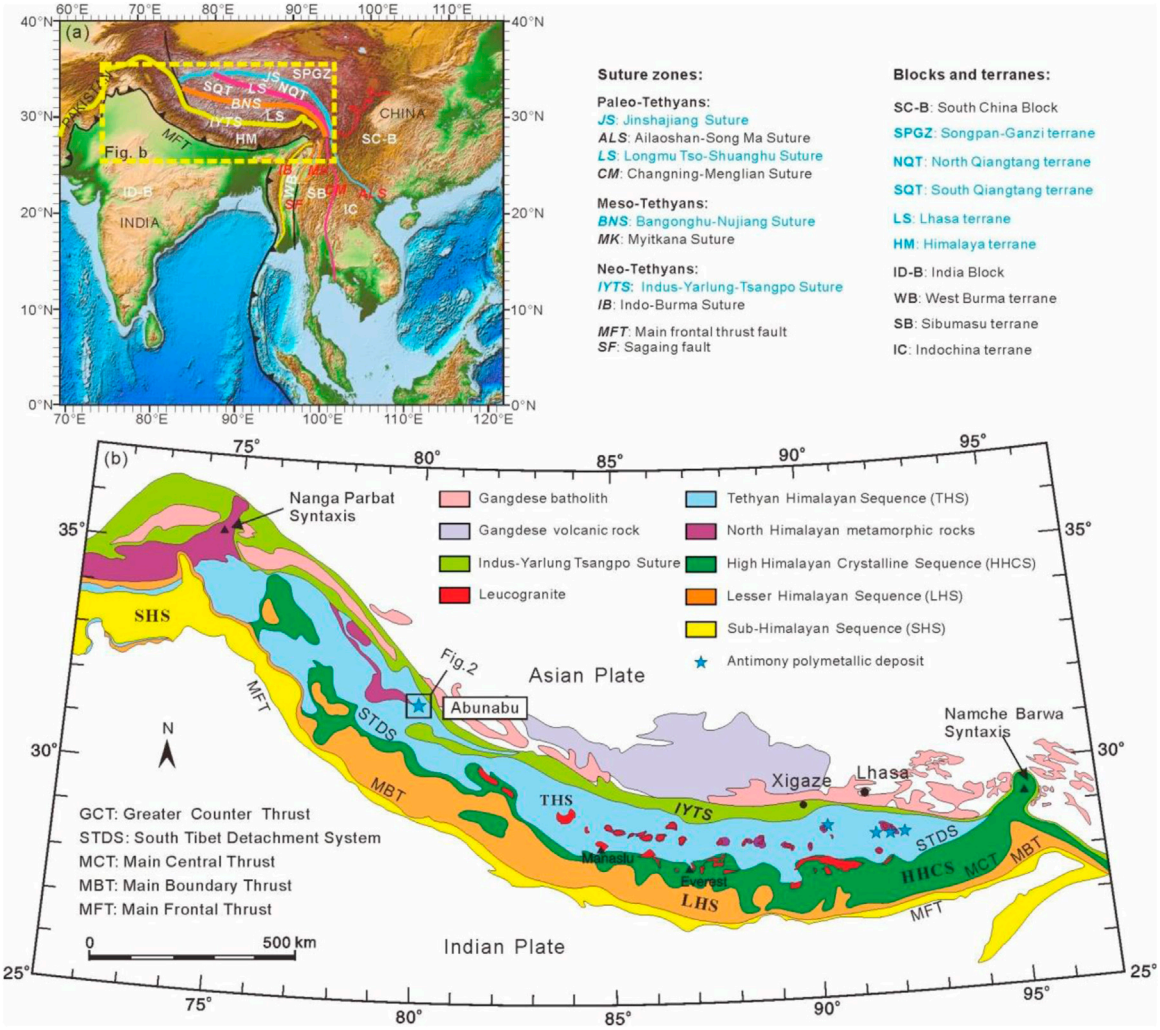

FIGURE 1
Tectonic map of the Himalaya–Tibetan Plateau region: **(A)** geotectonic sketch of southeastern Asia (Yin and Harrison, 2000; Cao et al., 2018); **(B)** simplified geological map of Himalaya, showing the major antimony polymetallic deposit (modified after Cao et al., 2018; Guillot et al., 2008; Zhang et al., 2019; Dai et al., 2020).

spatial relationship with antimony, antimony–gold, and gold deposits (Nie et al., 2005).

In terms of tectonic location, the Abunabu mining area is located in the southern margin of the Yarlung Tsangpo suture belt and the western section of the Tethys Himalayan metallogenic belt. The area contains mainly Silurian–Triassic, Palaeogene, and Quaternary strata (Figure 2). The main ore-bearing horizon is the Triassic Qiongguo Group ($T_{1\text{-}2}Q$), which is a set of lower-greenschist-facies metamorphic rock series with strong deformation. The primary lithology consists of slate, meta-sandstone (meta-conglomerate), and limestone, with mostly deep-sea turbidite deposits (Zhang et al., 2005).

The Late Cretaceous mélange (K_2mlg) is a tectonic–lithostratigraphic unit that is sporadically distributed as fragments and blocks. The exposed Nizha mélange (K_2nmlg) and Boku mélange (K_2bmlg) are material components of the ophiolite and mélange in the centre of the NW syncline in the western section of the Yarlung Tsangpo suture zone and together are also known as the northern tectonic mélange of the Brahmaputra junction. Magmatic rocks are distributed in the mining and surrounding areas and include Late Cretaceous Banguori lherzolite ($K_2b\varphi\sigma$), porphyritic quartz monzodiorite ($K_2\pi\eta\delta o$), and belugite ($K_2\delta\upsilon$). Medium–fine-grained ($E_2zx\eta\gamma$) and medium–coarse-grained ($E_2cz\eta\gamma$) monzogranites represent the products of plate subduction–collision events during the Mesozoic–Cenozoic evolution of the Tethyan tectonic regime (Zhang et al., 2005).

3 Ore deposit geology

The Hamuqu and Quzhen deposits (from old to new) are preserved in the Lower–Middle Triassic Qiongguo Group ($T_{1\text{-}2}Q$), the Palaeogene Liuqu Group ($E_{1\text{-}2}Lq$), and Quaternary strata (Figures 3A,B). Of these, the Quzhen deposit is hosted in Early Cretaceous ultramafic rocks ($K_1\Sigma$) and Late Cretaceous gabbros ($K_2\upsilon$) (Fang et al., 2006; Chen et al., 2011).

10.3389/feart.2022.1033124

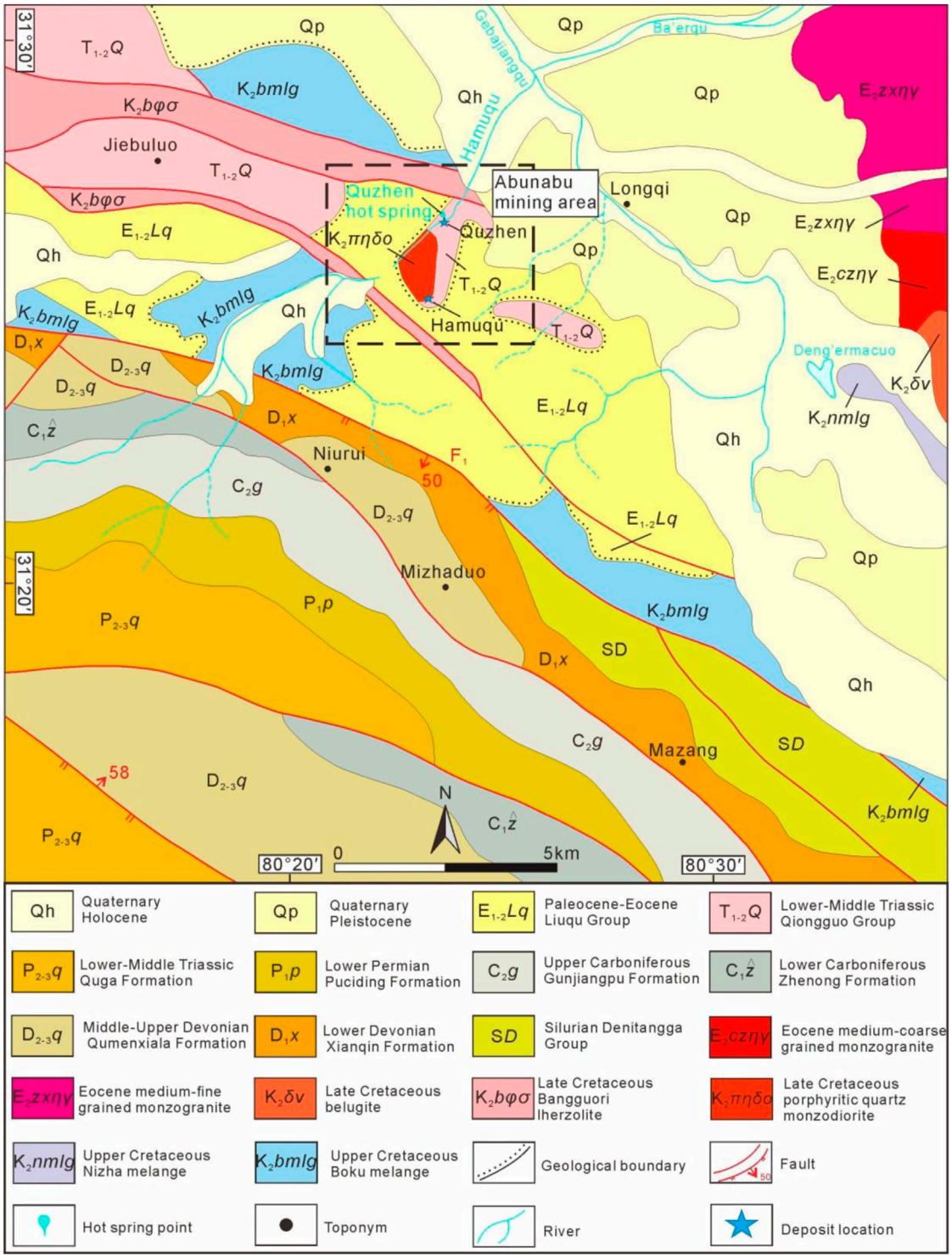

FIGURE 2
Regional geological map of Abunabu antimony ore concentration area (Zhang et al., 2005).

3.1 Hamuqu ore deposit

Two orebodies have been discovered in the Hamuqu antimony deposit. The mineralised alteration zone is formed in the Lower–Middle Triassic Qiongguo Group ($T_{1\text{-}2}Q$), which is a low-metamorphic-grade rock series composed of sericite slate and sericite siliceous slate. The No. I orebody is strictly controlled by the structure (faults) and is generally distributed along the NNE direction, with a steep dip angle of 65°–80° (Figure 4A). The No. II orebody is located to the northeast of the No. I orebody and is controlled by a NNE-trending pre-mineralisation fault; the wall-rock is Lower–Middle Triassic Qiongguo Group slate (Figure 3A). This orebody generally

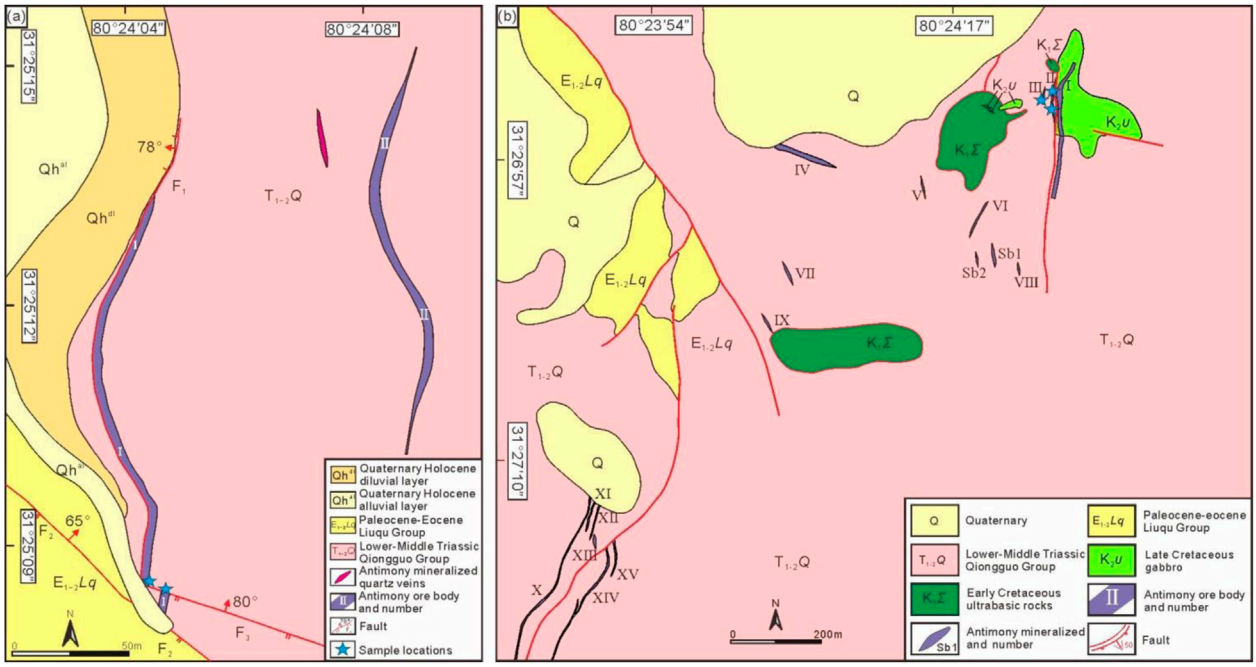

FIGURE 3
Geological maps of Hamuqu **(A)** and Quzhen **(B)** antimony deposits (Fang et al., 2006; Chen et al., 2011).

strikes NNE and is inclined WNW, with a dip angle of approximately 70°. The antimony orebodies of the Hamuqu deposit are mostly veined, bead-like, and lenticular. The ore minerals are primarily stibnite, with minor pyrite and arsenopyrite, whereas the gangue minerals are mainly quartz and sericite. The ore structure is dominated by columnar, columnar mosaic, and fragmentation and crush structures, appearing mostly in the form of crystal clusters, veinlet dissemination, agglomerates, and sparse dissemination (Figures 4C–F). Wall-rock alteration is dominated by silicification and sericitisation, with minor pyritisation. Stibnite mineralisation is closely related to silicification and sericitisation, with sericitisation occurring later than silicification (Fang et al., 2006).

3.2 Quzhen ore deposit

A total of 17 antimony orebodies have been found in the Quzhen deposit. Antimony orebodies I–II are developed primarily near Late Cretaceous altered gabbro ($K_2\upsilon$) plutons (Figure 4B), extending southwards to slate sandstone of the Lower–Middle Triassic Qiongguo Group ($T_{1\text{-}2}Q$). Antimony orebodies III–XV and Sb1–Sb2 occur in slate sandstone of the Lower–Middle Triassic Qiongguo Group ($T_{1\text{-}2}Q$) (Figure 3B). The antimony orebodies are mostly layered, veined and lenticular. The ore minerals are predominately stibnite, with minor pyrite, arsenopyrite, and valentinite; the gangue minerals are mainly quartz, muscovite, sericite, and chlorite. Stibnite crystals are primarily euhedral and subhedral, and some display fragmentation and metasomatic textures. Stibnite commonly occurs as granular aggregates with long columnar, radial, veinlet-disseminated, sparsely disseminated, crystal-cluster, and dense lumpy structures. Wall-rock alteration types are mainly silicification, carbonatisation, sericitisation, and pyritisation (Figures 4G–J). Silicification has generated numerous quartz veins and is closely related to mineralisation, as stibnite occurs mainly in zones of strong silicification (commonly containing quartz veins; Chen et al., 2011).

3.3 Stages of mineralisation in the abunabu deposits

Three stages of mineralisation can be identified in the deposits in the Abunabu mining area: (1) sedimentary metamorphic stage, (2) hydrothermal stage, and (3) supergene stage (Figure 5).

During the sedimentary metamorphic stage, sericite-, sericite–silica-, and sericite–silt-altered slates underwent regional dynamic metamorphism after undergoing regional N–S faulting and the formation of tectonic breccia. Sericite, muscovite, chlorite, and fine-grained quartz were generated by metamorphism of slate, without stibnite.

The hydrothermal stage was affected by regional extensional structures; early fault structures were reactivated, and numerous N–S-trending fault structures were formed. Deep ore-forming hydrothermal fluid ascended into shallow parts along fault structures and migrated into fault zones and the surrounding rocks. Multi-stage hydrothermal activity resulted in the alteration and mineralisation of slate, tectonic breccia, and magmatic rocks. Three different types of quartz formed during this stage and are spatially associated with large amounts of stibnite and quartz–sulphides and minor pyrite, arsenopyrite, and calcite.

Finally, in the supergene stage, after the hydrothermal stage and strong weathering, valentinite formed in orebodies at the surface. Simultaneously, some native sulphur formed as a result of hot spring activity.

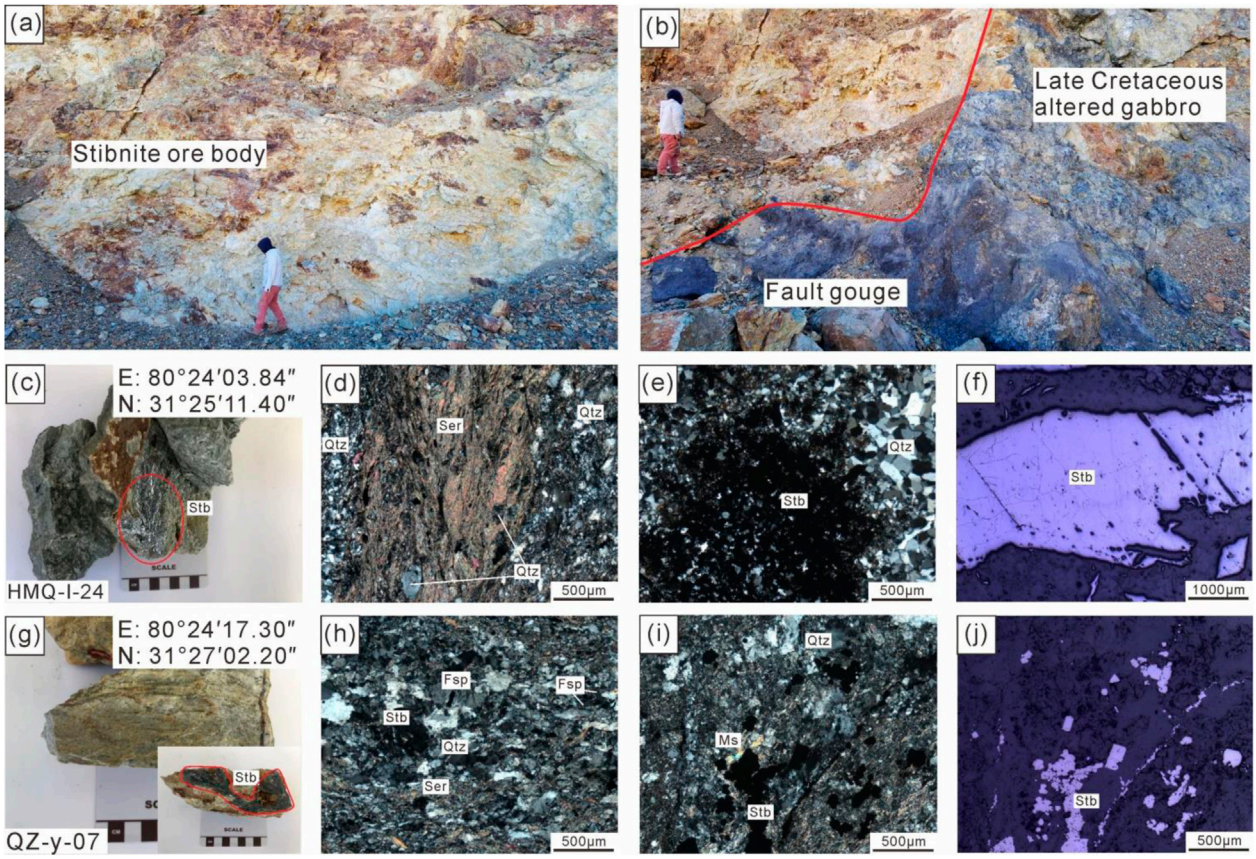

FIGURE 4
Field, hand specimens and microscopic photos of the Hamqu and Quzhen antimony de-posits **(A)**: field photo of Hamuqu I orebody; **(B)** field photo of Quzhen I orebody, the orebody is in contact with the fault zone and the late Cretaceous altered gabbro (K2υ); **(C–F)**: hand specimens and microscopic photographs of dark gray sericite silty slate in the Hamuqu deposit; **(G–J)**: hand specimens and microscopic photographs of greyish-green phyllitization sericeous slate in the Quzhen deposit; Qtz: quartz; Ser: sericite; Ms: muscovite; Fsp: feldspar; Stb: stibnite).

3.4 Controls on metallogenesis

Regional geological data and detailed field observations show that the strata most closely spatially associated with antimony mineralisation in the Abunabu deposits are the Middle–Upper Devonian Qumenxiala Formation ($D_{2\text{-}3}q$) and the Lower–Middle Triassic Qiongguo Group ($T_{1\text{-}2}Q$). Intrusive rocks exposed in the Quzhen deposit, which is located in the northern part of the mining area, are mostly Early Cretaceous ultramafic rocks ($K_1\Sigma$) and Late Cretaceous gabbros ($K_2\upsilon$). The mineralisation in this area is closely spatially related to the distribution and type of sedimentary strata, structures, and magmatic rocks, as follows (Chen et al., 2011).

1) Sedimentary strata. Strata including those of the Qumenxiala Formation ($D_{2\text{-}3}q$) and the Qiongguo Group ($T_{1\text{-}2}Q$) are found in the mining area. The orebodies are hosted mainly in certain rock types, including crystalline limestone, sericite slate, and meta-sandstone. The spatial distributions of the orebodies are thus associated with the distributions of particular stratigraphic units.
2) Structure. Well-developed fault structures occur in the mining area, such as NW–SE-trending and near-N–S-trending faults, which control the directional distribution of the orebodies.
3) Magmatic rocks. In the Quzhen deposit, some of the main metallogenic sites are found in the inner and outer contact zones between Early Cretaceous ultramafic rocks ($K_1\Sigma$) and Late Cretaceous gabbro ($K_2\upsilon$) and the Qiongguo Group ($T_{1\text{-}2}Q$) strata (Figure 3B). In general, magmatic rocks are expected to provide large amounts of gas, hydrothermal fluids, metals, and thermal energy for mineralisation and play a key role in the activation, migration, and enrichment of metallogenic elements.

4 Genetic mechanism of the ore deposits

4.1 Samples and analytical method

In this study, nine samples from fresh stibnite ores obtained from the Hamuqu and Quzhen deposits in the Abunabu antimony mining area were analysed for He, Ar, and S isotopes. Sample lithologies and sampling locations are given in Table 1. To characterize the mineralogy, textures, and mineral paragenesis of these samples, polished blocks and thin sections were examined by reflected and transmitted light microscopy.

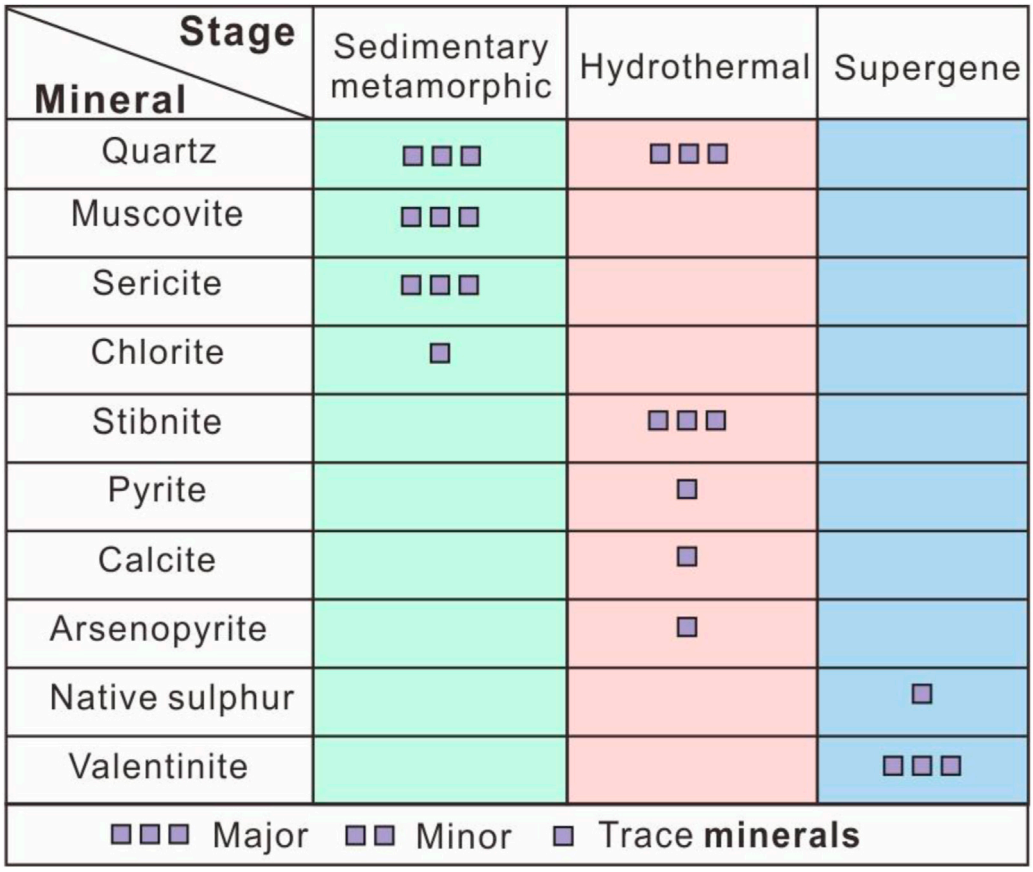

FIGURE 5
The metallogenic phase division and mineral paragenetic sequence of the Abunabu antimony deposits (Fang et al., 2006; Chen et al., 2011).

The He and Ar isotopic compositions of stibnite fluid inclusions were analysed at the Key Laboratory of Mineralisation and Resource Evaluation, Ministry of Natural Resources, Institute of Mineral Resources, Chinese Academy of Geological Sciences, Beijing, China, using a Helix SFT noble gas mass spectrometer. The setup consists of crushing, purification, and mass spectrometry systems. Analyses were performed under high-vacuum conditions, namely, $n \times 10^{-9}$ mbar for the crushing and purification system, and $n \times 10^{-10}$ mbar for the mass spectrometer system. A Nier-type ion source was used in the mass spectrometer, and the sensitivity was better than 2×10^{-4} amps/Torr for He under a trap current of 800 μA and better than 1×10^{-3} amps/Torr for Ar under a trap current of 200 μA. The static rise rate of ^{40}Ar was less than 1×10^{-12} cm^3 SPT/min, and the background value of ^{36}Ar was less than 5×10^{-14} cm^3 SPT. A Faraday cup resolution of >400 and an ion counter resolution of >700 allowed complete separation of the ^3He and ^4He, HD + H_3, and ^3He peaks. The procedure involved the following steps for each sample: (1) A high-purity 40–60 mesh sample was washed and dried. An amount of 0.5–1.0 g of the sample was placed in a stainless-steel crucible; the crucible was sealed, heated for de-gassing, and vacuumed. (2) The sample was crushed, inclusion gases were purified in multiple stages, and pure He and Ar were separated. (3) Testing of isotope composition of He and Ar was performed. (4) Isotope ratio results were corrected using test results of the air standard of the day and the air standard value. The standard value of $^3He/^4He$ in air is 1.4×10^{-6}, and the standard values of $^{40}Ar/^{36}Ar$ and $^{36}Ar/^{38}Ar$ are 295.5 and 5.35, respectively. (5) The ^4He and ^{40}Ar contents (cm^3 SPT/g) of the samples were evaluated using 0.1 ml standard gas ^4He (52.3×10^{-8} cm^3 SPT/g) and ^{40}Ar (4.472×10^{-8} cm^3 SPT/g); the isotopic signal intensity of the standard gas and the sample and the mass of the crushed and sieved (below 100 mesh) sample were used to calibrate the sample ^4He and ^{40}Ar contents (Li, et al., 2015).

Sulphur isotope analysis was conducted at the Isotope Laboratory of the Institute of Mineral Resources, Chinese Academy of Geological Sciences, using a MAT-251 mass spectrometer for analysis with Vienna Canyon Diablo Troilite (VCDT) as the standard. The specific procedure was as follows. First, single mineral specimens of stibnite were manually selected under a binocular microscope, with a purity of >95%. Subsequently, the selected specimens were ground to less than 200 mesh in an agate bowl, and a specific proportion of CuO was added. The mixture was mixed well and put in a container, which was placed into a muffle furnace. The reaction was performed at 1000°C for 15 min in a vacuum, during which sulphur in the minerals was oxidised to SO_2, which was collected and analysed for isotope composition. The analytical accuracy was ± 0.2‰ (Brian et al., 2002).

TABLE 1 Location and brief descriptions of the samples used for He–Ar–S isotopes analysis.

Mining area	Sample no.	Sample locations	Analytical mineral	Lithology	Paragenetic association of minerals	Petrographic description
Hamuqu	HMQ-I-24	Near the F_3 fault in the No. I orebody	Stibnite	Dark grey sericite silty slate	Quartz–stibnite–sericite–feldspar	The rock has a silty texture, lepidoblastic texture and plate structure. Mainly quartz and sericite, with a small amount of feldspar and muscovite. The quartz is mostly of a variable grain shape and has the characteristics of tensile orientation distribution as a whole. Sericites are arranged in parallel and oriented microscales. A small amount of mica, mixed in sheets with sericite, is the main result of sericite alteration. The feldspar is scattered in the rocks in a plate shape, and clays occur commonly
	HMQ-I-25		Stibnite		Quartz–stibnite–sericite–feldspar- muscovite	
	HMQ-I-28		Stibnite		Quartz–stibnite–sericite–feldspar–muscovite	
Quzhen	QZ-Y-7	The No. III orebody	Stibnite	Greyish-green phyllitisation sericeous slate	Quartz–stibnite–sericite–feldspar–muscovite	The rock is light grey-green, with a dense, massive structure and a lepidoblastic texture. The main mineral compositions are sericite and quartz, among which sericite is scaly and fibrous, with the directional or semi-directional arrangement. It is a shallow metamorphic product of argillaceous rock
	QZ-Y-23		Stibnite		Quartz–stibnite–sericite–feldspar–muscovite	
	QZ-Y-13	The contact of No. II ore body with faults and gabbro	Stibnite	Dark grey sericite silty slate	Quartz–stibnite–sericite–feldspar	The rock has a silty texture, lepidoblastic texture and plate structure. Mainly quartz and sericite, with a small amount of feldspar. The quartz is mostly of a variable grain shape and has the characteristics of tensile orientation distribution as a whole. Sericites are arranged in parallel and oriented microscales. The feldspar is scattered in the rocks in a plate shape, and clays occur commonly
	QZ-Y-15		Stibnite		Quartz–stibnite–sericite–feldspar	
	QZ-Y-16		Stibnite		Quartz–stibnite–sericite–feldspar	
	QZ-Y-17		Stibnite		Quartz–stibnite–sericite–feldspar	

5 Results

The analytical results for He–Ar–S isotopes of stibnite from the Hamuqu and Quzhen deposits in the Abunabu mining area are listed in Table 2 and Supplementary Table S3. Stibnite is the most important ore mineral in the study area and the main sulphide mineral, meaning that its fluid inclusions should be the best record of the original information of the ore-forming fluids of the metallogenic period. The ^{4}He contents of stibnite in the Hamuqu antimony deposit are 1.057×10^{-7}–1.584×10^{-7} cm^3 STP/g, and the ^{40}Ar contents are 1.37×10^{-7}–2.48×10^{-7} cm^3 STP/g. In addition, ^{40}Ar/^{36}Ar ratios vary widely between 303.8 and 320.7. Furthermore, ^{3}He/^{4}He (Ra) ratios range from 0.021 to 0.031. In stibnite from the Quzhen antimony deposit, the He signals of samples QZ-Y-13, QZ-Y-15, QZ-Y-16, and QZ-Y-17 samples were weak, and ^{4}He contents vary widely from 0.016×10^{-7} to 0.772×10^{-7} cm^3 STP/g. The ^{40}Ar contents are 1.40×10^{-7}–2.94×10^{-7} cm^3 STP/g, and ^{40}Ar/^{36}Ar ratios lie between 295.6 and 302.2. The ^{3}He/^{4}He (Ra) ratios have larger values of 0.025–0.351 (Table 2). As shown in Figure 6, there is a good correlation between the He and Ar isotopic compositions of the analysed fluid inclusions.

The δ^{34}S values of stibnite from the Hamuqu deposit in the Abunabu antimony mining area range from −4.9‰ to −4.4‰, with a mean of −4.7‰, whereas the δ^{34}S values of antimonite in the Quzhen deposit lie between −4.9‰ and −3.5‰, with a mean of −4.1‰ (Supplementary Table S3). The variation in sulphur isotope composition of the nine stibnite samples is narrow, indicating that the Hamuqu and Quzhen deposits shared a common or similar source of sulphur.

6 Discussion

6.1 Source of the ore-forming fluids

Isotopes of He and Ar have been widely used to determine the origin of ore-forming fluids (Hu et al., 1999; Ballentine and Burnard,

TABLE 2 He and Ar isotopic compositions of fluid inclusions of typical antimony polymetallic deposits in the Tethys Himalaya metallogenic belt.

Location	Sample number	Mineral	^4He	^{40}Ar	$^3He/^{36}Ar$	$^3He/^4He$	$^{40}Ar^*$	$^3He/^4He$	$^{40}Ar/^{36}Ar$	$^{40}Ar^*$	$^4He/^{36}Ar$	F_4He	Mantle derived He%	$^{40}Ar^*/^4He$	R/Ra	References
			($10^{-7}cm^3STP/g$)					(Ra)		(%)						
Mazhala	09MZL-2–12	stibnite	48	7.12	2206.161	0.790	2.042	0.056	414.3	28.675	2793.034	16876.337	0.562	0.043	0.040	Zhai et al. (2018)
	09MZL-1–5	stibnite	99.3	6.35	40947.547	0.549	5.957	0.039	4770.1	93.805	74593.847	450718.110	0.296	0.060	0.028	
	09MZL-1–7	stibnite	133.3	10.52	6055.692	0.604	6.591	0.043	791.3	62.656	10026.644	60583.949	0.357	0.049	0.031	
	09MZL-1-8a	stibnite	69.7	2.33	2007.206	0.193	0.345	0.014	346.8	14.792	10374.232	62684.180	–	0.005	0.010	
	09MZL-1–15	stibnite	42	4.21	1775.450	0.464	0.968	0.033	383.7	22.987	3827.886	23129.220	0.203	0.023	0.024	
	2010121	stibnite	63.1	3.52	2337.142	0.434	0.060	0.031	300.6	1.697	5388.597	32559.496	0.169	0.001	0.022	
	2010129	quartz	786	75.1	15674.091	0.557	66.847	0.040	2689.1	89.011	28144.242	170055.845	0.305	0.085	0.028	
	09MZL-1–9	pyrite	233	48.5	2858.856	0.469	37.195	0.034	1267.7	76.690	6090.188	36798.717	0.209	0.160	0.024	
	09MZL-1–14	pyrite	36.4	19.2	687.393	0.780	6.993	0.056	464.8	36.424	881.183	5324.371	0.551	0.192	0.040	
	09MZL-2–2	pyrite	24.7	13.37	790.181	1.224	2.063	0.087	349.4	15.426	645.488	3900.232	1.041	0.084	0.062	
	MZL-1	pyrite	70.2	3.03	20593.390	1.960	1.056	0.140	453.5	34.840	10506.832	63485.388	1.852	0.015	0.100	Zhang, (2012)
	MZL-3	pyrite	118.4	8.79	5825.172	1.400	0.381	0.100	308.9	4.338	4160.837	25141.011	1.235	0.003	0.071	
	MZL-2	pyrite	300	9.58	19791.733	1.540	2.682	0.110	410.4	27.997	12851.775	77654.227	1.389	0.009	0.079	
Shalagang	09SL-1–7	stibnite	52.6	12.01	1468.884	0.685	39.645	0.049	489.6	39.645	2144.293	12956.454	0.446	0.091	0.035	Zhai et al. (2018)
	09SL-1–8	stibnite	49.6	8.51	1207.858	0.422	39.792	0.030	490.8	39.792	2860.597	17284.574	0.157	0.068	0.022	
	09SL-1–10	stibnite	22.5	6.16	1378.259	0.813	36.356	0.058	464.3	36.356	1695.901	10247.136	0.587	0.100	0.041	
	09SL-7–2	stibnite	13.45	9.19	1040.167	1.608	33.130	0.115	441.9	33.130	646.742	3907.804	1.464	0.226	0.082	
	09SL-8–2	stibnite	114.2	11.09	3066.859	0.664	34.158	0.047	448.8	34.158	4621.547	27924.757	0.423	0.033	0.034	
	09SL-8–5	stibnite	89.4	9.4	1598.598	0.334	41.299	0.024	503.4	41.299	4787.655	28928.431	0.059	0.043	0.017	
	09SL-8–7	stibnite	146	16.9	2349.028	0.504	45.227	0.036	539.5	45.227	4660.769	28161.748	0.247	0.052	0.026	
	2010098	stibnite	18.9	6.22	758.743	0.569	32.719	0.041	439.2	32.719	1334.547	8063.726	0.318	0.108	0.029	
	2010105	stibnite	10.73	4.12	531.831	0.599	13.292	0.043	340.8	13.292	887.569	5362.954	0.352	0.051	0.031	
Zhaxikang	ZXKPD7-8e	sphalerite	39	2.46	100347.476	0.63	2.388	0.045	10047.0	97.059	159281.707	962427.235	0.386	0.061	0.032	Zhang, et al. (2010)
	ZXKPD7-8f	siderite	55.8	15	1906.987	1.106	5.437	0.079	463.5	36.246	1724.220	10418.248	0.910	0.097	0.056	
	ZXKPD6-1c	quartz	1.49	29.7	176.811	2.408	23.704	0.172	1463.6	79.810	73.426	443.664	2.346	15.908	0.123	
	ZXKPD6-2c	quartz	1.89	27.7	239.472	2.366	22.182	0.169	1483.4	80.080	101.214	611.565	2.299	11.737	0.121	

(Continued on following page)

10.3389/feart.2022.1033124

TABLE 2 (*Continued*) He and Ar isotopic compositions of fluid inclusions of typical antimony polymetallic deposits in the Tethys Himalaya metallogenic belt.

Location	Sample number	Mineral	^4He	^{40}Ar	$^3He/^{36}Ar$	$^3He/^4He$	$^{40}Ar^*$	$^3He/^4He$	$^{40}Ar/^{36}Ar$	$^{40}Ar^*$	$^4He/^{36}Ar$	F_4He	Mantle derived He%	$^{40}Ar^*/^4He$	R/Ra	References
			($10^{-7}cm^3STP/g$)					(Ra)		(%)						
	ZXKPD5-6d	stibnite	0.2	3.49	–	0.574	–	0.041	–	–	–	–	0.324	–	0.029	
	ZXKPD5-6e	quartz	0.09	32.6	1.543	0.672	21.015	0.048	831.5	64.462	2.296	13.870	0.432	233.495	0.034	
	ZXKPD5-8c	quartz	15.2	18	14798.538	18.270	12.455	1.305	959.2	69.193	809.991	4894.206	19.830	0.819	0.932	
	ZXK-1	pyrite	31.2	4.05	1340.814	0.560	0.199	0.040	310.8	4.923	2394.311	14467.137	0.309	0.006	0.029	Zhang, (2012)
	ZXK-2	pyrite	12.57	1.74	1168.750	0.560	-	0.040	288.9	-	2087.053	12610.595	0.309	–	0.029	
	ZXK-3	pyrite	21	2.68	1394.087	0.560	0.187	0.040	317.7	6.988	2489.440	15041.935	0.309	0.009	0.029	
Abunabu	HMQ-I-24	stibnite	1.584	2.48	60.212	0.310	0.070	0.022	304.1	2.828	194.232	1173.605	0.031	0.044	0.016	This study
	HMQ-I-25	stibnite	1.057	1.88	75.155	0.440	0.051	0.031	303.8	2.732	170.807	1032.065	0.170	0.049	0.022	
	HMQ-I-28	stibnite	1.058	1.37	74.299	0.300	0.108	0.021	320.7	7.858	247.665	1496.463	0.015	0.102	0.015	
	QZ-Y-5–7	stibnite	0.723	1.75	43.698	0.350	0.039	0.025	302.2	2.217	124.852	754.391	0.077	0.054	0.018	
	QZ-Y-23	stibnite	0.772	1.4	61.555	0.370	0.029	0.026	301.7	2.055	166.366	1005.233	0.093	0.037	0.019	
	QZ-Y-13	stibnite	0.053	1.7	13.277	1.430	0.013	0.102	297.8	0.772	9.284	56.099	1.265	0.248	0.073	
	QZ-Y-15	stibnite	0.025	2.66	8.835	3.180	0.001	0.227	295.6	0.034	2.778	16.787	3.194	0.036	0.162	
	QZ-Y-16	stibnite	0.017	2.94	7.215	4.190	0.023	0.299	297.8	0.772	1.722	10.405	4.306	1.336	0.214	
	QZ-Y-17	stibnite	0.016	2.54	9.208	4.910	0.019	0.351	297.7	0.739	1.875	11.331	5.108	1.173	0.251	

STP indicates the standard temperature and pressure state.

$^{40}Ar^*$ represents the relative content of radiogenic.

^{40}Ar in the ore-forming fluids; $n(^{40}Ar^*)= n(^{40}Ar)_{Sample}-295.5\times n(^{36}Ar)_{Sample}$; the F_4He value represents the amount of.

^4He in the fluids relative to air; $F_4He=[n(^4He)/n(^{36}Ar)]_{Sample}/[n(^4He)/n(^{36}Ar)]_{Air}$, $[n(^4He)/n(^{36}Ar)]_{Air}=0.1655$.

$^4He_{Mantle}$ represents the proportion of mantle source He, $n(^4He)_{Mantle} =100\%\times\{[n(^3He)/n(^4He)]_{Sample}-[n(^3He)/n(^4He)]_{Crustal}\}/\{[n(^3He)/n(^4He)]_{Mantle}-[n(^3He)/n(^4He)]_{Crustal}\}$, $[n(^3He)/n(^4He)]_{Mantle}=6.5Ra$, $[n(^3He)/n(^4He)]_{Crustal}=0.02Ra$, $Ra=[n(^3He)/n(^4He)]_{Air}=1.4\times10^{-6}$ (Stuart et al., 1995; Anderson, 2000).

10.3389/feart.2022.1033124

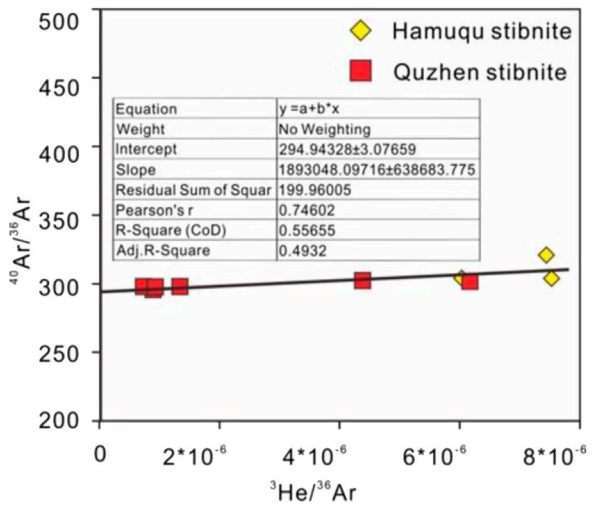

FIGURE 6
Diagram of fluid inclusions of 3He/36Ar-40Ar/36Ar in stibnite in the Abunabu antimony area.

2002). The gases He and Ar are present in minerals in three main forms: (1) in fluid inclusions that are captured by minerals; (2) radioactive ^{4}He and ^{40}Ar resulting from the decay of U, Th, and K in the mineral lattice; and (3) He and Ar from the atmosphere adsorbed onto mineral surfaces (Burnard et al., 1999). However, He and Ar in sulphides of hydrothermal deposits are found predominantly in mineral fluid inclusions (Turner and Stuart, 1992; Stuart et al., 1995). Owing to the low contents of U, Th, K, and other lithophile elements in fluid inclusions in the sulphide minerals of non-uranium deposits (with Th being almost insoluble in hydrothermal fluids), and because fluid inclusions in sulphide minerals are surrounded after closure, the presence of radiogenic He and Ar formed by the decay of U, Th, and K was considered negligible in the present study (Turner and Wang, 1992; Qiu, 1996; Burnard and Polya, 2004; Hu et al., 2004; 2012; Ding et al., 2014).

The content of He in the atmosphere is minimal and insufficient to substantially affect the content and isotopic composition of He in crustal fluids (Marty et al., 1989; Stuart et al., 1994; Hu et al., 2009). If a sample contains atmospheric He, then $F^{4}He$ should be equal to 1 (Kendrick et al., 2001; Mao and Li, 2004). As presented in Table 2, the $F^{4}He$ values of stibnite in the Abunabu antimony ore area range

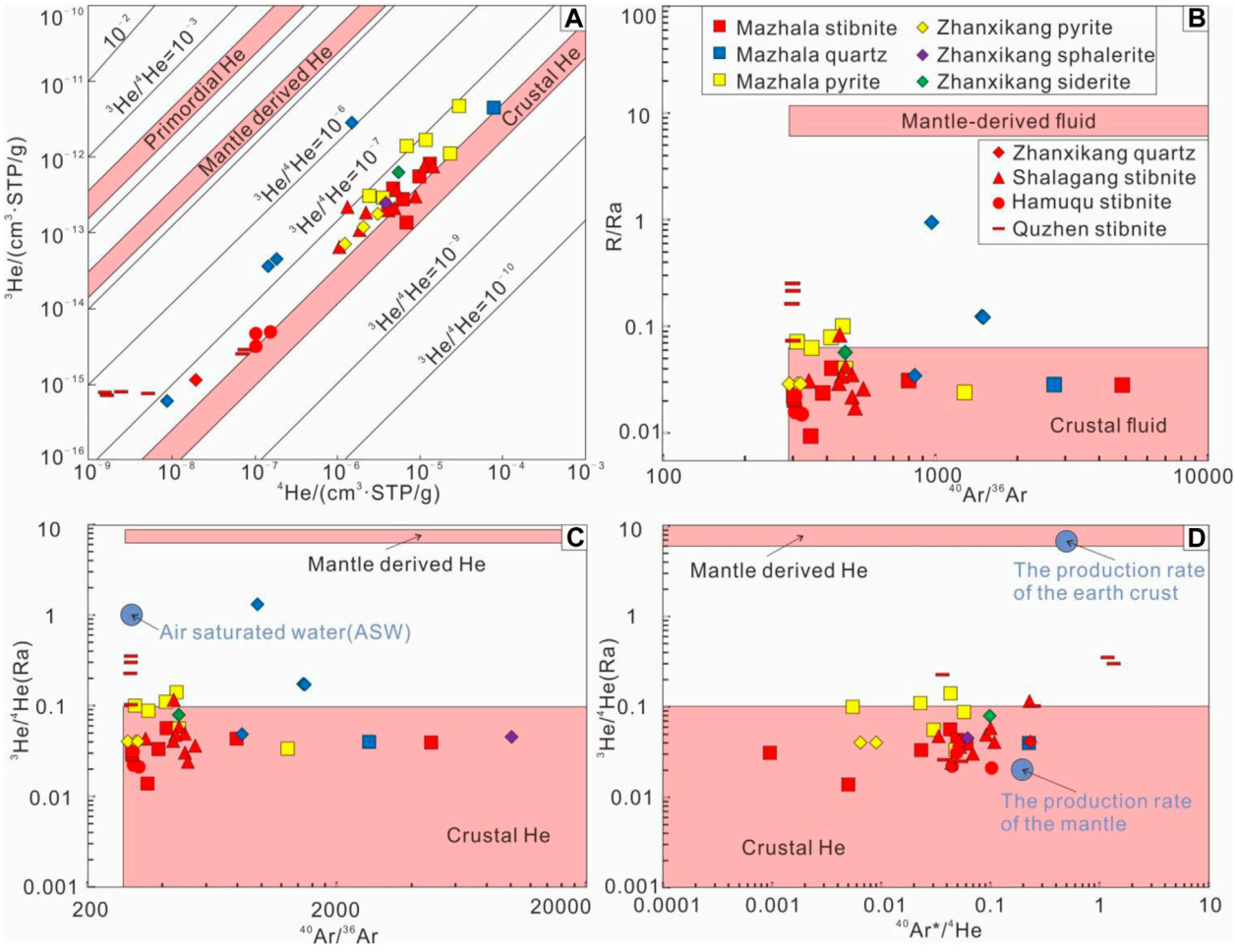

FIGURE 7
(A) plot of ^{4}He *versus* ^{3}He (basemap after Mamyrin and Tolstikhin, 1984); **(B)** plot of $^{40}Ar/^{36}Ar$ *versus* R/Ra (basemap after Burnard et al., 1999); **(C)** plot of $^{40}Ar/^{36}Ar$ vs $^{3}He/^{4}He(Ra)$ (crustal and mantle He from Andrews, 1985; Stuart et al., 1994); **(D)** plot of $^{40}Ar^{*}/^{4}He$ vs $^{3}He/^{4}He(Ra)$ (crustal and mantle He and He, Ar isotope production rations from Andrews, 1985; Stuart et al., 1994).

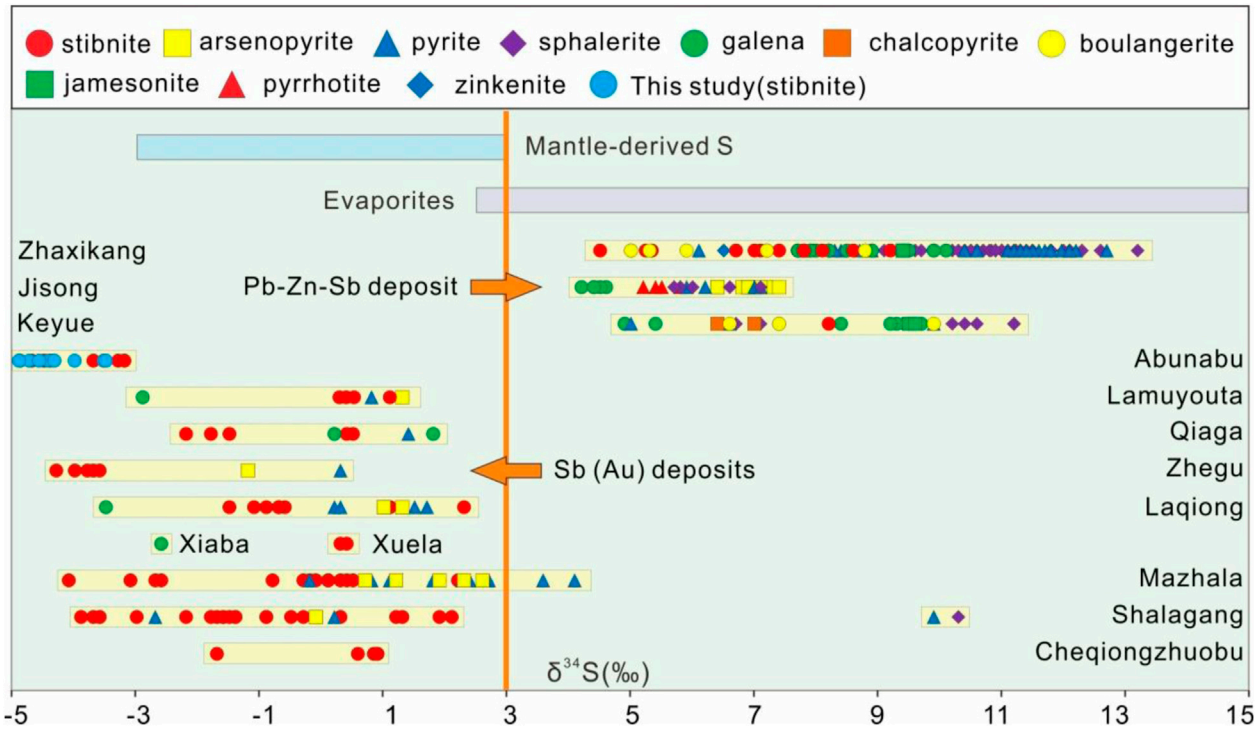

FIGURE 8
Sulphur isotopic composition of typical antimony polymetallic deposits in the Tethys Himalaya metallogenic belt [comparison of the S isotope composition derived from the mantle, and evaporates (Heyl et al., 1974; Zou et al., 2017; 2019; Cao et al., 2019)].

between 10.40 and 1,496.46, all greater than 1, suggesting no atmospheric He. Isotope data for He and Ar in this study were obtained from inclusions in stibnite, which should represent the initial values of the primary fluid inclusions. Owing to the unique nature of noble gases, no significant isotopic fractionation occurs whether the fluid inclusion samples are collected during mineralisation or obtained by crushing in a vacuum (Hu et al., 1999). Hu et al. (1999) studied the He–Ar isotopic geochemistry of ore-forming fluids of the Ailaoshan gold deposits and found that when fluid inclusions in chalcopyrite, galena, stibnite, and other minerals are diffused in large quantities to lose He, no obvious fractionation is observed in the He isotopes, meaning that the measured $^{3}He/^{4}He$ and $^{40}Ar/^{36}Ar$ ratios represent the initial values of the ore-forming fluids when the fluid inclusions were captured.

Noble gases have distinct He and Ar isotopic compositions in the atmosphere and crustal and mantle rocks. Thus, these gases are widely used to trace the source of ore-forming fluids. Isotopes of He and Ar in hydrothermal fluids are derived largely from the following sources (Burnard et al., 1999; Ballentine and Burnard, 2002), (1) The atmosphere or atmospheric saturated water (e.g., meteoric, sea, or sedimentary water). The atmosphere has a stable He–Ar isotopic composition, with $^{3}He/^{4}He = 1.399 \times 10^{-6}$ and $^{40}Ar/^{36}Ar = 295.5$. Atmospheric saturated water is in equilibrium with the atmosphere under certain temperature and pressure conditions and has a similar isotopic composition to that of the atmosphere. Because the He content in air is low and its solubility in aqueous solution is the lowest of the noble gases, the He content in saturated atmospheric water is low ($He/Ar \approx 1 \times 10^{-4}$; Simmons et al., 1987; Burnard et al., 1999). Due to the relatively high content of Ar in the atmosphere, the closure temperature of Ar in rocks is far higher than that of He (McDougall et al., 1988). Therefore, shallow groundwater contains almost no radioactive Ar but has characteristics consistent with the isotopic composition of atmospheric Ar. The radioactive-origin ^{4}He generated by the decay of U and Th in aquifer rocks diffuses into groundwater or geothermal fluids, the $^{3}He/^{4}He$ ratio of geological fluids derived from atmospheric water or seawater is lower than its atmospheric value, and the ^{4}He content of geological fluids is higher than that of atmospheric saturated water. Therefore, shallow groundwater or near-surface cryogenic fluids have lower $^{3}He/^{4}He$ ratios than those in the atmosphere and $^{40}Ar/^{36}Ar$ ratios that are similar to atmospheric values, indicating the characteristics of modified air-saturated water (Ballentine and Burnard, 2002). (2) Mantle-derived fluids. The $^{3}He/^{4}He$ ratio of fluids from the continental lithospheric mantle is in the range of six to eight Ra (where Ra is the atmospheric value), whereas that of oceanic lithospheric mantle fluids is in the range of six to nine Ra (Gautheron and Moreira, 2002). Mantle-derived Ar is mainly $^{40}Ar^{*}$ of radioactive origin, and the $^{40}Ar/^{36}Ar$ ratio varies considerably and is usually greater than 40,000 (Porcelli et al., 1992; Patterson et al., 1994; Reid and Graham, 1996). Because of the very large difference in the $^{3}He/^{4}He$ ratio between crust and mantle, even if there is a small amount of mantle He mixed in crustal fluids, this component can be easily identified using He isotopes (Simmons et al., 1987; Stuart et al., 1995; Hu et al., 1999). (3) Crustal fluids. Owing to the high content of large-ion lithophile elements in crustal rocks, the radioactive and nucleogenic He and Ar produced by these elements are characterised by a $^{40}Ar/^{36}Ar$ ratio of ≥295.5 and a $^{3}He/^{4}He$ ratio

of 0.01–0.05 Ra (Andrews and Lee, 1979; Stuart et al., 1995), such that metamorphic or magmatic fluids of crustal origin show similar He and Ar isotopic compositions to those of crustal rocks.

Data for a total of 41 analysed samples from four antimony deposits (Abunabu, Mazhala, Shalagang, and Zhaxikang) in the Tethys Himalayan metallogenic belt were compiled from this study and previous studies (Table 2). For these 41 analysed samples, the $^{3}He/^{4}He$ values of stibnite, pyrite, sphalerite, siderite, and quartz ranged from 0.014 to 1.305 Ra, with a mean of 0.105 Ra. Of these samples, the values for two stibnite samples (QZ-Y-7 and QZ-Y-23) from the Abunabu deposits fall within the crustal $^{3}He/^{4}He$ value range (0.01–0.05 Ra), whereas the remaining stibnite samples from the Quzhen deposit all display high $^{3}He/^{4}He$ values that are characteristic of the crust and lower $^{3}He/^{4}He$ values in the mantle range (six to nine Ra) (Stuart et al., 1995). The former values indicate that the He isotopes in the ore-forming fluids are of crustal origin; the latter values suggest that the He isotopes in the ore-forming fluids are a mixture of mantle and crustal origins. In an He isotopic composition distribution map (Figure 7A), the data points all fall in the transition zone between mantle-derived and crust-derived He, but they tend more towards the crust than the mantle. These data give estimated proportions of mantle-derived fluids in the stibnite samples from the Hamuqu and Quzhen deposits of 0.015%–0.169% (with a mean of 0.065%) and 0.077%–5.108% (with a mean of 2.341%), respectively. Regionally, one quartz sample from the Zhaxikang lead–zinc–antimony polymetallic deposit shows a proportion of mantle-derived fluids of 19.830%, whereas the proportion of mantle-derived fluids in samples from other deposits is less than 3% (Zhang et al., 2010). These results indicate that mantle-derived fluids made an overall minimal contribution to mineralisation and instead suggest a predominant crustal origin for the ore-forming fluids of antimony deposits in the Tethys Himalayan metallogenic belt. The involvement of mantle-derived fluids may be due to the water-rock reaction between the ore-forming fluid and the intermediate-basic magmatic rocks in the region, which activated part of the ore-forming materials such as Sb and Au. (Deng, 2020; Sun et al., 2020).

The $^{40}Ar/^{36}Ar$ ratios of the analysed fluid inclusions in stibnite from the Abunabu mining area range from 295.6 to 320.7, with a mean of 302.4, which is slightly higher than the characteristic value of $^{40}Ar/^{36}Ar$ in saturated atmospheric water (295.5) but substantially lower than that in the mantle ($^{40}Ar/^{36}Ar > 40{,}000$). Using least squares regression ($^{40}Ar/^{36}Ar = 294.94 + 1{,}893{,}048.09 \times {}^{3}He/^{36}Ar$) to fit the stibnite sample data in Figure 6, when $^{3}He/^{36}Ar = 5 \times 10^{-8}$ (the $^{3}He/^{36}Ar$ value of rainwater), $^{40}Ar/^{36}Ar \approx 295.03$, which is within error of the isotopic composition of atmospheric argon ($^{40}Ar/^{36}Ar \approx 295.5$). Moreover, this result is consistent with a considerably small amount of excess argon, which implies that the ore-forming fluids of the antimony deposits in the Abunabu mining area constitute a crustal end-member with the input of atmospheric precipitation (Hu et al., 1999; Chen et al., 2016).

A projection of the He and Ar isotopic compositions measured in this study onto a $R/Ra–^{40}Ar/^{36}Ar$ diagram (Figure 7B) shows that the compositions are distributed in the crustal fluid field or between crustal and mantle fluids (and closer to crustal fluids). Furthermore, the $^{40}Ar/^{36}Ar$ isotope ratios of all samples from the Abunabu mining area are greater than the atmospheric $^{40}Ar/^{36}Ar$ isotope ratio, implying the presence of crust-derived radiogenic Ar ($^{40}Ar^{*}/\%$) in the fluids. Calculations show that the proportion of radiogenic Ar in Abunabu mining area is in the range of 0.772%–7.858%, which indicates that only a low content of radiogenic Ar ($^{40}Ar^{*}/\%$) originated from the crust. Due to the different degrees of greenschist facies metamorphism of the host strata, the source of ore-forming fluid is also the result of the joint action of the modified air-saturated water and metamorphic fluid (Zhai et al., 2018; Li H et al., 2022). In comparison, Figure 7C shows that a few samples lie close to the atmospheric saturated water field, suggesting that in addition to crustal fluids, mantle-derived fluids and a small amount of atmospheric precipitation were involved in the mineralisation. Therefore, the antimony deposits in the Tethys Himalayan metallogenic belt display the characteristics of mixed mineralisation involving modified air-saturated water rich in atmospheric argon, crustal fluids containing He, and crustal fluids containing radioactively derived Ar.

The lithospheric mantle has $^{40}Ar^{*}/^{4}He = 0.5$ and $^{3}He/^{4}He$ = six to nine Ra, and crustal rocks have values of $^{40}Ar^{*}/^{4}He = 0.2$ and $^{3}He/^{4}He <$ 0.1 Ra (Andrews, 1985). $^{40}Ar^{*}/^{4}He$ values in the Hamuqu and Quzhen deposits are 0.0443–0.1018 and 0.0360–1.3357, respectively. Excluding the two samples whose values are higher than the mantle average in the Quzhen deposit (1.336 and 1.173), the rest fall substantially below the crustal mean. On a $^{40}Ar^{*}/^{4}He–^{3}He/^{4}He$ map (Figure 7D), most sample data for antimony deposits in the Tethys Himalayan metallogenic belt plot in the crustal source area. Furthermore, $^{40}Ar^{*}/^{4}He$ ratios lie between the average end-member of the crustal rock yield and the end-member of the crustal derived rock yield while being far lower than the end-member of the crustal rock yield. Previous studies have also found that in the antimony deposits of the Tethys Himalayan metallogenic belt (such as the Shalagang Sb deposit and Mazhala Sb-Au deposit), as well as the involvement of metamorphic fluids of crustal origin, there was addition of modified air-saturated water with low $^{40}Ar^{*}/^{4}He$ (Zhang, 2012; Zhai et al., 2018; Li et al., 2021; Liu et al., 2021). It is consistent with the results of hydrogen and oxygen isotope analysis, the ore-forming fluid is mainly composed of meteoric water and the addition of metamorphic fluid (Zhai et al., 2014).

Sphalerite, siderite, and pyrite from the Zhaxikang deposit have similar $^{3}He/^{4}He$ and $^{40}Ar/^{36}Ar$ values, which represent the characteristics of fluids during the early metallogenic stage. In an $R/Ra–^{40}Ar/^{36}Ar$ diagram, sphalerite, pyrite, and siderite all lie in the range of crustal fluids (Figure 7B). The He–Ar isotopic characteristics of quartz fluid inclusions in stibnite vein ores differ from those of the early zinc–lead ore-forming fluids, indicating the influence of mantle-derived fluids. Therefore, the ore-forming fluids of the early lead–zinc ore in the Zhaxikang deposit are composed mainly of crust-derived fluids, whereas the ore-forming fluids of the late stibnite are composed predominantly of mantle-derived fluids, which also suggests that the early ore-forming fluids of this deposit may have been seafloor hot brine (Zhang, 2016). Moreover, all data points for the particular same deposit are distributed parallel to the Y-coordinate axis (Figure 7C), implying that the variation in He isotopes in the ore-forming fluids was largely unaffected by Ar. Therefore, in the Tethys Himalayan metallogenic belt, the compositional variations in He and Ar isotopes in the ore-forming fluids of each antimony deposit are independent of each other. This result suggests that antimony deposits in the belt had similar fluid sources and mixing processes and that differences in the metallogenic tectonic setting within the belt emerged only in the later stages of evolution of the deposit.

6.2 Source of the ore-forming materials

Sulphur is an important metal transportation agent for ore-forming hydrothermal fluids and can therefore be used to infer the source of ore-forming materials (Li et al., 2020a; Li et al., 2021). The heavy S isotope, ^{34}S, tends to fractionate to sulphate relative to sulphide; however, under reducing environments, sulphide is the predominant S phase, meaning that ^{34}S values can approximately represent the bulk S isotopic composition (Ohmoto, 1972; Seal, 2006; Li et al., 2020b).

No sulphate minerals are found in the Hamuqu and Quzhen deposits of the Abunabu mining area, suggesting a reducing environment of formation, and the main sulphur-bearing mineral assemblages are sulphides such as stibnite, arsenopyrite, and pyrite. Therefore, the S isotopic compositions of the stibnite samples analysed in the present study are considered to represent the bulk S isotopic composition of the Abunabu mining area. The mean $\delta^{34}S$ value of stibnite in the Hamuqu and Quzhen deposits is −4.7‰, within the range of $\delta^{34}S$ values of antimonite in the Quzhen deposit of −4.9‰ to −3.5‰ (mean value of −4.1‰) and slightly lower than typical magmatic sulphur $\delta^{34}S$ values (−3‰ to +3‰; Chaussidon et al., 1989). The source of sulphur may have been mainly deep magmatic sulphur (Yang et al., 2009; Li et al., 2018; 2019; Cao et al., 2019; Li C L et al., 2022), with the slightly lower values reflecting the possible addition of small amounts of minerogenetic materials from the Qiongguo Group ($T_{1\text{-}2}Q$). Numerous intermediate–mafic dikes occur in the Abunabu mining area, and the Late Cretaceous gabbro body ($K_2\upsilon$) is the ore-bearing protolith of the No. I antimony orebody of the Quzhen deposit (Figure 3B), the mineralisation of which evidently occurred later than the intrusion of the intermediate–mafic dikes. Moreover, the intermediate–mafic dikes display alteration, suggesting that sulphur was not directly released by magma but may have been leached from the intermediate–mafic dikes during interaction between hydrothermal fluids and rocks.

A compilation of S isotope data (Supplementary Table 3) for sulphides from typical deposits in the Tethys Himalayan metallogenic belt is presented in Figure 8. The S isotopic compositions of the antimony–(gold) deposits and lead–zinc–antimony polymetallic deposits in this metallogenic belt allow the deposits to be divided into two categories (Figure 8). The first category includes antimony–(gold) deposits such as the Abunabu, Shalagang, Laqiong, Lamuyouta, and Cheqiongzhuobu deposits. The range of sulphide $\delta^{34}S$ for this category is relatively narrow, from −4.9‰ to −4.1‰, apart from two anomalously high $\delta^{34}S$ values for pyrite and sphalerite from the Shalagang deposit of 9.9‰ and 10.3‰, respectively, which are in marked contrast to the $\delta^{34}S$ values of sulphides from various deposits in the western Tethys Himalayan metallogenic belt, and are not discussed here. The $\delta^{34}S$ values of sulphides in these deposits are similar to those of skarn-type (−3.9‰ to −0.9‰) and porphyry-type (−1.7‰ to +2.1‰) deposits in Tibet (Zhou et al., 2017), suggesting that deep magma was the main source of sulphur for all of these deposits (Cao et al., 2019; Deng et al., 2019; Li B. L et al., 2022). In addition, the $\delta^{34}S$ values of antimony and gold deposits in the Tethys Himalayan metallogenic belt are similar to those in the Gangdese porphyry copper belt in Tibet (−6.3‰ to +1.8‰; Qu and Li, 2002), implying that the metallogenesis of antimony–(gold) in this metallogenic belt might be genetically related to large-scale leucogranite magmatism in southern Tibet (Zhou et al., 2017).

The second category of deposits is represented by lead–zinc–antimony polymetallic deposits such as Zhaxikang and Keyue, where sulphide $\delta^{34}S$ values vary from four‰ to 13‰, close to the $\delta^{34}S$ values (4.9‰–11.5‰) of the Ridang Formation; i.e., the main ore-bearing horizon in the study area (Zheng et al., 2003; Zhang, 2012). These deposits may contain sulphur that was derived from rocks deposited in a marine environment, and such sulphur was likely strongly involved in the mineralisation of Zhaxikang, Keyue, and other lead–zinc–antimony polymetallic deposits (Zhou et al., 2017; Sun et al., 2018). In summary, the two categories of deposits in the Tethys Himalayan metallogenic belt classified in terms of their sulphide $\delta^{34}S$ values had multiple sources of sulphur (Deng et al., 2019; Li et al., 2020b).

Although antimony–(gold) deposits and lead–zinc–antimony polymetallic deposits in the Tethys Himalayan metallogenic belt may have had the same sources of metal elements (deep metamorphic crystalline basement and leucogranite), the sources of sulphur of the associated ore-forming fluids differed considerably between these two types of deposit. Fluids of the former deposits were derived primarily from the magmatic system, whereas those of the latter deposits were derived predominantly from the surrounding black sedimentary rock series. In terms of the compositions of metallogenic elements, those deposits with magma-derived sulphur—including Abunabu—are dominated by antimony or antimony–gold mineralisation, whereas the element combination involved in sedimentary metallisation is mostly lead–zinc mineralisation, with antimony produced principally as associated ore. Therefore, sulphur isotopic compositions can be used to identify deposit types and give prospecting guidance for ore types in the Tethys Himalayan metallogenic belt (Du et al., 2011; Li et al., 2021).

6.3 Genesis of mineral deposits in the Tethys Himalayan metallogenic belt

Antimony deposits in southern Tibet have undergone three major stages of mineralisation (Fan et al., 2012; Li et al., 2014; Deng et al., 2019): the source bed formation stage, the preliminary mineral enrichment stage, and the superimposed mineral enrichment stage. The formation stage of the initial source beds occurred during the Late Triassic to Early Cretaceous, coinciding with the formation and development stage of the Neo-Tethys Ocean. In addition to rifting, the thick turbidite sedimentary structure that formed during this period laid the material foundation for mineralisation in southern Tibet. This structure included basalt-dominated magmatic rocks and hydrothermal sedimentary rocks. During the preliminary enrichment stage of minerals by dynamic hydrothermal metamorphism during the Late Cretaceous–Oligocene, the Indian plate subducted northwards beneath Asia, and the Tibetan Tethys Ocean gradually narrowed and closed, the crust thickened, and intra-continental orogenesis formed folds and thrust-nappe structures, resulting in regional low-temperature dynamic metamorphism. Subsequently, owing to the detachment of lithospheric mantle, mantle heat flow ascended, accompanied by granite emplacement and regional heat flow metamorphism, resulting in the extraction of H_2O, CO_2, Cl, S, Sb, As, Au, and other elements from the ore bearing formation-tectonic, thereby forming ore-bearing fluids. Under the influence of a temperature and pressure gradient, these fluids migrated and

precipitated minerals in the low-pressure dilatant zone, resulting in mineral enrichment (Li H et al., 2022). During the tectonic–magmatic superimposed enrichment mineralisation stage, which occurred after the Miocene, the Indian plate continued to subduct northwards, resulting in lateral extrusion and NE–SW-directed tensile stress. A series of near-N–S-trending high-angle normal faults were formed together with the emplacement of deep mafic magma, and some of these faults continued to develop to form horst–graben structures and faulted basins. This group of fault zones and horst–graben structures connected the magmatic–hydrothermal system with the groundwater hydrothermal system, providing favourable space for the migration and enrichment of ore-bearing hydrothermal solution, forming epithermal antimony–(gold) ore and 'hot spring type' antimony ore (Hou et al., 2006; Zhou et al., 2014; Liang, 2019).

Groves et al. (1998) considered that the temperature required for metamorphic fluids to activate Sb elements from surrounding rocks is the temperature corresponding to amphibolite-facies metamorphism. This temperature condition is much higher than that of the metamorphic grade of the rocks surrounding the Abunabu mining area, indicating that regional ore-forming fluids were derived predominantly from magmatic water. However, considering that most of the antimony–gold polymetallic deposits in the Tethys Himalayan metallogenic belt are distributed around metamorphic domes, the possible influence of metamorphic fluids on mineralisation cannot be ignored (Yang et al., 2009). Zheng et al. (2022) proposed that the Sb in antimony deposits of the Tethys Himalayan metallogenic belt was sourced from subvolcanic magmatism which involves rich volatiles formed from decompression and fusion of hypomagma and is responsible for the development of exhalative sedimentation-reworked, magmatic hydrothermal and hot spring deposits.

Although no metamorphic dome has been found near the Abunabu mining area, He–Ar isotope compositions indicate that metamorphic fluids of crustal origin were involved in the mineralisation process. We consider that the temperature of metamorphic fluids in the process of NE-directed tectonic migration decreased with increasing migration distance and was not sufficiently high to activate Sb, Au, and other ore-forming elements in the surrounding rock. Therefore, magmatic–hydrothermal fluids are inferred to have been responsible for the activation of Sb, Au, and other ore-forming elements. The mixing of magmatic fluids and metamorphic fluids involved in the migration of metallogenic materials is dependent on physical and chemical conditions, such as fluid composition, temperature, pressure, and pH. These conditions, together with mixing of atmospheric precipitation, provided favourable conditions for subsequent mineralisation in the Abunabu mining area (Yang et al., 2009; Deng, 2020).

The low $\delta^{34}S$ values of stibnite from the Abunabu mining area indicate that the ore-forming fluids involved in the mineralisation of the Hamuqu and Quzhen antimony deposits were a mixture of magmatic and metamorphic fluids. Moreover, the proportion of mantle-derived He in the analysed stibnite is less than 3%, implying that although mantle-derived materials were involved in the mineralisation, the degree of influence was much smaller than that of the dominant crustal source, from which the ore-forming fluids were mainly derived. Mafic magmatic rocks such as gabbro and ultramafic rocks are widely exposed in the regional strata, and the small amount of mantle-derived material in stibnite from the Abunabu mining area may be related to the magma that formed these rocks.

In summary, our analysis of ore-forming fluids and material sources leads us to conclude that the initial ore-forming fluids of the Hamuqu and Quzhen antimony deposits were a mixture of deep magmatic fluids and metamorphic–hydrothermal fluids derived from crust–mantle differentiation. When the magmatic fluids carrying metallogenic materials in the deep crust flowed and ascended into the low-grade-metamorphic sedimentary rocks of the Qiongguo Group ($T_{1\text{-}2}Q$) along a regional shear zone, large volumes of metamorphic fluids and extracted metallogenic materials from these sedimentary rocks were added to the magmatic fluids. Finally, the ore minerals were precipitated from these ore-forming fluids along tensional and torsional fracture zones (Liu et al., 2018; Li. L et al., 2022).

7 Conclusion

1) The Hamuqu and Quzhen deposits in the Abunabu mining area of the Tethys Himalayan metallogenic belt host antimony mineralisation that formed over three stages; i.e., the sedimentary metamorphic, hydrothermal, and supergene stages.
2) The He–Ar isotopic characteristics of fluid inclusions in stibnite indicate that the ore-forming fluids of the Hamuqu and Quzhen deposits were predominantly metamorphic fluids of crustal origin and included small proportions of magmatic-derived materials and modified air-saturated water with low $^{40}Ar^{*}/^{4}He$ ratios. Isotope compositional data for sulphides show that antimony deposits in the Tethys Himalayan metallogenic belt had similar fluid sources and mixing processes but that later evolutionary processes differed between the deposits as a result of variations in the metallogenic tectonic environment within the belt.
3) The $\delta^{34}S$ values of stibnite are consistent with magmatic sulphur, suggesting that the sulphur was derived mainly from a deep magmatic source. Analysis of compiled data for sulphide deposits in the Tethys Himalayan metallogenic belt reveals that antimony–(gold) and lead–zinc–antimony polymetallic deposits in the belt differ in their sulphur isotopic compositions and that multiple isotopic sulphur sources were involved in each of these types of deposit in the metallogenic belt.
4) Crustal fluids were the main contributors to the ore-forming fluids responsible for the metallogenesis of antimony deposits in the Abunabu mining area.

Data availability statement

The original contributions presented in the study are included in the article/supplementary material, further inquiries can be directed to the corresponding authors.

Author contributions

CW and YL; data curation, YL; writing—original draft preparation, YL; supervision, CW, YL, and YL; project administration, YS, YL, and MP. Funding acquisition, CW, YL, YS,

XZ, GM, and ZY. All authors have read and agreed to the published version of the manuscript.

Funding

This study was funded by "Geology of mineral resources in China" project from China Geological Survey (Grant No. DD20221695, DD20190379, DD20160346) and "Chengdu University of Technology Postgraduate Innovative Cultivation Program: Study on mineralization of the Abunabu antimony deposit in the western section of Tethys Himalayan antimony polymetallic metallogenic belt" (Grant No. CDUT2022BJCX002). The fieldwork was strongly supported by the Tibet Autonomous Region Geological Survey Institute. The experimental content was assisted by researcher Liu Feng and associate researcher Fan Changfu of the Institute of Mineral Resources (IMR), Chinese Academy of Geological Sciences (CAGS). Qin Jinhua, (IMR, CAGS), provided guidance for the revision of the manuscript, and reviewers and the editorial department put forward valuable comments and suggestions, which are hereby acknowledged.

Conflict of interest

The authors declare that the research was conducted in the absence of any commercial or financial relationships that could be construed as a potential conflict of interest.

Publisher's note

All claims expressed in this article are solely those of the authors and do not necessarily represent those of their affiliated organizations, or those of the publisher, the editors and the reviewers. Any product that may be evaluated in this article, or claim that may be made by its manufacturer, is not guaranteed or endorsed by the publisher.

Supplementary material

The Supplementary Material for this article can be found online at: https://www.frontiersin.org/articles/10.3389/feart.2022.1033124/full#supplementary-material

References

Andrews, J. N., and Lee, D. J. (1979). Inert gases in groundwater from the Bunter Sandstone of England as indicators of age and palaeoclimatic trends. *J. Hydrology* 41 (3-4), 233–252. doi:10.1016/0022-1694(79)90064-7

Andrews, J. N. (1985). The isotopic composition of radiogenic helium and itsuse to study groundwater movement in confined aquifers. *Chem. Geol.* 49 (1-3), 339–351. doi:10.1016/0009-2541(85)90166-4

Awang, J. C., Zheng, Y. Y., Yang, W. T., and Suolang, O. Z. (2017). Mineral typomorphic characteristics and sources of ore forming materials of Keyue lead zinc polymetallic deposit, southern Tibet. *Geol. Sci. Technol. Inf.* 36 (3), 53–63. doi:10.19509/j.cnki.dzkq.2017.0308

Ballentine, C. J., and Burnard, P. G. (2002). Production, release and transportof noble gases in the continental crust. *Rev. Mineralogy Geochem.* 47 (1), 481–538. doi:10.2138/rmg.2002.47.12

Brian, Fry., Steven, R. S., Carol, K., and Richard, K. A. (2002). Oxygen isotope corrections for online $\delta^{34}S$ analysis. *Rapid Commun. Mass Spectrom.* 16 (9), 854–858. doi:10.1002/rcm.651

Burchfiel, B. C., Chen, Z. L., Hodges, K. V., Liu, Y. P., Royden, L. H., Deng, C. R., et al. (1992). The south Tibetan detachment system, Himalayan orogen: Extension contemporaneous with and parallel to shortening in a collisional mountain belt. *Geol. Soc. Am. Spec. Pap.* 269, 1–41. doi:10.1130/SPE269-p1

Burnard, P. G., Hu, R. Z., Turner, G., and Bi, X. W. (1999). Mantle, crustal and atmospheric noble gases in Ailaoshan gold deposits, Yunnan Province, China. *Geochimica Cosmochimica Acta* 63 (10), 1595–1604. doi:10.1016/S0016-7037(99)00108-8

Burnard, P. G., and Polya, D. A. (2004). Importance of mantle derived fluids during granite associated hydrothermal circulation: He and Ar isotopes of ore minerals from panasqueira 1 1Associate editor: R. Wieler. *Geochimica Cosmochimica Acta* 68 (7), 1607–1615. doi:10.1016/j.gca.2003.10.008

Cao, H. W., Huang, Y., Li, G. M., Zhang, L. K., Wu, J. Y., Dong, L., et al. (2018). Late triassic sedimentary records in the northern tethyan Himalaya: Tectonic link with greater India. *Geosci. Front.* 9 (1), 273–291. doi:10.1016/j.gsf.2017.04.001

Cao, H. W., Li, G. M., Zhang, L. K., Dong, L., Gao, K., and Dai, Z. W. (2020). Monazite U-Th-Pb age of Liemai Eocene granites in the southern Tibet and its geological implications. *Sediment. Geol. Tethyan Geol.* 40, 31–42. doi:10.19826/j.cnki.1009-3850(2020)02-0031-12

Cao, H. W., Li, G. M., Zhang, R. Q., Zhang, Y. H., Zhang, L. K., Dai, Z. W., et al. (2021). Genesis of the Cuonadong tin polymetallic deposit in the Tethyan Himalaya: Evidence from geology, geochronology, fluid inclusions and multiple isotopes. *Gondwana Res.* 92, 72–101. doi:10.1016/j.gr.2020.12.020

Cao, H. W., Pei, Q. M., Santosh, M., Li, G. M., Zhang, L. K., Zhang, X. F., et al. (2022). Himalayan leucogranites: A review of geochemical and isotopic characteristics, timing of formation, Genesis, and rare metal mineralization. *Earth-Science Rev.* 234, 104229. doi:10.1016/j.earscirev.2022.104229

Cao, H. W., Zou, H., Bagas, L., Zhang, L. K., Zhang, Z., and Li, Z. Q. (2019). The Laqiong Sb–Au deposit: Implications for polymetallic mineral systems in the Tethys–Himalayan zone of southern Tibet, China. *Gondwana Res.* 72, 83–96. doi:10.1016/j.gr.2019.02.010

Chaussidon, M., Albarède, F., and Sheppard, S. M. (1989). Sulphur isotope variations in the mantle from ion microprobe analyses of micro–sulphide inclusions. *Earth Planet. Sci. Lett.* 92 (2), 144–156. doi:10.1016/0012-821X(89)90042-3

Chen, X., Su, W. C., and Huang, Y. (2016). He and Ar isotope geochemistry of ore-forming fluids for the Qinglong Sb deposit in Guizhou Province, China. *Acta Petrol. Sin.* 32 (11), 3312–3320.

Chen, Y. M., Da, P. Q., Xiao, N. C., Liu, J. J., Jing, K., Yang, L., et al. (2011). *Detailed investigation report of antimony deposit in Abunabu mine area, gar county, Tibet autonomous region*. Tibet Autonomous Region: Lhasa: Regional Geological Survey Team, Bureau of Geology and Mineral Resources Exploration and Development. (in Chinese).

Dai, Z. W., Dong, L., Li, G. M., Huizenga, M. J., Ding, J., Zhang, L. K., et al. (2020). Crustal thickening prior to 43 Ma in the Himalaya: Evidence from lower crust–derived adakitic magmatism in Dala, eastern Tethyan Himalaya, Tibet. *Geol. J.* 55, 4021–4046. doi:10.1002/gj.3639

Deng, Z. (2020). *Study on genesis of the Mazhala Au-Sb deposit in south tibet(thesis)*. Chengdu, China: Chengdu Univerisity of Technology. doi:10.26986/d.cnki.gcdlc.2020.000479

Deng, Z., Zhang, G. Y., Zheng, Y. Y., and Chen, Y. L. (2019). S–Pb isotope constrains for origin of ore forming material in Cheqiongzhuobu antimony deposit in southern Tibet. *J. Hefei Univ. Technol. Nat. Sci.* 42 (03), 337–345. doi:10.3969/j.iissn.1003-5060.2019.03.007

Ding, D. J., Liang, J. L., Sun, W. D., Guo, J. H., Li, H., and Ye, X. R. (2014). He–Ar isotopes tracing for ore genesis of the yangshan gold deposit. Bulletin of mineralogy. *Petrology Geochem.* 33 (06), 813–819. doi:10.3969/j.issn.1007-2802.2014.06.009

Du, Z. Z. (2011). *Geological, geochemical characteristics and genesis of the Lamuyouta Sb (Au) deposit, south Tibet (thesis)*. Beijing: China University of Geosciences.

Du, Z. Z., Gu, X. X., Li, G. Q., Zhang, Y. M., Cheng, W. B., Jing, L. B., et al. (2011). Sulfur, lead isotope composition characteristics and the relevant instructive significance of the Lamuyouta Sb (Au) deposit, south Tibet. *Geoscience* 25 (5), 853–860.

Duan, J. L., Tang, J. X., and Lin, B. (2016). Zinc and lead isotope signatures of the Zhaxikang Pb–Zn deposit, south Tibet: Implications for the source of the ore–forming metals. *Ore Geol. Rev.* 78, 58–68. doi:10.1016/j.oregeorev.2016.03.019

Fan, W. Y., Zhu, H. P., Gao, J. H., Yan, J., and Mima, C. R. (2012). Characteristics and Genesis of the Cheqiongzhuobu antimony deposit in Tibet. *Mineral. Deposits* 31 (S1), 1019–1020. (in Chinese). doi:10.16111/j.0258-7106.2012.s1.515

Fang, H. Y., Zou, P. X., Shentu, B. Y., Yu, Q. Z., and Zou, Y. X. (2006). *Antimony deposit, Hamuqu mining area, gaer county, xusong Tibet autonomous region*. Chengdu, China: Chengdu Institute of Geology and Mineral Resources. (in Chinese).

Groves, D., Goldfarb, R. J., Gebremariam, M., Hagemanna, S. G., and Robertd, F. (1998). Orogenic gold deposits: A proposed classification in the context of their crustal distribution and relationship to other gold deposit types. *Ore Geol. Rev.* 13 (1-5), 7–27. doi:10.1016/S0169-1368(97)00012-7

Guillot, S., Mahéo, G., De Sigoyer, J., Hattori, K. H., and Pêcher, A. (2008). Tethyan and Indian subduction viewed from the Himalayan high–to ultrahigh–pressure metamorphic rocks. *Tectonophysics* 451 (1-4), 225–241. doi:10.1016/j.tecto.2007.11.059

Guo, C. Y., Zhang, W. Z., Ge, L. S., Gao, B. F., and Xia, R. (2011). Several questions on tracing ore forming fluid by using hydrogen and oxygen isotope system. *Mineralogy Petrology* 31 (03), 41–47. doi:10.19719/j.cnki.1001-6872.2011.03.007

Heyl, A. V., Landis, G. P., and Zartman, R. E. (1974). Isotopic evidence for the origin of Mississippi valley–type mineral deposits: A review. *Econ. Geol.* 69 (6), 992–1006. doi:10.2113/gsecongeo.69.6.992

Hou, Z. Q., Qu, X. M., Yang, Z. S., Meng, X. J., Li, Z. Q., Yang, Z. M., et al. (2006). Metallogenesis in Tibetan collisional orogenic belt: III. Mineralization inpost–collisional extension setting. *Mineral. Deposits* 25 (6), 629–651. doi:10.16111/j.0258-7106.2006.06.001

Hou, Z. Q., and Zhang, H. R. (2015). Geodynamics and metallogenyof the eastern tethyan metallogenic domain. *Ore Geol. Rev.* 70, 346–384. doi:10.1016/j.oregeorev.2014.10.026

Hu, R. Z., Bi, X. W., Jiang, G. H., Chen, H. W., Peng, J. T., Qi, Y. Q., et al. (2012). Mantle-derived noble gases in ore–forming fluids ofthe granite-related Yaogangxian tungsten deposit, southeastern China. *Miner. Deposita* 47 (6), 623–632. doi:10.1007/s00126-011-0396-x

Hu, R. Z., Bi, X. W., and Turner, G. P. B. (1999). He and Ar isotope geochemistry of gold ore–forming fluids in Ailaoshan Gold belt. *Sci. China(Series D:Earth Sci.* 29 (04), 321–330. (in Chinese).

Hu, R. Z., Burnard, P. G., Bi, X. W., Zhou, M. F., Peng, J. T., Su, W. C., et al. (2004). Helium and argon isotope geochemistry of alkaline intrusion–associated gold and copper deposits along the Red River–Jinshajiang fault belt, SW China. *Chem. Geol.* 203 (3-4), 305–317. doi:10.1016/j.chemgeo.2003.10.006

Hu, R. Z., Burnard, P. G., Bi, X. W., Zhou, M. F., Peng, J. T., Su, W. C., et al. (2009). Mantle–derived gaseous components in ore–forming fluids of the Xiangshan uranium deposit, Jiangxi Province, China: Evidencefrom He, Ar and C isotopes. *Chem. Geol.* 266 (1-2), 86–95. doi:10.1016/j.chemgeo.2008.07.017

Hu, X. M., Garzanti, E., Wang, J. G., Huang, W. T., An, W., and Webb, A. (2016). The timing of India-Asia collision onset–facts, theories, controversies. *Earth Sci. Rev.* 160, 264–299. doi:10.1016/j.earscirev.2016.07.014

Huang, Y., Cao, H. W., Li, G. M., Brueckner, S. M., Zhang, Z., Dong, L., et al. (2018). Middle–late Triassic bimodal intrusive rocks from the Tethyan Himalaya in South Tibet: Geochronology, petrogenesis and tectonic implications. *Lithos* 318-319, 78–90. doi:10.1016/j.lithos.2018.08.002

Kali, E., Leloup, P. H., Arnaud, N., Mahéo, G., Liu, D., Boutonnet, E., et al. (2010). ExhumationHistory of the deepest central himalayan rocks, AmaDrime range:key Pressure-Temperature-Deformation-Time constraints on orogenic models. *Tectonics* 29 (2), 1–31. doi:10.1029/2009tc002551

Kendrick, M. A., Burgess, R., Pattrick, R. A. D., and Turner, G. (2001). Fluid inclusion noble gas and halogen evidence on theOrigin of Cu–porphyry mineralising fluids. *Geochim. Cosmochim. Acta* 65 (16), 2651–2668. doi:10.1016/S0016-7037(01)00618-4

Kohn, M. J. (2014). Himalayan metamorphism and its tectonic implications. *Annu. Rev. Earth Planet. Sci.* 42 (1), 381–419. doi:10.1146/annurev-earth-060313-055005

Li, B. L., Wang, L. Q., Zhang, X. G., Pingcuo, D, J., Gao, T., and Wang, Y. (2022). Sulfur and lead isotope compositions and their geological significances in the quzhen Sb mineralization section of the Hamuqu Sb–Au deposit, Tibet. *Acta Geosci. Sin.* 43 (2), 202–210.

Li, C. L., Li, S. R., Yuan, M. W., Du, B. Y., Li, W. L., Masroor, A. L. A. M., et al. (2020). Genesis of the keluo Au deposit in the nenjiang-heihe tectonic mélange belt, heilongjiang province: Evidence from chemical composition and pyrite He-Ar, S, Pb isotopes. *Earth Sci. Front.* 27 (5), 099–115. doi:10.13745/j.esf.sf.2020.5.37

Li, G. M., Zhang, L. K., Jiao, Y. J., Xia, X. B., Dong, S. L., Fu, J. G., et al. (2017). First discovery and implications of Cuonadong superlarge Be–W–Sn polymetallic deposit in Himalayan metallogenic belt, southern Tibet. *Mineral. Deposits* 36 (04), 1003–1008. doi:10.16111/j.0258-7106.2017.04.014

Li, G. Q., Gu, X. X., Cheng, W. B., Zhang, Y. M., Zhang, Y., Dai, H. Z., et al. (2014). The analysis of metallogenic material sources of the Zhaxikang antimony (sulfur salts) polymetallic deposits in Southern Tibet: Concurrent discussion on the differences of the ore sources of major mineral deposits in North Himalay an metallogenic belt. *Earth Sci. Front.* 21 (5), 090–104. doi:10.13745/j.esf.2014.05.008

Li, H., Danišík, M., Zhou, Z. K., Jiang, W. C., and Wu, J. H. (2020b). Integrated U–Pb, Lu–Hf and (U–Th)/He analysis of zircon from the Banxi Sb deposit and its implications for the low-temperature mineralization in South China. *Geosci. Front.* 11, 1323–1335. doi:10.1016/j.gsf.2020.01.004

Li, H., Kong, H., Guo, B. Y., Soh Tamehe, L., Zhang, Q., Wu, Q. H., et al. (2020a). Fluid inclusion, H–O–S isotope and rare Earth element constraints on the mineralization of the Dong'an Sb deposit, South China. *Ore Geol. Rev.* 126, 103759. doi:10.1016/j.oregeorev.2020.103759

Li, H., Kong, H., Zhou, Z. K., Tindell, T., Tang, Y. Q., Wu, Q. H., et al. (2019). Genesis of the Banxi Sb deposit, South China: Constraints from wall-rock geochemistry, fluid inclusion microthermometry, Rb–Sr geochronology, and H–O–S isotopes. *Ore Geol. Rev.* 115, 103162. doi:10.1016/j.oregeorev.2019.103162

Li, H., Wu, Q. H., Evans, N. J., Zhou, Z. K., Kong, H., Xi, X. S., et al. (2018). Geochemistry and geochronology of the Banxi Sb deposit: Implications for fluid origin and the evolution of Sb mineralization in central-Western Hunan, South China. *Gondwana Res.* 55, 112–134. doi:10.1016/j.gr.2017.11.010

Li, H., Zhu, D. P., Shen, L. W., Algeo, T. J., and Elatikpo, S. M. (2022). A general ore formation model for metasediment-hosted Sb-(Au-W) mineralization of the Woxi and Banxi deposits in South China. *Chem. Geol.* 607, 121020. doi:10.1016/j.chemgeo.2022.121020

Li, J. G. (2000). *Study on composite Sedex type Antimony and copper deposits in Mesozoic continental margin of central and southern Tibet (thesis)*. Chengdu, China: Chengdu Univerisity of Technology.

Li, J. J., Li, J., Liu, H. B., Zhang, J., Jin, G. S., Zhang, J. F., et al. (2015). Helium isotope composition of inclusions in mineral grains using Helix SFT noble gas mass spectrometer. *Acta Geol. Sin.* 89 (10), 1826–1831.

Li, Y., Wang, D. H., Wang, C. H., Sun, Y., and Mima, P. C. (2021). Geology and geochemistry of selected gold deposits in the ailaoshan metallogenic belt, China: Origin of ore-forming fluids. *Minerals* 11 (11), 1276. doi:10.3390/min11111276

Liang, W. (2019). Characteristics of Ore-Forming fluids in himalayan Au-Sb-Pb-Zn polymetallic belt: Constraints from H-O isotopes. *Earth Sci.* 44 (7), 2308–2321. doi:10.3799/dqkx.2019.172

Liang, W. (2014). *Metallogenesis of Au–Sb–Pb–Zn mineralization in Tethys Himalaya belt, south Tibet, China (thesis)*. Beijing: China University of Geosciences.

Liang, W., Zhang, L. K., Xia, X. B., Ma, G. T., Huang, Y., Zhang, Z., et al. (2018). Geology and preliminary mineral genesis of the cuonadong W–Sn polymetallic deposit, southern Tibet, China. *Earth Sci.* 43 (08), 2742–2754. doi:10.3799/dqkx.2018.154

Liu, H., Li, G. M., Huang, H. X., Xiao, W. F., Yan, G. Q., Ma, D. F., et al. (2018). Sources of ore-forming materials in the shangxu orogenic gold deposit, northern xizang(tibet): Constraints form C, S, and Pb isotopes. *Geol. Rev.* 64 (05), 1285–1301. doi:10.16509/j.georeview.2018.05.019

Liu, T., Tian, S. H., Wang, D. H., Hou, K. J., Zhang, Y. J., Li, X. F., et al. (2021). Characteristics of ore–forming fluids in kalu'an hard–rock–type lithium deposit in xinjiang province, China: Evidence from He–Ar isotopes. *Geol. Rev.* 67 (06), 1697–1708. doi:10.16509/j.georeview.2021.06.021

Lou, Y. L., Chen, W., Yuan, Y. S., and Yang, T. (2018). Fluid inclusion and H, O, and S isotopic composition of Qiaga stibnite deposit in Longzi County, Tibet. *Mineral. Deposits* 37 (5), 1124–1140. doi:10.16111/j.0258-7106.2018.05.014

Ma, Z. N., Han, Z. P., Li, Y. L., Bi, W. J., Xu, T. K., and Xiao, S. Q. (2022). Exhumation history of the Kampa dome in the southern Tibet: Evidence from low temperature thermochronology. *Sediment. Geol. Tethyan Geol.* 42, 300–309. doi:10.19826/j.cnki.1009-3850.2022.04009

Mamyrin, B. A., and Tolstikhin, I. N. (1984). *Helium isotopes in nature*. New York: Elsevier Science Publishers.

Mao, J. W., and Li, X. F. (2004). Mantle–derived fluids in relation to ore–forming and oil–forming processes. *Mineral. Deposits* 23 (4), 520–532. doi:10.16111/j.0258-7106.2004.04.013

Martin, A. J. (2017). A review of definitions of the himalayan main central thrust. *Int. J. Earth Sci.* 106 (6), 2131–2145. doi:10.1007/s00531-016-1419-8

Marty, B., Jambon, A., and Sano, Y. (1989). Helium isotopes and CO_2 in volcanic gases of Japan. *Chem. Geol.* 76 (1-2), 25–40. doi:10.1016/0009-2541(89)90125-3

McDougall, I., Mac Dougall, I., and Harrison, T. M. (1999). *Geochronology and thermochronology by the $^{40}Ar/^{39}Ar$ method*. Oxford, United Kingdom: Oxford University Press on Demand, 1–269.

Meng, X. J., Yang, Z. S., Qi, X. X., Hou, Z. Q., and Li, Z. Q. (2008). Silicon–oxygen–hydrogen isotopic compositions of Zaxikang antimony polymetallic deposit in southern Tibet and its responses to the ore–controling structure. *Acta Petrol. Sin.* 24 (7), 1649–1655.

Miao, H. Q., Li, G. M., Zhang, Z., Xia, B. B., and Liang, W. (2017). Origin of the Keyue Pb–Zn polymetallic deposit in southern Xizang: Evidences from sulfur and lead isotopic compositions. *Sediment. Geol. Tethyan Geol.* 37 (2), 14–22.

Nie, F. J., Hu, P., Jiang, S. H., Li, Z. X., Liu, Y., and Zhou, Y. Z. (2005). Type and temporal–spatial distribution of gold and antimony deposits (prospects) in southern Tibet, China. *Acta Geol. Sin.* 79 (03), 373–385.

Ohmoto, H. (1972). Systematics of sulfur and carbon isotopes in hydrothermal ore deposits. *Econ. Geol.* 67 (5), 551–578. doi:10.2113/gsecongeo.67.5.551

Olierook, H. K. H., Jiang, Q., Jourdan, F., and Chiaradia, M. (2019). Greater Kerguelen large igneous province reveals no role for Kerguelen mantle plume in the continental breakup of eastern Gondwana. *Earth Planet. Sci. Lett.* 511, 244–255. doi:10.1016/j.epsl.2019.01.037

Pan, G. T., Wang, L. Q., Yin, F. G., Geng, Q. R., Li, G. M., and Zhu, D. C. (2022). Researches on geological tectonic evolution of Tibetan plateau: A review, recent advances, and directions in the future. *Sediment. Geol. Tethyan Geol.* 42, 151–175. doi:10.19826/j.cnki.1009-3850.2022.05004

Patterson, D. B., Honda, M., and McDougall, I. (1994). Noble gases in mafic phenocrysts and xenoliths from New Zealand. *Geochimica Cosmochimica Acta* 58 (20), 4411–4427. doi:10.1016/0016-7037(94)90344-1

Porcelli, D. R., O'Nions, R. K., Galer, S. J. G., Cohen, A. S., and Mattey, D. P. (1992). Isotopic relationships of volatile and lithophile trace elements incontinental ultramafic xenoliths. *Contributions Mineralogy Petrology* 110 (4), 528–538. doi:10.1007/bf00344086

Qi, X. X., Li, T. F., Meng, X. J., and Yu, C. L. (2008). Cenozoic tectonic evolution of the Tethys Himalaya foreland fault–fold belt in southern Tibet, and its constraint on antimony–gold polymetallic minerogenesis. *Acta Petrol. Sin.* 24 (7), 1638–1648.

Qiu, H. N. (1996). ^{40}Ar-^{39}Ar dating of the quartz sample from two mineral deposits in Western Yunnan (SW China) by crushing in vacuum. *Chem. Geol.* 127 (1-3), 211–222. doi:10.1016/0009-2541(95)00093-3

Qu, X. M., Hou, Z. Q., and Li, Y. G. (2002). Implications of S and Pb isotopic compositions of the Gangdise porphyry copper belt for the ore–forming material source and material recycling within the orogenic belt. *Geol. Bull. China* 21 (11), 768–776.

Qu, X. M., Hou, Z. Q., and Zhang, Q. L. (2003). *The report of prospective value of Cu, Au, Sb poly–metallic mineral resources in Tibet*. CAGS: Unpublished open-file report, Institute of Mineral Resources, 194. (in Chinese).

Reid, M. R., and Graham, D. W. (1996). Resolving lithospheric and sub–lithospheric contributions to helium isotope variations in basalts from the southwestern US. *Earth Planet. Sci. Lett.* 144 (1-2), 213–222. doi:10.1016/0012-821X(96)00166-5

Richards, A., Argles, T., Harris, N., Parrish, R., Ahmad, T., Darbyshire, F., et al. (2005). Himalayan architecture constrained by isotopic tracers from clastic sediments. *Earth Planet. Sci. Lett.* 236 (3-4), 773–796. doi:10.1016/j.epsl.2005.05.034

Seal, R. R. (2006). Sulfur isotope geochemistry of sulfide minerals. *Rev. Mineralogy Geochem.* 61 (1), 633–677. doi:10.2138/rmg.2006.61.12

Searle, M. P. (2019). Timing of subduction initiation, arc formation, ophiolite obduction and India–Asia collision in the Himalaya. *Geol. Soc. Lond., Spec. Publ.* 483, 19–37. doi:10.1144/SP483.8

Simmons, S. F., Sawkins, F. J., and Schlutter, D. J. (1987). Mantle-derived heliumin two Peruvian hydrothermal ore deposits. *Nature* 329 (6138), 429–432. doi:10.1038/329429a0

Stuart, F. M., Burnard, P. G., Taylor, R. P., and Turner, G. (1995). Resolving mantle and crustal contributions to ancient hydrothermal fluids: He–Ar isotopes in fluid inclusions from dae hwa W–Mo mineralisation, South Korea. *Geochimica Cosmochimica Acta* 59 (22), 4663–4673. doi:10.1016/0016-7037(95)00300-2

Stuart, F., Turner, G., and Taylor, R. P. (1994). "He-Ar isotope systematics of fluid inclusions: Resolving mantle and crustal contributions to hydrothermal fluids," in *Noble gas geochemistry and cosmochemistry*. Editor J. Matsuda (Tokyo: Terra Scientific Publishing Company), 261–277.

Sun, J., Zhou, C., Lu, W., Guo, A. M., Xiao, R., Wei, H. T., et al. (2020). He–Ar–Sr isotope geochemistry of ore–forming fluids in the gutaishan Au–Sb deposit in hunan province and its significance for deep prospecting. *Acta Geosci. Sin.* 41 (2), 267–279. doi:10.3975/cagsb.2020.021101

Sun, X., Wei, H., Zhai, W., Shi, G., Liang, Y., Mo, R. W., et al. (2016). Fluid inclusion geochemistry and Ar–Ar geochronology of the Cenozoic Bangbu orogenic gold deposit, southern Tibet, China. *Ore Geol. Rev.* 74, 196–210. doi:10.1016/j.oregeorev.2015.11.021

Sun, X., Zheng, Y. Y., Pirajno, F., McCuaig, T. C., Yu, M., Xia, S. L., et al. (2018). Geology, S–Pb isotopes, and ^{40}Ar/^{39}Ar geochronology of the Zhaxikang Sb–Pb–Zn–Ag deposit in southern Tibet: Implications for multiple mineralization events at Zhaxikang. *Miner. Deposita* 53 (3), 435–458. doi:10.1007/s00126-017-0752-6

Turner, G., and Stuart, F. M. (1992). Helium/heat ratios and deposition temperatures of sulphides from the ocean floor. *Nature* 357 (6379), 581–583. doi:10.1038/357581a0

Turner, G., and Wang, S. S. (1992). Excess argon, crustal fluids and apparent isochrons from crushing K–Feldspar. *Earth Planet. Sci. Lett.* 110 (1-4), 193–211. doi:10.1016/0012-821X(92)90048-Z

Wang, C. L., Huang, H., Tong, X. X., Zheng, M. T., Peng, Z. D., Nan, J. B., et al. (2016). Changing provenance of late Neoarchean metasedimentary rocks in the Anshan-Benxi area, North China Craton: Implications for the tectonic setting of the worldclass Dataigou banded iron formation. *Gondwana Res.* 40, 107–123. doi:10.1016/j.gr.2016.08.010

Wang, D. H. (2019b2019). Discussion on issues related to strategic key mineral resources. *Geol. Chem. Minerals* 41 (2), 65–72.

Wang, D. H. (2019a). Study on critical mineral resources: Significance of research, determination of types, attributes of resources, progress of prospecting, problems of utilization, and direction of exploitation. *Acta Geol. Sin.* 93 (6), 1189–1209. doi:10.19762/j.cnki.dizhixuebao.2019186

Wang, D., Sun, X., Zheng, Y. Y., Wu, S., Xia, S. L., Chang, H. F., et al. (2017). Two pulses of mineralization and Genesis of the Zhaxikang Sb–Pb–Zn–Ag deposit in southern Tibet: Constraints from Fe–Zn isotopes. *Ore Geol. Rev.* 84, 347–363. doi:10.1016/j.oregeorev.2016.12.030

Wang, D., Zheng, Y. Y., Zhang, J. F., Wu, S., Zhang, S. K., Yu, M., et al. (2020). The Sr–He–Ar isotopic and elemental evidence constraints on the ore Genesis of the Zhaxikang Sb–Pb–Zn–Ag deposit in southern Tibet. *Geol. J.* 55 (4), 2631–2645. doi:10.1002/gj.3537

Wen, C. Q., Duo, J., Fan, X. P., Hu, X. C., Li, B. H., Sun, Y., et al. (2006). Characteristics of ore fluids of the Mayum gold deposit, Western Tibet, China. *Geol. Bull. China* 25 (1), 261–266.

Wu, F. Y., Liu, Z. C., Liu, X. C., and Ji, W. Q. (2015). Himalayan leucogranite: Petrogenesis and implications to orogenesis and plateau uplift. *Acta Petrol. Sin.* 31 (1), 1–36.

Xie, Y. L., Li, L. M., Wang, B. G., Li, G. M., Liu, H. F., Li, Y. X., et al. (2017). Genesis of the Zhaxikang epithermal Pb–Zn–Sb deposit in southern Tibet, China: Evidence for a magmatic link. *Ore Geol. Rev.* 80, 891–909. doi:10.1016/j.oregeorev.2016.08.007

Yang, Z. S., Hou, Z. Q., Gao, W., Wang, H. P., Li, Z. Q., Meng, X. J., et al. (2006). Metallogenic characteristics and genetic model of antimony and gold depositsin south Tibetan detachment system. *Acta Geol. Sin.* 80 (09), 1377–1391.

Yang, Z. S., Hou, Z. Q., Meng, X. J., Liu, Y. C., Fei, H. C., Tian, S. H., et al. (2009). Post–collisional Sb and Au mineralization related to the South Tibetan detachment system, Himalayan orogen. *Ore Geol. Rev.* 36 (1-3), 194–212. doi:10.1016/j.oregeorev.2009.03.005

Yin, A. (2006). Cenozoic tectonic evolution of the Himalayan orogen as constrained by along–strike variation of structural geometry, exhumation history, and foreland sedimentation. *Earth Sci. Rev.* 76, 1–131. doi:10.1016/j.earscirev.2005.05.004

Yin, A., and Harrison, T. M. (2000). Geologic evolution of the Himalayan–Tibetan orogen. *Annu. Rev. Earth Planet. Sci.* 28 (1), 211–280. doi:10.1146/annurev.earth.28.1.211

Zhai, W., Sun, X. M., Yi, J. Z., Zhang, X. G., Mo, R. W., Zhou, F., et al. (2014). Geology, geochemistry, and genesis of orogenic gold–antimony mineralization in the himalayan orogen, south Tibet, China. *Ore Geol. Rev.* 58, 68–90. doi:10.1016/j.oregeorev.2013.11.001

Zhai, W., Zheng, S. Q., Sun, X. M., Wei, H. X., Mo, R. W., Zhang, L. Y., et al. (2018). He–Ar isotope compositions of orogenic Mazhala Au–Sb and Shalagang Sb deposits in Himalayan orogeny, southern Tibet: Constrains to ore–formingfluid origin. *Acta Petrol. Sin.* 34 (12), 3525–3538.

Zhang, G. Y. (2012). *Metallogenic model and prospecting potential in southern Tibet Au–Sb polymetallic belt (thesis)*. Wuhan: China University of Geosciences.

Zhang, J. F., Zheng, Y. Y., Zhang, G. Y., Gao, S. B., Ye, X. R., Zhang, Z., et al. (2010). Genesis of Zhaxikang Pb–Zn–Sb–Ag deposit in northern Himalaya:constraints from multi-isotope geochemistry. *Earth Science-Journal China Univ. Geosciences* 35 (6), 1000–1010. doi:10.3799/dqkx.2010.113

Zhang, J. J., Santosh, M., Wang, X. X., Guo, L., Yang, X. Y., and Zhang, B. (2012). Tectonics of the northern Himalaya since the India–Asia collision. *Gondwana Res.* 21 (4), 939–960. doi:10.1016/j.gr.2011.11.004

Zhang, K. J., Xia, B. D., Wang, G. M., Li, Y. T., and Ye, H. F. (2004). Early Cretaceous stratigraphy, depositional environments, sandstone provenance, and tectonic setting of central Tibet, Western China. *Geol. Soc. Am. Bull.* 116 (9-10), 1202–1222. doi:10.1130/B25388.1

Zhang, K. J., Zhang, Y. X., Li, B., and Zhong, L. F. (2007). Nd isotopes of siliciclastic rocks from Tibet, Western China: Constraints on provenance and pre-Cenozoic tectonic evolution. *Earth Planet. Sci. Lett.* 256 (3), 604–616. doi:10.1016/j.epsl.2007.02.014

Zhang, L. K., Li, G. M., Santosh, M., Cao, H. W., Dong, S. L., Zhang, Z., et al. (2019). Cambrian magmatism in the Tethys Himalaya and implications for the evolution of the proto–tethys along the northern gondwana margin: A case study and overview. *Geol. J.* 54, 2545–2565. doi:10.1002/gj.3311

Zhang, S. K. (2016). *Geological and geochemistrical characteristics of Zhaxikang antimony polym etallic deposit, southern tibet(thesis)*. Beijing: China University of Geosciences.

Zhang, S. Z., Li, J. H., Li, G. D., Zhang, H. B., Gao, X., Wu, L. H., et al. (2005). *Report of 1: 250000 Zada county regional geological survey in Tibet*. Hebei: Hebei Institute of Geological Survey. (in Chinese).

Zheng, Y. Y., Fan, W. Y., Zhang, X. B., Yan, J., Liu, M. Y., Zhang, H. P., et al. (2003). *Geological report on resource investigation and evaluation of Gyantz–Longzi gold and antimony polymetallic metallogenic belt in Tibet*. Lhasa: Geological Survey Institute of Tibet Autonomous Region. (in Chinese).

Zheng, Y. Y., Liu, M. Y., Sun, X., Yuan, E. H., Tian, L. M., Zheng, H. T., et al. (2012). Type, discovery process and significance of Zhaxikang antimony polymetallic ore deposit, Tibet. *Earth Science-Journal China Univ. Geosciences* 37 (5), 1003–1014. doi:10.3799/dqkx.2012.108

Zheng, Y. Y., Sun, X., Tian, L. M., Zheng, H. T., Yu, M., Yang, W. T., et al. (2014). Mineralization, deposit type and metallogenic age of the gold antimony polymetallic belt in the eastern part of north Himalayan. *Geotect. Metallogenia* 38 (1), 108–118.

Zheng, Y. Y., Wang, D., Yi, J. Z., Yu, Z. Z., Jiang, Z. X., Li, X. X., et al. (2022). Antimony mineralization and prospecting orientation in the north Himalayan metallogenic belt, Tibet. *Earth Sci. Front.* 29 (01), 200–230. doi:10.13745/j.esf.sf.2021.8.5

Zhou, Q., Li, G. M., Xia, X. B., Wu, J. Y., Lai, Y., Li, Y. X., et al. (2014). Metallogenic model of Zhaxikang Pb-Zn polymetallic ore cluster in South Tibet. *Mineral. Deposits* 33 (S1), 353–354. (in Chinese). doi:10.16111/j.0258-7106.2014.s1.179

Zhou, Q., Li, W. C., Qing, C. S., Lai, Y., Li, Y. X., Liao, Z. W., et al. (2017). Origin and tectonic implications of the Zhaxikang Pb–Zn–Sb–Ag deposit in northern Himalaya: Evidence from structures, Re–Os–Pb–S isotopes, and fluid inclusions. *Miner. Deposita* 53 (4), 585–600. doi:10.1007/s00126-017-0760-6

Zhu, D. C., Zhao, Z. D., Pan, G. T., Lee, H. Y., Kang, Z. Q., Liao, Z. L., et al. (2009). Early cretaceous subduction–related adakite–like rocks of the Gangdese Belt, southern Tibet: Products of slab melting and subsequent melt–peridotite interaction? *J. Asian Earth Sci.* 34 (3), 298–309. doi:10.1016/j.jseaes.2008.05.003

Zhu, L. K., Gu, X. X., Li, G. Q., Zhang, Y. M., Cheng, W. B., and Bian, X. D. (2012). Fluid inclusions in the Zhaxikang Pb–Zn–Sb polymetallic deposit, south Tibet, and its geological significance. *Geoscience* 26 (3), 453–463.

Zou, H., Cao, H. W., Bagas, L., Zhang, Y. H., Zhang, S. T., Zhang, Q., et al. (2019). Origin of the Mo-bearing xiaoshuijing syenogranite in the tengchong terrane, SW China. *Ore Geol. Rev.* 105, 258–272. doi:10.1016/j.oregeorev.2018.12.018

Zou, H., Fang, Y., Zhang, S. T., and Zhang, Q. (2017). The source of fengjia and langxi barite–fluorite deposits in southeastern sichuan, China: Evidence from rare Earth elements and S, Sr, and Sm–Nd isotopic data. *Geol. J.* 52 (3), 470–488. doi:10.1002/gj.2779

frontiers | Frontiers in Earth Science

TYPE Original Research
PUBLISHED 06 January 2023
DOI 10.3389/feart.2022.1104197

OPEN ACCESS

EDITED BY
Hu Wang,
Southwest Jiaotong University, China

REVIEWED BY
Xu Zhao,
Guangzhou Institute of Geochemistry (CAS), China
Yong Wang,
Chengdu University of Technology, China

*CORRESPONDENCE
Zhiming Yang,
zm.yang@hotmail.com
Huawen Cao,
caohuawen1988@126.com

SPECIALTY SECTION
This article was submitted to Structural Geology and Tectonics, a section of the journal Frontiers in Earth Science

RECEIVED 21 November 2022
ACCEPTED 14 December 2022
PUBLISHED 06 January 2023

CITATION
Dai Z, Yang Z, Li G, Xie Y, Dong L, Gao K and Cao H (2023), Partial melting of amphibolitic lower crust and subsequent melt-crystal separation for generation of the Early Eocene magmatism in eastern Himalaya. *Front. Earth Sci.* 10:1104197. doi: 10.3389/feart.2022.1104197

Partial melting of amphibolitic lower crust and subsequent melt-crystal separation for generation of the Early Eocene magmatism in eastern Himalaya

Zuowen Dai[1], Zhiming Yang[1,2]*, Guangming Li[3], Yuling Xie[1], Lei Dong[3], Ke Gao[3] and Huawen Cao[3]*

[1]School of Civil and Resource Engineering, University of Science and Technology Beijing, Beijing, China, [2]Institute of Geology, Chinese Academy of Geological Sciences, Beijing, China, [3]Chengdu Center, China Geological Survey, Chengdu, China

The Himalayan leucogranites provide a good opportunity to investigate the crustal evolution of the southern Qinghai-Tibet Plateau. In this study, we present zircon U-Pb and monazite U-Th-Pb ages, zircon Hf isotopes and whole-rock Sr-Nd-Pb isotopes and major and trace elements for the Liemai two-mica granite, eastern Himalaya. Together with previously published data we revalued the petrogenesis of the Early Eocene magmatic rocks in this region and their geological implications. The zircon and monazite U-(Th)-Pb dating results showed that the Liemai two-mica granite was generated at ~ 43 Ma, similar to adjacent Yardoi, Dala and Quedang adakitic two-mica granites, Ridang subvolcanic rocks and Yardoi leucogranite. The Liemai two-mica granite, similar to these coeval adakitic two-mica granites, is enriched in SiO_2, Al_2O_3, Th, U, Pb, La, and Sr, and depleted in MgO, total iron, Yb and Y with high Sr/Y and (La/Yb)N ratios (showing adakitic affinities), and exhibits enriched Sr-Nd-Pb-Hf isotopic compositions, suggesting an origin of a thickened lower crust consisting mainly of garnet amphibolite. Although the Ridang subvolcanic rocks and Yardoi leucogranite show similar Sr-Nd-Hf isotopes to these adjacent coeval two-mica granites, perceptible differences in whole-rock major and trace elements can be observed. Broadly, these granites can be divided into high-Mg# granites (HMGs, the two-mica granites) and low-Mg# granites (LMGs, the Ridang subvolcanic rocks and Yardoi leucogranite). The former has relatively higher contents of total iron, MgO, Mg#, TiO_2, P_2O_5, LREE, Y, Th, Sr, incompatible elements (Cr and Ni) and Eu/Eu* values, and lower contents of SiO_2 and Rb/Sr and Rb/Ba ratios, thus is less evolved than the latter. According to recent studies of differentiation processes in silicic magma reservoirs, we proposed that the HMGs represent a congealed crystal mush that was composed of 'cumulate crystals' and a trapped interstitial liquid, while the LMGs represent the almost pure liquid that was extracted from the crystal mush. Modeling using the trace elements Sr and Ba shows that the extraction probably occurred when the crystallinity of the mush was ~ 60%–63%, at least for the most evolved LMGs sample. The HMGs correspond to a residual crystal mush that had a terminal porosity of ~ 21%–25%

filled with a trapped interstitial liquid. Underplating of mafic magmas following slab breakoff of the Neo-Tethys oceanic lithosphere caused partial melting of the amphibolitic lower crust, which had been thickened to ~50 km prior to ~43 Ma.

KEYWORDS

adakitic rocks, crystal mush, melt-crystal separation, crustal thickening, Liemai, Himalaya

1 Introduction

Magma is an important carrier for material and energy exchange among inner spheres of our planet (Mo et al., 2007; Yang et al., 2015a; Yang et al., 2015b; Yang et al., 2016a; Zheng et al., 2016; Cao et al., 2022a). Magmatic rocks are regarded as a "probe" for exploring the deep Earth, and carry crucial information for crustal evolution, plate movement and tectonic events (Mo et al., 2007; Zhu et al., 2009a; Mo, 2011; Hou et al., 2015; Li et al., 2020). It is noteworthy that significant breakthroughs have been made in qualitative and even quantitative estimation for crustal thickness in ancient orogens using some geochemical indices of intermediate-felsic magmatic rocks or accessory minerals therein (Profeta et al., 2015; Hu et al., 2017; Tang et al., 2020; Luffi and Ducea, 2022). For example, magmatic rocks with high Sr/Y and $(La/Yb)_N$ ratios, i.e., adakites or adakitic rocks (Martin, 1986; Defant and Drummond, 1990), are typically considered as prototypical products of high pressure condition, thus indicating an abnormally thick crust (>50 km) (Xu et al., 2002; Chung et al., 2003; Dai et al., 2020a; 2020b; Zeng et al., 2020). The theoretical basis for this crustal thickness estimation is the pressure-dependent behavior of Sr, Y, La, and Yb during partial melting of lower crustal mafic rocks (or their metamorphic equivalents) and fractionation of mantle-derived mafic magmas in the lower crust. At low pressure (<~1.0 GPa), Sr preferentially incorporates into plagioclase, whereas Y and Yb still remain in the melt, resulting in low Sr/Y and La/Yb ratios in the melt. However, at high pressure (>~1.0 GPa), Y and Yb preferentially partitions into garnet and amphibole, while Sr and La remain in the melt, resulting in melts with high Sr/Y and La/Yb values (Davidson et al., 2007; Moyen, 2009).

In southern Qinghai-Tibet Plateau, voluminous Cenozoic leucogranites were well developed along the Himalaya orogenic belt forming a 2,000 km-long west-east trending leucogranite belt (Liu et al., 2017; Wu et al., 2020; Cao et al., 2022b). These massive magmatic rocks were formed during the collision between India and Eurasia, thus play a crucial role in exploring the evolution of the orogenic belt (Hou et al., 2012; Wu et al., 2015; Fu et al., 2020; Zhang et al., 2020). For instance, the Early Eocene granites were normally considered as adakitic rocks based on their high Sr/Y ratios, thus were viewed as products of partial melting of a thickened (>50 km) lower crust (Zeng et al., 2011, 2015; Hou et al., 2012; Dai et al., 2020a). However, a recent study proposed that the fractional crystallization (plagioclase accumulation), rather than melting at the base of the thickened crust, was probably responsible for generation of the high Sr/Y ratios of these adakitic rocks (Gao et al., 2021). Undoubtedly, this novel viewpoint pushes us to rethink the traditional perception for generation of these Early Eocene magmatic rocks as well as the evolutionary history of crust in the Himalayan orogen.

In this study we present monazite U-Th-Pb and zircon U-Pb ages, zircon Hf and whole-rock Sr-Nd-Pb isotopes and whole-rock major and trace elements for two-mica granite exposed in Liemai (village), southeastern Yardoi dome. Together with previously published data we revalued the petrogenesis of the Early Eocene magmatic rocks in this region and their geological implications.

2 Geological setting and sample description

Himalaya, the south most component of the Qinghai-Tibet plateau, is the highest and youngest collisional orogen on Earth resulted from collision between India and Asia during Late Cretaceous to Paleocene (Figure 1; Yin and Harrison, 2000; Yin, 2006; Pan et al., 2012; Kohn, 2014). It is bound by the Indus-Yarlung Tsangpo Suture zone in the north from the Lhasa terrane and the Main Frontier Thrust (MFT) in the south from the Indian plate. The Himalaya can be subdivided into the Tethyan Himalayan Sequence (THS), Higher Himalayan Crystalline Sequence (HHCS), Lower Himalayan Sequence (LHS), and the Sub-Himalayan Sequence (SHS) (Figure 1). These subterranes are separated by several north-dipping fault systems, from north to south including the south Tibet detachment system (STDS), the Main Central Thrust (MCT), and the Main Boundary Thrust (MBT) (Figure 1). The STDS represents a normal fault system while the other two are reverse faults (Leloup et al., 2010; Zhang et al., 2012). The THS represents the Indian passive continental margin sedimentary sequences and mainly comprises Late Proterozoic to Mesozoic unmetamorphosed or low-grade metamorphic siliciclastic and carbonate rocks; The HHCS represents a series of Late Proterozoic to Paleozoic metasedimentary sequences (typically upper amphibolite to lower granulite facies) that were derived from the basement of the Indian continent; The LHS represents a suite of Proterozoic low-grade metamorphic rocks (typically greenschist to amphibolite facies); While the SHS represents a series of coarse-grained clastic sediments (Siwalik Group), which

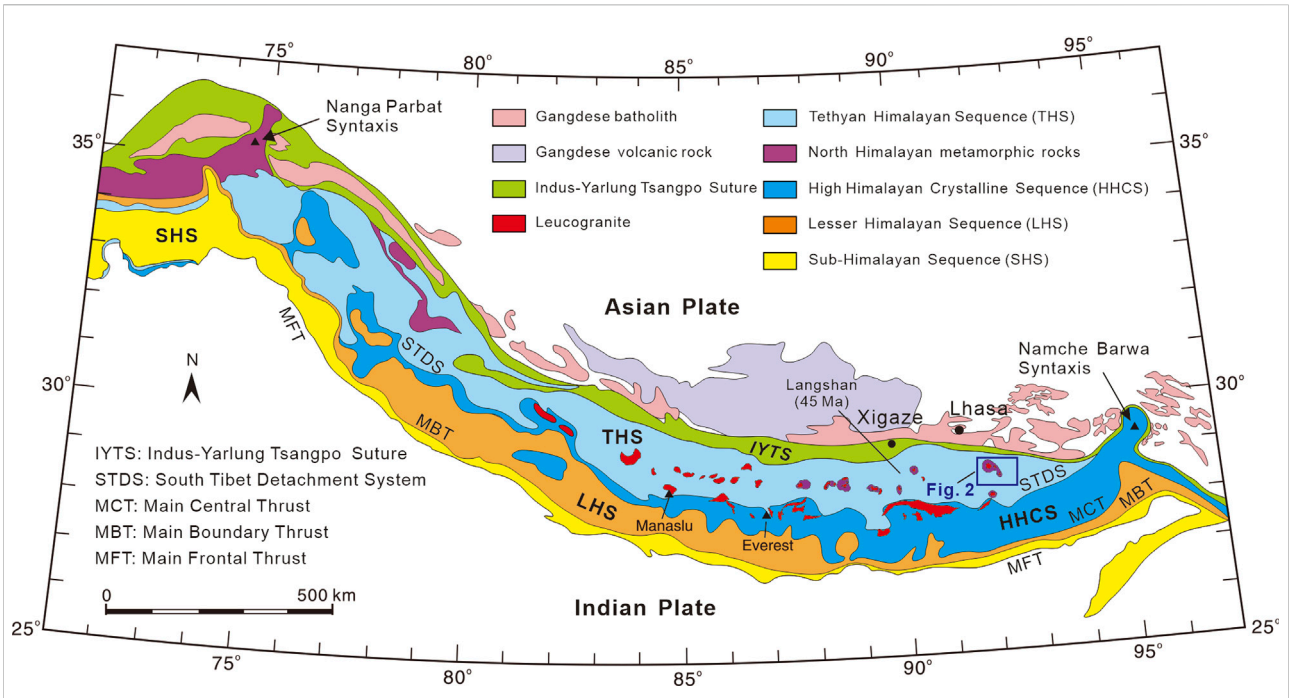

FIGURE 1
Simplified geological map of Himalaya, showing the subdivision of this orogen and distribution of leucogranites (modified after Yin and Harrison (2000), Yin (2006), Pan et al. (2012) and Kohn (2014)).

were deposited during foreland molasse sedimentation following the uplift of the Himalaya (Kohn, 2014; Cao et al., 2018; Myrow et al., 2019).

Owing to continuous collision between India and Asia, the Himalayan crust experienced intense and extensive deformation, metamorphism and anatexis, which resulted in formation of voluminous leucogranites. These leucogranites constitute two huge sub-parallel leucogranite belts, i.e. the Tethyan Himalayan leucogranite belt (also konwn as the North Himalayan leucogranite belt) to the north and the Higher Himalayan leucogranite belt to the south (Figure 1; Wu et al., 2015). Normally, the Higher Himalayan leucogranites were emplaced into the HHCS adjacent to the STDS forming a discontinuous chain of sheets, dykes, sills, and laccolithic bodies (Figure 1; Wu et al., 2015). In contrast, most Tethyan Himalayan leucogranites are exposed in the cores of the north Himalayan gneiss domes, except for a few isolated intrusions and sills that intruded into the THS (such as the Dala and Quedang two-mica granites) (Figure 1; Wu et al., 2015). The Himalayan leucogranites are composed of biotite granite, two-mica granite, muscovite granite, tourmaline granite, and garnet granite, and were emplaced between 48.5 and 0.7 Ma (Wu et al., 2015, 2020; Cao et al., 2022b). Typically, the Miocene leucogranites are considered as highly fractionated (strong) peraluminous S-type granites (Wu et al., 2015, 2020). While the majority of Eocene granites are characterized by high Sr/Y ratios and, therefore, considered as products of partial melting of a thickened amphibolitic lower crust with minor metapelites (Zeng et al., 2011, 2015; Hou et al., 2012; Dai et al., 2020a).

The Himalayan Eocene granites were mainly exposed in Yardoi (Yalaxiangbo) gneiss dome and areas nearby, occurred as stocks (Yardoi, Dala and Quedang), and dikes or sills (Liemai and Ridang) (Figure 2; Zeng et al., 2015; Cao et al., 2022b). The majority of granites in this region were generated in the Early Eocene (Ca. 40~48 Ma; Qi et al., 2008; Aikman et al., 2008, 2012; Zeng et al., 2011, 2015; Hou et al., 2012; Wu et al., 2014; Tian et al., 2018; Dai et al., 2020a; Cao et al., 2020) except for minor that were formed at the Early Eocene (~35 Ma; Zeng et al., 2009; Wu et al., 2014). On the basis of lithologic features, these Early Eocene granites can be divided into two types, i.e., two-mica granite and leucogranite granite (almost without biotite). The former constituted the main part of the Early Eocene granites in Yardoi area, including Yardoi, Dala and Quedang two-mica granite and the majority of adjacent sills (Hou et al., 2012; Zeng et al., 2015; Dai et al., 2020a). While the latter exposed as minor sills or dikes in Yardoi dome (Yardoi leucogranite) or in County Longzi (near Ridang town) (subvolcanic rocks) (Hu et al., 2011b; Zeng et al., 2015). Samples in this study were collected from a sill with a width of 5–8 m that was exposed 10 km away from east of Liemai village (GPS: 92°41′44.37″, 28°25′12.59″; Figures 2, 3A). The rock (two-mica granite) shows fine-grained

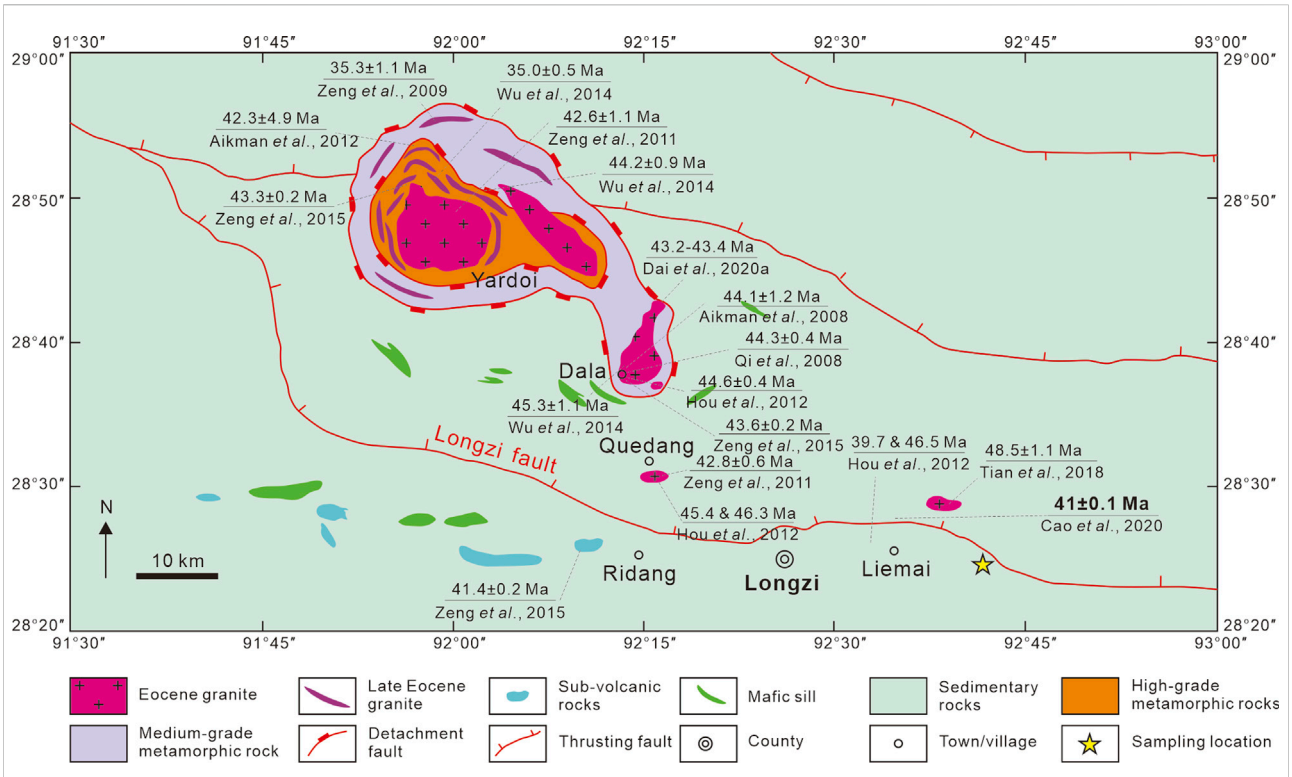

FIGURE 2
Simplified geological map of the Yardoi area showing the Yardoi gneiss dome and distribution of Eocene granites (modified after Dai et al. (2020a) and Cao et al. (2021)).

granitic texture and are composed of eu - to subhedral K-feldspar (35~40 vol.%) and plagioclase (30~35 vol.%), anhedral quartz (15~20 vol.%), sub- to anhedral biotite (10~15 vol.%) and muscovite (~5 vol%), and accessory minerals (zircon, monazite, apatite and titanite). Polysynthetic twinning well-developed in plagioclase. Sericitization is very common in K-feldspar (Figures 3B–F).

3 Analytical methods

3.1 Zircon U-Pb dating and Hf isotopes

Rock sample was crushed and washed, followed by conventional heavy-liquid and magnetic separation to separate zircon grains. Representative zircon grains were handpicked under a binocular microscope and then mounted in epoxy resin and polished to a smooth flat surface. Sample processing was conducted at the Langfang Regional Geological Survey (Hebei Province, China). Prior to U-Pb dating, internal factures of zircons were observed using transmitted, reflected, and cathodoluminescence images. These images were obtained at the Wuhan Sample Solution Analytical Technology Co., Ltd. (Hubei Province, China).

U-Pb dating and trace element analysis of zircon were simultaneously conducted by LA-ICP-MS at the Wuhan Sample Solution Analytical Technology Co., Ltd. Detailed operating conditions for the laser ablation system and the ICP-MS instrument and data reduction are the same as description by Zong et al. (2017). Laser sampling was performed using a GeolasPro laser ablation system that consists of a COMPexPro 102 ArF excimer laser (wavelength of 193 nm) and a MicroLas optical system. An Agilent 7700e ICP-MS instrument was used to acquire ion-signal intensities. Helium was applied as a carrier gas. Argon was used as the make-up gas and mixed with the carrier gas *via* a T-connector before entering the ICP. A "wire" signal smoothing device is included in this laser ablation system (Hu et al., 2015). The spot size and frequency of the laser were set to 32 μm and 8 Hz, respectively, in this study. Zircon 91,500 and glass NIST610 were used as external standards for U-Pb dating and trace element calibration, respectively. Each analysis incorporated a background acquisition of approximately 20–30 s followed by 50 s of data acquisition from the sample. An Excel-based software ICPMSDataCal was used to perform off-line selection and integration of background and analyzed signals, time-drift correction and quantitative calibration for trace element analysis and U-Pb dating (Liu et al., 2008, 2010). Concordia

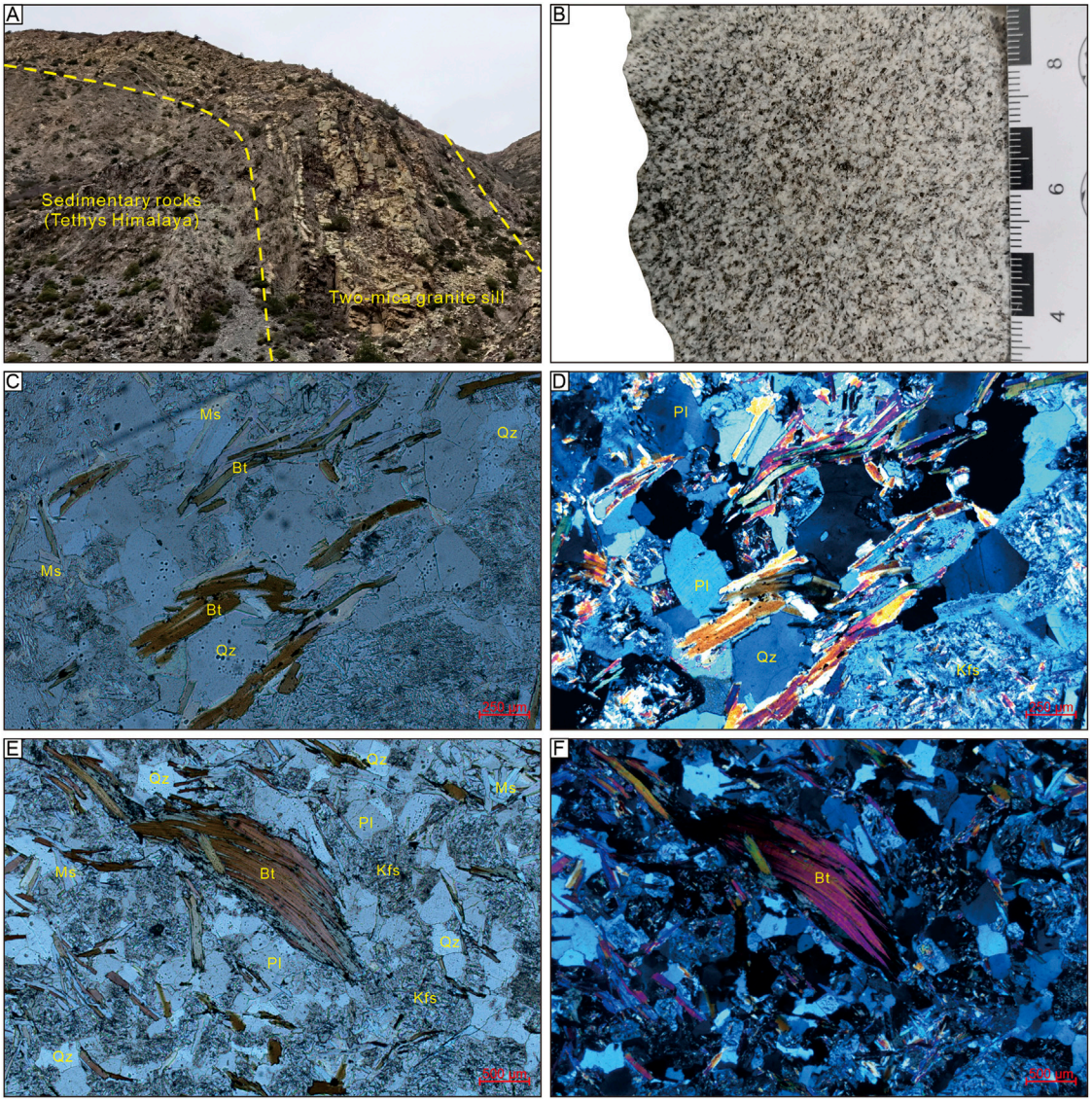

FIGURE 3
(A) Field photograph, **(B)** hand specimen photograph, and **(C–F)** representative photomicrographs of the Liemai two-mica granite [**(C)** and **(E)**, plane-polarized light; **(D)** and **(F)**, crossed-polarized light]. Bt, biotite; Kfs, K-feldspar; Pl, plagioclase; Qz, quartz.

diagrams and weighted mean calculations were made using Isoplot/Ex_ver3 (Ludwig, 2003).

Experiments of *in situ* Hf isotope ratio analysis were conducted using a Neptune Plus MC-ICP-MS (Thermo Fisher Scientific, Germany) in combination with a Geolas HD excimer ArF laser ablation system (Coherent, Göttingen, Germany) that was hosted at the Wuhan Sample Solution Analytical Technology Co., Ltd. All the Hf analyses were done on the same or equivalent spots as those for U-Pb laser ablation analyses. A stationary laser ablation spot with a beam diameter of 32 μm was used for the analyses. Detailed operating conditions for the laser ablation system and the MC-ICP-MS instrument and analytical method were described in Hu et al. (2012). The major limitation to accurate *in situ* zircon Hf isotope determination by LA-MC-ICP-MS is the very large isobaric interference from ^{176}Yb and, to a much lesser extent ^{176}Lu on ^{176}Hf. It has been shown that the mass fractionation of Yb (β_{Yb}) isn't constant over time and that the β_{Yb} that is obtained from the introduction of solutions is unsuitable for *in situ* zircon measurements (Woodhead et al., 2004). The under- or over-estimation of the β_{Yb} value would undoubtedly affect the accurate correction of ^{176}Yb and thus the determined ^{176}Hf/^{177}Hf ratio. We applied the directly obtained β_{Yb} value from the zircon sample itself in real-time in this study. The ^{179}Hf/^{177}Hf and ^{173}Yb/^{171}Yb ratios were used to calculate the

mass bias of Hf (β_{Hf}) and Yb (β_{Yb}), which were normalized to $^{179}Hf/^{177}Hf = 0.7325$ and $^{173}Yb/^{171}Yb = 1.132685$ (Fisher et al., 2014) using an exponential correction for mass bias. Interference of ^{176}Yb on ^{176}Hf was corrected by measuring the interference-free ^{173}Yb isotope and using $^{176}Yb/^{173}Yb = 0.79639$ (Fisher et al., 2014) to calculate $^{176}Yb/^{177}Hf$. Similarly, the relatively minor interference of ^{176}Lu on ^{176}Hf was corrected by measuring the intensity of the interference-free ^{175}Lu isotope and using the recommended $^{176}Lu/^{175}Lu = 0.02656$ (Blichert-Toft et al., 1997) to calculate $^{176}Lu/^{177}Hf$. We used the mass bias of Yb (β_{Yb}) to calculate the mass fractionation of Lu because of their similar physicochemical properties. Off-line selection and integration of analyte signals, and mass bias calibrations were performed using ICPMSDataCal (Ludwig, 2003).

3.2 Monazite U-Th-Pb dating

Similar to zircons, monazite separation and sample processing were conducted at the Langfang Regional Geological Survey. Transmitted, reflected, and BSE images, which were obtained at the Wuhan Sample Solution Analytical Technology Co., Ltd (Hubei Province, China), were used to determine internal features of monazite grains. Twenty-five eu- to subhedral monazite grains without obvious inclusions were selected for *in situ* LA-ICP-MS isotopic and compositional analyses. U-Pb dating of monazite was conducted by LA-ICP-MS at the Wuhan Sample Solution Analytical Technology Co., Ltd. Laser sampling was performed using a GeolasPro laser ablation system that consists of a COMPexPro 102 ArF excimer laser (wavelength of 193 nm) and a MicroLas optical system. An Agilent 7700e ICP-MS instrument was used to acquire ion-signal intensities. Helium was applied as a carrier gas. Argon was used as the make-up gas and mixed with the carrier gas *via* a T-connector before entering the ICP. A "wire" signal smoothing device is included in this laser ablation system, by which smooth signals are produced even at very low laser repetition rates down to 1 Hz (Hu et al., 2015). It is very useful for *in-situ* U-Pb dating of high-U mineral (Zong et al., 2015). The spot size and frequency of the laser were set to 16 μm and 2 Hz, respectively. The laser energy was set to 80 mJ. Monazite standard 44069 and glass NIST610 were used as external standards for U-Pb dating and trace element calibration, respectively. Each analysis incorporated a background acquisition of approximately 20–30 s followed by 50 s of data acquisition from the sample. An Excel-based software ICPMSDataCal was used to perform off-line selection and integration of background and analyzed signals, time-drift correction and quantitative calibration for trace element analysis and U-Pb dating (Liu et al., 2008, 2010). Concordia diagrams and weighted mean calculations were made using Isoplot/Ex_ver3 (Ludwig, 2003).

3.3 Whole-rock major and trace elements

Major and trace element contents were analyzed at the Beijing Research Institute of Uranium Geology. The fresh rock samples were chipped and powdered to a mesh size of ~200 using a tungsten carbide ball mill. The details of the analytical procedures are described by Gao et al. (2003). Major oxide analyses were conducted using a PANalytical Axios MAX X-ray Fluorescence Spectrometer with an analytical uncertainty of <5%. The trace element concentrations were analyzed using a Perkin-Elmer NexIon 300D ICPMS with an analytical precision of <1% for elements with concentrations >200 ppm and 1%–3% for elements with concentrations <200 ppm.

3.4 Whole-rock Sr-Nd-Pb isotopes

Whole-rock Sr-Nd-Pb isotopes were analyzed at the Beijing Research Institute of Uranium Geology. Approximately 200 mg of each sample powder was dissolved in an HF + HNO_3 acid mixture for 48 h in a Teflon beaker. All samples were prepared in duplicate. The digests were dried, dissolved in hydrochloric acid and heated in closed vials at 160 C for 1 h, and evaporated to dryness. The Sr and Nd were separated and purified by conventional cation-exchange techniques. The initial $^{87}Sr/^{86}Sr$ ratios and ε_{Nd} (t) values at the time of crystallization were calculated from the weighted mean zircon U-Pb age and the Rb, Sr, Sm and Nd contents. When calculating the ε_{Nd} (t) values, we assumed the model composition of a chondritic uniform reservoir at the estimated age. The T_{DM1} and T_{DM2} values are the estimated ages of extraction from the depleted mantle according to the one-stage and two-stage crustal pre-histories, respectively, as assumed by Depaolo (1988) and Depaolo et al. (1991). The precision of the calculated initial $^{87}Sr/^{86}Sr$ values is limited by the errors in the parent/daughter ratios calculated from the geochemical data. Nevertheless, in most cases, errors as high as ±10% in the Rb/Sr ratio introduce uncertainties below 0.0001 in the initial $^{87}Sr/^{86}Sr$ values (Dolgopolova et al., 2013), and a 10% error in the Nd isotopes results in an uncertainly of about 0.4–0.7 in the ε_{Nd} (t) values. The measured Pb isotopic ratios were corrected for the instrumental mass fractionation of 0.1 amu-1 by referencing to repeat analyses of the standard NBS-981.

4 Results

4.1 Zircon U-Pb ages and Hf isotopes

U-Pb dating and trace elements results for zircons of the Liemai two-mica granite are shown in appendix (Supplementary Table S1). Cathodoluminescence (CL) images of representative zircon grains from the Liemai two-mica granite are shown in

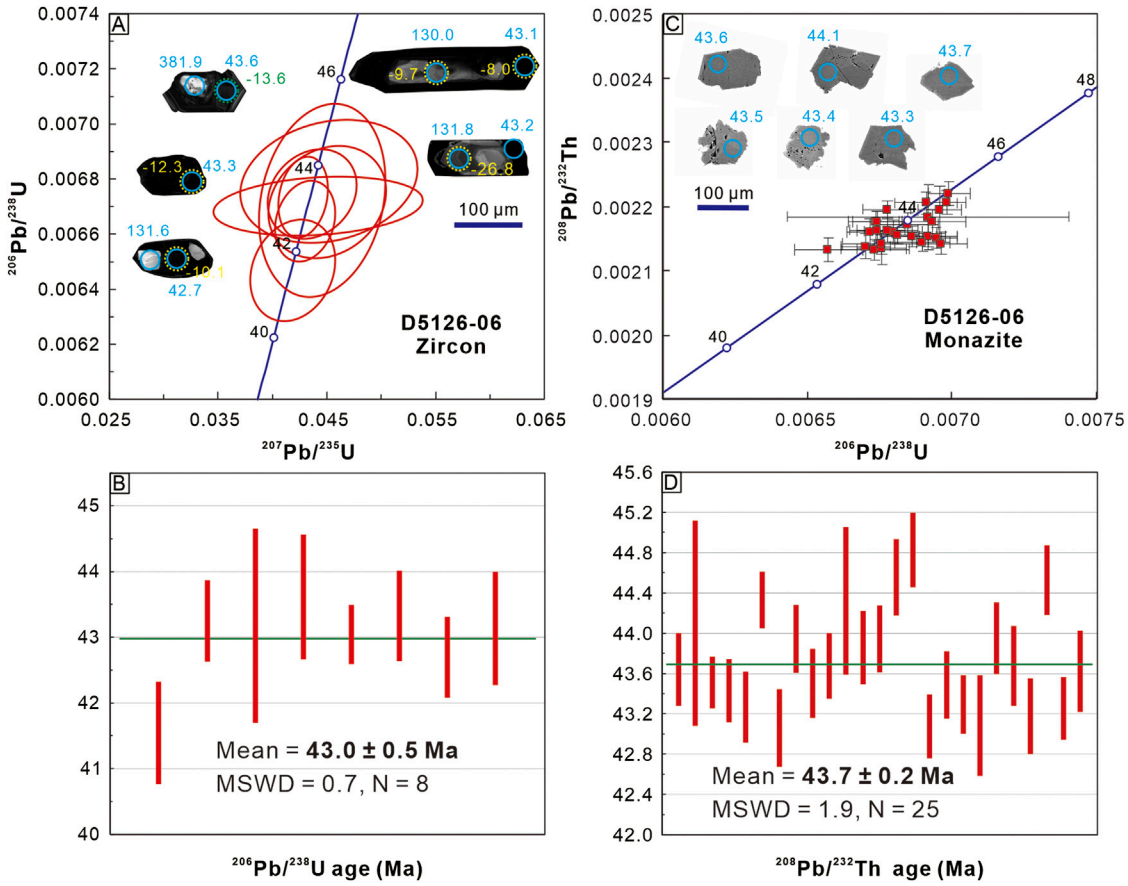

FIGURE 4
(A) U-Pb concordia diagram of zircons and cathodoluminescence images of representative zircons with corresponding $^{206}Pb/^{238}U$ ages and ε_{Hf} (t) values and **(B)** the weighted mean age for zircons of the Liemai two-mica granite; **(C)** U-Th-Pb concordia diagram of monazites and BSE images of representative monazites with corresponding $^{208}Pb/^{232}Th$ ages and **(D)** the weighted mean age for monazites of the Liemai two-mica granite.

Figure 4A. Eu- to subhedral zircon crystals are long prismatic (80–200 μm), with aspect ratios of 2:1 to 5:1. Most zircon grains exhibit core-(mantle)-rim structure with gray subhedral to anhedral cores and dark rims (Figure 4A). The inherited cores normally show obvious oscillatory growth zoning (Figure 4A), suggesting magmatic origin (Wu and Zheng, 2004). In contrast, some rims display weak but visible oscillatory overgrowth zoning indicating magmatic origin, some others show no oscillatory overgrowth zoning and are homogeneous suggesting metamorphosed origin (Figure 4A; Wu and Zheng, 2004; Hoskin, 2005). Detailed description of zircon structure and analytical position are shown in appendix (Supplementary Table S1). Twenty-three analyses (with a concordance of >90%) yield $^{206}Pb/^{238}U$ ages ranging from 41.6 to 1721.5 Ma. Fifteen analyses on inhibited cores yield $^{206}Pb/^{238}U$ ages ranging from 130.0 to 1721.5 Ma. Eight analyses on dark rims or zircons without inherited cores yield $^{206}Pb/^{238}U$ ages ranging from 41.6 to 43.6 Ma with a weighted Eocene mean age of 43.0 ± 0.5 Ma (MSWD = 0.7) (Figure 4B).

Thirteen spots were also analyzed for Lu-Hf isotopes. The analytical results are listed in appendix (Supplementary Table S2). The analyzed zircon grains have $^{176}Lu/^{177}Hf$ ratios of 0.000018–0.003409 and $^{176}Hf/^{177}Hf$ ratios of 0.281963–0.282520. Except for one analysis (D5126-06-24), zircon crystals display $^{176}Lu/^{177}Hf$ ratios <0.002, indicating extremely low accumulations of the radioactive Hf isotope after crystallization (Wu et al., 2007). Seven analyses on juvenile zircon rims yield calculated ε_{Hf} (t) (t = 43 Ma) values of −14.3 to −8.0 (average of −11.1) with two stage Hf model ages (T_{DM2}) of 1,027–1,256 Ma.

4.2 Monazite U-Th-Pb ages

The monazite U-Th-Pb dating and trace elements results for the Liemai two-mica granite are listed in appendix (Supplementary Table S3). The BSE images of representative monazites are showed in Figure 4C. All monazite grains are grey in BSE images, and most of them are homogeneous, although some grains show zoning

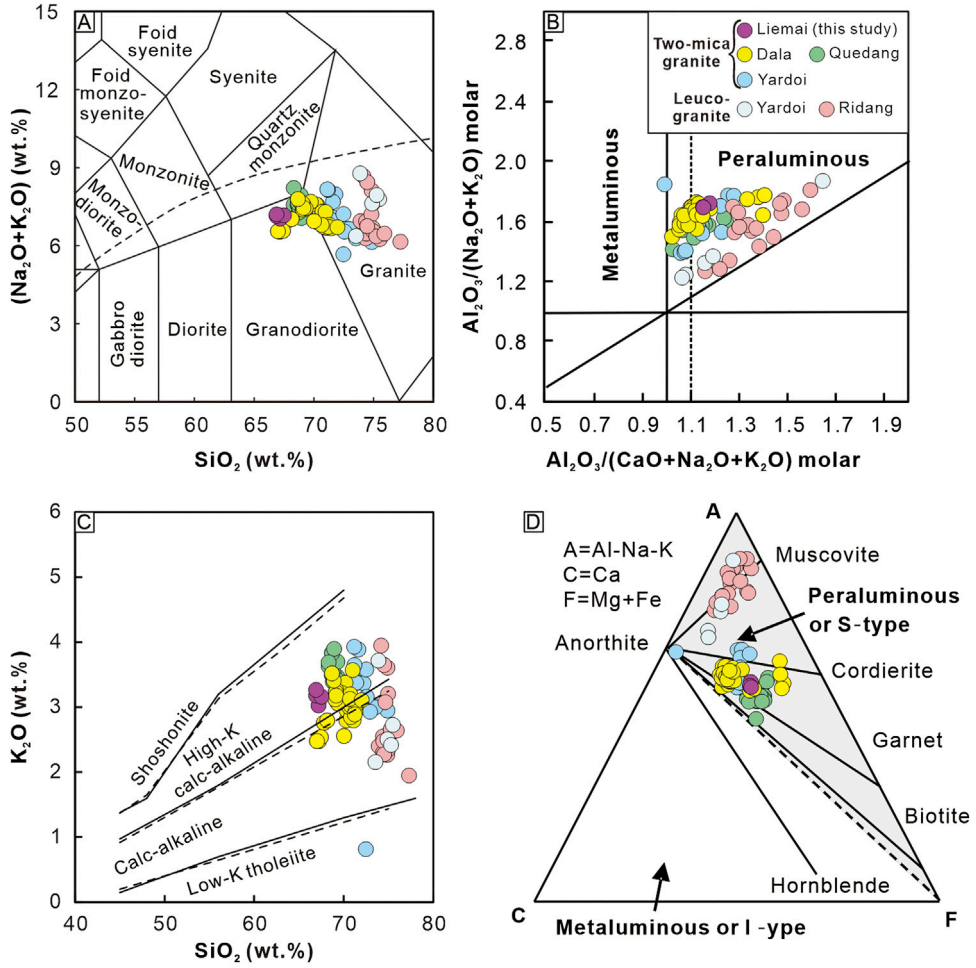

FIGURE 5
(A) SiO_2 vs. K_2O + Na_2O (Middlemost, 1994), **(B)** A/CNK vs. A/NK (Maniar and Piccoli, 1989), **(C)** SiO_2 vs. K_2O (Rickwood, 1989), and **(D)** A-C-F (Chappell and White, 1992) diagrams for the Liemai two-mica granite. Data source: Quedang two-mica granites are from Zeng et al. (2011) and Hou et al. (2012); Dala two-mica granites are from Zeng et al. (2011, 2015), Hou et al. (2012) and Dai et al. (2020a); Yardoi two-mica granites are from Zeng et al. (2011, 2015); Yardoi leucogranites are from Zeng et al. (2015); Ridang leucogranites (subvolcanic rocks) are from Hu et al. (2011b) and Zeng et al. (2015).

(Figure 4C). The monazites in the Liemai two-mica granite have high contents of Th (37,794~113,394 ppm) and U (1,663~9,254 ppm), and relatively low Pb contents (83~245 ppm). The $^{207}Pb/^{235}U$ ages of these monazites are scattered, ranging from 59.3 to 251.9 Ma. In contrast, the $^{206}Pb/^{238}U$ ages (42.2~44.9 Ma) and $^{208}Pb/^{232}Th$ ages (43.1~44.8 Ma with a weighted Eocene mean age of 43.7 ± 0.2 Ma, N=25, MSWD = 0.7; Figure 4D) are very concentrated. In addition, the $^{206}Pb/^{238}U$ ages and $^{208}Pb/^{232}Th$ ages are very concordant with each other (Figure 4D).

4.3 Whole-rock major and trace elements

The whole-rock major and trace element data for the Liemai two-mica granite are listed in appendix (Supplementary Table S4). Samples are characterized by high contents of SiO_2 (66.88–67.48 wt.%), Al_2O_3 (16.24–16.44 wt.%), Na_2O (3.72–3.83 wt.%) and K_2O (3.03–3.27 wt.%), and relatively low contents of CaO (2.42–2.52 wt%), total iron (TFeO = 2.06–2.11 wt.% TiO_2 (0.31–0.33 wt.%), MnO (0.03–0.04 wt.%), MgO (1.24–1.29 wt.%), and P_2O_5 (0.13–0.14 wt.%) with relatively high Na_2O/K_2O mass ratios (1.14–1.25) and Mg# [Mg# = $MgO\times100/(MgO+FeO^T)$ (molar ratio)] values (51.75–52.20) (Supplementary Table S4). The total alkali contents (K_2O+Na_2O) range from 6.82 to 6.99 wt%, indicative of sub-alkaline series in the total alkalis vs. silica (TAS) diagram (Figure 5A; Middlemost, 1994). The A/CNK values [A/CNK = $Al_2O_3/(CaO + Na_2O + K_2O)$ (molar ratio)] vary from 1.15 to 1.17, whereas the A/NK values [A/NK = $Al_2O_3/(Na_2O + K_2O)$ (molar ratio)] range from 1.69 to 1.72, indicating peraluminous features

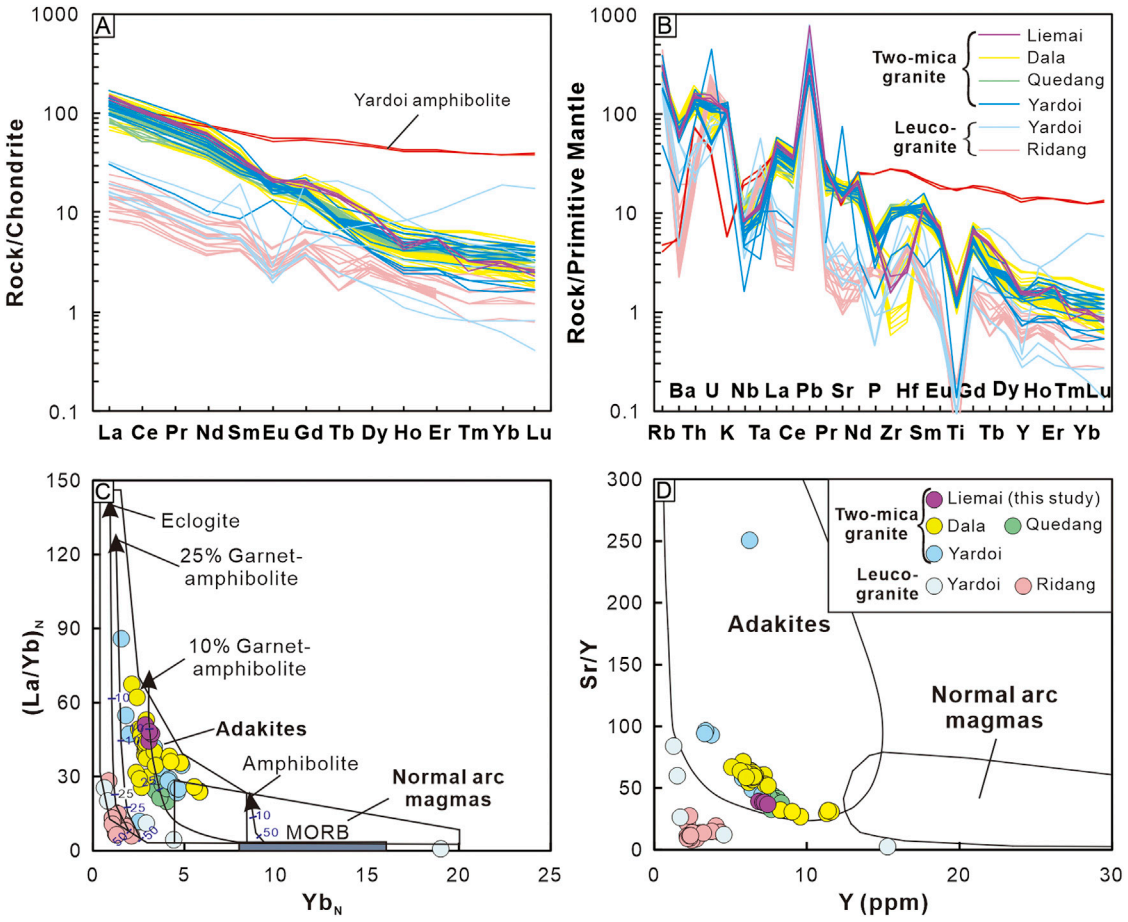

FIGURE 6
(A) Chondrite-normalized REE patterns, **(B)** primitive mantle-normalized trace element patterns, **(C)** Yb_N vs. La_N/Yb_N and **(D)** Y vs. Sr/Y diagrams for the Liemai two-mica granite (Martin, 1986; Defant and Drummond, 1990). Subscript N represents chondrite-normalized value. Chondrite and primitive mantle values are from Sun and McDonough (1989). Data source: the amphibolite in the Yardoi area was from Hou et al. (2012); the granites/leucogranites are same as in Figure 5.

(Figure 5B; Maniar and Piccoli, 1989). On the K_2O vs. SiO_2 diagram, the samples show high-K calc-alkaline characteristics (Figure 5C; Peccerillo and Taylor, 1976). On the A-F-C diagram, the Liemai two-mica granite samples plot in the peraluminous granitoid-type field (Figure 5D; Chappell and White, 1992).

The Liemai two-mica granite is characterized by LREE (light rare Earth element) enrichment and HREE (heavy rare Earth element) depletion with high LREE/HREE ratios (16.0–16.7; Supplementary Table S4), suggesting significant differentiation of LREE from HREE. This is in accordance with the right-leaning chondrite-normalized REE patterns (Figure 6A). The Liemai two-mica granite displays an indistinctive negative Eu anomaly (Eu/Eu^*=0.7~0.8; Supplementary Table S4; Figure 6A). The rock is enriched in LILE (large ion lithophile element) such as Rb and K and depleted in HFSE (high field strength element) such as Nb, Ta, Zr, Hf, and Ti (Figure 6B). Importantly, the Liemai two-mica granite has low concentrations of Y (6.9~7.4 ppm) and Yb (~0.5 ppm) and relatively high concentrations of Sr (269~278 ppm) and La (32.3~36.0 ppm) with high Sr/Y (36.8~39.2) and $(La/Yb)_N$ (44.5~50.9) ratios (subscript N represents chondrite-normalized value based on Sun and McDonough, 1989), showing adakitic features (Figures 6C, D; Martin, 1986; Defant and Drummond, 1990).

4.4 Whole-rock Sr-Nd-Pb isotopes

The whole-rock Sr-Nd-Pb isotopic compositions of the Liemai two-mica granite are listed in appendix (Supplementary Table S5). The samples have low $(^{87}Sr/^{86}Sr)_i$ ratios (0.718414–0.718423) and negative ε_{Nd} (t) values (–14.7 to –13.9), with T_{DM2} ranging from 1,803 to 1,852 Ma. The $(^{206}Pb/^{204}Pb)_i$, $(^{207}Pb/^{204}Pb)_i$, and $(^{208}Pb/^{204}Pb)_i$ values are 18.781–18.791, 15.687–15.695 and 39.214–39.236, respectively. All initial values are calculated for 43 Ma.

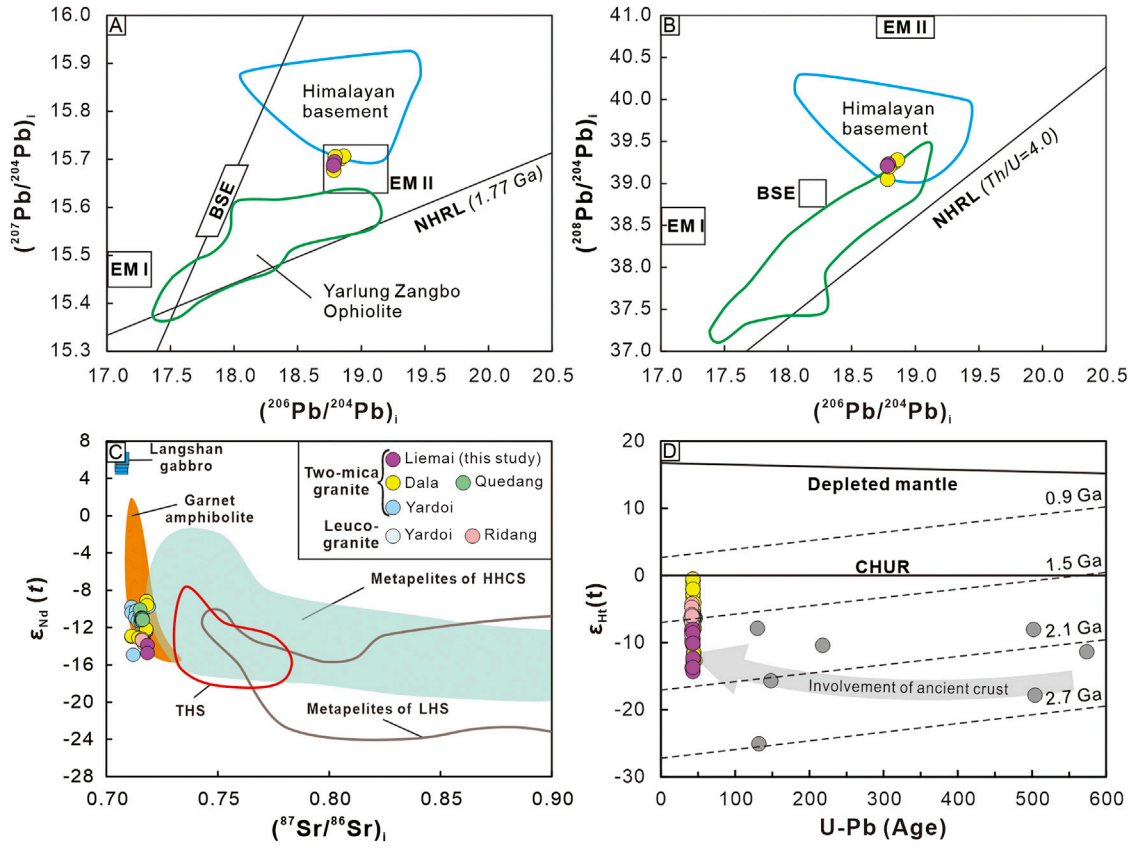

FIGURE 7
(A) $(^{207}Pb/^{204}Pb)_i$ vs. $(^{206}Pb/^{204}Pb)_i$, **(B)** $(^{208}Pb/^{204}Pb)_i$ vs. $(^{206}Pb/^{204}Pb)_i$, **(C)** ε_{Nd} (t) vs. $(^{87}Sr/^{86}Sr)_i$, and **(D)** ε_{Hf} (t) vs. U-Pb age diagrams for the Liemai two-mica granite. Data source: the Himalayan basement is from Vidal et al. (1982) and Harrison et al. (1999); the Yarlung Zangbo Ophiolite are from Xu and Castillo (2004), Zhang et al. (2005) and Niu et al. (2006); the Bulk Silicate Earth (BSE) and enriched mantle components (EM I and EM II) are from Zindler and Hart (1986); the Langshan gabbro is from Ji et al. (2016); the garnet amphibolite is from Zeng et al. (2011); the metapelites of HHCS are from Inger and Harris (1993), Yang and Jin (2001), Richards et al. (2005) and Zeng et al. (2009, 2012); the LHS and THS are from Richards et al. (2005); the granites/leucogranites are the same as in Figure 5. Northern Hemisphere Reference Line (NHRL): $^{207}Pb/^{204}Pb = 0.1084 \times {}^{206}Pb/^{204}Pb + 13.491$; $^{208}Pb/^{204}Pb = 1.209 \times {}^{206}Pb/^{204}Pb + 15.627$. All initial isotopic ratios are corrected to t = 43 Ma.

5 Discussion

5.1 Formation age for the Liemai two-mica granite

As mentioned above, the juvenile zircon rims with oscillatory zoning in the Liemai two-mica granite are magmatic while those without oscillatory zoning are of metamorphosed origin. Interestingly, these rims have undistinguishable $^{206}Pb/^{238}U$ ages (Supplementary Table S1). This indicates that metamorphism and partial melting of the source rock for the Liemai two-mica granite were possibly coeval. This phenomenon has been recorded in the Yardoi dome (Zeng et al., 2011). Therefore, the weighted $^{206}Pb/^{238}U$ age of juvenile zircon rims (43.0 ± 0.5 Ma) can be interpreted as the timing of partial melting of the source rock and the formation age of the Liemai two-mica granite.

Monazite incorporates a significant amount of ^{230}Th into its crystal structure during crystallization, which will lead to generation of "excess" ^{206}Pb and result in disequilibrium in the $^{238}U \rightarrow {}^{206}Pb$ decay. In juvenile monazite (Cenozoic), the "excess" ^{206}Pb will lead to apparent $^{206}Pb/^{238}U$ ages that are older than measured $^{207}Pb/^{235}U$ and $^{208}Pb/^{232}Th$ ages. Besides, due to their young age, such monazites normally contain low contributions of radiogenic ^{207}Pb, which will result in $^{207}Pb/^{235}U$ ages that are less precise than $^{206}Pb/^{238}U$ and $^{208}Pb/^{232}Th$ ages. In contrast, owing to high contents of ^{232}Th (wt.% levels) and therefore significant ^{208}Pb in monazite, $^{208}Pb/^{232}Th$ ages can be taken as the best estimate of the monazite crystallization age (Cottle et al., 2015). Therefore, the weighted $^{208}Pb/^{232}Th$ age (43.7 ± 0.2 Ma) are interpreted as crystallization age of monazites in the Liemai two-mica granite. Owing to relatively low closure temperature and high sensitivity, inherited monazites are very rare even in low-temperature granites (Parrish, 1990). Thus, the weighted $^{208}Pb/^{232}Th$ age (43.7 ± .2 Ma) of

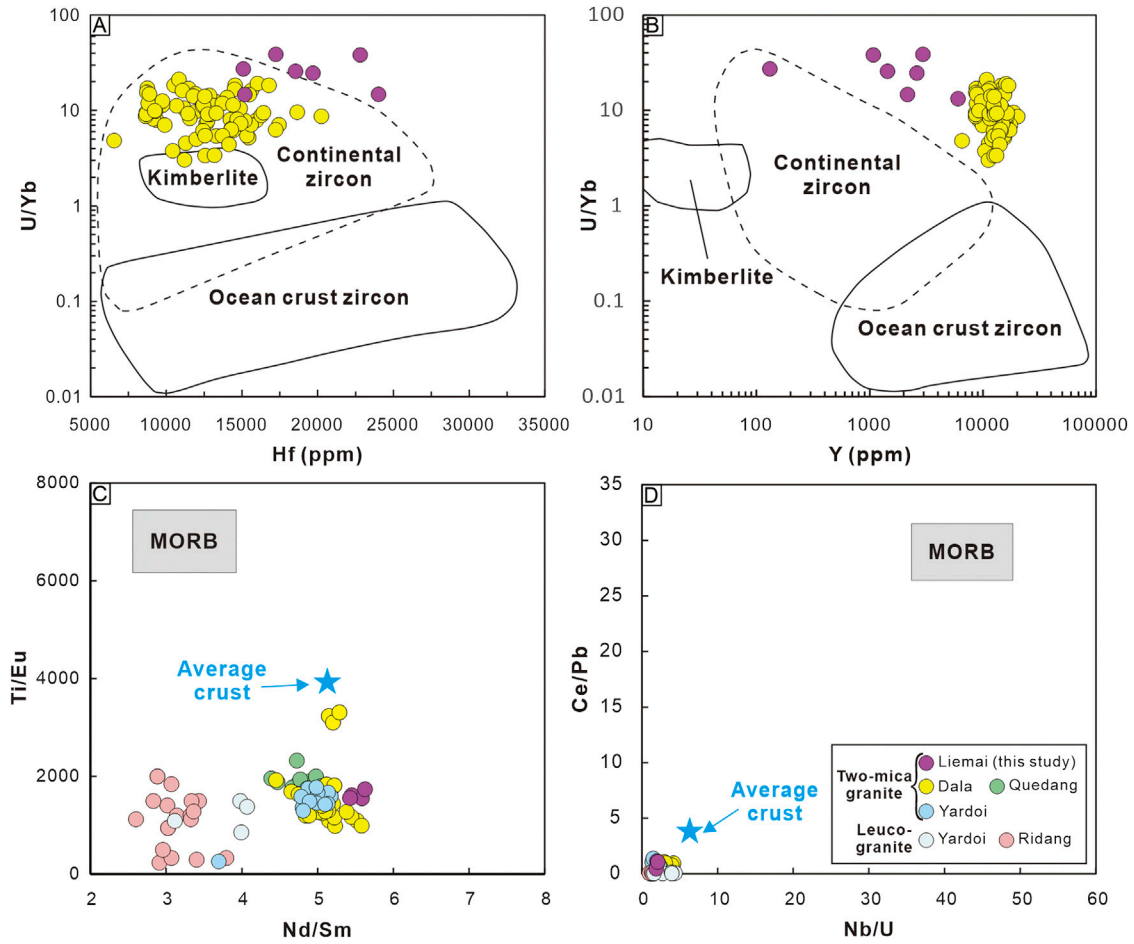

FIGURE 8
(A) U/Yb vs. Hf and **(B)** U/Yb vs. Y diagrams of zircons from the Liemai two-mica granite (Grimes et al., 2007); **(C)** Ti/Eu vs. Nd/Sm and Ce/Pb vs. Nb/U diagrams for the Liemai two-mica granite. The fields of MORB (mid-ocean-ridge basalt) and average crust are from Klein (2003) and Rudnick and Gao (2003), respectively. The granites and leucogranites are the same as in Figure 5.

monazites in the Liemai two-mica granite can be interpreted as formation age of the rock.

In summary, the weighted $^{206}Pb/^{238}U$ age of juvenile zircons are consistent with the weighted $^{208}Pb/^{232}Th$ age of monazites within errors, indicating that the Liemai two-mica granite was generated at ~43.5 Ma, coeval to two-mica granites in Yardoi, Dala, Quedang (Figure 2).

5.2 Petrogenesis of the Early Eocene granites in the Yardoi area

5.2.1 Petrogenesis of the Liemai two-mica granite

In despite of strong peraluminous features, the high Sr/Y (36.8~39.2) and $(La/Yb)_N$ (44.5~50.9) ratios of the Liemai two-mica are indicative of its adakitic attribution (Figures 6C, D; Martin, 1986; Defant and Drummond, 1990). Several models have been proposed for the genesis of adakitic rocks since Defant and Drummond (1990) defined this rock type based on its geochemical features: 1) partial melting of subducted oceanic crust (Defant and Drummond, 1990; Zhu et al., 2009b; Dai et al., 2018); 2) crustal assimilation and fractional crystallization (AFC) processes from parental basaltic magmas (Castillo et al., 1999; Macpherson et al., 2006; Wang et al., 2020); 3) mixing of felsic and basaltic magmas (Streck et al., 2007; Chu et al., 2020); 4) partial melting of thickened lower crust (Long et al., 2015; Yang et al., 2016b); 5) partial melting of delaminated lower crust (Xu et al., 2002; Dai et al., 2020b) and 6) partial melting of subducted continental crust (Jiang et al., 2011; Lai and Qin, 2013). These possibilities will be discussed below.

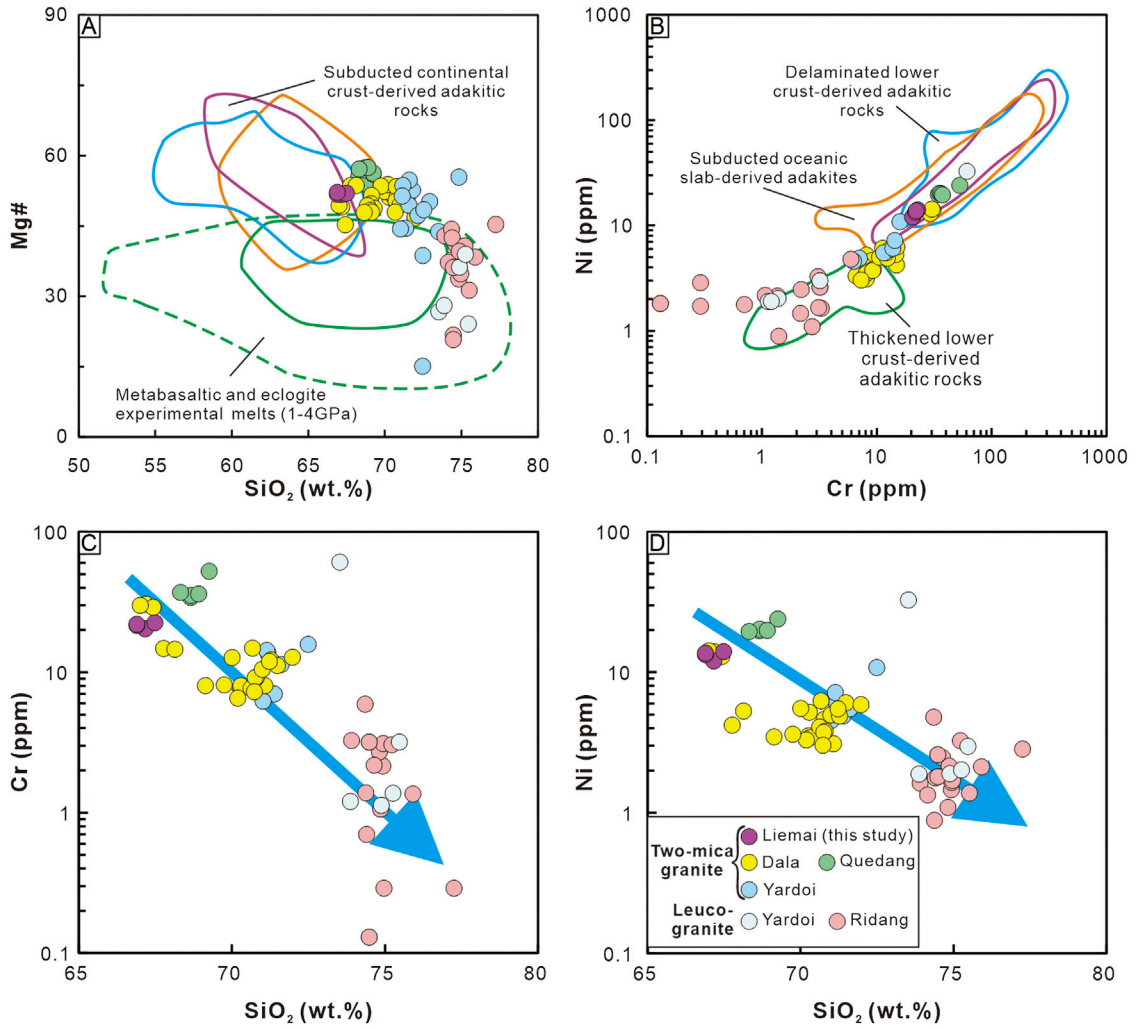

FIGURE 9
(A) Mg# vs. SiO_2, **(B)** Ni vs. Cr, **(C)** Cr vs. SiO_2 and **(D)** Ni vs. SiO_2 diagrams for the Liemai two-mica granite. Data source: metabasaltic and eclogite experimental melts (1–4 GPa) are from Rapp et al. (1999, 2002); subducted oceanic slab-derived adakites are from Zhu et al. (2009b), Zhang et al. (2010), Jiang et al. (2012), Ma et al. (2013) and Dai et al. (2018); subducted continental crust-derived adakitic rocks are from Jiang et al. (2011) and Lai and Qin (2013); thickened lower crust-derived adakitic rocks are from Ma et al. (2014), Long et al. (2015) and Yang et al. (2016b); delaminated lower crust-derived adakitic rocks are from Xu et al. (2002, 2006), Gao et al. (2004), Wang et al. (2006, 2014), Karsli et al. (2010) and Chen et al. (2013); other granites and leucogranites are the same as in Figure 5.

The Pb isotopes of the Liemai two-mica granite are similar to those of the Himalayan basement but differ from those of the Yarlung Zangbo ophiolite (Figures 7A, B), precluding the subducted oceanic crust and supporting the Himalayan crust as a possible magma source. The distinct Sr-Nd isotopes of the Liemai two-mica granite from those of the coeval Langshan gabbro (Figure 7C; Ji et al., 2016) and absent of dark enclaves (Figure 3B) are inconsistent with hypotheses of fractional crystallization (Macpherson et al., 2006; Wang et al., 2020) and mixing of felsic and basaltic magmas (Chu et al., 2020), respectively. Instead, enrichment of Th, U and Pb, and large negative zircon ε_{Hf} (t) values (−14.3 to −8.0) with old T_{DM2} (1,027–1,256 Ma) of the Liemai two-mica suggest an ancient crustal source. In addition, the Liemai two-mica granite shows notable continental crust affinities on the U/Yb vs. Hf and U/Yb vs. Y diagrams of zircons and whole-rock Ti/Eu vs. Nd/Sm and Ce/Pb vs. Nb/U diagrams (Figure 8).

Commonly, crust-derived melts display low concentrations of MgO, Mg# values and compatible elements (such as Cr and Ni) (Ma et al., 2014; Long et al., 2015; Yang et al., 2016b). However, delaminated thickened lower crust- and subducted continental crust-derived melts typically shows elevated MgO,

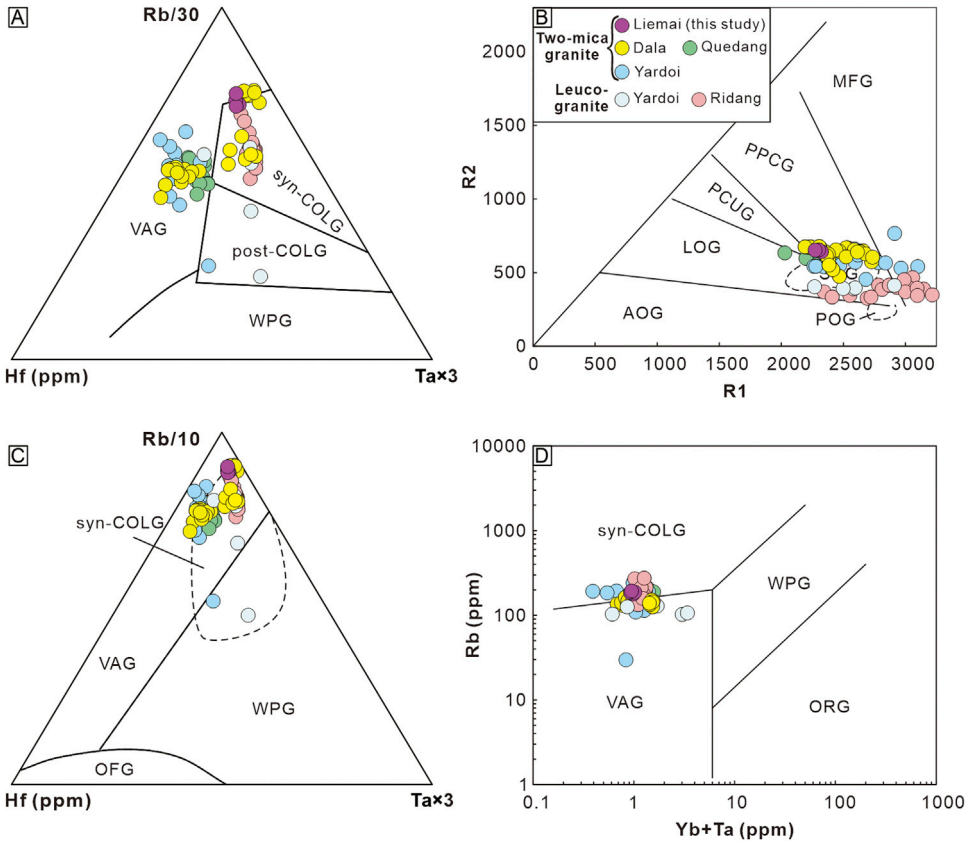

FIGURE 10
Geochemical discrimination diagrams of **(A)** Rb/30-Hf-Tax3 (Harris et al., 1986), **(B)** R1 vs. R2 (Batchelor and Bowden, 1985), **(C)** Rb/10-Hf-Tax3 (Harris et al., 1986), and **(D)** Rb vs. Yb + Ta (Pearce et al., 1984) for the Liemai two-mica granite. Abbreviations: MFG, mantle fractionate granitoids; PPCG, pre-plate collision granitoids; PCUG, post-collision uplift granitoids; LOG, late-orogenic granitoids; AOG, anorogenic granitoids; SCG, syn-collision granitoids; POG, post-orogenic granitoids; VAG, volcanic arc granitoids; syn-COLG, syn-collision granitoids; post-COLG, post-collision granitoids; WPG, within-plate granitoids; ORG, ocean ridge granitoids; OFG, ocean-floor granitoids. Data source: the granites and leucogranites are the same as in Figure 5.

Mg# values and compatible element concentrations owing to interaction with overlying mantle peridotite during ascent (Xu et al., 2002; Jiang et al., 2011; Lai and Qin, 2013; Dai et al., 2020b). The Liemai two-mica granite show a little bit higher concentrations of Mg# (52 on average) and Cr (21.7 ppm on average) and Ni (13.4 ppm on average) than typical thickened lower crust-derived magmas and experimental products of partial melting of metabasalt and ecologite (Mg#<45; Cr<15 ppm; Ni<5 ppm; Figures 9A, B), seemingly suggesting an origin related to subduction of oceanic or continental crust or delamination of lower continental crust. Subduction origin can be easily excluded since subduction-related magmas occur in active continental margin while the Himalayan terrane was a passive continental margin of the Neo-Tethys Ocean (Pan et al., 2012; Zhu et al., 2015). In addition, delamination of lower crust typically occurs at an extensional tectonic background typically during late stage of collision (Hou et al., 2004; Wang et al., 2006, 2014). Although a temporary extension tectonic regime could be possible owing to continental rebound owing to pull force loss resulted from slab detachment of the Noe-Tethys lithosphere. In the Paleogene, owing to intensive collision between India and Eurasia, compressional and contractional tectonic regime dominated the Himalaya orogen (Hou et al., 2006a; 2006b). This is consistent with syn-collisional geochemical signatures of the Liemai two-mica granites (Figure 10). Thus, partial melting of a thickened lower crust is a more preferable interpretation for genesis of the Liemai two-mica granite. Relatively higher contents of Mg#, Ni and Cr could probably be caused by relatively high contents of biotite (Figures 9B–F, 3B–F).

Zircon U-Pb and monazite U-Th-Pb dating results in this study imply that the metamorphism and anatexis of the source rock of the Liemai two-mica granite occurred at ~43.5 Ma. This is coincidence with the contemporaneous metamorphism and partial melting of garnet amphibolite (43.5 ± 1.3 Ma; Zeng

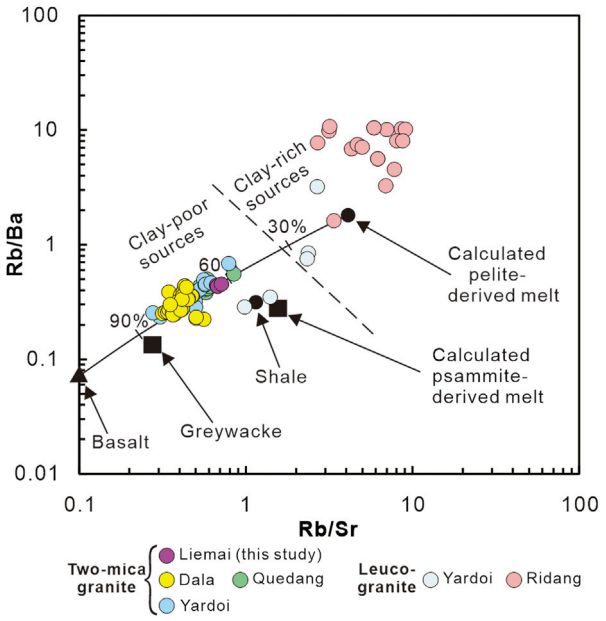

FIGURE 11
Rb/Ba vs. Rb/Sr diagram for the Liemai two-mica granite (Sylvester, 1998). Data source: the granites and leucogranites are the same as in Figure 5.

et al., 2011) in the Yardoi dome. In addition, Sr-Nd isotopes of the Liemai two-mica granite are similar to those of the garnet amphibolite (Figure 7C). This indicates that the garnet amphibolite would be the major source rock for the Liemai two-mica granite. Relatively high Rr/Sr and Rb/Ba values indicate that minor metapelites were also probably present in the source region (Figure 11), although the abnormally high Rr/Sr and Rb/Ba ratios could have probably been caused by extreme magma evolution.

In summary, the Liemai two-mica granite is a product of partial melting of thickened lower crust consisting mainly of amphibolite with minor metapelites. This, in turn, manifests that the Early Eocene adakitic rocks in the Yardoi area share a same origin, which is supported by their similar formation ages (Figure 2), geochemical (Figures 5, 6, 8–11) and isotopic (Figure 7) compositions.

5.2.2 Genetic relationship between the high-Mg# granites and low-Mg# granites

Besides two-mica granite, there are also some other types of coeval granites exposed in the Yardoi area, including subvolcanic porphyritic leucogranite and leucogranite. These adjacent granites have similar formation ages (Figure 2) and Sr–Nd–Hf isotope systematics (Figure 7), suggesting an identical origin. Nevertheless, discernible differences in mineral assemblage and some major and trace elements demonstrate that these granites likely experienced different magma processes (Hu et al., 2011a; Zeng et al., 2011, 2015; Hou et al., 2012; Dai et al., 2020a). Based on geochemical features, the Eocene granites in the Yardoi area can be broadly divided into two major types: high-Mg# granites (HMGs) and low-Mg# granites (LMGs). The HMGs are mainly composed of two-mica granites including several relatively large intrusions such as Yardoi, Dala, Quedang, and a series of sills or dikes, such as Liemai (Figure 2; Zeng et al., 2011, 2015; Hou et al., 2012; Dai et al., 2020a). Thus, these granites show overwhelming superiority in volume. The HMGs are characterized by relatively high contents of TFeO, MgO, Mg#, TiO_2, P_2O_5, LREE, Y, Th, Sr, incompatible elements (Cr and Ni) and Eu/Eu*, and low contents of SiO_2 and Rb/Sr and Rb/Ba ratios (Figures 6, 9, 11, 12). Typically, the HMGs have high Sr/Y and $(La/Yb)_N$ values showing adakitic characteristics (Figures 6C, D). Besides, these granites show higher degree of REE differentiation, but less remarkable negative Eu anomalies (Figure 6A). The LMGs consist mainly of minor sub-volcanic leucogranite in Longzi County and leucogranite sills or dikes in Yardoi dome (Hu et al., 2011a; Zeng et al., 2015). These granites are poor in dark minerals and have low Sr/Y and $(La/Yb)_N$ ratios precluding their adakitic signatures (Figures 6C, D; Hu et al., 2011a; Zeng et al., 2015). In contrast, in spite of less degree of REE differentiation, the LMGs show remarkable negative Eu anomalies (Figure 6A).

The linear correlations between HMGs and LMGs on the Harker diagrams (Figure 12) are indicative of their evolutionary relationship. Especially, more notable negative Eu and Sr anomalies (Figures 6A, B, 12I) of the LMGs demonstrate that the LMGs represent granitic magmas that were evolved from the HMGs by crystal fractionation of plagioclase (Zeng et al., 2015). However, perceptible geochemical discontinuities in the whole-rock geochemistry can be identified between these two granite types (Figure 12), which differs from the continuum in chemical compositions that is commonly assumed to be resulted from a continuous separation of crystals and derivative melts (e.g., Bonnefoi et al., 1995). In addition, generation of high evolved melts through segregation of crystals from a high-silica magma isn't easy due to relatively high viscosity of the silica-rich magma and low-density contrast between the crystals and the liquid. Thus, a simple continuous fractional crystallization process is probably inefficient to interpret the compositional gaps between these two types of granite (Liu et al., 2019).

Alternatively, fractional crystallization of a crystal mush (Michael, 1984; Lee and Morton, 2015) has been proposed to interpret the genetic relationships between the less evolved granites and the adjacent highly evolved derivative granites in the Tibet-Himalaya orogen (Liu et al., 2019; Wang et al., 2021). In this model, intensive crystal fractionation is unnecessary. Instead, separation of residual liquid from the crystal mush is enough to generate highly evolved melts (Michael, 1984; Lee and Morton, 2015). Obviously, separation of liquid is much more viable than that of mineral crystals from a crystal mush. Especially, the high

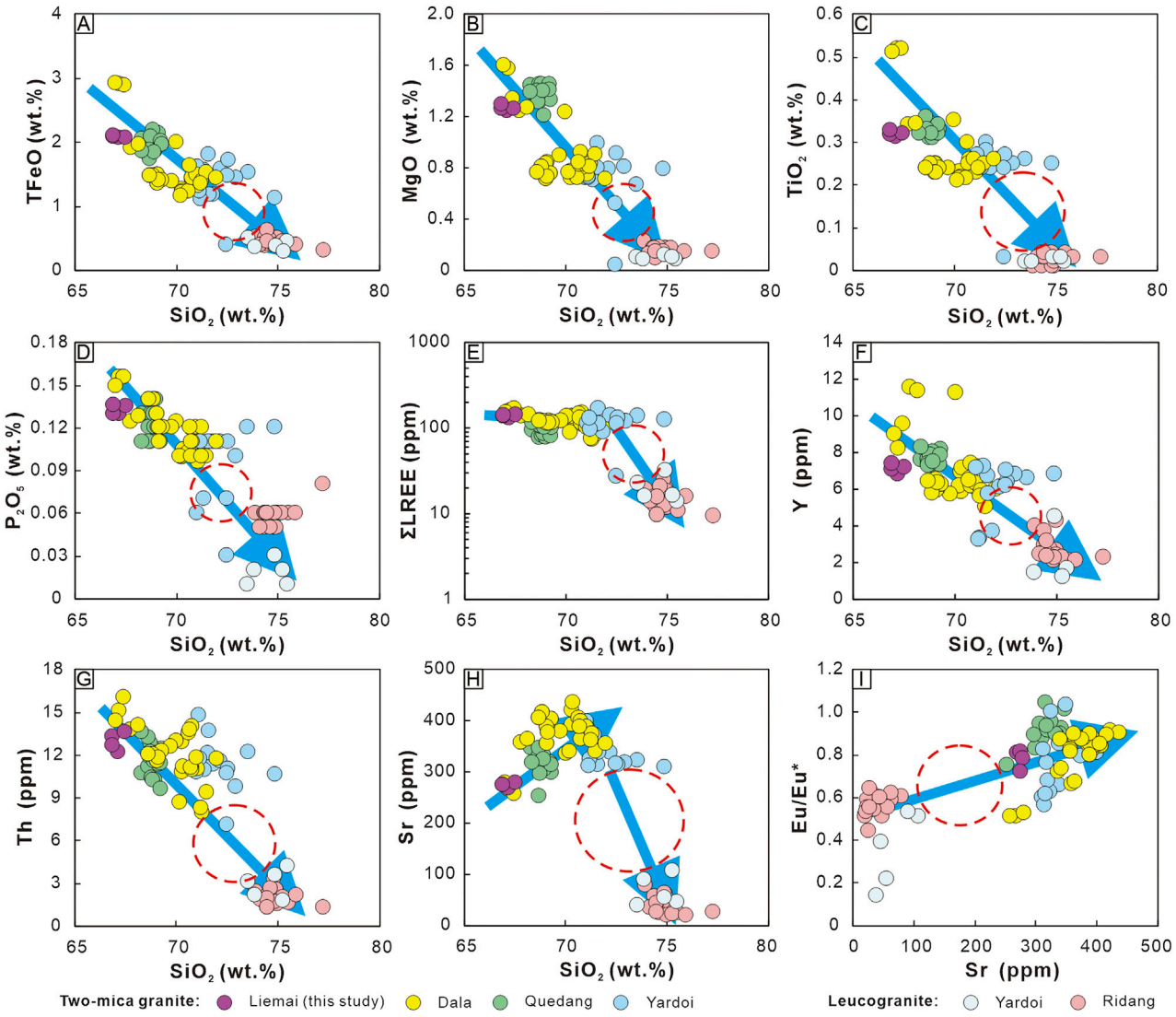

FIGURE 12
(A) TFeO, **(B)** MgO, **(C)** TiO_2, **(D)** P_2O_5, **(E)** ΣLREE, **(F)** Y, **(G)** Th, **(H)** Sr vs. SiO_2, and **(I)** Eu/Eu* vs. Sr diagrams for the Liemai two-mica granite. Data source: the granites and leucogranites are the same as in Figure 5. The red dotted circle denotes the compositional gaps between the two-mica granites and the leucogranites.

volatile (i.e., H_2O, F and B) contents can lowered magma solidus and decreased the melt viscosity (Baker and Vaillancourt, 1995; Scaillet et al., 1996; Sirbescu and Nabelek, 2003), allowing sufficient time and melt activity for the extraction of interstitial liquid. REE tetrad effect-like buckling on the chondrite-normalized REE patterns and deviation of Y/Ho, Nb/Ta and Zr/Hf values from the chondrite values indicate an interaction between the melts and volatile-enriched fluids (Hu et al., 2011a; 2011b). Therefore, the crystal mush model is probably a more suitable candidate for interpreting the relationship between the HMGs and LMGs. The less evolved HMGs can be viewed as the crystal mush (crystal cumulate with trapped/interstitial melts), whereas the highly evolved LMGs can be regarded as residual liquids extracted from the trapped melts in crystal mush. To assess whether this suggestion is in accordance with the observed geochemical fractionation patterns, we performed trace element modeling on these Eocene granites.

Sr and Ba were selected to verify the fractional crystallization process because their geochemical behaviors are strongly controlled by the main minerals (feldspar and micas) in granites (Liu et al., 2019). The modeling calculations were based on the Rayleigh fractionation equation $C_L/C_0 = F^{D-1}{}_d$, where F_d refers to the fraction of the derived liquid, D refers to the

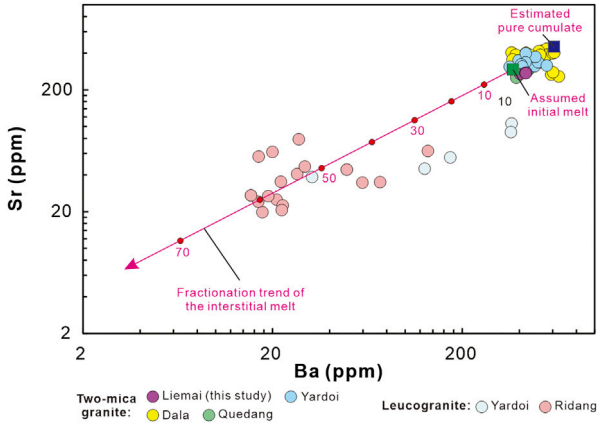

FIGURE 13
Ba-Sr modeling of melt extraction from the Early Eocene two-mica granite crystal mush for the generation of the coeval leucogranites in the Yardoi area. The detailed modeling process can be found in Liu et al. (2019), and the related calculation parameters are presented in Supplementary Table S6). Data source: the granites and leucogranites are the same as in Figure 5.

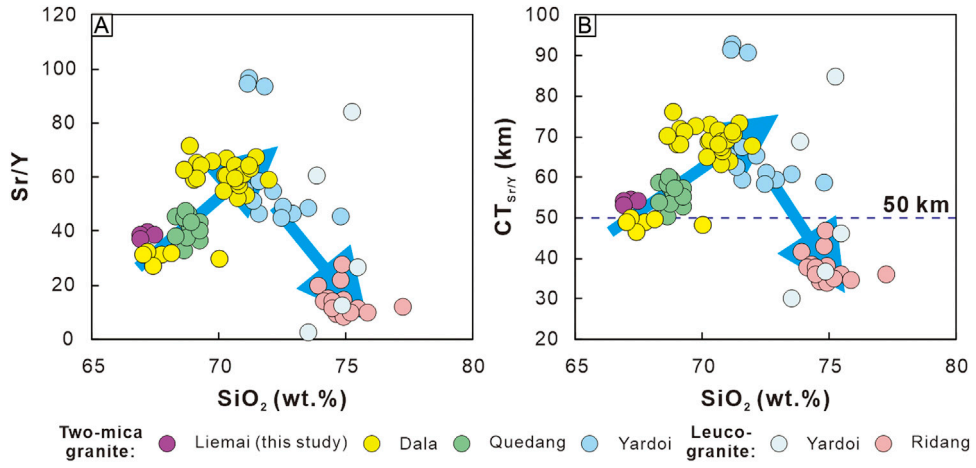

FIGURE 14
(A) Sr/Y vs. SiO_2 and **(B)** $CT_{Sr/Y}$ vs. SiO_2 diagrams for the Liemai two-mica granite. $CT_{Sr/Y}$ represents crustal thickness calculated using the equations from Hu et al. (2017). Data source: the granites and leucogranites are the same as in Figure 5.

bulk partition coefficient, C_L and C_0 refer to the trace element compositions of the fractionated liquid and the initial melt, respectively. The assumed extracted liquid was from the most-evolved LMGs (represented by sample 0473-4 with lowest sum of Ba+Sr from Hu et al., 2011b, Ba = 17.7 ppm, Sr = 19.8 ppm). The average Ba (459.9 ppm) and Sr (362.6 ppm) contents of the HMGs, represent the assumed composition of the residual crystal mush (including data from this study and previously reported data in Zeng et al., 2011, 2015; Hou et al., 2012; Dai et al., 2020a). Partition coefficients for micas were sourced from Icenhower and London (1995) while partition coefficients for feldspars were sourced from Michael (1984). The detailed calculating process can be found in Liu et al. (2019), and the related calculation parameters are presented in Supplementary Table S6. As illustrated in Figure 13, the theoretical calculations of the evolution of Ba and Sr are broadly in accordance with the actual compositional variations observed in the LMGs. According to the calculation, the most evolved LMGs sample (0473-4) represents the liquid extracted from a crystal mush at crystal fractions of ~60%–63% (F^{Sr}_{d} = 0.37, F^{Ba}_{d} = 0.40; Supplementary Table S6). The other less-evolved LMGs are probably due to involvement of a certain number of cumulate

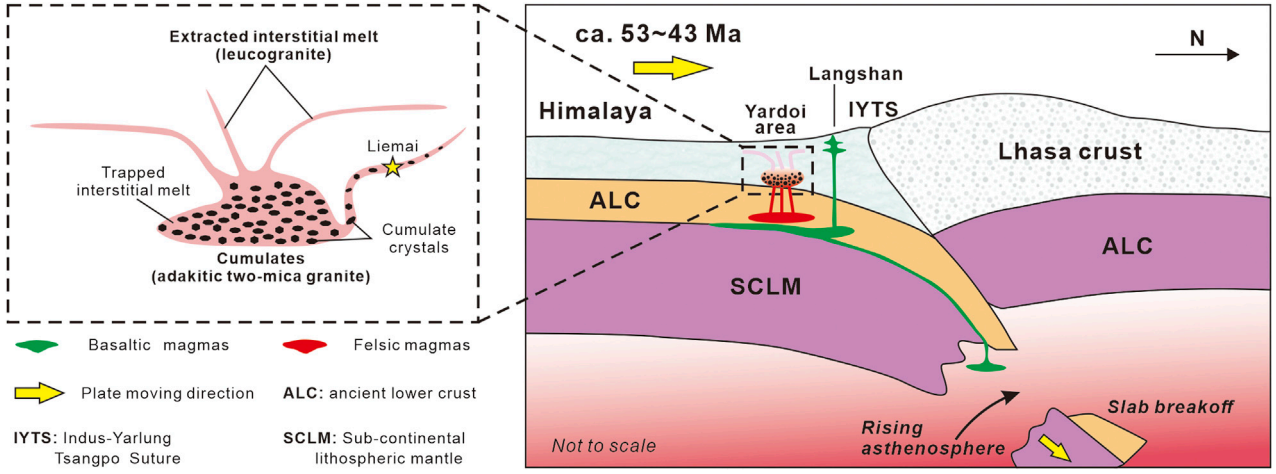

FIGURE 15
Schematic illustration shows the geodynamic setting and formation of the Early Eocene granites in the Yardoi area. The Langshan gabbro is from Ji et al. (2016).

crystals. In addition, the calculation results show that residual melt trapped in the HMGs crystal mush accounts for ~21%–25% (f^{Sr}_{tra} = 0.21 and $f^{Ba\ tra}$ = 0.25; Supplementary Table S6). Broadly, the results in accordance with previous predictions of a terminal porosity of 20–30 vol% for a residual crystal mush (Lee and Morton, 2015).

Therefore, the modeling calculations based on the Rayleigh fractionation using Sr and Ba indicate that the LMGs were extracted from the HMGs crystal mush at crystal fractions less than or equal to 60%–63%, in which crystal cumulates are plagioclase (41%), K-feldspar (17%), biotite (10%), and muscovite (5%) (Figure 13; Supplementary Table S6). Considering remarkable depletion of LREE and Ti in the LMGs compared to the HMGs, LREE-bearing minerals (e.g., monazite and apatite) and Ti-bearing minerals would have also been cumulative minerals.

5.3 Geological implications of the Early Eocene granitoids in eastern Himalaya

A pronounced magmatic flare-up with intensive input of mantle materials along the southern Gangdese at ca. 52–51 Ma (Zhu et al., 2015), together with a sudden drop of the India-Asia convergence rate (Patriat and Achache, 1984; van Hinsbergen et al., 2011), marked the slab breakoff of the subducting Neo-Tethyan oceanic lithosphere. In addition, the crustal thickness beneath the Gangdese reached a thickness>50 km at the beginning of the Eocene (Zhu et al., 2017; Tang et al., 2020). These observations signify that the Neo-Tethys Ocean has been completely closed prior to the Eocene and the Gangdese already had an abnormally thick crust.

Ultra-high pressure metamorphism (~55 Ma) and high amphibolite facies to granulite facies metamorphism (~43–47 Ma) in the Tethyan Himalaya suggest that intensive collision and crustal thickening occurred following closure of the Neo-Tethyan Ocean (Zeng et al., 2011; Gao et al., 2012). This is followed by intensive anatexis of the amphibolitic lower crust to generate Early Eocene adakitic magmas in the Yardoi area (Zeng et al., 2011, 2015; Hou et al., 2012; Dai et al., 2020a). It is worth mentioning that the garnet amphibolites, as the major source rocks for the adakitic rocks, show negligible Eu anomalies and differentiation of REE with low Sr/Y values (< 5) (Figure 6; Hou et al., 2012). In contrast, the garnet amphibolite-derived adakitic rocks are obviously depleted in MREE, HREE and Y, in despite of their comparable LREE and Sr contents and Eu anomalies to the garnet amphibolites (Figure 6). Therefore, MREE-enriched amphibole and HREE-enriched garnet should serve as residual minerals while the plagioclase should serve as melting phase during partial melting to produce melts with remarkable depletion of MREE and HREE and high Sr/Y ratios. Therefore, generation of these Early Eocene adakitic granites in the Yardoi area are indicative of a thickened crust.

In the past, the Sr/Y ratio was used to qualitatively estimate the paleo-crustal thickness. Recently, Chiaradia (2015) found that the Sr/Y ratios of magmatic rocks show positive correlation with crustal thickness in young arcs. Subsequently, Chapman et al. (2015) and Profeta et al. (2015) reconstructed the global and regional correlations between the whole-rock Sr/Y and $(La/Yb)_N$ ratios of intermediate-felsic arc magmatic rocks and arc crustal thickness, providing quantitative constraints on the paleo-crustal thickness in ancient arcs. More recently, Hu et al. (2017) successfully extended this method to continental collisional zones. The Eocene granites in the Yardoi area were formed

posterior India-Eurasia collision and slab breakoff of the Noe-Tethys oceanic lithosphere thus can be used to estimate the paleo-crustal thickness using the equations from Hu et al. (2017). Interestingly, granite sills (e.g., Liemai two-mica granite) or small intrusions (e.g., Quedang two-mica granite) show relatively lower Sr/Y ratios than big intrusions in Yardoi and Dala (Figure 14A). This is probably because small volume of magmas cooled faster than big ones, thus preserved relatively primitive Sr/Y values. In contrast, magmas with large volume could remain a relative long period at crystal mush state, which could result in elevated Sr/Y ratios due to extraction of low-Sr/Y melts. Therefore, although the extraction of low-Sr/Y melts (LMGs) could have increased the Sr/Y ratios of the crystal mush (HMGs) to some degree (Gao et al., 2021), the small intrusions (e.g., Liemai and Queang two-mica granites) with relatively primitive Sr/Y values can be preferably used to estimate the paleo-crustal thickness. This is supported by the close sample plotting sites of these granites to that of the assumed initial melt in the Sr vs. Ba diagram (Figure 13). The calculated $CT_{Sr/Y}$ values (crustal thickness based on whole-rock Sr/Y ratios) are broadly range from 50 to 90 km (Figure 14B) using the equation from Hu et al. (2017). Thus, the crustal thickness beneath the Himalaya was inferred to ~50 km during the Early Eocene.

Therefore, both sides of the IYTS experienced notable crustal thickening and gained an abnormally thick crust (~50 km) in the Early Eocene due to the India-Asia collision. Importantly, ascent of hot asthenospheric materials though slab windows caused by slab breakoff of the Neo-Tethys oceanic lithosphere triggered generation of mafic magmas (Ji et al., 2016). Mafic magmas that underplated to the crust-mantle boundary caused partial melting of the thickened lower crust to form adakitic rocks while those intruded in the middle-upper crust formed mafic rocks (Figure 15).

6 Conclusion

The following conclusions can be drawn from this study.

(1) The Liemai two-mica granite was emplaced at ca. 43 Ma similar to adjacent Yardoi, Dala, Quedang two-mica granites, and sub-volcanic leucogranite in Longzi County and leucogranite sills or dikes in Yardoi dome.
(2) The Liemai two-mica granite, similar to other coeval two-mica granites in the Yardoi area, shows adakitic features and was derived from partial melting of thickened lower crust consisting mainly of garnet amphibolite with minor metapelites.
(3) The high- and low-Mg# granites in the Yardoi area should be cogenetic. The highly evolved low-Mg granites were extracted from the high-Mg# granitic crystal mush at crystal fractions less than or equal to 52%–53%, in which crystal cumulates are plagioclase, K-feldspar, biotite, muscovite, LREE-bearing minerals (e.g., monazite and apatite) and Ti-bearing minerals.
(4) Underplating of basaltic magmas triggered by slab breakoff of the Neo-Tethyan oceanic lithosphere was the most possible mechanism supplying heat to induce partial melting of the thickened (~50 km) amphibolitic lower crust in Himalaya orogen to generate granites with adakitic signatures.

Data availability statement

The original contributions presented in the study are included in the article/Supplementary Material, further inquiries can be directed to the corresponding authors.

Author contributions

ZD and HC contributed to field investigation, experiments, and writing the manuscript. ZY, GL and YX contributed specifically to funding acquisition and supervision. LD and KG contributed to field investigation.

Funding

This study was financially supported by the National Natural Science Foundation of China (grant/award numbers: 92155305, 42103066 and 91955208).

Conflict of interest

The authors declare that the research was conducted in the absence of any commercial or financial relationships that could be construed as a potential conflict of interest.

Publisher's note

Supplementary material

The Supplementary Material for this article can be found online at: https://www.frontiersin.org/articles/10.3389/feart.2022.1104197/full#supplementary-material

References

Aikman, A. B., Harrison, T. M., and Hermann, J. (2012). The origin of eo- and neo-himalayan granitoids, eastern Tibet. *J. Asian Earth Sci.* 58 (30), 143–157. doi:10.1016/j.jseaes.2012.05.018

Aikman, A. B., Harrison, T. M., and Lin, D. (2008). Evidence for early (>44 Ma) himalayan crustal thickening, tethyan Himalaya, southeastern Tibet. *Earth Planet. Sci. Lett.* 274 (1–2), 14–23. doi:10.1016/j.epsl.2008.06.038

Baker, D. R., and Vaillancourt, J. (1995). The low viscosities of F+ H_2O-bearing granitic melts and implications for melt extraction and transport. *Earth Planet. Sci. Lett.* 132 (1-4), 199–211. doi:10.1016/0012-821x(95)00054-g

Batchelor, R. A., and Bowden, P. (1985). Petrogenetic interpretation of granitoid rock series using multicationic parameters. *Chem. Geol.* 48 (1–4), 43–55. doi:10.1016/0009-2541(85)90034-8

Blichert-Toft, J., Chauvel, C., and Albarède, F. (1997). Separation of Hf and Lu for high-precision isotope analysis of rock samples by magnetic sector-multiple collector ICP-MS. *Contributions Mineralogy Petrology* 127 (3), 248–260. doi:10.1007/s004100050278

Bonnefoi, C., and Provost and, A. (1995). The 'Daly gap' as a magmatic catastrophe. *Nature* 378, 270–272. doi:10.1038/378270a0

Cao, H. W., Huang, Y., Li, G. M., Zhang, L. K., Wu, J. Y., Dong, L., et al. (2018). Late triassic sedimentary records in the northern tethyan Himalaya: Tectonic link with greater India. *Geosci. Front.* 9 (1), 273–291. doi:10.1016/j.gsf.2017.04.001

Cao, H. W., Li, G. M., Zhang, L. K., Dong, L., Gao, K., and Dai, Z. W. (2020). Monazite U-Th-Pb age of Liemai Eocene granites in the southern Tibet and its geological implications. *Sediment. Geol. Tethyan Geol.* 40 (2), 31–42. (in Chinese with English abstract). doi:10.19826/j.cnki.1009-3850.(2020)02-0031-12

Cao, K., Yang, Z. M., White, N. C., and Hou, Z. Q. (2022a). Generation of the giant porphyry Cu-Au deposit by repeated recharge of mafic magmas at pulang in eastern Tibet. *Econ. Geol.* 117 (1), 57–90. doi:10.5382/econgeo.4860

Cao, H. W., Pei, Q. M., Santosh, M., Li, G. M., Zhang, L. K., Zhang, X. F., et al. (2022b). Himalayan leucogranites: A review of geochemical and isotopic characteristics, timing of formation, Genesis, and rare metal mineralization. *Earth-Science Rev.* 234, 104229. doi:10.1016/j.earscirev.2022.104229

Castillo, P. R., Janney, P. E., and Solidum, R. U. (1999). Petrology and geochemistry of camiguin island, southern Philippines: Insights to the source of adakites and other lavas in a complex arc setting. *Contributions mineralogy petrology* 134, 33–51. doi:10.1007/s004100050467

Chapman, J. B., Ducea, M. N., DeCelles, P. G., and Profeta, L. (2015). Tracking changes in crustal thickness during orogenic evolution with Sr/Y: An example from the North American Cordillera. *Geology* 43 (10), 919–922. doi:10.1130/g36996.1

Chappell, B. W., and White, A. J. R. (1992). I- and S-type granites in the lachlan fold belt. *Earth Environ. Sci. Trans. R. Soc. Edinb.* 83 (1-2), 1–26. doi:10.1017/s0263593300007720

Chen, J. L., Wu, J. B., Xu, J. F., Dong, Y. H., Wang, B. D., and Kang, Z. Q. (2013). Geochemistry of Eocene high-Mg# adakitic rocks in the northern Qiangtang terrane, central Tibet: Implications for early uplift of the plateau. *Geol. Soc. Am. Bull.* 125 (11-12), 1800–1819. doi:10.1130/b30755.1

Chiaradia, M. (2015). Crustal thickness control on Sr/Y signatures of recent arc magmas: An earth scale perspective. *Sci. Rep.* 5, 8115. doi:10.1038/srep08115

Chu, G. B., Chen, H. Y., Falloon, T. J., Han, J. S., Zhang, S. T., Cheng, J. M., et al. (2020). Early cretaceous mantle upwelling and melting of juvenile lower crust in the middle-lower yangtze river metallogenic belt: Example from tongshankou Cu-(Mo W) ore deposit. *Gondwana Res.* 83, 183–200. doi:10.1016/j.gr.2020.02.004

Chung, S. L., Liu, D. Y., Ji, J. Q., Chu, M. F., Lee, H. Y., Wen, D. J., et al. (2003). Adakites from continental collision zones: Melting of thickened lower crust beneath southern Tibet. *Geology* 31 (11), 1021–1024. doi:10.1130/g19796.1

Cottle, J. M., Searle, M. P., Jessup, M. J., Crowley, J. L., and Law, R. D. (2015). Rongbuk re-visited: Geochronology of leucogranites in the footwall of the south Tibetan detachment system, everest region, southern Tibet. *Lithos* 227, 94–106. doi:10.1016/j.lithos.2015.03.019

Dai, Z. W., Dong, L., Li, G. M., Huizenga, J. M., Ding, J., Zhang, L. K., et al. (2020a). Crustal thickening prior to 43 Ma in the Himalaya: Evidence from lower crust-derived adakitic magmatism in Dala, eastern tethyan Himalaya, Tibet. *Geol. J.* 55 (5), 4021–4046. doi:10.1002/gj.3639

Dai, Z. W., Huang, H. X., Li, G. M., Huizenga, J. M., Santosh, M., Cao, H. W., et al. (2020b). Formation of Late Cretaceous high-Mg granitoid porphyry in central Lhasa, Tibet: Implications for crustal thickening prior to India-Asia collision. *Geol. J.* 55 (10), 6696–6717. doi:10.1002/gj.3834

Dai, Z. W., Li, G. M., Ding, J., Huang, Y., and Cao, H. W. (2018). Late cretaceous adakite in Nuri area, Tibet: Products of ridge subduction. *Earth Sci.* 43 (8), 2727–2741. (in Chinese with English abstract). doi:10.3799/dqkx.2018.230

Davidson, J., Turner, S., Handley, H., Macpherson, C., and Dosseto, A. (2007). Amphibole "sponge" in arc crust? *Geology* 35 (9), 787. doi:10.1130/g23637a.1

Defant, M. J., and Drummond, M. S. (1990). Derivation of some modern arc magmas by melting of young subducted lithosphere. *Nature* 347 (6294), 662–665. doi:10.1038/347662a0

Depaolo, D. J. (1988). Age dependence of the composition of continental crust: Evidence from Nd isotopic variations in granitic rocks. *Earth Planet. ence Lett.* 90 (3), 263–271. doi:10.1016/0012-821x(88)90130-6

Depaolo, D. J., Linn, A. M., and Schubert, G. (1991). The continental crustal age distribution: Methods of determining mantle separation ages from Sm-Nd isotopic data and application to the southwestern United States. *J. Geophys. Res.* 96, 2071. doi:10.1029/90jb02219

Dolgopolova, A., Seltmann, R., Armstrong, R., Belousova, E., Pankhurst, R. J., and Kavalieris, I. (2013). Sr-Nd-Pb-Hf isotope systematics of the Hugo Dummett Cu-Au porphyry deposit (Oyu Tolgoi, Mongolia). *Lithos* 164-167, 47–64. doi:10.1016/j.lithos.2012.11.017

Fisher, C. M., Vervoort, J. D., and Hanchar, J. M. (2014). Guidelines for reporting zircon Hf isotopic data by LA-MC-ICPMS and potential pitfalls in the interpretation of these data. *Chem. Geol.* 363, 125–133. doi:10.1016/j.chemgeo.2013.10.019

Fu, J. G., Li, G. M., Wang, G. H., Zhang, L. K., Liang, W., Zhang, X. Q., et al. (2020). Structural analysis of sheath folds and geochronology in the cuonadong dome, southern Tibet, China: New constraints on the timing of the south Tibetan detachment system and its relationship to North Himalayan gneiss domes. *Terra nova.* 32 (4), 300–323. doi:10.1111/ter.12462

Gao, J. F., Lu, J. J., Lai, M. Y., Lin, Y. P., and Pu, W. (2003). Analysis of trace elements in rock samples using HR-ICPMS. *J. Nanjing Univ. Nat. Sci.* 39 (6), 844–850. (in Chinese with English abstract).

Gao, L. E., Zeng, L. S., and Xie, K. J. (2012). Eocene high grade metamorphism and crustal anatexis in the North Himalaya gneiss domes, southern Tibet. *Chin. Sci. Bull.* 57 (6), 639–650. doi:10.1007/s11434-011-4805-4

Gao, P., Zheng, Y. F., Yakymchuk, C., Zhao, Z. F., and Meng, Z. Y. (2021). The effects of source mixing and fractional crystallization on the composition of Eocene granites in the Himalayan Orogen. *J. Petrology* 62 (7), 1–23. doi:10.1093/petrology/egab037

Gao, S., Rudnick, R. L., Yuan, H. L., Liu, X. M., Liu, Y. S., Xu, W. L., et al. (2004). Recycling lower continental crust in the North China craton. *Nature* 432, 892–897. doi:10.1038/nature03162

Grimes, C. B., John, B. E., Kelemen, P. B., Mazdab, F. K., Wooden, J. L., Cheadle, M. J., et al. (2007). Trace element chemistry of zircons from oceanic crust: A method for distinguishing detrital zircon provenance. *Geology* 35 (7), 643–646. doi:10.1130/g23603a.1

Harris, N. B. W., Pearce, J. A., and Tindle, A. G. (1986). Geochemical characteristics of collision-zone magmatism. *Geol. Soc. Lond. Spec. Publ.* 19, 67–81. doi:10.1144/gsl.sp.1986.019.01.04

Harrison, T. M., Grove, M., Mckeegan, K. D., Coath, C. D., Lovera, O. M., and Fort, P. L. (1999). Origin and episodic emplacement of the manaslu intrusive complex, central Himalaya. *J. Petrology* 40 (1), 3–19. doi:10.1093/petroj/40.1.3

Hoskin, P. W. O. (2005). Trace-element composition of hydrothermal zircon and the alteration of Hadean zircon from the Jack Hills, Australia. *Geochimica Cosmochimica Acta* 69 (3), 637–648. doi:10.1016/j.gca.2004.07.006

Hou, Z. Q., Duan, L. F., Lu, Y. J., Zheng, Y. C., Zhu, D. C., Yang, Z. M., et al. (2015). Lithospheric architecture of the Lhasa terrane and its control on ore deposits in the himalayan-Tibetan orogen. *Econ. Geol.* 110 (6), 1541–1575. doi:10.2113/econgeo.110.6.1541

Hou, Z. Q., Gao, Y. F., Qu, X. M., Rui, Z. Y., and Mo, X. X. (2004). Origin of adakitic intrusives generated during mid-Miocene east–west extension in southern Tibet. *Earth Planet. Sci. Lett.* 220 (1–2), 139–155. doi:10.1016/s0012-821x(04)00007-x

Hou, Z. Q., Pan, G. T. W., An, J., Mo, X. X., Tian, S. H., Sun, X. M., et al. (2006a). Metallogenesis in Tibetan collisional orogenic belt: II. Mineralization in late-collisional transformation setting. *Mineral. Deposits* 25 (5), 521–543. (in Chinese with English abstract).

Hou, Z. Q., Yang, Z. S., Xu, W. Y., Mo, X. X., Ding, L., Gao, Y. F., et al. (2006b). Metallogenesis in Tibetan collisional orogenic belt: I. Mineralization in main collisional orogenic setting. *Mineral. Deposits* 25 (4), 337–358. (in Chinese with English abstract).

Hou, Z. Q., Zheng, Y. C., Zeng, L. S., Gao, L. E., Huang, K. X., Li, W., et al. (2012). Eocene–Oligocene granitoids in southern Tibet: Constraints on crustal anatexis and tectonic evolution of the Himalayan orogen. *Earth Planet. Sci. Lett.* 349 (350), 38–52. doi:10.1016/j.epsl.2012.06.030

Hu, F. Y., Ducea, M. N., Liu, S. W., and Chapman, J. B. (2017). Quantifying crustal thickness in continental collisional belts: Global perspective and a geologic application. *Sci. Rep.* 7, 7058. doi:10.1038/s41598-017-07849-7

Hu, G. Y., Zeng, L. S., and Qi, X. X. (2011a). The mid-eocene subvolcanic field in the lhunze-qiaga area, tethyan Himalaya, southern Tibet: A high-level magmatic suite related to the yardio two-mica granite. *Acta Petrol. Sin.* 27 (11), 3308–3318. (in Chinese with English abstract).

Hu, G. Y., Zeng, L. S., Gao, L. E., and Xie, K. J. (2011b). Lanthanide kinked shape, similar to Tetrad effect, observed in sub-volcanic rocks from Qiaga, southern Tibet, China. *Geol. Bull. China* 30 (1), 82–94. (in Chinese with English abstract).

Hu, Z. C., Liu, Y. S., Gao, S., Liu, W. G., Zhang, W., Tong, X. R., et al. (2012). Improved *in situ* Hf isotope ratio analysis of zircon using newly designed X skimmer cone and jet sample cone in combination with the addition of nitrogen by laser ablation multiple collector ICP-MS. *J. Anal. Atomic Spectrom.* 27, 1391–1399. doi:10.1039/c2ja30078h

Hu, Z. C., Zhang, W., Liu, Y. S., Gao, S., Li, M., Zong, K. Q., et al. (2015). "Wave" signal-smoothing and mercury-removing device for laser ablation quadrupole and multiple collector ICPMS analysis: Application to lead isotope analysis. *Anal. Chem.* 87 (2), 1152–1157. doi:10.1021/ac503749k

Icenhower, J., and London, D. (1995). An experimental study of element partitioning among biotite, muscovite, and coexisting peraluminous silicic melt at 200 MPa (H2O). *Am. Mineralogist* 80 (11-12), 1229–1251. doi:10.2138/am-1995-11-1213

Inger, S., and Harris, N. (1993). Geochemical constraints on leucogranite magmatism in the langtang valley, Nepal Himalaya. *J. Petrology* 34 (2), 345–368. doi:10.1093/petrology/34.2.345

Ji, W. Q., Wu, F. Y., Chung, S. L., Wang, X. C., Liu, C. Z., Li, Q. L., et al. (2016). Eocene Neo-Tethyan slab breakoff constrained by 45 Ma oceanic island basalt-type magmatism in southern Tibet. *Geology* 44 (4), 283–286. doi:10.1130/g37612.1

Jiang, Z. Q., Wang, Q., Li, Z. X., Wyman, D. A., Tang, G. J., Jia, X. H., et al. (2012). Late Cretaceous (ca. 90 Ma) adakitic intrusive rocks in the Kelu area, Gangdese Belt (southern Tibet): Slab melting and implications for Cu–Au mineralization. *J. Asian Earth Sci.* 53, 67–81. doi:10.1016/j.jseaes.2012.02.010

Jiang, Z. Q., Wang, Q., Wyman, D. A., Tang, G. J., Jia, X. H., Yang, Y. H., et al. (2011). Origin of ~30Ma chongmuda adakitic intrusive rocks in the southern gangdese region, southern Tibet: Partial melting of the northward subducted Indian continent crust? *Geochimica* 40 (2), 126–146. (in Chinese with English abstract). doi:10.19700/j.0379-1726.2011.02.002

Karsli, O., Dokuz, A., Uysal, I., Aydin, F., Kandemir, R., and Wijbrans, J. (2010). Generation of the early Cenozoic adakitic volcanism by partial melting of mafic lower crust, eastern Turkey; implications for crustal thickening to delamination. *Lithos* 114 (1–2), 109–120. doi:10.1016/j.lithos.2009.08.003

Klein, E. M. (2004). "Geochemistry of the igneous oceanic crust," in *Treatise on geochemistry*. Editor H. D. Holland and K. K. Turekian. Amsterdam: Elsevier 3, 433–463.

Kohn, M. J. (2014). Himalayan metamorphism and its tectonic implications. *Annu. Rev. Earth Planet. Sci.* 42, 381–419. doi:10.1146/annurev-earth-060313-055005

Lai, S. c., and Qin, J. f. (2013). Adakitic rocks derived from the partial melting of subducted continental crust: Evidence from the Eocene volcanic rocks in the northern Qiangtang block. *Gondwana Res.* 23 (2), 812–824. doi:10.1016/j.gr.2012.06.003

Lee, C.-T. A., and Morton, D. M. (2015). High silica granites: Terminal porosity and crystal settling in shallow magma chambers. *Earth Planet. Sci. Lett.* 409, 23–31. doi:10.1016/j.epsl.2014.10.040

Leloup, P. H., Mahéo, G., Arnaud, N., Kali, E., Boutonnet, E., Liu, D., et al. (2010). The South Tibet detachment shear zone in the Dinggye area: Time constraints on extrusion models of the Himalayas. *Earth Planet. Sci. Lett.* 292 (1–2), 1–16. doi:10.1016/j.epsl.2009.12.035

Li, W. K., Yang, Z. M., Chiaradia, M., Lai, Y., and Zhang, J. Y. (2020). Redox state of southern Tibetan upper mantle and ultrapotassic magmas. *Geology* 48 (7), 733–736. doi:10.1130/g47411.1

Liu, Y. S., Gao, S., Hu, Z. C., Gao, C. G., Zong, K. Q., and Wang, D. B. (2010). Continental and oceanic crust recycling-induced melt–peridotite interactions in the trans-north China orogen: U–Pb dating, Hf isotopes and trace elements in zircons from mantle xenoliths. *J. Petrology* 51 (1-2), 537–571. doi:10.1093/petrology/egp082

Liu, Y. S., Hu, Z. C., Gao, S., Günther, D., Xu, J., Gao, C. G., et al. (2008). *In situ* analysis of major and trace elements of anhydrous minerals by LA-ICP-MS without applying an internal standard. *Chem. Geol.* 257 (1-2), 34–43. doi:10.1016/j.chemgeo.2008.08.004

Liu, Z. C., Wu, F. Y., Liu, X. C., Wang, J. G., Yin, R., Qiu, Z. L., et al. (2019). Mineralogical evidence for fractionation processes in the Himalayan leucogranites of the Ramba Dome, southern Tibet. *Lithos* 340-341, 71–86. doi:10.1016/j.lithos.2019.05.004

Liu, Z. C., Wu, F. Y., Qiu, Z. L., Wang, J. G., Liu, X. C., Ji, W. Q., et al. (2017). Leucogranite geochronological constraints on the termination of the South Tibetan Detachment in eastern Himalaya. *Tectonophysics* 721, 106–122. doi:10.1016/j.tecto.2017.08.019

Long, X. P., Wilde, S. A., Wang, Q., Yuan, C., Wang, X. C., Li, J., et al. (2015). Partial melting of thickened continental crust in central Tibet: Evidence from geochemistry and geochronology of Eocene adakitic rhyolites in the northern Qiangtang Terrane. *Earth Planet. Sci. Lett.* 414, 30–44. doi:10.1016/j.epsl.2015.01.007

Ludwig, K. R. (2003). User's manual for a geochronological toolkit for Microsoft Excel (Isoplot/Ex version 3.0). *Spec. Publ.* 4, 1–71.

Luffi, P., and Ducea, M. N. (2022). Chemical mohometry: Assessing crustal thickness of ancient orogens using geochemical and isotopic data. *Rev. Geophys.* 60 (2), 1–42. doi:10.1029/2021rg000753

Ma, L., Wang, B. D., Jiang, Z. Q., Wang, Q., Li, Z. X., Wyman, D. A., et al. (2014). Petrogenesis of the early eocene adakitic rocks in the napuri area, southern Lhasa: Partial melting of thickened lower crust during slab break-off and implications for crustal thickening in southern Tibet. *Lithos* 196-197, 321–338. doi:10.1016/j.lithos.2014.02.011

Ma, L., Wang, Q., Wyman, D. A., Li, Z. X., Jiang, Z. Q., Yang, J. H., et al. (2013). Late Cretaceous (100–89 Ma) magnesian charnockites with adakitic affinities in the Milin area, eastern Gangdese: Partial melting of subducted oceanic crust and implications for crustal growth in southern Tibet. *Lithos* 175–176, 315–332. doi:10.1016/j.lithos.2013.04.006

Macpherson, C. G., Dreher, S. T., and Thirlwall, M. F. (2006). Adakites without slab melting: High pressure differentiation of island arc magma, Mindanao, the Philippines. *Earth Planet. Sci. Lett.* 243, 581–593. doi:10.1016/j.epsl.2005.12.034

Maniar, P. D., and Piccoli, P. M. (1989). Tectonic discrimination of granitoids. *Geol. Soc. Am. Bull.* 101 (5), 635–643. doi:10.1130/0016-7606(1989)101<0635:tdog>2.3.co;2

Martin, H. (1986). Effect of steeper Archean geothermal gradient on geochemistry of subduction-zone magmas. *Geology* 14 (9), 753–756. doi:10.1130/0091-7613(1986)14<753:eosagg>2.0.co;2

Michael, P. J. (1984). Chemical differentiation of the Cordillera Paine granite (southern Chile) by *in situ* fractional crystallization. *Contributions Mineralogy Petrology* 87 (2), 179–195. doi:10.1007/bf00376223

Middlemost, E. A. K. (1994). Naming materials in the magma/igneous rock system. *Earth-Science Rev.* 37 (3), 215–224. doi:10.1016/0012-8252(94)90029-9

Mo, X. X., Hou, Z. Q., Niu, Y. L., Dong, G. C., Qu, X. M., Zhao, Z. D., et al. (2007). Mantle contributions to crustal thickening during continental collision: Evidence from Cenozoic igneous rocks in southern Tibet. *Lithos* 96 (1–2), 225–242. doi:10.1016/j.lithos.2006.10.005

Mo, X. X. (2011). Magmatism and evolution of the Tibetan plateau. *Geol. J. China Univ.* 17 (3), 351–367. (in Chinese with English abstract). doi:10.16108/j.issn1006-7493.2011.03.004

Moyen, J.-F. (2009). High Sr/Y and La/Yb ratios: The meaning of the "adakitic signature". *Lithos* 112 (3), 556–574. doi:10.1016/j.lithos.2009.04.001

Myrow, P. M., Fike, D. A., Malmskog, E., Leslie, S. A., Zhang, T., Singh, B. P., et al. (2019). Ordovician–Silurian boundary strata of the Indian Himalaya: Record of the latest ordovician boda event. *Geol. Soc. Am. Bull.* 131 (5-6), 881–898. doi:10.1130/b31860.1

Niu, X. L., Zhao, Z. D., Mo, X. X., DePaolo, D., Dong, G. C., Zhang, S. Q., et al. (2006). Elemental and Sr-Nd-Pb isotopic geochemistry for basic rocks from decun-angren ophiolites in xigaze area, Tibet: Implications for the characteristics of the tethyan upper mantle domain. *Acta Petrol. Sin.* 22 (12), 2875–2888. (in Chinese with English abstract).

Pan, G. T., Wang, L. Q., Li, R. S., Yuan, S. H., Ji, W. H., Yin, F. G., et al. (2012). Tectonic evolution of the Qinghai-Tibet Plateau. *J. Asian Earth Sci.* 53, 3–14. doi:10.1016/j.jseaes.2011.12.018

Parrish, R. R. (1990). U–Pb dating of monazite and its application to geological problems. *Can. J. Earth Sci.* 27 (11), 1431–1450. doi:10.1139/e90-152

Patriat, P., and Achache, J. (1984). India-Eurasia collision chronology has implications for crustal shortening and driving mechanism of plates. *Nature* 311 (5987), 615–621. doi:10.1038/311615a0

Pearce, J. A., Harris, N. B., and Tindle, A. G. (1984). Trace element discrimination diagrams for the tectonic interpretation of granitic rocks. *J. petrology* 25 (4), 956–983. doi:10.1093/petrology/25.4.956

Peccerillo, A., and Taylor, S. R. (1976). Geochemistry of eocene calc-alkaline volcanic rocks from the Kastamonu area, Northern Turkey. *Contributions Mineralogy Petrology* 58, 63–81. doi:10.1007/bf00384745

Profeta, L., Ducea, M. N., Chapman, J. B., Paterson, S. R., Gonzales, S. M., Kirsch, M., et al. (2015). Quantifying crustal thickness over time in magmatic arcs. *Sci. Rep.* 5, 17786. doi:10.1038/srep17786

Qi, X. X., Zeng, L. S., Meng, X. J., Xu, Z. Q., and Li, T. F. (2008). Zircon SHRIMP U-Pb dating for Dala granite in the Tethyan Himalaya and its geological implication. *Acta Petrol. Sin.* 24 (7), 1501–1508. (in Chinese with English abstract).

Rapp, R. P., Shimizu, N., Norman, M. D., and Applegate, G. S. (1999). Reaction between slab-derived melts and peridotite in the mantle wedge: Experimental constraints at 3.8 GPa. *Chem. Geol.* 160, 335–356. doi:10.1016/s0009-2541(99)00106-0

Rapp, R. P., Xiao, L., and Shimizu, N. (2002). Experimental constraints on the origin of potassium-rich adakites in eastern China. *Acta Petrol. Sin.* 18 (3), 293–302.

Richards, A., Argles, T., Harris, N., Parrish, R., Ahmad, T., Darbyshire, F., et al. (2005). Himalayan architecture constrained by isotopic tracers from clastic sediments. *Earth Planet. Sci. Lett.* 236 (3-4), 773–796. doi:10.1016/j.epsl.2005.05.034

Rickwood, P. C. (1989). Boundary lines within petrologic diagrams which use oxides of major and minor elements. *lithos* 22 (4), 247–263. doi:10.1016/0024-4937(89)90028-5

Rudnick, R. L., and Gao, S. (2003). "Composition of the continental crust," in *Treatise on geochemistry*. Editor K. K. Turekian (Oxford: Pergamon), 1–64.

Scaillet, B., Holtz, F., Pichavant, M., and Schmidt, M. (1996). Viscosity of Himalayan leucogranites: Implications for mechanisms of granitic magma ascent. *J. Geophys. Res. Solid Earth* 101 (B12), 27691–27699. doi:10.1029/96jb01631

Sirbescu, M.-L. C., and Nabelek, P. I. (2003). Crustal melts below 400 C. *Geology* 31 (8), 685–688. doi:10.1130/g19497.1

Streck, M. J., Leeman, W. P., and Chesley, J. (2007). High-magnesian andesite from mount shasta: A product of magma mixing and contamination, not a primitive mantle melt. *Geology* 35 (4), 351–354. doi:10.1130/g23286a.1

Sun, S. S., and McDonough, W. F. (1989). Chemical and isotopic systematics of oceanic basalts: Implications for mantle composition and processes. *Geol. Soc. Lond. Spec. Publ.* 42, 313–345. doi:10.1144/gsl.sp.1989.042.01.19

Sylvester, P. J. (1998). Post-collisional strongly peraluminous granites. *Lithos* 45 (1–4), 29–44. doi:10.1016/s0024-4937(98)00024-3

Tang, M., Ji, W. Q., Chu, X., Wu, A. B., and Chen, C. (2020). Reconstructing crustal thickness evolution from europium anomalies in detrital zircons. *Geology* 49 (1), 76–80. doi:10.1130/g47745.1

Tian, L. M., Wang, L. Y., Zheng, H. T., and Yang, B. (2018). Eocene magmatism from the Liemai intrusion in the eastern tethyan himalayan belt and tectonic implications. *Geol. Mag.* 156, 510–524. doi:10.1017/s0016756817000966

van Hinsbergen, D. J. J., Steinberger, B., Doubrovine, P. V., and Gassmöller, R. (2011). Acceleration and deceleration of India-Asia convergence since the Cretaceous: Roles of mantle plumes and continental collision. *J. Geophys. Res.* 116 (B6), B06101. doi:10.1029/2010jb008051

Vidal, P., Cocherie, A., and Le Fort, P. (1982). Geochemical investigations of the origin of the Manaslu leucogranite (Himalaya, Nepal). *Geochimica Cosmochimica Acta* 46 (11), 2279–2292. doi:10.1016/0016-7037(82)90201-0

Wang, L. Q., Cheng, W. B., Gao, T., and Wang, Y. (2021). A model involving amphibolite lower crust melting and subsequent melt extraction for leucogranite generation. *GSA Bull.* 134, 1160–1179. doi:10.1130/b36055.1

Wang, Q., Xu, J. F., Jian, P., Bao, Z. W., Zhao, Z. H., Li, C. F., et al. (2006). Petrogenesis of adakitic porphyries in an extensional tectonic setting, dexing, south China: Implications for the genesis of porphyry copper mineralization. *J. Petrology* 47 (1), 119–144. doi:10.1093/petrology/egi070

Wang, Q., Zhu, D. C., Zhao, Z. D., Liu, S. A., Chung, S. L., Li, S. M., et al. (2014). Origin of the ca. 90Ma magnesia-rich volcanic rocks in SE Nyima, central Tibet: Products of lithospheric delamination beneath the Lhasa-Qiangtang collision zone. *Lithos* 198–199, 24–37. doi:10.1016/j.lithos.2014.03.019

Wang, Y. J., Wang, X. S., Bi, X. W., Tao, Y., and Lan, T. G. (2020). Intraplate adakite-like rocks formed by differentiation of mantle-derived mafic magmas: A case study of eocene intermediate-felsic porphyries in the machangqing porphyry Cu-Au mining district, se Tibetan plateau. *J. Asian Earth Sci.* 196, 104364. doi:10.1016/j.jseaes.2020.104364

Woodhead, J., Hergt, J., Shelley, M., Eggins, S., and Kemp, R. (2004). Zircon Hf-isotope analysis with an excimer laser, depth profiling, ablation of complex geometries, and concomitant age estimation. *Chem. Geol.* 209 (1–2), 121–135. doi:10.1016/j.chemgeo.2004.04.026

Wu, F. Y., Li, X. H., Zheng, Y. F., and Gao, S. (2007). Lu-Hf isotopic systematics and their applications in petrology. *Acta Petrol. Sin.* 23 (2), 185–220. (in Chinese with English abstract).

Wu, F. Y., Liu, X. C., Liu, Z. C., Wang, R. C., Xie, L., Wang, J. M., et al. (2020). Highly fractionated Himalayan leucogranites and associated rare-metal mineralization. *Lithos* 352-353, 105319. doi:10.1016/j.lithos.2019.105319

Wu, F. Y., Liu, Z. C., Liu, X. C., and Ji, W. Q. (2015). Himalayan leucogranite: Petrogenesis and implications to orogenesis and plateau uplift. *Acta Petrol. Sin.* 31 (1), 1–36. (in Chinese with English abstract).

Wu, Y. B., and Zheng, Y. F. (2004). Genesis of zircon and its constraints on interpretation of U-Pb age. *Chin. Sci. Bull.* 49 (15), 1554–1569. doi:10.1360/04wd0130

Wu, Z. H., Ye, P. S., Wu, Z. H., and Zhao, Z. (2014). LA-ICP-MS zircon U-Pb ages of tectonic-thermal events in the Yalaxiangbo dome of Tethys Himalayan belt. *Geol. Bull. China* 33 (5), 595–605. (in Chinese with English abstract).

Xu, J. F., and Castillo, P. R. (2004). Geochemical and Nd-Pb isotopic characteristics of the tethyan asthenosphere: Implications for the origin of the Indian ocean mantle domain. *Tectonophysics* 393 (1-4), 9–27. doi:10.1016/j.tecto.2004.07.028

Xu, J. F., Shinjo, R., Defant, M. J., Wang, Q., and Rapp, R. P. (2002). Origin of Mesozoic adakitic intrusive rocks in the Ningzhen area of east China: Partial melting of delaminated lower continental crust? *Geology* 30 (12), 1111–1114. doi:10.1130/0091-7613(2002)030<1111:oomair>2.0.co;2

Xu, W. L., Wang, Q. H., Wang, D. Y., Guo, J. H., and Pei, F. P. (2006). Mesozoic adakitic rocks from the Xuzhou–Suzhou area, eastern China: Evidence for partial melting of delaminated lower continental crust. *J. Asian Earth Sci.* 27, 230–240. doi:10.1016/j.jseaes.2005.03.005

Yang, D. B., Xu, W. L., Zhao, G. C., Huo, T. F., Shi, J. P., and Yang, H. T. (2016b). Tectonic implications of Early Cretaceous low-Mg adakitic rocks generated by partial melting of thickened lower continental crust at the southern margin of the central North China Craton. *Gondwana Res.* 38, 220–237. doi:10.1016/j.gr.2015.11.013

Yang, X. S., and Jin, Z. M. (2001). Studies on Rb-Sr and Sm-Nd isotope of yadong leucogranite in Tibet: Constraint on its age and source materal. *Geol. Rev.* 47 (3), 294–300. (in Chinese with English abstract). doi:10.16509/j.georeview.2001.03.013

Yang, Z. M., Chang, Z. S., Paquette, J., White, N. C., Hou, Z. Q., and Ge, L. S. (2015a). Magmatic Au mineralization at the Bilihe Au deposit, China. *Econ. Geol.* 110 (7), 1661–1668. doi:10.2113/econgeo.110.7.1661

Yang, Z. M., Lu, Y. J., Hou, Z. Q., and Chang, Z. S. (2015b). High-Mg diorite from Qulong in southern Tibet: Implications for the Genesis of adakite-like intrusions and associated porphyry Cu deposits in collisional orogens. *J. Petrology* 56, 227–254. doi:10.1093/petrology/egu076

Yang, Z. M., Goldfarb, R. J., and Chang, Z. S. (2016a). Generation of postcollisional porphyry copper deposits in southern Tibet triggered by subduction of the Indian continental plate. *Soc. Econ. Geol. Spec. Pub* 19, 279–300. doi:10.5382/SP.19.11

Yin, A. (2006). Cenozoic tectonic evolution of the Himalayan orogen as constrained by along-strike variation of structural geometry, exhumation history, and foreland sedimentation. *Earth-Science Rev.* 76 (1–2), 1–131. doi:10.1016/j.earscirev.2005.05.004

Yin, A., and Harrison, T. M. (2000). Geologic evolution of the Himalayan-Tibetan orogen. *Annu. Rev. Earth Planet. Sci.* 28, 211–280. doi:10.1146/annurev.earth.28.1.211

Zeng, L. S., Gao, L. E., Dong, C. Y., and Tang, S. H. (2012). High-pressure melting of metapelite and the formation of Ca-rich granitic melts in the Namche Barwa Massif, southern Tibet. *Gondwana Res.* 21 (1), 138–151. doi:10.1016/j.gr.2011.07.023

Zeng, L. S., Gao, L. E., Tang, S. H., Hou, K. J., Guo, C. L., and Hu, G. Y. (2015). Eocene magmatism in the tethyan Himalaya, southern Tibet. *Geol. Soc. Lond. Spec. Publ.* 412, 287–316. doi:10.1144/sp412.8

Zeng, L. S., Gao, L. E., Xie, K. J., and Jing, L. Z. (2011). Mid-Eocene high Sr/Y granites in the Northern Himalayan Gneiss Domes: Melting thickened lower continental crust. *Earth Planet. Sci. Lett.* 303, 251–266. doi:10.1016/j.epsl.2011.01.005

Zeng, L. S., Liu, J., Gao, L. E., Xie, K. J., and Wen, L. (2009). Early Oligocene anatexis in the Yardoi gneiss dome, southern Tibet and geological implications. *Chin. Sci. Bull.* 54 (1), 104–112. doi:10.1007/s11434-008-0362-x

Zeng, Y. C., Ducea, M. N., Xu, J. F., Chen, J. L., and Dong, Y. H. (2020). Negligible surface uplift following foundering of thickened central Tibetan lower crust. *Geology* 49 (1), 45–50. doi:10.1130/g48142.1

Zhang, J. J., Santosh, M., Wang, X. X., Guo, L., Yang, X. Y., and Zhang, B. (2012). Tectonics of the northern Himalaya since the India–Asia collision. *Gondwana Res.* 21, 939–960. doi:10.1016/j.gr.2011.11.004

Zhang, L. K., Li, G. M., Cao, H. W., Zhang, Z., Dong, S. L., Liang, W., et al. (2020). Activity of the south Tibetan detachment system: Constraints from leucogranite ages in the eastern Himalayas. *Geol. J.* 55 (7), 5540–5573. doi:10.1002/gj.3756

Zhang, S. Q., Mahoney, J. J., Mo, X. X., Ghazi, A. M., Milani, L., Crawford, A. J., et al. (2005). Evidence for a widespread tethyan upper mantle with Indian-Ocean-Type isotopic characteristics. *J. Petrology* 46 (4), 829–858. doi:10.1093/petrology/egi002

Zhang, Z. M., Zhao, G. C., Santosh, M., Wang, J. L., Dong, X., and Shen, K. (2010). Late Cretaceous charnockite with adakitic affinities from the Gangdese batholith, southeastern Tibet: Evidence for Neo-Tethyan mid-ocean ridge subduction? *Gondwana Res.* 17 (4), 615–631. doi:10.1016/j.gr.2009.10.007

Zheng, Y. C., Hou, Z. Q., Fu, Q., Zhu, D. C., Liang, W., and Xu, P. Y. (2016). Mantle inputs to Himalayan anatexis: Insights from petrogenesis of the Miocene Langkazi leucogranite and its dioritic enclaves. *Lithos* 264, 125–140. doi:10.1016/j.lithos.2016.08.019

Zhu, D. C., Chung, S. L., Mo, X. X., Zhao, Z. D., Niu, Y. L., Song, B., et al. (2009a). The 132 Ma Comei-Bunbury large igneous province: Remnants identified in present-day southeastern Tibet and southwestern Australia. *Geology* 37 (7), 583–586. doi:10.1130/g30001a.1

Zhu, D. C., Wang, Q., Cawood, P. A., Zhao, Z. D., and Mo, X. X. (2017). Raising the gangdese mountains in southern Tibet. *J. Geophys. Res. Solid Earth* 122, 214–223. doi:10.1002/2016jb013508

Zhu, D. C., Wang, Q., Zhao, Z. D., Chung, S. L., Cawood, P. A., Niu, Y. L., et al. (2015). Magmatic record of India-Asia collision. *Sci. Rep.* 5, 14289. doi:10.1038/srep14289

Zhu, D. C., Zhao, Z. D., Pan, G. T., Lee, H. Y., Kang, Z. Q., Liao, Z. L., et al. (2009b). Early cretaceous subduction-related adakite-like rocks of the Gangdese Belt, southern Tibet: Products of slab melting and subsequent melt–peridotite interaction? *J. Asian Earth Sci.* 34 (3), 298–309. doi:10.1016/j.jseaes.2008.05.003

Zindler, A., and Hart, S. (1986). Chemical geodynamics. *Annu. Rev. earth Planet. Sci.* 14, 493–571. doi:10.1146/annurev.ea.14.050186.002425

Zong, K. Q., Chen, J. Y., Hu, Z. C., Liu, Y. S., Li, M., Fan, H. H., et al. (2015). *In-situ* U-Pb dating of uraninite by fs-LA-ICP-MS. *Sci. China Earth Sci.* 58 (10), 1731–1740. doi:10.1007/s11430-015-5154-y

Zong, K. Q., Klemd, R., Yuan, Y., He, Z. Y., Guo, J. L., Shi, X. L., et al. (2017). The assembly of Rodinia: The correlation of early Neoproterozoic (ca. 900 Ma) high-grade metamorphism and continental arc formation in the southern Beishan Orogen, southern Central Asian Orogenic Belt (CAOB). *Precambrian Res.* 290, 32–48. doi:10.1016/j.precamres.2016.12.010

frontiers | Frontiers in Earth Science

TYPE Original Research
PUBLISHED 09 January 2023
DOI 10.3389/feart.2022.1097778

OPEN ACCESS

EDITED BY
Qiuming Pei,
Southwest Jiaotong University, China

REVIEWED BY
Wenyan Ge,
Northwest A&F University, China
Jie Dou,
China University of Geosciences Wuhan, China
Shubin Zhou,
Macquarie University, Australia

*CORRESPONDENCE
Ling Zeng,
zengling18@cdut.edu.cn
Shoutao Jiao,
jshoutao@mail.cgs.gov.cn

SPECIALTY SECTION
This article was submitted to Structural Geology and Tectonics, a section of the journal Frontiers in Earth Science

RECEIVED 14 November 2022
ACCEPTED 22 December 2022
PUBLISHED 09 January 2023

CITATION
Zeng L, Li T, Huang H, Zeng P, He Y, Jing L, Yang Y and Jiao S (2023), Identifying Emeishan basalt by supervised learning with Landsat-5 and ASTER data. *Front. Earth Sci.* 10:1097778. doi: 10.3389/feart.2022.1097778

Identifying Emeishan basalt by supervised learning with Landsat-5 and ASTER data

Ling Zeng[1]*, Tianbin Li[2], Haitao Huang[3], Peng Zeng[2], Yuanxiao He[4], Linhai Jing[5], Yan Yang[6] and Shoutao Jiao[6]*

[1]Geomathematics Key Laboratory of Sichuan Province, College of Mathematics and Physics, Chengdu University of Technology, Chengdu, China, [2]State Key Laboratory of Geohazard Prevention and Geoenvironment Protection, Chengdu University of Technology, Chengdu, China, [3]College of Earth Sciences, Chengdu University of Technology, Chengdu, China, [4]Sichuan Geological Survey, Chengdu, China, [5]Aerospace Information Research Institute, Chinese Academy of Sciences, Beijing, China, [6]Development Research Center of China Geological Survey, Beijing, China

Multispectral-sensor images are advantageous in terms of discriminating major lithologies due to their high spatial resolution and intermediate spectral resolution, in addition to their low cost and high accessibility in comparison to hyperspectral images. In this study, Landsat-5 Thematic Mapper ™ and the Advanced Spaceborne Thermal Emission and Reflection Radiometer (ASTER) data—which are the most widely used multispectral data for the discrimination of the mixed rock units—are utilized to identify basalts in our study area. Further, prior knowledge regarding basalt-distribution areas in our study region is obtained from the geological-survey results conducted by the Sichuan Geological Survey at 2005, which is used as the reference of correction to assess our identified results. Small portions of this prior area of basalt distribution were verified through field checks, which were then determined as sites for use as training data for remote-sensing imagery. Three supervised-classification algorithms within ENVI 5.3—k-nearest neighbors (KNN), maximum likelihood classification (MLC), and support vertical machine (SVM)—were utilized for model identification. As a result, six models were constructed, including the KNN prediction of basalts by ASTER images, SVM prediction by ASTER, MLC prediction by ASTER, KNN prediction by Landsat-5 images, SVM prediction by Landsat-5, and MLC prediction by Landsat-5. The performances of the six models, in terms of precision and accuracy, show that the optimum model is Landsat-5 by SVM, with a precision of 70.92% and accuracy of 99.97%, followed by the ASTER by SVM model, with a precision of 67.72% and accuracy of 99.89% and the Landsat-5 by KNN model, with a precision of 57.23% and accuracy of 99.85%.

KEYWORDS

identifying basalt, Landsat-5, ASTER, supervised learning, machine-learning algorithms

1 Introduction

Generally, various rock types—with their own specific rock-forming minerals—have their own reflectance signatures, and can thus be discriminated based on their spectral characteristics using different spectral wavelengths of optical remote-sensing images (Kang et al., 2001; Corumluoglu et al., 2015; Hassan and Ramadan, 2015). Satellite images have been used to map the Earth for decades (Dou et al., 2015a; Dou et al., 2015b; Lillesand et al., 2015; Moghtaderi et al., 2022), and multispectral sensors are widely used for lithological discrimination in areas where rock units are exposed (Haselwimmer et al., 2010; Nair and Mathew, 2012; Arivazhagan and Anbazhagan, 2017). In comparison to hyperspectral imagery, multispectral imagery is

more advantageous in terms of classifying major lithologies (e.g., basalt, granite, and rhyolite) due to its high quality, high spatial resolution, low cost, and high accessibility (Ge et al., 2018). Nevertheless, hyperspectral imagery is more suitable for the finer classifications of rocks (e.g., tholeiitic basalt, alkali basalt, etc.).

Landsat Thematic Mapper™, the Advanced Spaceborne Thermal Emission and Reflection Radiometer (ASTER), and Sentinel-2 are the most widely used multispectral sensors for the discrimination of mixed rock units. Of the three, ASTER and Sentinel-2 are regarded to be more suitable due to their increased availability of infrared bands and better spatial resolution than the Landsat Thematic Mapper (Gomez et al., 2005; Perry and Kruse, 2010; Ehlers and Klonus, 2014). In this study, we use the geological survey of the basalt distribution by the Sichuan Geological Survey in 2005 as prior knowledge to assess the remote-sensing identifications. Further, the Sentinel-2 sensor began collecting images after 2015; therefore, we did not use Sentinel-2 imageries here considering that the vegetation coverage changed significantly in the geological-survey area from 2005 to 2015. Instead, we used ASTER and Landsat-5 TM images collected from 2003 to 2007 and in 2004. Three machine learning methods, including k-nearest neighbors (KNN), maximum likelihood classification (MLC), and support vertical machine (SVM), were compared to identify basalts based on both ASTER and Landsat-5 data. Therefore, the prediction results of six models, including the KNN prediction of basalts by ASTER images, SVM prediction by ASTER, MLC prediction by ASTER, KNN prediction by Landsat-5 images, SVM prediction by Landsat-5, and MLC prediction by Landsat-5, were compared based on the area of bare basalt in the geological-survey scope, to calculate the performance metrics (precision and accuracy). The geological-survey basalt is partly covered by vegetation that is thus hard to be identified by remote-sensing imageries, so we just used the bare-basalt distribution of the geological-survey, that is without vegetation coverage, to assess the identified results. The bare-basalt distribution is extracted through land-use classification for the geological-survey scope (bare land and vegetation).

Furthermore, the flood basalts are the signature feature of the Emeishan Large Igneous Province (LIP) in spite that there are also ultramafic and silicic volcanic rocks and layered mafic-ultramafic and silicic plutonic rocks exposed (Shellnutt, 2014). There were much substantial researches on ELIP in the past, and the reason why it is of particular interest is that it contains numerous world-class orthomagmatic Fe-Ti-V deposits and series of smaller economically important Ni-Cu-(OGE) sulphide deposits but also is contemporaneous with the Late Capitanian (~260 Ma) mass extinction (Zhou et al., 2002; Zhang et al., 2006; Ganino and Arndt 2009). Numerous researches on ELIP in the past covered a wide scope of geology, paleomagnetism, geochronology, geochemistry, biostratigraphy and so on. But remote sensing technology was seldom used in the researches on ELIP flood basalts. This paper conducted the studies of remote-sensing identification on flood basalts in the Panxi part of ELIP.

2 Materials and methods

2.1 Study area

The study area filled in red in Figure 1, including the three counties of Miyi, Huili, and Ningnan, is located in the Panzhihua-Xichang (Panxi) region, Sichuan Province, SW China, which is part of the Emeishan LIP, and lies between the latitudes of 26°02′54″N to 27°18′33″N and longitudes of 101°59′53″E to 102°54′50″E, covering an approximate area of 8,328 km^2. The Panxi region lies in the central-western part of the Emeishan LIP, where the flood basalts include high-Ti and Low-Ti lavas in addition to many other continental flood basalts (Xiao et al., 2004; Zhong et al., 2005). Magmatic Fe-Ti oxide deposits are documented in several layered intrusions in this region and, thus, account for a total ore reserve of ~7,209 Mt total Fe, ~559 Mt TiO_2, and ~17.4 Mt V_2O_5 (Vapnik, 1982).

2.2 Data

2.2.1 Geological-survey basalts

The regional geological map of basalt distribution was provided by the Sichuan Geological Survey (Figure 2). The geological map, at a scale of 1:50,0000, was created in 2005. This map served as prior knowledge for the flood basalt distribution in our study area and to determine the sampling sites and to assess our identifications by remote-sensing imageries.

2.2.2 Sampling sites

The five sampling sites of basalts (Figure 2) were initially selected based on both the prior knowledge of the location of geological-survey basalts in 2005 and the visual interpretation of optical remote-sensing imagery; this was verified through field surveys in 2022. The five sampling sites have the central locations of (27°07′59″N, 102°54′22″E), (27°07′05″N,102°54′14″E), (27°06′14″N, 102°53′20″E), (27°05′10″N, 102°53′24″E), and (27°43′59″N, 102°53′17″E). The areas of the five sampling sites on remote-sensing imageries are utilized as the training data in our modeling analyses.

2.2.3 Landsat-5 and ASTER imagery

Developed by NASA, Landsat-5 is a low Earth orbit satellite that was launched on 1 March 1984, and decommissioned on 5 June 2013, and carried multispectral scanner (MSS) and the thematic mapper (TM) instruments. The Landsat-5 MSS supplies four bands, from .5 to 1.1 μm, with a 60-m spatial resolution; the Landsat-5 TM supplies seven bands, with a 30-m spatial resolution (Markham et al., 1998; Chander and Markham, 2003). In our study, we use Landsat-5 TM imagery.

The Advanced Spaceborne Thermal Emission and Reflection Radiometer (ASTER) is a high spatial resolution instrument on the Terra satellite launched by NASA in 1999, and has been collecting data since February 2000. ASTER is a 15-m, 14-band multispectral resolution instrument, including six shortwave infrared (SWIR) bands, three visible and near-infrared (VNIR) bands, and five thermal infrared (TIR) bands (Argany et al., 2018). It can be used for land cover and change detection, calibration, validation, and land-surface studies. +

Generally, we used images around 2005, when the geological survey of basalt was conducted. Landsat-5 and ASTER were utilized as comparison data here. Three Landsat-5 images in 2004 covered our study area, and eleven ASTER images—from 2003 to 2007—covered our study area. All imagery techniques mentioned herein are described in Table 1. Both Landsat-5 and ASTER images were obtained through the U.S. Geological Survey

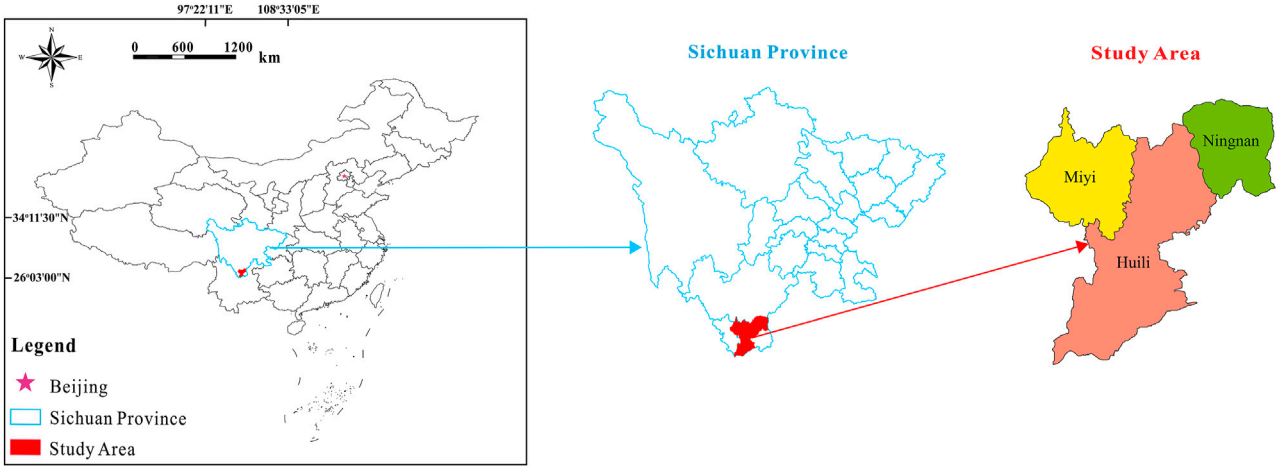

FIGURE 1
Location of the study area.

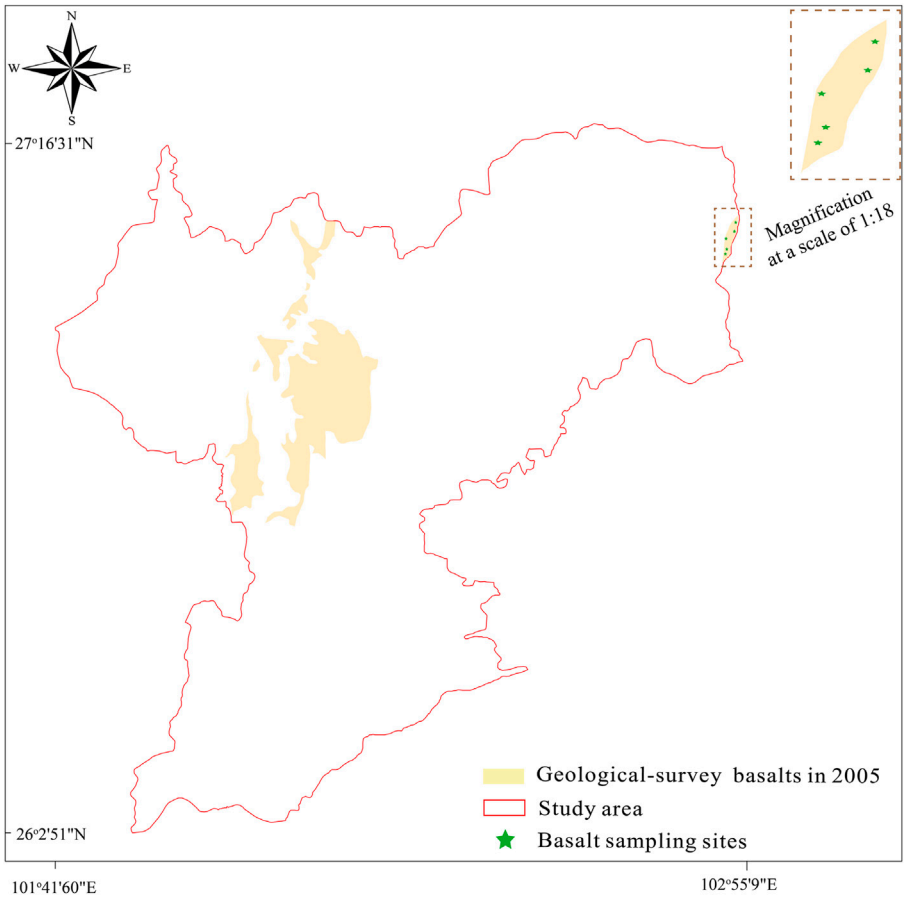

FIGURE 2
Location of geological-survey basalts in 2005 by the Sichuan Geological Survey and the sampling sites of basalts in 2022.

TABLE 1 Descriptions of Landsat-5 and ASTER images.

Data type	Data description	Acquisition time
Landsat-5 Imageries	LT51300412004045BKT02	2004.02.14 03:19:36
	LT51300422004029BJC01	2004.01.29 03:19:36
	LT51310412004004BJC00	2004.01.04 03:25:18
ASTER	AST_L1T_00302242005035655_20150508102813_112444	2005.02.24 03:56:55
	AST_L1T_00303072003035822_20150427134321_27841	2003.03.07 03:58:22
	AST_L1T_00303072003035831_20150427134317_112024	2003.03.07 03:58:31
	AST_L1T_00303072003035840_20150427134327_106647	2003.03.07 03:58:40
	AST_L1T_00311092003040420_20150501223438_108363	2003.11.09 04:04:20
	AST_L1T_00311092003040429_20150501223445_108567	2003.11.09 04:04:29
	AST_L1T_00311092003040438_20150501223445_108561	2003.11.09 04:04:38
	AST_L1T_00312152007035749_20150522093942_60394	2007.12.15 03:57:49
	AST_L1T_00312242007035142_20150522114242_120399	2007.12.24 03:51:42
	AST_L1T_00312242007035151_20150522114256_1171	2007.12.24 03:51:51
	AST_L1T_00312242007035200_20150522114310_17801	2007.12.24 03:52:00

Earth Resources Observation and Science Center (EROS) (http://earthexplorer.usgs.gov). The cloud coverage of these images ranged approximately from 2% to 8%, which is a relatively low level.

2.3 Methods

2.3.1 Land-use classification

Generally, the remote-sensing identification of lithologic units prefers bare land, and is less efficient when detecting lithology under dense vegetation. However, geological field surveys by geological experts can help observe lithology under vegetation. The geological-survey mapping of basalts in 2005 contains vegetated subareas. Here, we used Landsat-5 data in 2004 for land-use classification and, thus, extracted the bare-land type in our study area (Figure 3A). Figure 3B shows a magnification of the coverage of geological-survey basalts with land-use types.

2.3.2 Supervised-classification algorithms

2.3.2.1 KNN

The k-nearest neighbors (KNN) algorithm is a non-parametric supervised learning method (Altman, 1992). When using KNN for the binary classification of remote-sensing images in our study, the output is either a basalt class or non-basalt class. In this study, an unknown object is classified by a plurality vote of its neighbors that are metricized in the spectral–spatial distance. Here, we calculate the spectral–spatial distances of the unknown object with all training samples of two categories (basalt category and non-basalt category), and the five nearest neighbors to vote for classification: if three or more of the five nearest neighbors are related to basalt, then an unknown sample is classified as basalt, and *vice versa*.

2.3.2.2 MLC

Maximum likelihood classification (MLC) is a supervised classification method based on Bayes theorem, which makes use of a discriminant function to assign a pixel to the class with the highest likelihood (Ahmad and Quegan 2012a). The advantage of MLC as a parametric classifier is that it takes into account the variance–covariance within the class distributions and for normally distributed data (Ahmad and Quegan, 2012a; Ahmad and Quegan, 2012b).

2.3.2.3 SVM

support vertical machine (SVM), as a non-parametric supervised machine learning algorithm, is often used in binary-classification problems (Merghadi et al., 2020). SVM is one of the most robust prediction methods, based on the statistical learning frameworks proposed by Vapnik (1982), Vapnik (1995). An SVM training algorithm builds a model that assigns new examples to one category or the other, making it a non-probabilistic binary linear classifier. SVM maps training examples to points in space to maximize the width of the gap between the two categories.

2.3.3 Model evaluation metrics

To evaluate the performance of the three aforementioned supervised-classification methods, two metrics were utilized here: precision and accuracy. Precision refers to the correctness of basalt identification based on the geological-survey mapping basalts as shown in Figure 3, and accuracy is the ratio of the number of correct predictions made to all predictions.

$$\textit{Precison}\ (P) = \frac{TP}{TP + FP} \tag{1}$$

$$\textit{Accuracy}\ (A) = \frac{TP + TN}{TP + FP + FN + TN} \tag{2}$$

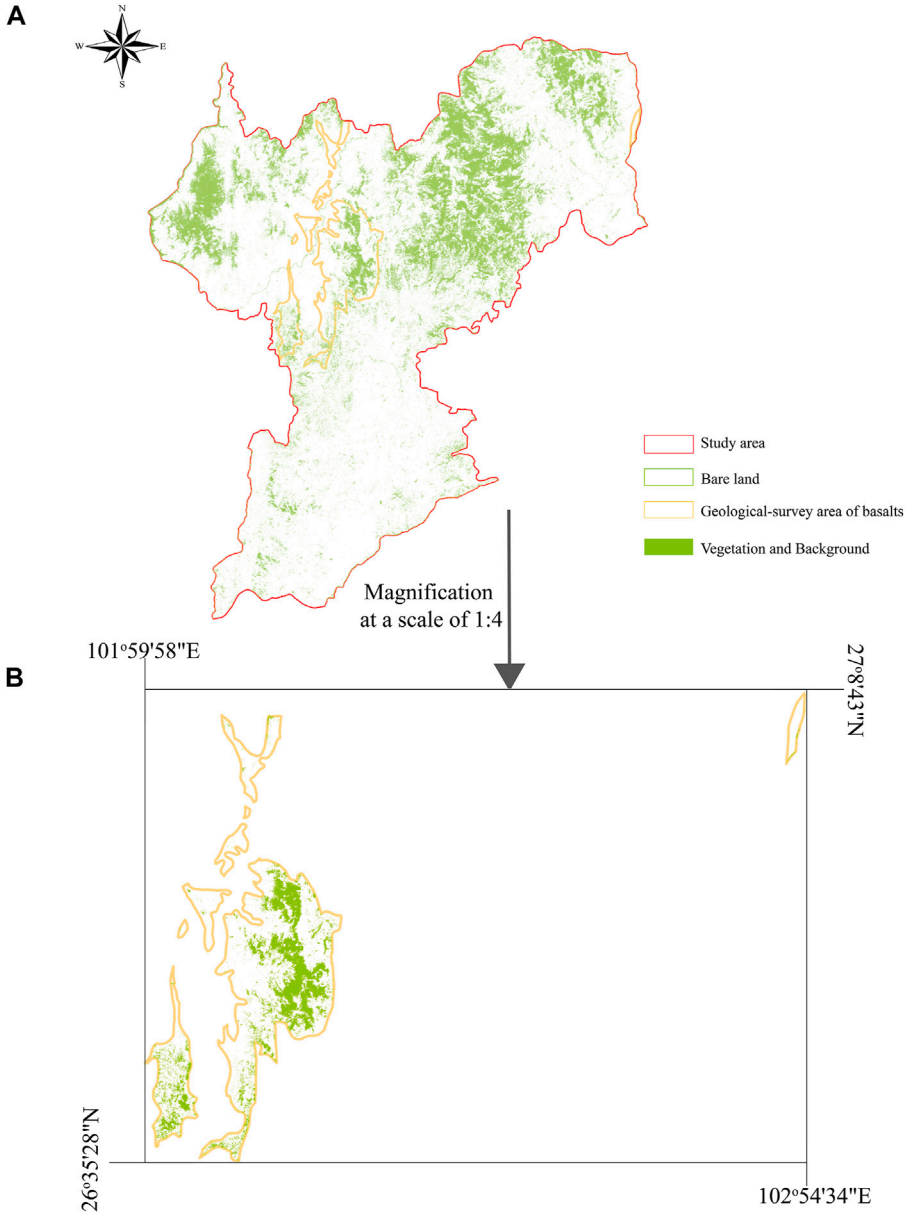

FIGURE 3
(A) Land-use type distribution in the study area. **(B)** The land-use type distribution in the area of geological-survey basalts.

where 1) FPs (false positives) mean that pixels belonging to non-basalt were misclassified as belonging to basalt, 2) FNs (false negatives) mean that pixels belonging to basalt were misclassified as belonging to non-basalt, 3) TPs (true positives) mean that pixels belonging to basalt were correctly classified as belonging to basalt, and 4) TNs (true negatives) mean that pixels belonging to non-basalt were correctly classified as belonging to non-basalt (Costa et al., 2019; Zeng et al., 2022).

3 Results

We analyzed three supervised-classification algorithms and two kinds of remote-sensing imageries, as mentioned previously, to identify basalts using the training images. These training images are part of the Landsat-5 imagery data located at the sampling sites, as described in Figure 2, when identification uses Landsat-5 images; they are also part of ASTER imagery, when identification uses ASTER images. In total, six identification methods are used: the KNN prediction of basalts by ASTER images, SVM prediction by ASTER, MLC prediction by ASTER, KNN prediction of basalts by Landsat-5 images, SVM prediction by Landsat-5, and MLC prediction by Landsat-5. All identifications are carried out using ENVI 5.3.

When using MLC, the probability threshold is set at 99%. This threshold is a probability minimum for inclusion in a class, and the ENVI does not classify pixels with a value lower than this value. As a binary-classification method, we tried changing the probability threshold of MLC from 51% to 99.9%; it was found that a threshold below 99% led to anomalous data that deviated from prior-knowledge basalt areas.

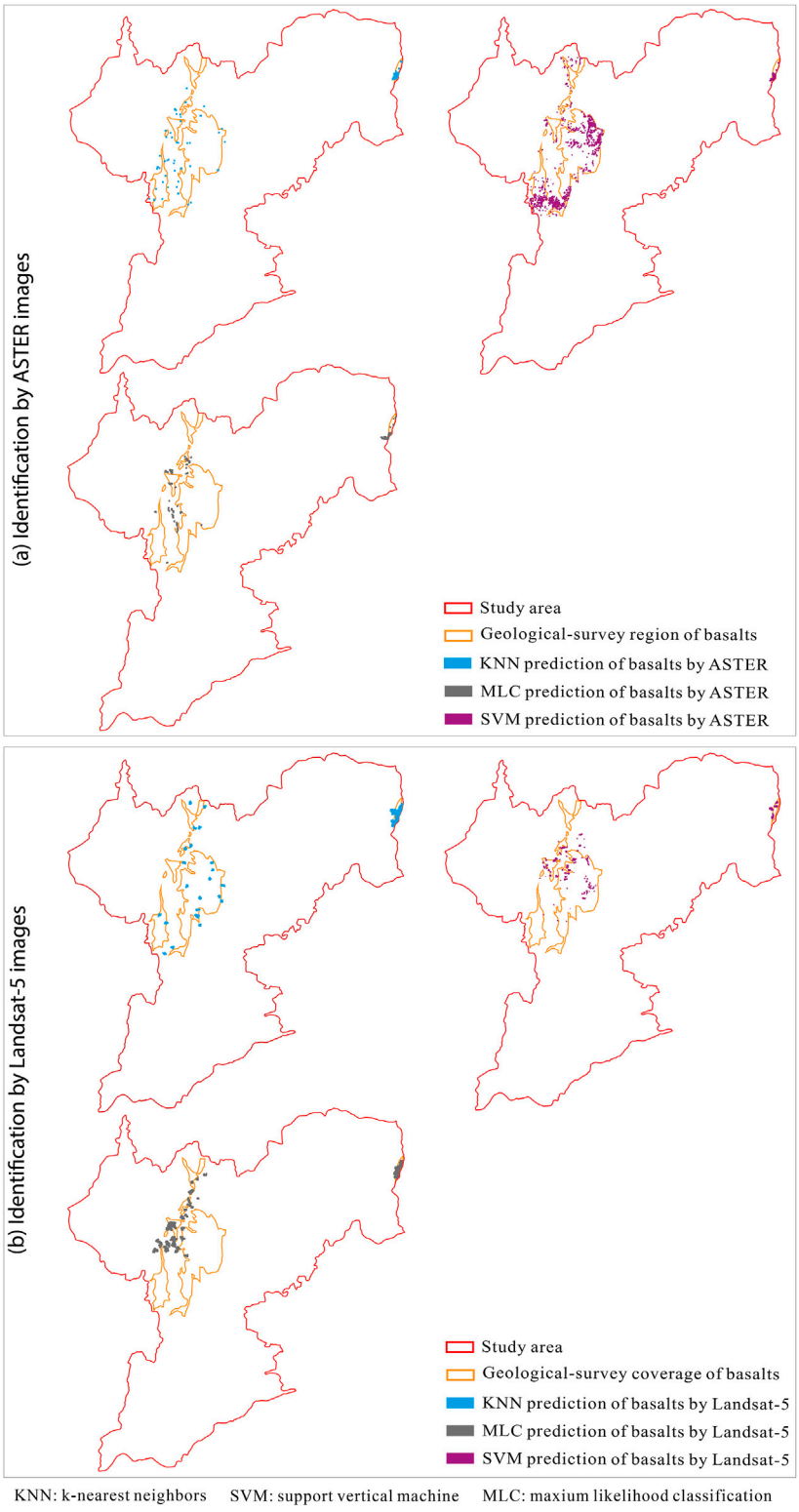

Lorem ipsum

FIGURE 4
Results of basalt identification by the three algorithms respectively on Landsat-5 and ASTER imageries.

The results of the six identification methods are shown in Figure 4. Generally, the identified locations of basalts are concentrated in the prior areas of geological-survey basalt, which indicates that the methods of identification used (including the selections of both remote-sensing images and algorithms) are reasonable. Furthermore, in past research, remote-sensing images for identifying the lithology exhibit poor performance with significant vegetation coverage (Grebby et al., 2014). Therefore, in our study, the

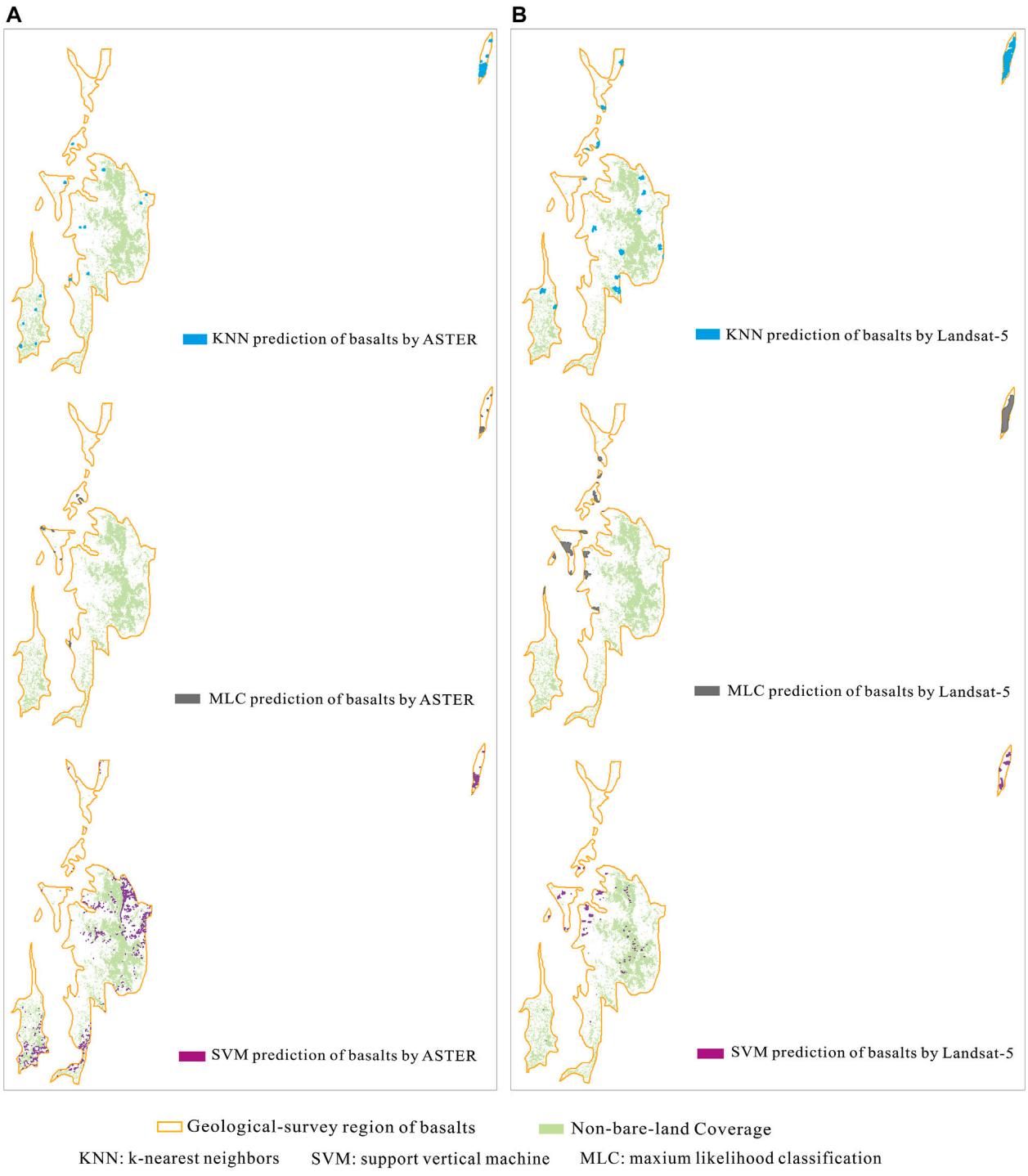

FIGURE 5
(A) Three identifications by ASTER falling into the scope of geological-survey basalts. **(B)** Three identifications by Landsat-5 falling into the scope of geological-survey basalts.

samples used for training are chosen to be bare and without vegetation coverage; here, remote-sensing images simply identify basalts that are exposed and cannot detect basalts under vegetation. We overlap bare land (Figure 3) with the identified results (Figure 4), taking the area of geological-survey basalts as prior knowledge to calculate the precision and accuracy for the six identification methods. Figure 5A shows that how the three ASTER identification results fall into the prior area of basalts, and Figure 5B shows that how the three Landsat-5 identification results fall into the prior area of basalts. Assuming that the geological-survey basalt areas are correct, the performance metrics (including precision and accuracy) of the six identification methods are shown in Table 1.

TABLE 2 Performance metrics of the six identification methods.

Identification way	Precision (%)	Accuracy (%)
Landsat-5 + KNN	57.23	99.85
Landsat-5 + MLC	39.83	99.65
Landsat-5 + SVM	70.92	99.97
ASTER + KNN	53.67	99.97
ASTER + MLC	23.03	99.91
ASTER + SVM	67.72	99.89

4 Discussion

As shown in Figure 5, most of the identified area falling into the geological-survey scope is on bare land, except a minor portion of the identified area from SVM by Landsat-5, which slightly overlaps with vegetation. It is inevitable that all methods exhibit certain errors, but the overall identification of basalts by remote-sensing images, with the training data of bare-basalt images, is still correct for bare land.

The three algorithms of KNN, MLC, and SVM are all object-oriented identifications; therefore, the identified basalts have many clusters with various sizes. Generally, the identified clusters by Landsat-5 show larger sizes than those by ASTER (Figure 4; Figure 5), possibly because Landsat-5 has a lower spatial resolution of 30 m for identification, than ASTER's 15 m, which is better for our study area with the total area of 8328 km^2.

Moreover, it seems that the SVM algorithm performs most effectively on both ASTER and Landsat-5 imageries than the other two algorithms, because the total identified area of basalts by SVM is slightly more. KNN performed very well on Landsat-5; MLC performed poorest on both ASTER and Landsat-5 imageries (Figure 5 and Table 2), compared to SVM and KNN. The SVM algorithm is essentially a two-category classifier of deep learning and is possibly more robust than the other two algorithms of simple machine learning. When the probability threshold of MLC is set lower, it produces results that deviate from prior knowledge; when it is set higher, it produces a smaller area of prediction. The error emergence of singular solutions possibly occurs when solving the covariance matrix in the MLC algorithm. KNN performs intermediately between SVM and MLC, and predicts more area based on Landsat-5 than based on ASTER, possibly only because the spatial resolution of Landsat-5 TM imagery is 30 m, in contrast to the 15-m resolution of ASTER imagery.

5 Conclusion

Although ASTER is widely used for the discrimination of mixed rock units, Landsat-5 data has advantages in certain cases, especially when the total area for identification is large. However, ASTER data would be more advantageous for more detailed identification in smaller areas. Furthermore, for machine learning algorithms for the supervised classification within ENVI, SVM may perform relatively more robustly.

Generally, in this study, we use both ASTER and Landsat-5 data for discrimination of the mixed rocks by three supervised-classification algorithms, and in the training, small-size training images are utilized. As a result, a total of six models are constructed. The modeling results by training small-size images are generally in accordance with the trends of the prior area of geological-survey basalt distributions. This verifies the capability of remote-sensing imagery for lithological discrimination and the capability of the SVM algorithm for deep learning in supervised classification. However, there are still issues in terms of how remote-sensing imagery can identify rocks with high vegetation coverage. Under the constraints of present remote-sensing technology, the only possibility may be to develop algorithms of deep learning neural networks.

Besides, this work of the remote-sensing identification of flood basalts in Panxi part of Emeishan LIP is significant, which will promote us to launch a wider-scope identification across Emeishan LIP in the future. Remote-sensing identification of flood basalts all over the Emeishan LIP will not only help map the distribution of flood basalts, but also help explore the world-class Fe-Ti-V deposits and Ni-Cu-(OGE) sulphide deposits that are both closely related to flood basalt distributions.

Data availability statement

The original contributions presented in the study are included in the article/Supplementary Material, further inquiries can be directed to the corresponding authors.

Author contributions

LZ: Conceptualization, methodology, investigation, formal analysis, writing-original draft; TL: Supervision, funding acquisition, validation, writing–review and editing; HH: Visualization, data curation; PZ: Funding acquisition, supervision; YH: Resource; LJ: Resource, writing–review and editing; YY: Visualization; SJ: Conceptualization, investigation, formal analysis, validation, project administration, writing–review and editing.

Funding

The funding for this work was supported by the National Natural Science Foundation of China (No. 42002294, No. 41972308, No. U19A20111, No. 42130719), China Geological Survey project (No. DD20221785), State Key Laboratory of Geohazard Prevention and Geoenvironment Pretection Research Project (SKLGP 2017Z001), Research Foundation for Talents of Chengdu University of Technology (10912-KYQD2021-07430), and the Second Tibetan Plateau Scientific Expedition and Research (2019QZKK0806)

Conflict of interest

The authors declare that the research was conducted in the absence of any commercial or financial relationships that could be construed as a potential conflict of interest.

Publisher's note

References

Ahmad, A., and Quegan, S. (2012a). Analysis of maximum likelihood classification on multispectral data. *Appl. Math. Sci.* 6, 6425–6436.

Ahmad, A., and Quegan, S. (2012b). "Analysis of maximum likelihood classification technique on Landsat 5 TM satellite data of tropical land covers," in 2012 IEEE International Conference on Control System, Computing and Engineering, Penang, Malaysia, 23-25 November 2012, 280–285. doi:10.1109/ICCSCE.2012.6487156

Altman, N. S. (1992). An introduction to kernel and nearest-neighbor nonparametric regression. *Am. Stat.* 46, 175–185. doi:10.1080/00031305.1992.10475879

Argany, M., Ramezani, A., and Ahmadi, A. (2018). Determination of basalt zones using basalt extraction index (BEI) and ASTER image classification. *Cogent. Geosci.* 4 (1), 1466672. doi:10.1080/23312041.2018.1466672

Arivazhagan, S., and Anbazhagan, S.Centre for Geoinformatics and Planetary Studies, Periyar University, Salem – 636 011, India (2017). ASTER data analyses for lithological discrimination of sittampundi anorthositic complex, southern India. *Geosciences Res.* 2, 196–209. doi:10.22606/gr.2017.23005

Chander, G., and Markham, B. (2003). Revised Landsat-5 TM radiometric calibration procedures and postcalibration dynamic ranges. *IEEE Trans. Geosci. Remote Sens.* 41, 2674–2677. doi:10.1109/tgrs.2003.818464

Corumluoglu, O., Vural, A., and Asri, I. (2015). Determination of Kula basalts (geosite) in Turkey using remote sensing techniques. *Arab. J. Geosci.* 8, 10105–10117. doi:10.1007/s12517-015-1914-4

Costa, M. G. F., Campos, J. P. M., de Aquino, E. A. G., de Albuquerque Pereira, W. C., and Costa Filho, C. F. F. (2019). Evaluating the performance of convolutional neural networks with direct acyclic graph architectures in automatic segmentation of breast lesion in US images. *Bmc. Med. Imaging.* 19, 85. doi:10.1186/s12880-019-0389-2

Dou, J., Chang, K. T., Chen, S., Yunus, A. P., Liu, J. K., Xia, H., et al. (2015a). Automatic case-based reasoning approach for landslide detection: Integration of object-oriented image analysis and a genetic algorithm. *Remote Sens.* 7, 4318–4342. doi:10.3390/rs70404318

Dou, J., Li, X., Yunus, A. P., Paudel, U., Chang, K. T., Zhu, Z., et al. (2015b). Automatic detection of sinkhole collapses at finer resolutions using a multi-component remote sensing approach. *Nat. Hazards* 78, 1021–1044. doi:10.1007/s11069-015-1756-0

Ehlers, M., and Klonus, S. (2014). "Scale issues in multisensory image fusion," in *Scale issues in remote sensing*. Editor Q. Weng (Hoboken, New Jersey: John Wiley & Sons), 13–33.

Ganino, C., and Arndt, N. T. (2009). Climate changes caused by degassing of sediments during the emplacement of large igneous provinces. *Geology* 37, 323–326. doi:10.1130/g25325a.1

Ge, W., Cheng, Q., Tang, Y., Jing, L., and Gao, C. (2018). Lithological classification using sentinel-2A data in the shibanjing ophiolite complex in inner Mongolia, China. *Remote. Sens.* 10, 638–722. doi:10.3390/rs10040638

Gomez, C., Delacourt, C., Allemand, P., Ledru, P., and Wackerle, R. (2005). Using ASTER remote sensing dataset for geological mapping, in Namibia. *Phys. Chem. Earth.* 30, 97–108. doi:10.1016/j.pce.2004.08.042

Grebby, S., Cunninghan, D., Tansey, K., and Naden, J. (2014). The impact of vegetation on lithological mapping using airborne multispectral data: A case study for the north troodos region, Cyprus. *Remote. Sens.* 6, 10860–10887. doi:10.3390/rs61110860

Haselwimmer, C. E., Riley, T. R., and Liu, J. G. (2010). Assessing the potential of multispectral remote sensing for lithological mapping on the Antarctic Peninsula: Case study from eastern Adelaide Island, Graham Land. *Antarct. Sci.* 22, 299–318. doi:10.1017/s0954102010000015

Hassan, S. M., and Ramadan, T. M. (2015). Mapping of the late Neoproterozoic Basement rocks and detection of the gold-bearing alteration zones at Abu Marawat-Semna area, Eastern Desert, Egypt using remote sensing data. *Arab. J. Geosci.* 8, 4641–4656. doi:10.1007/s12517-014-1562-0

Kang, K. K., Song, K. Y., Ahn, C. H., and Won, J. S. (2001). Reflectance of geological media by using a field spectrometer in the Ungsang area, Kyungsang Basin. *Korean. J. remote. Sens.* 17, 165–181.

Lillesand, T. M., Kieffer, R. W., and Chipman, J. W. (2015). *Remote sensing and image interpretation*. Hoboken: John Wiley & Sons.

Markham, B. L., Seiferth, J. C., Smid, J., and Barker, J. L. (1998). <title>Lifetime responsivity behavior of the Landsat-5 thematic mapper</title>. *Proc. SPIE* 3427, 420–431. doi:10.1117/12.328513

Merghadi, A., Yunus, A. P., Dou, J., Whiteley, J., ThaiPham, B., Bui, D. T., et al. (2020). Machine learning methods for landslide susceptibility studies: A comparative overview of algorithm performance. *Earth-Science Rev.* 207, 103225. doi:10.1016/j.earscirev.2020.103225

Moghtaderi, A., Moore, F., and Ranjbar, H. (2022). Testing ASTER and sentinel-2 MSI images to discriminate igneous and metamorphic rock units in the chadormalu paleocrater, central Iran. *Can. J. Remote. Sens.* 48, 214–238. doi:10.1080/07038992.2021.1997347

Nair, A., and Mathew, G. (2012). Lithological discrimination of the phenaimata felsic-mafic complex. Gujarat, India, using the advanced Spaceborne thermal emission and reflection radiometer (ASTER). *Int. J. Remote. Sens.* 33, 198–219. doi:10.1080/01431161.2011.591441

Perry, S., and Kruse, F. (2010). "ASTER data use in mining applications," in *Land remote sensing and global environmental change. Remote sensing and digital image processing*. Editors B. Ramachandran, C. Justice, and M. Abrams (New York: Springer), 301–324.

Shellnutt, J. G. (2014). The Emeishan large igneous province: A synthesis. *Geosci. Front.* 5, 369–394.

Vapnik, V. (1982). *Estimation of dependences based on empirical data*. Berlin: Springer.

Vapnik, V. (1995). *The nature of statistical learning theory*. New York: Springer.

Xiao, L., Xu, Y. G., Mei, H. J., Zheng, Y. F., He, B., and Pirajno, F. (2004). Distinct mantle sources of low-Ti and high-Ti basalts from the Western emeishan large igneous province, SW China: Implications for plume-lithosphere interaction. *Earth. Planet. Sc. Lett.* 228, 525–546. doi:10.1016/j.epsl.2004.10.002

Zeng, L., Li, T. B., Wang, X. K., Chen, L., Zeng, P., and Herrin, J. S. (2022). UNetGE: A U-Net-based software at automatic grain extraction for image analysis of the grain size and shape characteristics. *Sensors* 22, 5565. doi:10.3390/s22155565

Zhang, Z., Mahoney, J. J., Mao, J., and Wang, F. (2006). Geochemistry of picritic and associated basalt flows of the Western Emeishan flood basalt province, China. *J. Pet.* 47, 1997–2019. doi:10.1093/petrology/egl034

Zhong, H., Hu, R. Z., Wilson, A. H., and Zhu, W. G. (2005). Review of the link between the hongge layered intrusion and emeishan flood basalts, southwest China. *Int. Geol. Rev.* 47, 971–985. doi:10.2747/0020-6814.47.9.971

Zhou, M.-F., Malpas, J., Song, X.-Y., Robinson, P. T., Sun, M., Kennedy, A. K., et al. (2002). A temporal link between the Emeishan large igneous province (SW China) and the end-Guadalupian mass extinction. *Earth. Planet. Sc. Lett.* 196, 113–122. doi:10.1016/s0012-821x(01)00608-2

frontiers | Frontiers in Earth Science

TYPE Original Research
PUBLISHED 12 January 2023
DOI 10.3389/feart.2022.1037727

OPEN ACCESS

EDITED BY
Stanislaw Mazur,
Institute of Geological Sciences, Polish Academy of Sciences, Poland

REVIEWED BY
Wang Fangyue,
Hefei University of Technology, China
Yi-Xiang Chen,
University of Science and Technology of China, China
Yongsheng He,
China University of Geosciences, China

*CORRESPONDENCE
Huawen Cao,
caohuawen1988@126.com

SPECIALTY SECTION
This article was submitted to Structural Geology and Tectonics, a section of the journal Frontiers in Earth Science

RECEIVED 06 September 2022
ACCEPTED 01 November 2022
PUBLISHED 12 January 2023

CITATION
Pei Q, Ma S, Li C, Liu F, Zhang Y, Xiao Y, Wang S, Wu J and Cao H (2023), *In-situ* boron isotope and chemical composition of tourmaline in the Gyirong pegmatite, southern Tibet: Implications for petrogenesis and magma source.
Front. Earth Sci. 10:1037727.
doi: 10.3389/feart.2022.1037727

In-situ boron isotope and chemical composition of tourmaline in the Gyirong pegmatite, southern Tibet: Implications for petrogenesis and magma source

Qiuming Pei[1], Shaobing Ma[1], Chenghong Li[1], Fei Liu[2], Yunhui Zhang[1], Yong Xiao[1], Shiming Wang[1], Jianfei Wu[3] and Huawen Cao[4]*

[1]Faculty of Geosciences and Environmental Engineering, Southwest Jiaotong University, Chengdu, China, [2]Institute of Mountain Hazards and Environment, Chinese Academy of Sciences, Chengdu, China, [3]Information Center, Ministry of Natural Resources of China, Beijing, China, [4]Chengdu Center, China Geological Survey, Chengdu, China

Leucogranitic rocks, mainly including leucogranite-pegmatite systems, have been found to be widely distributed in the South Tibetan Himalaya, and they have received considerable interest because of their significance in crustal evolution and associated rare-metal mineralization. Although the nature and geodynamic setting of the Himalayan leucogranites have been well documented by numerous studies, the pegmatites spatially associated with these leucogranites are still poorly understood. Tourmaline is a ubiquitous phase from the leucogranite to the pegmatite. We have therefore conducted *in situ* major and trace element and boron isotope investigations of tourmaline from the Gyirong pegmatite, synthesizing published data on the Gyirong leucogranite, to document the origin of tourmaline and its genetic implications. Two types of tourmaline (Tur-I & Tur-II) have been identified in this contribution and they are enriched in Fe, Si and Al but depleted in Mg and Ca, with Mg/(Mg+Fe) ratios ranging from 0.22 to 0.45. Accordingly, the tourmalines belong to the alkali group and have schorl composition. Trace elements, such as Zn, Ga, V, Sc, Li, Sn, Sr, and Co in the tourmalines are relatively enriched, whereas, other trace elements record low concentrations less than 10 ppm. The trace element concentrations of tourmaline are mainly controlled by melt composition. Morphological and geochemical characteristics reflect that the tourmalines from the Gyirong pegmatite are magmatic in origin. The Gyirong pegmatitic tourmalines have S-type granitoids and pegmatites boron isotopic signatures with a tight range of $\delta^{11}B$ values between –11.8 and –9.7‰, which is consistent with the magmatic tourmalines (Mg-poor) of the Gyirong leucogranite. This study suggests that the Gyirong pegmatite was the product of crustal anatexis and that the crustal metapelitic rocks within the Greater Himalayan Crystalline Complex were the most likely source components.

KEYWORDS
tourmaline, boron isotope, leucogranite, pegmatite, Tibet

1 Introduction

The India-Asia collision since the Early Cenozoic formed the largest Himalayan-Tibetan orogenic system on Earth (Yin and Harrison, 2000; Najman et al., 2010; Hu et al., 2016; Xu et al., 2017). Meanwhile, the ongoing continental collision-convergence processes triggered large-scale anatexis of the crust during the Late Eocene to Miocene and eventually generated the world's most famous voluminous leucogranite belt (Le Fort et al., 1987; Hou et al., 2012; Wu et al., 2015; Fan et al., 2021). As a probe, the Himalayan leucogranites carry ample information, such as their origin, age, emplacement mechanisms and related economic mineralization, which is critical for understanding the tectonic-magmatic-metamorphic evolution of the Himalayan orogeny (Searle et al., 2010; Liu et al., 2019; Wang et al., 2020; Wu et al., 2020; Tang et al., 2021; Xu et al., 2021; Cao H. et al., 2022). These leucogranitic rocks mainly include leucogranite-pegmatite systems, which are widely distributed in the South Tibetan Himalaya (Zhou et al., 2019). Considerable attention has been paid to the nature and geodynamic setting of the Himalayan leucogranites (Cao et al., 2022a and reference therein), while the pegmatites spatially associated with these leucogranites are still poorly understood.

Tourmaline, as a ubiquitous cyclosilicate mineral in rocks of the Earth's crust, forms in a wide range of geological settings and is particularly prevalent in evolved granitic rocks (Trumbull et al., 2008; van Hinsberg et al., 2011; Wadoski et al., 2011; Čopjaková et al., 2021). The chemical compositions of tourmaline have negligible diffusion rates with wide temperature (150 °C–900 °C) and pressure (6 MPa to >6 GPa) stability ranges, making it an ideal petrogenetic indicator (Henry et al., 2011; Wei and Zhao, 2020). Importantly, tourmaline is the dominant boron-bearing mineral, and its boron isotopes show significant variations. Therefore, tourmaline boron isotope geochemistry has been widely applied to trace boron sources and magmatic-hydrothermal processes (Marschall and Jiang, 2011; Grew et al., 2016; Guo et al., 2021; Guo et al., 2022). In addition, tourmaline occurs widely in Himalayan leucogranites and associated pegmatites, and often has well-defined crystal faces with complex zonal structures (Yang et al., 2015; Zhou et al., 2019; Liu et al., 2022; Zhang et al., 2022). Such convoluted chemical zoning retains the history of physicochemical conditions of the melt or fluid from which it crystallized and provides major insights into petrologic processes (Hawthorne and Dirlam, 2011; Bosi, 2018; Liu and Jiang, 2021).

The Gyirong aera, located in the central Himalayan orogenic belt, contains the vital record of sedimentary sequence, drainage development and magmatic-tectonic events of the Himalaya (Shen et al., 2016; Dong et al., 2017). Previous studies mainly focused on climatic and tectonic uplift evolution (Hong et al., 2010; Shen et al., 2016; Wolff et al., 2022), paleoenvironmental analysis (Xu et al., 2012), gneiss dome and associated granitoids (Gao and Zeng, 2014; Dong et al., 2017; Gao et al., 2017; Wang et al., 2017) and potential rare metal mineralization (Wu et al., 2020). The geochemical variations in accessory minerals such as zircon, monazite, tourmaline and garnet from the leucogranites are also involved in the above investigations (Gao et al., 2017; Hu et al., 2022), whereas there is a lack of studies on tourmaline from the pegmatites therein. In this contribution, we present *in situ* major and trace elements and boron isotopes of tourmalines from the Gyirong pegmatite of southern Tibet. Our results, combined with the geochemical data of the tourmalines from other regions along the Himalayan leucogranite belt, allow us to document the geochemical behavior of tourmaline precipitation and its origin, and also contribute additional constraints on the genetic mechanisms of the Himalayan leucogranites as well as the architecture and evolution of the Himalayan orogen.

2 Geological setting and samples

The roughly east-west-trending Himalayan orogen (extending ~2500 km long), bounded by the Indus-Yarlung Tsangpo suture to the north and the Main Front Thrust (MFT) to the south, is a classic example of collisional belts worldwide (Figure 1A) (Hodges, 2000; Zhao Z-b et al., 2021; Yu et al., 2021; Pan et al., 2022). It has experienced a prolonged and complicated history that included several periods of oceanic spreading, subduction and continental collision and eventually formed *via* the amalgamation of multiple terranes (Pan et al., 2012; Metcalfe, 2021; Xu et al., 2022). Tectonically, from north to south, four major lithotectonic units have been defined within this orogen: the Tethyan Himalayan Sequence (THS), the Greater Himalayan Crystalline Complex (GHC), the Lesser Himalayan Sequence (LHS) and the sub-Himalayan Sequence (SHS, or defined as the Siwalik Sequence), which are separated sequentially by the South Tibet Detachment System (STDS), the Main Central Thrust (MCT) and the Main Boundary Thrust (MBT) (Figure 1B) (Yin, 2006; Goscombe et al., 2018; Cao et al., 2020). The THS located in the northernmost part of the orogenic belt mainly exposed Early Paleozoic-Eocene clastic and carbonate rocks that experienced low-grade greenschist- and low amphibolite-facies metamorphism (Cao et al., 2018). A series of discontinuously distributed gneiss domes (e.g., the Malashan dome, Kawakami et al., 2007), belonging to the North Himalayan gneiss domes (NHGD) (Alsdorf et al., 1998; Fu et al., 2017; Ma et al., 2022), are recognized within the THS. The GHC consists of Proterozoic-Early Paleozoic high-grade metasediments, orthogneiss and magmatic rocks (Grujic et al., 2002; Gou et al., 2016; Gou et al., 2022; Ji et al., 2022),

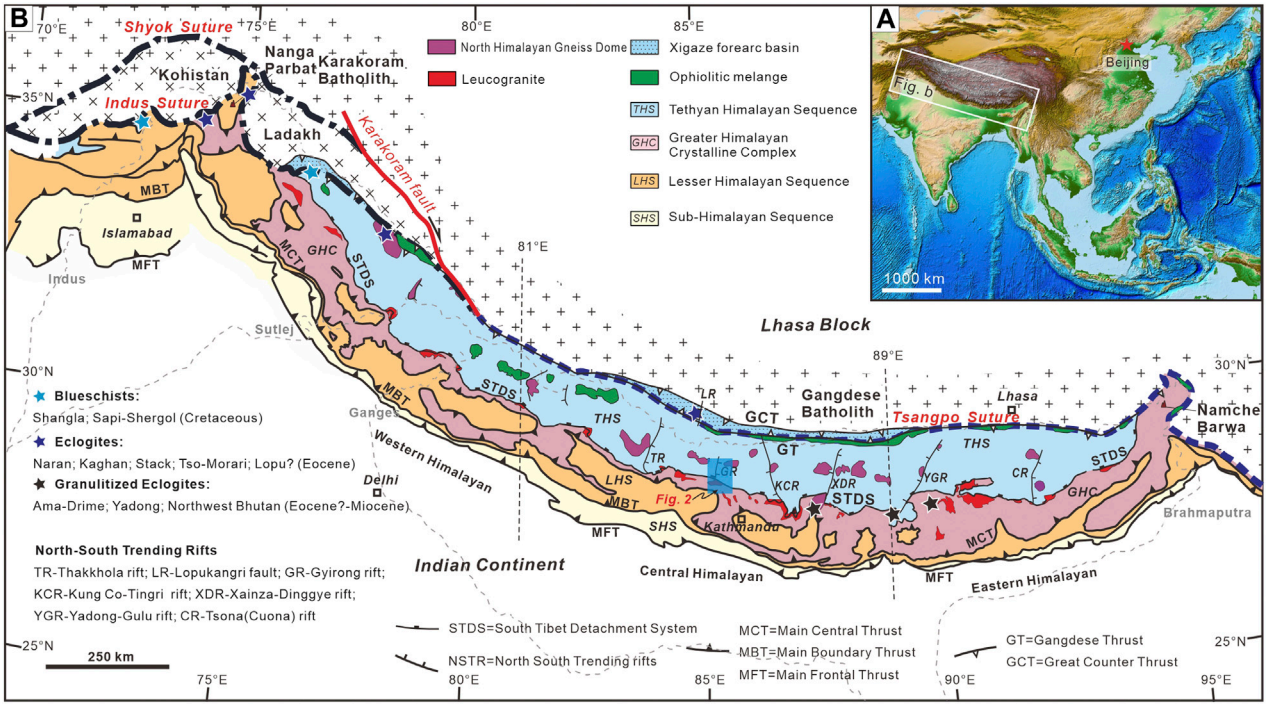

FIGURE 1
(A) Geographical location of the Himalaya. **(B)** Simplified geological map of the Himalayan Orogen (modified after Cao et al., 2021).

representing the core of the Himalayan orogenic belt. Further evidence suggests that it exhumed from the middle-lower crust to near the surface in the Cenozoic (Webb et al., 2017). The LHS principally comprises Paleoproterozoic to Early Paleozoic greenschist-to amphibolite-facies metasedimentary rocks, augen gneisses and metavolcanic rocks (Imayama et al., 2010; Martin, 2017). Two subparallel Cenozoic leucogranite belts with nearly east-west direction are discontinuously exposed along Himalayan orogen (Figure 1B): the northern belt occurs in the THS and NHGD, and the southern belt is distributed at the top of the GHC or involved in the shear zone beneath the STDS (Searle, 1999). Petrographically, the Himalayan leucogranites are generally equivalent to monzonite granites and dominated by two-mica (muscovite and biotite), biotite-, tourmaline- and garnet-bearing leucogranites (Wu et al., 2020). Their mineralogical composition includes quartz, euhedral plagioclase, perthitic potassic feldspar, muscovite, tourmaline, biotite and garnet (Guillot and Le Fort, 1995).

Our study area, which is located near the Gyirong County of southern Tibet, encompasses the Malashan-Paiku Co dome, the THS, the STDS, and the GHC from north to south (Figure 2). In addition, several Late Cenozoic fault basins, such as Gyirong and Oma, are also distributed in this area, which may be controlled by the north-south extension related to the STDS (Yang et al., 2009). The Malashan-Paiku Co dome acts as a segment of the NHGD and consists essentially of two-mica granite and Paiku composite leucogranite in the core and metamorphic rocks such as gneiss, schist and phyllite toward the margin (Wang et al., 2016; Gao et al., 2017), accompanied by multistage ductile deformation (Aoya et al., 2005). To the south, there is a set of Ordovician-Jurassic sedimentary rocks containing a small amount of Early Paleozoic and Mesozoic volcanic rocks. The cross-section of Gyirong area shows that folds and normal faults are developed in this set of strata. The STDS in the Gyirong area is a large ductile shear zone with a width of more than 10 km. It is mainly composed of Paleozoic granitic gneiss and Cenozoic foliated two-mica granites with syn-deformational features (Yang et al., 2009) and was emplaced by late undeformed leucogranites (~17.7 Ma, Gao et al., 2016). The GHC in the study area exposes medium-grade metamorphic rocks mainly consisting of augen gneiss, amphibole-biotite gneiss, metapelite, meta-sandstone, plagioclase-amphibole gneiss and schist. Leucogranites occurring as sills, dikes, dykes, dendritic and lenticular shapes intruded into the metamorphic rocks within the GHC. These leucogranitic veins were emplaced at 22–16 Ma (Wang et al., 2013; Gao et al., 2016), which record a long duration of anatexis and a tectonic transformation.

Two tourmaline-bearing samples (JL-4 and JL-5) were collected from the granitic pegmatites within the GHC (Figures 3A,B,D. Sample JL-4 is garnet tourmaline granitic

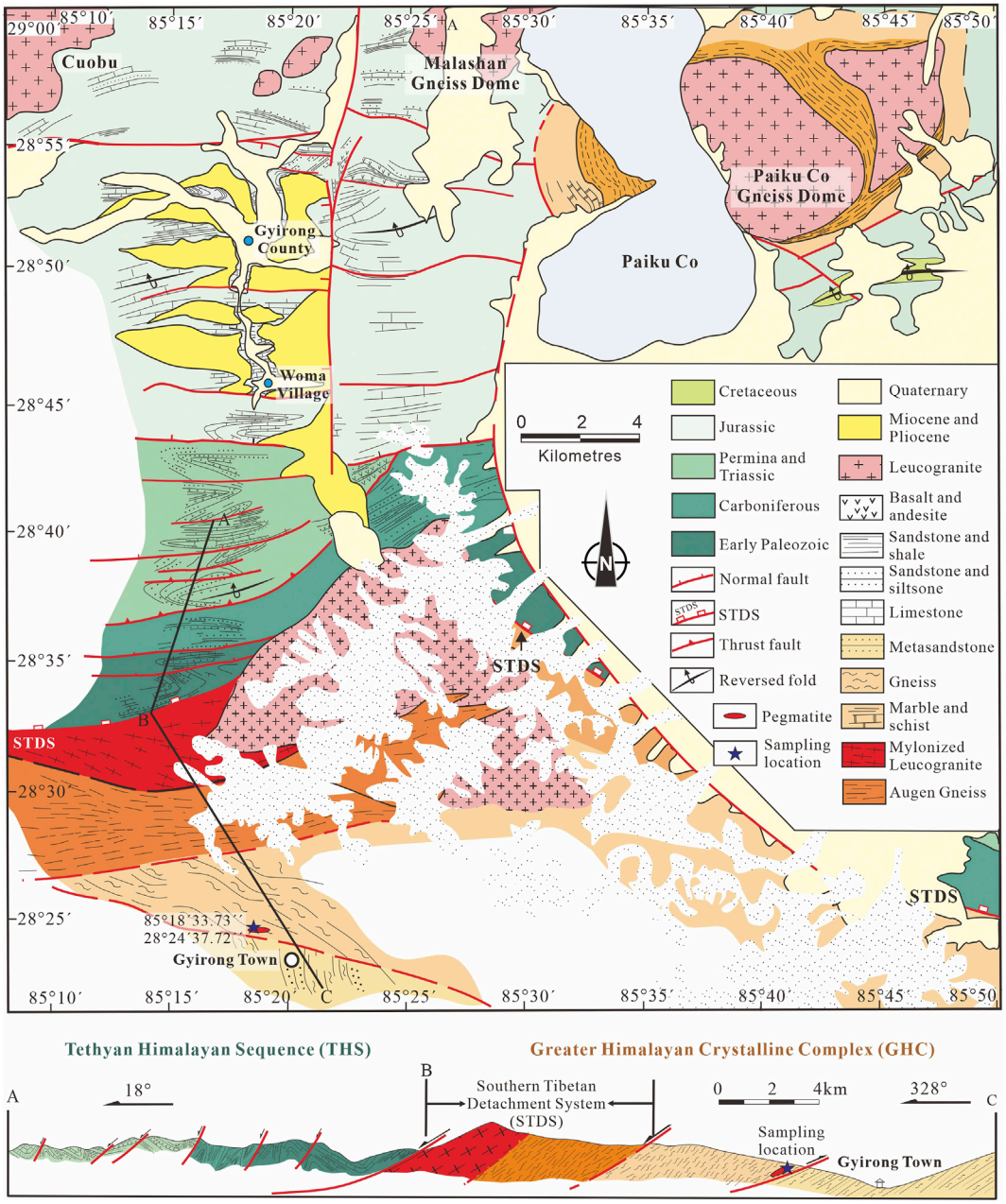

FIGURE 2
Geological map of the Malashan-Gyirong area (modified after Wang et al., 2017).

pegmatite. Plagioclase, potassium feldspar, tourmaline, garnet, muscovite and biotite dominate sample JL-4 (Figure 3C). Some tourmaline occurs as rounded inclusions within garnet (Figure 3C). In contrast, sample JL-5 displays similar mineral assemblages (Figures 3D–F) but much less garnet, thus it can be defined as tourmaline granitic pegmatite. Tourmaline in two samples shows diverse colors (e.g., green, brownish, yellow, pale blue) and usually has a dark- or light-colored core surrounded by a zoned rim. These tourmaline grains commonly occur as large crystals and are predominantly prismatic or granular in shape with sizes mainly ranging from 0.1 to 4 cm (Figures 3C,E–H). In this study, we select large tourmaline grains with complex zoning (Tur-Ⅰ type) within sample JL-4 and granular tourmaline (Tur-Ⅱ type) in sample JL-5 for further chemical and B isotope investigation.

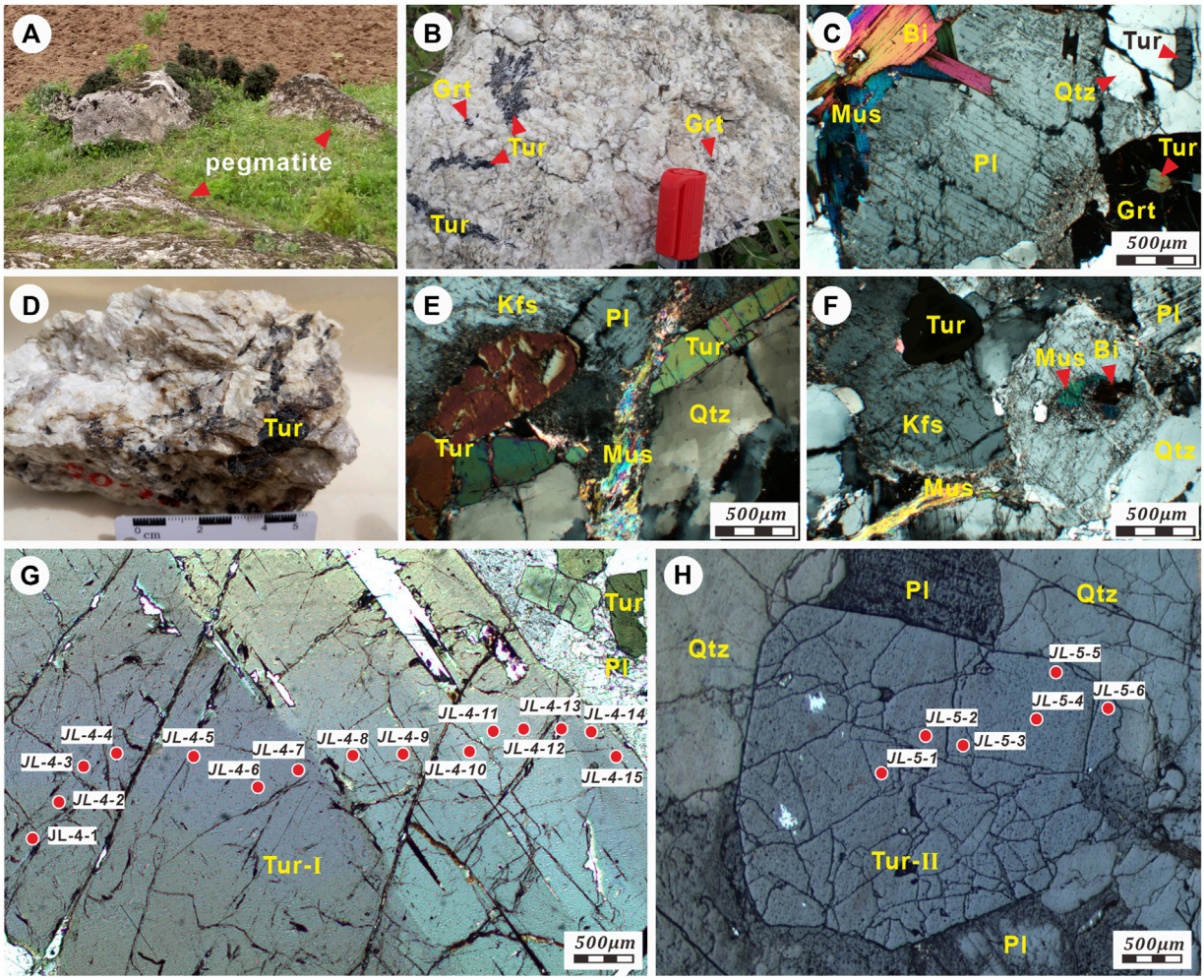

FIGURE 3
Representative photographs of tourmalines in the Gyirong pegmatite. **(A)** Outcrops of the Gyirong pegmatite. **(B)** Hand specimen of garnet tourmaline granitic pegmatite. **(C)** Granular tourmalines as rounded inclusions within garnet and quartz. **(D)** Hand specimen of tourmaline granitic pegmatite. **(E)** Large columnar tourmalines showing diverse colors. **(F)** Tourmaline grains, K-feldspar, plagioclase, quartz, muscovite and biotite in pegmatite. **(G)** Large tourmaline with complex zoning (Tur-I type). **(H)** Granular tourmaline (Tur-II type). The red circles are the points of *in situ*major and trace elements and boron isotope analyses. Abbreviations: Bi, Biotite; Grt, Garnet; Kfs, K-feldspar; Mus, Muscovite; Pl, Plagioclase; Qtz, Quartz; Tur, Tourmaline.

3 Analytical techniques

Major element compositions of tourmaline were obtained from polished thin sections using an EMPA-1600 electron microprobe with wavelength dispersive spectrometry at the Chengdu Center of the Geological Survey of China. The operating conditions were at 15 kV acceleration potential, 20 nA beam current and a 20 μm defocused spot with counting times between 10 and 30 s.

The trace element concentrations of tourmaline in polished thin sections were determined using an Agilent 7700E inductively coupled plasma mass spectrometer (ICP-MS) equipped to a GeolasPro laser ablation (LA) system at Wuhan Sample Solution Analytical Technology Co., Ltd., Wuhan, China. In this experiment, the ablating diameter for the LA-ICP-MS trace element analysis was set at 35 μm on the equivalent locations where the EPMA had been conducted. The detailed testing procedures and conditions were similar to those described by Zheng and Chen (2021). Data processing was performed offline using ICPMSDataCal software (Liu et al., 2008).

In situ boron isotopic compositions of tourmaline were measured in polished thin sections by the RESOlution S-155 laser ablation system coupled to a Nu plasma II multi-collector ICP-MS (LA-MC-ICP-MS). Analyses were carried out with laser spot size of 50 μm, 10 Hz repetition rate, and energy of ~5 J/cm^2. Two Faraday cups were used to collect $^{11}B/^{10}B$ signals of

TABLE 1 Summary of EPMA results and calculated atoms per formula (apfu) for tourmalines from the Gyirong pegmatites.

Sample	Tur-I-cores			Tur-I-rims			Tur-II		
	Min	Max	Mean	Min	Max	Mean	Min	Max	Mean
SiO_2	33.09	34.15	33.63	33.37	34.65	34.04	33.45	34.30	33.98
TiO_2	0.42	0.89	0.62	0.68	0.95	0.84	0.71	0.92	0.79
Al_2O_3	31.46	32.39	31.80	32.15	33.80	32.96	32.56	33.18	32.90
FeO	14.12	14.68	14.36	9.08	11.56	10.13	9.14	11.43	9.86
MnO	0.05	0.22	0.12	0.01	0.17	0.08	0.00	0.08	0.05
MgO	2.01	4.19	2.24	4.15	4.95	4.55	4.15	5.19	4.81
CaO	0.60	0.93	0.68	0.75	0.93	0.83	0.77	0.95	0.85
Na_2O	1.87	2.03	1.94	1.76	2.00	1.92	1.84	2.08	2.00
K_2O	0.07	0.11	0.09	0.07	0.10	0.08	0.06	0.10	0.07
B_2O_3	10.04	10.23	10.09	10.23	10.44	10.30	10.24	10.37	10.30
H_2O	3.28	3.36	3.30	3.32	3.40	3.37	3.33	3.42	3.37
O=F	0.00	0.00	0.00	0.00	0.03	0.00	0.00	0.06	0.02
Total(wt.%)	98.55	99.56	98.97	98.58	99.93	99.20	98.78	99.53	99.11
Structural formula on the basis of 15 Cations (T+Z+Y)									
B (apfu)	3.00	3.00	3.00	3.00	3.00	3.00	3.00	3.00	3.00
T site: Si	5.73	5.86	5.79	5.65	5.79	5.74	5.68	5.79	5.73
T site: Al	0.14	0.27	0.21	0.21	0.35	0.26	0.21	0.32	0.27
Z site: Al	6.00	6.00	6.00	6.00	6.00	6.00	6.00	6.00	6.00
Y site: Al	0.19	0.29	0.24	0.17	0.40	0.30	0.19	0.33	0.28
Y site: Fe^{2+}	2.03	2.12	2.07	1.26	1.64	1.43	1.29	1.62	1.39
Y site: Mg	0.52	1.06	0.58	1.05	1.23	1.14	1.05	1.31	1.21
X site: Ca	0.11	0.17	0.12	0.14	0.17	0.15	0.14	0.17	0.15
X site: Na	0.62	0.68	0.65	0.58	0.65	0.63	0.60	0.68	0.66
X site: K	0.02	0.03	0.02	0.01	0.02	0.02	0.01	0.02	0.02
X vacancy	0.18	0.24	0.21	0.18	0.25	0.20	0.14	0.22	0.17
V+W sites: OH	3.76	3.82	3.79	3.74	3.82	3.79	3.73	3.86	3.80
Mg/(Mg+Fe)	0.20	0.41	0.22	0.39	0.49	0.45	0.39	0.50	0.47

tourmaline samples and various standards. The standard-sample-standard bracketing (SSB) method was adopted to calibrate the instrumental mass fractionation (IMF). The international tourmaline standard IAEA B4 from Tonarini et al. (2003) served as an external standard, whereas tourmaline reference material IMR RB1 was adopted as the monitoring standard. Replicate analyses of standard tourmaline IMR RB1 yielded an average $\delta^{11}B$ of -13.3‰ (Supplementary Table S1), which is consistent with the reference value of −12.97‰ ± 0.97 (2σ; n = 57) obtained by LA-MC-ICP-MS (Hou et al., 2010). The external precision is estimated to be better than 0.5‰ (±2σ) based on the replicated analyses of reference tourmalines during the process of this study. The internal precision (1 SD) in per mil for individual analysis was calculated from approximately 100 cycles during each analysis (Zhao K-D. et al., 2021). Detailed analytical procedure broadly followed that presented in Yang and Jiang (2012).

4 Results

4.1 Tourmaline chemical compositions and classification

4.1.1 Major element crystal chemistry

Tourmaline has a fairly complicated crystal structure framework and varied constituents with empirical crystallochemical formula of XY_3Z_6 $[T_6O_{18}][BO_3]_3V_3W$ followed by (Hawthorne and Henry, 1999), where X = Na^+, Ca^{2+}, $X_{[vacancy]}$, K^+, Pb^{2+}; Y = Mg^{2+}, Fe^{2+}, Al^{3+}, Li^+, Ti^{4+}, Mn^{2+}, Fe^{3+}, Zn^{2+}; Z = Al^{3+}, Cr^{3+}, Fe^{3+}, Mg^{2+}, Fe^{2+}; T = Si^{4+}, B^{3+}, Al^{3+}; V = OH^-, O^{2-} ; and W = OH^- , F^- and O^{2-}. Tourmaline formulas were calculated by normalizing to 15 cations apfu (atoms per formula unit) in the tetrahedral and octahedral sites (T+Y+Z) and assuming B=3 pfu following the procedure of (Henry and Dutrow, 1996). The calculation was undertaken with the WinTcac program of Yavuz et al. (2014) based on the EPMA

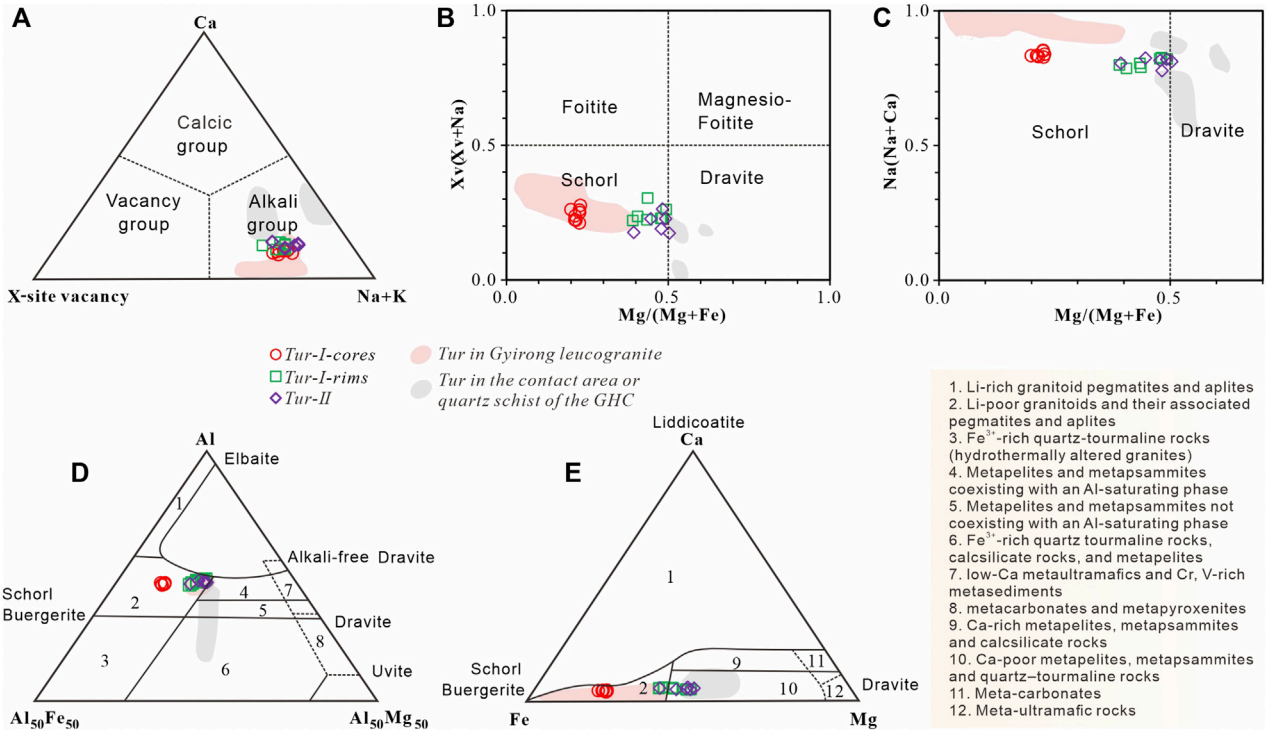

FIGURE 4
Ternary and binary diagrams for tourmaline in the Gyirong pegmatite. **(A)** Principal groups of tourmalines based on X-site occupancy (Henry et al., 2011). Plots of Mg/(Mg + Fe) vs. Xv/(Xv + Na) **(B)** and Mg/(Mg + Fe) vs. Na/(Na+Ca) **(C)** of tourmalines (Henry et al., 2011). **(D)** Ternary Al-Fe-Mg **(D)** and Ca-Fe-Mg **(E)** diagrams for tourmalines (Henry and Guidotti, 1985). Data sources: Hu et al.,(2018); Hu et al. (2022) and references therein.

data (Table 1). A complete list of the major element analyses can be found in Supplementary Table S2.

Tourmalines from the Gyirong pegmatite show large variable contents of FeO (9.08–4.68 wt.%) and MgO (2.01–0.19 wt.%) but restricted ranges of SiO_2 (33.09–34.65 wt.%), TiO_2 (0.42–0.95 wt.%), Al_2O_3 (31.46–3.80 wt.%), CaO (0.60–0.95 wt.%), Na_2O (1.76–0.08 wt.%) and K_2O (0.06–0.11 wt.%), with low K_2O (0.06–0.11 wt.%), MnO (0–0.22 wt.%) and F (0–0.06 wt.%). According to the X site classification of (Henry et al., 2011), all the tourmalines from the Gyirong pegmatite belong to the alkali group (Figure 4A). From the cores to the rims of Tur-I, a trend of lower FeO (14.68–0.13 wt.%) and higher MgO (2.24–0.55 wt.%) were found during crystal growth, whereas the concentrations of other major elements did not show clear differences. For tourmaline of Tur-II, its chemical composition is consistent with that of tourmaline rims of Tur-I. Thus, tourmalines from the Gyirong pegmatite are distributed in two groups: group-I of tourmaline cores of Tur-I, and group-II of tourmaline rims of Tur-I & tourmaline of Tur-II, with average $Mg^{\#}$ ($Mg^{\#}$=Mg/(Mg+Fe)) ratios of 0.22 and 0.45, respectively. The variations in the Y site $Mg^{\#}$ are shown in the plots of Mg/(Mg+Fe) versus the X-site occupancy (Xv/Xv+Na) (Figure 4B) and Mg/(Mg+Fe) v*ersus*the X-site occupancy (Na/Na+Ca) (Figure 4C). All the tourmaline samples exhibit small Na/Na+Ca and Xv/Xv+Na variations on the X-site, combined with $Mg^{\#}$ ratios, classifying them as schorl type (Figures 4B,C). As illustrated in Al-Fe-Mg and Ca-Fe-Mg ternary diagrams (Figures 4D,E) (Henry and Guidotti, 1985), tourmaline cores of Tur-I fall in field 2, equal to Li-poor granitoids and associated pegmatites and aplites. This is consistent with the negligible content of Li (less than 50 ppm) confirmed by the LA-ICP-MS analysis (see below). In contrast, some analyses of tourmalines from Tur-I rims and Tur-II fall in the range of Ca-poor metapelites, metapsammites and quartz-tourmaline rocks (field 10).

4.1.2 Trace element contents

The trace element compositions analyzed by LA-ICP-MS are summarized in Table 2, and the whole data set can be found in Supplementary Table S2. All types of tourmalines in the Gyirong pegmatite contain low contents of rare earth elements (REEs), with the majority of analyses yielding concentrations below 1 ppm. The total contents of REEs range from 13.3 to 23.9 ppm. Tourmalines of Tur-I and Tur-II from the Gyirong pegmatite share similar chondrite-normalized REE patterns

TABLE 2 Representative LA-ICP-MS trace element analyses of tourmaline from the Gyirong pegmatite (in ppm)

Sample	Tur-I-cores			Tur-I-rims			Tur-II		
	Min	Max	Mean	Min	Max	Mean	Min	Max	Mean
Li	21.13	44.95	33.49	17.27	21.95	19.37	16.05	21.36	18.54
Be	1.69	7.67	4.04	2.03	7.24	4.36	4.39	8.70	5.97
Sc	47.64	53.38	50.80	18.06	27.75	22.67	21.70	34.43	25.99
V	15.30	52.75	19.56	52.75	114.60	66.60	36.35	106.39	69.62
Co	9.49	16.64	10.51	16.64	19.29	18.17	15.12	19.75	17.77
Ni	0.12	6.53	1.51	6.53	13.63	10.80	3.02	18.52	9.75
Zn	299.74	333.63	315.98	195.69	228.70	212.44	207.77	259.31	224.08
Ga	79.92	94.54	84.88	83.99	97.23	90.08	89.17	97.50	93.34
Rb	0.02	0.10	0.05	0.02	0.12	0.07	0.02	0.15	0.09
Sr	15.71	26.43	17.47	20.11	26.43	22.86	17.08	25.49	20.64
Y	0.09	0.27	0.13	0.13	0.27	0.18	0.06	0.14	0.11
Sn	24.35	34.25	28.42	17.19	24.84	20.55	20.29	32.35	26.33
Sb	—	0.20	0.14	0.05	0.19	0.11	0.15	0.39	0.25
Pb	5.99	7.60	6.67	4.81	6.25	5.70	4.21	6.18	5.27
La	3.75	6.47	4.40	3.40	6.47	4.85	3.46	6.22	4.38
Ce	6.14	12.12	7.56	6.35	12.12	8.76	6.80	11.76	8.36
Pr	0.52	1.17	0.74	0.51	1.17	0.81	0.59	0.98	0.76
Nd	1.82	2.94	2.21	1.86	2.96	2.35	1.48	3.28	2.25
Sm	0.20	0.52	0.38	0.24	0.52	0.40	0.21	0.58	0.34
Eu	0.10	0.20	0.15	0.14	0.23	0.19	0.11	0.24	0.16
Gd	0.18	0.41	0.32	0.16	0.45	0.26	0.17	0.55	0.33
Tb	0.01	0.04	0.02	—	0.05	0.02	0.02	0.07	0.03
Dy	0.11	0.20	0.15	0.03	0.19	0.09	0.05	0.13	0.07
Ho	0.01	0.04	0.02	0.01	0.05	0.03	0.01	0.01	0.01
Er	0.02	0.04	0.04	0.04	0.07	0.05	0.03	0.06	0.05
Tm	0.02	0.02	0.02	0.01	0.04	0.02	0.02	0.02	0.02
Yb	0.01	0.16	0.06	0.08	0.16	0.11	0.06	0.12	0.09
Lu	0.01	0.03	0.02	0.01	0.02	0.02	0.03	0.03	0.03
ΣREE	13.7	23.9	16.0	13.3	23.9	17.8	13.7	23.2	16.8

"-" means below detection level.

(Figure 5), which are characterized by marked light REE enrichment with positive Eu anomalies and weak to negligible Ce anomalies. The concentrations of most trace elements except REEs vary from 0.1 to tens of parts per million (ppm) (Figure 6). Tourmalines are relatively enriched in Zn (195.56–333.63 ppm), Ga (79.92–7.50 ppm), V (15.30–14.60 ppm), Sc (18.06–3.38 ppm), Li (16.05–4.95 ppm), Sn (17.19–4.25 ppm), Sr (15.71–6.43 ppm) and Co (9.49–9.75 ppm). Whereas, trace elements such as Be, Ni, Rb, Y, Sb and Pb show concentrations less than 10 ppm. A few elements exhibit large variations in tourmaline of different types. Tourmalines in group-I display higher Li, Sc, Zn, Sn, and Pb contents than those in group-II. In contrast, elements such as V, Co, Ni and Sr are highly enriched in group-II.

4.2 Boron isotopic composition of tourmaline

The LA-MC-ICP-MS analytical results of boron isotopic compositions of tourmalines from the Gyirong pegmatite are available in Table 3 and Figure 7A. The tourmalines show a tight range of $\delta^{11}B$ values between -11.8 and -9.7‰. There seem to be no obvious differences in B-isotope compositions between the two types of tourmalines. More specifically, the $\delta^{11}B$ values of Tur-I from sample JL-4 and Tur-II from sample JL-5 are concentrated from −11.8 to −9.9‰ (mean −10.4‰) and from −11.8 to −9.7‰ (mean −11.1‰), respectively. With regard to compositional zonation, Tur-I shows slight core-rim variation, with mean $\delta^{11}B$ values ranging from −10.6‰ (core) to −10.2‰ (rim).

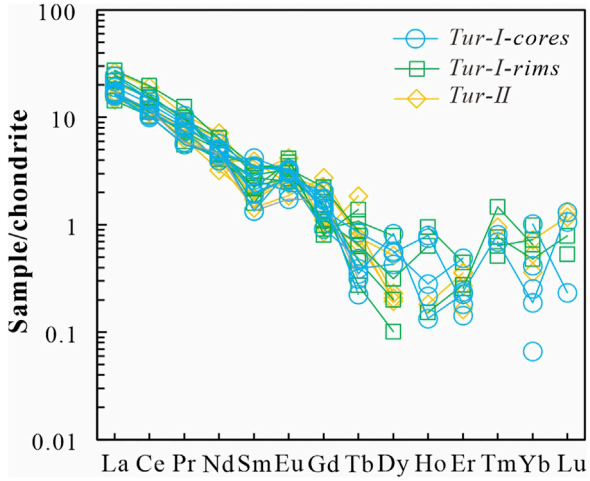

FIGURE 5
Chondrite-normalized REE diagrams of tourmalines in the Gyirong pegmatite.

5 Discussion

5.1 Formation of tourmaline in the Gyirong pegmatite

Tourmaline is a common accessory mineral in many evolved granitic rocks (Trumbull and Chaussidon, 1999; uriánek and Novák, 2007; Yang and Jiang, 2012), especially peraluminous leucogranites and related pegmatites, which widely exist in continental collision zones such as the Himalayan orogenic belt (Le Fort et al., 1987; Guillot and Le Fort, 1995; Wu et al., 2020; Liu et al., 2022). Abundant boron in melt-fluid system is the main factor for the crystallization of tourmaline (Wolf and London, 1997; London, 2011). Due to the incompatibility of boron and the crystallization of boron-poor materials (e.g., feldspar and quartz) during magma evolution, boron-rich magma may have been produced at late stage, causing tourmaline to crystallize (Pesquera et al., 2013). However, in the magmatic-hydrothermal stage, boron is preferentially partitioned into the fluid phase (London, 1999), and boron-rich fluid reacted with crystallized minerals and residual melts to form tourmaline nodules accordingly (Trumbull et al., 2008; Balen and Broska, 2011). Thus, tourmaline in the granite-pegmatite system could be magmatic in origin as documented by prior studies (Trumbull and Chaussidon, 1999; Chakraborty, 2021). Alternatively, it could also be generated from the reaction between boron-rich fluid with crystallized granite at shallow levels, as proven by field investigations and experimental works (Morgan and London, 1989; Cheng et al., 2019). Moreover, there are also examples of tourmaline in the pegmatite reported to be of magmatic-hydrothermal origin at the late magmatic stage (e.g., Gou et al., 2017). Accordingly, tourmaline in the pegmatite could potentially crystallize from a melt or (magmatic-) hydrothermal fluid, which requires comprehensive information to distinguish.

Tourmalines in the Gyirong pegmatite mainly act as isolated grains or long columnar coexisting with the major rock-forming minerals (quartz, plagioclase, K-feldspar, muscovite, etc.) with planar and arc-shaped contacts (Figures 3B,C,F–I). Furthermore, tourmaline crystals are found enveloped by quartz, feldspar and garnet grains (Figures 3B,C,F–I), suggesting that these tourmalines occurred early in the crystallization sequence. There is no textural evidence to show that pegmatite has undergone hydrothermal alteration. Geochemically, all the tourmaline samples reflect relatively homogeneous compositions and are characterized by low Mg# (0.20~0.50) and CaO (0.60–0.95 wt.%), high Al_2O_3 (31.46–3.80 wt.%) and FeO (9.08–4.68 wt.%), and high Al contents at the Y-site (0.19–40 apfu). All tourmalines belong to the alkali group (Figure 4A) and plot in the schorl (Fe-rich) field (Figures 4B,C). In the ternary diagrams of Al-$Al_{50}Fe_{50}$-$Al_{50}Mg_{50}$ (Figure 4D) and Ca-Fe-Mg (Figure 4E), tourmalines plot mostly in the magmatic range, whereas few analyses of Tur-I rims and Tur-II lie across field 2 (Li-poor granitoids and associated pegmatites and aplites) to field 10 (Ca-poor metapelites, metapsammites and quartz-tourmaline rocks). All tourmaline analyses from the Gyirong pegmatite display high Zn concentrations (195.56–33.63 ppm), which indicate that they were crystallized from hydrous borosilicate melts (Veksler and Thomas, 2002; Hazarika et al., 2017). The above morphology and geochemistry of the tourmaline in the Gyirong pegmatite indicate that they are magmatic in nature (London and Manning, 1995), which is clearly different in composition from tourmaline of hydrothermal origin (Yang et al., 2015; Zhao H-D. et al., 2021; Liu et al., 2022). These features are consistent with those of magmatic tourmaline reported in other Himalayan leucogranites (Yang et al., 2015; Dai et al., 2019; Zhou et al., 2019; Cheng et al., 2021; Liu et al., 2022).

It is noteworthy that the Tur-I rims and Tur-II show slightly Mg (Ca)-rich and Fe-poor signatures compared to the Tur-I cores. The common explanation for the significant increase in $Mg^{\#}$ from the core to rim of tourmaline is magma mixing and input of external (Mg-rich) fluid (Jiang et al., 2008; Cheng et al., 2021). However, there is no field evidence, such as the presence of secondary tourmaline veins. Besides, the uniform B-isotope compositions (Tur-I & Tur-II) also argue against magma mixing or the involvement of external fluids (Palmer and Swihart, 1996; Albert et al., 2018; Qiu et al., 2021). Alternatively, considering that the composition of magmatic tourmaline depends on the nature of the melt (Liu and Jiang, 2021), the insignificant variations (e.g., Fe, Mg, Ca) in core-rim compositions of tourmaline might suggest that slight assimilation and contamination by wall rocks have occurred (Liu and Jiang, 2021; Qiu et al., 2021). The high-grade metamorphosed rocks with high-Mg/low-Fe compositions in the GHC have the

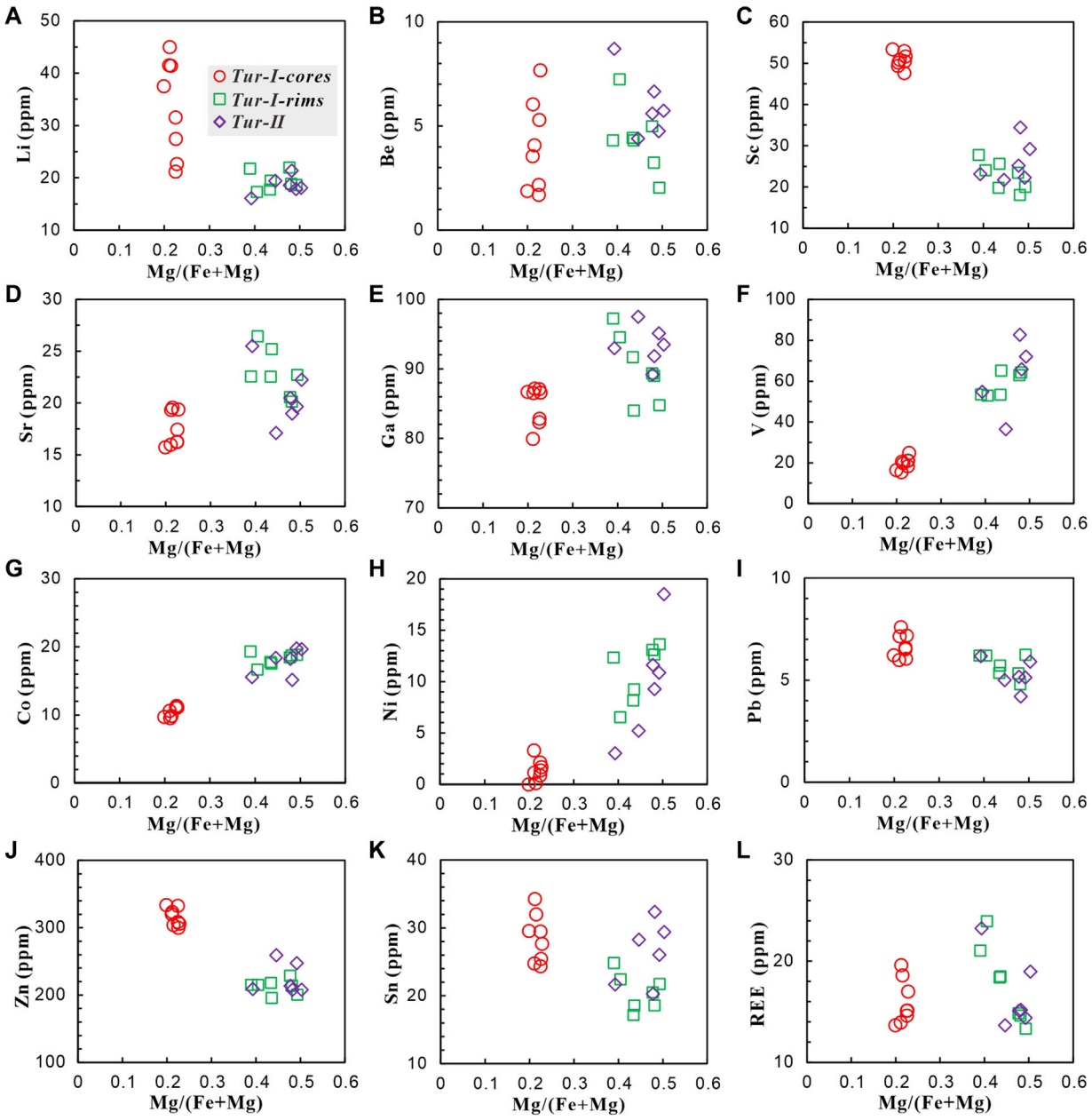

FIGURE 6
(A–L) Correlation diagrams between selected trace elements (Li, Be, Sc, Sr, Ga, V, Co, Ni, Pb, Zn, Sn, and REE) and Mg/(Mg + Fe) ratios in tourmalines from the Gyirong pegmatite.

potential to supply magnesium (Harris and Massey, 1994; Yin, 2006). The increase in V, Co and Ni and the decrease in Li with Mg/(Mg + Fe) from the Tur-Ⅰ cores to the Tur-Ⅰ rims and Tur-Ⅱ is consistent with contamination by the surrounding strata. This hypothesis is also supported by the distinct chemical variations in tourmalines in different lithologic units within the Gyirong area (Hu et al., 2022). Similarly, a transition trend recorded in elemental and Sr-Nd isotopic compositions of granitic dikes through Bendui intrusion to Himalayan leucogranites within the THS by a case study by Ji et al. (2020) also supports this scenario. It is worth noting that even if contamination by wall rocks might have occurred, the tourmaline composition only changes slightly (e.g., Mg# does not exceed 0.5). In this case, their boron isotopes can still represent the original B isotopic composition of the source (Hu et al., 2018).

TABLE 3 LA-MC-ICP-MS boron isotope analyses for tourmaline from the Gyirong granitic pegmatite

Analysis no.	Type	δ^{11}B (‰)	1 SD (‰)	Analysis no.	Type	δ^{11}B (‰)	1 SD (‰)
Sample JL-4							
JL-4-1	Tur-I	−11.6	0.9	JL-4-12	Tur-I	−9.9	0.7
JL-4-2	Tur-I	−11.3	0.8	JL-4-13	Tur-I	−9.9	0.8
JL-4-3	Tur-I	−11	0.8	JL-4-14	Tur-I	−9.9	0.7
JL-4-4	Tur-I	−11.8	0.8	JL-4-15	Tur-I	−9.9	0.7
JL-4-5	Tur-I	−10.6	0.9	Sample JL-5			
JL-4-6	Tur-I	−10.2	0.8	JL-5-1	Tur-II	−11	0.7
JL-4-7	Tur-I	−9.9	0.8	JL-5-2	Tur-II	−11.7	0.7
JL-4-8	Tur-I	−10	0.9	JL-5-3	Tur-II	−11.8	0.6
JL-4-9	Tur-I	−10.1	0.9	JL-5-4	Tur-II	−11.1	0.7
JL-4-10	Tur-I	−9.9	1	JL-5-5	Tur-II	−9.7	0.7
JL-4-11	Tur-I	−10	0.9	JL-5-6	Tur-II	−11	0.7

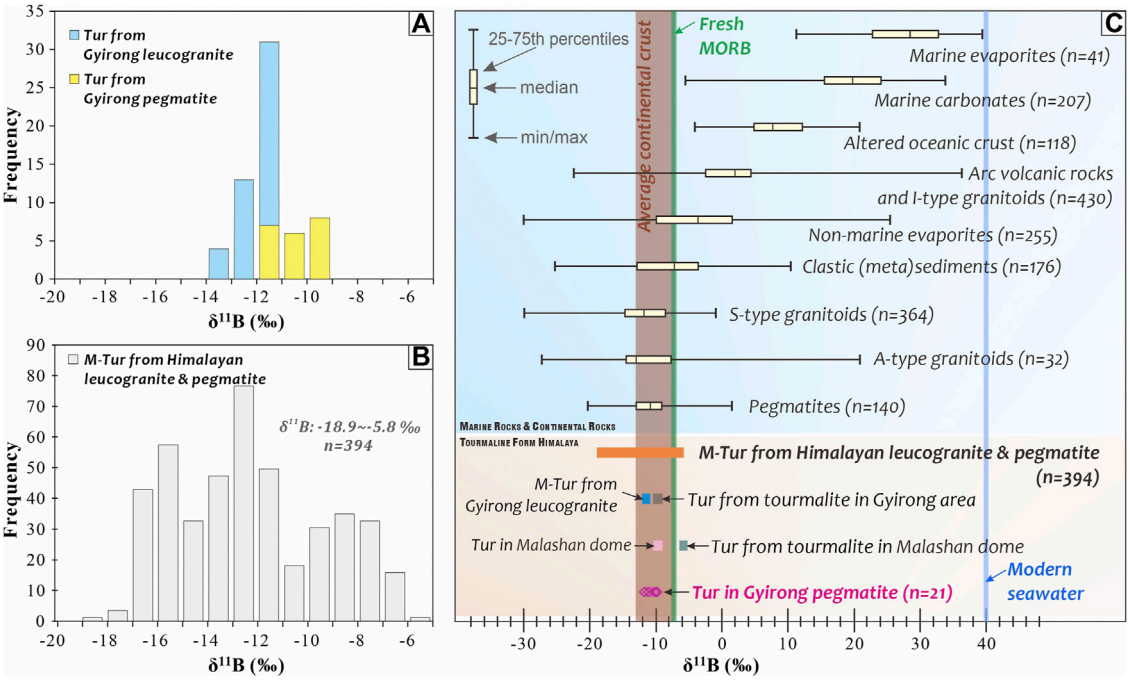

FIGURE 7
Histograms representing the δ^{11}B values of **(A)** tourmalines from the Gyirong leucogranite and pegmatite; and **(B)** magmatic tourmalines from Himalayan leucogranite and pegmatite. **(C)** Summary of boron isotope compositions for marine and crustal rocks and for tourmaline from the Gyirong and Malashan areas. Date sources: tourmalines from the Gyirong leucogranite (Hu et al., 2022), tourmalines from Himalayan leucogranites and pegmatites (Supplementary Table S3), average continental crust (Marschall and Jiang, 2011), and other boron reservoirs (Trumbull et al., 2020 and references therein). Abbreviations: Tur: tourmaline, M-Tur: magmatic tourmaline.

The trace elements of tourmaline could record the compositional signature of its host melt (e.g., van Hinsberg, 2011). According to the correlation diagrams of trace elements versus Mg/(Mg + Fe), only V, Ni and Co (not obvious) are positively correlated with Mg/(Mg + Fe) (Figure 6), which may be related to the potential crystal chemical effects on their incorporation (Zhao et al., 2019). Most trace elements did not show apparent correlations with

Mg/(Mg+Fe), which indicates that the trace element concentrations of tourmaline are mainly controlled by melt composition. This supports the scenario that tourmalines in the Gyirong pegmatite were crystallized directly from melt. In summary, we suggest that the tourmalines from the Gyirong pegmatite are of magmatic origin and are a product of direct crystallization from a boron-rich pegmatitic magma.

5.2 Boron isotope variation and genetic implications

We compiled a total of 394 boron isotopic analyses (Supplementary Table S3) on magmatic tourmalines (free of hydrothermal effects) from Himalayan leucogranites and pegmatites reported in the literature (Figure 7B, Chaussidon and Albarède, 1992; Yang et al., 2015; Gou et al., 2017; Hu et al., 2018; Dai et al., 2019; Zhou et al., 2019; Han et al., 2020; Cheng et al., 2021; Hu et al., 2022; Liu et al., 2022), which define an ample range of $\delta^{11}B$ values from −18.9 to −5.8. The large boron isotopic compositional variations in tourmalines in the Himalaya may result from heterogeneous melt sources (magma mixing) or fractions of boron isotopes during magma evolution (Trumbull et al., 2013; Kawakami et al., 2019; Xiang et al., 2020).

The measured tourmaline boron isotopes from the Gyirong pegmatite define a narrow range of −11.8 to −9.7 ‰ (concentrated at approximately −10 ‰) with negligible boron isotopic zonation within tourmalines, which indicates that no significant isotopic fractionation has occurred. Similarly, magmatic tourmalines (Mg-poor) of the Gyirong leucogranite have $\delta^{11}B$ values of −12.1 to −11.2 ‰ (Hu et al., 2022). Note that minimal boron isotope fractionation occurs between boric granitic or pegmatitic melt and tourmaline at common anatectic temperatures (Palmer and Swihart 1996; Smith and Yardley, 1996; Meyer et al., 2008). In this case, the boron isotopes of magmatic tourmaline should approximate that of the primary $\delta^{11}B$ value of the parental magma. The light boron isotopic compositions of magmatic tourmalines in the Gyirong leucogranite and pegmatite are consistent with the global database of average continental crust (−10 ± 3‰), S-type granitoids and pegmatites (Figure 7C), reflecting a continental source of boron (Trumbull et al., 2020).

As addressed by numerous studies (e.g., Gao and Zeng, 2014; Gou et al., 2017; Fan et al., 2021), the Himalayan leucogranites were mainly generated by metapelite dehydration melting or fluid-present melting. The Gyirong leucogranite shows high $(^{87}Sr/^{86}Sr)_i$ ratios (0.7548–7586), high Rb contents, and low Sr and Ba contents (Gao et al., 2017; Wang et al., 2017), which can be ascribed to fluid-absent melting of muscovite in metasedimentary sources. This interpretation is also supported by recent Mg-Fe-Sr-Nd isotope studies (e.g., Tian et al., 2020; Shi et al., 2021). Note that some authors found that the Himalayan leucogranites do not record any mantle material contribution to the sources (Inger and Harris, 1993; opkinson et al., 2017). In addition, some studies emphasized the contribution from the LHS fluids with regard to the anatectic sources of the Greater Himalayan leucagranites (Guo and Wilson, 2012; Liu et al., 2022). In contrast, there are also recent studies arguing that the contribution of the LHS is unnecessary (e.g., Ji et al., 2022). In our case, homogeneous tourmaline $\delta^{11}B$ values are consistent with the average crust and S-type granite, likely supporting the latter hypothesis in the Gyirong area. Hence, the crustal metapelitic rocks within the GHC were the most likely source components for the Gyirong pegmatite, which is consistent with most Himalayan leucogranites (Inger and Harris, 1993; Gao et al., 2017; Xie et al., 2018; Khanal et al., 2020; Hu et al., 2022; Ji et al., 2022).

Considering the close spatial and temporal relationship between the Gyirong leucogranite and pegmatite, it is easy to assume that the pegmatite originated from the highly differentiated evolution of granites. However, if this happened, the tourmaline in pegmatite could display lighter $\delta^{11}B$ values than that in leucogranite since the crystallization of tourmalines would result in depletion of ^{11}B in the residual melt (Chakraborty, 2021). As the melt cools, B-rich fluid exsolution from the magma often occurs in the granite-pegmatite systems (e.g., Thomas et al., 2003). Accordingly, tourmaline crystallized from the residual melt to show a lower $\delta^{11}B$ value (Liu et al., 2022). We have no conclusive evidence to confirm or deny the existence of hydrothermal tourmaline in the Gyirong pegmatite, which requires further investigation. In the present case, our measured boron isotope compositions of pegmatite ($\delta^{11}B$ of −11.8 to −9.7‰) show slightly higher values than those of the leucogranite ($\delta^{11}B$ of −12.1 to −11.2‰), which preclude the possibility of fractional crystallization (e.g., Rayleigh fractionation) as well as fluid exsolution (Ghosh et al., 2021). Such overlapping or similar B isotopic compositions in the granite-pegmatite system favor a genetic relationship between the Gyirong leucogranite and pegmatite (Montenegro et al., 2021). The Gyirong pegmatite displays high $^{87}Sr/^{86}Sr_{16Ma}$ (~0.762), $^{208}Pb/^{204}Pb_{16Ma}$ (~39.72), $^{207}Pb/^{204}Pb_{16Ma}$ (~15.79) and $^{206}Pb/^{204}Pb_{16Ma}$ (~19.6), and low εNd_{16Ma} value of −16.0 (authors' unpublished data). Their Sr-Nd-Pb isotopic signatures are consistent with those of the Gyirong leucogranite, suggesting that they have similar origins. Furthermore, the whole-rock geochemical data (authors' unpublished data) indicate that the Gyirong pegmatite did not experience a high degree of differentiation. Combined with the typical peraluminous mineral assemblage (e.g., tourmaline, muscovite and garnet) of the Gyirong pegmatite, we thus propose that the Gyirong pegmatite was the product of crustal anatexis rather than formed *via* the highly differentiated evolution of the granite. The anatectic metamorphism was linked to crustal thinning (28–5 a) caused by the STDS within the Himalayan orogen (Harris and Massey, 1994; Wang et al., 2017; Ding et al., 2021; Ji et al., 2022).

6 Conclusion

Based on petrographic and geochemical studies conducted on tourmaline from the Gyirong pegmatite within the South Tibet Himalaya, we reached the following conclusions.

1) Mineralogical characteristics show that Gyirong pegmatite belongs to the peraluminous S-type pegmatite and contains abundant tourmaline. Two types of tourmalines (Tur-Ⅰ & Tur-Ⅱ) were identified in this contribution and they are all Fe-rich schorl with low Mg# ratios (0.22 –.45). The trace element concentrations of tourmaline are mainly controlled by melt composition.
2) Morphological and geochemical characteristics indicate that the tourmalines from the Gyirong pegmatite are magmatic in origin. Insignificant variations in tourmaline boron isotopic composition from −11.8 to −9.7‰ indicate that the Gyirong pegmatite was derived from the continental crust. And the crustal metapelitic rocks within the GHC were the most likely source components for the Gyirong pegmatite.
3) We hypothesize that the Gyirong pegmatite was the product of crustal anatexis rather than formed *via*the highly differentiated evolution of the Gyirong leucogranite.

Data availability statement

The original contributions presented in the study are included in the article/supplementary material, further inquiries can be directed to the corresponding author.

Author contributions

QP and HC designed the project and helped to supervise this study. QP, FL, YZ, and YX conducted field investigations. QP, SM, and CL carried out EMPA and LA-ICP-MS analysis for major and trace element compositions. SM, CL, and SW are responsible for iin situboron isotope analysis. FL and JW assisted in data collection and analysis. All authors listed participated in the discussion and contributed to the writing of the manuscript.

Funding

This research received funding from the Second Tibetan Plateau Scientific Expedition and Research (SQ2019QZKK2203), the Key subject of Science and Technology Projects of Chinese Academy of Sciences (XDA19030303-02), the Sichuan Natural Science Foundation (2022NSFSC0410) and the National Natural Science Foundation of China (41802095).

Acknowledgments

We thank Kuidong Zhao for assistance in tourmaline boron isotope analysis. We also greatly appreciate the constructive comments and suggestions from the editor and three reviewers, which helped us considerably improve the paper.

Conflict of interest

The authors declare that the research was conducted in the absence of any commercial or financial relationships that could be construed as a potential conflict of interest.

Publisher's Note

All claims expressed in this article are solely those of the authors and do not necessarily represent those of their affiliated organizations, or those of the publisher, the editors and the reviewers. Any product that may be evaluated in this article, or claim that may be made by its manufacturer, is not guaranteed or endorsed by the publisher.

Supplementary material

The Supplementary Material for this article can be found online at: https://www.frontiersin.org/articles/10.3389/feart.2022.1037727/full#supplementary-material

References

Abert, C., Lana, C., Gerdes, A., Schannor, M., Narduzzi, F., and Queiroga, G. (2018). Archean magmatic-hydrothermal fluid evolution in the Quadrilátero Ferrífero (SE Brazil) documented by B isotopes (LA MC-ICPMS) in tourmaline. *Chemi. Geolo.* 481, 95–109. doi:10.1016/j.chemgeo.2018.02.002

Alsdorf, D., Brown, L., Nelson, K. D., Makovsky, Y., Klemperer, S., and Zhao, W. (1998). Crustal deformation of the Lhasa terrane, Tibet plateau from Project INDEPTH deep seismic reflection profiles. *Tectonics* 17 (4), 501–159. doi:10.1029/98tc01315

Aoya, M., Wallis, S. R., Terada, K., Lee, J., Kawakami, T., Wang, Y., et al. (2005). North-south extension in the Tibetan crust triggered by granite emplacement. *Geol.* 33 (11), 853–685. doi:10.1130/g21806.1

Balen, D., and Broska, I. (2011). Tourmaline nodules: Products of devolatilization within the final evolutionary stage of granitic melt? *Geolo. Soci. Londo. Speci. Publi.* 350 (1), 53–68. doi:10.1144/sp350.4

Bosi, F. (2018). Tourmaline crystal chemistry. *Ame. Mineralogist* 103 (2), 298–306. doi:10.2138/am-2018-6289

Buriánek, D., and Novák, M. (2007). Compositional evolution and substitutions in disseminated and nodular tourmaline from leucocratic granites: Examples from the Bohemian Massif, Czech Republic. *Lithos* 95 (1-2), 148–614. doi:10.1016/j.lithos.2006.07.006

Cao, H., Huang, Y., Li, G., Zhang, L., Wu, J., Dong, L., et al. (2018). Late Tiassic sedimentary records in the northern Tethyan Himalaya: Tectonic link with Greater India. *Geoscie. Fronti.* 9 (1), 273–921. doi:10.1016/j.gsf.2017.04.001

Cao, H. W., Li, G. M., Zhang, L. K., Dong, L., Gao, K., and Dai, Z. W. (2020). Monazite U-Th-Pb age of Liemai Eocene granites in the southern Tibet and its geological implications. *Sedimenta. Geolo. Tethyan Geolo.* 40, 31–42. doi:10.19826/j.cnki.1009-3850.(2020)02-0031-12

Cao, H-W., Li, G-M., Zhang, R-Q., Zhang, Y-H., Zhang, L-K., Dai, Z-W., et al. (2021). Genesis of the Cuonadong tin polymetallic deposit in the Tethyan Himalaya: Evidence from geology, geochronology, fluid inclusions and multiple isotopes. *Gondwana Rese.* 92, 72–101. doi:10.1016/j.gr.2020.12.020

Cao, H-W., Pei, Q-M., Santosh, M., Li, G-M., Zhang, L-K., Zhang, X-F., et al. (2022a). Himalayan leucogranites: A review of geochemical and isotopic characteristics, timing of formation, genesis and rare metal mineralization. *Earth-Science Revi.* 234, 104229. doi:10.1016/j.earscirev.2022.104229

Cao, H., Li, G., Zhang, L., Zhang, X., Yu, X., Chen, Y., et al. (2022b). Genesis of Himalayan leucogranite and its potentiality of rare-metal mineralization. *Sedimenta. Geolo. Tethyan Geolo.* 42 (2), 189–211. doi:10.19826/j.cnki.1009-3850.2022.04004

Chakraborty, T. (2021). Tourmaline growth and evolution in S-type granites and pegmatites: Constraints from textural, chemical and B-isotopic study from the Gingpur Shist Belt granitoids, eastern India. *Geol. Mag.* 158, 1657–1670. doi:10.1017/s0016756821000224

Chaussidon, M., and Albarède, F. (1992). Secular boron isotope variations in the continental crust: A ion microprobe study. *Earth Alaneta. Scie. Lette.* 108 (4), 229–421. doi:10.1016/0012-821x(92)90025-q

Cheng, L., Zhang, C., Yang, X., Qi, D., Zhou, Y., and Holtz, F. (2019). Experimental investigation of reactions between two-mica granite and boron-rich fluids: Implications for the formation of tourmaline granite. *Sci. China Earth Sci.* 62 (1674-7313), 1630–1644. doi:10.1007/s11430-019-9442-y

Cheng, L., Zhang, C., Liu, X., Yang, X., Zhou, Y., Horn, I., et al. (2021). Significant boron isotopic fractionation in the magmatic evolution of Himalayan leucogranite recorded in multiple generations of tourmaline. *Chemi. Geolo.* 571, 120194. doi:10.1016/j.chemgeo.2021.120194

Čopjaková, R., Prokop, J., Novák, M., Losos, Z., Gadas, P., Škoda, R., et al. (2021). Hydrothermal alteration of tourmaline from pegmatitic rocks enclosed in serpentinites: Multistage processes with distinct fluid sources. *Lithos* 308-381, 105823. doi:10.1016/j.lithos.2020.105823

Dai, Z., Li, G., Ding, J., Zhang, L., Cao, H., Zhang, Z., et al. (2019). Chemical and Boron Iiotopic Composition, and Significance of Tourmaline from the Conadong Tourmaline Granite, Tibet. *Earth Scie.* 44 (6), 1849–5189. doi:10.3799/dqkx.2019.043

Ding, H., Kohn, M. J., and Zhang, Z. (2021). Long-lived (ca. 22-24 Myr) partial melts in the eastern Himalaya: Petrochronologic constraints and tectonic implications. *Earth Alaneta. Scie. Lette.* 558, 116764. doi:10.1016/j.epsl.2021.116764

Dong, X., Liu, G., and Gou, Z. (2017). Cenozoic metamorphism and tectonic significance of the greater himalayan crystalline complex from the Gyirong area, southern Tibet. *Acta Petrolo. Sini.* 33 (8), 2342–5236.

Fan, J-J., Wang, Q., Li, J., Wei, G-J., Ma, J-L., Ma, L., et al. (2021). Boron and molybdenum isotopic fractionation during crustal anatexis: Constraints from the conadong leucogranites in the Himalayan Block, South Tibet. *Geochimica Geosmochimica Acta* 297, 120–412. doi:10.1016/j.gca.2021.01.005

Fu, J., Li, G., Wang, G., Huang, Y., Zhang, L., Dong, S., et al. (2017). First field identification of the conadong dome in southern Tibet: implications for EW extension of the North Himalayan gneiss dome. *Int. J. Earth Sci.* 106 (5), 1581–9156. doi:10.1007/s00531-016-1368-2

Gao, L-E., and Zeng, L. (2014). Fluxed melting of metapelite and the formation of Miocene high-CaO two-mica granites in the Malashan gneiss dome, southern Tibet. *Geochimica Geosmochimica Acta* 130, 136–515. doi:10.1016/j.gca.2014.01.003

Gao, L., Zeng, L., Wang, L., Hou, K., Gao, J., and Shang, Z. (2016). Timing of Different Crustal Partial Mmlting in the Himalayan Orogenic Belt and Its Tectonic Implications. *Acta Geolo. Sini.* 90 (11), 3039–5309.

Gao, L-E., Zeng, L., and Asimow, P. D. (2017). Contrasting geochemical signatures of fluid-absent versus fluid-fluxed melting of muscovite in metasedimentary sources: The Himalayan leucogranites. *Geology* 45 (1), 39–42. doi:10.1130/g38336.1

Ghosh, U., Upadhyay, D., Abhinay, K., and Mishra, B. (2021). Nature of the mineralizing fluids in the Balda and Motiya W-prospects, Western India: Constraints from chemical and B-isotope composition of tourmaline. *Chemi. Geolo.* 582, 120439. doi:10.1016/j.chemgeo.2021.120439

Goscombe, B., Gray, D., and Foster, D. A. (2018). Metamorphic response to collision in the Central Himalayan Orogen. *Gondwana Rese.* 57, 191–265. doi:10.1016/j.gr.2018.02.002

Gou, Z., Zhang, Z., Dong, X., Xiang, H., Ding, H., Tian, Z., et al. (2016). Petrogenesis and tectonic implications of the Yadong leucogranites, southern Himalaya. *Lithos* 256-257, 300–130. doi:10.1016/j.lithos.2016.04.009

Gou, G. N., Wang, Q., Wyman, D. A., Xia, X. P., Wei, G. J., and Guo, H. F. (2017). *In situ* boron isotopic analyses of tourmalines from Neogene magmatic rocks in the northern and southern margins of Tibet: Evidence for melting of continental crust and sediment recycling. *Solid Earth Scie.* 2 (2), 43–54. doi:10.1016/j.sesci.2017.03.003

Gou, Z. B., Liu, H., Li, J., Zhang, S. Z., Zhao, X. D., and Wang, S. W. (2022). Petrogenesis and geological implications of the Yadong Migmatites, South Tibet. *Sedimenta. Geolo. Tethyan Geolo.* 42, 279–287. doi:10.19826/j.cnki.1009-3850.2022.05008

Grew, E. S., Krivovichev, S. V., Hazen, R. M., and Hystad, G. (2016). Evolution of Structural Complexity in Boron Minerals. *Can. Mineral.* 54 (1), 125–413. doi:10.3749/canmin.1500072

Grujic, D., Hollister, L. S., and Parrish, R. R. (2002). Himalayan metamorphic sequence as an orogenic channel: insight from Bhutan. *Earth Plalaneta. Scie. Lette.* 198 (1), 177–911. doi:10.1016/s0012-821x(02)00482-x

Guillot, S., and Le Fort, P. (1995). Geochemical constraints on the bimodal origin of High Himalayan leucogranites. *Lithos* 35 (3), 221–324. doi:10.1016/0024-4937(94)00052-4

Guo, Z., and Wilson, M. (2012). The Himalayan leucogranites: Constraints on the nature of their crustal source region and geodynamic setting. *Gondwana Rese.* 22 (2), 360–736. doi:10.1016/j.gr.2011.07.027

Guo, R., Hu, X., Garzanti, E., and Lai, W. (2021). Boron isotope composition of detrital tourmaline: A new tool in provenance analysis. *Lithos* 400–401, 106360. doi:10.1016/j.lithos.2021.106360

Guo, J., Xiang, L., Zhang, R., Yang, T., Wu, K., and Sun, W. (2022). Chemical and boron isotopic variations of tourmaline deciphering magmatic-hydrothermal evolution at the Gejiu Sn-polymetallic district, South China. *Chemi. Geolo.* 593, 120698. doi:10.1016/j.chemgeo.2021.120698

Han, J., Hollings, P., Jourdan, F., Zeng, Y., and Chen, H. (2020). Inherited Eocene magmatic tourmaline captured by the Miocene Himalayan leucogranites. *Ame. Mineralogist* 105 (9), 1436–4140. doi:10.2138/am-2020-7608

Harris, N., and Massey, J. (1994). Decompression and anatexis of Himalayan metapelites. *Tectonics* 13 (6), 1537–4156. doi:10.1029/94tc01611

Hawthorne, F. C., and Dirlam, D. M. (2011). Tourmaline the indicator mineral: From atomic arrangement to viking navigation. *Elements* 7 (5), 307–132. doi:10.2113/gselements.7.5.307

Hawthorne, F. C., and Henry, D. J. (1999). Classification of the minerals of the tourmaline group. *Eur. J. Mineral.* 11, 201–216. doi:10.1127/ejm/11/2/0201

Hazarika, P., Upadhyay, D., and Pruseth, K. L. (2017). Episodic tourmaline growth and re-equilibration in mica pegmatite from the Bihar Mica Belt, India: Major-and trace-element variations under pegmatitic and hydrothermal conditions. *Geol. Mag.* 154 (1), 68–86. doi:10.1017/s0016756815000916

Henry, D. J., and Dutrow, B. L. (1996). Metamorphic tourmaline and its petrologic applications. *Revi. Mineralogy Geochemi.* 33 (1), 503–557.

Henry, D. J., and Guidotti, C. V. (1985). Tourmaline as a petrogenetic indicator mineral: A example from the staurolite-grade metapelites of NW Maine. *Ame. Mineralogist* 70 (1-2), 1–15.

Henry, D. J., Novak, M., Hawthorne, F. C., Ertl, A., Dutrow, B. L., Uher, P., et al. (2011). Nomenclature of the tourmaline-supergroup minerals. *Ame. Mineralogist* 96 (5-6), 895–913. doi:10.2138/am.2011.3636

Hodges, K. V. (2000). Tectonics of the Himalaya and southern Tibet from two perspectives. *Geol. Soc. Am. Bull.* 112 (3), 324–530. doi:10.1130/0016-7606(2000)112<324:tothas>2.0.co;2

Hong, H., Zhang, K., and Li, Z. (2010). Climatic and tectonic uplift evolution since ~7 Ma in Gyirong basin, southwestern Tibet plateau: cay mineral evidence. *Int. J. Earth Sci.* 99 (6), 1305–1135. doi:10.1007/s00531-009-0457-x

Hopkinson, T. N., Harris, N. B. W., Warren, C. J., Spencer, C. J., Roberts, N. M. W., Horstwood, M. S. A., et al. (2017). The identification and significance of pure sediment-derived granites. *Earth alaneta. Scie. Lette.* 467, 57–63. doi:10.1016/j.epsl.2017.03.018

Hou, K., Li, Y., Xiao, Y., Liu, F., and Tian, Y. (2010). *In situ* boron isotope measurements of natural geological materials by LA-MC-ICP-MS. *Chin. Sci. Bull.* 55 (29), 3305–1331. doi:10.1007/s11434-010-4064-9

Hou, Z-Q., Zheng, Y-C., Zeng, L-S., Gao, L-E., Huang, K-X., Li, W., et al. (2012). Eocene–Oligocene granitoids in southern Tibet: Constraints on crustal anatexis and tectonic evolution of the Himalayan orogen. *Earth Plalaneta. Scie. Lette.* 349-350, 38–52. doi:10.1016/j.epsl.2012.06.030

Hu, X., Garzanti, E., Wang, J., Huang, W., An, W., and Webb, A. (2016). The timing of India-Asia collision onset–Facts, theories, controversies. *Earth-Science Revi.* 160, 264–929. doi:10.1016/j.earscirev.2016.07.014

Hu, G., Zeng, L., Gao, L-E., Liu, Q., Chen, H., and Guo, Y. (2018). Diverse magma sources for the Himalayan leucogranites: Evidence from B-Sr-Nd isotopes. *Lithos* 314-315, 88–99. doi:10.1016/j.lithos.2018.05.022

Hu, G., Gao, L., Zeng, L., and Li, Y. (2022). Geochemical and Boron Isotopic Evidence that Tourmaline Records Country Rock Assimilation of Leucogranites in the Himalayan Orogen. *Acta Geolo. Sini.* 96 (1), 123–314. doi:10.1111/1755-6724.14800

Imayama, T., Takeshita, T., and Arita, K. (2010). Metamorphic P–T profile and P–T path discontinuity across the far-eastern Nepal Himalaya: investigation of channel flow models. *Jo.Metamorphi. Geolo.* 28 (5), 527–459. doi:10.1111/j.1525-1314.2010.00879.x

Inger, S., and Harris, N. (1993). Geochemical Constraints on Leucogranite Megmatism in the Langtang Valley, Nepal Himalaya. *Jo.Metrology* 34 (2), 345–638. doi:10.1093/petrology/34.2.345

Ji, W-Q., Wu, F-Y., Liu, X-C., Liu, Z-C., Zhang, C., Liu, T., et al. (2020). Pervasive Miocene melting of thickened crust from the Lhasa terrane to Himalaya, southern Tibet and its constraint on generation of Himalayan leucogranite. *Geochimica eosmochimica Acta* 278, 137–516. doi:10.1016/j.gca.2019.07.048

Ji, M., Gao, X-Y., and Zheng, Y-F. (2022). Geochemical evidence for partial melting of progressively varied crustal sources for leucogranites during the Oligocene–Miocene in the Himalayan orogen. *Chemi. Geolo.* 589, 120674. doi:10.1016/j.chemgeo.2021.120674

Jiang, S-Y., Radvanec, M., Nakamura, E., Palmer, M., Kobayashi, K., Zhao, H-X., et al. (2008). Chemical and boron isotopic variations of tourmaline in the Hnilec granite-related hydrothermal system, Slovakia: Constraints on magmatic and metamorphic fluid evolution. *Lithos* 106 (1–2), 1–11. doi:10.1016/j.lithos.2008.04.004

Kawakami, T., Aoya, M., Wallis, S. R., Lee, J., Terada, K., Wang, Y., et al. (2007). Contact metamorphism in the Malashan dome, North Himalayan gneiss domes, southern Tibet: a example of shallow extensional tectonics in the Tethys Himalaya. *Jo. Metamorphi. Geolo.* 25 (8), 831–583. doi:10.1111/j.1525-1314.2007.00731.x

Kawakami, T., Sakai, H., and Sato, K. (2019). Syn-metamorphic B-bearing fluid infiltrations deduced from tourmaline in the Main Central Thrust zone, eastern Nepal Himalayas. *Lithos* 348-349, 105175. doi:10.1016/j.lithos.2019.105175

Khanal, G. P., Wang, J-M., Wu, F-Y., Wang, J-G., and Yang, L. (2020). In-sequence buoyancy extrusion of the Himalayan Metamorphic Core, central Nepal: Constraints from monazite petrochronology and thermobarometry. *Jo.Asian Earth Scie.* 199, 104406. doi:10.1016/j.jseaes.2020.104406

Le Fort, P., Cuney, M., Deniel, C., France-Lanord, C., Sheppard, S. M. F., Upreti, B. N., et al. (1987). Crustal generation of the Himalayan leucogranites. *Tectonophysics* 134 (1), 39–57. doi:10.1016/0040-1951(87)90248-4

Liu, T., and Jiang, S-Y. (2021). Multiple generations of tourmaline from Yushishanxi leucogranite in South Qilian of Western China record a complex formation history from B-rich melt to hydrothermal fluid. *Ame. Mineralogist* 106 (6), 994–1008. doi:10.2138/am-2021-7473

Liu, Y., Hu, Z., Gao, S., Günther, D., Xu, J., Gao, C., et al. (2008). *In situ* analysis of major and trace elements of anhydrous minerals by LA-ICP-MS without applying an internal standard. *Chemi. Geolo.* 257 (1–2), 34–43. doi:10.1016/j.chemgeo.2008.08.004

Liu, Z-C., Wu, F-Y., Liu, X-C., Wang, J-G., Yin, R., Qiu, Z-L., et al. (2019). Mineralogical evidence for fractionation processes in the Himalayan leucogranites of the Ramba Dome, southern Tibet. *Lithos* 340, 71–86. doi:10.1016/j.lithos.2019.05.004

Liu, S., Zhang, G., Zhang, L., Liu, Z., and Xu, J. (2022). Boron isotopes of tourmalines from the central Himalaya: Implications for fluid activity and anatexis in the Himalayan orogen. *Chemi. Geolo.* 596, 120800. doi:10.1016/j.chemgeo.2022.120800

London, D., and Manning, D. A. C. (1995). Chemical variation and significance of tourmaline from Southwest England. *Econo. Geolo.* 90 (3), 495–519. doi:10.2113/gsecongeo.90.3.495

London, D. (1999). Stability of tourmaline in pei aluminous granite systems: Te boron cycle from anatexis to hydrothermal aureoles. *Eur. J. Mineral.* 11 (2), 253–622. doi:10.1127/ejm/11/2/0253

London, D. (2011). Experimental synthesis and stability of tourmaline: a historical overview. *Tana. Mineralogist* 49 (1), 117–316. doi:10.3749/canmin.49.1.117

Ma, Z. N., Han, Z. P., Li, Y. L., Bi, W. J., Xu, T. K., and Xiao, S. Q. (2022). Exhumation history of the Kampa dome in the southern Tibet: Evidence from low temperature thermochronology. *Sedimenta. Geolo. Tethyan Geolo.* 42, 300–309. doi:10.19826/j.cnki.1009-3850.2022.04009

Marschall, H. R., and Jiang, S-Y. (2011). Tourmaline Isotopes: No Element Lift Behind. *Elements* 7 (5), 313–931. doi:10.2113/gselements.7.5.313

Martin, A. J. (2017). A review of Himalayan stratigraphy, magmatism, and structure. *Gondwana Rese.* 49, 42–80. doi:10.1016/j.gr.2017.04.031

Metcalfe, I. (2021). Multiple Tethyan ocean basins and orogenic belts in Asia. *Gondwana Rese.* 100, 87–130. doi:10.1016/j.gr.2021.01.012

Meyer, C., Wunder, B., Meixner, A., Romer, R., and Heinrich, W. (2008). Boron-isotope fractionation between tourmaline and fluid: a experimental re-investigation. *Contrib. Mineral. Petrol.* 156 (2), 259–627. doi:10.1007/s00410-008-0285-1

Montenegro, T., Wul, J., de Luchi, M. L., Ribacki, E., and Trumbull, R. B. (2021). Chemical and boron isotope composition of tourmaline from pegmatites and their host rocks, Sierra de San Luis, Argentina. *Tana. Mineralogist* 59 (3), 467–944. doi:10.3749/canmin.2000072

Morgan, G. B., and London, D. (1989). Experimental reactions of amphibolite with boron-bearing aqueous fluids at 200 MPa: implications for tourmaline stability and partial melting in mafic rocks. *Contrib. Mineral. Petrol.* 102 (3), 281–927. doi:10.1007/bf00373721

Najman, Y., Appel, E., Boudagher-Fadel, M., Bown, P., Carter, A., Garzanti, E., et al. (2010). Timing of India-Asia collision: Geological, biostratigraphic, and palaeomagnetic constraints. *J. Geophys. Res.* 115 (B12), B12416. doi:10.1029/2010jb007673

Palmer, M. R., and Swihart, G. H. (1996). Boron isotope geochemistry; an overview. *ReviMineralogy aeochemi.* 33 (1), 709–474.

Pan, G., Wang, L., Li, R., Yuan, S., Ji, W., Yin, F., et al. (2012). Tectonic evolution of the Qinghai-Tibet Plateau. *Jo. of Asian Earth Scie.* 53, 3–14. doi:10.1016/j.jseaes.2011.12.018

Pan, G. T., Wang, L. Q., Yin, F. G., Geng, Q. R., Li, G. M., and Zhu, D. C. (2022). Researches on geological tectonic evolution of Tibetan Plateau: A review, recent advances, and directions in the future. *Sedimenta. Geolo. Tethyan Geolo.* 42, 151–175. doi:10.19826/j.cnki.1009-3850.2022.05004

Pesquera, A., Torres-Ruiz, J., García-Casco, A., and Gil-Crespo, P. P. (2013). Evaluating the Controls on Tourmaline Formation in Ganitic Systems: a Ccse Study on Paraluminous Granites from the Central Iierian Zzne (CIZ), Western Spain. *Jo. Metrology* 54 (3), 609–364. doi:10.1093/petrology/egs080

Qiu, K-F., Yu, H-C., Hetherington, C., Huang, Y-Q., Yang, T., and Deng, J. (2021). Tourmaline composition and boron isotope signature as a tracer of magmatic-hydrothermal processes. *Ame. Mineralogist* 106 (7), 1033–4104. doi:10.2138/am-2021-7495

Searle, M., Cottle, J., Streule, M., and Waters, D. (2010). Crustal melt granites and migmatites along the Himalaya: mMlt source, segregation, transport and granite emplacement mechanisms. *Earth anvironm. Scie. Transa. ofo. Soci. odinbu.* 100 (1-2), 219–323. doi:10.1017/s175569100901617x

Searle, M. P. (1999). Emplacement of Himalayan leucogranites by magma injection along giant sill complexes: examples from the Co Ou, Gachung King and Everest leucogranites (Nepal Himalaya). *Jo.Asian Earth Scie.* 17 (5), 773–873. doi:10.1016/s1367-9120(99)00020-6

Shen, T., Wang, G., Leloup, P. H., van der Beek, P., Bernet, M., Cao, K., et al. (2016). Controls on Cenozoic exhumation of the Tethyan Himalaya from fission-track thermochronology and detrital zircon U-Pb geochronology in the Gyirong basin area, southern Tibet. *Tectonics* 35 (7), 1713–3174. doi:10.1002/2016tc004149

Shi, Q., He, Y., Zhao, Z., Liu, D., Harris, N., and Zhu, D-C. (2021). Petrogenesis of Himalayan Lucogranites: Perspective From a Combined Elemental and Fe-Sr-Nd Isotope Study. *JGR. Solid Earth* 126 (8), e2021JB021839. doi:10.1029/2021jb021839

Smith, M. P., and Yardley, B. W. D. (1996). The boron isotopic composition of tourmaline as a guide to fluid processes in the southwestern England orefield: An ion microprobe study. *Geochimica Geosmochimica Acta* 60 (8), 1415–2147. doi:10.1016/0016-7037(96)00007-5

Tang, J-X., Yang, H-H., Song, Y., Wang, L-Q., Liu, Z-B., Li, B-L., et al. (2021). The copper polymetallic deposits and resource potential in the Tibet Plateau. *China Geolo.* 4 (1), 1–16. doi:10.31035/cg2021016

Thomas, R., Förster, H-J., and Heinrich, W. (2003). The behaviour of boron in a peraluminous granite-pegmatite system and associated hydrothermal solutions: a melt and fluid-inclusion study. *Contrib. Mineral. Petrol.* 144 (4), 457–472. doi:10.1007/s00410-002-0410-5

Tian, S., Hou, Z., Chen, X., Tian, H., Gong, Y., Yang, Z., et al. (2020). Magnesium isotopic behaviors between metamorphic rocks and their associated leucogranites, and implications for Himalayan orogenesis. *Gondwana Rese.* 87, 23–40. doi:10.1016/j.gr.2020.06.006

Tonarini, S., Pennisi, M., Adorni-Braccesi, A., Dini, A., Ferrara, G., Gonfiantini, R., et al. (2003). Intercomparison of Boron Iiotope and Concentration Measurements. Part I: Selection, Preparation and Homogeneity Tests of the

Iltercomparison Materials. *Geostand. Geoanal. Res.* 27 (1), 21–39. doi:10.1111/j.1751-908x.2003.tb00710.x

Trumbull, R. B., and Chaussidon, M. (1999). Chemical and boron isotopic composition of magmatic and hydrothermal tourmalines from the Sinceni granite–pegmatite system in Swaziland. *Chemi. Geolo.* 153 (1–4), 125–317. doi:10.1016/s0009-2541(98)00155-7

Trumbull, R., Krienitz, M-S., Gottesmann, B., and Wiedenbeck, M. (2008). Chemical and boron-isotope variations in tourmalines from an S-type granite and its source rocks: Te Eaongo granite and tourmalinites in the Dimara Belt, Namibia. *Contrib. Mineral. Petrol.* 155 (1), 1–18. doi:10.1007/s00410-007-0227-3

Trumbull, R. B., Beurlen, H., Wiedenbeck, M., and Soares, D. R. (2013). The diversity of B-isotope variations in tourmaline from rare-element pegmatites in the Borborema Province of Brazil. *Chemi. Geolo.* 352, 47–62. doi:10.1016/j.chemgeo.2013.05.021

Trumbull, R. B., Codeço, M. S., Jiang, S-Y., Palmer, M. R., and Slack, J. F. (2020). Boron isotope variations in tourmaline from hydrothermal ore deposits: a review of controlling factors and insights for mineralizing systems. *Ore Geolo. Revi.* 125, 103682. doi:10.1016/j.oregeorev.2020.103682

van Hinsberg, V. J., Henry, D. J., and Marschall, H. R. (2011). Tourmaline: a ideal indicator of its host environment. *Tana. Mineralogist* 49 (1), 1–16. doi:10.3749/canmin.49.1.1

van Hinsberg, V. J. (2011). Preliminary experimental data on trace-element partitioning between tourmaline and silicate melt. *Tana. Mineralogist* 49 (1), 153–613. doi:10.3749/canmin.49.1.153

Veksler, I. V., and Thomas, R. (2002). An experimental study of B-P- and F-rich synthetic granite pegmatite at 0.1 and 0.2 GPa. *Contrib. Mineral. Petrol.* 143 (6), 673–863. doi:10.1007/s00410-002-0368-3

Wadoski, E. R., Grew, E. S., and Yates, M. G. (2011). Compositional evolution of tourmaline-supergroup minerals from granitic pegmatites in the Larsemann Hills, East Antarctica. *Tana. Mineralogist* 49 (1), 381–405. doi:10.3749/canmin.49.1.381

Wang, X., Zhang, J., Liu, J., Yan, S., and Wang, J. (2013). Middle-Miocene transformation of tectonic regime in the Himalayan orogen. *Chin. Sci. Bull.* 58 (1), 108–117. doi:10.1007/s11434-012-5414-6

Wang, X., Zhang, J., and Wang, J. (2016). Geochronology and Formation Mechanism of the Paiku Granite in the Northern Himalaya, and is Tectonic implications. *Earth Scie.* 41 (6), 982–998. doi:10.3799/dqkx.2016.082

Wang, X., Zhang, J., and Yang, X. (2017). Geochemical Characteristics of the Leucogranites from Gyirong, South Tibet: Formation Mechanism and Tectonic Implications. *Geotectonica et Metallogenia* 41 (2), 354–638. doi:10.16539/j.ddgzyckx.2017.02.011

Wang, Z-Z., Liu, S-A., Liu, Z-C., Zheng, Y-C., and Wu, F-Y. (2020). Extreme Mg and Zn isotope fractionation recorded in the Himalayan leucogranites. *Geochimica eosmochimica Acta* 278, 305–231. doi:10.1016/j.gca.2019.09.026

Webb, A. A. G., Guo, H., Clift, P. D., Husson, L., Müller, T., Costantino, D., et al. (2017). The Himalaya in 3D: Slab dynamics controlled mountain building and monsoon intensification. *Lithosphere* 9 (4), L636.1–51. doi:10.1130/l636.1

Wei, S-D., and Zhao, J-H. (2020). Neoproterozoic tourmaline-bearing peraluminous granitoids in the Western Jiangnan Orogen, South China: Geochemistry, petrogenesis and tectonic implications. *Precambrian Rese.* 347, 105831. doi:10.1016/j.precamres.2020.105831

Wolf, M. B., and London, D. (1997). Boron in granitic magmas: sability of tourmaline in equilibrium with biotite and cordierite. *Contributions tineralogy metrology* 130 (1), 12–30. doi:10.1007/s004100050346

Wolff, R., Hölzer, K., Hetzel, R., Xu, Q., Dunkl, I., Anczkiewicz, A. A., et al. (2022). Spatially focused erosion in the High Himalaya and the geometry of the Main Himalayan Thrust in Central Nepal (85°E) from thermo-kinematic modeling of thermochronological data in the Gyirong region (southern China). *Tectonophysics* 834, 229378. doi:10.1016/j.tecto.2022.229378

Wu, F., Liu, Z., Liu, X., and Ji, W. (2015). Himalayan leucogranite: Petrogenesis and implications to orogenesis and plateau uplift. *Acta Petrolo. Sini.* 31 (1), 1–36.

Wu, F-Y., Liu, X-C., Liu, Z-C., Wang, R-C., Xie, L., Wang, J-M., et al. (2020). Highly fractionated Himalayan leucogranites and associated rare-metal mineralization. *Lithos* 352-353, 105319. doi:10.1016/j.lithos.2019.105319

Xiang, L., Romer, R. L., Glodny, J., Trumbull, R. B., and Wang, R. (2020). Li and B isotopic fractionation at the magmatic-hydrothermal transition of highly evolved granites. *Lithos* 376-377, 105753. doi:10.1016/j.lithos.2020.105753

Xie, J., Qiu, H., Bai, X., Zhang, W., Wang, Q., and Xia, X. (2018). Geochronological and geochemical constraints on the Cuonadong leucogranite, eastern Himalaya. *Acta Geochimi.* 37 (3), 347–539. doi:10.1007/s11631-018-0273-8

Xu, Y-D., Zhang, K-X., Wang, G-C., Jiang, S-S., Chen, F-N., Xiang, S-Y., et al. (2012). Extended stratigraphy, palynology and depositional environments record the initiation of the Himalayan Gyirong Basin (Neogene China). *Jo. osian Earth Scie.* 44, 77–93. doi:10.1016/j.jseaes.2011.04.007

Xu, B., Griffin, W. L., Xiong, Q., Hou, Z. Q., O'Reilly, S. Y., Guo, Z., et al. (2017). Ultrapotassic rocks and xenoliths from South Tibet: Contrasting styles of interaction between lithospheric mantle and asthenosphere during continental collision. *Geology* 45 (1), 51–45. doi:10.1130/g38466.1

Xu, B., Hou, Z. Q., Griffin, W. L., Zheng, Y. C., Wang, T., Guo, Z., et al. (2021). Cenozoic lithospheric architecture and metallogenesis in Southeastern Tibet. *Earth-Science Revi.* 214, 103472. doi:10.1016/j.earscirev.2020.103472

Xu, B., Hou, Z. Q., Griffin, W. L., O'Reilly, S. Y., Long, T., Zhao, Y., et al. (2022). Apatite halogens and Sr–O and zircon Hf–O isotopes: recycled volatiles in Jurassic porphyry ore systems in southern Tibet. *Chemi. Geolo.* 605, 120924. doi:10.1016/j.chemgeo.2022.120924

Yang, S-Y., and Jiang, S-Y. (2012). Chemical and boron isotopic composition of tourmaline in the Xiangshan volcanic–intrusive complex, Southeast China: Evidence for boron mobilization and infiltration during magmatic–hydrothermal processes. *Chemi. Geolo.* 312-313 (0), 177–819. doi:10.1016/j.chemgeo.2012.04.026

Yang, X., Zhang, J., Qi, G., Wang, D., Guo, L., Li, P., et al. (2009). Structure and deformation around the Gyirong basin, north Himalaya, and onset of the south Tibetan detachment system. *Sci. China Ser. D-Earth. Sci.* 39 (8), 1046–5108. doi:10.1007/s11430-009-0111-2

Yang, S-Y., Jiang, S-Y., and Palmer, M. R. (2015). Chemical and boron isotopic compositions of tourmaline from the Nyalam leucogranites, South Tibetan Himalaya: Implication for their formation from B-rich melt to hydrothermal fluids. *Chemi.Geolo.* 419, 102–113. doi:10.1016/j.chemgeo.2015.10.026

Yavuz, F., Karakaya, N., Yıldırım, D. K., Karakaya, M. Ç., and Kumral, M. (2014). A Windows program for calculation and classification of tourmaline-supergroup (IMA-2011). *Compute.&eosciences* 63, 70–87. doi:10.1016/j.cageo.2013.10.012

Yin, A., and Harrison, T. M. (2000). Geologic evolution of the Himalayan-Tibetan orogen. *Annu. Rev. Earth Planet. Sci.* 28 (1), 211–820. doi:10.1146/annurev.earth.28.1.211

Yin, A. (2006). Cenozoic tectonic evolution of the Himalayan orogen as constrained by along-strike variation of structural geometry, exhumation history, and foreland sedimentation. *Earth-Science Revi.* 76 (1), 1–131. doi:10.1016/j.earscirev.2005.05.004

Yu, S-m., Ma, X-d., Hu, Y-c., Chen, W., Liu, Q-p., Song, Y., et al. (2021). Post-subdution evolution of the Northern Llasa Terrane, Tibet: Constraints from geochemical anomalies, chronology and petrogeochemistry. *China Geolo.* 5 (1), 84–95. doi:10.31035/cg2021045

Zhang, Y., Yin, C., Davis, D. W., Li, S., Qian, J., Zhang, J., et al. (2022). Mechanism of crustal thickening and exhumation of southern Lhasa terrane during the Late Cretaceous: Evidence from high-pressure metamorphic rocks of the Eastern Himalayan Syntaxis. *GSA Bulle.* doi:10.1130/b36366.1

Zhao, H-D., Zhao, K-D., Palmer, M. R., and Jiang, S-Y. (2019). *In-situ*elemental and boron isotopic variations of tourmaline from the Sanfang granite, South China: Insights into magmatic-hydrothermal evolution. *Chemi. Geolo.* 504, 190–204. doi:10.1016/j.chemgeo.2018.11.013

Zhao, H-D., Zhao, K-D., Palmer, M. R., Jiang, S-Y., and Chen, W. (2021a). Magmatic-Hydrothermal Mineralization Processes at the Yudong Ttn Deposit, South China: Insights from In Situ Chemical and Boron Isotope Changes of Tourmaline. *Econo. Geolo.* 116 (7), 1625–4167. doi:10.5382/econgeo.4868

Zhao, K-D., Zhang, L-H., Palmer, M. R., Jiang, S-Y., Xu, C., Zhao, H-D., et al. (2021b). Chemical and boron isotopic compositions of tourmaline at the Dachang Sn-polymetallic ore district in South China: Constraints on the origin and evolution of hydrothermal fluids. *Mine Depos.* 56, 1589–6108. doi:10.1007/s00126-021-01045-4

Zhao, Z-b., Li, C., and Ma, X-x. (2021c). How does the elevation changing response to crustal thickening process in the central Tibetan Plateau since 120 Ma?. *China Geolo.* 4 (1), 32–43. doi:10.31035/cg2021013

Zheng, B., and Chen, M. (2021). Gem Elbaite as a Recorder of Pigmatite Evolution: *In situ* Major, Trace Elements and Boron sotope Analysis of a Colour-Zoning Tourmaline Crystal. *Crystals* 11, 1363. doi:10.3390/cryst11111363

Zhou, Q., Wenchang, L., Wang, G., Liu, Z., Lai, Y., Huang, J., et al. (2019). Chemical and boron isotopic composition of tourmaline from the Conadong leucogranite-pegmatite system in South Tibet. *Lithos* 326-327, 529–359. doi:10.1016/j.lithos.2019.01.003

frontiers | Frontiers in Earth Science

TYPE Original Research
PUBLISHED 02 February 2023
DOI 10.3389/feart.2023.1118118

OPEN ACCESS

EDITED BY
Qiuming Pei,
Southwest Jiaotong University, China

REVIEWED BY
Himan Shahabi,
University of Kurdistan, Iran
Shaohua Zhao,
Ministry of Ecology and Environment Center for Satellite Application on Ecology and Environment, China
Salim Heddam,
University of Skikda, Algeria

*CORRESPONDENCE
Shan Zhao,
475283764@qq.com

SPECIALTY SECTION
This article was submitted to Structural Geology and Tectonics, a section of the journal Frontiers in Earth Science

RECEIVED 07 December 2022
ACCEPTED 20 January 2023
PUBLISHED 02 February 2023

CITATION
Guo H, Dai W, Zhang R, Zhang D, Qiao B, Zhang G, Zhao S and Shang J (2023), Mineral content estimation for salt lakes on the Tibetan plateau based on the genetic algorithm-based feature selection method using Sentinel-2 imagery: A case study of the Bieruoze Co and Guopu Co lakes. *Front. Earth Sci.* 11:1118118. doi: 10.3389/feart.2023.1118118

Mineral content estimation for salt lakes on the Tibetan plateau based on the genetic algorithm-based feature selection method using Sentinel-2 imagery: A case study of the Bieruoze Co and Guopu Co lakes

Hengliang Guo[1], Wenhao Dai[2], Rongrong Zhang[2], Dujuan Zhang[1], Baojin Qiao[2], Gubin Zhang[3], Shan Zhao[2]* and Jiandong Shang[1]

[1]National Supercomputing Center in Zhengzhou, Zhengzhou University, Zhengzhou, China, [2]School of Geoscience and Technology, Zhengzhou University, Zhengzhou, China, [3]Henan Geological Research Institute, Zhengzhou, China

Salt lakes on the Tibetan Plateau (TP) are rich in lithium (Li), boron (B) and other mineral resources, and accurate assessment of the mineral content and spatial distribution of the brine in those salt lakes is important to guide the development and utilization of their mineral resources. There are few studies estimating the mineral content of salt lakes on the TP due to the lack of *in situ* investigation data. This study introduced an intelligent prediction model combining a feature selection algorithm with a machine learning algorithm using Sentinel-2 satellite data to estimate the Li, B, and TDS contents of Bieruoze Co and Guopu Co lakes on the TP. First, to enrich the spectral information, four mathematical transformations (reciprocal, logarithmic, reciprocal of logarithm, and first-order derivative) were applied to the original bands. Then, feature selection was performed using the genetic algorithm (GA) to select the optimal input variables for the model. Finally, prediction models were constructed by partial least squares regression (PLSR), multiple linear regression (MLR), and random forest (RF). The results showed that: 1) The spectral mathematical transformation provided rich spectral information for the mineral content estimation. 2) The performance of the estimation model constructed by the feature optimization method using GA was better than that of the estimation model constructed based on all spectral bands. Based on GA for feature optimization, the MAPE of GA-RF for estimating Li, B and TDS contents on the testing set was reduced by 77.52%, 28.54% and 36.79%, respectively. 3) Compared with the GA-MLR and GA-PLSR models, GA-RF estimated Li (R^2=0.99, RMSE=1.15 mg L^{-1}, MAPE=3.00%), B (R^2=0.97, RMSE=10.65 mg L^{-1}, MAPE=2.73%), and TDS (R^2=0.93, RMSE=0.60 g L^{-1}, MAPE=1.82%) all obtained the optimal performance. This study showed that the combination of the GA-based feature selection method and the RF model has excellent performance and applicability for monitoring the content of multiple minerals using Sentinel-2 imagery in salt lakes on the TP.

KEYWORDS

mineral content, salt lake, Tibetan plateau, Sentinel-2, random forest, genetic algorithm, feature selection

1 Introduction

The Tibetan Plateau (TP), known as the "Water Tower of Asia", is rich in lake resources, most of which are saltwater lakes and saline lakes (Ma et al., 2011; Liu et al., 2021; Qiao et al., 2021). The brine of salt lakes is not only high in salinity but also rich in potassium, magnesium, lithium (Li), boron B), uranium and other salt resources, which have high development potential and strategic value. With the advancement of Li battery technology, Li has gained notoriety as a strategic asset. Li brine resources are abundant in China, which has the third-largest Li reserves in the world. Li brines are primarily found on the TP. Due to the growing demand and the lower production cost of Li extraction from brines, the technology for Li extraction from salt lake brines has received much attention (He et al., 2020; Zhang et al., 2022). B is a crucial essential raw ingredient for the production of ceramics, detergents, fertilizers, and glass. Salt lake brines account for 80% of the world's Li and 25% of its B salt production (Kong et al., 2021). Total dissolved solids (TDS) reflect the overall content of anions and cations in salt lakes. The TP is relatively minimally influenced by humans, and changes in brine mineral content are mainly affected by natural conditions. In recent years, due to climate change and other factors, some salt lakes on the TP have shown varying degrees of lake desalination and decreases in brine mineral content (Yan and Zheng, 2015). Investigation and monitoring of the mineral content of salt lakes can provide an important theoretical basis for the study of the mineralization law, mineralization mechanism, and geological survey of salt lakes in the TP region (Ding et al., 2022).

Traditional monitoring methods involve conducting field sampling and laboratory analysis. However, owing to the extreme natural environment of the TP and the poor accessibility of some salt lakes, traditional methods cannot reflect the spatial distribution of the mineral content in salt lakes as a whole. The use of remote sensing to estimate water parameters has been used in salt lakes (Wang et al., 2015; Wang et al., 2021), estuaries (Geiger et al., 2013; Fang et al., 2017), seas (Chen and Hu, 2017), inland freshwater lakes (Bayati and Danesh-Yazdi, 2021; Li et al., 2022) and other regions. Compared with traditional measures, the use of satellite remote sensing to monitor mineral content has the advantages of a large range, long duration, and periodicity (Sun et al., 2022), which overcome the shortcomings and limitations of traditional methods. Remote sensing technology can be used to quickly and accurately search for areas with high mineral content in the salt lake and to fully grasp the spatial distribution and changes in resources, thus scientifically guiding the development and production of mineral resources in the salt lake. The multispectral satellite data have high spatial resolution and are suitable for mineral content studies of salt lakes on the TP. Sentinel-2 is a multispectral satellite with publicly available free data that is commonly used for hydrological remote sensing studies (Miles et al., 2017; Marinho et al., 2021).

The models commonly used for hydrological remote sensing are multiple linear regression (MLR) (Chen and Hu, 2017), partial least squares regression (PLSR) (Song et al., 2013; Cao et al., 2018), random forest (RF) models (Hafeez et al., 2019; Cao et al., 2020; Maier et al., 2021; Sun et al., 2022), and artificial neural network models (Bayati and Danesh-Yazdi, 2021). Due to the lack of actual measurement data, there are few studies on the estimation of Li, B, and TDS contents of salt lakes on the TP. The available studies estimated the mineral content of the salt lake mainly through empirical and machine learning models. For example, Zhang et al. (2007) used the ratio method and principal component analysis to reveal the spatial distribution pattern of boron oxide content in Zabuye Salt Lake. This method is easy to implement, but the estimation accuracy is low. The second approach used machine learning algorithms to construct estimation models. For example, Zhou et al. (2016) used an adaptive band selection method to determine the optimal band combination and a BP neural network algorithm to construct an inversion model for the ion content of the salt lake. Liu et al. (2021) used the LightGBM algorithm to invert the Li content of the Zabuye salt lake. Machine learning methods have been shown to be a better way to address complex problems without prior knowledge (Saberioon et al., 2020), and machine learning methods can address non-linear and other complicated regression issues. Therefore, machine learning models also have great potential for mineral content estimation in salt lakes.

Wang (2019) performed mathematical transformations such as logarithmic transformation and first-order differential transformation on Sentinel-2 data and predicted the Li content of Alisallo salt lake, and the results showed that spectral transformation played an important role in the prediction model. Spectral transformation has been proven to be an effective spectral preprocessing method. The spectral mathematical transformation can enrich the spectral information and extract information that is more sensitive than the original spectrum, thus improving the accuracy of the prediction model (Wang et al., 2022). In remote sensing inversion studies, input irrelevant bands can affect the accuracy of the model and even lead to overfitting. The spectral feature band selection method can improve the prediction of the model, effectively eliminate redundant information and retain valid information. The above study on mineral content estimation of salt lakes used principal component analysis for data dimensionality reduction work. The principal component analysis, as a heuristic feature selection method, is simple to operate but cannot handle the complex relationships between input and output variables. Meta-heuristic algorithms avoid these limitations. The genetic algorithm (GA) is a meta-heuristic intelligent algorithm based on natural selection and genetics (Katoch et al., 2021). Sun et al. (2022) used the GA for band selection and used the chosen bands and PLSR to estimate the soil organic matter content. Shekofteh and Masoudi (2019) designed an algorithm combining the GA with the artificial neural network (ANN) to select five soil properties that have the most influence on soil quality indicators. The GA has now been used to solve optimization problems in many fields, including feature selection (Cao et al., 2018). So far, the GA has not been applied to the study of the estimation of minerals in salt lakes. Based on this, our innovation is to use the GA for feature selection and machine learning models to estimate the mineral content.

Current studies on mineral content estimation of salt lakes on the TP have focused on Zabuye Salt Lake (Tian et al., 2005; ZHANG et al., 2007; Xu et al., 2017; Liu et al., 2021). It is necessary to investigate and survey other salt lakes on the TP using remote sensing technology and machine learning algorithms. This study investigates the feasibility of a strategy combining feature selection based on the GA and machine learning in estimating the content of multiple minerals in salt lakes, and provides an application example and theoretical support for future assessment and monitoring of mineral resources in salt lakes on the TP. In this work, we proposed an intelligent method for estimating the Li, B, and TDS contents of salt lakes on the TP using Sentinel-2 imagery and *in situ* data from two typical salt

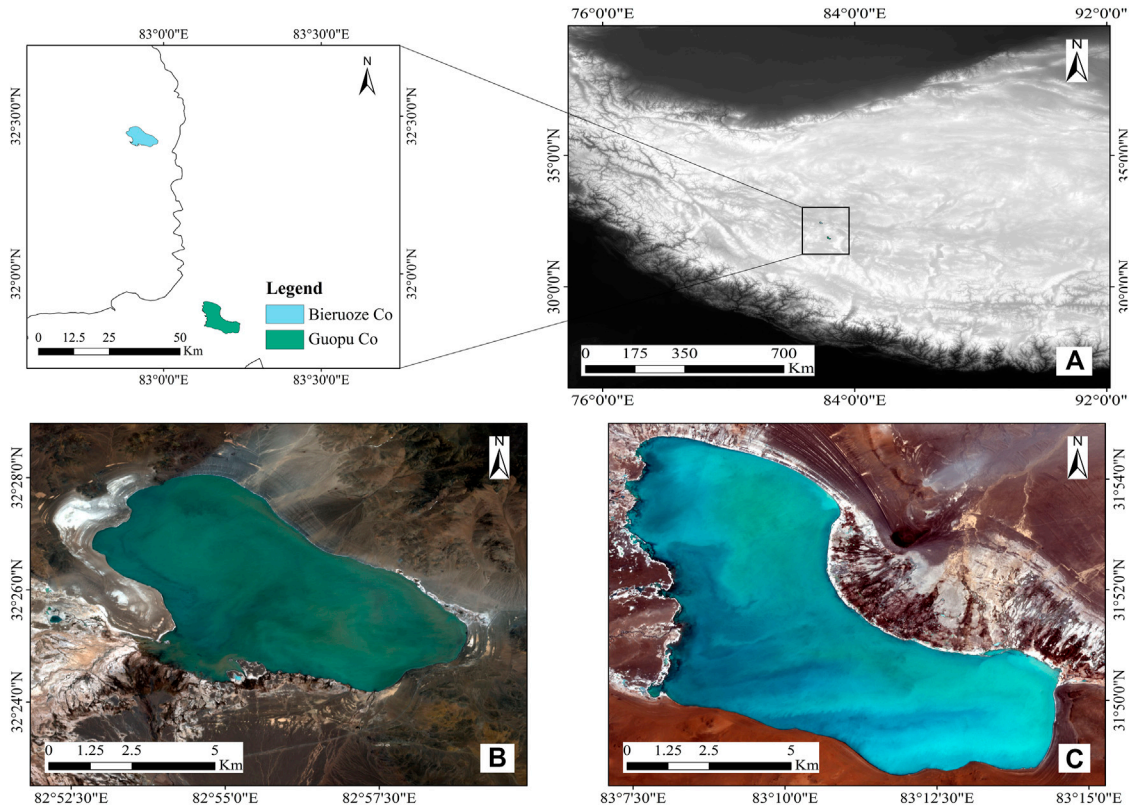

FIGURE 1
Location of the research region. **(A)** Topographic map of the TP. **(B)** and **(C)** are the Sentinel-2 imagery of Bieruoze Co and Guopu Co, respectively, in May 2018.

lakes. 1) The feature bands were constructed by mathematical transformations, which can enhance the spectral information and raise the predictive model's accuracy. 2) Using the GA for feature band selection, the best input band combination was intelligently selected. 3) PLSR, MLR, and RF models were constructed using the optimal band combination, and the accuracy of the three models was contrasted. 4) The best estimation model was used to monitor and map the mineral content of the salt lakes.

2 Study area and data

2.1 Study area

The research area is made up of two lakes, Bieruoze Co and Guopu Co, and is situated in the southeastern Ali region of the TP (Figure 1). Based on the results of the 2018 field survey, Bieruoze Co is located at 32°24′-32°28′N, 82°52′-82°59′E, with an altitude of 4,400 m. The lake is approximately 9.6 km long from east to the west and 4.8 km wide, with a surface area of 36 km^2 and an average water depth of 3.3 m. Guopu Co is located at 31°49′-31°55′N, 83°7′-83°15′E, with an altitude of 4,700 m. The east–west length of the lake is approximately 14 km, it is approximately 5.9 km at its widest point, its surface area is approximately 61 km^2, and its average water depth is 2.8 m.

Bieruoze Co and Guopu Co are both salt lakes, blue in color, and are non-discharge lakes without outlets. The lake water is colorless, odorless, salty, and transparent. The lake contains a large number of brine worms, and the soluble mineral salts in the area around the lake constantly converge in the lake through surface runoff. The dynamic changes in the lake are barely affected by human activities, mainly relying on atmospheric precipitation, snow and ice melt and spring recharge; the discharge relies on strong evaporation.

2.2 *In situ* data

In May-June 2018, field measurements of the Li, B, and TDS contents of Bieruoze Co and Guopu Co were conducted. According to the "salt lake and salt mineral geological survey specification", the surface area of Bieruoze Co was between 10 and 50 km^2, the observation network degree was 2 km, and the point distance was 1–2 km; the surface area of Guopu Co was between 50 and 100 km^2, the observation network degree was 2–4 km, and the point distance was 2 km. To obtain more sample data, the observation network and sampling point spacing were established at 2 km × 1 km intervals, and the local sampling point spacing was set to 0.5 km. Figure 2 depicts the locations of the 32 sampling points in Bieruoze Co and the 50 sampling points in Guopu Co. Water samples were collected at a depth of 0.2 m from the lake surface using a 0.55 L polyethylene water bottle, and all samples were forwarded to the laboratory for analysis.

Table 1 displays the maximum, minimum, mean, standard deviation (SD) and coefficient of variation (CV) of the measured values at all sampling points. The measured data show that the two salt

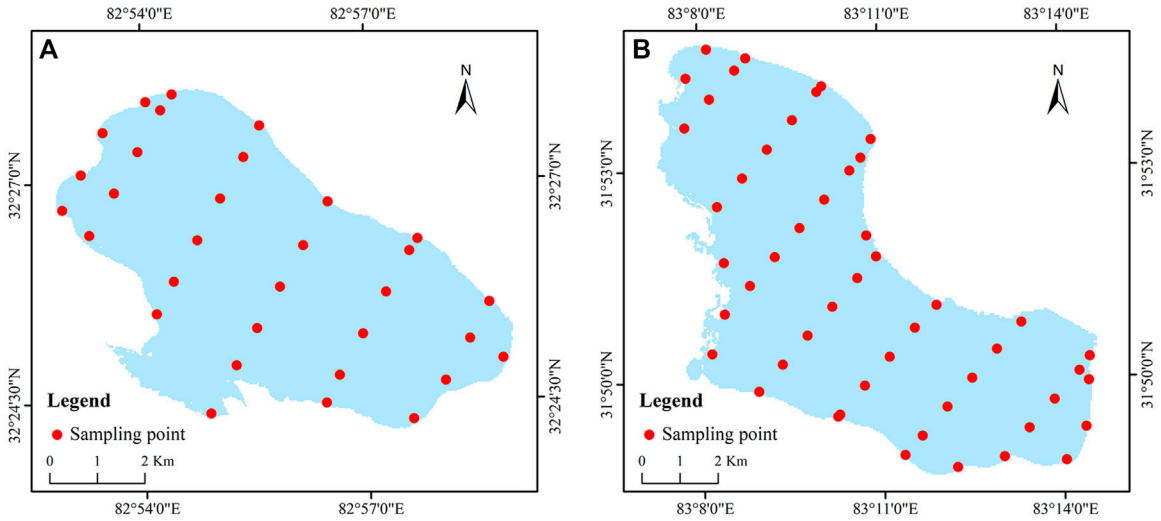

FIGURE 2
The spatial distribution of sampling points. **(A)** Bieruoze Co. **(B)** Guopu Co.

TABLE 1 Statistical information on the measured values of all the sampling points of Bieruoze Co and Guopu Co.

Lake name	Measured plots	Parameters	Max value	Min value	Mean value	SD	CV
Bieruoze Co	32	Li ($mg{\cdot}L^{-1}$)	44.35	36.84	41.71	1.79	0.04
		B ($mg{\cdot}L^{-1}$)	232.48	194.23	222.66	7.70	0.03
		TDS ($g{\cdot}L^{-1}$)	23.43	19.61	22.21	0.92	0.04
Guopu Co	50	Li ($mg{\cdot}L^{-1}$)	10.06	8.18	9.37	0.37	0.04
		B ($mg{\cdot}L^{-1}$)	358.46	302.95	338.52	11.84	0.04
		TDS ($g{\cdot}L^{-1}$)	28.14	25.20	26.90	0.73	0.03

lakes, Bieruoze Co and Guopu Co, are rich in Li, B and TDS resources. The variation in Li content in Bieruoze Co Lake ranged from 36.84 to 44.35 mg L^{-1}, with an average content of 41.71 mg L^{-1}. The concentration of B was greater than that of Li, with the variation in B content ranging from 194.23 to 232.48 mg L^{-1}, with an average content of 222.66 mg L^{-1}. The variation in TDS content ranged from 19.61 to 23.43 g L^{-1}, with an average content of 22.21 g L^{-1}. The Li content of Guopu Co was lower than that of Bieruoze Co, and the B and TDS concentrations were higher than those of Bieruoze Co. The variation in Li content was small, ranging from 8.18 to 10.06 mg L^{-1}, with an average content of 9.37 mg L^{-1}. The variation in B content ranged from 302.95 to 358.46 mg L^{-1}, with an average of 338.52 mg L^{-1}. The variation in TDS content ranged from 25.20 to 28.14 g L^{-1}, with an average of 26.90 g L^{-1}.

We used 82 sampling points data from two salt lakes to construct the model, 70% were randomly selected as the training dataset, and 30% were selected as the testing dataset. The number of samples in the training dataset was 57 (including 22 from Bieruoze Co and 35 from Guopu Co); the number of samples in the test dataset was 25 (including 10 from Bieruoze Co and 15 from Guopu Co). To ensure comparability among the tested models, the training and testing sets of each model were identical.

2.3 Satellite data and preprocessing

Sentinel-2 is a high-resolution multispectral imaging satellite with an orbital altitude of 786 km. Sentinel-2 carries a multispectral instrument covering 13 bands from visible to shortwave infrared with a maximum spatial resolution of 10 m. The revisit period is 10 days for a single satellite and 5 days for two complementary satellites (Sentinel-2A/B). Sentinel-2 data were obtained from the Copernicus Data Centre of the European Space Agency (https://scihub.copernicus.eu/). To obtain more accurate experimental results, the satellite data time needs to be as close as possible to the *in situ* measurement time, and there should be no clouds covering the lake, so we selected Sentinel-2 satellite image data from May 2018. We used the Sen2Cor processing tool for atmospheric correction to obtain the Level-2A products, resampled all spectral band images to a 10 m resolution, and finally extracted the lake extent using the normalized difference water body index (NDWI) (Gao, 1996; Liu et al., 2019).

$$NDWI = (Green - NIR)/(Green + NIR) \quad (1)$$

where Green denotes the B_3 band of Sentinel-2 and NIR denotes the B_8 band of Sentinel-2.

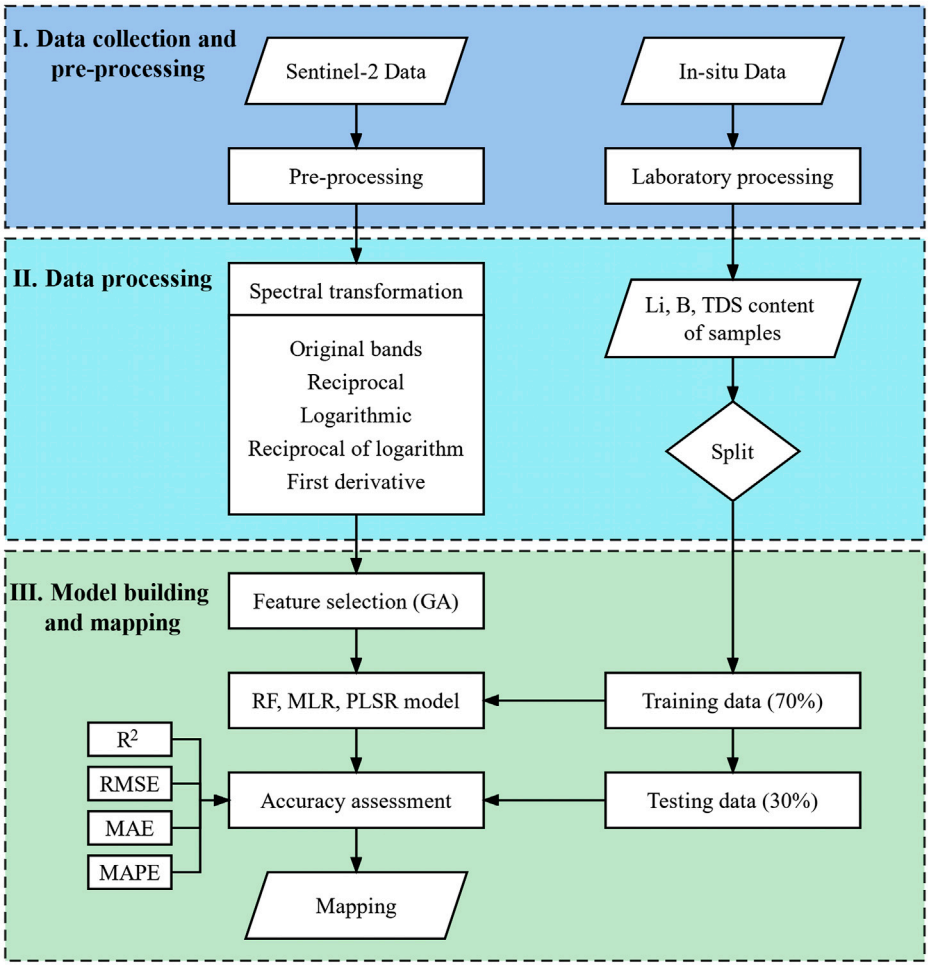

FIGURE 3
Flow chart.

3 Methods

The methodology used in this study is shown in Figure 3. In the first step, we collected *in situ* data from two salt lakes on the TP, including Li, B, and TDS contents. Sentinel-2 data of the corresponding periods were obtained and pre-processed. In the second step, the spectral bands of Sentinel-2 were processed by mathematical transformations, including reciprocal transformation (RT), logarithmic transformation (LT), reciprocal of logarithm (RL), and first-order derivative (FD). The sample data were randomly divided into the training set and testing set. In the third step, firstly, the spectral bands obtained after the mathematical transformation in the second step and the original bands were put into the GA for spectral feature selection. The GA adaptively selected the feature bands according to the fitness function. Subsequently, the feature bands obtained by GA screening were used as input variables of RF, MLR, and PLSR models to construct estimation models. Finally, the performance of the three estimation models was evaluated using the evaluation function, and the optimal model was used for the mineral content estimation of the two salt lakes.

3.1 Spectral feature transformation

First-order derivative transformation is a common preprocessing method for hyperspectral data that is capable of extracting more delicate spectral data than the original spectrum and has been widely used for water quality parameter estimation (Wang et al., 2022) and soil parameter estimation (Wang et al., 2021). The introduction of spectral derivative transformation into multispectral images can further exploit the differences between spectral data to retrieve valuable information and thus improve the accuracy of prediction models (Wang et al., 2021). The spectral mathematical transformation allows the extraction of hidden features of water body spectra and the effective use of differences in spectral data to estimate different water body parameters.

We used the reciprocal transformation (RT), logarithmic transformation (LT), reciprocal of logarithm (RL), and first-order derivative (FD) for the Sentinel-2 spectrum.

$$RT(B_i) = 1/(B_i) \quad (2)$$

$$LT(B_i) = Ln(B_i) \quad (3)$$

$$RL(B_i) = 1/Ln(B_i) \quad (4)$$

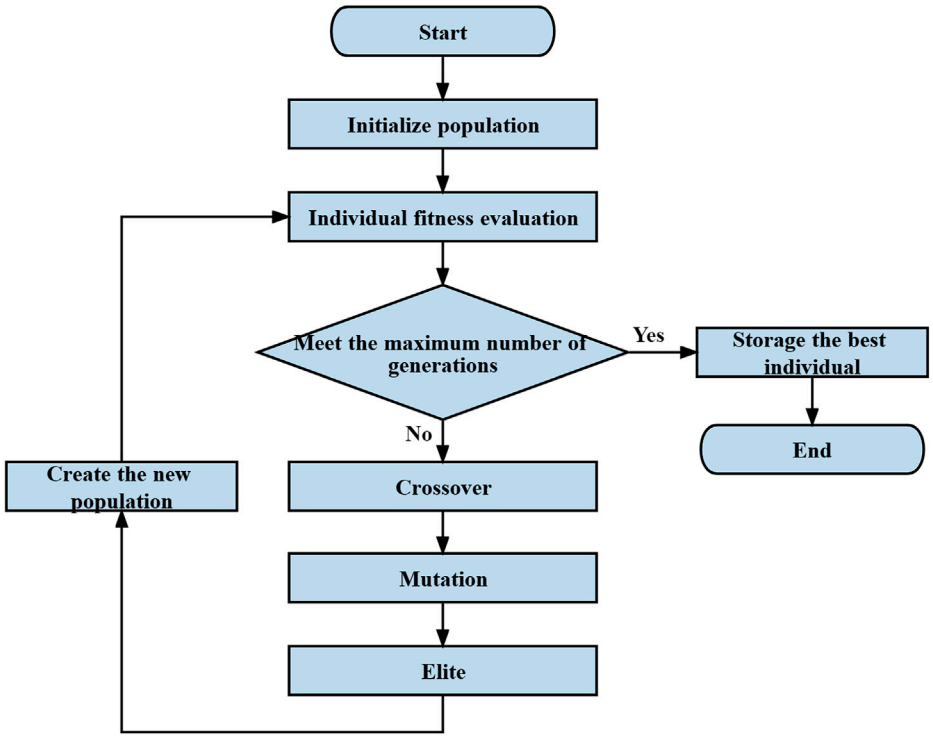

FIGURE 4
Flow chart of GA.

$$FD(B_i) = \frac{B_{(i+1)} - B_i}{\lambda_{i+1} - \lambda_i} \quad (5)$$

where B_i denotes a single band of Sentinel-2 and λ_i denotes the central wavelength. In this study, the above four transformations and the untreated original spectral bands (OR) are used as input variables for the estimation model.

3.2 Feature optimization using GA

The number of input variables for machine learning models can have a considerable impact on how accurate the prediction model is; extraneous variables complicate the structure of the prediction model and increase the number of calibration parameters, which confounds training (Bayati and Danesh-Yazdi, 2021). Additionally, keeping useless bands raises the computational cost (Han et al., 2022). To avoid these problems, we used the GA to determine the best combination of bands for predicting mineral contents.

The GA is a metaheuristic global optimization algorithm that has been used to solve spectral subset selection problems. The GA was designed and proposed based on evolutionary laws of organisms in nature (Abba et al., 2022), and it is founded on the ideas of natural selection and evolution, applying the concepts of superiority and inferiority to find optimal solutions to optimization problems (Li et al., 2015). As a non-deterministic method of choosing variables (Tiyasha et al., 2021), the GA finds the best combination of bands by the following steps.

1. Initialize the population: Spectral variables are encoded as binary data, with 0 and 1 as individuals, and a population consists of multiple individuals.
2. Selection: According to the fitness function, suitable parents are chosen, with individuals with greater fitness levels having a larger chance of being chosen.
3. Crossover: Genetic exchange between individuals of the parental generation produces two new offspring individuals.
4. Mutation: Random variation in the individual for a particular gene value.

The above process simulates the stages of natural evolution, leading to the creation of generations that are more suited. The flow chart of the GA is demonstrated in Figure 4.

3.3 Model construction

3.3.1 RF model

RF is a machine learning technique based on decision trees for classification and regression. The basic unit of the RF is a decision tree, and several decision trees are created during the training process. Each decision tree creates a number of weak classifiers for local learning using randomly chosen samples and characteristics and then combines them to create a powerful global classifier. The final output is the mean of the predicted values for each decision tree (Wang et al., 2022). RF reflects the non-linear regression relationship between water parameters and spectral data without the need to explicitly know their functional correlation. RF has the advantage of a strong ability to handle multidimensional data and avoid overfitting.

The RF model is run in Python 3.7, and the hyperparameters are determined by a “grid search” strategy.

3.3.2 PLSR model

A multivariate regression technique called PLSR combines the benefits of principal component analysis with those of standard correlation analysis (Wold et al., 2001; Cao et al., 2018). PLSR compresses the input data matrix by choosing consecutive orthogonal elements to maximize the covariance between Y (water body parameters) and X (spectral bands) (Zhu et al., 2022). It successfully addresses the issue of multicollinearity between spectral data and maintains accurate predictions even with few samples (Xie et al., 2022).

3.3.3 MLR model

MLR is the most widely used linear regression method (Hestir et al., 2015). MLR attempts to fit the relationship between multiple independent variables and dependent variables through a linear equation (Abba et al., 2017). Although MLR has lower predictive accuracy than machine learning-based models, it can be easily interpreted (Nemati et al., 2015).

3.4 Accuracy evaluation

Four evaluation metrics are used to assess the estimation effectiveness of the models, namely, the coefficient of determination (R^2), root mean square error (RMSE), mean absolute error (MAE) and mean absolute percentage error (MAPE). R^2 is a metric for how well a model matches the data and illustrates the model's capacity for prediction, so the best model can be selected based on R^2. Usually, an R^2 value closer to one indicates a more robust model. RMSE is used to evaluate the deviation between the estimated and true values, and MAE and MAPE metrics are used to measure the closeness of the estimated values to the true data. The smaller the RMSE, MAE, and MAPE are, the better the predictive performance of the model (Wagle et al., 2019). The following is the calculation for these metrics:

$$R^2 = \frac{\sum_{i=1}^{n}(P_i - \bar{M}_i)^2}{\sum_{i=1}^{n}(M_i - \bar{M}_i)^2} \quad (6)$$

$$RMSE = \sqrt{\frac{1}{n}\sum_{i=1}^{n}(M_i - P_i)^2} \quad (7)$$

$$MAE = \frac{1}{n}\sum_{i=1}^{n}|(M_i - P_i)| \quad (8)$$

$$MAPE = \frac{100\%}{n}\sum_{i=1}^{n}\left|\frac{M_i - P_i}{Mi}\right| \quad (9)$$

where M_i is the *in situ* data, P_i is the predicted value, $\bar{M}$ is the average of the *in situ* data.

4 Results

4.1 Mineral content prediction model results

4.1.1 Modeling results without feature selection

Before constructing the prediction model using feature selection, we used the OR and all four transformed spectral bands as the input bands and the Li, B, and TDS contents as the dependent variables to build the PLSR, MLR, and RF prediction models. Table 2 lists the modeling results for all bands. The PLSR model estimated R^2 and MAPE values of 0.81% and 38.93% for Li, 0.82% and 6.29% for B, and 0.70% and 4.11% for TDS, respectively, for the testing set. The RF model estimated R^2 and MAPE values of 0.91% and 13.33% for Li, 0.88% and 3.82% for B, and 0.87% and 2.88% for TDS, respectively, for the testing set. By comparing these two models, the estimation performance of the RF model was higher than that of the PLSR model. In addition, the MLR model performed poorly in estimating the three mineral contents (MAPE >30%), possibly due to too many independent variables. Using all the bands to build the estimation model does not achieve satisfactory results. In addition, redundant bands increase the cost of model training and reduce the model accuracy. Therefore, this study used the strategy of spectral feature band selection to solve these problems and improve the model prediction accuracy.

4.1.2 Results of the prediction model based on GA feature optimization

The GA-PLSR, GA-MLR, and GA-RF models were constructed based on the GA for feature selection. The number of generations of the GA was 500, and the number of populations was 50. The model accuracy evaluation is shown in Table 3. In all the models, the accuracy of the training was higher than that of the testing, which indicated that all the models were not overfitted.

From the modeling results, the performance of all three models built based on the GA for feature band selection was better than that of the models constructed based on all bands. The model performance for estimating three mineral contents was the GA-RF > GA-MLR > GA-PLSR. The plots of the predicted *versus* measured contents of the models obtained using the GA-PLSR, GA-MLR, and GA-RF are shown in Figure 5, Figure 6, Figure 7. Table 4 showed the 17, 20, and 17 feature bands selected by GA for use in the GA-RF model. The GA-RF model estimated Li (R^2=0.99, RMSE=1.15 mg L^{-1}, MAE=0.78 mg L^{-1}, MAPE=3.00%); B (R^2=0.97, RMSE=10.65 mg L^{-1}, MAE=7.91 mg L^{-1}, MAPE=2.73%); TDS (R^2=0.93, RMSE=0.60 g L^{-1}, MAE=0.46 g L^{-1}, MAPE=1.82%) all achieved the best performance.

Figure 8 displays the spatial distribution of the MAPE for the three mineral contents that were estimated using the GA-RF model. Overall, the sampling point errors for model training were smaller than those for model testing. The MAPE values of the three mineral contents estimated in Bieruoze Co ranged from 0.04% to 8.38% (Li), 0.01%–12.97% B), and 0.06%–6.22% (TDS); the average MAPEs were 2.29% (Li), 1.67% B), and 1.58% (TDS). The MAPE for the three mineral contents estimated at Guopu Co ranged from 0.02% to 8.76% (Li), 0.04%–5.56% B), and 0.08%–5.65% (TDS); the mean MAPE were 1.74% (Li), 1.62% B), and 1.31% (TDS).

4.2 Mapping of the spatial distribution of mineral content

We mapped the geographic distribution of Li, B, and TDS contents in Bieruoze Co and Guopu Co using the GA-RF model and Sentinel-2 imagery (Figure 9). The variation in the three mineral contents in Bieruoze Co ranged from 33.93 to 43.46 mg L^{-1} (Li), 201.43–250.37 mg L^{-1} B), and 20.29–23.78 g L^{-1} (TDS). The distribution of Li content in the northwest was high, and that in the southeast was low; the spatial distribution of B content was relatively uniform; and the TDS content in the west was slightly higher than that in the east. The variation in the three minerals in

TABLE 2 Results of estimation models based on all spectral bands.

		Training				Testing			
		R^2	RMSE	MAE	MAPE	R^2	RMSE	MAE	MAPE
Li	MLR	0.67	9.13	2.89	22.63	0.66	9.16	6.95	47.35
	PLSR	0.89	5.27	4.42	35.60	0.81	6.90	4.98	38.93
	RF	0.99	1.15	0.54	3.50	0.91	4.81	1.97	13.33
B	MLR	0.38	77.68	33.27	11.50	0.19	142.67	108.37	37.45
	PLSR	0.87	20.27	15.77	5.33	0.82	24.79	17.59	6.29
	RF	0.97	9.51	6.92	2.40	0.88	20.29	11.61	3.82
TDS	MLR	0.28	13.10	5.76	22.63	0.16	13.34	10.97	43.71
	PLSR	0.77	1.18	0.92	3.77	0.70	1.25	1.05	4.11
	RF	0.92	0.71	0.44	1.79	0.87	0.84	0.71	2.88

TABLE 3 Performance of the estimation model based on the feature selection method.

		Training				Testing			
		R^2	RMSE	MAE	MAPE	R^2	RMSE	MAE	MAPE
Li	GA-PLSR	0.91	4.75	3.78	28.81	0.87	5.66	3.94	28.85
	GA-MLR	0.98	2.15	1.52	9.64	0.93	4.15	2.30	13.75
	GA-RF	0.99	0.60	0.32	1.50	0.99	1.15	0.78	3.00
B	GA-PLSR	0.89	18.79	14.67	5.03	0.85	22.69	14.87	5.57
	GA-MLR	0.96	11.27	8.29	2.88	0.91	18.00	11.39	4.00
	GA-RF	0.99	4.30	3.40	1.16	0.97	10.65	7.91	2.73
TDS	GA-PLSR	0.80	1.11	0.84	3.48	0.77	1.10	0.88	3.48
	GA-MLR	0.89	0.81	0.64	2.65	0.86	0.87	0.67	2.70
	GA-RF	0.97	0.43	0.30	1.24	0.93	0.60	0.46	1.82

Guopu Co ranged from 8.51 to 9.93 mg L^{-1} (Li), 305.01–353.23 mg L^{-1} B), and 24.31–27.61 g L^{-1} (TDS); the three minerals were high in the north and east of Guopu Co.

5 Discussion

5.1 Advantages of spectral feature transformation

In this study, spectral transformation had a significant part in estimating the mineral content of salt lakes on the TP. Li, B, and TDS, as non-optically active substances, have more complex optical properties (Alparslan et al., 2009). We mathematically transformed the Sentinel-2 spectral band using four methods: RT, LT, RL, and FD. The correlation coefficient plots were obtained by analyzing the Pearson correlations of Li, B, and TDS contents and different spectral variables (Figure 10). For Li, the correlation coefficients of the original reflectance (OR) and LT spectra with Li content were negative, the correlation coefficients of the RL spectra with Li content were positive, and the correlation coefficients of RT and FD with Li content were alternately positive or negative. For B, the correlation coefficients of the OR and LT bands with B were all positive, the correlation coefficients of RL with B content were all negative, and the correlation coefficients of RT and FD with Li content were alternately positive or negative. The trends of the correlation coefficients of the spectra with TDS content and B content were basically the same. The correlations of the RT-, LT-, RL-, and FD-treated spectra with Li, B, and TDS were all improved to different degrees compared to the OR, and the bands with the highest correlations were all RTB_1 (Li = 0.93, B = −0.93, TDS = −0.84). RT showed the highest correlations, followed by LT and OR. The results suggested that the mathematical transformation of the spectra can significantly reduce the negative effects in the spectra, enhance the small fluctuations in the reflectance spectral features, enrich the spectral details of images, highlight spectral features, and provide effective information for prediction models.

5.2 Advantages of the GA-RF model

The GA-RF model has two advantages, the first one is the advantage of using the GA for feature optimization extraction, and the second one is the advantage of the RF model.

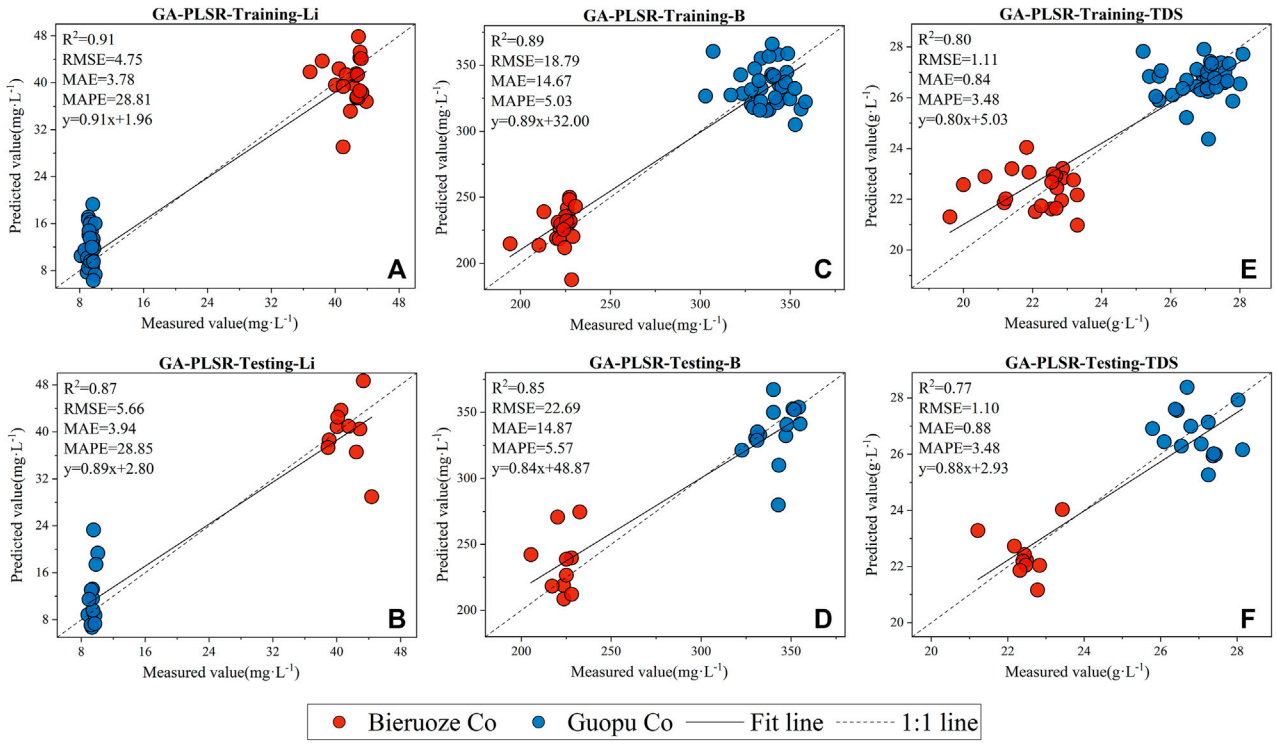

FIGURE 5
Fitting of measured and predicted values using GA-PLSR models. Estimated Li contents based on the training **(A)** and testing **(B)**. Estimated B contents based on the training **(C)** and testing **(D)**. Estimated TDS content during training **(E)** and testing **(F)**.

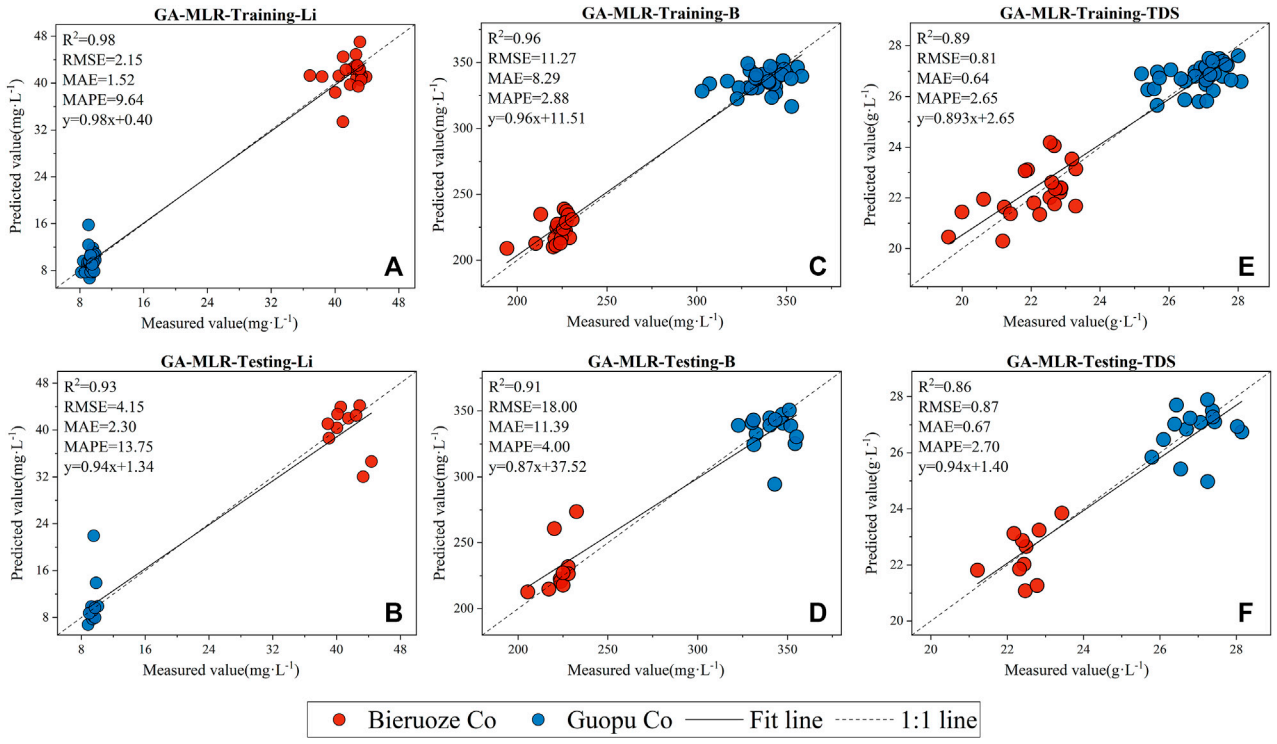

FIGURE 6
Fitting of measured and predicted values using GA-MLR models. Estimated Li content based on the training **(A)** and testing **(B)**. Estimated B content based on the training **(C)** and testing **(D)**. Estimated TDS content based on the training **(E)** and testing **(F)**.

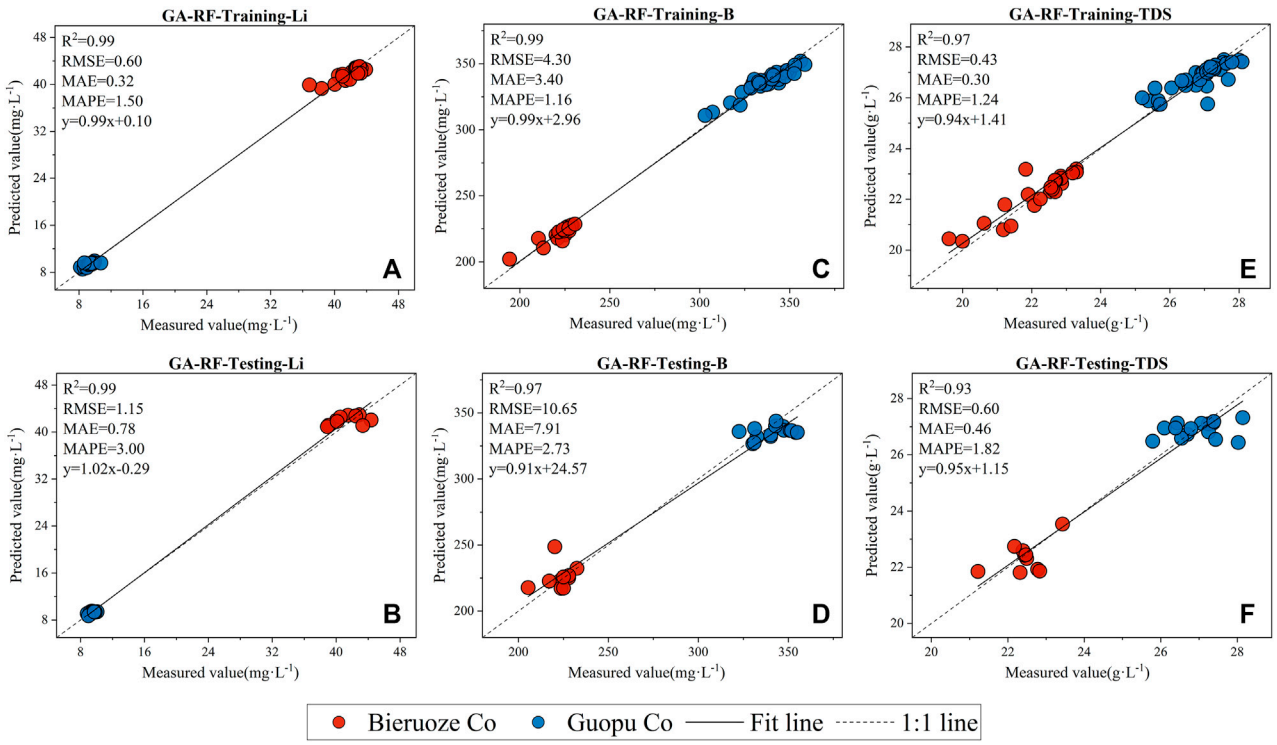

FIGURE 7
Fitting of measured and predicted values using GA-RF models. Estimated Li content based on the training **(A)** and testing **(B)**. Estimated B content based on the training **(C)** and testing **(D)**. Estimated TDS content based on the training **(E)** and testing **(F)**.

TABLE 4 Spectral feature bands of GA-RF model obtained by GA.

Model	Parameters	Spectral bands	Number of bands
GA-RF	Li	B_1, B_4, B_5, RTB_4, RTB_5, RTB_7, LTB_4, RLB_4, RLB_5, RLB_6, RLB_{8a}, FDB_2, FDB_4, FDB_5, FDB_8, FDB_{8a}, FDB_9	17
	B	B_6, B_7, B_8, RTB_8, LTB_1, LTB_7, LTB_8, LTB_{8a}, LTB_9, LTB_{12}, RLB3, RLB_8, FDB_1, FDB_2, FDB_6, FDB_7, FDB_8, FDB_{8a}, FDB_9, FDB_{11}	20
	TDS	B_1, RTB_1, RTB_{8a}, RTB_9, RTB_{11}, RTB_{12}, LTB_1, LTB_{8a}, LTB_{12}, RLB_2, RLB_3, RLB_9, FDB_1, FDB_2, FDB_5, FDB_8, FDB_9	17

Table 2 displays the results of modeling based on the full spectral bands; however, the accuracy of all models was not satisfactory. This was due to the presence of invalid information in the spectral band, which affects the estimation performance of the models. In machine learning, selecting the best input variables remains a difficult task; too many input spectral variables not only complicate the operation and increase the time cost but also reduce the prediction performance of models with limited samples, which is known as a dimensional catastrophe and leads to models suffering from the "curse of dimensionality" (Bach, 2017). In contrast, using too few input spectral bands could prevent the spectrum from fully revealing its hidden information. Therefore, it is essential to select the best input variables. Common feature selection methods include both heuristics and metaheuristics. Heuristics are simple to operate but cannot handle complex relationships between input and output variables, such as principal component analysis, while metaheuristics avoid these limitations. The GA is a classical artificial intelligence algorithm among metaheuristics (Katoch et al., 2021). In the GA, a single spectral variable is considered a gene on a chromosome, represented by a binary code: 0 means that the band is unselected, and 1 means that it is selected. Second, the genes are dynamically modified by the probability of crossover and variation to change the search process and reach the optimal solution. The GA can evaluate all individuals and output the result of optimal feature selection; therefore, the GA has better global search capability. Figure 11 exhibits the MAPE of the test set of the model constructed based on full bands and the model based on the GA for feature selection. The performance improvement of the GA-MLR and GA-RF models is large. Compared with the MLR model, the MAPE of the GA-MLR model on the testing set was reduced by 70.96% (Li), 89.32% (B), and 93.83% (TDS). Compared with the PLSR model, the MAPE of the GA-PLSR model on the testing set was reduced by 25.90% (Li), 11.47% (B), and 15.39% (TDS). Compared with the RF model, the MAPE of the GA-RF model on the testing set was reduced by 77.52% (Li), 28.54% B) and 36.79% (TDS). In general, the accuracy of various prediction models

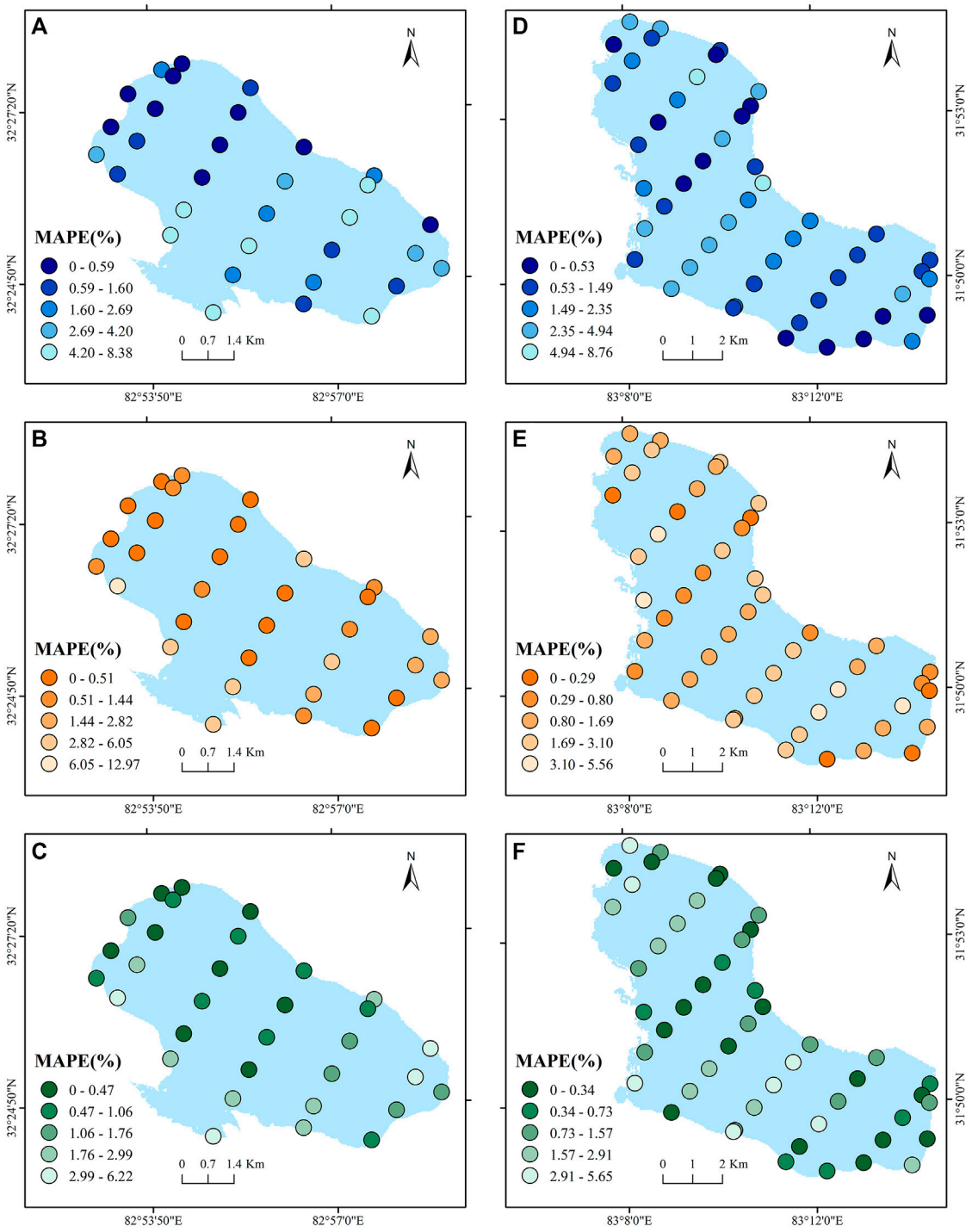

FIGURE 8
Spatial distribution map of MAPE at sampling points in Bieruoze Co and Guopu Co by using GA-RF model. **(A)**, **(B)** and **(C)** are the MAPE of Li, B, and TDS, respectively, estimated by Bieruoze Co. **(D)**, **(E)** and **(F)** are the MAPE of Li, B, and TDS, respectively, estimated by Guopu Co.

with feature optimization by the GA was improved compared with the estimation models constructed based on all spectral bands. This indicates that the GA can extract the necessary information from all bands and reduce the interference of non-essential information, thus improving the accuracy of model prediction. Therefore, the GA can be used as an effective spectral band feature selection algorithm for estimating mineral content.

Zaman Zad Ghavidel and Montaseri. (2014) estimated the TDS content in the Zarinehroud Basin, Iran, using a gene expression programming algorithm with R=0.96 and RMSE=28.99. Zhou et al. (2016) used a BP neural network inversion model to invert the salt lake mineral ion content of the Taijinar Salt Lake in the Qaidam Basin. The inversion accuracy was above 85%. Wang. (2019) used Sentinel-2 data and BP and RF models to invert the Li content of Alisaro Salt Lake

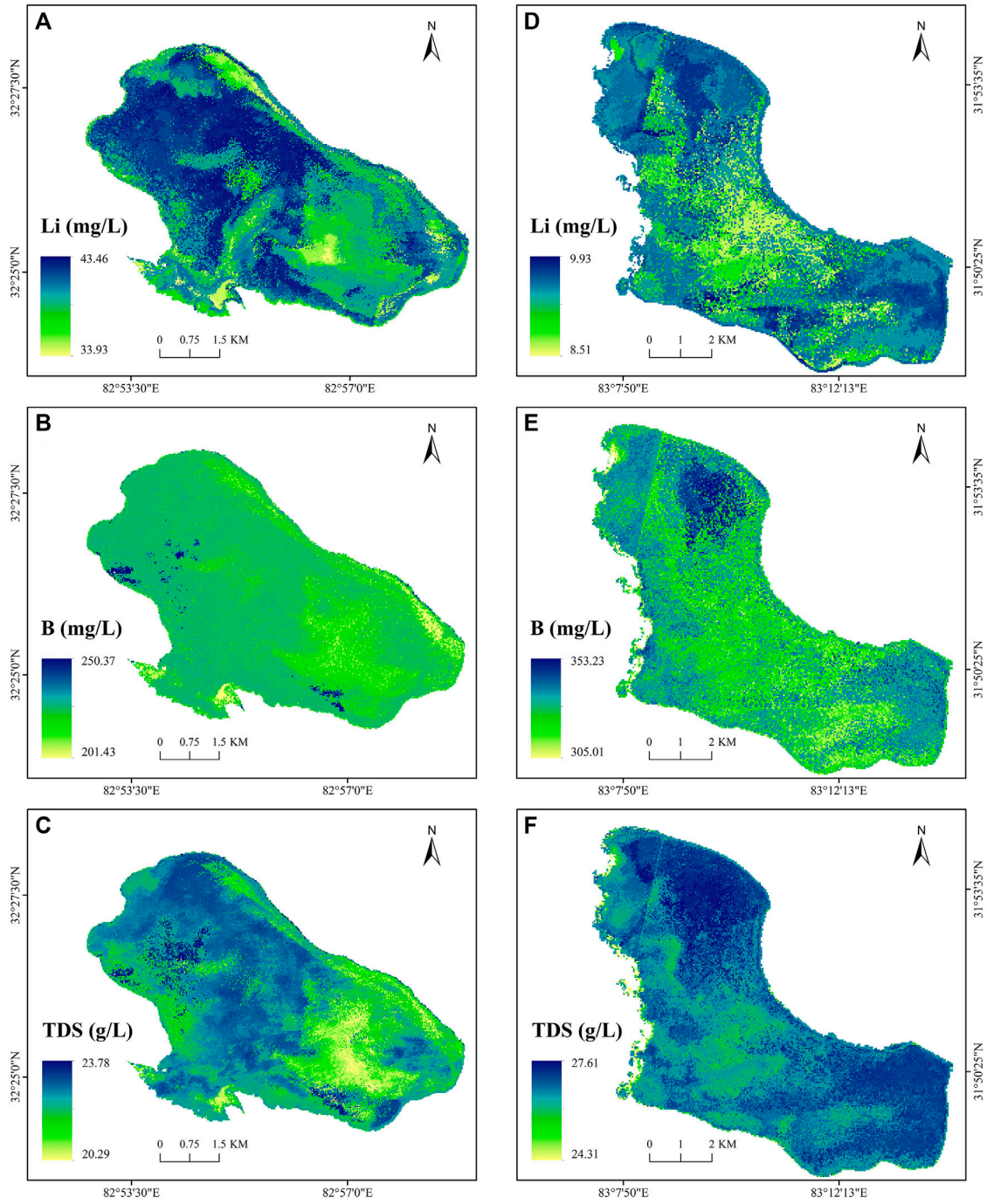

FIGURE 9
Spatial distribution of mineral content in Bieruoze Co and Guopu Co by using GA-RF model. **(A)**, **(B)**, **(C)** are the distribution maps of the Li, B, and TDS contents of Bieruoze Co. **(D)**, **(E)**, **(F)** are the distribution maps of the Li, B, and TDS contents of Guopu Co.

with R^2=0.731 and R^2=0.771, and the results showed that the RF model achieved the best results. As a machine learning model, RF can train the model with less data and a lower computational cost while possessing high accuracy and generalization performance, which is suitable for mineral content inversion of salt lakes on the TP. Figure 12 illustrates the boxplots of the three models, with the first box indicating the results of the measured values in the field and the other three boxes indicating the results of the different model estimates. The results of the GA-RF model were more similar to the results of the field measurements, and the GA-RF model estimates were the closest to the mean, median, and range of values of the field measurements of the two lakes, as well as fewer outliers. Taylor diagram allows a visual comparison of the three different statistical indicators RMSE, SD and correlation. It is obvious from Figure 13 that the predictive performance of the GA-RF model was higher than the other models. The merits of the GA-RF model can be summarized as lower errors and higher correlations. Although the accuracy of GA-MLR, GA-PLSR models was improved by the GA for feature selection.

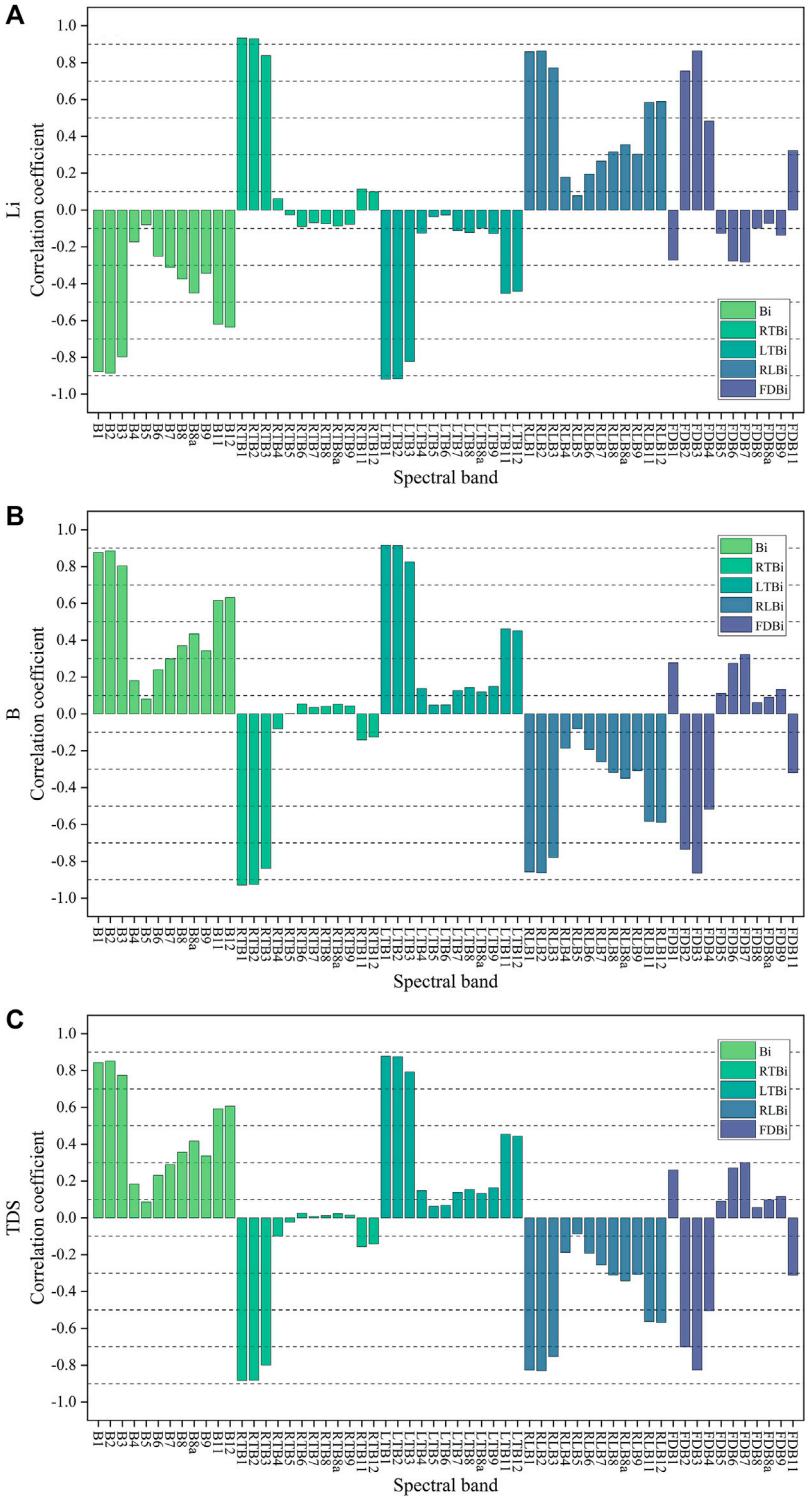

FIGURE 10
Correlation coefficients between spectral bands and Li, B, and TDS. **(A)** Li; **(B)** B; **(C)** TDS.

However, the performance of the two models is still lower than that of the GA-RF model because the MLR and PLSR models are weaker in dealing with non-linear complex problems. Figure 7 demonstrates that GA-RF can handle complex non-linearities between spectral variables and has a high sensitivity for predicting mineral content. In this study, four evaluation metrics were used to assess the accuracy of the model, and the GA-RF model possessed the highest R^2 and the lowest RMSE, MAE, and MAPE values. MAPE, as one of the most popularly used accuracy evaluation metrics, has the advantages of scale independence and interpretability. The GA-RF model indicated that the MAPEs were all below 3%. Therefore, the GA-RF model proposed in this study also performs well compared to previous studies.

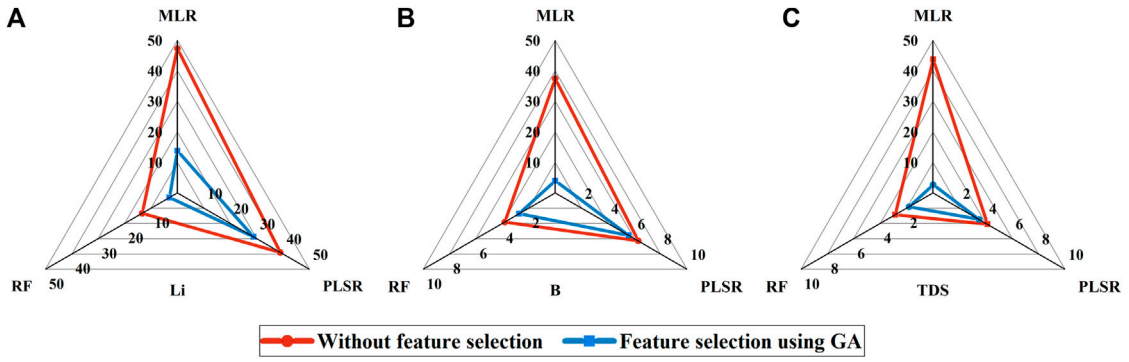

FIGURE 11
Radar plot of MAPE on the testing set of the three models. **(A–C)** are the model results for estimated Li, B, and TDS contents, respectively.

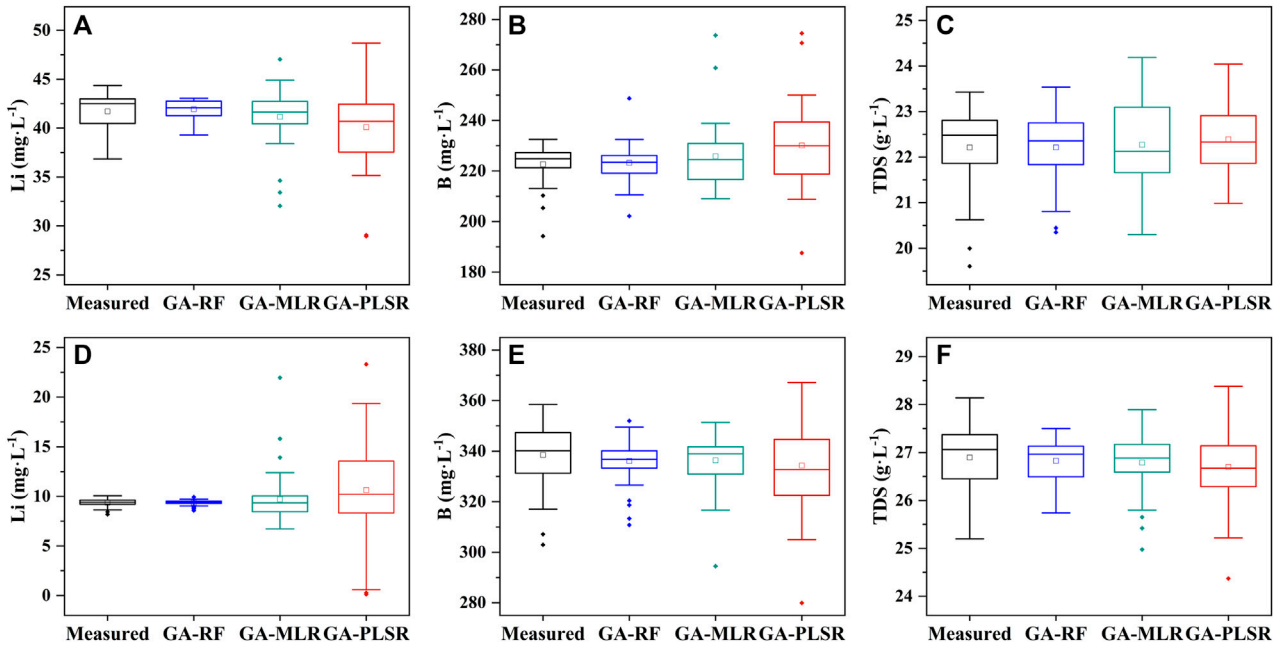

FIGURE 12
Boxplots of field measurements and three model estimates of Li, B, and TDS contents. **(A)**, **(B)** and **(C)** indicate the measured and model estimates of Li, B, and TDS contents of Bieruoze Co, respectively. **(D)**, **(E)** and **(F)** indicate the measured and estimated values of Li, B, and TDS contents of Guopu Co.

5.3 Importance analysis of variables for the GA-RF model

A variable importance analysis was performed on the input spectral variables of the optimal model (GA-RF) to help interpret the model results and the importance of each spectral feature in the model. The variable importance value indicates the degree of influence of that input variable on the model. Theoretically, the higher the variable importance is, the more important that input variable is to the prediction model (Wei et al., 2015). The importance of the different bands in the GA-RF is shown in Figure 13. The analysis shows that for Li, the importance of B_1 is greater than 0.35 and the importance of FDB_2 and FDB_8 is greater than 0.15. For B, LTB_1 has the highest variable importance (0.43), followed by FDB_8 (0.11) and FDB_6 (0.08). The importance of LTB_1 is much higher than that of the other input bands. For TDS, RLB_2 (0.31) and RTB_1 (0.24) are the two bands with the highest importance. Although the importance of the other input variables is relatively low, their role in the prediction model still cannot be ignored. In addition, the bands with the highest importance are also the bands with higher correlations, so feature optimization using the GA can obtain spectral bands that are more sensitive to minerals and enhance the performance of the prediction model. Figure 14.

5.4 Future research

Our study showed that Sentinel-2 satellite data can estimate the brine mineral content of salt lakes on the TP with high accuracy.

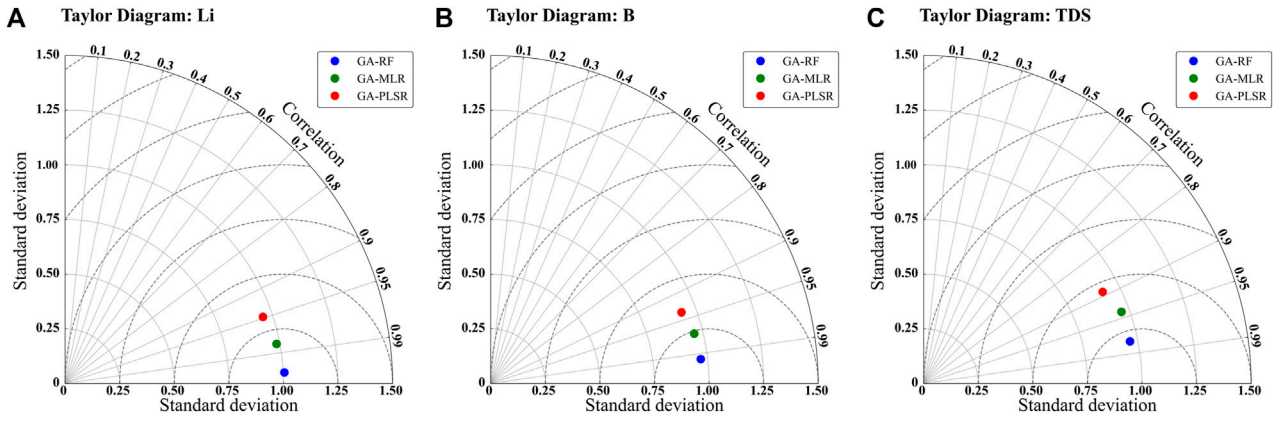

FIGURE 13
Taylor diagram of the GA-RF, GA-MLR, and GA-PLSR models. **(A)** Li; **(B)** B; **(C)** TDS.

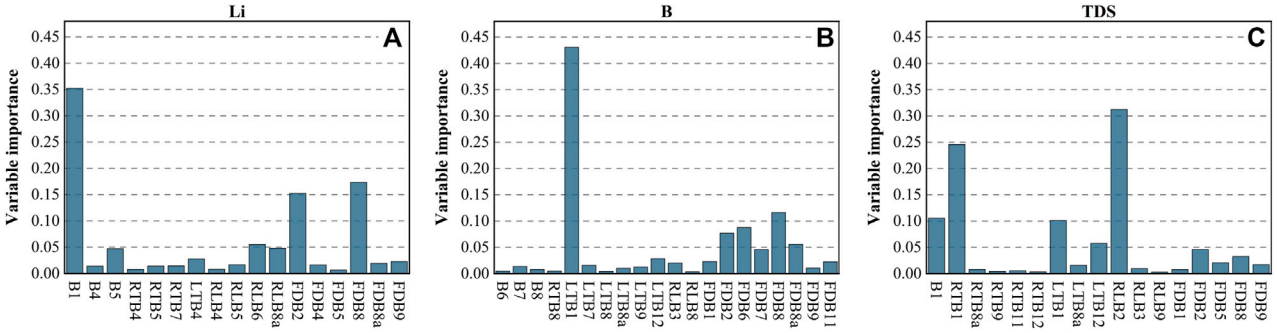

FIGURE 14
Importance of input variables for the GA-RF model. **(A)** Li; **(B)** B; **(C)** TDS.

According to the industrial standard in the Code for Geological Exploration of Salt Lakes and Salt Minerals (DZ/T0212-2002), the Li and B contents of Bieruoze Co and Guopu Co have reached the boundary grade, which has the potential for the development and prospecting of those minerals. The inversion method of mineral content of salt lakes on the TP based on machine learning algorithms will provide a more comprehensive, objective and accurate response to the spatial distribution of mineral content of salt lakes, and enable long-term dynamic monitoring.

Although the strategy of combining GA with RF improved the estimation accuracy, there are still some unexplained variations in information, which may be due to the influence of water body information by other environmental factors (e.g., water depth). By incorporating these environmental variables, it may be possible to enhance the estimation performance of the mineral content prediction model further. The performance of the RF model is limited by the data and the study area. If there is noise in the training data, it may cause overfitting. In addition, the generalizability of machine learning models has been a popular research topic, and it is still challenging to construct a general machine learning model. Different saline lakes on the TP vary widely, and we will collect data from different regions and periods to conduct large-scale dynamic monitoring in the future. At the same time, the method will be tested in lakes or other aquatic systems with different salinities to check the applicability of the method as a larger-scale tool in different types of aquatic environments and at different salinity levels.

The multispectral satellites commonly used in water quality inversion are Landsat and Sentinel. Sentinel-2 satellite has 13 bands with a maximum spatial resolution of 10 m. In recent years, China has launched some multispectral satellites with similar characteristics, such as GF-1 and GF-6. The Gaofen-6 satellite is an optical remote sensing satellite in China's Gaofen series, which was launched in 2018. The GF-6 satellite combines high-resolution and wide-field-of-view (WFV) imaging capabilities with a spatial resolution of 8 m, and has great potential for remote sensing inversion monitoring (Wang et al., 2019). In addition, feature selection algorithms have been widely used for spectral subset selection of hyperspectral satellites. In 2021, China launched the GF5-02 satellite, which carries a hyperspectral camera Advanced Hyperspectral Imager (AHSI) with 330 bands and a maximum spectral resolution of 5 nm. Compared with multispectral satellites, hyperspectral satellites have a higher spectral resolution. The emergence of new remote sensing satellites provides more possibilities and higher quality data for salt lake monitoring on the TP. In future work, we will apply the model to

new satellite data to explore the potential of new satellites for mineral content estimation and monitoring of salt lakes.

The GA-RF model proposed in this study managed to improve the accuracy of the prediction model and generated a set of modeling methods with some generalization. With the field data, the adaptive intelligent prediction model developed in this study can be used for mineral content estimation of salt lakes on the TP and prediction of other water body parameters such as total phosphorus, total nitrogen, and chlorophyll a.

6 Conclusion

The use of remote sensing to monitor lake parameters has proven to be a mature technique; however, there are fewer studies on brine mineral content monitoring in saline lakes. We conducted *in situ* measurements of two typical salt lakes on the TP and collected Li, B, and TDS content data. An intelligent model for estimating the mineral resource content of salt lakes on the TP was developed using Sentinel-2 high spatial resolution remote sensing data. The original spectral images were first processed by four mathematical transformations (RT, LT, RL, FD). Then, the optimal input bands were selected by feature selection through the GA. Finally, three estimation models of PLSR, MLR and RF were developed. The research conclusions were as follows.

(1) Spectral transformations played an important role in estimating the mineral content of salt lakes on the TP. The correlation between spectral bands and Li, B, and TDS contents was increased to different degrees by spectral mathematical transformations while providing rich spectral information for the model.
(2) The estimation model using GA for feature selection method outperforms the estimation model based on all spectral bands. Compared with the MLR model, the MAPE of the GA-MLR model on the testing set was reduced by 70.96% (Li), 89.32% B) and 93.83% (TDS), respectively. Compared with the PLSR model, the MAPE of the GA-PLSR model on the testing set was reduced by 25.90% (Li), 11.47% B), and 15.39% (TDS), respectively. Compared with the RF model, the MAPE of the GA-RF model on the testing set was reduced by 77.52% (Li), 28.54% B), and 36.79% (TDS). The genetic algorithm can be used as an effective spectral band feature selection algorithm for estimating the mineral content of salt lakes.
(3) For all three parameters, the GA-RF model showed the best results compared with the GA-MLR and GA-PLSR models. For Li, the GA-RF model performance was R^2=0.99, RMSE=1.15 mg L^{-1}, MAE=0.78 mg L^{-1}, MAPE=3.00%; for B content, the GA-RF model performance was R^2=0.97, RMSE=10.65 mg L^{-1}, MAE=7.91 mg L^{-1}, MAPE=2.73%; for TDS content, the GA-RF model performance was R^2=0.93, RMSE=0.60 g L^{-1}, MAE=0.46 g L^{-1}, MAPE=1.82%. The GA-RF model predicted MAPE below 3% for all three mineral contents.
(4) The combined strategy of the GA-based feature selection method and the RF showed excellent performance and applicability in mineral content prediction of salt lakes on the TP, and realized intelligent salt lake mineral search. This study provided an application example for remote sensing inversion and monitoring of mineral resources in salt lakes on the TP.

Data availability statement

The original contributions presented in the study are included in the article/supplementary material, further inquiries can be directed to the corresponding author.

Author contributions

HG: Conceptualization, Methodology, Writing–original draft, Funding acquisition. WD: Methodology, Formal analysis, Writing–Original Draft, Editing. RZ: Formal analysis, Writing–original draft, Editing. DZ: Validation, Reviewing. BQ: Validation, Reviewing. GZ: Investigation, Resources. SZ: Supervision, Funding acquisition. JS: Funding acquisition.

Funding

This study was funded by the Major Science and Technology Special Projects in Henan Province (221100210600; 201400211000 and 201400210100); the Science and Technology Tackling Plan of Henan Province (222102320220).

Conflict of interest

The authors declare that the research was conducted in the absence of any commercial or financial relationships that could be construed as a potential conflict of interest.

Publisher's note

All claims expressed in this article are solely those of the authors and do not necessarily represent those of their affiliated organizations, or those of the publisher, the editors and the reviewers. Any product that may be evaluated in this article, or claim that may be made by its manufacturer, is not guaranteed or endorsed by the publisher.

References

Abba, S. I., Abdulkadir, R. A., Sammen, S. S., Pham, Q. B., Lawan, A. A., Esmaili, P., et al. (2022). Integrating feature extraction approaches with hybrid emotional neural networks for water quality index modeling. *Appl. Soft. Comput.* 114, 108036. doi:10.1016/j.asoc.2021.108036

Abba, S. I., Hadi, S. J., and Abdullahi, J. (2017). River water modelling prediction using multi-linear regression, artificial neural network, and adaptive neuro-fuzzy inference system techniques. *Procedia Comput. Sci.* 120, 75–82. doi:10.1016/j.procs.2017.11.212

Alparslan, E., Coskun, H. G., and Alganci, U. (2009). Water quality determination of küçükçekmece lake, Turkey by using multispectral satellite data. *Sci. World J.* 9, 1215–1229. doi:10.1100/tsw.2009.135

Bach, F. (2017). Breaking the curse of dimensionality with convex neural networks. *J. Mach. Learn. Res.* 18, 1–53. doi:10.48550/arXiv.1412.8690

Bayati, M., and Danesh-Yazdi, M. (2021). Mapping the spatiotemporal variability of salinity in the hypersaline Lake Urmia using Sentinel-2 and Landsat-8 imagery. *J. Hydrol.* 595, 126032. doi:10.1016/j.jhydrol.2021.126032

Cao, Y., Ye, Y., Zhao, H., Jiang, Y., Wang, H., Shang, Y., et al. (2018). Remote sensing of water quality based on HJ-1A HSI imagery with modified discrete binary particle swarm optimization-partial least squares (MDBPSO-PLS) in inland waters: A case in weishan lake. *Ecol. Inf.* 44, 21–32. doi:10.1016/j.ecoinf.2018.01.004

Cao, Z., Ma, R., Duan, H., Pahlevan, N., Melack, J., Shen, M., et al. (2020). A machine learning approach to estimate chlorophyll-a from Landsat-8 measurements in inland lakes. *Remote Sens. Environ.* 248, 111974. doi:10.1016/j.rse.2020.111974

Chen, S., and Hu, C. (2017). Estimating sea surface salinity in the northern Gulf of Mexico from satellite ocean color measurements. *Remote Sens. Environ.* 201, 115–132. doi:10.1016/j.rse.2017.09.004

Ding, T., Zheng, M., Nie, Z., Ma, L., Ye, C., Wu, Q., et al. (2022). Impact of regional climate change on the development of lithium resources in Zabuye Salt Lake, tibet. *Front. Earth Sci.* 10, 865158. doi:10.3389/feart.2022.865158

Fang, Y., Chen, X., and Cheng, N. (2017). Estuary salinity prediction using a coupled GA-SVM model: A case study of the min river estuary, China. *Water Supply* 17, 52–60. doi:10.2166/ws.2016.097

Gao, B. (1996). NDWI—a normalized difference water index for remote sensing of vegetation liquid water from space. *Remote Sens. Environ.* 58, 257–266. doi:10.1016/S0034-4257(96)00067-3

Geiger, E. F., Grossi, M. D., Trembanis, A. C., Kohut, J. T., and Oliver, M. J. (2013). Satellite-derived coastal ocean and estuarine salinity in the Mid-Atlantic. *Cont. Shelf Res.* 63, S235–S242. doi:10.1016/j.csr.2011.12.001

Hafeez, S., Wong, M., Ho, H., Nazeer, M., Nichol, J., Abbas, S., et al. (2019). Comparison of machine learning algorithms for retrieval of water quality indicators in case-II waters: A case study of Hong Kong. *Remote Sens.* 11, 617. doi:10.3390/rs11060617

Han, J., Pei, J., and Tong, H. (2022). *Data mining: Concepts and techniques*. Cambridge, MA, United States: Morgan Kaufmann.

He, M., Luo, C., Yang, H., Kong, F., Li, Y., Deng, L., et al. (2020). Sources and a proposal for comprehensive exploitation of lithium brine deposits in the Qaidam Basin on the northern Tibetan Plateau, China: Evidence from Li isotopes. *Ore Geol. Rev.* 117, 103277. doi:10.1016/j.oregeorev.2019.103277

Hestir, E. L., Brando, V., Campbell, G., Dekker, A., and Malthus, T. (2015). The relationship between dissolved organic matter absorption and dissolved organic carbon in reservoirs along a temperate to tropical gradient. *Remote Sens. Environ.* 156, 395–402. doi:10.1016/j.rse.2014.09.022

Katoch, S., Chauhan, S. S., and Kumar, V. (2021). A review on genetic algorithm: Past, present, and future. *Multimed. Tools Appl.* 80, 8091–8126. doi:10.1007/s11042-020-10139-6

Kong, F., Yang, Y., Luo, X., Sha, Z., Wang, J., Ma, Y., et al. (2021). Deep hydrothermal and shallow groundwater borne lithium and boron loadings to a mega brine lake in Qinghai Tibet Plateau based on multi-tracer models. *J. Hydrol.* 598, 126313. doi:10.1016/j.jhydrol.2021.126313

Li, L., Chen, Y., Xu, T., Liu, R., Shi, K., and Huang, C. (2015). Super-resolution mapping of wetland inundation from remote sensing imagery based on integration of back-propagation neural network and genetic algorithm. *Remote Sens. Environ.* 164, 142–154. doi:10.1016/j.rse.2015.04.009

Li, S., Chen, F., Song, K., Liu, G., Tao, H., Xu, S., et al. (2022). Mapping the trophic state index of eastern lakes in China using an empirical model and Sentinel-2 imagery data. *J. Hydrol.* 608, 127613. doi:10.1016/j.jhydrol.2022.127613

Liu, C., Zhu, L., Wang, J., Ju, J., Ma, Q., Qiao, B., et al. (2021a). *In-situ* water quality investigation of the lakes on the Tibetan Plateau. *Sci. Bull.* 66, 1727–1730. doi:10.1016/j.scib.2021.04.024

Liu, T., Dai, J., Zhao, Y., Tian, S., and Ye, C. (2021b). Remote sensing inversion of lithium concentration in salt lake using LightGBM:a case study of northern Zabuye salt lake in Tibet. *Acta Geol. Sin.* 95, 2249–2256. doi:10.19762/j.cnki.dizhixuebao.2021222

Liu, Z., Yao, Z., and Wang, R. (2019). Automatic identification of the lake area at Qinghai–Tibetan Plateau using remote sensing images. *Quat. Int.* 503, 136–145. doi:10.1016/j.quaint.2018.10.023

Ma, R., Yang, G., Duan, H., Jiang, J., Wang, S., Feng, X., et al. (2011). China's lakes at present: Number, area and spatial distribution. *Sci. China Earth Sci.* 54, 283–289. doi:10.1007/s11430-010-4052-6

Maier, P. M., Keller, S., and Hinz, S. (2021). Deep learning with WASI simulation data for estimating chlorophyll a concentration of inland water bodies. *Remote Sens.* 13, 718. doi:10.3390/rs13040718

Marinho, R. R., Harmel, T., Martinez, J., and Filizola Junior, N. P. (2021). Spatiotemporal dynamics of suspended sediments in the negro river, amazon basin, from *in situ* and sentinel-2 remote sensing data. *ISPRS Int. J. Geo-Inf.* 10, 86. doi:10.3390/ijgi10020086

Miles, K. E., Willis, I. C., Benedek, C. L., Williamson, A. G., and Tedesco, M. (2017). Toward monitoring surface and subsurface lakes on the Greenland ice sheet using sentinel-1 SAR and landsat-8 OLI imagery. *Front. Earth Sci.* 5, 58. doi:10.3389/feart.2017.00058

Nemati, S., Fazelifard, M. H., Terzi, Ö., and Ghorbani, M. A. (2015). Estimation of dissolved oxygen using data-driven techniques in the Tai Po River, Hong Kong. *Environ. Earth Sci.* 74, 4065–4073. doi:10.1007/s12665-015-4450-3

Qiao, B., Ju, J., Zhu, L., Chen, H., Kai, J., and Kou, Q. (2021). Improve the accuracy of water storage estimation—a case study from two lakes in the hohxil region of north Tibetan plateau. *Remote Sens.* 13, 293. doi:10.3390/rs13020293

Saberioon, M., Brom, J., Nedbal, V., Souček, P., and Císař, P. (2020). Chlorophyll-a and total suspended solids retrieval and mapping using Sentinel-2A and machine learning for inland waters. *Ecol. Indic.* 113, 106236. doi:10.1016/j.ecolind.2020.106236

Shekofteh, H., and Masoudi, A. (2019). Determining the features influencing the-S soil quality index in a semiarid region of Iran using a hybrid GA-ANN algorithm. *Geoderma* 355, 113908. doi:10.1016/j.geoderma.2019.113908

Song, K., Li, L., Tedesco, L. P., Li, S., Duan, H., Liu, D., et al. (2013). Remote estimation of chlorophyll-a in turbid inland waters: Three-band model versus GA-PLS model. *Remote Sens. Environ.* 136, 342–357. doi:10.1016/j.rse.2013.05.017

Sun, W., Liu, S., Zhang, X., and Li, Y. (2022a). Estimation of soil organic matter content using selected spectral subset of hyperspectral data. *Geoderma* 409, 115653. doi:10.1016/j.geoderma.2021.115653

Sun, X., Zhang, Y., Shi, K., Zhang, Y., Li, N., Wang, W., et al. (2022b). Monitoring water quality using proximal remote sensing technology. *Sci. Total Environ.* 803, 149805. doi:10.1016/j.scitotenv.2021.149805

Tian, S., Qin, X., Zheng, M., Hong, Y., and Kuang, S. (2005). Quantitative analysis of remote sensing on the total salinity of zhabuye Salt Lake in tibet. *Geoscience* 19, 596–602. doi:10.3969/j.issn.1000-8527.2005.04.016

Tiyasha, T., Tung, T. M., Bhagat, S. K., Tan, M. L., Jawad, A. H., Mohtar, W. H. M. W., et al. (2021). Functionalization of remote sensing and on-site data for simulating surface water dissolved oxygen: Development of hybrid tree-based artificial intelligence models. *Mar. Pollut. Bull.* 170, 112639. doi:10.1016/j.marpolbul.2021.112639

Wagle, N., Pote, R., Shahi, R., Lamsal, S., Thapa, S., and Acharya, T. D. (2019). Estimating and mapping chlorophyll-A concentration of phewa lake of kaski district using Landsat imagery. *ISPRS Ann. Photogrammetry, Remote Sens. Spatial Inf. Sci.* IV-5/W2, 127–132. doi:10.5194/isprs-annals-IV-5-W2-127-2019

Wang, D. (2019). *Models for predicting the Li content in salt lake based on remote sensing: A case study of Argentina's arzaro salt lake*. Jilin, China: Jilin University.

Wang, J., Liu, J., Li, Z., Liu, D., and Wang, D. (2015). High resolution remote sensing estimation of salinity in Salt Lake with uranium resources. *Earth Sci. - J. China Univ. Geosciences* 40, 1409–1414. doi:10.3799/dqkx.2015.126

Wang, J., Lu, D., Zhou, M., Wu, D., and Hao, W. (2021). WV-II high resolution data based quantitative inversion of salinity content for Salt Lake: A case study of gasikule Salt Lake. *Uranium Geol.* 37, 78–86. doi:10.3969/j.issn.1000-0658.2021.37.010

Wang, M., Cheng, Y., Guo, B., and Jin, S. (2019). Parameters determination and sensor correction method based on virtual CMOS with distortion for the GaoFen6 WFV camera. *ISPRS-J. Photogramm. Remote Sens.* 156, 51–62. doi:10.1016/j.isprsjprs.2019.08.001

Wang, S., Peng, H., and Liang, S. (2022a). Prediction of estuarine water quality using interpretable machine learning approach. *J. Hydrol.* 605, 127320. doi:10.1016/j.jhydrol.2021.127320

Wang, X., Song, K., Liu, G., Wen, Z., Shang, Y., and Du, J. (2022b). Development of total suspended matter prediction in waters using fractional-order derivative spectra. *J. Environ. Manage.* 302, 113958. doi:10.1016/j.jenvman.2021.113958

Wang, Z., Zhang, F., Zhang, X., Chan, N. W., Kung, H., Ariken, M., et al. (2021). Regional suitability prediction of soil salinization based on remote-sensing derivatives and optimal spectral index. *Sci. Total Environ.* 775, 145807. doi:10.1016/j.scitotenv.2021.145807

Wei, P., Lu, Z., and Song, J. (2015). Variable importance analysis: A comprehensive review. *Reliab. Eng. Syst. Saf.* 142, 399–432. doi:10.1016/j.ress.2015.05.018

Wold, S., Trygg, J., Berglund, A., and Antti, H. (2001). Some recent developments in PLS modeling. *Chemom. Intell. Lab. Syst.* 58, 131–150. doi:10.1016/S0169-7439(01)00156-3

Xie, S., Ding, F., Chen, S., Wang, X., Li, Y., and Ma, K. (2022). Prediction of soil organic matter content based on characteristic band selection method. *Spectrochimica Acta Part A Mol. Biomol. Spectrosc.* 273, 120949. doi:10.1016/j.saa.2022.120949

Xu, W., Bu, L., Kong, W., Zheng, M., and Nie, Z. (2017). Monitoring of the dynamic change of Zabuye Salt Lake: A remote sensing approach. *Sci. Technol. Rev.* 35, 89–96. doi:10.3981/j.issn.1000-7857.2017.06.011

Yan, L. J., and Zheng, M. P. (2015). Influence of climate change on saline lakes of the Tibet Plateau, 1973-2010. *Geomorphology* 246, 68–78. doi:10.1016/j.geomorph.2015.06.006

Zaman Zad Ghavidel, S., and Montaseri, M. (2014). Application of different data-driven methods for the prediction of total dissolved solids in the Zarinehroud basin. *Stoch. Environ. Res. Risk Assess.* 28, 2101–2118. doi:10.1007/s00477-014-0899-y

Zhang, D., Tian, S., and Luan, X. (2007). Remote sening research on the spatial distribution of boric anhydride in the zhabuye Salt Lake of tibet. *Remote Sens. Land & Resour.* 32-35, 48. doi:10.3969/j.issn.1001-070X.2007.01.006

Zhang, L., Li, J., Liu, R., Zhou, Y., Zhang, Y., Ji, L., et al. (2022). Recovery of lithium from salt lake brine with high Na/Li ratio using solvent extraction. *J. Mol. Liq.* 362, 119667. doi:10.1016/j.molliq.2022.119667

Zhou, Y., Zhang, R., Ma, H., Zhang, J., and Zhang, X. (2016). Retrieving of salt lake mineral ions salinity from hyper-spectral data based on BP neural network. *Remote Sens. Land & Resour.* 28, 34–40. doi:10.6046/gtzyyg.2016.02.06

Zhu, C., Ding, J., Zhang, Z., and Wang, Z. (2022). Exploring the potential of UAV hyperspectral image for estimating soil salinity: Effects of optimal band combination algorithm and random forest. *Spectrochimica Acta Part A Mol. Biomol. Spectrosc.* 279, 121416. doi:10.1016/j.saa.2022.121416

frontiers | Frontiers in Earth Science

TYPE Original Research
PUBLISHED 06 February 2023
DOI 10.3389/feart.2023.1113377

OPEN ACCESS

EDITED BY
Hu Wang,
Southwest Jiaotong University, China

REVIEWED BY
Jianzhang Pang,
Institute of Geology, China Earthquake Administration, China
Xibin Tan,
Institute of Geology, China Earthquake Administration, China
Xi Chen,
China University of Geosciences, China

*CORRESPONDENCE
Zhiwu Li,
lizhiwu06@mail.cdut.edu.cn

SPECIALTY SECTION
This article was submitted to Structural Geology and Tectonics, a section of the journal Frontiers in Earth Science

RECEIVED 01 December 2022
ACCEPTED 03 January 2023
PUBLISHED 06 February 2023

CITATION
Wang Z, Li Z, Ran B, Liu S, Wu W, Ye Y, Tong K, Hua T and Li J (2023), Mid-cretaceous rapid denudation of Eastern Tibetan plateau: Insights from detrital records at the Southwestern corner of Sichuan basin.
Front. Earth Sci. 11:1113377.
doi: 10.3389/feart.2023.1113377

Mid-cretaceous rapid denudation of Eastern Tibetan plateau: Insights from detrital records at the Southwestern corner of Sichuan basin

Zijian Wang[1], Zhiwu Li[1]*, Bo Ran[1], Shugen Liu[1,2], Wenhui Wu[1], Yuehao Ye[1], Kui Tong[1], Tian Hua[1] and Jinxi Li[1]

[1]State Key Laboratory of Oil and Gas Reservoir Geology and Exploitation, Chengdu University of Technology, Chengdu, China, [2]Xihua University, Chengdu, Sichuan, China

Reconstruction of the Cretaceous tectonic evolution of the eastern margin of the Tibetan Plateau is of great significance to understanding the formation and early evolution of the Tibetan Plateau. The thick late Mesozoic sedimentary sequence in the Western Sichuan Basin may record the evolution of the basin itself and the tectonic uplift history of the eastern margin of the Tibetan Plateau during the Cretaceous period. Here we provide new multi-proxy provenance data from conglomerate clast populations, sandstone petrography, heavy mineral assemblages, U-Pb dating of detrital zircon, paleocurrent data, and detrital garnet geochemistry from the Cretaceous clastic units in the southwest corner of Sichuan Basin. Our analysis reveals two distinct changes in sediment provenance recorded in the Cretaceous strata at the southwest corner of the Sichuan Basin. The first significant change of detrital provenance was identified in the mid-Cretaceous Jiaguan Formation. Metamorphic rocks and volcanic rocks clast, as well as feldspar and mica, increased significantly, a heavy mineral assemblage dominated by hematite–limonite and ilmenite with high ATi and RuZi and low ZTR values, predominantly type Bi garnet and mostly 164 Ma, 207 Ma, 440 Ma, 780 Ma–824 Ma, and 1840 Ma detrital zircon ages, interpreted to be sourced from the Songpan-Ganzi fold belt and Longmenshan orogenic belt. The second shift, in the Guankou Formation, is marked by a low compositional maturity, a distinct increase in fossiliferous carbonate clasts and high GZi index with type Bii garnet, and Triassic zircon ages, indicating the exhumation of Longmenshan orogenic belt during the late Cretaceous. These data collectively indicate that the significant surface uplift and rapid denudation of the eastern margin of the Tibetan Plateau were probably initiated in the mid-Cretaceous (~120 Ma). In conclusion, a detailed hands-on provenance analysis of the clastic sedimentary sequences in the southwest corner of the Sichuan Basin enabled us to determine catchment areas and shifts hitherto unstudied, thus contributing to the exhumation history of the eastern margin of the Tibetan Plateau.

KEYWORDS

Cretaceous denudation, detrital zircon dating, heavy mineral analysis, detrital garnet geochemistary, eastern Tibetan plateau, Sichuan basin

1 Introduction

The surface uplift and growth mechanism of the Tibetan Plateau is a research hotspot (Fielding, 1996; Chung et al., 1998; Mulch and Chamberlain, 2006; Rowley and Currie, 2006; Wang et al., 2008; Rohrmann et al., 2012; Ding et al., 2017, 2022; Spicer et al., 2021). Due to the special tectonic position and unique geological structure and structural characteristics of the eastern Tibetan Plateau (Figure 1), its tectonic evolution history is of great significance to reveal the early uplift and growth of the plateau and its dynamic mechanism (Lin et al., 1996; Harrowfield and Wilson, 2005; Li et al., 2008; Li et al., 2010b; Liu et al., 2019), and has become an important research field. Numerous studies have been conducted on the tectonic uplift history of the eastern Tibetan Plateau in the past decades. However, most of the previous studies have only been concentrated on tectonic uplift history studies on the early Late Mesozoic (Late Triassic—early Jurassic) and Cenozoic (Wang et al., 2012; Tian et al., 2013, 2014a, Tian et al., 2018; Tan et al., 2017; Shen et al., 2019; Tan et al., 2019; Yang et al., 2019), while the tectonic evolution history of the Late Mesozoic (Middle and Late Jurassic—Cretaceous), especially the Cretaceous period, remains unclear (Xue et al., 2017; Wang et al., 2021), hindering our understanding of the early formation and evolution of the Tibetan Plateau.

In recent years, low-temperature thermochronology studies have shown that the Songpan—Ganzi fold belt experienced regional uplift and denudation in Late Jurassic—Early Cretaceous (Tian et al., 2014b) and rapid uplift in the Middle-Late Cretaceous (Kamp et al., 2013; Liu et al., 2019; Yang et al., 2019). Influenced by the remote effect of the Lhasa—Qiangtang terrane collision, the inherited structures of the Longmenshan orogenic belt were reactivated (Arne et al., 1997; Wallis et al., 2003; Roger et al., 2004, 2010; Airaghi, 2017a; Airaghi et al., 2017b, 2018) and denudated significantly during the Cretaceous (Xu et al., 2007, Xu et al., 2016; Airaghi et al., 2018; Xue et al., 2021). In addition, more and more information indicated that there was a significant erosion event in the eastern margin of the Tibetan Plateau in the Middle Cretaceous (Xu and Kamp. 2000; Reid et al., 2005; Kamp et al., 2013; Tian et al., 2014b; Airaghi, 2017a; Liu-Zeng et al., 2018; Liu et al., 2019; Yang et al., 2019). The accumulated denudation thickness is more than 5,000 m, which should be uplifted in a large area and form obvious high terrain (Liu et al., 2019). Thus, the results of thermochronology indicate that the early plateauing of the eastern Plateau began at least during the Cretaceous period prior to the India-Asia collision and produced a large amount of denudative material (Xu et al., 2016; Liu et al., 2019), but the whereabouts of these detritus is unknown. The tectonic uplift in the eastern margin of the Tibetan Plateau and the coupled subsidence of the adjacent sedimentary basins fundamentally control the evolution of the topography, geomorphology, drainage system, and sourcing-sink system in the eastern Tibetan Plateau. However, there are still many controversies about the sedimentary filling process of the Cretaceous basins on the eastern edge of the Tibetan Plateau, as well as the source-sink system associated with its early uplift denudation.

Precambrian basement complex code: KD, Kangdian; BX, Baoxing; PG, Pengguan; XLB, Xuelongbao; JZD, Jiaoziding; MCS, Micang Shan; HN, Hannan. Suture zone code: SDS, Shangdan; AMS, Anyemaqen; MLS, Mianlve; GLS, Ganzi—Litang; JSJS, Jinshajiang; BNS, Banggong–Nujiang. Fault zone code: NQLF, North Qinling; LPSF, Liupanshan; TBF, Tianshui—Baoji; WQLF, West Qinling; HMF, Hezuo-Minxian; DZF, Dieshan-Zhouqu; EKLF, East Kunlun; MJF, Minjiang; LRF, Longriba; QCF, Qingchuan; WMF, Wenchuan—Maoxian; YBF, Yingxiu—Beichuan; GAF, Guanxian—Anxian; XSHF, Xianshuihe; ANHF, Anlinghe; DLSF, Daliangshan; ZMHF, Zemuhe; XJF, Xiaojiang. Construction unit Code: LMS, Longmenshan orogenic belt; KQQ, Kunlun—Qilian—Qinling composite orogenic belt; HXSG, Hoh Xil—Songpan—Ganzi terrane; YD, Yidun Terrane; NQT, North Qiangtang terrane; SQT, Sourth Qiangtang terrane; LS, Lhasa terrane; HM, Himalayan terrane.

Sediments deposited in the sedimentary basin provide key information about paleo-tectonic events during orogenic development (Baral et al., 2017). Detailed analysis of these basin sediments allows one to trace them back to their original provenance and reconstruct uplift events (DeCelles and Giles, 1996; Jian et al., 2013) and the contemporaneous orogenic exhumation processes (Pettijohn et al., 1987; Najman and Garzanti, 2000; Weltje and Eynatten, 2004; Panaiotu et al., 2007; Rahl et al., 2018). In the past several decades, U-Pb dating based on detrital zircon (chemically stable and mechanically durable within different depositional environments and weathering conditions) (e.g., Veevers & Saeed, 2013; Gehrels, 2014; Allen, 2017) combined with heavy mineral assemblage analysis and single mineral geochemistry from clastic rocks in the basin (Hartley & Otava, 2001; Linka & Stawikowski, 2013; Morton & Hallsworth, 1994 and references therein; Morton et al., 2016) has become a precise tool for provenance analysis and for paleogeography and paleotectonic reconstruction (Dickinson and Suczek, 1979; Dickinson, 1988; Cawood and Nemchin, 2000; Cawood et al., 2012).

Sichuan Basin is the largest Mesozoic sedimentary basin in the Upper Yangtze plate, adjoining the eastern Tibetan Plateau (Figure 1), which is an ideal place to provide crucial information about the formation and depositional history of the basin itself and the tectonic evolution of the eastern Tibetan Plateau (Guo et al., 1996; Lin et al., 1996; Liu et al., 2003; Li et al., 2016a; Li et al., 2016b). Near the entire NE–SW-trending Longmenshan orogenic belt was deposited over 4 km of Late Triassic to Late Cretaceous foreland basin sedimentary rocks (BGMRSP, 1991; Liu, 2006), which are exposed along the eastern margin of the orogenic belt front. This sequence has been used to study the rate of sedimentation and exhumation history of the source region, climatic changes, and paleogeography, and for provenance analysis (Meng et al., 2005; Li et al., 2018; Zhu et al., 2016). So far, previous provenance analysis of the Western Sichuan basin deposits mainly focused on the Upper Triassic Xujiahe Formation (Deng et al., 2008; Li et al., 2010a; Chen et al., 2011; Luo et al., 2014; Zhang et al., 2015; Shao et al., 2016; Zhu et al., 2017; Yan et al., 2019; Mu et al., 2019; Chen et al., 2020), Lower Jurissic Batianba Formation (Qian et al., 2015; Shao et al., 2016; Tian, 2018; Lv et al., 2022), Middle-Late Jurassic Shaoximiao Formation, Sunning Formation and Penglaizhen Formation (Li et al., 2010a; Yang et al., 2010; Luo et al., 2014; Qian et al., 2015; Li et al., 2018), Lower Cretaceous Chengqiangyan Group of the northwest basin (Li et al., 2016b; Li et al., 2018), Late Cretaceous Wotoushan to Gaokanba Formation, and Paleogene Liujia Formation in the Yibin-Liujia area of the southwest Sichuan Basin (Deng et al., 2018; Jiang et al., 2019), and few investigations have been conducted on the Cretaceous red beds based on the age of U-Pb in zircons (Li et al., 2018) in the southwestern corner of the Sichuan Basin (SWCSB) where the largest accumulations of foreland basin

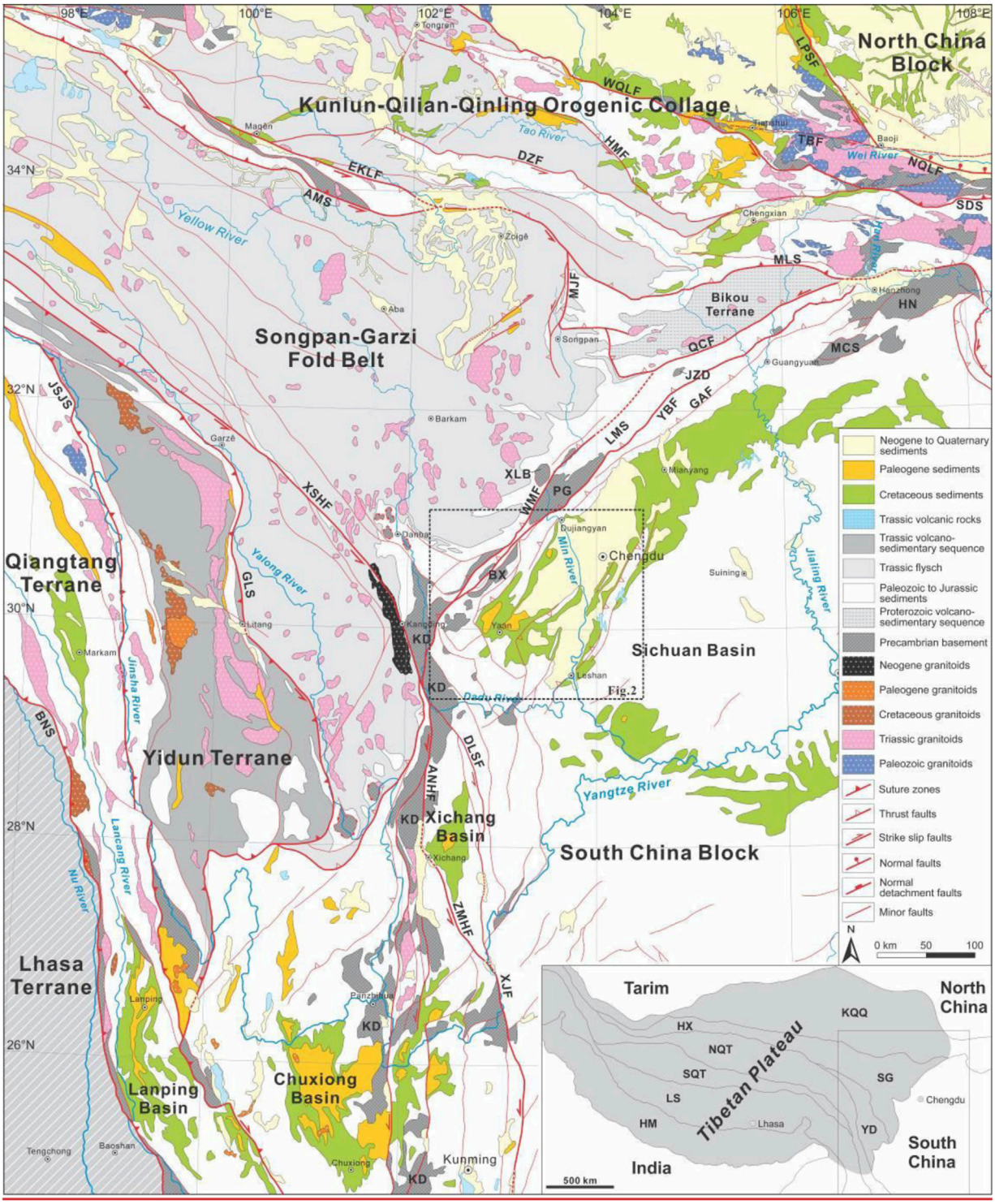

FIGURE 1
Simplified geological and structuctural map of the eastern Tibetan Plateau (after Liu et al., 2019).

syntectonic deposits are preserved (Figure 2). Meanwhile, it has been suggested that Cretaceous sediments of the southwest Sichuan Basin were supplied by multiple sources systems, and a single U-Pb age component can contribute to multiple potential provenance regions (Li et al., 2018), but the relative contribution of each source region cannot be quantified.

Due to the lack of constraints of other provenance indexes, the precise provenance of these sediments remains unclear, which seriously restricts our understanding of source areas' tectonic events and basin evolution during the Cretaceous. Given that the deposition of the Tianmashan, Jiaguan, and Guankou Formations records key information in the Cretaceous of the Sichuan Basin, it

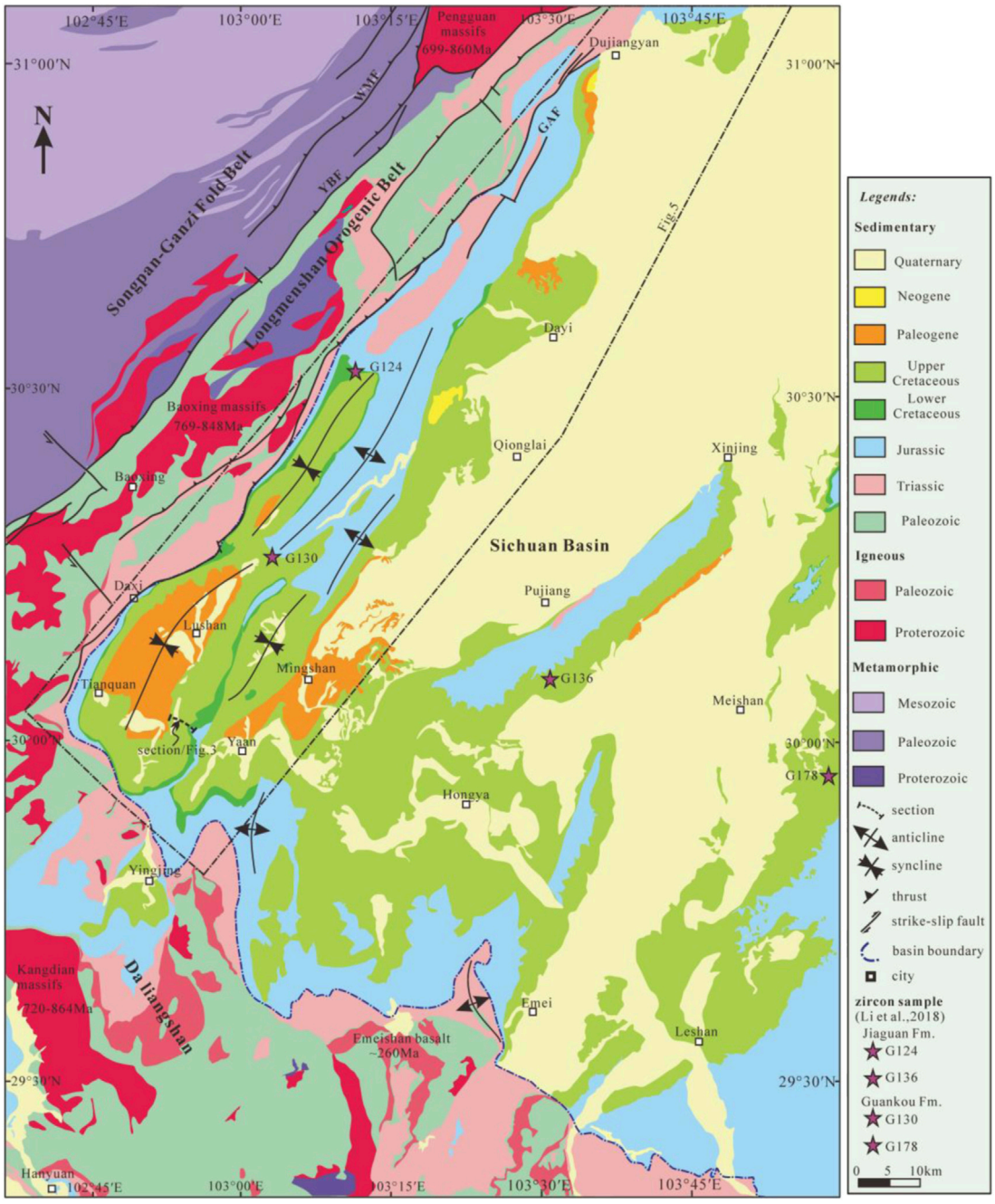

FIGURE 2
Geological map of the southwestern corner of the Sichuan basin showing the location of measured sections and sampling localities. Geology map modified after Burchfiel et al. (1995), 1:200,000 geologic maps (Ministry of Geology and Mineral Resources, 1991), and our own observations. WMF- Wenchuan-maoxian fault; YBF- Yinxiu-Beichuan fault; GAF- Guanxian-Anxian fault.

requires further research. This comprehensive analysis of multi-proxy provenance will help to overcome the multiple solutions and uncertainties caused by the above single research methods.

In this study, we have selected the continuous 1.2 km thick Cretaceous strata from a river section exposed at the southwestern corner of the Sichuan Basin (SWCSB) around the village of "Feixianguan" (completely unrelated to the Lower Triassic "Feixianguan" Formation found elsewhere in the Sichuan Basin) is analyzed here in this multi-proxy provenance study (Figure 2). This section was magneto-stratigraphically dated in detail (Zhuang et al., 1988; Otofuji et al., 1990; Enkin et al., 1991), and predecessors have accumulated abundant sedimentology, paleontological and elemental geochemistry data near it (Li, 1979; Wei, 1979; Li, 1982; Ye, 1983; Gou, 1998; Li, 1988; Yang et al., 2010; Li et al., 2013). For our study we combined fieldwork and modal framework grain composition of the sandstones, conglomerate clasts composition, heavy mineral analysis, and detrital garnet geochemistry from the Tianmashan, Jiaguan, and Guankou Formations to characterize the lithologies in the source areas

of the Sichuan Basin though Cretaceous period. These data, in combination with stratigraphic records and tectonothermal events evidence, provide important constraints on the early uplift and denudation history of the eastern margin of the Tibetan Plateau.

2 Geology setting and potential provenance

The hinterland of the southwest corner of the Sichuan Basin comprises, from west to east, potential source rocks derived from the following tectonic units: Songpan-Ganzi fold belt, Yidun terrane, and Longmenshan orogenic belt. Here we summarize the age, lithology, and tectonic association of potential sources for recent work of the detrital zircon geochronology and heavy mineral analysis from the Cretaceous basin fill.

2.1 Songpan Ganzi fold belt (SPGZ)

The West of the Longmenshan orogenic belt, the triangular-shaped Songpan-Ganzi turbidite fold belt (Figure 1), which represents a Paleo-Tethyan accretionary complex (Chen et al., 1995), is dominated by a thick succession of Middle-Upper Triassic flysch turbidites that settled mainly during Ladinian through Norain (230 Ma–203 Ma) (Huang and Chen, 1987; Brugier et al., 1997; Weislogel et al., 2006; Enkelmann et al., 2007; Zhang et al., 2008; Zhang et al., 2012). Moreover, the only deep oil exploratory well HC1 of 7,012.4 m located in the area shows at least six times tectonic repetitions, resulting in more than ~46% thickening of the Triassic sequence (Liu et al., 2013b). It indicates that the true thickness of the Songpan–Ganzi Triassic flysch is not 10 km–15 km as previously assumed (BGMRSP, 1991), but not more than 3 km–5 km (Liu et al., 2013b). From the end of the Late Triassic to the Early Jurassic, most flysches were intensely folded and uplifted (Burchfiel et al., 1995), which is associated with the amalgamation involving the Qiangtang block and accompanied by synchronous east-directed emplacement of the Longmenshan orogenic belt (Chen et al., 1995). The Songpan–Ganzi Triassic flysch has a multi-provenance origin with peak zircon ages of 265 Ma, 440 Ma, 740 Ma, 1,860, and ca.2,450 Ma (Weislogel et al., 2006, 2010; Enkelmann et al., 2007; Deng et al., 2008; Ding et al., 2013; Zhang et al., 2014; Tang et al., 2017; Jian et al., 2019; Gong et al., 2021), and experienced low-to medium-grade greenschist facies metamorphism during the Late Triassic–Early Jurassic (BGMRSP, 1991; Dirks et al., 1994; Brugier et al., 1997; Huang et al., 2003; Wilson et al., 2006; Roger et al., 2010). In contrast, the underlying upper Sinian–Palaeozoic sequences, predominantly composed of carbonates, experienced higher-grade, medium-pressure metamorphism (Huang et al., 2003). Heavy mineral assemblages in the Triassic flysch contain abundant zircon, apatite, garnet, leucoxene, haematite-limonite, tourmaline, epidote, and rutile (Zhang et al., 2008; Yan et al., 2014; Tang et al., 2017). The geochemical analysis of clastic garnet shows that the type of garnet is mainly Bi (70%) type and Type A (18%) (Zhang et al., 2008; Yan et al., 2014). During the Mesozoic, large amounts of granodiorite to monzonite with ages of 228 Ma–185 Ma were emplaced in the flysch turbidites (Roger et al., 2010; Ding et al., 2013; Zhang et al., 2014).

2.2 Yidun terrane

The Yidun terrane is located to the southwest of the SPGZ, bounded by the Jinsha and Ganzi-Litang suture zone in the south and north respectively (Figure 1). From west to east, it includes the Precambrian–Paleozoic Zhongza massif, Middle Triassic-Early Jurassic eastern Yidun felsic plutons, and middle Cretaceous West Yidun felsic plutons (120 Ma) (Jian et al., 2019). The Zhongza massif is composed of Neoproterozoic basement rocks consisting of granitic gneisses and metavolcanic rocks (Bureau of Geology and Mineral Resources of Sichuan Province (BGMRSP, 1991) and a cover sequence of Paleozoic greenschist facies metasedimentary rocks, shallow-to deep-marine carbonates, and clastic rocks intercalated with sporadic mafic volcanic rocks (BGMRSP, 1991; Chang, 2000). The eastern Yidun Terrane includes widespread exposure of the Triassic Yidun Group flysch that is intruded by large Late Triassic dioritic - granitic plutons (230 Ma-210 Ma) (Reid et al., 2007; Weislogel, 2008; Jackson et al., 2018a; Jackson et al., 2018b). Detrital zircon ages from the Yidun Group in the northern part of the Yidun terrane show prominent bimodal characteristics of 400 Ma–480 Ma and 880 Ma–980 Ma, with a small number of ages of 2,450 Ma–2,500 Ma (Wang et al., 2013). The detrital zircons from the southern Yidun Group are mainly ~220 Ma–240 Ma, ~400 Ma–480 Ma, ~720 Ma–1,000 Ma, ~1,700 Ma–1,900 Ma, and ~2,400 Ma–2,500 Ma (Ding et al., 2013; Wang et al., 2013; Liu et al., 2021).

2.3 Longmenshan orogenic belt (LMS)

The Longmenshan orogenic belt, separating the Songpan-Ganzi turbidite fold belt to the west from the Western Sichuan foreland basin to the east (Figure 1), evolved into an intracontinental transpressional orogen in the Late Triassic (Burchfiel et al., 1995; Chen et al., 1995; Worley and Wilson, 1996). It is NE-SW trending, approximately 500 km long by 30 km–50 km wide (Lin et al., 1996; Jia et al., 2006; Lin, 2008). This belt is characterized by numerous large-scale nappes separated by several NW-dipping thrusts (Jia et al., 2006), in which deformed Paleozoic passive margin carbonate rocks of South China Block and Precambrian crystalline basement massifs are involved (Ministry of Geology and Mineral Resources, 1991; Burchfiel et al., 1995). The massifs consist of high-grade metamorphic quartzofeld-spathic gneisses and associated granitoids with an age of 699 Ma–864 Ma (Zhou et al., 2002a; Zhou et al., 2002b; Zhou et al., 2006a; Druschke et al., 2006; Sun et al., 2007; Zhao and Zhou, 2007; Yan et al., 2008). The passive margin sequence itself consists primarily of shallow water marine rocks of Neoproterozoic (Sinian) to Permian age (BGMRSP, 1991; Guo et al., 1996; Yan et al., 2008). Directly northwest of Longmenshan, Paleozoic metasedimentary units of the Maoxian Group are exposed within the Maoxian-Wenchuan shear zone (BGMRSP, 1991; Worley and Wilson, 1996; Yan et al., 2011). The detrital zircons of Paleozoic sedimentary rocks in the Longmenshan orogenic belt are aged 490 Ma–670 Ma, 730 Ma–850 Ma, 900 Ma–1,000 Ma, and 2,450 Ma–2,550 Ma. The peak ages were ~554 Ma, ~800 Ma, ~940 Ma, and ~2,500 Ma, respectively (Duan et al., 2011; Chen et al., 2016, 2018). Heavy mineral assemblages in the Longmenshan region contain abundant garnet, sillimanite, staurolite, and kyanite (BGMRSP, 1991; Worley and Wilson, 1996). Airaghi et al. (2017b)

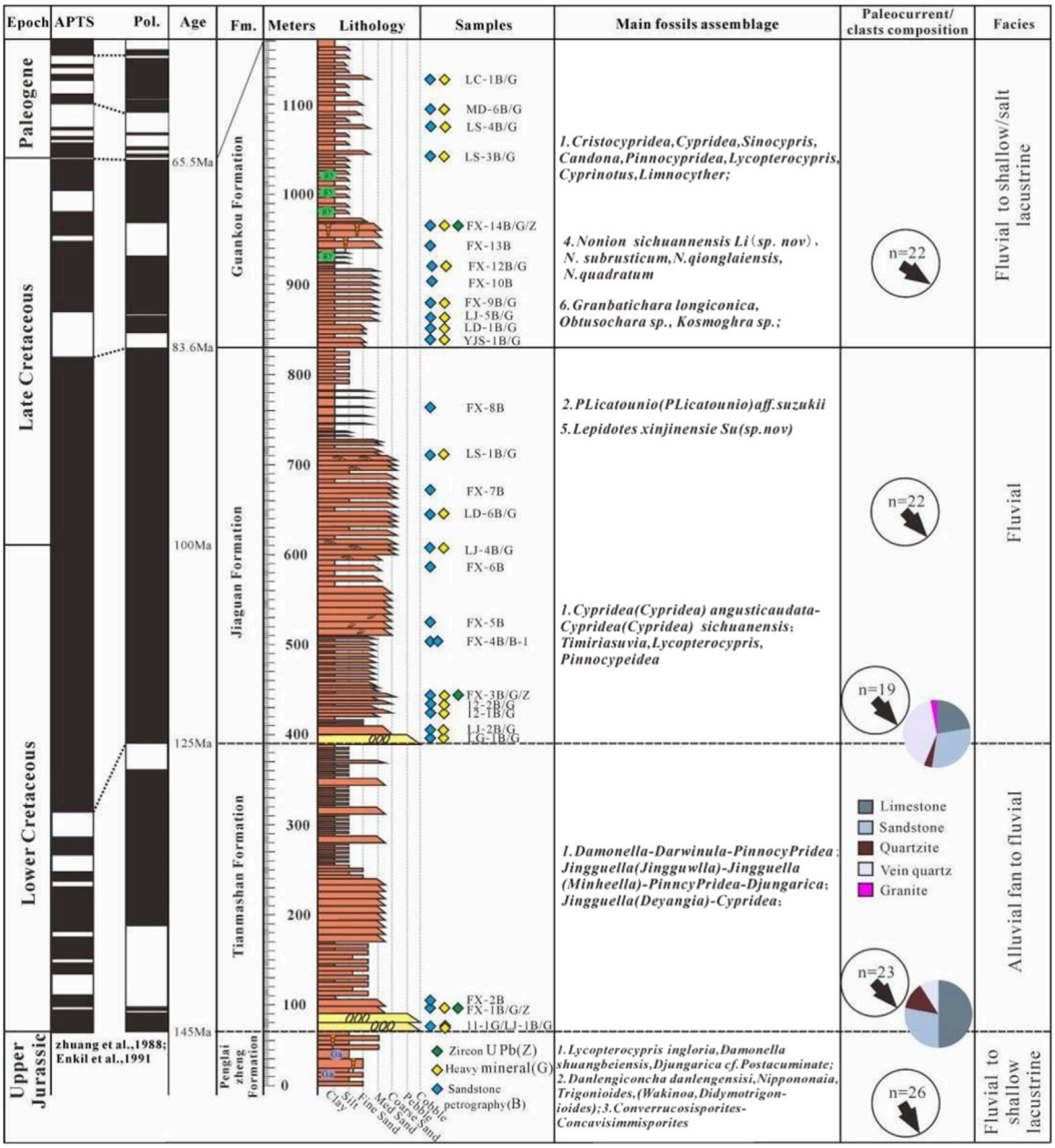

FIGURE 3
Comprehensive stratigraphic column of the Cretaceous in the SW Sichuan Basin, indicating the position of analyzed samples, and upward compositional variations in conglomerates. The geomagnetic polarity time scale (GPTS) is from Harland et al. (1982), and the observed polarity data are from Zhuang et al. (1988), Enkin et al. (1991). Fossil data are compiled from BGMRSP (1991), Wei (1979), Ye (1983), Chen (1983), Su (1983), Li (1987), Gou (1998) and Wang et al. (2006). 1 Ostracoda; 2 Lamellibranchia; 3 Pollen; 4 Foraminifera; 5 Fish; 6 Charophyte.

showed that there was obvious uplift and denudation in the lower Cretaceous (137 Ma) of Longmenshan orogenic belt.

2.4 Cretaceous sedimentary strata in Western Sichuan Basin

Mesozoic sedimentary basins are widespread along the eastern Tibetan Plateau. As the largest Mesozoic sedimentary basin of the Upper Yangtze plate (Figure 1), the Sichuan Basin is located to the east of the Tibetan Plateau with a total area of 18 $\times 10^4$ km^2 (Tong, 1992). It is a multi-stage, superimposed basin characterized by three main basin evolution processes: marine carbonate platform (Ediacaran to Late Triassic), Indosinian-Yanshanian orogeny foreland basin (Late Triassic to Late Cretaceous), and uplift and tectonic modification (Late Cretaceous to Quaternary) (Chen et al., 1995; Guo et al., 1996; Liu et al., 2018; Deng et al., 2013a, b; Li Z W et al., 2012; Li J Z et al., 2009; Li W et al., 2009; Shen et al., 2009; Liu et al., 2008; Richardson et al., 2008). Since the Late Triassic, the Sichuan Basin had become a typical continental sedimentary basin (Liu, 1993; Li Y et al., 2003).

The exposed Cretaceous terrestrial sediments sequence consists entirely of non-marine synorogenic deposits, including lacustrine,

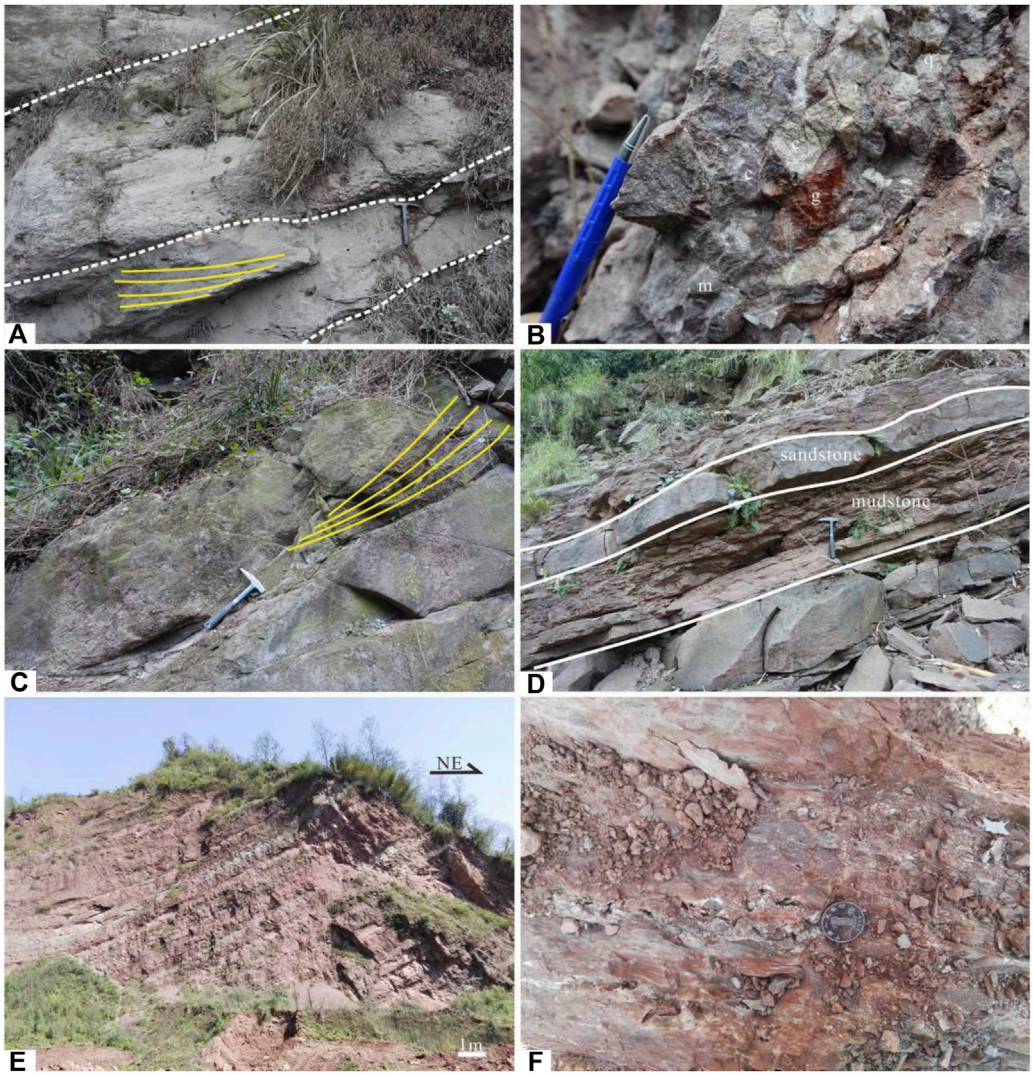

FIGURE 4
Typical outcrops photographs from the Feixianguan section. **(A)** Channel bottom scour surface and conglomerate in the Tianmashan Formation. **(B)** Basal conglomerate in the Jiaguan Formation. **(C)** Massive medium-coarse sandstone with low-angle oblique bedding, Jiaguan Formation. **(D)** Interbedded sandstone and mudstone at the top of the Jiaguan Formation. **(E)** Brownish red lacustrine mudstone of Guankou Formation. **(F)** Brownish red mudstone with dissolved pores in the Guankou Formation. c-Limestone clast. m- Metasandstone clast. g- Granite clast.

alluvial fan and fluvial sandstone and conglomerate, siltstone, and mudstone [Bureau of Geology and Mineral Resources of Sichuan Province (BGMRSP), 1991]. Cretaceous strata exist only in the southeast, west, and northwest of the Sichuan Basin, with the central basin dominated by Jurassic red beds (Bureau of Geology and Mineral Resources of Sichuan Province (Compiling Group of Continental Mesozoic Stratigraphy and Palaeontology in Sichuan Basin of China, 1982; Zhuang et al., 1988; BGMRSP, 1991).

In the study area (Figure 2), the Cretaceous strata are composed of (from oldest to youngest) the Tianmashan (K_1t), Jiaguan ($K_{1\text{-}2}j$), and Guankou(K_2g) Formations (Figure 3). These strata locally exceed 3,000 m in total thickness in the Southwest corner of the Sichuan Basin (Figures 1, 2). Sedimentary rocks interpreted to have been deposited in the foreland basin thin eastward toward the interior of the Sichuan Basin. This Cretaceous succession in the southwestern corner of the Sichuan Basin is mainly composed of brown red sandstone interbedded with red mudstone and conglomerate, which exhibit decreasing compositional and textural maturity with time (BGMRSP, 1991; SBGMR, 1997; Gou, 1998).

The sedimentary age of the Cretaceous foreland deposits is well constrained by magnetostratigraphic and fossil data (Wei, 1979; Su, 1983; Li, 1987; Ye, 1983; Chen, 1983; Zhuang et al., 1988; BGMRSP, 1991; Gou, 1998; Wang et al., 2006) (Figure 3). Paleomagnetic and paleontological data show that the depositional ages of Tianmashan, Jianguan, and Guanguou Formations are, in turn, early Cretaceous Berriasian-Barremian, middle Cretaceous Aptian-Santonian and late Cretaceous Campanian-Maastrichtian stage (Figure 3) (Zhuang et al., 1988; Li and Ji, 1993; Gou, 1998).

The Early Cretaceous Tianmashan Formation is 350 m thick and parallel unconformably overlies the Upper Jurassic Penglaizheng Formation (Chengdu Institute of Geology and Mineral Resources (CGMR), 1979; BGMRSP, 1991; Wang et al., 2006) (Figure 3). It is composed of brown-red quartz-lithic sandstone interbedded with

mudstone and conglomerate lenses, with thick-bedded massive conglomerate at the base (Figure 4A). The depositional environment is interpreted as alluvial fan and fluvial deposits (CGMR, 1979; BGMRSP, 1991; Gou, 1998; Li et al., 2016b). The conglomerate bed is commonly present in the basal portion of the Tianmashan Formation, approximately 10 m thick and consists of massive, light brown-red, matrix to clast supported, calcium cemented. The matrix is sandy to siltly and normally is purple to reddish-purple in color. The clasts are ranging from 2 mm to 15 mm in size (average 5 mm), and are mainly composed of sub-rounded to rounded limestone, quartz sandstone, quartzite, and vein quartz. They often show fining-upward sequence and occasional gravel shingle imbricate structures, and we interpret this conglomerate bed as a lag deposit of a meandering river. Non-marine Cretaceous ostracod assemblages of the Tianmashan Formation are characterized by *Jingguella—Pinnocypridea—Damonella—Minheella* (Wei, 1979; Ye, 1983; Chen, 1983; Li, 1987; Wang et al., 2006), combined with paleomagnetic data (Zhuang et al., 1988), the sedimentary age corresponding to ca. 145 Ma–125 Ma (Figure 3).

The ~420-m-thick Jiaguan Formation was parallel unconformity above the Tianmashan Formation (Figure 3) and consists of a fining-upwards unit of red, conglomerate, feldspar-quartz sandstone, siltstone, and mudstone (Figures 4C, D). Whereas the Jiaguan Formation corresponds to a braided river environment (SBGMR, 1993; Gou, 1998; Li J. et al., 2016). Non-marine Cretaceous ostracod assemblages of the Jiaguan Formation are characterized by *Cypridea—Monosulcocypris* (Wei, 1979; Ye, 1983; Chen, 1983; Li, 1987; Wang et al., 2006), combined with paleomagnetic data (Zhuang et al., 1988), corresponding to ca. 125 Ma–83.6 Ma (Figure 3). The conglomerate beds are commonly present at the bottom of the Jiaguan Formation. Their composition and texture are varied. Pebbles and cobbles are generally rounded to subangular and are composed of metamorphic rocks and volcanic rocks, quartzite, vein quartz, sandstone, and carbonate clasts (Figure 4B).

The Upper Cretaceous Guankou Formation overlies the Jiaguan Formation and has an age of ca. 83.6 Ma–66 Ma (Zhuang et al., 1988), with non-marine Cretaceous ostracod assemblages characterized by *Cristocypridea—Sinocypris (Quadracypris)—Lunicypris* (Wei, 1979; Ye, 1983; Chen, 1983; Li, 1983; Li, 1987; Wang et al., 2006). This formation consists predominantly of 800 m brown-red mudstone with unequal siltstone and comparatively thick marlstone, fine conglomerates, gypsums, and halite (BGMRSP, 1991; Wang et al., 2006) (Figures 4E, F), which were deposited in fluvial to closed lacustrine sedimentary environment (BGMRSP, 1991; SBGMR, 1993; Gou, 1998) (Figure 3).

3 Sampling and methodology

A combination of paleocurrent data, sandstone modal framework point-count data, conglomerate clast compositions, heavy mineral analysis, detrital zircon U-Pb age dating, and single grain detrital garnet major element geochemistry analysis was performed to determine the provenance of the Cretaceous sediments in the southwest corner of the Sichuan Basin, and the tectonic evolution of the source area. Analytical methods, including separation, identification, and quantification techniques, are described as flowing:

3.1 Paleocurrent

To determine the paleotransport directions, paleocurrent indicators (trough-cross, conglomerate clast imbrications, and oblique bedding) were measured wherever possible in the stratigraphic sections to infer the input direction of the detrital material. A total number of 112 directional data were collected from the Late Jurassic Penglaizheng to Late Cretaceous Guankou Formation (Figure 3). All the paleocurrent data were corrected to horizontal by standard stereonet techniques (DeCelles et al., 1983), and the corrected data are then plus or minus 180°C (Wu et al., 2012), and plotted the average value represented by a black arrow (Figure 3).

3.2 Gravel and sandstone petrography

The lithology, size, sorting and roundness of conglomerate clasts were assessed by conducting *in situ* clast counts at bottom of Tianmashan and Jiaguan Formations, respectively (Figure 3). Locations of the clast counts and various lithological types at each site are shown in the stratigraphic column (Figure 3). In addition, we collected clasts composition data from 20 locations on the western margin of the Sichuan Basin from published literature to compare regional provenance changes in clast types and identify specific sediment sources (Figure 5).

Sandstone framework compositions were collected from 27 standard petrographic thin sections of samples obtained from Cretaceous sandstones (Figures 3, 6). These medium-grained sandstone samples were systematically collected to represent the variations in stratigraphy, lithology, and composition through the Tianmashan, Jiagaun, and Guankou Formations along the log of the SW of the Sichuan Foreland Basin. The logged section and the position of selected samples for different analyses are given in the stratigraphic column (Figures 3, 6). Thin sections were stained for potassium and calcium feldspar, and at least 300 relevant grains of quartz, feldspar, and lithic rock fragments per thin section were counted according to the Gazzi-Dickinson method to reduce the influence of grain size (Dickinson, 1970; Dickinson and Suczek, 1979; Dickinson et al., 1983; Ingersoll et al., 1984). This allows us to examine the detrital framework and understand the composition of sandstones within the Cretaceous strata, which ultimately provides additional information on the composition of source rocks from which the sediment was derived (e.g., Dickinson and Suczek, 1979; Dickinson et al., 1983; Ingersoll et al., 1984). Provenance data from the light mineral assemblage is displayed on the QFL (quartz–feldspar–lithics) and QmFLt (quartz monocrystalline–feldspar–lithic total) diagrams to indicate possible derivation from "continental block", "recycled orogen" or "magmatic arc" settings (Dickinson et al., 1983). Recent studies have highlighted issues with over-simplified interpretation of these plots when applied in tropical settings (van Hattum et al., 2006; Garzanti et al., 2007; Smyth et al., 2008; Sevastjanova et al., 2012). Therefore, the two triangular diagrams are used to show the composition differences between different Formations without much discussion about the tectonic background of the potential source (Zimmermann and Hall, 2016).

Textural categories from 1 to 4 were assigned for sorting and roundness of grains (Zimmermann and Hall, 2016, 2019; Löwen

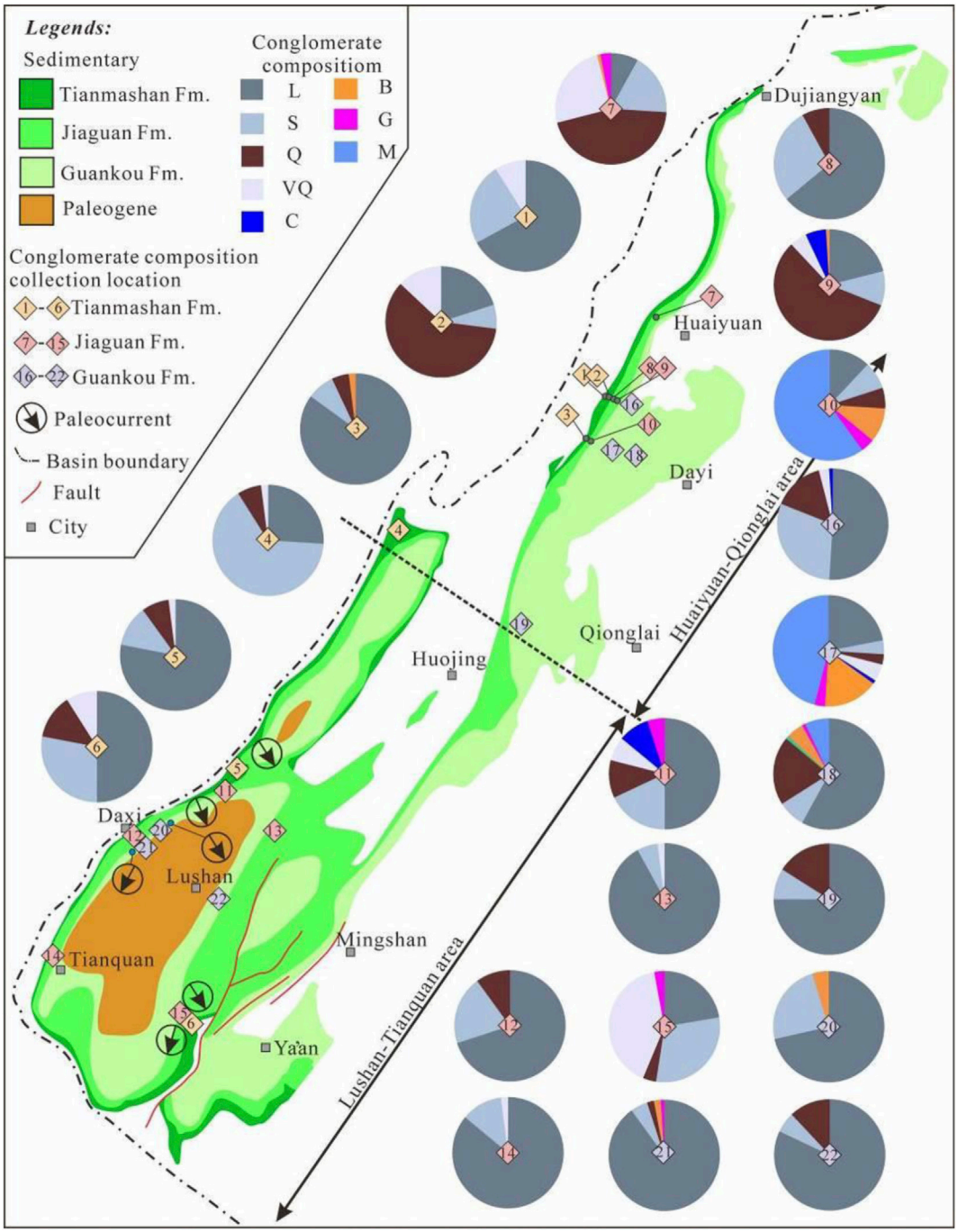

FIGURE 5
The pie charts showing clasts composition of conglomerate from the southwest corner of Sichuan Basin. Clast types in the Cretaceous sandstones: L-limestone, S-sandstone, Q-quartzite, VQ-vein quartz, C-chert, B-basalt, G-granite, M-metamorphic. Clasts composition data from Chengdu Institute of Geology and Mineral Resources (CGMR). (1979), Zeng et al. (2004), Ji and Li, 1995, Li and Ji (1993), Gou (2001), and this study.

et al., 2018). Sorting categories are 1) poorly sorted, 2) moderately sorted, 3) well sorted, and 4) very well sorted. Rounding categories are 1) angular, 2) sub-angular, 3) subrounded, and 4) rounded. Typical examples of Cretaceous rocks are shown in Figure 3. The collection of conglomerate compositional data was conducted at two outcrop localities, they come from the bottom of the Tianmashan Formation and the Jiaguan Formation, respectively (Figure 3).

3.3 Heavy mineral assemblages

There were 21 heavy mineral separates analyzed, comprising three samples from the Tianmshan Formation sandstones, eight samples from the Jiaguan Sandstone, and 10 samples from the Guankou, respectively (Figure 3). To make sure the samples were representative, each sandstone sample is fresh fine-to coarse-grained with an average grain size between 0.2 mm–2 mm,

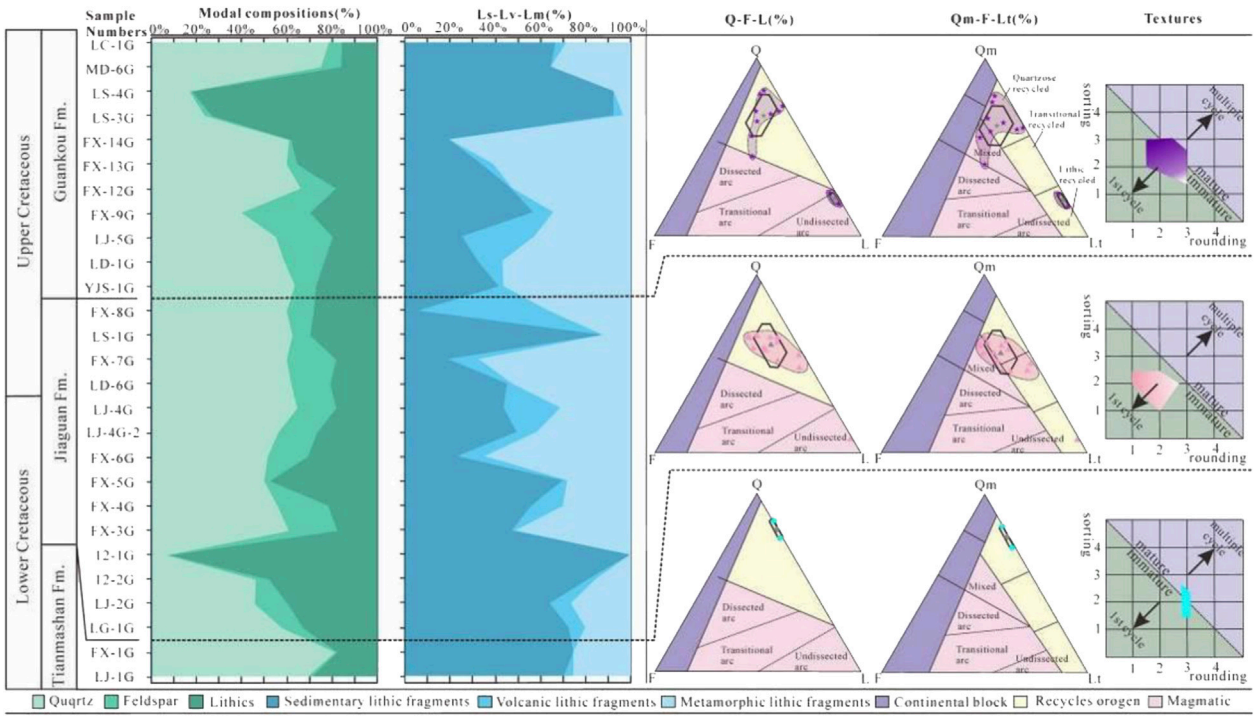

FIGURE 6
Summary of light mineral point counting of Cretaceous sandstones from the SW Sichuan basin. Ternary plots after Dickinson et al. (1983) showing possible provenance affiliation (Q–Quartz, F—Feldspar, L–Lithic fragments, Qm–Monocrystalline quartz, Lt–Total lithic fragments). Textures after Zimmermann and Hall (2016, 2019) showing assessments of sorting and rounding using simple number schemes which were used to estimate maturity.

weighing at least ~1.5 kg–2 kg. Heavy mineral separation was disaggregated using a ceramic mortar and pestle, and wet-sieved into four grain-size categories: > 1 mm, 0.25 mm–1 mm, 0.0625 mm–0.25 mm, and < 0.0625 mm, and the 0.0625 mm–0.25 mm sand fraction was then processed by density separation using sodium polytungstate with a density of 2.89 g cm^{-3} (Morton, 1985; Mange and Maurer, 1992; Morton & Hallsworth 1994). 300 heavy mineral grains per sample were classified.

Heavy mineral analysis is one of the most sensitive and widely used methods to determine possible provenance areas of sandstones (e.g., Mange and Maurer, 1992; Morton and Hallsworth, 1994, 1999). Hence, they often do not reflect the original composition of the source area (Morton and Hallsworth, 1994). Common ultra-stable heavy minerals were categorized into groups corresponding to their most likely protoliths, based on suggested source rocks (Feo-Codecido, 1956; Mange, 2002; Nichols, 2009). Based on the types of heavy minerals isolated from the samples and the background information of potential provenance, common heavy minerals were grouped by their most likely protoliths, based on suggested source rock associations (Mange, 2002; Nichols, 2009; Zimmermann and Hall, 2016, 2019) zircon, tourmaline, anatase, monazite, and apatite are considered to indicate acid igneous (granitic) sources. Magnetite, ilmenite, and chromium spinel represent basic igneous and ultrabasic sources. Rutile and garnet are interpreted to indicate metamorphic sources, mainly of continental character. Other minerals, such as barite, haematite-limonite, and leucoxene are thought to be sedimentary rock sources.

The provenance-sensitive heavy mineral ratios ATi (apatite: tourmaline index), GZi (garnet: zircon index), RuZi (rutile: zircon index), MZi (monazite: zircon index) and CZi (chrome spinel: zircon index) were determined following Morton and Hallsworth (1994) and Morton et al. (2005). In addition, the ZTR index (zircon, tourmaline, rutile) was calculated as defined by Hubert (1962) (Figure 8).

3.4 Detrital garnet geochemistry

Garnet is a very common heavy mineral that occurs in a wide range of metamorphic and igneous rocks and is relatively stable during sedimentary transport and burial diagenetic conditions (Wright, 1938; Morton, 1985; Deer et al., 1992). Its comparatively wide range of major and trace element composition is primarily controlled by host rock composition and reflects changes in pressure and temperature conditions during mineral growth as well (Mange and Morton, 2007; Krippner et al., 2014). Therefore, the mineral chemistry of detrital garnet is widely used as a provenance indicator in studies of sedimentary rocks (Mange and Morton, 2007; Krippner et al., 2014, 2015, 2016; Huang et al., 2019b).

In order to characterize the detrital garnets in the Western Sichuan foreland, three samples were taken from the Tianmashan, Jiaguan, and Guankou Formation, fine-to medium-grained fluvial sandstones, respectively. Garnet major element geochemistry analysis was performed with a JEOL JXA8230 RL EMP equipped with five wavelength dispersive spectrometers at the Sample Solution, Wuhan, Hebei Province. Measuring conditions for garnet include a beam current of 20 nA and an accelerating voltage of 15 kV. The counting times per spot were 15 s for Si, Mg, Ca, Fe, and Al, and 30 s for Ti, Cr, and Mn. Garnet assemblages have been compared by

determining the relative abundances of garnet types A (low -Ca, high-Mg), Bi (low-Mg, Ca < 10%), Bii (low-Mg, Ca > 10%), and C (high-Mg, high-Ca), as defined by Mange and Morton (2007). Previous studies have shown that garnets from felsic crystalline rocks (e.g., intermediate–acidic igneous rocks and metapelites) often have similar major element composition (Mange and Morton, 2007), while there are significant differences in trace elements, which can be effectively used to distinguish garnets from medium-acidic igneous rocks and different metapelite rocks (Lenaza et al., 2018; Hong et al., 2020a, 2020b).

It is possible to compare potential source compositions to the detrital ones because the potential source rocks were already narrowed down to particular regions based on other provenance proxies and because many of these rocks are still preserved in the western provenance of the basin today. For comparison we used data from published source rocks data from different units including Triassic flysch from the southern Songpan-Ganzi (Zhang et al., 2008), Early and Middle Triassic sandstones in the West Qinling (Yan et al., 2014), Triassic granite within the Ganzi-Litang suture zone (Li et al., 2017), Metamorphic crystalline basement of Yidun terrane (Tian et al., 2018), Metamorphic massifs in Longmenshan orogenic belt (He et al., 1988), Metamorphic rocks in Danba area of the southeast corner of Tibetan Plateau (Huang et al., 2003; Billerot et al., 2017), and garnet from modern river sands in the upper Reaches of the Yangtze River (Wang et al., 2018).

3.5 Detrital zircon U-Pb age

Three middle-coarse sandstone samples (FX-1G, from Tianmashan Formation; FX-3G, from Jiaguan Formation, and FX-14G from Guankou Formation) were used for zircon U-Pb dating analysis. At least 250 zircon grains were randomly selected and mounted in epoxy resin and polished to nearly half their original width to expose the internal structures. The internal texture of the zircons was observed with transmitted and reflected light micrographs and cathodoluminescence (CL) images. U–Pb dating was generated from detrital zircons using laser-ablation inductively coupled plasma mass spectroscopy (LA–ICP–MS) at the State Key Laboratory of Continental Dynamics, Department of Geology, Northwest University, Xi'an, China, following a procedure similar to that reported by Yuan et al. (2007). Eighty detrital zircons from each sample were analyzed with a spot size of 32 μm using an Agilent 7,500a ICP–MS coupled to a Lambda Physik Geolas 200 M excimer laser ablation system (193 nm). U–Th–Pb isotopic data were simultaneously acquired on the same spot.

Isotopic ratios and element concentrations of zircon grains were calculated by GLITTER (ver. 4.0, Macquarie University), and were corrected for both instrumental mass bias and depth-dependent elemental and isotopic fractionation using Harvard zircon 91,500 as an external standard with a recommended $^{206}Pb/^{238}U$ age of 1,065.4 Ma ± 0.6 Ma (Wiedenbeck et al., 2004). Concordia ages and diagrams were obtained using Isoplot/Ex (ver. 3.0; Ludwig, 2003). Common lead was corrected by the LA-ICP-MS common lead correction (ver. 3.15) method, following Andersen (2002). Interpreted ages were based on $^{206}Pb/^{238}U$ for younger than 1,000 Ma grains and on $^{206}Pb/^{207}Pb$ for older than 1,000 Ma grains. Only zircon ages with 90%–110% concordance were used to estimate percentages and build a probability plot of each sample, and considered in the following discussions. The analytical data are reported in Supplementary data (See Supplementary Material for details).

We also collected detrital zircon geochronological data of four published samples to compare with the new data (Figure 2), including sample G124 (Jiaguan Formation), G136 (Jiaguan Formation), G130 (Guankou Formation), and G178 (Guankou Formation) (Li et al., 2018).

4 Results

4.1 Paleocurrent

To reconstruct the organization of flow direction during the foreland basin evolution in the study area, 86 new palaeocurrent data (23 in Tianmashan Formation, 41 in Jiaguan Formation, 22 in Guankou Formation) were measured from the gravel slant plane and the direction of inclination of the oblique bedding and combined with 124 palaeocurrent measurements previously published from the Jiaguan and Guankou Formations (Li and Ji, 1993; SBGMR, 1993). Measurements indicate a clear SE-directed transport direction (Figure 3). There is no significant change that occurs in paleocurrent patterns. Paleocurrent data show that from the Early Cretaceous Tianmashan Formation to the Late Cretaceous Guankou Formation in the southwestern Sichuan Basin, the palaeoflow pattern was inherited, and the main body was SE 110°C–220°C with an average of 130°C (Figures 3, 5). It is suggested that the source area of sediments is located at the West and Northwest of the basin from Longmenshan orogenic belt and the Songpan-Ganzi fold belt.

4.2 Gravel and sandstone petrography

4.2.1 Conglomerate clasts composition

In the Feixianguan section, clasts at the bottom of the Tianmashan Formation consist of gray-white carbonate (85%), quartz sandstone (8%), quartzite (5%), and a little volcanic rock (2%) (Figures 3, 5). In contrast, the conglomerate clasts composition at the bottom of the Jiaguan Formation changed significantly and is mainly composed of subrounded vein quartz (42%), followed by sub-angular sandstone (31%), limestone (23%), and minor amounts of quartzite (4%) and granite (3%). There is an upsection increase in sandstone and vein quartz clast, while decrease significantly in carbonate clasts (Figure 3).

Regional stratigraphy and sedimentology studies show that the conglomerates in each formation mainly developed in the front of the Longmenshan orogenic belt in the western margin of the Sichuan Basin (SBGMR, 1993; Gou, 1998). In order to better understand the provenance information in the region, we collected the conglomerate clasts composition data of the front edge of the Longmenshan orogenic belt from the published literature (CGMR, 1979; Zeng et al., 2004; Li and Ji, 1993; SGMB, 1993; Ji and Li, 1995; Gou, 2001) and discussed together with our new statistical data. Spatially, the conglomerates can be divided into two small ranges: Huaiyuan—Qionglai area and Lushan—Tianquan area (Figure 5).

At the Dayi—Qionglai area, clasts in the Tianmashan Formation are mainly limestone (26%–85%), sandstone (7%–65%), quartzite (0%–60%), and vein quartz (0%–13%). The average proportions are as follows: limestone, 50%; sandstone, 26%; quartzite, 18%; vein

FIGURE 7
Selection of thin section photomicrographs of light minerals (crossed polarized light) in the Tianmashan **(A–C)**, Jiaguan **(D–I)**, and Guankou **(J–L)** Formations. Qm, monocrystalline quartz; Lm, metamorphic lithic; Lc, carbonate lithic; Ch, chert lithic; Mic, microcline; P, plagioclase.

quartz, 6%. Major clast types in the Jiaguan Formation are quartzite (average 29%), limestone (average 26%), sandstone (average 16%), metamorphic rocks (average 15%), and vein quartz (average 10%). Minor clasts include basalt (average 3%), chert (average 2%), and granite (average 2%). Major clast types in the Guankou Formation are the same as those in the Jiaguan Formation, namely limestone (22%–75%, average 52%), quartzite (3%–20%, average 14%), metamorphic rocks (1%–46%, average 14%), sandstone (4%–30%, average 13%) and basalt (0%–16%, average 5%). The quartz conglomerate is mainly developed near Dayi and is related to the ancient river course, their parent rocks may be the Devonian Pingyipu Formation or the Precambrian basement (SBGMR, 1993; Gou, 2001).

In the Lushan—Tianquan area, major clast types in the three Formations are the same, namely limestone, sandstone, quartzite, and vein quartz. According to the stratigraphic order from Tianmashan to Guankou Formation, the amount of limestone clast increases upsection from an average of 64%–82%, and the amount of sandstone clasts decreases from an average of 20%–12%, and the amount of quartzite clasts decreases from an average of 11%–5%, the amount of vein quartz increases upsection from an average of 4.5%–11% and then to decreases zero (Figure 5).

The carbonate clasts in Tianmashan Formation are mainly purple micrite, and their parent rock is supposed to be the Triassic Feixianguan Formation. The limestone clasts of the Jianguan Formation are mainly microcrystalline limestone. The fusulinids and bivalve fossils in the limestone gravel indicate that the source rocks of the clasts were mainly from the Permian-Triassic carbonate rocks (Gou, 2001). The abundant microfossil assemblages (stromatoporoid and brachiopoda) in the Guankou Formation carbonate clasts are similar to reported microfauna from the upper Devonian Yangmaba and Guanwushan Formation (SBGMR, 1993; Li and Ji, 1993; Gou, 2001). In addition, the microfossils of foraminifera and gastropods indicate the some clasts of the Guankou Formation are derived from Permian-early-mid-Triassic Carbonates (Gou, 2001).

4.2.2 Sandstones petrology

Figure 6 shows the results of point counting and textural analysis of sandstones from the southwest corner of the Sichuan Basin. In

general, samples are dominated by quartz, lithic fragments with varying abundances of feldspar. The lithic is mainly sedimentary rock and metamorphic rock fragments. Textural immaturity is indicated by poor sorting and (sub) angular grain shape.

The sandstones of the Tianmashan Formation are medium to coarse-grained, moderately to poorly sorted (1–2), and consist of sub-rounded to rounded grains 3) (Figures 7A, B). Compositions are dominated by quartz (74%–83%), lithic fragments (16%–24%) (Figures 7B, C), and feldspar (1%–2%). Among them chert rock fragments (5%), carbonate rock fragments (7%), and sandstone and metamorphic rocks (1.5%). The unstable lithic fragment grains are normally less than 10%. Quartz contains a small amount of undulating extinction polycrystalline quartz, with monocrystalline quartz accounting for 80%, and polycrystalline quartz for 2%. Carbonate is the dominant cement. Samples studied, commonly show a "Recycled orogen" and "Quartzose recycled" modal composition on the QFL diagram and the QmFLt diagram (Figure 6).

A major petrographic shift occurs across the boundary between the Tianmashan and the Jiaguan Formations in the Mid-Cretaceous. Above this boundary, a marked decrease in structural and compositional maturity is seen Figure 6. The content of quartz gradually decreases, and the unstable components of feldspar and mica increase. 14 samples from the Cretaceous Jiaguan Formation are fine—to very coarse-grained and moderately to poorly sorted (1–2) and consist of angular to sub-rounded grains (1–3) (Figure 6). Compositions are dominated by monocrystalline quartz (57%) and polycrystalline quartz (4%), with varying content of feldspar (microcline and plagioclase) (6%–22%) and lithic fragments (13%–46%) (Figures 7D–I), except for sample 12-1G. Rock fragments are c. 30% on average of the modal composition and are mostly sedimentary (23%) and metamorphic (7%) grains (Figures 7D–F). Among them, chert accounted for 2%, carbonate rock fragments accounted for 5%, sandstone fragments accounted for 2%, phyllite and quartz schist fragments accounted for 1%, granite fragments accounted for 0.27%, and mica accounted for 5%. The sample 12-1G was mainly carbonate lithic fragments, with only 8% quartz. As shown in Figure 5, the QFL and QmFLt diagrams indicate a "Quartzose recycled orogen" modal composition (Ingersoll and Suczek 1979; Dickinson 1985). On the textures plot (Zimmermann and Hall, 2016, 2019), samples concentration in the immature field (Figure 6).

Sandstones of the upper Cretaceous Guankou Formation are petrographically identical to the lower part. They are fine-to coarse-grained, poorly to moderately sorted (1–2), and consisting of angular to subround grains (1–3) (Figures 7J–L). There are similarities between sand-type detrital components in the Jiaguan Formation and the Guankou Formation (Figure 6), in which monocrystalline quartz (Figure 7J) accounted for 59.8%, polycrystalline quartz accounted for 7%, feldspar (Figure 7K) accounted for 18%, chert accounted for 3%, and carbonate rocks accounted for 6% of rock fragments, 5% of sandstone debris, 1.52% of metamorphic rock fragments, and 1.5% of mica. The lithic fragments comprise dominantly sedimentary rocks and some metamorphic rocks and represent 13%–2% of the rock. Sample LS-3G and LS-4G were mainly carbonate lithic fragments. As shown in the QFL and QmFLt diagrams indicate a "Quartzose recycled orogen" and "Mixed" modal composition (Ingersoll and Suczek 1979; Dickinson 1985). On the textures plot (Zimmermann and Hall, 2016; Zimmermann and Hall, 2019), most of the sample concentration is in the immature field (Figure 6). Almost all sandstone samples show contains ≥ 60% quartz, possibly due to quartz grains mainly coming from felsic parent rocks. The unsorted sediments of the Jiaguan and Guankou Formations indicate that they were deposited not far from the source by the fluvial process.

4.3 Heavy mineral assemblages

Figure 8 summarises heavy mineral assemblages, ZTR index, heavy mineral ratios, protoliths, and zircon morphology types of the Lower Cretaceous to Upper Cretaceous sediments. Hematite-limonite and ilmenite are the dominant phase in the Feixianguan section sandstones (average of 72%) and together with zircon and rutile comprises 73%–99% of the heavy mineral fraction. The main heavy minerals detected in the studied samples are haematite–limonite (granular), ilmenite (granular), zircon (euhedral, subhedral, and subrounded), rutile (brown red, columnar, and granular), leucoxene (irregular granular), garnet (pink, irregular granular), apatite (columnar, subhedral, and rounded granular), and barite (granular). However, their relative percentages vary widely, and zircon and apatite exhibit different crystal shapes, indicating the coexistence of two provenances of proximal and distant sources, which might be related to sediment recycling. Other minerals, such as tourmaline (dark brown and columnar), anatase (granular), monazite (granular), and magnetite (granular) are present, either in very low percentages. Chrome spinel (granular) occurs only in a few samples.

Samples 11-1G, LJ-1G, and FX-1G collected from the Early Cretaceous Tianmashan Formation contain the highest abundances of Hematite-limonite (average 46.5%), zircon (average 25.2%), rutile (average 6.9%), leucoxene (average 5%), tourmaline (average 1.8%), and anatase (average 1.7%) and the lowest abundances of ilmenite, apatite, magnetite, and monazite. Sample 11-1G also yields abundant garnet (11.36%), and sample LJ-1G contains abundant barite (15%). These two samples also contain a small amount of chrome-spinel (0.2%). The highest ZTR index value (49.7) is measured in this formation, along with the lowest average ATi (2) and RuZi (20) indices. While intermediate-basic volcanic accessory minerals such as hornblende, epidote, and pyroxene, and aluminosilicate accessory minerals characteristic of medium-to high-grade metamorphic sources, such as andalusite, kyanite, and sillimanite, are absent. Their heavy mineral assemblage reflects their mineralogical maturity and is dominated by the ultra-stable phases with high ZTR value. Less stable accessories are apatite and garnet, and there is a lack of ilmenite and magnetite. The high ZTR index indicates enhanced recycling or chemical weathering.

The Tianmashan Formation in Yaan has a significant acidic igneous (9%–43%) and metamorphic signal (9%–14%) that reflects the abundance of mainly zircon, rutile, and garnet (Figure 8). Sandstones contain on average 59.3% sedimentary rocks and 0.2% basic igneous grains. There is a mixture of angular (39%), subangular (23%), and subround-rounded zircon grains (38%).

In contrast, there is a significant change in provenance in the overlying Jiaguan and Guankou Formations, which have similar heavy mineral assemblage characteristics. Hematite–limonite (average 60%), ilmenite (average 16%), magnetite (average 7.5%), garnet (average 2.2%), apatite (average 1%) and monazite

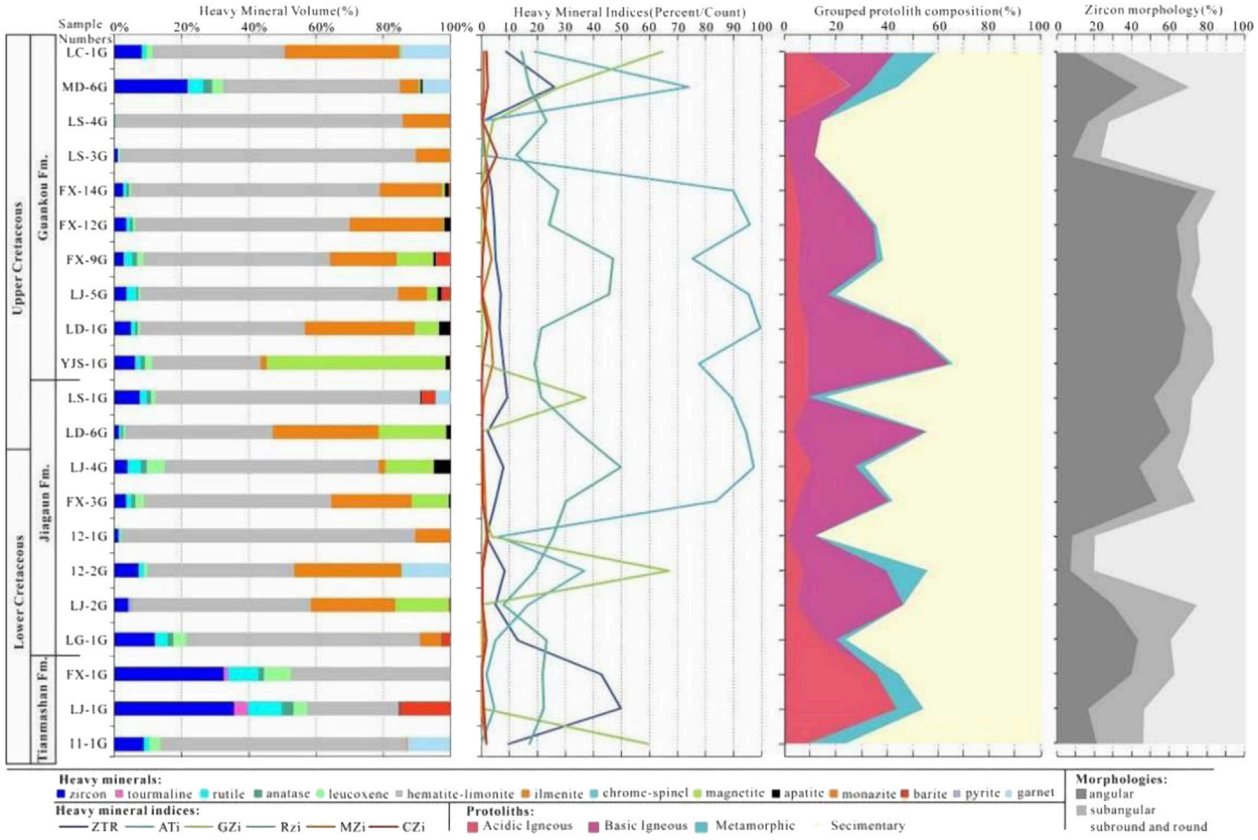

FIGURE 8
Overview of heavy mineral assemblages in the 63 μm–125 μm fraction, and provenance-sensitive heavy minerals index ratios, interpreted protoliths and varietal morphology of zircon from the Cretaceous sediments in the southwest corner of Sichuan Basin, arranged in reconstructed stratigraphic order. ZTR: zircon-tourmaline-rutile index (zircon + tourmaline + rutile counts); ATi: apatite-tourmaline index [100 × apatite count/(total apatite + tourmaline)]; GZi: garnet-zircon index [100 × garnet count/(total garnet + tourmaline)]; RuZi: Rutile-zircon index [100 ×Rutile/(rutile + zircon)]. MZi: Monazite-zircon index [100 × monazite count/(total monazite + zircon)]. CZi: Chromium spinel-zircon index [100 × chromium spine count/(total chromium spine + zircon)]. The detailed position of the samples is shown in Figure 3.

(average 0.1%) abundances are higher, while zircon (average 4.8%), rutile (average 1.6%), leucoxene (average 1.4%) and tourmaline (average 0.1%) abundances are lower. This stratigraphic interval has the highest mean ATi (56), GZi (11.6), RuZi (26), and MZi (1.32) indices, and the lowest mean ZTR index (6.7). Hematite–limonite and leucoxene represent strong oxidation conditions, are widely distributed in the study area, possibly reflecting the dry oxidation of the climate environment or the decreasing water scale at that time (An et al., 2011; Zhang et al., 2016; Tang et al., 2017), and a very low percentage of zircon, which is interpreted to indicate basic igneous rock sources. The Jiaguan and Guankou Formation sandstones contain a basic igneous (24.5%) and acidic igneous (7.2%) signal indicated by a high percentage of ilmenite, magnetite, and apatite (Figure 8). Zircon grains are a mixture of subround-rounded (38%–44%), subangular (18%), and angualr (43%). At the same time, the rutile index also slightly increased (Figure 8). Thus, we infer an increased source input from basic igneous rocks and medium-to high-grade metapelite during the deposition of the Jiaguan and Guankou Formations. Compared with all the samples from the Guankou Formation, the zircon and rutile of the top two samples MD-6G and LC-1G increased, which may be related to the enhanced recycling in the Late Cretaceous (Li et al., 2018).

4.4 Detrital garnet geochemistry

A total of 239 single grains of detrital garnet were analyzed from three samples of the Lower Cretaceous Tianmashan Formation (Sample 11-1G), the Mid-Cretaceous Jiaguan Formation (Samples 12-2G), and the Late Cretaceous Guankou Formation (Sample LC-1G). Results of the garnet single-grain geochemical analysis are shown in the classification scheme after Mange and Morton (2007) (Figure 9). Garnets from the three samples predominantly scatter in fields A and B of the diagram but, non-etheless, show distinct characteristics. Garnet type distribution for the three studied formations is displayed as pie charts in Figure 9.

The most diverse garnet population is present in the Tianmashan Formation with dominant input of type A (granulite-facies metasediments-70%), Bi (intermediate to felsic igneous rocks-28%), and small amounts of type Bii (amphibolite-facies metasediments -2%) garnet (Figure 9A). In contrast, the Jiaguan Formation exhibits considerably higher amounts of Bi (39%) and Bii (23%), but a lower percentage of A type (36%), grains with negligible amounts of garnet from high-grade metamafic igneous rocks (Ci type) (2%) (Figure 9B). Compositional data of garnets from sample LC-1G of the Guankou Formation suggest mainly amphibolite-facies metasediments (45%) and granulite-facies metasediments (45%) as host lithologies with only

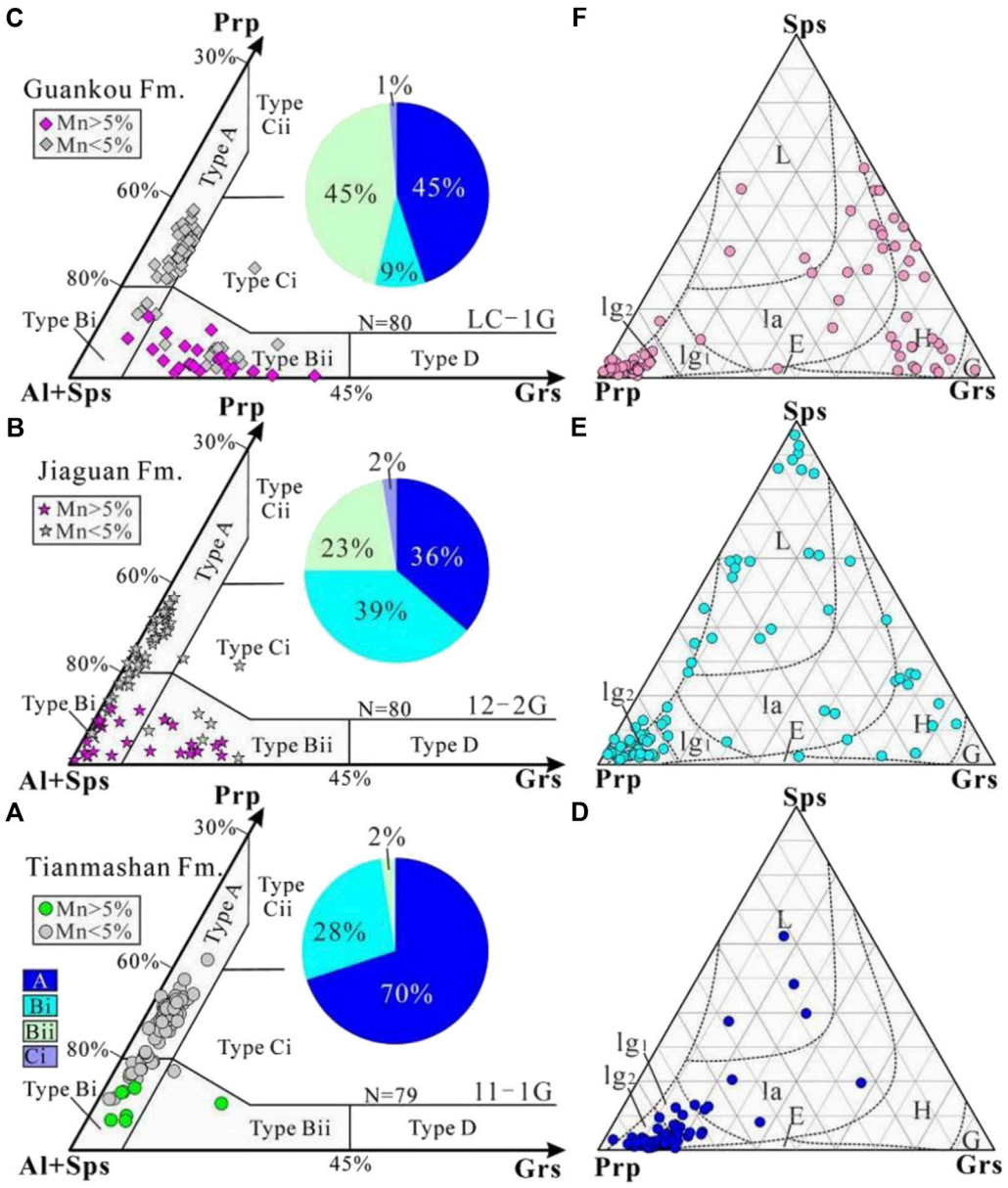

FIGURE 9
(A–C) Results of garnet chemical analysis in the ternary classification scheme of Mange and Morton (2007) with idealised almandine + spessartine (Alm + Sps), pyrope (Prp) and grossular (Grs) compositions as poles. Prp = pyrope, Alm = almandine, Sps = spessartine, Grs = grossular. A-sourced from granulite facies metasediments, charnockites, or intermediate to acidic deeper crust rocks; Bi-from intermediate to acidic igneous rocks; Bii-from amphibolite-facies metasediments; Ci–from high-grade metamafic rocks; Cii-from ultramafic rocks with high Mg; D-from Ca-rich metamorphites like metasomatic rocks (skarns), very low-grade metabasic rocks or ultra-high temperature calc-silicate granulites. **(D–F)** Ternary discrimination diagram with proportions of pyrope, grossular, and spessartine as poles after Teraoka et al. (1997, 1998). L-low P–T, la -intermediate P–T (up to amphibolites facies), H—high P–T, lg1, lg2—intermediate P -T (granulite facies), E-eclogite, G-grandite garnets.

minor input of Bi (9%) and Ci (1%) type garnets (Figure 9C). Up section, type Bii garent increased significantly.

Using the scheme of Teraoka et al. (1997, 1998) we see a wide range in compositions but with some coherent differences between the different samples (Figures 9D–F). The sample 11-1G has a strong preference for garnets plotting in the lg1 + lg2 (intermediate P–T, 87%) field. In contrast, sample 12-2G has some grains of that composition but some grains are biased towards common L (low P-T, 28%) and H (high P-T, 15%) garnets. More obviously, more garnet grains appeared in the la (intermediate P–T, 14%) and H (high P-T, 31%) regions of the sample LC-1G. Almost all the samples have a significant number of grains plotting within the lg2 (intermediate-granulite facies) field. Grains plotting in the H (high P–T) field are quite common in the Guankou Formation. Such grains are rare in the Tianmashan Formation.

4.5 Detrital zircon U-Pb age

Three sandstone samples yield a total of 235 U–Pb ages with concordance within 90%–110% (Figure 10). More than 90% of the

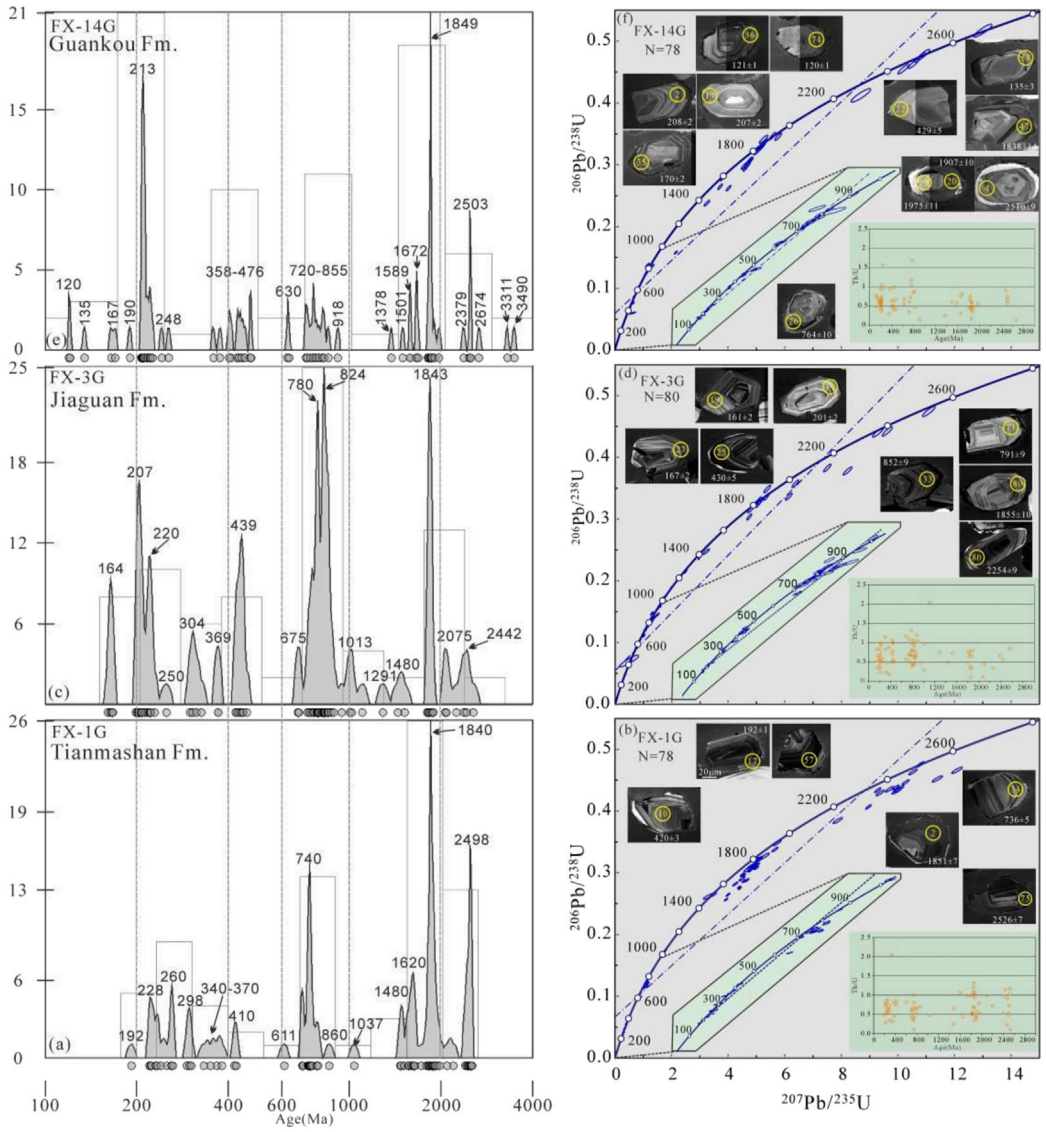

FIGURE 10
Cathodoluminescence images of the selected zircon grains and zircon U-Pb concordia and kernel density estimation (KDE) of samples of the Tianmashan Formation **(A, B)**, Jiaguan Formation **(C, D)**, and Guankou Formation **(E, F)**.

zircons are short prisms, with small cores, well-developed crystal faces, and well-preserved magmatic oscillatory zoning visible in the CL images. These grains are identified as magmatic in origin and are supported by a high Th/U (> 0.2). U–Pb results (Figure 10) from three stratigraphic units are preliminarily presented in the light of stratigraphic order.

Sample FX-1G from the Early Cretaceous Tianmashan Formation. Seventy-eight grains yield six age populations of 192 Ma–240 Ma (*n*=7, 8.9%), 252 Ma–425 Ma (*n*=13, 16.7%), 700 Ma–860 Ma (*n*=14, 17.9%), 1,473 Ma–1,644 Ma (*n*=9, 11.5%), 1731 Ma–2098 Ma (*n*=21, 26.9%), and 2,405 Ma–2,528 Ma (*n*=11, 14.1%). The main peaks are at 740 Ma, 1840 Ma, and 2,498 Ma (Figure 10A), with three weaker peaks at age 1,620, 260, and 228 Ma. Only two zircons (grains FX-1G-68 and FX-1G-75) of 742 Ma and 2,526 Ma have low Th/U values of <0.2 and blastopsammitic textures in the CL images, suggesting metamorphic origin. All other grains have relatively high Th/U values and well-developed crystal faces and are identified as magmatic sources. 22% of the zircon grains have a good roundness, 26% of the zircon grains are sub-angular, and 52% of the zircon grains are angular (Figures 8, 10B).

Sample FX-3G from the Mid-Cretaceous Jiaguan Formation. Eighty zircon grains with five major age populations at 201 Ma–250 Ma (*n*=13, 16.25%), 300 Ma–461 Ma (*n*=14, 17.5%), 679 Ma–945 Ma (*n*=27, 33.75%), 1,804 Ma–1,900 Ma (*n*=8, 10%) and 161 Ma–192 Ma (*n*=5, 6.25%). Six zircon grains with ages ranging 1,006 Ma–1,521 Ma (*n*=6, 7.5%). Relative major peaks are at 164 Ma, 215 Ma, 440 Ma, 780 Ma, and 1,860 Ma (Figure 10C). Five zircon grains (6%) have round shape, blastopsammitic textures in the CL images, and relatively low Th/U values (0.11–0.18), and they are likely metamorphism origin. The remaining grains are clearly of magmatic origin, with high Th/U values of > 0.2 and well-

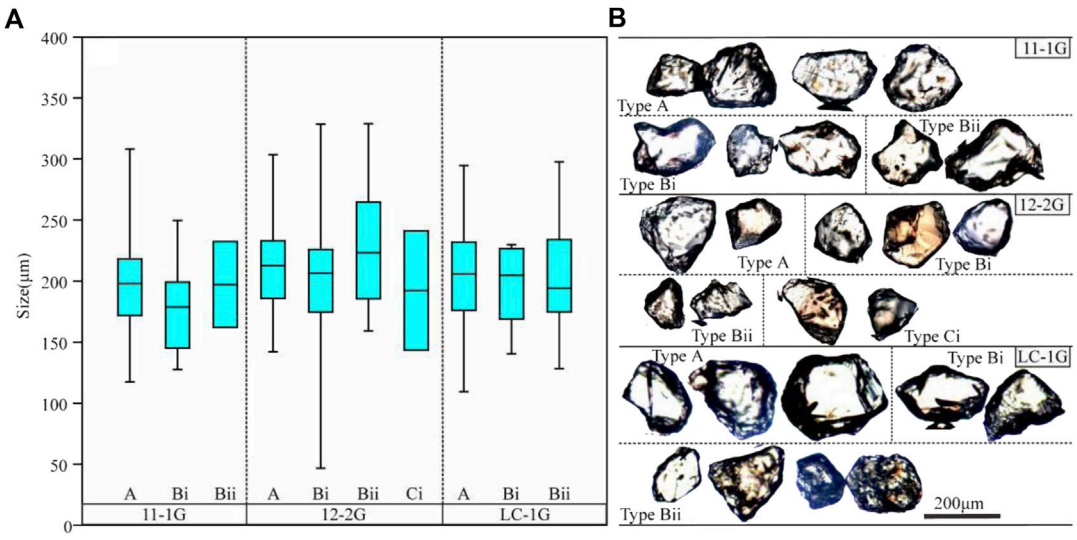

FIGURE 11
Detrital garnet type and its grain size **(A)** and morphological characteristics **(B)**.

preserved oscillatory zoning. 9% of the zircon grains have a good roundness, 19% of the zircon grains are sub-angular, and 72% of the zircon grains are angular (Figures 8, 10D).

Sample FX-14G from the Late Cretaceous Guankou Formation. Seventy-seven grains with five major age populations at 207 Ma–242 Ma (n = 20, 25.97%), 1,800 Ma–1900 Ma (n = 12, 15.6%), 720 Ma–860 Ma (n = 9, 11%), 400 Ma–476 Ma (n = 8, 10%) and 2,509 Ma–2,674 Ma (n = 5, 6.49%), and three subordinate age populations of 165 Ma–190 Ma (n = 3, 3.89%), 120 Ma–135 Ma (n = 3, 3.89%), and 627–690 Ma (n = 3, 3.89%) (Figure 10E). Seven zircon grains with ages ranging 1,360 Ma–1,700 Ma. The sample had two dominant peak ages at 213 Ma, and 1849 Ma. Only two zircon grains (3%) have round shape, blastopsammitic textures in the CL images, and relatively low Th/U values (0.11–0.17), and they are likely metamorphism origin. The remaining grains are clearly of magmatic origin, with high Th/U values of > 0.2 and well-preserved oscillatory zoning. 5% of the zircon grains have a good roundness, 11% of the zircon grains are sub-angular, and 84% of the zircon grains are angular (Figures 8, 10F).

5 Discussion

5.1 Source analysis of garnet

Previous studies showed that hydrodynamic has a certain effect on the separation of garnet geochemistry, thus affecting the geochemistry-based provenance interpretation (Huang et al., 2019a). Specifically, the smaller size of grains (63–125 microns) are more abundant in Fe^{2+} and Mn^{2+}, and indicate that the provenance is mainly low-level metamorphic rocks of amphibolite facies. Other larger grains (125–250 microns) have higher Ca^{2+} and Mg^{2+}, and their source rocks are more diverse including low-grade metamorphic rocks, intermediate-acid igneous rocks, and eclogite, etc. In this study, the grains size of detrital garnet is mainly distributed in the range of 110–230 microns, and most of the grains are angular and a few are subangular-subround (Figure 11). Our analysis result shows that there was no significant difference in grain size between each type of garnet, suggesting that hydrodynamic sorting has less effect on the analysis results. It may be due to the sample itself having a similar sedimentary environment, implying the result is reliable. Therefore, the geochemical differences of garnet between samples are directly related to their provenance.

Garnets typically occur in a wide variety of metamorphic and igneous rocks, as well as in peraluminous rocks. According to the classification of Mange and Morton (2007) (Figure 9), detrital garnets from the Cretaceous sandstones are composed of type A, Bi, and Bii (Figure 9), which account for about 50%, 25.3%, and 23.4% of the analyzed garnet grains, respectively. Thus, they probably derived from granulite-facies metasedimentary rocks, intermediate to acidic igneous rocks, and amphibolite-facies metasedimentary rocks, rather than from high-grade metabasic rocks and skarns and low-grade metabasic rocks. Moreover, some low- Ca and high- Mg garnets (type A) can also be derived from charnockites and intermediate-acidic igneous rocks (Sabeen et al., 2002; Morton et al., 2004). Type Bii grains are Mg- and Ca-poor but Mn-rich (> 5%) garnets that most likely originated from amphibolite-facies metasedimentary rocks (Deer et al., 1997). This suggests that ultrahigh-temperature metamorphic calcsilicate granulites, amphibolite-facies metasedimentary rocks, and intermediate-acidic igneous rocks are the major source of detrital garnets in the Cretaceous sandstones from the southwest corner of the Sichuan Basin.

There are three possible sources of garnet in Cretaceous sandstones in the Sichuan Basin: 1) Songpan-Ganzi Triassic flysch sediments; 2) Metamorphic basement, massifs, and amphibolite -facies metasedimentary rocks of the Longmenshan orogenic belt; 3) Recycling of older pre- Cretaceous sedimentary rocks in the Western margin of the Sichuan Basin. The possibilities and contributions of these three sources are discussed in more detail below.

Previous studies have shown that Songpan-Ganzi flysch has a multi-provenance origin, such as the east Kunlun high-grade metamorphic rock used to be one of its main source (Weislogel

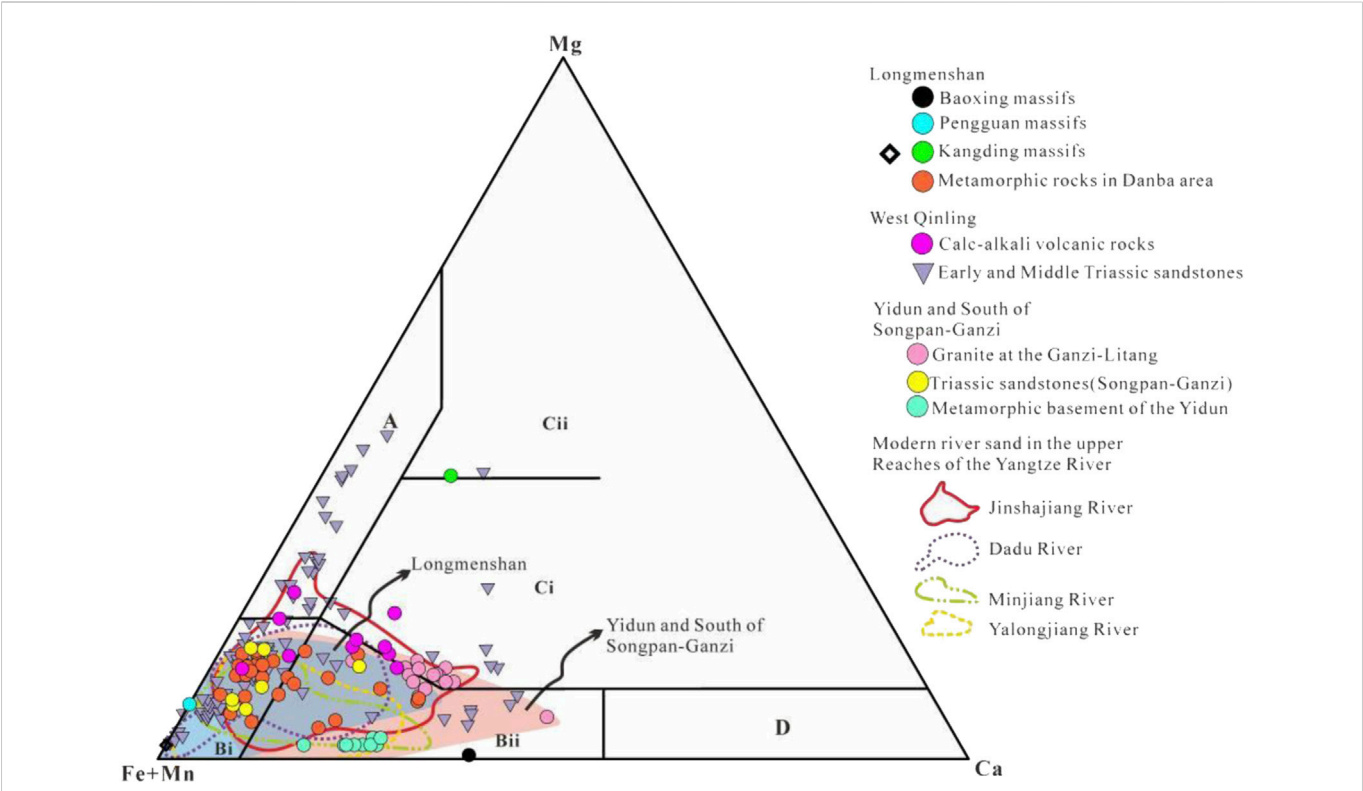

FIGURE 12
The G-P-AS triangular diagram (Mange and Morton, 2007) of garnet geochemistry from literature. Garnet geochemistry data form the Triassic flysch from the southern Songpan-Ganzi (Zhang et al., 2008), Early and Middle Triassic sandstones in the West Qinling (Yan et al., 2014), Triassic granite of the Ganzi-Litang suture zone (Li et al., 2017), Metamorphic crystalline basement of Yidun Terrane (Tian et al., 2018), Metamorphic massifs in Longmenshan orogenic belt (He et al., 1988), Metamorphic rocks in Danba area of the southeast corner of Tibetan Plateau (Huang et al., 2003; Billerot et al., 2017), and garnet from modern river sands in the upper Reaches of the Yangtze River (Wang et al., 2018).

et al., 2006, 2010; Enkelmann et al., 2007). The detrital garents in Triassic flysch sediments in the West Qinling and Songpan-Ganzi fold belt are mainly type Bi (>76%) and type A (18%) (Figure 12) (Zhang et al., 2008; Yan et al., 2014). At the same time, the metamorphic strata of the Triassic in the Songpan-Ganzi metamorphic belt generally do not exceed the low green schist facies (BGMRSP, 1991; Dirks et al., 1994; Brugier et al., 1997; Huang et al., 2003; Roger et al., 2010). Therefore, type Bi garnet should be the main type of garnet supplied by the Songpan-Ganzi fold belt. Our provenance analysis shows that the material supply by the Songpan-Ganzi fold belt is gradually stronger from the Lower Cretaceous Tianmashan to Upper Cretaceous Guankou Formation. Based on this, Bi type garnet should take up a higher proportion in the sediments of the Late Cretaceous, which is inconsistent with the actual analysis results.

Li et al. (2018) showed that the continental clastic rocks deposition in the Sichuan Basin had increased recirculation since the Middle Jurassic period. Although there are abundant detrital garnets in the Upper Triassic Xujiahe Formation and the Middle Jurassic Shaximiao Formation sandstones in the Sichuan Basin (An et al., 2011; Shi et al., 2011), the morphological characteristics of garnets in the Cretaceous sandstones do not support the strong recirculation deposition (Figure 11). All the heavy mineral analysis samples showed that the content of garnet in the Early Cretaceous sandstone samples was relatively low (average 3.8%), and the most obvious rich garnet sediments in the region appeared in the Upper Cretaceous Guankou Formation (this study) and Gaokanba Formation (Deng et al., 2018; Jiang et al., 2019), whose geochemical analysis indication takes type Bii as the absolute advantage. The presence of Type A garnets in all formations is interesting. Type A garnet accounts for a major proportion (70%) in Early Cretaceous and has a similar proportion in Middle-Late Cretaceous, still maintaining at about 40% (Figure 9). They are most likely derived from high-grade granulite-facies metasedimentary rocks or charnockite and intermediate felsic igneous rock (Sabeen et al., 2002; Morton et al., 2004; Mange and Morton, 2007; Krippner et al., 2014). There was no charnockites reported from the potential source area of the Sichuan Basin.

Regional geological research shows that high-grade metamorphic complexes exist in the widely outcropping metamorphic massifs and Kangdian grey gneisses in the Longmenshan orogenic belt (SBGMR, 1982; He et al., 1988; Zhou et al., 2006b; Liu, 2006; Xu et al., 2016). Granitic gneisses, locally accompanied by variable amounts of amphibolite and garnet or amphibole two-pyroxene granulite, are the most voluminous rocks in these complexes (Zhou et al., 2006a). In the mixed gneiss of these metamorphic complexes, mainly garnet assemblage consists of pyrope, almandine, grossularite, and andradite (He et al., 1988). Moreover, the posterior mountain metamorphic belt in the Longmenshan orogenic belt is an important garnet-rich metamorphic belt in the East margin of the Tibetan Plateau (Dirks et al., 1994; Worley and Wilson, 1996; Wallis et al., 2003) (Figure 1). It is especially represented by the kyanite-sillimanite-garnet belt in Danba area and the garnet belt in the Maoxian-Wenchuan ductile shear zone (SBGMR, 1982; Worley et al., 1995). The garnet in the

Damba metamorphic complex and garnet zone is mainly almandine and a small amount of grossular (Huang et al., 2003; Billerot et al., 2017).

More importantly, the garnet geochemistry of modern river sand samples in the upper reaches of the Yangtze River reveals that the garnet produced by numerous parent rocks (magmatic rocks + metamorphic rocks) in the Yangtze River catchment is mainly type B, while type A garnet is significantly lacking (Figure 12), indicating that garnet came from the medium-low grade metamorphic rocks (Wang et al., 2018). This further confirms that the garnet supplied by the Songpan-Ganzi fold belt is mainly of type B. All of the garnets from the Triassic granite plot are close to the discrimination line between the Ci and Bii fields (Figure 12), but the garnet in the Cretaceous sandstones in the Sichuan Basin is rarely near this boundary. It is suggested that there may be few garnets from granite, while metamorphic rocks are the main provenance. The Cretaceous sandstones in the Sichuan Basin obviously lack Type C garnet, which is significantly different from the garnet type in Jurassic sandstones in the Hefei Basin, which was provided by ultrahigh pressure eclogite from the Qinling-Dabieshan orogenic belt (Li R. W. et al., 2000; Wang Q. C., 2013), indicating that the provenance areas of the Sichuan Basin are lack of high-grade basic-ultrabasic metamorphic rocks, which is also consistent with the actual geological background. In conclusion, the most likely explanation for the type A garnet is that it comes from the metamorphic complexes or relatively high-grade metamorphic rocks in the Longmenshan orogenic belt, and kyanite was detected in the Tianmashan Formation (Cao et al., 2008), which supports the interpretation of proximal high metamorphic rocks provenance. Due to its special structure-geographical location, the Longmenshan orogenic belt is not only the main provenance of the basin sediments, but also the only way for the detrital materials from western source areas to flow into the basin, so the type A garnet can be continuously reflected in the sediments. The type B garnet mainly comes from the joint contribution of the Songpan-Ganzi fold belt and the metamorphic belt of the Longmenshan orogenic belt (Figure 12). The garnet in the Late Cretaceous sediments is mainly composed of intermediate P-T metamorphic rocks, which is more suitable for the Longmenshan orogenic belt.

5.2 Interpretation of detrital zircon ages

U-Pb detrital-zircon age signatures of the Cretaceous strata of the southwest corner of the Sichuan Basin (SWCSB) contain distinct age distributions that can be linked to particular source regions (Figure 13). To assess the provenance of the Cretaceous strata preserved in the SWCSB, we include previously reported DZ results from the Jiaguan and Guankou Formation sandstones (Li et al., 2018) (Figure 2). The results obtained from the U–Pb geochronology provide a wide range of ages. Age populations occur at ~2,569 Ma–2,200 Ma, ~1,976 Ma–1,464 Ma, ~865 Ma–610 Ma, ~485 Ma–322 Ma, ~242 Ma–200 Ma, and ~167 Ma–120 Ma (Figures 10, 13). By comparing the age populations of zircons in seven sediment samples and potential source areas, the results show that the age spectra of zircons have significant temporal and spatial differences (Figure 13).

In terms of time, the Early Cretaceous Tianmashan Formation shows 2,498 Ma, 1,840 Ma, 740 Ma, and 230 Ma peaks, but the 440 Ma population is significantly lower. In the Mid-Cretaceous Jiaguan Formation, the peak of the oldest age component (2,569 Ma–2,200 Ma) decreased or even disappeared, but the 440 Ma peak became one of the dominant age peaks. The most striking feature in the Late Cretaceous Guankou Formation is the abundance of late Triassic zircons (with a peak at 213 Ma) (Zhang et al., 2015) that are missing in Lower Cretaceous Tianmashan Formation sandstone. Spatially, the samples (G124 and 130) at the west edge of the basin were enriched to 1,840 Ma (48%–56%) at the peak, while those at 740 Ma, 440 Ma, and 230 Ma peak ages were poorer than samples at the interior of the basin (Figure 13A).

Figure 13C shows zircon age normalized probability density for the eastern margin of Tibetan Plateau units that contain ca. 2,480, 1,840 Ma, 750 Ma, 441 Ma, 260 Ma, and 230 Ma zircons, such as the Upper Triassic-Jurassic sediments in the southwestern and western Sichuan Basin (Deng et al., 2008; Chen et al., 2011; Zhang et al., 2015; Shao et al., 2016; Li et al., 2018), Triassic flysch sediments in Songpan-Ganzi fold belt (Weislogel et al., 2006, 2010; Enkelmann et al., 2007; Tang et al., 2017; Jian et al., 2019), Yidun group in the Yiduan terrane (Wang B. Q. et al., 2013), and the Longmenshan orogenic belt and Kangdian rift (Li X. H. et al., 2002; Li Z. X. et al., 2002; Li Z. X. et al., 2003; Zhou et al., 2006b; Zhao and Zhou, 2007; Zhao J. H. et al., 2008; Zhao X. F. et al., 2008; Huang et al., 2009; Sun et al., 2009; Duan et al., 2011; Wang L. J. et al., 2012; Chen et al., 2016, 2018), including the Emeishan large igneous province (Shellnutt, 2014 and references there in). It can be observed that the Yidun group has a significant peak at 970 Ma, while the early Paleozoic of Longmen shan orogenic belt includes more ages of 944 Ma and 513 Ma (Figure 13C). These ages are not obviously reflected in Cretaceous sediments in the Sichuan Basin. Meanwhile, MDS analysis shows that the above two potential sources are far away from the Cretaceous sandstone samples, indicating that they are less likely to provide clastic materials to the sediments in the Sichuan Basin (Figure 13D).

The oldest age population within the sample FX-1G from the Lower Cretaceous Tianmashan Formation illustrates Palaeoproterozoic ages, and shows bimodal characteristics (with a peak at 1,840 Ma and 2,498 Ma) (Figure 13C). The two age populations make up 52% of 78 concordant zircon ages. Although the sandstones were from the Jurassic and Upper Triassic Xujiahe Formations in the western margin of the Sichuan Basin, and the Songpan-Ganzi Triassic flysch may provide zircons of 1,850 Ma and 2,500 Ma ages for the Tianmashan Formation, but the detrital materials from Songpan-Ganzi are obviously enriched with zircons of 440 Ma ages. Significant Paleoproterozoic, Neoproterozoic, and Triassic populations show similarities to Upper Triassic-Jurassic sandstones in the southwestern and western Sichuan Basin (Figure 13C), indicating that their provenance is mainly from recycling sediments, while in Early Cretaceous period Songpan-Ganzi fold belt was not the main provenance area. This also explains the high ZTR index and higher percentage of rounded zircons in the Lower Cretaceous Tianmashan Formation than in overlying strata (Figure 8).

Samples from the Jiaguan and Guankou Formations, the detrital U-Pb zircon age spectra display four major age peaks at ca. 1,840 Ma, 780 Ma–830 Ma, 440 Ma, and ca. 207 Ma–230 Ma, with two minor U-Pb age peaks at ca. 167 Ma and 2,450 Ma. The peak at ca. 240 Ma–188 Ma is consistent with the occurrence of widespread granites in the Songpan-Ganzi fold belt (Zhang et al., 2007). The major age peak encountered at ca. 860 Ma–760 Ma can be linked to the Kangdian rift. The detrital U-Pb age spectra indicate that the dominant provenance of the Jiaguan Formation sediments during

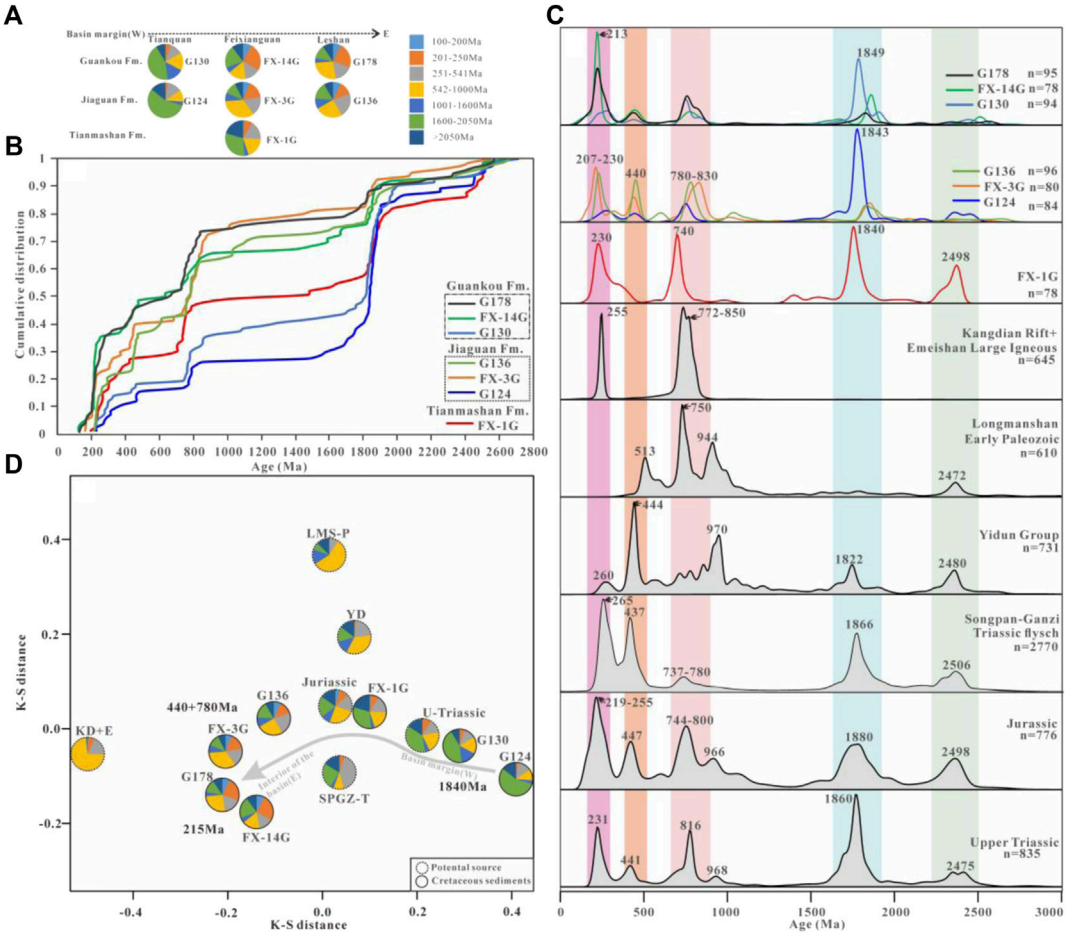

FIGURE 13
Detrital zircon U-Pb age result of the Cretaceous sediments in the Southwest corner of Sichuan Basin compared to age spectra from potential source regions. Data are shown as **(A)** pie diagrams, **(B)** cumulative distributions, **(C)** normalized probability density plots, and **(D)** a multi-dimensional scaling (MDS) plot. Data sources: Triassic flysh sediments in the Songpan-Ganzi fold belt (SPGZ-T) (Weislogel et al., 2006, 2010; Enkelmann et al., 2007; Tang et al., 2017; Jian et al., 2019); Yidun Group in the Yiduan terrane (YD) (Wang B. Q. et al., 2013); Kangdian rift (late Neoproterozoic complexes: Li X. H. et al., 2002; Li Z. X. et al., 2002, Li Z. X. et al., 2003; Zhou et al., 2006a; Zhao and Zhou, 2007; Huang et al., 2009; Zhao X. F. et al., 2008; Zhao J. H. et al., 2008; Sun et al., 2009; Wang L. J. et al., 2012) and Emeishan Large Igneous Province (Shellnutt, 2014 and references therein) (KD+E); Early Paleozoic sediments from the Longmenshan orogenic belt (LMS-P): Duan et al., 2011; Chen et al., 2016, 2018; Upper Triassic sediments in southwestern and western Sichuan Basin: Deng et al. (2008), Chen et al. (2011), and Zhang et al. (2015); Jurassic sediments in the southwestern and western Sichuan Basin: Shao et al. (2016); Li et al. (2018). Cretaceous sediments (Li et al., 2018): Jiaguan Formation (G124) and Guankou Formation (G130) from Tianquan; Jiaguan Formation (G136) and Guankou Formation (G178) Formation from Leshan. The sample position is shown in Figure 2.

the Mid-Cretaceous was the Songpan-Ganzi fold belt and Longmenshan orogenic belt (Figure 13D).

5.3 Provenance change and interpretation

Using the multi-proxy provenance data, we were able to determine the provenance evolution of a thick stratigraphic succession within the southwest corner of the Sichuan Basin and two significant provenance shifts (Figure 14). The two shifts are characterized by different compositions attributed to changes in denudation areas.

Our analysis indicates that the first significant provenance change occurs at the bottom of the Mid-Cretaceous Jiaguan Formation (ca. 125 Ma) (Figure 14). This initial transition is interpreted to reflect the introduction of sediment from the Longmenshan orogenic belt and decreasing sediment input from the Pre-Cretaceous clastic rocks in the Western margin of the Sichuan Basin. Sandstones modal analysis indicates that the lithology of the Early Cretaceous Tianmashan Formation sandstone is mainly lithic-quartz sandstone with high quartz and low plagioclase. This composition strongly indicates recycled orogen in a collision orogen as the sediment source for Tianmashan sandstones (Figure 6) (Dickinson, 1985). However, in the Jiaguan Formation sandstone, the content of microcline, plagioclase, and mica increased significantly, while the content of quartz decreased, and granite lithic fragments appeared, and few samples of Jiaguan Formation are shown in the mixed field in the Qm-F-Lt diagram, which clearly shows the composition difference with that of the Tianmashan Formation (Figure 6). Coincidentally, conglomerate clast compositions indicate from the Tianmashan Formation to the upper Jiaguan Formation, the amount of carbonate and sandstone clasts decreases while igneous and metamorphic rocks clasts increase (Figures 5, 14).

Our garnet geochemical data, based on provenance fields of idealized compositions, show that the Tianmashn Formation has more type A and less type Bii garnets than the younger Jiaguan Formation sediments

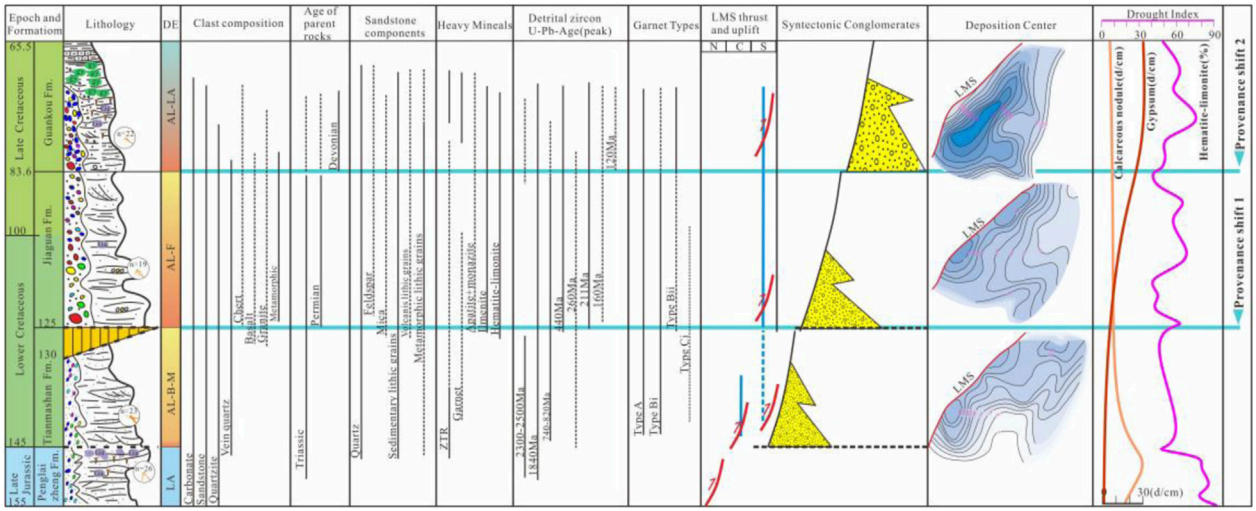

FIGURE 14
Generalized geological correlation between tectonic events (history of thrust and uplift, Longman Shan thrust belt in Longmanshan orogen), sedimentary events (depositional environment, paleocurrents, clast composition, stratigraphy, and depocenter) in the southwest corner of Cretaceous Sichuan Basin. Data for the history of the thrust and uplift were modified from Liu et al. (2018). Paleocurrent data, clast compositions, and parent rocks age data from the Cretaceous strata were modified from SBGMR (1993), Li and Ji (1993), Gou (2001), and this study. Data for the stratigraphy and depocenter were modified from SBGMR (1993). Indicators of climate change (gypsum and calcareous nodule) come from field observations and measurements. Hematite–limonite data are based on our heavy mineral analysis. DE. depositional environment; LA. lacustrine; AL-B-M. Alluvial fan, braided river, and meandering river; AL-F. Alluvial fan and fluvial; AL-LA. Alluvial fan and lacustrine.

(Figure 9). This provenance shift is also indicated in the detrital zircons age distribution diagrams (Figures 10A,C). The zircon U-Pb data presented here record a dramatic change in sediment provenance from the Tianmashan Formation to the upper Jiaguan Formation, and they refine existing constraints on sediment sources for both formations, which were deposited during the transition from fluvial system to alluvial fan-braided river system in the Southwest corner of Sichuan Basin. The Tianmashan Formation zircon age population is dominated by three peaks at 740 Ma, 1,840 Ma, and 2,498 Ma (Figure 10A). By contrast, the Jiaguan Formation is dominated by ca. 164 Ma, 213 Ma, 440 Ma, ca. 800 Ma, and 1,840 Ma zircons, whereas ca. 2,440 Ma ages are minor (Figure 10B). By comparing the previous studies on Late Triassic—Late Jurassic detrital rocks in the basin and the potential provenance data (Figures 13C,D), the detrital zircon ages of the Tianmashan Formation are very consistent with the late Triassic Xujiahe Formation in the western margin of the Sichuan Basin, reflecting the bimodal characteristics of 1,840 Ma and 2,500 Ma. This indicates the migration of the erosion center from the Late Triassic Xujiahe Formation ranges to the Longmenshan orogenic belt and Songpan-Ganzi fold belt. Heavy mineral compositions support this migration: samples of Tianmashan Formation have higher ZTR values (42.58%–52%) and leucoxene with low garnet compared to that of the Jiaguan Formation. Moreover, ilmenite, monazite, and biotite with unstable physical properties are increased in the Jiaguan Formation. In addition, chromium spinel and ilmenite, which represent the basic-ultrabasic parent rocks, began to increase.

A new significant compositional change occurred in the Guankou Formation, with a Late Cretaceous age indicated by provenance shift 2. This compositional change is characterized by the increase of fossiliferous carbonate clasts and the substantial decrease of sandstone, quartzite, and vein quartz clasts (Figure 5). The content of carbonate clasts in the conglomerate can reach up to 92% (average 82%). The microfossil assemblages in the Guankou Formation carbonate clasts are similar to the reported microfauna from the Devonian Carbonates (Gou, 2001). The unstable carbonate clasts had a shorter transport distance and were probably derived from proximal sources such as the southern section of the Longmenshan orogenic belt. This provenance change is also evidenced by the slight decrease lithic fragments of metamorphic rocks. The heavy mineral is reflected in the increase of garnet content, and the geochemical characteristics show that garnet is mainly of Type Bii, indicating that the main source is low-grade metasediments (up to amphibolite metamorphic facies). The Guankou Formation zircon age population is dominated by two peaks at 213 Ma and 1,840 Ma, with only minor Mid-Cretaceous (120 Ma–135 Ma) and Paleozoic ages (358 Ma–476 Ma), but lacking ages of 720 Ma–860 Ma. The provenance change is also reflected in the Liujia area of Yibin in southeastern Sichuan, which shows that the garnet content in the Late Cretaceous Sanhe and Gaokangba Formation is suddenly increased compared with that in the underlying strata (Deng et al., 2018; Jiang et al., 2019).

In summary, the above analyses based on multi-proxy provenance data reveal that two marked changes of sedimentary provenances occurred in the Cretaceous: a local source region for the Lower Cretaceous clastic rocks and SPGZ and LMS source regions for the Middle-Late Cretaceous successions.

5.4 Implication for mid-cretaceous rapid denudation of Eastern Tibetan plateau

Cretaceous strata of the southwestern corner of the Sichuan Basin provide an excellent opportunity to decipher changes in sediment provenance during the transition from Longmenshan thrusting through the formation of regional Cretaceous Plateau uplifts.

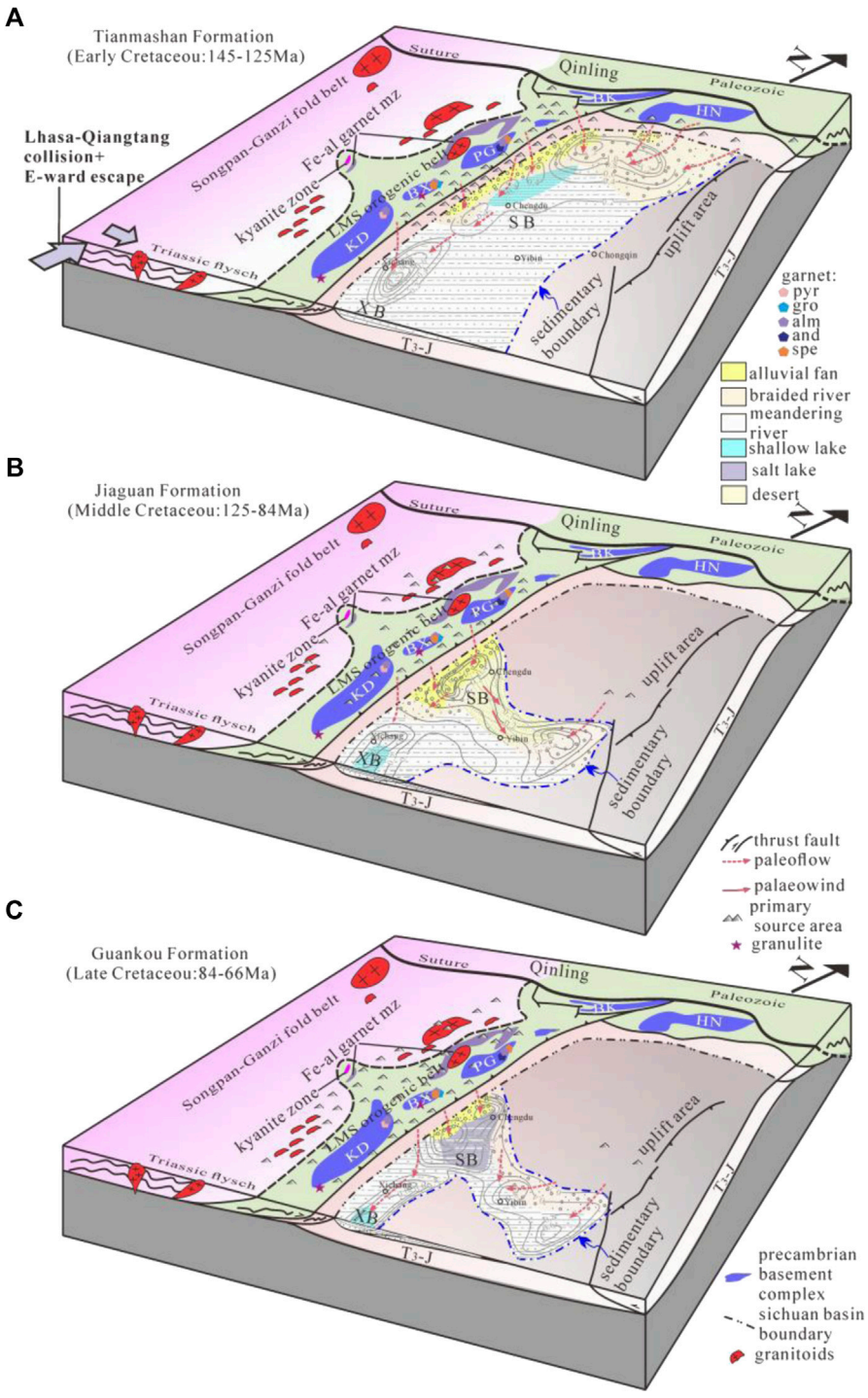

FIGURE 15
Schematic block diagrams illustrating exhumation history of the East margin of Tibetean Plateau, and tectonosedimentary evolution of its foreland basin. **(A)** Early Cretaceous, **(B)** Middle Cretaceous, and **(C)** Late Cretaceous. Isopach maps after Guo et al. (1996). HN. Hannan; BK. Bikou; KD. Kangdian; BX. Baoxing. PG. Pengguan; mz. metamorphic zone; SB. Sichuan Basin; XB. Xichang Basin.

Our detailed provenance analysis revealed that two provenance shifts were located at the bottom of the Jiangaun Formation and within the Guankou Formation, respectively (Figure 14). The two provenance changes were accompanied by the change of sedimentary environment from fluvial facies to alluvial fan and alluvial fan-lacustrine sedimentary systems (Gou, 1998; Gou, 2001).

Abrupt shifts in sediment provenance at geologic timescales can be an indication of tectonic reconfiguration of upland source areas (Horton et al., 2004). A Cretaceous palaeogeographic reconstruction with major sediment transport directions (Figure 15) shows suggested sources for Cretaceous in the Sichuan Basin that are SPGZ, LMS, and pre-Cretacepous sediments in the west edge of the Sichuan Basin. The changes in sedimentary facies and provenance indicate that the eastern

margin of the Tibetan Plateau has become the main provenance area of Cretaceous clastic rocks, and rapid uplift and denudation began to occur during the sedimentary period of the Jiaguan Formation. In other words, intense tectonic activity began in the eastern margin of the Tibetan Plateau began from Middle Cretaceous (125 Ma).

Tectonic reconstructions indicate that the Mountain Frontal Fault (Beichaun Fault), involving crystalline basement at depth, would have been most reactive during the Lower Cretaceous Tianmashan and Jiaguan syntectonic depositions, as observed at Pengguan massif (Airaghi et al., 2017b). There is a good agreement between the uplift denudation events of sedimentary records and cooling events of the Cretaceous at the eastern margin of the Tibetan Plateau revealed by low-temperature thermochronology (Liu et al., 2018).

Reviewing the history of regional tectonic evolution, the most important tectonic transformation occurred in the late Early Cretaceous, when the tectonic environment of the Sichuan Basin changed from the Qinling tectonic domain to the Tibetan Plateau tectonic domain (Liu et al., 2013a; Liu et al., 2018). On the one hand, the tectonic nature of the Qinling orogenic belt has undergone a major transformation and the structural deformation of the northwestern boundary of the basin and the northern part of the basin was basically finalized in this event, and the deposition has since ended and entered a state of uplift and denudation. Since then, the tectonic activities of the Qinling orogenic belt have no significant influence on the western Sichuan foreland basin. At the same time, affected by the long-range effects of the collision between the Lhasa and Qiangtang terranes and the collision between the Indian plate and the Eurasian plate, the central and southern section of Longmen mountains, became active again, forming a new foredeep on its front edge. The subsidence center migrated from early northwestern Sichuan to southwestern Sichuan, and then entered the Late Cretaceous to Paleogene foreland basin evolution stage under the control of the Tibetan Plateau tectonic domain. The regional uplift in the late Early Cretaceous made the Lower Cretaceous in the northern part of the basin and the Tianmashan Formation in the southern part of the basin suffered different degrees of denudation. During the deposition of the Jiaguan Formation, the depositional range was reduced, and the basin turned into a differential evolution stage of north uplift-south down. The provenance transition of the Guankou Formation responded to the late Cretaceous period (~80 Ma) with another significant uplift and denudation of Longmen Mountain at the eastern edge of the Tibetan Plateau.

6 Conclusion

Based on sedimentology and new provenance data from the Early Cretaceous Tianmashan Formation to Late Cretaceous Guankou Formation together with a thorough literature compilation, we conclude as follows:

1) Detrital garnet geochemistry of three Cretaceous sandstone samples from Feixianguan outcrop show distinct characteristics. The detrital garnets from the Tianmashan Formation with dominant input of type A and Bi, while the Jiaguan and Guankou Formations have significantly increased Bii type. Our results indicated the intermediate P-T metamorphic rocks had uplifted and suffered from erosion in the eastern Tibetan Plateau during the Mid-Cretaceous.
2) Major provenance changes were observed at 125 Ma and 80 Ma. Denudation of the SPGZ occurred after 125 Ma resulting in the change in the sediment source from the Triassic in the Longmenshan orogenic belt front to flysh sediments of the SPGZ. After 80 Ma, considerable amounts of sediments were supplied from the Longmenshan orogenic belt.
3) The significant surface uplift and rapid denudation of the eastern margin of the Tibetan Plateau were probably initiated in the mid-Cretaceous (~120 Ma).

Data availability statement

The datasets presented in this study can be found in online repositories. The names of the repository/repositories and accession number(s) can be found in the article/Supplementary Material.

Author contributions

ZW and SL conceived and designed the study. ZJ measured Chronological data and wrote the first draft of the manuscript. BR and JX provided constructive suggestions to improve the work. WH, YH, KT, and TH edited and reviewed the manuscript.

Funding

This study was financially supported by the National Natural Science Foundation of China (No. 42230310).

Acknowledgments

We thank Bin Deng and Chihua Wu from Chengdu University of Technology for constructive advice, as well as Lei Jiang for his field assistance. And we thank the reviewers for the review suggestions for this work.

Conflict of interest

The authors declare that the research was conducted in the absence of any commercial or financial relationships that could be construed as a potential conflict of interest.

Publisher's note

Supplementary material

The Supplementary Material for this article can be found online at: https://www.frontiersin.org/articles/10.3389/feart.2023.1113377/full#supplementary-material

References

Airaghi, L. (2017a). "A petro-chronological study of the longmen Shan thrust belt (eastern tibet): Geological inheritance and implication for the present geodynamics," in *Earth sciences* (Université Grenoble Alpes). English. <NNT: 2017GREAU029>. <tel-01712320>.

Airaghi, L., De Sigoyer, J., Lanari, P., Guillot, S., Vidal, O., Monie, P., et al. (2017b). Total exhumation across the Beichuan fault in the longmen Shan (eastern Tibetan plateau, China): Constraints from petrology and thermobarometry. *J. Asian Earth ences* 140, 108–121.

Airaghi, L., Sigoyer, J., Guillot, S., Robert, A., Warren, C. J., and Deldicque, D. (2018). The Mesozoic along-strike tectono-metamorphic segmentation of Longmen Shan (eastern Tibetan plateau). *Tectonics* 37, 4655–4678. doi:10.1029/2018tc005005

Allen, P, A. (2017). *Sediment routing systems: The fate of sediment from source to sink*. Cambridge, UK: Cambridge University Press.

An, H. Y., Shi, Z. Q., Zhang, H. J., Zeng, D. Y., and Zhung, H. (2011). On material source of sandstone reservoir of the middle jurassic Shaximiao Formation in west sichuan depression. *J. Sichuan Geol.* 31 (1), 29–33. (in Chinese with English abstract).

Andersen, T. (2002). Correction of common lead in U–Pb analyses that do not report 204Pb. *Chem. Geol.* 192, 59–79. doi:10.1016/s0009-2541(02)00195-x

Arne, D., Worley, B., Wilson, C., Chen, S. F., Foster, D., Luo, Z. L., et al. (1997). Differential exhumation in response to episodic thrusting along the eastern margin of the Tibetan Plateau. *Tectonophysics* 280, 239–256. doi:10.1016/s0040-1951(97)00040-1

Baral, U., Lin, D., and Chamlagain, D. (2017). Detrital zircon ages and provenance of Neogene foreland basin sediments of the Karnali River section, Western Nepal Himalaya. *J. Asian Earth Sci.* 138, 98–109. doi:10.1016/j.jseaes.2017.02.003

Billerot, A., Duchene, S., Vanderhaeghe, O., and de Sigoyer, J. (2017). Gneiss domes of the Danba metamorphic complex, songpan ganze, eastern tibet. *J. Asian Earth Sci.* 140, 48–74. doi:10.1016/j.jseaes.2017.03.006

Brugier, O., Lancelot, J. R., and Malavieille, J. (1997). U–Pb dating on single detrital zircon grains from the triassic songpan–ganze flysch (central China): Provenance and tectonic correlations. *Earth Planet. Sci. Lett.* 152 (1-4), 217–231. doi:10.1016/s0012-821x(97)00138-6

Burchfiel, B. C., Chen, Z., Liu, Y., and Royden, L. H. (1995). Tectonics of the Longmen Shan and adjacent regions, central China. *Int. Geol. Rev.* 37, 661–735. doi:10.1080/00206819509465424

Bureau of Geology and Mineral Resources of Sichuan Province (BGMRSP) (1991). *Regional geology of sichuan province*. Beijing: Geological Publishing House, 1–730. (in Chinese).

Cao, K., Li, X. H., and Wang, C. S. (2008). The cretaceous clay minerals and paleoclimate in Sichuan Basin. *Acta Geol. Sin.* 82 (1), 115–123.

Cawood, P. A., Hawkesworth, C. J., and Dhuime, B. (2012). Detrital zircon record and tectonic setting. *Geology* 40 (10), 875–878. doi:10.1130/g32945.1

Cawood, P. A., and Nemchin, A. A. (2000). Provenance record of a rift basin: U/Pb ages of detrital zircons from the perth basin, western Australia. *Sediment. Geol.* 134 (3-4), 209–234. doi:10.1016/s0037-0738(00)00044-0

Chang, E. Z. (2000). Geology and tectonics of the Songpan-Ganzi fold belt, southwestern China. *Int. Geol. Rev.* 42 (9), 813–831. doi:10.1080/00206810009465113

Chen, H. L., Zhu, M., Chen, S. Q., Xiao, A. C., Jia, D., and Yang, G. (2020). Basin-orogen patterns and the late Triassic foreland basin conversion process in the Western Yangtze Block, China. *J. Asian Earth Sci.* 194, 104311. doi:10.1016/j.jseaes.2020.104311

Chen, P. J. (1983). A Survey of the non-marine cretaceous in China. *Cretaceous Research* 4, 123–143.

Chen, Q., Sun, M., Long, X. P., Zhao, G. C., Wang, J., Yu, Y., et al. (2018). Provenance study for the paleozoic sedimentary rocks from the West yangtze block: Constraint on possible link of Southsouth China to the gondwana supercontinent reconstruction. *Precambrian Res.* 309, 271–289. doi:10.1016/j.precamres.2017.01.022

Chen, Q., Sun, M., Long, X., Zhao, G., and Yuan, C. (2016). U–Pb ages and Hf isotopic record of zircons from the late neoproterozoic and silurian–devonian sedimentary rocks of the Western yangtze block: Implications for its tectonic evolution and continental affinity. *Gondwana Res.* 31, 184–199. doi:10.1016/j.gr.2015.01.009

Chen, S. F., Wilson, C. J. L., and Worley, B. A. (1995). Tectonic transition from the Songpan-Garzê fold belt to the Sichuan Basin, south-Western China. *Basin Res.* 7, 235–253. doi:10.1111/j.1365-2117.1995.tb00108.x

Chen, Y., Liu, S. G., Li, Z. W., Deng, B., Zeng, X. L., and Lin, J. (2011). LA-ICP-MS detrital zircon u-pb geochronology approaches to the sediment provenance of the Western Sichuan Foreland Basin and limited uplift of the Longmen Mountains during the Early stage of Late Triassic. *Geotect. Metallogenia* 35 (2), 315–323.

Chengdu Institute of Geology and Mineral Resources (CGMR) (1979). *Stratigraphic summary of southwest China (cretaceous)*, 1–176.

Chung, S. L., Lo, C. H., Lee, T. Y., Zhang, Y. Q., Xie, Y. W., Li, X. H., et al. (1998). Diachronous uplift of the Tibetan plateau starting 40 Myr ago. *Nature* 394, 769–773. doi:10.1038/29511

Compiling Group of Continental Mesozoic Stratigraphy and Palaeontology in Sichuan Basin of China (1982). *Continental mesozoic stratigraphy and paleontology in sichaun Basin of China*. Chengdu: People's Publishing House of Sichuan, 5–235.

DeCelles, P. G., and Giles, K. A. (1996). Foreland basin systems. *Basin Res.* 8, 105–123. doi:10.1046/j.1365-2117.1996.01491.x

DeCelles, P. G., Langford, R. P., and Schwartz, R. K. (1983). Two new methods of paleocurrent detemination from trough cross-stratifi cation. *J. Sediment. Petrology* 53, 629–642.

Deer, W. A., Howie, R. A., and Zussman, J. (1992). *Rock-forming minerals*. Harlow, UK: Longman Group Ltd., 712.

Deer, W. A., Howie, R. A., and Zussman, J. (1997). *Rock-forming minerals volume 2B Double-chain silicates*. 2nd ed. London: The Geol. Soc., 784.

Deng, B., David, C., Jiang, L., Mark, C., Cogné, N., Wang, Z. J., et al. (2018). Heavy mineral analysis and detrital u-pb ages of the intracontinental paleo-yangzte basin: Implications for a transcontinental source-to-sink system during late cretaceous time. *Geol. Soc. Am. Bull.* 130 (11-12), 2087–2109. doi:10.1130/b32037.1

Deng, B., Liu, S. G., Jansa, L., Yong, S., and Zhang, Z. (2013a). Fractal analysis of veins in permian carbonate rocks in the lingtanchang anticline, western China. *Geofluids* 14 (2), 160–173. doi:10.1111/gfl.12059

Deng, B., Liu, S. G., Li, Z. W., Jansa, L., Liu, S., Wang, G. Z., et al. (2013b). Differential exhumation at eastern margin of the Tibetan plateau, from apatite fission-track thermochronology. *Tectonophysics* 591, 98–115. doi:10.1016/j.tecto.2012.11.012

Deng, F., Jia, D., Luo, L., Li, H. B., Li, Y. Q., and Wu, L. (2008). The contrast between provenances of songpan–ganze and Western sichuan foreland basin in the late triassic: Clues to the tectonics and paleography. *Geol. Rev.* 54, 561–573. (in Chinese with English abstract). doi:10.16509/j.georeview.2008.04.005

Dickinson, W. R., Beard, L. S., Brakenridge, G. R., Erjavic, J. L., Ferguson, R. C., Inman, K. F., et al. (1983). Provenance of North American Phanerozoic sandstones in relation to tectonic setting. *Geol. Soc. Am. Bull.* 94, 222–235. doi:10.1130/0016-7606(1983)94<222:ponaps>2.0.co;2

Dickinson, W. R. (1970). Interpreting detrital modes of graywacke and arkose. *J. Sediment. Petrology* 40, 695–707.

Dickinson, W. R. (1985). "Interpreting provenance relations from detrital modes of sandstones," in *Provenance of arenites. NATO ASI series, mathematical and physical sciences*. Editor G. G. Zuffa, 148, 333–361.

Dickinson, W. R. (1988). "Provenance and sediment dispersal in relation to paleotectonics and paleogeography of sedimentary basins," in *New perspectives in basin analysis*. Editors K. L. Kleinspehn and C. Paola (New York, NY: Springer), 3–25.

Dickinson, W. R., and Suczek, C. A. (1979). Plate tectonics and sandstone compositions. *Am. Assoc. Petroleum Geol. Bull.* 63, 2164–2182.

Ding, L., Kapp, P., Cai, F., Garzione, C. N., Xiong, Z., Wang, H., et al. (2022). Timing and mechanisms of Tibetan Plateau uplift. *Nat. Rev. Earth Environ* 3, 652–667. doi:10.1038/s43017-022-00318-4

Ding, L., Spicer, R. A., Yang, J., Xu, Q., Cai, F., Li, S., et al. (2017). Quantifying the rise of the Himalaya orogen and implications for the south Asian monsoon. *Geology* 45 (3), 215–218. doi:10.1130/g38583.1

Ding, L., Yang, D., Cai, F. L., Pullen, A., Kapp, P., Gehrels, G. E., et al. (2013). Provenance analysis of the mesozoic hoh-xil-songpan-ganzi turbidites in northern tibet: Implications for the tectonic evolution of the eastern paleo-tethys ocean. *Tectonics* 32, 34–48. doi:10.1002/tect.20013

Dirks, P. H. G. M., Wilson, C. G. L., Chen, S. F., Luo, Z. L., and Liu, S. G. (1994). Tectonic evolution of the NE margin of the Tibetan plateau: Evidence from the central longmenshan, sichuan province, China. *J. Southeast Asian Earth Sci.* 9, 181–192. doi:10.1016/0743-9547(94)90074-4

Druschke, P., Hanson, A. D., Yan, Q., Wang, Z. Q., and Wang, T. (2006). Stratigraphic and U-Pb SHRIMP detrital zircon evidence for a Neoproterozoic continental arc, Central China: Rodinia implications. *J. Geol.* 114, 627–636. doi:10.1086/506162

Duan, L., Meng, Q. R., Zhang, C. L., and Liu, X. M. (2011). Tracing the position of the southsouth China block in gondwana: U–Pb ages and Hf isotopes of devonian detrital zircons. *Gondwana Res.* 19, 141–149. doi:10.1016/j.gr.2010.05.005

Enkelmann, E., Weislogel, A., Ratschbacher, L., Eide, E., Renno, A., and Wooden, J. (2007). How was the triassic songpan-ganze basin filled? A provenance study. *Tectonics* 26. doi:10.1029/2006TC002078

Enkin, R. J., Courtillot, V., Xing, L., Zhang, Z., Zhuang, Z., and Zhang, J. (1991). The stationary Cretaceous paleomagnetic pole of Sichuan (south China block). *Tectonics* 10 (3), 547–559. doi:10.1029/90tc02554

Feo-Codecido, G. (1956). Heavy-mineral techniques and their application to Venezuelan stratigraphy. *Am. Assoc. Petroleum Geol. Bull.* 40, 984–1000.

Fielding, E. J. (1996). Tibet uplift and erosion. *Tectonophysics* 260, 55–84. doi:10.1016/0040-1951(96)00076-5

Garzanti, E., Doglioni, C., Vezzoli, G., and Ando, S. (2007). Orogenic belts and orogenic sediment provenance. *J. Geol.* 115, 315–334. doi:10.1086/512755

Gehrels, G. (2014). Detrital zircon U-Pb geochronology applied to tectonics. *Annu. Rev. Earth Planet. Sci.* 42, 127–149. doi:10.1146/annurev-earth-050212-124012

Gong, D. X., Wu, C. H., Zou, H., Zhou, X., Zhou, Y., Tan, H. Q., et al. (2021). Provenance analysis of late triassic turbidites in the eastern songpan–ganzi flysch complex:

Sedimentary record of tectonic evolution of the eastern PaleoTethys ocean. *Mar. Petroleum Geol.* 126, 104927. doi:10.1016/j.marpetgeo.2021.104927

Gou, Z. H. (2001). Characteristics of Jurassic-Tertiary conglomerates and depositional environment in the Dayi-Wenchuan area, Sichuan. *Regional Geol. China* 17 (2), 124–131. (in Chinese with English abstract).

Gou, Z. H. (1998). The jurassic-cretaceous in the yaan-baoxing area, sichuan. *Regional Geol. China* 20 (1), 25–32. (in Chinese with English abstract).

Guo, Z. W., Deng, K. L., and Han, Y. F. (1996). *Formation and evolution of the Sichuan Basin*. Beijing: Geologic Publishing House.

Harland, W. B., Cox, A. V., Llewellyn, P. G., Pickton, C. A., Smith, A. G., and Walted, R. (1982). *A geologic time scale*. New York: Cambridge University Press.

Harrowfield, M. J., and Wilson, C. J. L. (2005). Indosinian deformation of the songpan garzê fold belt, northeast Tibetan plateau. *J. Struct. Geol.* 27 (1), 101–117. doi:10.1016/j.jsg.2004.06.010

Hartley, A. J., and Otava, J. (2001). Sediment provenance and dispersal in a deep marine foreland basin: The Lower Carboniferous Culm Basin, Czech Republic. *J. Geol. Soc. Lond.* 158, 137–150. doi:10.1144/jgs.158.1.137

He, J. M., Chen, G. H., Yang, Z. L., Min, J. K., and Liu, Q. X. (1988). *The Kangdian gray gneisses*. Chongqing: Chengdu Institute of Geology and Mineral ResourcesChongqing Publishing House. (in Chinese with English abstract).

Hong, D. M., Jian, X., Fu, L., and Zhang, W. (2020b). Garnet trace element geochemistry as a sediment provenance indicator: An example from the Qaidam basin, northern Tibet. *Mar. Petroleum Geol.* 116, 104316. doi:10.1016/j.marpetgeo.2020.104316

Hong, D. M., Jian, X., Huang, X., Zhang, W., and Ma, J. G. (2020a). Garnet trace elemental geochemistry and its application in sedimentary provenance analysis. *Earth Sci. Front.* 27 (3), 191–201. (in Chinese with English abstract). doi:10.13745/j.esf.sf.2020.1.1

Horton, B. K., Constenius, K. N., and DeCelles, P. G. (2004). Tectonic control on coarse-grained foreland-basin sequences: An example from the Cordilleran foreland basin, Utah. *Utah. Geol.* 32, 637–640. doi:10.1130/g20407.1

Huang, H. Y., He, D. F., Li, D., and Li, Y. D. (2019a). Detrital zircon U-Pb ages of Paleogene deposits in the southwestern Sichuan foreland basin, China: Constraints on basin-mountain evolution along the southeastern margin of the Tibetan Plateau. *Geol. Soc. Am. Bull.* 131 (3-4), 668–686. doi:10.1130/b35211.1

Huang, M. H., Buick, I. S., and Hou, L. W. (2003). Tectonometamorphic evolution of the eastern tibet plateau: Evidence from the central songpan-garze orogenic belt, western China. *J. Petrology* 44 (2), 255–278. doi:10.1093/petrology/44.2.255

Huang, T. K., and Chen, B. W. (1987). *The evolution of the tethys in China and adjacent regions: Beijing*. Beijing: Geological Publishing House, 108–109. (in Chinese).

Huang, X., Jian, X., Zhang, W., Hong, D. M., Guan, P., and Du, J. X. (2019b). Detrital garnet geochemistry-based provenance analysis and interpretation: The effect of grain size. *Acta Sedimentol. Sin.* 37 (3), 511–518. (in Chinese with English abstract). doi:10.14027/j.issn.1000.0550.2018.161

Huang, X. L., Xu, Y. G., Lan, J. B., Yang, Q. J., and Luo, Z. Y. (2009). Neoproterozoic adakitic rocks from mopanshan in the Western yangtze craton: Partial melts of a thickened lower crust. *Lithos* 112, 367–381. doi:10.1016/j.lithos.2009.03.028

Hubert, J. F. (1962). A zircon-tourmaline-rutile maturity index and the interdependance of the composition of heavy mineral assemblages with the gross composition and texture of sandstones. *J. Sediment. Petrology* 32, 440–450.

Ingersoll, R. V., Fullard, T. F., Ford, R. L., Grimm, J. P., Pickle, J. D., and Sares, S. W. (1984). The effect of grain size on detrital modes; a test of the Gazzi–Dickinson point-counting method. *J. Sediment. Res.* 54, 103–116.

Ingersoll, R. V., and Suczek, C. A. (1979). Petrology and provenance of neogene sand from nicobar and bengal fans, dsdp sites 211 and 218. *J. Sediment. Res.* 49 (4), 1228–1271.

Jackson, W. T., Jr., Robinson, D. M., Weislogel, A. L., Jian, X., and McKay, M. P. (2018a). Cenozoic development of the nonmarine Mula basin in the Southern Yidun terrane: Deposition and deformation in the eastern Tibetan Plateau associated with the India-Asia collision. *Tectonics* 37, 2446–2465. doi:10.1029/2018TC004994

Jackson, W. T., Jr., Robinson, D. M., Weislogel, A. L., Shang, F., and Jian, X. (2018b). Mesozoic development of nonmarine basins in the northern Yidun terrane: Deposition and deformation in the eastern Tibetan Plateau prior to the India-Asia collision. *Tectonics* 37, 2466–2485. doi:10.1029/2018TC004995

Ji, X. T., and Li, Y. L. (1995). Alluvial fan-lake facies association in the late Cretaceous-Palaeogene continental basin of the Tianquan-Lushan area. *J. Chengdu Inst. Technol.* 22 (02), 15–21. (in Chinese with English abstract).

Jia, D., Wei, G. Q., Chen, Z. X., Li, B. L., Zeng, Q., and Yang, G. (2006). Longmen Shan fold-thrust belt and its relation to the Western Sichuan Basin in central China: New insights from hydrocarbon exploration. *AAPG* 90, 1425–1447. doi:10.1306/03230605076

Jian, X., Guan, P., Zhang, D. W., Zhang, W., Feng, F., Liu, R. J., et al. (2013). Provenance of Tertiary sandstone in the northern Qaidam basin, northeastern Tibetan Plateau: Integration of framework petrography, heavy mineral analysis and mineral chemistry. *Sediment. Geol.* 290, 109–125. doi:10.1016/j.sedgeo.2013.03.010

Jian, X., Weislogel, A., and Pullen, A. (2019). Triassic sedimentary filling and closure of the eastern paleo-tethys ocean: New insights from detrital zircon geochronology of songpan-ganzi, Yidun, and West Qinling flysch in eastern tibet. *Tectonics* 38, 767–787. doi:10.1029/2018TC005300

Jiang, L., Liu, S. G., Wang, Z. J., Li, Z. W., Lai, D., He, Y., et al. (2019). Provenance change and its indication of late cretaceous in the west margin of upper yangtze basin. *Geol. Rev.* 65 (2), 477–490. (in Chinese with English abstract). doi:10.16509/j.georeview.2019.02.017

Kamp, P. J. J., Liu, S. G., Xu, G. Q., Li, Z. W., Danisik, M., and Deng, B. (2013). Cooling history of a crustal section in eastern tibet (well HC1) constrained by thermochronology. *Acta Geol. Sin.*, 57–58. (English Edition) 87(supp.

Krippner, A., Meinhold, G., Morton, A. C., Russell, E., and von Eynatten, H. (2015). Grain-size dependence of garnet composition revealed by provenance signatures of modern stream sediments from the Western Hohe Tauern (Austria). *Sediment. Geol.* 321, 25–38. doi:10.1016/j.sedgeo.2015.03.002

Krippner, A., Meinhold, G., Morton, A. C., Schönig, J., and von Eynatten, H. (2016). Heavy minerals and garnet geochemistry of stream sediments and bedrocks from the almklovdalen area, western gneiss region, SW Norway: Implications for provenance analysis. *Sediment. Geol.* 336, 96–105. doi:10.1016/j.sedgeo.2015.09.009

Krippner, A., Meinhold, G., Morton, A. C., and von Eynatten, H. (2014). Evaluation of garnet discrimination diagrams using geochemical data of garnets derived from various host rocks. *Sediment. Geol.* 306, 36–52. doi:10.1016/j.sedgeo.2014.03.004

Lenaza, D., Mazzolib, C., Velicognaa, M., and Princivalle, F. (2018). Trace and Rare Earth Elements chemistry of detrital garnets in the SE Alps and Outer Dinarides flysch basins: An important tool to better define the source areas of sandstones. *Mar. Petroleum Geol.* 98, 653–661. doi:10.1016/j.marpetgeo.2018.09.025

Li, J., Wen, X. Y., and Huang, C. M. (2016c). Lower cretaceous paleosols and paleoclimate in Sichuan Basin, China. *Cretac. Res.* 62, 154–171. doi:10.1016/j.cretres.2015.10.002

Li, J. Z., Dong, D. Z., Chen, G. S., Wang, S. Q., and Chen, K. M. (2009). Prospects and strategic position of shale gas Resources in China. *Nat. Gas. Ind.* 29 (5), 11–16. (in Chinese with English Abstract). doi:10.3787/j.issn.1000.0976.2009.05.003

Li, M. X., Liang, B., Wang, Q. W., Zhu, B., Hao, X. F., Ying, L. C., et al. (2013). Geochemistry of cretaceous argillaceous rocks in longquan mountain, western sichuan. *Geol. J. China Univ.* 19 (2), 346–354.

Li, Q. H., Zhang, Y. X., Zhang, K. J., Yan, L. L., Zeng, L., Jin, X., et al. (2017). Garnet amphibolites from the ganzi–litang fault zone, eastern Tibetan plateau: Mineralogy, geochemistry, and implications for evolution of the eastern palaeo-tethys realm. *Int. Geol. Rev.* 60, 1954–1967. doi:10.1080/00206814.2017.1396563

Li, R. B., Pei, X. Z., Liu, Z. Q., Li, Z. C., Ding, S. P., Liu, Z. G., et al. (2010a). Basin-Mountain coupling relationship of foreland basins between Dabashan and northeastern Sichuan-the evidence from LA–ICP–MS U– Pb dating of the detrital zircons. *Acta Geol. Sin.* 84, 1118–1134. (in Chinese with English abstract). doi:10.19762/jcnkidizhixuebao.2010.08.005

Li, R. W., Li, C., Jiang, M. S., Sun, S., Jin, F. Q., and Zhang, W. H. (2000). Composition of clastic garnet in the Hefei Basin and its significance to source restoration and stratigraphic correlation. *Sci. China (Series D).* 30, 91–98. (in Chinese with English abstract).

Li, W., Yang, J. L., Jiang, J. W., Liu, J. M., and Liu, Z. C. (2009). Origin of upper triassic formation water in middle Sichuan Basin and its natural gas significance. *Petroleum Explor. Dev.* 36 (4), 428–435. doi:10.1016/s1876-3804(09)60138-5

Li, X. H., Li, Z. X., Zhou, H. W., Liu, Y., and Kinny, P. D. (2002). U–Pb zircon geochronology, geochemistry and Nd isotopic study of neoproterozoic bimodal volcanic rocks in the Kangdian rift of Southsouth China: Implications for the initial rifting of rodinia. *Precambrian Res.* 113, 135–154. doi:10.1016/s0301-9268(01)00207-8

Li, Y., Allen, P. A., Densmore, A. L., and Xu, Q. (2003). Evolution of the longmen Shan foreland basin (western sichuan, China) during the late triassic indosinian orogeny. *Basin Res.* 15, 117–138. doi:10.1046/j.1365-2117.2003.00197.x

Li, Y. L., and Ji, X. T. (1993). Petrological character of Daxi conglomerate in Lushan-Tianquan and its provenance. *J. Mineral Petrol* 13 (3), 68–73. (in Chinese wieh English abstract). doi:10.19719/j.cnki.1001-6872.1993.03.011

Li, Y. Q., He, D. F., Chen, L. B., Mei, Q. H., Li, C. X., and Zhang, L. (2016a). Cretaceous sedimentary basins in sichuan, SW China: Restoration of tectonic and depositional environments. *Cretac. Res.* 57, 50–65. doi:10.1016/j.cretres.2015.07.013

Li, Y. Q., He, D. F., Li, D., Lu, R. Q., Fan, C., Sun, Y. P., et al. (2018). Sedimentary provenance constraints on the jurassic to cretaceous paleogeography of Sichuan Basin, SW China. *Gondwana Res.* 60, 15–33. doi:10.1016/j.gr.2018.03.015

Li, Y. Q., He, D. F., Li, D., Wen, Z., Mei, Q. H., Li, C. X., et al. (2016b). Detrital zircon U–Pb geochronology and provenance of Lower Cretaceous sediments: Constraints for the northwestern Sichuan pro-foreland basin. *Palaeogeogr. Palaeoclimatol. Palaeoecol.* 453, 52–72. doi:10.1016/j.palaeo.2016.03.030

Li, Y. W. (1979). Discovery of cretaceous brackish-water foraminifera and ostracoda in the Sichuan Basin, and their significance. *Geol. Rev.* 25 (1), 2–9. (in Chinese with English abstract). doi:10.16509/j.georeview.1979.01.002

Li, Y. W. (1982). "Late jurassic-paleogene ostracods in Sichuan Basin, and their significance of stratigraphy," in *Continental mesozoic stratigraphy and paleontology in Sichuan Basin of China, Part II, paleontological professional papers, 274-345* (Chengdu, China: People's Publishing House of Sichuan). (in Chinese with English abstract).

Li, Y. W. (1983). On the non-marine jurassic-cretaceous boundary in Sichuan Basin by ostracoda. *Bull. Chengdu Inst. Geol. Min. Res. Chin. Acad. Geol. Sci.* 4, 77–89. (in Chinese with English abstract). doi:10.16509/j.georeview.1983.05.013

Li, Y. W. (1988). The application of ostracoda to the location of the non-marine jurassic-cretaceous boundary in the sichuan basin of China. *Dev. Palaeontol. Stratigr.* 11, 1245–1260.

Li, Y. W. (1987). The cretaceous geological history of the Sichuan Basin. *Regional Geol. China* 1, 51–56. (in Chinese with English abstract).

Li, Z. W., Chen, H. D., Liu, S. G., Hou, M. C., and Deng, B. (2010b). Differential uplift driven by thrusting and its lateral variation along the Longmenshan belt, Western Sichaun, China: Evidence from fission track thermochronology. *Chin. J. Geol.* 45 (4), 944–968. (in Chinese with English abstract).

Li, Z. W., Liu, S. G., Chen, H. D., Deng, B., Hou, M. C., Wu, W. H., et al. (2012). Spatial variation in MesoCenozoic exhumation history of the longmen Shan thrust belt (eastern Tibetan plateau) and the adjacent western Sichuan Basin: Constraints from fission track thermochronology. *J. Asian Earth Sci.* 47 (1), 185–203. doi:10.1016/j.jseaes.2011.10.016

Li, Z. W., Liu, S. G., Chen, H. D., Liu, S., Guo, B., and Tian, X. B. (2008). Structural segmentation and zonation and differential deformation across and along the Longmen thrust belt, west Sichuan, China. *J. Chengdu Univ. Technol. Sci. Technol. Ed.* 35, 440–455. (in Chinese with English abstract). doi:10.3969/j.issn.1671-9727.2008.04.0440.15

Li, Z. X., Li, X. H., Kinny, P. D., Wang, J., Zhang, S., and Zhou, H. (2003). Geochronology of neoproterozoic syn-rift magmatism in the yangtze craton, south China and correlations with other continents: Evidence for a mantle superplume that broke up rodinia. *Precambrian Res.* 122, 85–109. doi:10.1016/s0301-9268(02)00208-5

Li, Z. X., Li, X. H., Zhou, H. W., and Kinny, P. D. (2002). Grenvillian continental collision in south China: New SHRIMP U–Pb zircon results and implications for the configuration of rodinia. *Geology* 30, 163–166. doi:10.1130/0091-7613(2002)030<0163:gccisc>2.0.co;2

Lin, M. B., Gou, Z. H., Wang, G. Z., Deng, J. H., Li, Y., Wang, D. Y., et al. (1996). *A research on the Orogenic model of Longmen mountains orogenic belt*. Chengdu: Press of Chengdu University of Science and Technology. (in Chinese with English abstract).

Lin, M. B. (2008). The huge Wenchaun earthquake and Longmen tectonic belt. *J. Chengdu Univ. Technol. Sci. Technol. Ed.* 35 (4), 366–370. (in Chinese with English abstract).

Linka, K. M., and Stawikowski, W. (2013). Garnet and tourmaline as provenance indicators of terrigenous material in epicontinental carbonates (Middle Triassic, S Poland). *Sediment. Geol.* 291 (4), 27–47. doi:10.1016/j.sedgeo.2013.03.005

Liu, S. G., Deng, B., Jansa, L., Li, Z. W., Sun, W., Wang, G. Z., et al. (2018). Multi-stage basin development and hydrocarbon accumulations: A review of the sichuan basin at eastern margin of the Tibetan plateau. *J. Earth Sci.* 29 (2), 307–325. doi:10.1007/s12583-017-0904-8

Liu, S. G., Deng, B., Jansa, L., Wang, G. Z., Li, X. H., Wang, C. S., et al. (2013b). Late triassic thickening of the songpan-ganzi triassic flysch at the edge of the northeastern Tibetan plateau. *Int. Geol. Rev.* 55 (16), 2008–2015. doi:10.1080/00206814.2013.812705

Liu, S. G., Deng, B., Li, Z. W., Jansa, L., Liu, S., Wang, G. Z., et al. (2013a). Geological evolution of the longmenshan intracontinental composite orogen and the eastern margin of the Tibetan plateau. *J. Earth Sci.* 24 (6), 874–890. doi:10.1007/s12583-013-0391-5

Liu, S. G., Luo, Z. L., Zhao, X. K., Xu, G. S., Wang, G. Z., and Zhang, C, J. (2003). Coupling relationships of sedimentary basin-orogenic belt systems and their dynamic models in west China. *Acta Geol. Sin.* 77 (2), 177–186. (in Chinese with English abstract).

Liu, S. G., Sun, W., Li, Z. W., Deng, B., and Liu, S. (2008). Tectonic uplifting and gas pool formation since late cretaceous epoch, Sichuan Basin. *Nat. Gas. Geosci.* 19 (3), 293–300. (in Chinese with English Abstract). doi:10.11764/j.issn.1672-1926.2008.03.0293.08

Liu, S. G. (1993). *The Formation and evolution of longmengshan thrust zone and western sichuan*. ChinaChengdu: Press of Chengdu University of Science and Technology.

Liu, S., Li, Z., Kamp, P. J. J., Ran, B., Li, J., Deng, B., et al. (2019). Discovery of the Mesozoic Zoige paeo-plateau in eastern Tibetan Plateau and its geological significance. *J. Chengdu Univ. Technol. Sci. Technol. Ed.* 46 (1), 1–28. (in Chinese with English abstract). doi:10.3969/j.issn.1671-9727.2019.01.01

Liu, W. Z. (2006). The Formation age and tectonic setting of the kangding complex in the western margin of the yangtze block. *J. Anhui Univ. Sci. Technol. Nat. Sci.* 26 (4), 1–5. (in Chinese with English abstract). doi:10.3969/j.issn.1672-1098.2006.04.0001.05

Liu, X., Zhan, Q. Y., Zhu, D. C., Wang, Q., Xie, J. C., and Zhang, L. L. (2021). Provenance and tectonic uplift of the Upper Triassic strata in the southern Songpan-Ganzi fold belt, SW China: Evidence from detrital zircon geochronology and Hf isotope. *Acta Petrol. Sin.* 37 (11), 3513–3526. (in Chinese with English abstract). doi:10.18654/1000-0569/2021.11.16

Liu-Zeng, J., Zhang, J. Y., McPhillips, D., Reiners, P., Wang, W., Pik, R., et al. (2018). Multiple episodes of fast exhumation since Cretaceous in southeast Tibet, revealed by low-temperature thermochronology. *Earth Planet. Sci. Lett.* 490, 62–76. doi:10.1016/j.epsl.2018.03.011

Löwen, A. K., Meinhold, G., and Güngör, T. (2018). Provenance and tectonic setting of carboniferous–triassic sandstones from the karaburun peninsula, Western Turkey: A multi-method approach with implications for the palaeotethys evolution. *Sediment. Geol.* 375, 232–255. doi:10.1016/j.sedgeo.2017.11.006

Ludwig, K. R. (2003). *User's manual for isoplot/ex v3.0a geochronology toolkit for microsoft excel*. Berkely: Berkeley Geochronological Center Special Publications, 25–31.

Luo, L., Qi, J. F., Zhang, M. Z., Wang, K., and Han, Y. Z. (2014). Detrital zircon U–Pb ages of late triassic–late jurassic deposits in the Western and northern Sichuan Basin margin: Constraints on the foreland basin provenance and tectonic implications. *Int. J. Earth Sci. Geol. Rundsch.* 103, 1553–1568. doi:10.1007/s00531-014-1032-7

Lv, F., Ran, B., Liu, S. G., Wang, Z. J., Sun, T., Li, X. H., et al. (2022). Provenance of the Lower Jurassic quartz-rich conglomerate in northwestern sichuan basin and its link with the pre-collisional unroofing history of the northlongmen Shan thrust belt, NE Tibetan plateau margin. *Front. Earth Sci.* 10, 982354. doi:10.3389/feart.2022.982354

Mange, M. A., and Maurer, H. F. W. (1992). *Heavy minerals in colour*. London: Chapman & Hall, 147.

Mange, M. A., and Morton, A. C. (2007). "Chapter 13 geochemistry of heavy minerals," in *Developments in sedimentology*. Editors A. M. Maria and T. W. David (Elsevier), 345–391.

Mange, M. A. (2002). *16th international sedimentological congress*. South Africa: Rand Afrikaans University, 34.New look at heavy minerals—A short course

Meng, Q. R., Wang, E. Q., and Hu, J. M. (2005). Mesozoic sedimentary evolution of the northwest Sichuan basin: Implication for continued clockwise rotation of the southsouth China block. *GSA Bull.* 117, 396. doi:10.1130/B25407.1

Ministry of Geology and Mineral Resources (1991). *Regional geology of sichaun province*. Beijing: Geological Publishing House, 1–689. (in Chinese with English abstract).

Morton, A. C. (1985). A new approach to provenance studies: Electron microprobe analysis of detrital garnets from middle jurassic sandstones of the northern north sea. *Sedimentology* 32, 553–566. doi:10.1111/j.1365-3091.1985.tb00470.x

Morton, A. C., Hallsworth, C. R., and Chalton, B. (2004). Garnet compositions in scottish and Norwegian basement terrains: A framework for interpretation of north sea sandstone provenance. *Mar. Petrol. Geol.* 21, 393–410. doi:10.1016/j.marpetgeo.2004.01.001

Morton, A. C., and Hallsworth, C. R. (1994). Identifying provenance specific features of detrital heavy mineral assemblages in sandstones. *Sediment. Geol.* 90, 241–256. doi:10.1016/0037-0738(94)90041-8

Morton, A. C., and Hallsworth, C. R. (1999). Processes controlling the composition of heavy mineral assemblages in sandstones. *Sediment. Geol.* 124, 3–29. doi:10.1016/s0037-0738(98)00118-3

Morton, A. C., Whitham, A. G., and Fanning, C. M. (2005). Provenance of late cretaceous to paleocene submarine fan sandstones in the Norwegian sea: Integration of heavy mineral, mineral chemical and zircon age data. *Sediment. Geol.* 182, 3–28. doi:10.1016/j.sedgeo.2005.08.007

Morton, A., Knox, R., and Frei, D. (2016). Heavy mineral and zircon age constraints on provenance of the sherwood sandstone group (Triassic) in the eastern Wessex basin, UK. *Proc. Geol. Assoc.* 127 (4), 514–526. doi:10.1016/j.pgeola.2016.06.001

Mu, H. X., Yan, D. P., Qiu, L., Yang, W. X., Kong, R. Y., Gong, L. X., et al. (2019). formation of the late triassic Western sichuan foreland basin of the qinling orogenic belt, SW China: Sedimentary and geochronological constraints from the Xujiahe Formation. *J. Asian Earth Sci.* 183, 103938. doi:10.1016/j.jseaes.2019.103938

Mulch, A., and Chamberlain, C. P. (2006). The rise and growth of Tibet. *Nature* 439, 670–671. doi:10.1038/439670a

Najman, Y., and Garzanti, E. (2000). Reconstructing early Himalayan tectonic evolution and paleogeography from Tertiary foreland basin sedimentary rocks, northern India. *Geol. Soc. Am. Bull.* 112 (3), 435–449. doi:10.1130/0016-7606(2000)112<435:rehtea>2.0.co;2

Nichols, G. (2009). *Sedimentology and stratigraphy*. John Wiley & Sons.

Otofuji, Y., Inoue, Y., Funahara, S., Murata, F., and Zheng, X. (1990). Palaeomagnetic study of eastern tibet-deformation of the three rivers region. *Geophys. J. Int.* 103, 85–94. doi:10.1111/j.1365-246x.1990.tb01754.x

Panaiotu, C. E., Vasiliev, I., Panaiotu, C. G., Krijgsman, W., and Langereis, C. G. (2007). Provenance analysis as a key to orogenic exhumation: A case study from the East carpathians (Romania). *Terra nova.* 19 (2), 120–126. doi:10.1111/j.1365-3121.2006.00726.x

Pettijohn, F. J., Potter, P. E., and Siever, R. (1987). *Sand and sandstone*. third ed. New York: Springer.

Qian, T., Liu, S. F., Li, W. P., Gao, T. J., and Chen, X. L. (2015). Early–middle jurassic evolution of the northern yangtze foreland basin: A record of uplift following triassic continent–continent collision to form the qinling–dabieshan orogenic belt. *Int. Geol. Rev.* 57, 327–341. doi:10.1080/00206814.2015.1006270

Rahl, J. M., Harbor, D. J., Galli, C. I., and O'Sullivan, P. (2018). Foreland basin record of uplift and exhumation of the Eastern Cordillera, northwest Argentina. *Tectonics* 37, 4173–4193. doi:10.1029/2017TC004955

Reid, A. J., Fowler, A. P., Phillips, D., and Wilson, C. J. L. (2005). Thermochronology of the Yidun arc, central eastern Tibetan plateau: Constraints from 40Ar/39Ar K-feldspar and apatite fission track data. *J. Asian Earth Sci.* 25, 915–935. doi:10.1016/j.jseaes.2004.09.002

Reid, A., Wilson, C. J. L., Shun, L., Pearson, N., and Belousova, E. (2007). Mesozoic plutons of the Yidun arc, SW China: U/Pb geochronology and Hf isotopic signature. *Ore Geol. Rev.* 31 (1-4), 88–106. doi:10.1016/j.oregeorev.2004.11.003

Richardson, N. J., Densmore, A. L., Seward, D., Fowler, A., Wipf, M., Ellis, M. A., et al. (2008). Extraordinary denudation in the Sichuan Basin: Insights from low-temperature thermochronology adjacent to the eastern margin of the Tibetan plateau. *J. Geophys. Res.* 113 (B4), B04409. doi:10.1029/2006jb004739

Roger, F., Jolivet, M., and Malavieille, J. (2010). The tectonic evolution of the songpan garze (north tibet) and adjacent areas from proterozoic to present: A synthesis. *J. Asian Earth Sci.* 39, 254–269. doi:10.1016/j.jseaes.2010.03.008

Roger, F., Malavieille, J., Leloup, P. H., Calassou, S., and Xu, Z. (2004). Timing of granite emplacement and cooling in the Songpan-Garzê Fold Belt (eastern Tibetan Plateau) with tectonic implications. *J. Asian Earth Sci.* 22 (5), 465–481. doi:10.1016/s1367-9120(03)00089-0

Rohrmann, A., Kapp, P., Carrapa, B., Reiners, P. W., Guynn, J., Ding, L., et al. (2012). Thermochronologic evidence for plateau formation in central Tibet by 45 Ma. *Geology* 40, 187–190. doi:10.1130/g32530.1

Rowley, D. B., and Currie, B. S. (2006). Palaeo–altimetry of the late eocene to miocene lunpola basin, central tibet. *Nature* 439, 677–681. doi:10.1038/nature04506

Sabeen, H. M., Ramanujam, N., and Morton, A. C. (2002). The provenance of garnet: Constraints provided by studies of coastal sediments from southern India. *Sediment. Geol.* 152, 279–287. doi:10.1016/s0037-0738(02)00083-0

Sevastjanova, I., Hall, R., and Alderton, D. (2012). A detrital heavy mineral viewpoint on sediment provenance and tropical weathering in SE Asia. *Sediment. Geol.* 280, 179–194. doi:10.1016/j.sedgeo.2012.03.007

Shao, T. B., Cheng, N. F., and Song, M. S. (2016). Provenance and tectonic-paleogeographic evolution: Constraints from detrital zircon U–Pb ages of late triassic–early jurassic deposits in the northern Sichuan basin, central China. *J. Asian Earth Sci.* 127, 12–31. doi:10.1016/j.jseaes.2016.05.027

Shellnutt, J. G. (2014). The emeishan large igneous province: A synthesis. *Geosci. Front.* 5, 369–394. doi:10.1016/j.gsf.2013.07.003

Shen, C. B., Mei, L. F., and Xu, S. H. (2009). Fission track dating of mesozoic sandstones and its tectonic significance in the eastern Sichuan Basin, China. *Radiat. Meas.* 44 (9/10), 945–949. doi:10.1016/j.radmeas.2009.10.001

Shen, X. M., Tian, Y. T., Zhang, G. H., Zhang, S. M., Carter, A., Kohn, B. P., et al. (2019). Late Miocene hinterland crustal shortening in the Longmen Shan thrust belt, the eastern margin of the Tibetan Plateau. *J. Geophys. Res. Solid Earth* 124 (11), 11972–11991. doi:10.1029/2019jb018358

Shi, Z. S., Wang, X. Q., and Wu, C. J. (2011). The heavy minerals and provenances of the upper triassic Xujiahe Formation in Sichuan Basin. *Nat. Gas. Geosci.* 22 (4), 618–627. (in Chinese with English Abstract).

Sichuan Bureau of Geology and Mineral Resources (SBGMR) (1997). *Stratigraphy (lithostratic) of sichuan province*. Wuhan: China University of Geosciences Press.

Sichuan Bureau of Geology and Mineral Resources (SBGMR) (1982). "Writing group of continental mesozoic stratigraphy and paleontology," in *Continental mesozoic stratigraphy and paleontology in sichuan basin of China*. Editor S. Basin (Chengdu: People's Publishing House of Sichuan), 622–179 (in Chinese).

Sichuan Bureau of Geology and Mineral Resources (SBGMR) (1993). *Report of 1: 50,000 tianquan and lingguan regional geological survey*. Chengdu: Chengdu University of Technology.

Smyth, H. R., Hall, R., and Nichols, G. J. (2008). Significant volcanic contribution to some quartz-rich sandstones, east java, Indonesia. *J. Sediment. Res.* 78 (5), 335–356. doi:10.2110/jsr.2008.039

Spicer, R. A., Su, T., Valdes, P. J., Farnsworth, A., Wu, F. X., Shi, G., et al. (2021). Why 'the uplift of the Tibetan Plateau' is a myth? *Natl. Sci. Rev.* 8 (1), nwaa091. doi:10.1093/nsr/nwaa091

Su, D. Z. (1983). Note on a new lepidotes from the cretaceous of sichaun. *Vertebr. Palasiat.* 21 (3), 177–185. (in Chinese with English abstract).

Sun, W. H., Zhou, M. F., Gao, J. F., Yang, Y. H., Zhao, X. F., and Zhao, J. H. (2009). Detrital zircon U–Pb geochronological and Lu–Hf isotopic constraints on the Precambrian magmatic and crustal evolution of the Western Yangtze Block, SW China. *Precambrian Res.* 172, 99–126. doi:10.1016/j.precamres.2009.03.010

Sun, W. H., Zhou, M. F., and Zhao, J. H. (2007). Geochemistry and tectonic significance of basaltic lavas in the neoproterozoic yanbian group, southern sichuan province, southwest China. *Int. Geol. Rev.* 49, 554–571. doi:10.2747/0020-6814.49.6.554

Tan, X. B., Liu, Y, D., Lee, Y. H., Lu, R. Q., Xu, X. W., Suppe, J., et al. (2019). Parallelism between the maximum exhumation belt and the Moho ramp along the eastern Tibetan Plateau margin: Coincidence or consequence? *Earth Planet. Sci. Lett.* 507, 73–84. doi:10.1016/j.epsl.2018.12.001

Tan, X. B., Xu, X. W., Lee, Y. H., Lu, R. Q., Xu, C., Li, K., et al. (2017). Late Cenozoic thrusting of major faults along the central segment of Longmen Shan, eastern Tibet: Evidence from low-temperature thermochronology. *Tectonophysics* 712-713, 145–155. doi:10.1016/j.tecto.2017.05.016

Tang, Y., Zhang, Y., and Tong, L. (2017). Provenance of middle to late triassic sedimentary rocks in the zoige depression in the ne part of the songpan-ganzi flysch basin: Petrography, heavy minerals, and zircon U-Pb geochronology. *Geol. J.* 52, 449–462. doi:10.1002/gj.3001

Teraoka, Y., Suzuki, M., Hayashi, T., and Kawakami, K. (1997). Detrital garnets from paleozoic and mesozoic sandstones in the onogawa area, east kyushu, southwest Japan. *Bull. Fac. Educ. Hiroshima Univ.* 19, 87–101.

Teraoka, Y., Suzuki, M., and Kawakami, K. (1998). Provenance of cretaceous and Paleogene sediments in the median zone of southwest Japan. *Bull. Geol. Surv. Jpn.* 49, 395–411.

Tian, Q. (2018). *Provenance analysis of the lower jurassic baitianba Formation in northwestern Sichuan Basin and its tectonic significance*. Master's thesis. Chengdu, China: Chengdu University of Technology, 1–81. (in Chinese with English abstract).

Tian, Y. T., Kohn, B. P., Gleadow, A. J. W., and Hu, S. B. (2014a). A thermochronological perspective on the morphotectonic evolution of the southeastern Tibetan Plateau. *J. Geophys Res. Solid Earth* 119 (1), 676–698. doi:10.1002/2013jb010429

Tian, Y. T., Kohn, B. P., Gleadow, A. J. W., and Hu, S. B. (2013). Constructing the Longmen Shan eastern Tibetan Plateau margin: Insights from low-temperature thermochronology. *Tectonics* 32, 576–592. doi:10.1002/tect.20043

Tian, Y. T., Kohn, B. P., Hu, S. B., and Gleadow, A. J. W. (2014b). Postorogenic rigid behavior of the eastern Songpan-Ganze terrane: Insights from low-temperature thermochronology and implications for intracontinental deformation in central Asia. *Geochem. Geophys. Geosystems* 15 (2), 453–474. doi:10.1002/2013gc004951

Tian, Y. T., Li, R., Tang, Y., Xu, X., Wang, Y. J., and Zhang, P. Z. (2018). Thermochronological constraints on the late Cenozoic morphotectonic evolution of the Min Shan, the eastern margin of the Tibetan Plateau. *Tectonics* 37, 1733–1749. doi:10.1029/2017tc004868

Tian, Z. D., Leng, C. B., Zhang, X. C., Yin, C. J., Zhang, W., Cuo, J. H., et al. (2018). Mineralogical and petrogeochemical characteristics of the metamorphic basement of Yidun terrane and their geological implication. *Acta Mineral. Sin.* 38 (2), 152–165. (in Chinese with English abstract).

Tong, C. G. (1992). *Tectonic evolution of Sichuan Basin and gas/oil accumulation*. Beijing: Geological Publishing House.

van Hattum, M. W. A., Hall, R., Pickard, A. L., and Nichols, G. J. (2006). Southeast asian sediments not from asia: Provenance and geochronology of north borneo sandstones. *Geology* 34, 589–592. doi:10.1130/g21939.1

Veevers, J. J., and Saeed, A. (2013). Age and composition of Antarctic sub-glacial bedrock reflected by detrital zircons, erratics, and recycled microfossils in the Ellsworth Land–Antarctic Peninsula–Weddell Sea– Dronning Maud Land sector (240°E–0°–015°E). *Gondwana Res.* 23, 296–332. doi:10.1016/j.gr.2012.05.010

Wallis, S., Tsujimori, T., Aoya, M., Kawakami, T., Terada, K., Suzuki, K., et al. (2003). Cenozoic and mesozoic metamorphism in the longmenshan orogen: Implications for geodynamic models of eastern tibet. *Geology* 31 (9), 745–748. doi:10.1130/g19562.1

Wang, B. Q., Wang, W., Chen, W. T., Gao, J. F., Zhao, X. F., Yan, D. P., et al. (2013). Constraints of detrital zircon U–Pb ages and Hf isotopes on the provenance of the Triassic Yidun Group and tectonic evolution of the Yidun Terrane, eastern Tibet. *Sediment. Geol.* 289, 74–98. doi:10.1016/j.sedgeo.2013.02.005

Wang, C. S., Zhao, X. X., Liu, Z. F., Lippert, P. C., Graham, S. A., Coe, R. S., et al. (2008). Constraints on the early uplift history of the Tibetan Plateau. *Proc. Natl. Acad. Sci. U. S. A.* 105, 4987–4992. doi:10.1073/pnas.0703595105

Wang, E., Kirby, E., Furlong, K. P., van Soest, M., Xu, G., Shi, X., et al. (2012). Two-phase growth of high topography in eastern Tibet during the Cenozoic. *Nat. Geosci.* 5, 640–645. doi:10.1038/ngeo1538

Wang, L. C., Shen, L. J., Liu, C. L., Chen, K., Ding, L., and Wang, C. S. (2021). The late cretaceous source-to-sink system at the eastern margin of the Tibetan plateau: Insights from the provenance of the lanping basin. *Geosci. Front.* 12, 101102. doi:10.1016/j.gsf.2020.11.002

Wang, L. J., Yu, J. H., Griffin, W. L., and O'Reilly, S. Y. (2012). Early crustal evolution in the Western yangtze block: Evidence from U–Pb and Lu–Hf isotopes on detrital zircons from sedimentary rocks. *Precambrian Res.* 222–223, 368–385. doi:10.1016/j.precamres.2011.08.001

Wang, Q. C. (2013). Erosion and sedimentary record of orogenic belt. *Chin. J. Geol.* 48 (1), 1–31. (in Chinese with English abstract).

Wang, Q. W., Kan, Z. Z., Liang, B., and Zeng, Y. J. (2006). Stratigraphic division and corrlation of the continental meso-cenozoic group in ya'an, west Sichuan Basin. *Acta Geol. Sichuan* 26 (2), 65–69. (in Chinese with English abstract).

Wang, Z. B., Yang, S. Y., Mei, X., and Lu, K. (2018). Detrital garnet chemistry of the Changjiang (Yangtze River) sediments and their provenance implication. *J. Tongji Univ. Nat. Sci.* 46 (10), 1455–1472.

Wei, M. (1979). Ostracoda and geological age of the Tianmashan Formation in sichuan. *Geol. Rev.* 25 (02), 7–14.

Weislogel, A. L., Graham, S. A., Chang, E. Z., Wooden, J. L., and Gehrels, G. E. (2010). Detrital zircon provenance from three turbidite depocenters of the Middle-Upper Triassic Songpan–Ganzi complex, central China: Record of collisional tectonics, erosional exhumation, and sediment production. *Geol. Soc. Am. Bull.* 122 (11–12), 2041–2062. doi:10.1130/b26606.1

Weislogel, A. L., Graham, S. A., Chang, E. Z., Wooden, J. L., Gehrels, G. E., and Yang, H. (2006). Detrital zircon provenance of the late triassic songpan-ganzi complex: Sedimentary record of collision of the north and south China blocks. *Geology* 34, 97–100. doi:10.1130/g21929.1

Weislogel, A. L. (2008). Tectonostratigraphic and geochronologic constraints on evolution of the northeast Paleotethys from the Songpan-Ganzi complex, central China. *Tectonophysics* 451, 331–345. doi:10.1016/j.tecto.2007.11.053

Weltje, G, J., and Eynatten, H. V. (2004). Quantitative provenance analysis of sediments: Review and outlook. *Sediment. Geol.* 171 (1/4), 1–11. doi:10.1016/j.sedgeo.2004.05.007

Wiedenbeck, M., Hanchar, J. M., Peck, W. H., Sylvester, P., Valley, J., Whitehouse, M., et al. (2004). Further characterisation of the 91500 zircon crystal. *Geostand. Geoanalytical Res.* 28 (1), 9–39. doi:10.1111/j.1751-908x.2004.tb01041.x

Wilson, C. J. L., Harrowfield, M. J., and Reid, A. J. (2006). Brittle modification of triassic architecture in eastern tibet: Implications for the construction of the cenozoic plateau. *J. Asian Earth Sci.* 27, 341–357. doi:10.1016/j.jseaes.2005.04.004

Worley, B. A., and Wilson, C. J. L. (1996). Deformation partitioning and foliation reactivation during transpressional orogenesis, an example from the Central Longmen Shan, China. *J. Struct. Geol.* 18, 395–411. doi:10.1016/0191-8141(95)00095-u

Worley, B. A., Wilson, C. J. L., Liu, S. G., and Luo, Z. L. (1995). Structural observations from the wenchuan-maowen metamorphic belt, longmen mountains, China. *J. Chengdu Inst. Technol. Nat. Sci.* 22 (1), 24–41.

Wright, W. I. (1938). The composition and occurrence of garnets. *Am. Mineral.* 23, 436–449.

Wu, L., Xiao, A., Yang, S., Wang, L., Mao, L., Wang, L., et al. (2012). Two stage evolution of the altyn tagh fault during the cenozoic: New insight from provenance analysis of a geological section in NW qaidam basin, NW China. *Terra nova.* 24 (5), 387–395. doi:10.1111/j.1365-3121.2012.01077.x

Xu, G., and Kamp, P. J. J. (2000). Tectonics and denudation adjacent to the Xianshuihe Fault, eastern Tibetan Plateau: Constraints from fission track thermochronology. *J. Geophys. Res.* 105, 19231–19251. doi:10.1029/2000jb900159

Xu, Z. Q., Fu, X. F., Ma, X. X., Qi, X. X., Wu, C., Hou, L. W., et al. (2016). The gneiss domes in Tibetan Plateau and their potential for prospecting. *Acta Geol. Sin.* 90 (11), 2971–2981. (in Chinese with English abstract).

Xu, Z. Q., Li, H. Q., Hou, L. W., Fu, X. F., Chen, W., Zeng, L. S., et al. (2007). Uplift of the Longmen- Jinping orogenic belt along the eastern margin of the Qinghai- Tibet Plateau: Large-scale detachment faulting and extrusion mechanism. *Geol. Bull. China* 26 (10), 1262–1276. (in Chinese with English abstract).

Xu, Z. Q., Zhao, Z. B., Peng, M., Ma, X. X., Li, H. Q., and Zhao, J. M. (2016). Review of "orogenic plateau". *Acta Petrol. Sin.* 32 (12), 3557–3571. (in Chinese with English abstract).

Xue, Z. H., Lin, W., Chu, Y., Faure, M., Chen, Y., Ji, W. B., et al. (2021). An intracontinental orogen exhumed by basement-slice imbrication in the Longmenshan Thrust Belt of the Eastern Tibetan Plateau. *Geol. Soc. Am. Bull.* 134, 15–38. doi:10.1130/B35826.1

Xue, Z. H., Martelet, G., Lin, W., Faure, M., Chen, Y., Wei, W., et al. (2017). Mesozoic crustal thickening of the Longmenshan belt (NE Tibet, China) by imbrication of basement slices: Insights from structural analysis, petrofabric and magnetic fabric studies, and gravity modeling. *Tectonics* 36 (3-4), 3110–3134. doi:10.1002/2017tc004754

Yan, D. P., Zhou, M. F., Li, S. B., and Wei, G. Q. (2011). Structural and geochronological constraints on the Mesozoic -Cenozoic tectonic evolution of the Longmen Shan thrust belt, eastern Tibetan Plateau. *Tectonics* 30. doi:10.1029/2011TC002867

Yan, D. P., Zhou, M. F., Wei, G. Q., Gao, J. F., Liu, S. F., Xu, P., et al. (2008). The pengguan tectonic dome of longmen mountains, sichuan province: Mesozoic denudation of a neoproterozoic magmatic arc-basin system. *Sci. China Ser. D-Earth Sci.* 51, 1545–1559. doi:10.1007/s11430-008-0126-0

Yan, Z., Guo, X. Q., Fu, C. L., Aitchison, J., Wang, Z. Q., and Li, J. L. (2014). Detrital heavy mineral constraints on the triassic tectonic evolution of the West qinling terrane, NW China: Implications for understanding subduction of the paleotethyan ocean. *J. Geol.* 122, 591–608. doi:10.1086/677264

Yan, Z. K., Tian, Y. T., Li, R., Vermeesch, P., Sun, X. L., Li, Y., et al. (2019). Late triassic tectonic inversion in the upper yangtze block: Insights from detrital zircon u–pb geochronology from south-Western sichuan basin. *Basin Res.* 31, 92–113. doi:10.1111/bre.12310

Yang, G. C., Yu, B. S., Chen, J. Q., Yao, J. M., Li, S. Y., and Wu, Y. H. (2010). Geochemical research on rare Earth elements of argillaceous rocks of upper jurassic and cretaceous in the western sichuan foreland basin. *Geoscience* 24 (1), 140–149. (in Chinese with English abstract).

Yang, L., Yuan, W. M., Zhu, X. Y., and Shi, Z. (2019). Late triassic-cenozoic thermochronology in the southern sanjiang tethys, SW China, new insights from zircon fission track analysis. *J. Earth Sci.* 30 (5), 996–1004. doi:10.1007/s12583-019-1014-6

Ye, C. H. (1983). Cretaceous ostracod assemblages in Sichuan Basin, southwest China. *Acta Palaeontol. Sin.* 22 (02), 204–208.

Yuan, H. L., Gao, S., Dai, M. N., Zong, C. L., Günther, D., Fontaine, G. H., et al. (2007). Simultaneous determinations of U–Pb age, Hf isotopes and trace element compositions of zircon by excimer laser-ablation quadrupole and multiple-collector ICP-MS. *Chem. Geol.* 247, 100–118. doi:10.1016/j.chemgeo.2007.10.003

Zeng, Y. J., Yang, X. J., Li, Y. Q., Xie, Q. X., Zhu, B., and Hao, X. F. (2004). Tectonic significance of meso-cenozoic conglomerate in the south of the West sichuan foreland basin. *Acta Geol. Sichuan* 22 (4), 198–201.

Zhang, H. F., Parrish, R., Zhang, L., Xu, W. C., Yuan, H. L., Gao, S., et al. (2007). A-type granite and adakitic magmatism association in Songpan-Garze fold belt, eastern Tibetan Plateau: Implication for lithospheric delamination. *Lithos* 97, 323–335. doi:10.1016/j.lithos.2007.01.002

Zhang, K. J., Li, B., Wei, Q. G., Cai, J. X., and Zhang, Y. X. (2008). Proximal provenance of the Western Songpan–Ganzi turbidite complex (Late Triassic, eastern Tibetan plateau): Implications for the tectonic amalgamation of China. *Sediment. Geol.* 208 (1), 36–44. doi:10.1016/j.sedgeo.2008.04.008

Zhang, K. J., Li, B., and Wei, Q. G. (2012). Diversified provenance of the songpan-ganzi triassic turbidites, central China: Constraints from geochemistry and Nd isotopes. *J. Geol.* 120 (01), 69–82. doi:10.1086/662716

Zhang, Y., Jia, D., Shen, L., Yin, H. W., Chen, Z. X., Li, H. B., et al. (2015). Provenance of detrital zircons in the late triassic sichuan foreland basin: Constraints on the evolution of the qinling orogen and longmen Shan thrustfold belt in central China. *Int. Geol. Rev.* 57, 1806–1824. doi:10.1080/00206814.2015.1027967

Zhang, Y. L., Wang, Z. Q., Wang, G., Li, Q., and Lin, J. F. (2016). Chromian spinel, zircon age constraints on the provenance of early triassic feixianguan Formation sandstones. *Geol. Rev.* 62 (01), 54–72.

Zhang, Y. X., Tang, X. C., Zhang, K. J., Tang, X. C., and Gao, C. L. (2014). U–Pb and Lu–Hf isotope systematics of detrital zircons from the Songpan–Ganzi Triassic flysch, NE Tibetan Plateau: Implications for provenance and crustal growth. *Int. Geol. Rev.* 56 (1), 29–56. doi:10.1080/00206814.2013.818754

Zhang, Y. X., Zeng, L., Li, Z. W., Wang, C. S., Zhang, K. J., Yang, W. G., et al. (2015). Late permian–triassic siliciclastic provenance, palaeogeography, and crustal growth of the songpan terrane, eastern Tibetan plateau: Evidence from U–Pb ages, trace elements, and Hf isotopes of detrital zircons. *Int. Geol. Rev.* 57 (2), 159–181. doi:10.1080/00206814.2014.999356

Zhao, J. H., and Zhou, M. F. (2007). Geochemistry of Neoproterozoic mafic intrusions in the Panzhihua district (Sichuan Province, SW China): Implications for subduction-related metasomatism in the upper mantle. *Precambrian Res.* 152, 27–47. doi:10.1016/j.precamres.2006.09.002

Zhao, J. H., Zhou, M. F., Yan, D. P., Yang, Y. H., and Sun, M. (2008). Zircon Lu–Hf isotopic constraints on Neoproterozoic subduction–related crustal growth along the Western margin of the Yangtze Block, South China. *Precambrian Res.* 163, 189–209. doi:10.1016/j.precamres.2007.11.003

Zhao, X. F., Zhou, M. F., Li, J. W., and Wu, F. Y. (2008). Association of neoproterozoic A- and I-type granites in south China: Implications for generation of A-type granites in a subduction–related environment. *Chem. Geol.* 257, 1–15. (in Chinese with English abstract). doi:10.1016/j.chemgeo.2008.07.018

Zhou, M. F., Ma, Y. X., Yan, D. P., Xia, X. P., Zhao, J. H., and Sun, M. (2006a). The yanbian terrane (southern sichuan province, SW China): A neoproterozoic arc assemblage in the Western margin of the yangtze block. *Precambrian Res.* 144, 19–38. doi:10.1016/j.precamres.2005.11.002

Zhou, M. F., Kennedy, A. K., Sun, M., Malpas, J., and Lesher, M. (2002b). Neoproterozoic Arc-Related mafic intrusions along the northern margin of South China: Implications for the accretion of rodinia. *J. Geol.* 110, 611–618. doi:10.1086/341762

Zhou, M. F., Yan, D. P., Kennedy, A. K., Li, Y. Q., and Ding, J. (2002a). SHRIMP U–Pb zircon geochronological and geochemical evidence for Neoproterozoic arc-magmatism along the Western margin of the Yangtze Block, South China. *Earth Planet Sci. Lett.* 196, 51–67. doi:10.1016/s0012-821x(01)00595-7

Zhou, M. F., Yan, D. P., Wang, C. L., Qi, L., and Kennedy, A. (2006b). Subduction-related origin of the 750 Ma xuelongbao adakitic complex (sichuan province, China): Implications for the tectonic setting of the giant neoproterozoic magmatic event in south China. *Earth Planet. Sci. Lett.* 248, 286–300. doi:10.1016/j.epsl.2006.05.032

Zhu, C. Q., Hu, S. B., Qiu, N. S., Rao, S., and Yuan, Y. S. (2016). The thermal history of the Sichuan Basin, SW China: Evidence from the deep boreholes. *Sci. China (Earth Sci.* 59, 70–82. doi:10.1007/s11430-015-5116-4

Zhu, M., Chen, H., Zhou, J., and Yang, S. (2017). Provenance change from the middle to late triassic of the southwestern Sichuan basin, southwest China: Constraints from the sedimentary record and its tectonic significance. *Tectonophysics* 700–701, 92–107. doi:10.1016/j.tecto.2017.02.006

Zhuang, Z. H., Tian, D. X., Ma, X. H., Ren, X. F., Jiang, X. C., and Xu, S. J. (1988). A paleomagnetic study along the yanan-tianquan cretaceous-eogene section in Sichuan Basin. *Geophys. Geochem. Explor.* 12 (03), 224–228.

Zimmermann, S., and Hall, R. (2019). Provenance of Cretaceous sandstones in the Banda Arc and their tectonic significance. *Gondwana Res.* 67, 1–20. doi:10.1016/j.gr.2018.09.008

Zimmermann, S., and Hall, R. (2016). Provenance of triassic and jurassic sandstones in the banda arc: Petrography, heavy minerals and zircon geochronology. *Gondwana Res.* 37, 1–19. doi:10.1016/j.gr.2016.06.001

frontiers | Frontiers in Earth Science

TYPE Original Research
PUBLISHED 22 February 2023
DOI 10.3389/feart.2023.1138360

OPEN ACCESS

EDITED BY
Qiuming Pei,
Southwest Jiaotong University, China

REVIEWED BY
Gang Zhang,
Southwest University of Science and Technology, China
Dewei Li,
China Geological Survey, China
Gang Min,
Chengdu University of Technology, China

*CORRESPONDENCE
Qiao Wang,
540363176@qq.com

SPECIALTY SECTION
This article was submitted to Structural Geology and Tectonics, a section of the journal Frontiers in Earth Science

RECEIVED 05 January 2023
ACCEPTED 06 February 2023
PUBLISHED 22 February 2023

CITATION
Wan H and Wang Q (2023), Electrical structure of Gulu geothermal field in Southern Tibet and its implication for the high-temperature geothermal system. *Front. Earth Sci.* 11:1138360. doi: 10.3389/feart.2023.1138360

Electrical structure of Gulu geothermal field in Southern Tibet and its implication for the high-temperature geothermal system

Hanping Wan[1] and Qiao Wang[2]*

[1]Beijing Research Institute of Uranium Geology, Beijing, China, [2]China Geological Survey, Chengdu Centre, Chengdu, China

The Yadong-Gulu rift (YGR) South Tibet is a Cenozoic active rift, which is endowed with abundant geothermal resources. The Gulu geothermal field (GGF) is located in the Northern section of the rift, where a large number of high-temperature hot springs develop, but its geothermal system is mysterious. In this study, the three-dimensional (3D) electrical structure of GGF is revealed by broad magnetotelluric (MT) and audio magnetotelluric (AMT). MT reveals that middle and upper crust conductors are developed in the subsurface of GGF. The conductors may originate from the partial melting that drives the geothermal system. AMT reveals that the electrical structure of GGF is conductive alternation cap overlying more resistive reservoir, which is consistent with the classical electrical structure of geothermal systems in worldwide active tectonic zones. According to the geothermal system model, cold fluids may converge from the periphery of GGF to the middle, wherein fault F1 (the Western branch of Jiulazi-Sanxung fault) may be the main channel for cold fluids to migrate downward. The fluids are heated by partial melting in the middle and upper crust, and may migrate upward along fault F2 (the middle branch of Jiulazi-Sanxung fault) and develop into heat reservoirs.

KEYWORDS

magnetotelluric, audio magnetotelluric, Gulu geothermal filed, geothermal system model, electrical structure

1 Introduction

The YGR in the Southern Tibet is a Cenozoic active rift, which is characterized by active normal faults, frequent earthquakes, widespread thermal springs and high terrestrial heat flow, being endowed with abundant geothermal energy (Armijo et al., 1986; Hu et al., 2000; Yin and Harrison, 2000; Wu et al., 2011; Chevalier et al., 2020; Bian et al., 2022), Figure 1. High-temperature geothermal energy is renewable and can be used for power generation (Barbier, 2002; Rybach, 2010). The only two commercial geothermal power stations in China are located in the middle of YGR, that is Yangbajing geothermal field and Yangyi geothermal

Abbreviations: CSR, Cona-Sangri rift; GGF, Gulu geothermal field; JF, Jiali fault; MFT, Main front thrust; NS, Bangong-Nujiang Suture; PXR, Pumqu-Xainza rift; TYR, Tangra-Yumco rift; YGR, Yadong-Gulu rift; YZS, Yarlung-Zangbo suture.

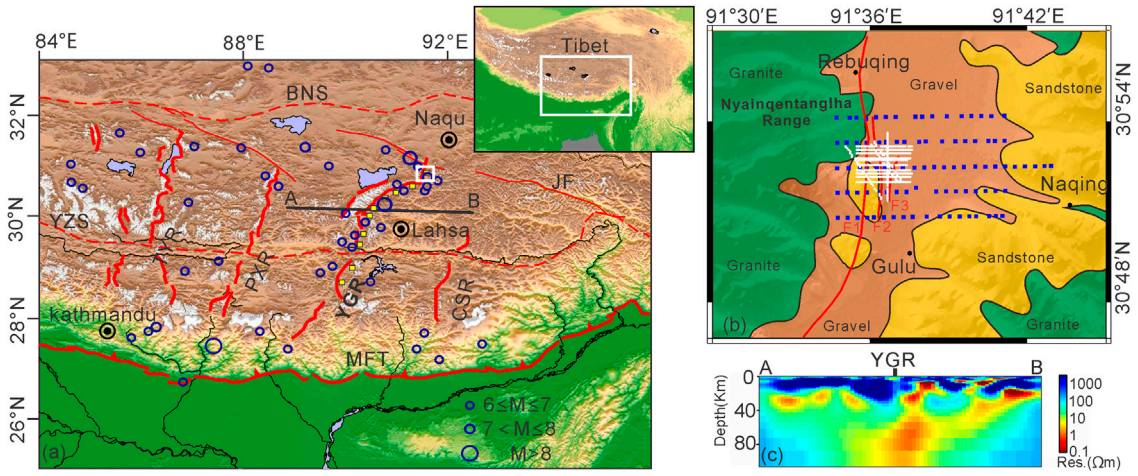

FIGURE 1
Geologic setting and sounding sites **(A)** Tectonic framework of Yadong-Gulu rift (modified from Shi et al., 2020). A large number of earthquakes are distributed around YGR, suggesting that YGR has intense activity. Red dots are sutures. Red lines are faults. Blue circles are earthquakes. Yellow diamonds are geothermal manifestations. Black line is the previous MT section, as shown in Figure 1C. **(B)** Sounding sites overlap on the geology of Gulu geothermal filed. Jiulazi-SanXung fault is consist of fault F1, F2 and F3. Nyainqentanglha Range is mainly composed of granite. The middle Jurassic Mali formation sandstone (J_2m) and Quaternary gravel (Q) are the sedimentary strata of GGF. Blue diamonds are MT sites. White dots are AMT sites. **(C)** Electrical model of section AB (modified from Wang G et al., 2017). High conductors of mantle origin are distributed in the subsurface of YGR.

field, whose installed capacity is 25.15 MW and 16 MW, respectively (Dorji, 2003; Wang and Guo, 2010). A large number of high-temperature hot springs are developed on the surface of GGF, which is located in the north of YGR (Liu et al., 2014), Figure 1A. The unclear geothermal system of GGF limits the development of commercial power generation.

Geothermal systems are generally composed of shallow structures and deep heat sources, the former is key to understand geothermal systems (Cumming, 2009; Liao, 2017). Water geochemistry indicates that atmospheric precipitation is the main source of groundwater, including a small amount of magmatic water (Liu et al., 2014; Su et al., 2020; Wang et al., 2020; Yu et al., 2022). Tensional faults constitute fluid circulation channels and thermal reservoirs (Zhang et al., 2014; Wang S et al., 2017). The Quaternary hydrothermal sinter seals off the geothermal reservoirs, and the widely distributed hot springs imply good geothermal potential (Gao et al., 2022). The north-south active normal fault obviously controls the hydrothermal activity (Li and hou, 2005; Wu et al., 2006; Guo et al., 2007). Previous studies on the formation mechanism of geothermal system are mainly based on surface investigation (Zhao et al., 2002; Liu et al., 2009; Feng et al., 2012; Hu et al., 2022), laying a foundation for understanding of GGF geothermal systems. However, the lack of deep structure seriously restricts the understanding of GGF geothermal system.

Electrical resistivity in the subsurface is sensitive to characterize geothermal context, such as the shallow geothermal structure and deep heat source (Newman et al., 2008; Muñoz, 2013; Spycher et al., 2014). Fluid-bearing faults (or fractures) and heat sources are the main components of geothermal systems, which often show high conductivity and are easy to be imaged by MT (Abiye and Haile, 2008; Piña-Varas, et al., 2014; Peacock et al., 2016; Paolo et al., 2020). In this study, MT and AMT imagining have been carried out, and 3D inversion has been implemented to obtain the electrical structure of the middle and upper crust of GGF. Combining with previous researches, the origin of heat source is discussed on the electrical structure of MT. This study reveals the distribution of shallow geothermal systems by AMT. On this basis, the geothermal systems in tectonically active zones around the world are compared and analyzed, and the geothermal system model of GGF is constructed, which provides an important basis for understanding the geothermal system model of YGR in the South Tibet.

2 Materials and methods

To clarify the origin of deep heat source in the GGF, we deployed 3D MT. The space of MT sites is about 0.6 km, and the collecting time is about 24 h with five components of electromagnetic field (Ex, Ey, Hx, Hy, Hz). In addition, in order to understand the fault and fluid distribution, 3D AMT was carried out in the hot springs developed area. The AMT space is about 0.05 km, the collecting time is 1 h with 5 components of electromagnetic field. Both MT and AMT data were collected by Phoenix V5-2000. On this basis, impedance tensors were estimated through the robust technique (Egbert, 1997).

The 3D inversion of MT and AMT data were carried out on the ModEM modules (Egbert, 2012; Kelbert et al., 2014). 3D inversion can effectively minimize the influence of off-profile structure and reveal a more real subsurface structure (Siripunvaraporn, 2011). Input data for the 3D inversions are all components of the MT and AMT impedance tensor for period range from 0.0001–1,000 s. The error floor for all tensors were 5% of sqrt (|Zxy×Zyx|). The starting model was set to a uniform half space with background resistivity of 100 Ωm, which was divided in a grid of 94 × 130 × 80 cells in the x, y, and z directions, respectively. In the data coverage part, horizontal

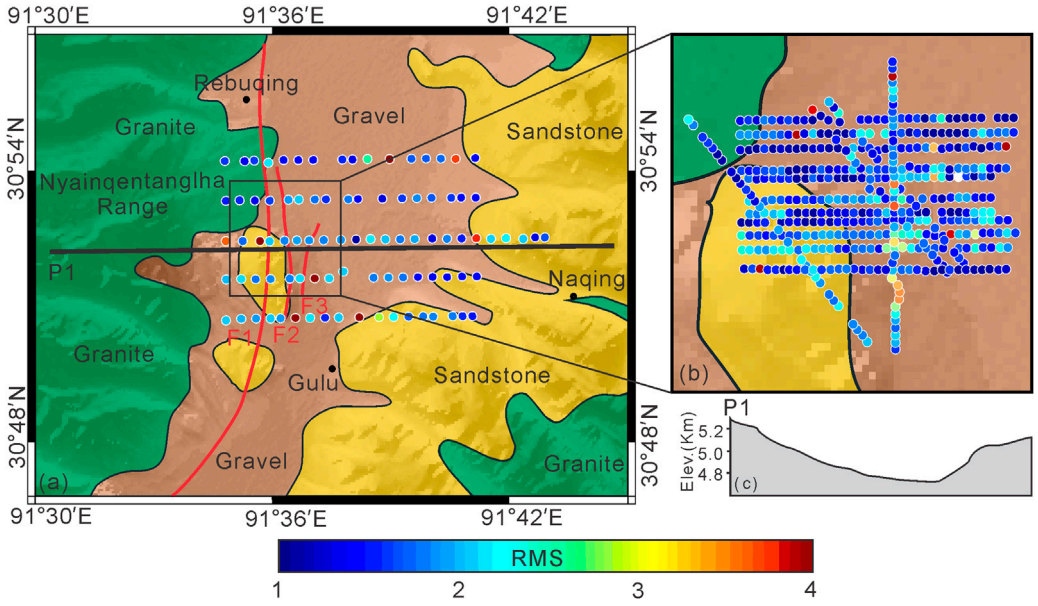

FIGURE 2
RMS of Magnetotelluric 3D inversion and tomographic section. **(A)** RMS of MT 3D inversion. RMS of most MT sites is less than 3. **(B)** RMS of AMT 3D inversion. RMS of a few AMT sites is around 4. **(C)** Topographic section of P1. The high terrain on both sides of GGF facilitates fluid migration to the center.

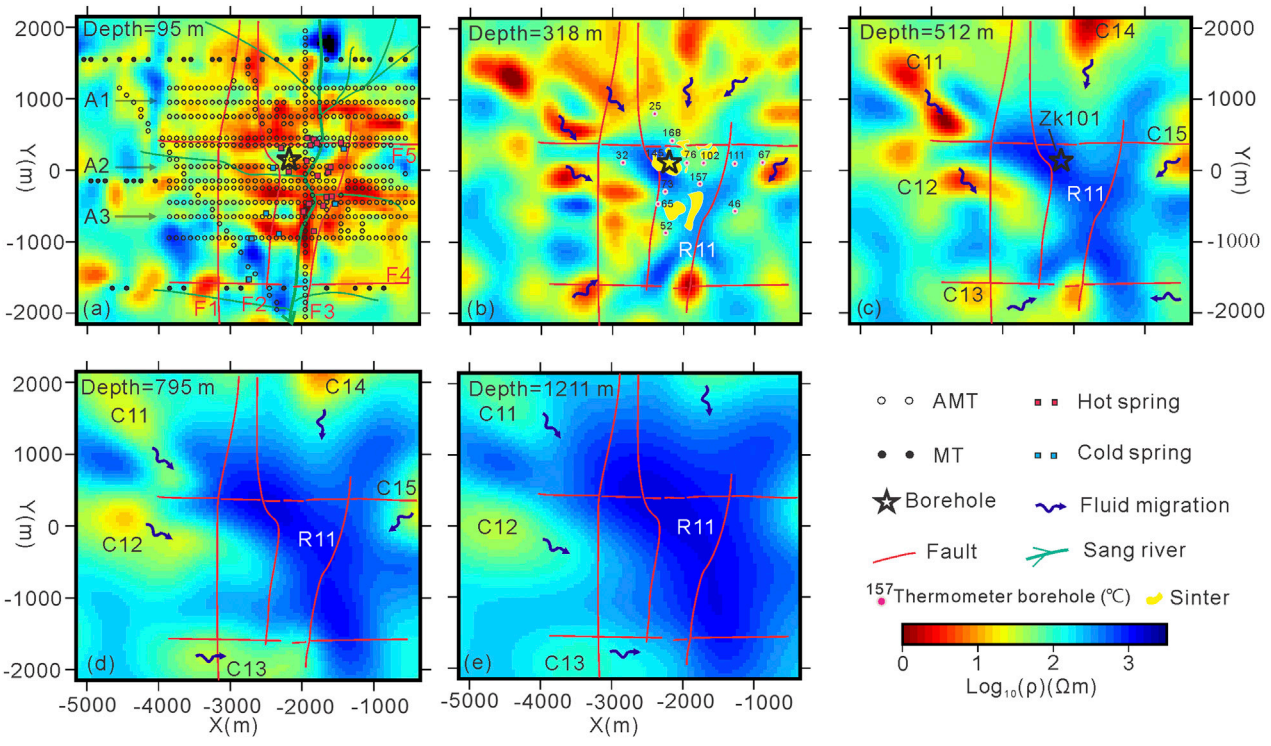

FIGURE 3
Horizontal slices of electrical model at different depths revealed by AMT. **(A–E)** Horizontal slices at depths of 95 m, 318 m, 512 m, 795 m, 1,211 m, respectively. The electrical model has the characteristics of high conductivity in the shallow depth **(A–C)** and high resistivity in the deep depth **(D–E)**. Thermometer boreholes with depths of 57.1–83.1 m give out temperatures at the bottoms, as shown in Figure 3B.

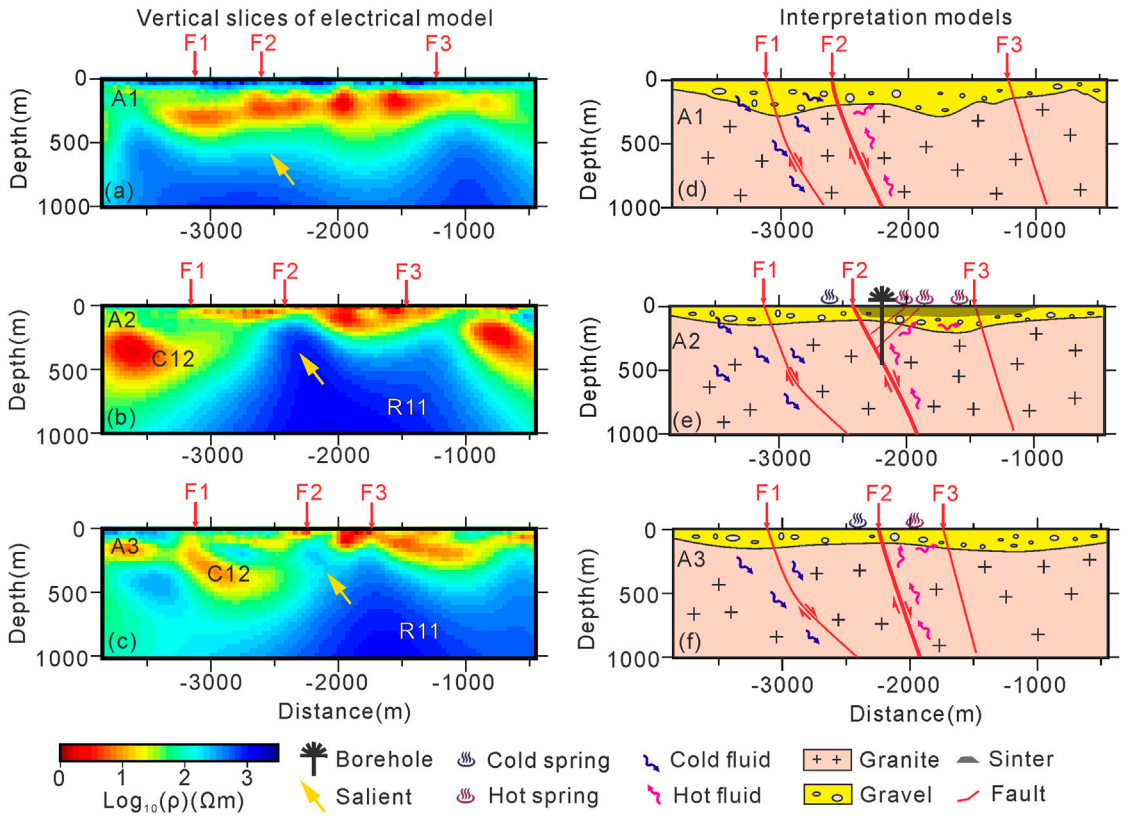

FIGURE 4
Vertical slices of electrical model and interpretation revealed by AMT. **(A–C)** Section resistivity models of A1-A3. High resistivity salient is an important feature in the electrical model, as shown by yellow arrows. **(D–F)** Interpretation models of A1-A3. Faults F1 and F2 may be the cold and hot fluids migration channel, respectively. The resistor R11 may imply presence of granite.

cell sizes are set to 0.1 × 0.1 km. Ten padding cells with an increasing factor of 1.5 were also included. In the vertical direction, first layer is set to 50 m thickness, followed by 79 layers increasing thicknesses gradually by a factor of 1.1. After 103 times of iteration, the root-mean-square (RMS) misfit reached 2.18 (Figure 2), and a reliable resistivity model was obtained.

3 Results

3.1 Electrical structure of shallow depth revealed by AMT

The electrical structure in shallow depth is characterized by high resistivity in the middle and high conductivity in the periphery. Geothermal systems typically consist of faults and fractures filled with geothermal fluids that may contain high concentrations of dissolved salts resulting in the presence of conductive electrolytes in the rock matrix (Muñoz, 2013). Hence, the resistivity of geothermal systems composed of fluids and electrolytes is about n × 10 Ωm (high conductivity), and that of granites is about n × 100 Ωm (high resistivity) (Newman et al., 2008; Peacock et al., 2012; Muñoz, 2013). These features provide an important basis for the interpretation of AMT data. Resistivity models at depths less than 0.4 km show that high conductivity (ρ<10 Ωm) is the dominant feature (Figure 3A, B), which may be related to the Quaternary strata, faults or fluids. Resistivity models of depths greater than 0.4 km show that there is a resistor R11 (ρ>1,000 Ωm), implying the presence of granite. The conductors C11, C12 and C13 located around the resistor R11 extends below 1 km, while the thickness of Quaternary strata in this area is generally less than 0.2 km (Armijo et al., 1986). We conclude that the shallow conductors may be related to the fluid migration.

Section A3 reveals fluid migration in the GGF. Conductor C12 is distributed beneath fault F1, extending to a depth of less than 1 km, which is inferred to be the migration direction of cold fluids. The migration direction is consistent with the topographic distribution of the surface, as shown in Figure 2C. In addition, a large number of cold springs distributed near fault F1, indicating that fault F1 may be the cold fluid channel, as shown in Figure 3A. The resistivity anomaly that cannot be ignored in Figure 4 is the high resistivity salient, marked by yellow arrows. The high resistivity salient may be caused by fault F2. The fault F2 may be a deep fault that controls granite invasion and also constitutes a heat-conducting channel. Borehole ZK101 revealed 5 layers of heat reservoirs and dozens of hydrothermal alteration zones in the hanging wall of fault F2 (Gao et al., 2022). In addition, there are a large number of hot springs and sinters on the eastern side of the fault F2 (Figures 3A, B), suggesting that the fault F2 may be an important heat-conducting channel for the GGF.

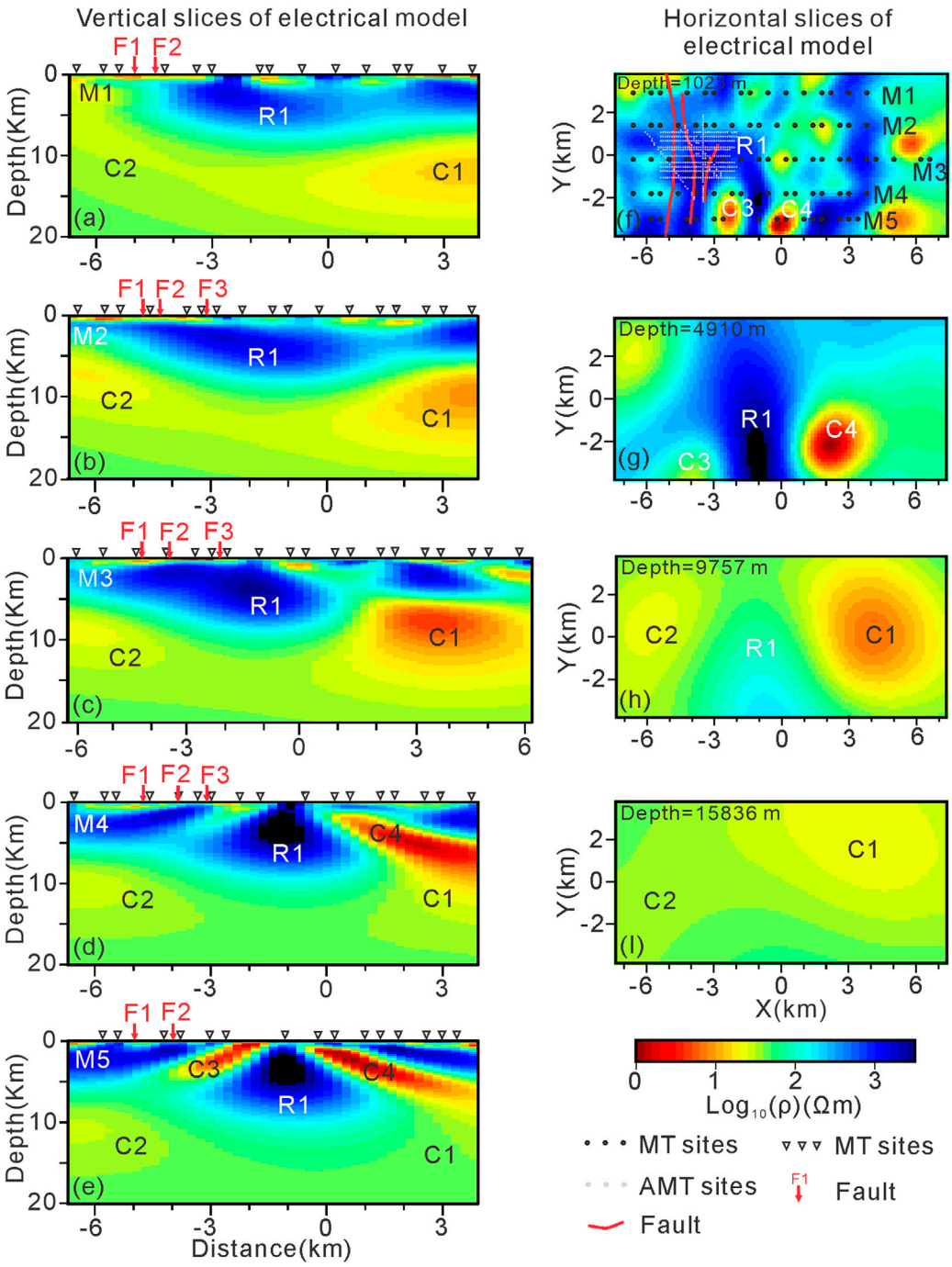

FIGURE 5
Horizontal and vertical slices of resistivity in GGF revealed by the MT. Figure **(A–E)** are vertical resistivity slices of M1 - M5, respectively. The vertical models are characterized by high resistivity at depth above ~8 km and high conductivity at depth below 8 km. Figure **(F–I)** are horizontal resistivity slices of depths at 1,028 m, 4,910 m, 9,757 m, 15,836 m, respectively. Conductors C1 and C2 dominate the electrical anomaly of horizontal models. AMT sites indicate the location of GGF.

Different from section A2 and A3, section A1 reveals that there is a continuous and stable layer of high conductivity in the shallow depth, suggesting different geothermal context between the South and North of GGF. The nearly continuous conductivity layer in Figure 4A may suggest that there is an abundance of subsurface fluids and even good connectivity between these fluids. The influx of cold fluid will reduce the temperature of hot fluid, which is not conducive to the exploration of high-temperature geothermal system. This may also be the main reason why there is no surface hydrothermal activity in the

north of GGF, as shown in Figure 3B. Combined with surface geology, boreholes, and resistivity anomalies, we deduce the deep extension of the faults F1, F2 and F3, Figures 4D–F. After clarifying the superficial fluid and fault system, it is the key to understand the deep heat source.

3.2 Electrical structure of middle and upper crust revealed by MT

The horizontal slice of 3D electrical structure is important for understanding the transverse distribution of anomalous electrical bodies. According to the 3D inversion results, the electrical structures with depths of 1,023 m, 4,910 m, 9,757 m and 15,836 m were plotted, as shown in Figures 5A–D. The resistor R1 (ρ>1,000 Ωm) and the conductors C1 and C2 (ρ<30 Ωm) are distributed at different depths. Resistor R1 may represent intact granite and is an important medium for deep heat conduction to the surface (Newman et al., 2008; Piña-Varas, et al., 2014). The resistor R11 in Figure 4 is the shallow part of resistor R1 in Figure 5 on account of the same electrical anomaly and similar resistivity value. Resistors R11 and R1 represent the nearly intact granites. In Figure 5A, four conductors (C1, C2, C3, C4) are distributed around the resistor R1. They gradually become discrete on the shallow surface, which may indicate fluid migration, which has been elaborated on the AMT section. Conductors C3 and C4 are located above the R1 in Figures 5D, E, implying that there might be two blind faults bearing fluids in the southern GGF (Figures 5F, G). Conductors C1 and C2, located in the either side of GGF, extend deep and are more clearly shown in the sections.

High conductivity domains the main resistivity feature in the subsurface of GGF. Conductors C1 and C2 (ρ<30 Ωm) has been imagined in these sections, among of which the section M3 is representative, Figure 5C. Section M3 shows different conductivity anomaly at the east and west of GGF. The west is characterized by resistivity, while the East is characterized by conductivity, which are also reflected in the horizontal slices. Conductors C1 and C2 extends to depth of 20 km and has no trap at the bottom, implying that they have a deep origin (Bertrand et al., 2012).

The middle and upper crust conductors C1 and C2 may originate from the upper mantle. Wang S et al. (2017) reveals that there are the conductors with approximately continuous distribution from the upper mantle to the middle and upper crust beneath the YGR, Figure 1C. In addition, Jin et al. (2022) reveals the similar conductivity anomaly characteristics through sparse 3D magnetotelluric data. Due to large site spacing (>20 km), previous researches mainly reveal crust-mantle scale structures of YGR (Lei et al., 2023). On the contrary, the authors deployed the MT with site space of ~0.6 km in the GGF, which can reveal the fine electrical structure of the middle-upper crust. It is concluded that conductors C1 and C2 has a good spatial coupling relationship with the middle and lower crust conductors originating from upper mantle revealed by previous researches (Figure 1C), suggesting that they may have a high-temperature.

4 Discussion

4.1 Conductors C1 and C2 revealed by MT implying the heat source originating from mantle upwelling

Partial melting may contribute to the conductors C1 and C2 beneath the GGF. For active tectonic zones, the main mechanisms for generating conductors are partial melting and aqueous fluids (Yang, 2011). It may be more appropriate to interpret conductors C1 and C2 by partial melting (Chen et al., 1996; Unsworth et al., 2005), because partial melting can continuously provide high terrestrial heat flow values (~100 mW/m^2, significantly higher than the surrounding areas, Hu et al., 2000) to the GGF. The resistivity revealed by MT can be used to estimate the fluid fraction (Le Pape et al., 2015). Partial melting zones may exist below C1 and C2 at depths of ~8 km, with resistivity values of about 30 Ωm, indicating the presence of 2%–5% partial melting (Gaillard and Marziano, 2005). High-temperature and high-pressure experiments show that a small amount of water can affect partial melting fraction (Yang, 2011). The minor difference of resistivity between C1 and C2 may be due to the difference of water content in partial melting (Holtz et al., 2001).

Partial melting may originate from tearing of Indian slab (IS). The IS subducted beneath the Tibet at different angles (gentle in the west and steep in the east, Liang and Song, 2006; Li et al., 2008; Zhao J et al., 2010; Shi et al., 2020). Since the uneven gravitational field of IS triggering the differential dragging, it gives rise to the tearing of IS into multiple pieces (Chen et al., 2015; Li and Song, 2018). Mantle hot materials upwelled into the crust along the IS tearing windows and are geophysically imaged as low velocity bodies or high conductivity bodies in the middle and lower crust (Nelson, 1996; Wei et al., 2001; Unsworth et al., 2005; Jin et al., 2022). In addition, the tearing of IS caused the East-West extension of the upper crust, and several North-South trending rifts were formed in the Southern Tibet, such as the YGR (Wang Y et al., 2022; Lei et al., 2023). Mantle upwelling brought a large number of hot materials to the middle and lower crust (Li and Song, 2018), which lead to partial melting of crust. Partial melting of the middle and lower crust would penetrate the middle and upper crust along the tensile faults, forming the deep heat source of GGF. They are imagined as conductors C1 and C2 by MT (Figures 5H, I), which may be the origin of high terrestrial heat flow in the YGF. They are also supported by other evidences, such as seismic wave velocity (Tian et al., 2015; Wu et al., 2019; Shi et al., 2020), mantle CO_2 emission (Kapp and Guynn, 2004; Zhang et al., 2021). Therefore, it is suggested that partial melting is the heat source driving high-temperature geothermal system of GGF, confirming the previous conjecture that heat source exists in the middle and upper crust (Dorji, 2003; Li and Hou, 2005; Gao et al., 2022; Wang R et al., 2022).

4.2 Shallow geothermal system revealed by the AMT

The north-south normal fault is an important channel for fluid migration. In the GGF, the east-dipping active normal fault is a part

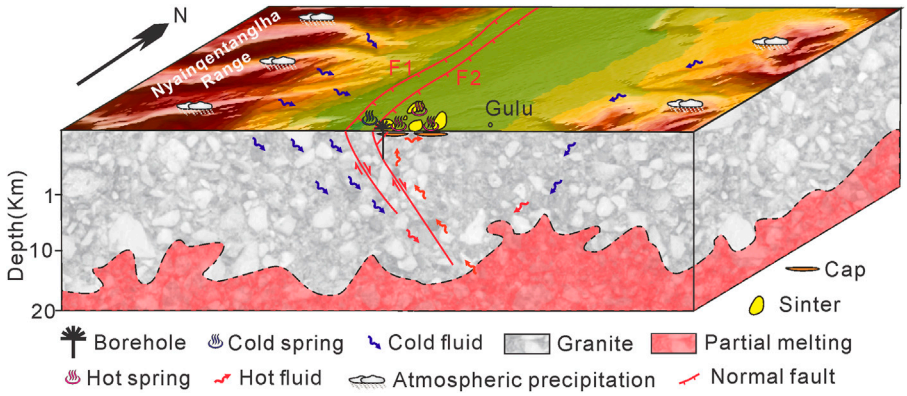

FIGURE 6
Cartoon model of geothermal system in Gulu geothermal field. Atmospheric precipitation feeds the underground fluids. The cold and hot fluids mainly migrate along the faults F1 and F2, respectively. The hydrothermal alternation zones below ~30–50 m of surface revealed by boreholes are the cap of geothermal system of Gulu geothermal field. Partial melting in middle and upper crust drives the geothermal system.

of the Nyainqentanglha fault, which undertakes the east-west stretching (~6 mm/yr) and triggered the 1952 Mw7.4 Gulu earthquake (Tapponnier et al., 1981; Armijo et al., 1986; Chevalier et al., 2020), laying the foundation for the development of hot springs (Gao et al., 2022). The ages of fault and sinters overlap since Miocene, suggesting a strong correlation between fault and geothermal fluids (Shen, 1992; Zhao Y et al., 2010). The five geothermal reservoirs and hidden geothermal alteration zones revealed by borehole ZK101 in the middle of GGF, suggesting that fault F2 is a geothermal fluid channel (Gao et al., 2022). The geothermal system elements, such as hot springs at the surface with high conductivity and geothermal reservoirs at the depth with high resistivity, are well imagined by AMT, Figures 3, 4, which are consistent with high-temperature geothermal systems worldwide (Ussher et al., 2000). Due to the low permeability and high resistivity of granite (Newman et al., 2008), geothermal reservoirs (n × 100 Ωm) tend to have higher resistivity than geothermal alteration zones (1–10 Ωm) (Wright et al., 1985; Pellerin et al., 1996; Piña-Varas et al., 2014). Based on such features, we believe that the yellow arrows in Figure 4 may represent geothermal reservoirs, and the fault F2 may be the upward migration channel of geothermal fluids.

Hydrothermal alternation zones, as the cap of geothermal system, seal off the hot fluids. Due to clays and brines, the hydrothermal alteration zones are often characterized by high conductivity (Wright et al., 1985; Muñoz, 2014). Horizontal resistivity slice of depth at 95 m shows that there is a large area of shallow conductors in GGF, Figure 3A. Not all conductors are the hydrothermal alternation zones (Muñoz, 2013). Fortunately, thermometer borehole can directly reveal the existence of hydrothermal alternation zone. Except for the thermometer boreholes below 50°C in Figure 3B, all the other boreholes reveal that there are hydrothermal alteration zones with a thickness of ~20–40 m distributed below 10 m on the surface, constituting the cap of the GGF geothermal system. In addition, the cold fluid migration is also worth identifying.

Fault F1 may be the channel for cold fluid migration. Fissures generated by faulting are important channels for surface fluids to migrate to the depth (Dorji, 2003). On the horizontal slices, the conductors (C11-C14) with increasing depth clearly show that the migration pathways of cold fluids are converging from the periphery to the middle (Figures 3D,E), which are consistent with the topographic relief of GGF (Figure 3C). The resistivity models A2 and A3 indicate that the fluids in the east may not be deeply circulating, while the conductor C12 in the west may indicate deep circulation of fluids (Figure 4). In general, high-temperature geothermal reservoirs can only be formed through deep circulation of fluids (Cumming and Mackie, 2010; Muñoz, 2014). Hydrogen and oxygen isotopes reveal that atmospheric precipitation is an important supply source of underground fluids (Zhang et al., 1995; Liu et al., 2014). Some of them migrate deeply into the West of Nyainqentanglha range, and the others overflow to the surface on the east side of fault F1 in the form of cold spring (Figure 3A). The fluids with deep migrating have the characteristics of high conductivity, which is imaged as conductor C12 by AMT, Figures 4C, E. Therefore, it is suggested that fault F1 may be an important channel for the deep migration of cold fluids.

4.3 Implications for the geothermal system in the Gulu geothermal field

Conceptionally, an ideal high-temperature geothermal system (temperature above 150°C–200°C, Muffler and Cataldi, 1978; Benderitter and Cormy, 1990) consists of heat source, heat reservoirs and cap, which are disputed in the tectonic active zones, such as plate boundaries, volcanic zones and rift zones (Majorowicz and Grasby, 2010; Muñoz, 2014). Conductive alteration cap overlying a more resistive reservoir is the classical electrical structure in the high-temperature geothermal systems, such as Taupo volcanic zone in New Zealand, Basin and Range province in California (Heise et al., 2007; Newman et al., 2008). The partially molten magma chambers are believed to be the heat source driving the geothermal systems (Wannamaker et al., 2004). Similar electrical structure and heat source also appear in the GGF. Unlike

them, the electrical structure in the GGF appears to be shallower in the depth and higher in resistivity value, possibly due to young geothermal fluids activity. Based on above analyses, the authors establish the geothermal system model of GGF, Figure 6.

The atmospheric precipitation migrates to the depth along the normal fault F1. With the depth increases, these cold fluids are gradually heated by partial melting, and transform into high-temperature geothermal fluids. Due to the upward geothermal buoyancy (Dorji, 2003), the geothermal fluids begin to migrate upward along the normal fault F2, and form hot springs and geothermal alteration zones on the surface.

5 Conclusion

The Yadong-Gulu rift in southern Tibetan is a tensile active rift, which gives rise to high-temperature geothermal systems, and the Gulu geothermal field is located in its northern section. Through three-dimensional inversion of integrated magnetotelluric and audio magnetotelluric data, the electrical model of the Gulu geothermal field is obtained. MT and AMT imagine conductors (C11, C12 and C13 in shallow depth, C1 and C2 in the deep) and resistors (R11 and R1) beneath Gulu geothermal field. Combined with geology, boreholes and previous researches, this paper explains the conductors and resistors and obtains the following understandings.

(1) Magnetotelluric reveals that conductors C1 and C2 are developed beneath the middle and upper crust of the Gulu geothermal field. The conductors may be the partial melting originating from the mantle upwelling, which drives the high-temperature geothermal system in the Gulu geothermal field.
(2) Audio magnetotelluric reveals the shallow electrical structure of Gulu geothermal system. The hydrothermal alternation cap with high conductivity overlies the high-temperature geothermal reservoirs with high resistivity, which is consistent with the classical electrical structure of active rifts geothermal systems worldwide. Faults F1 and F2 may be the cold and hot fluids migration channels, respectively.
(3) The geothermal system model of Gulu geothermal field constraining from the electrical structure is constructed. Cold fluids migrate from the periphery of Gulu geothermal field to the middle and supplies to the subsurface. Fault F1 may be the main downward migration channel of cold fluids. Due to the partial melting in the middle and upper crust, cold fluids are heated into hot fluids. Hot fluids may migrate upward along the fault F2, forming a large number of thermal alteration zones and hot springs in the Gulu geothermal field.

Data availability statement

The raw data supporting the conclusion of this article will be made available by the authors, without undue reservation.

Author contributions

HW designed and organized the project. HW and QW analyzed the data. HW and QW interpreted the results and wrote the manuscript.

Funding

This research was partially supported by the Centralized R&D project of China National Nuclear Corporation ([2019] No. 419).

Acknowledgments

We thank Gary Egbert and Anna Kelbert for providing their 3D MT inversion code ModEM. We thank the associate editor and the reviewers for constructive comments that helped to improve this paper. We thank the researchers involved with collecting these valuable data. We are grateful to Shibing Xia for his assistance in mapping part of pictures.

Conflict of interest

The authors declare that this study received funding from China National Nuclear Corporation ([2019] No. 419). The funder had the following involvement in the study: design, data collection and analysis, decision to publish, and preparation of the manuscript.

Publisher's note

References

Abiye, T. A., and Haile, T. (2008). Geophysical exploration of the boku geothermal area, central Ethiopian rift. *Geothermics* 37, 586–596. doi:10.1016/j.geothermics.2008.06.004

Armijo, R., Tapponnier, P., Mercier, J. L., and Han, T. L. (1986). Quaternary extension in Southern Tibet – field observations and tectonic implications. *J. Geophys. Res. Solid Earth* 91, 13803–13872. doi:10.1029/jb091ib14p13803

Barbier, E. (2002). Geothermal energy technology and current status: An overview. *Renew. Sustain Energy Rev.* 6, 3–65. doi:10.1016/s1364-0321(02)00002-3

Benderitter, Y., and Cormy, G. (1990). "Possible approach to geothermal research and relative costs," in *Small geothermal resources: A guide to development and utilization*. Editors M. H. Dickson and M. Fanelli (New York: UNITAR), 59–69.

Bertrand, E. A., Caldwell, T. G., Hill, G. J., Wallin, E., Bennie, S., Cozens, N., et al. (2012). Magnetotelluric imaging of upper-crustal convection plumes beneath the Taupo Volcanic Zone, New Zealand. *Geophys Res. Lett.* 39, L02304. doi:10.1029/2011GL050177

Bian, S., Gong, J., Zuza, A. V., Yang, R., Chen, L., Ji, J., et al. (2022). Along-strike variation in the initiation timing of the north-trending rifts in southern Tibet as revealed from the Yadong-Gulu rift. *Tectonics* 41, e2021TC007091. doi:10.1029/2021tc007091

Chen, L. S., Booker, J. R., Jones, A. G., Wu, N., Unsworth, M. J., Wei, W. B., et al. (1996). Electrically conductive crust in southern Tibet from Indepth magnetotelluric surveying. *Science* 274 (5293), 1694–1696. doi:10.1126/science.274.5293.1694

Chen, Y., Li, W., Yuan, X., Badal, J., and Teng, J. (2015). Tearing of the Indian lithospheric slab beneath southern Tibet revealed by SKS-wave splitting measurements. *Ear. Pla. Sci. Let.* 413, 13–24. doi:10.1016/j.epsl.2014.12.041

Chevalier, M., Tapponnier, P., van der Woerd, J., Leloup, P. H., Wang, S., Pan, J., et al. (2020). Late Quaternary extension rates across the northern half of the Yadong-Gulu rift: Implication for east-west extension in southern Tibet. *Jour. Geoph. Res. Sol. Ear.* 125, e2019JB019106. doi:10.1029/2019JB019106

Cumming, W. (2009). Geothermal resource conceptual models using surface exploration data[C], *proceedings, 34th workshop on geothermal reservoir engineering*, 187. SGP-TR-: Stanford University, 1–6.

Cumming, W., and Mackie, R. (2010). "Resistivity imaging of geothermal resources using 1D, 2D and 3D MT inversion and TDEM static shift correction illustrated by a glass mountain case history," in proceedings of world geothermal congress 2010, Bali, Indonesia, 25–29 April.

Dorji, X. (2003). The basic characteristics of the yangbajing geothermal field— a typical high-temperature geothermal system. *China Eng. Sci.* 5 (1), 42–47. doi:10.3969/j.issn.10091742.2003.01.008

Egbert, G. (2012). Hybrid conjugate gradient-Occam algorithms for inversion of multi-frequency and multi-transmitter EM data. *Geophys. J. Int.* 190, 255–266. doi:10.1111/j.1365-246x.2012.05523.x

Egbert, G. (1997). Robust multiple-station magnetotelluric data processing. *Geophys. J. Int.* 130, 475–496. doi:10.1111/j.1365-246X.1997.tb05663.x

Feng, Z., Zhao, Y., Zhou, A., and Zhang, N. (2012). Development program of hot dry rock geothermal resource in the Yangbajing Basin of China. *Renew. energy* 39 (1), 490–495. doi:10.1016/j.renene.2011.09.005

Gaillard, F., and Marziano, G. I. (2005). Electrical conductivity of magma in the course of crystallization controlled by their residual liquid composition. *J. Geophys. Res.* 110, B06204. doi:10.1029/2004JB003282

Gao, H., Hu, Z., Wan, H., Weilin, H., Song, Z., and Xiao, L. (2022). Characteristics of geothermal geology of the Gulu geothermal field in Tibet. Available at: https://kns.cnki.net/kcms/detail/42.1874.P.20220506.0949.006.html.

Guo, Q. H., Wang, Y., and Wei, L. (2007). Major hydrogeochemical processes in the two reservoirs of the Yangbajing geothermal field, Tibet, China. *Jour. Vol Geo. Res.* 166 (3-4), 255–268. doi:10.1016/j.jvolgeores.2007.08.004

Heise, W., Bibby, H. M., Caldwell, T. G., Bannister, S. C., Ogawa, Y., Takakura, S., et al. (2007). Melt distribution beneath a young continental rift: The Taupo volcanic zone, New Zealand. *Geophys Res. Lett.* 34, L14313. doi:10.1029/2007GL029629

Holtz, F., Johannes, W., Tamic, N., and Behrens, H. (2001). Maximum and minimum water contents of granitic melts generated in the crust: A reevaluation and implications. *Lithos* 56 (1), 1–14. doi:10.1016/S0024-4937(00)00056-6

Hu, S. B., He, L., and Wang, J. (2000). Heat flow in the continental area of China: A new data set. *Ear. Plan. Sci. Let.* 179 (2), 407–419. doi:10.1016/s0012-821x(00)00126-6

Hu, Z. H., Gao, H. L., and Wan, H. P., (2022). Temporal and spatial evolution of hydrothermal alteration in the Yangbajing geothermal field, Tibet. *Geol. Rev.* 68 (1), 359–374. doi:10.16509/j.georeview.2021.12.105

Jin, S., Sheng, Y., Comeau, M. J., Becken, M., Wei, W., Ye, G., et al. (2022). Relationship of the crustal structure, rheology, and tectonic dynamics beneath the Lhasa-Gangdese terrane (southern Tibet) based on a 3-D electrical model. *J. Geophys. Res. Solid Earth* 127, e2022JB024318. doi:10.1029/2022JB024318

Kapp, P., and Guynn, J. H. (2004). Indian punch rifts Tibet. *Geology* 32, 993. doi:10.1130/g20689.1

Kelbert, A., Meqbel, N., Egbert, G., and Tandon, K. (2014). ModEM: A modular system for inversion of electromagnetic geophysical data. *Comput. Geosciences* 66, 40–53. doi:10.1016/j.cageo.2014.01.010

Le Pape, F., Jones, A. G., Unsworth, M. J., Vozar, J., Wei, W., Jin, S., et al. (2015). Constraints on the evolution of crustal flow beneath northern Tibet. *Geochem. Geophys. Geosystems* 16 (12), 4237–4260. doi:10.1002/2015GC005828

Lei, L., Jin, S., Dong, H., Wei, W., Ye, G., and Zhang, L. (2023). 3-D electrical structure and tectonic dynamics in the Yangbajing area based on the array magnetotelluric data. *Front. Earth Sci.* 10, 1089675. doi:10.3389/feart.2022.1089675

Li, C., van der Hilst, R. D., Meltzer, A. S., and Engdahl, E. R. (2008). Subduction of the indian lithosphere beneath the Tibetan plateau and Burma. *Ear. Plan. Sci. Lett.* 274 (1-2), 157–168. doi:10.1016/j.epsl.2008.07.016

Li, J. T., and Song, X. D. (2018). Tearing of Indian mantle lithosphere from highresolution seismic images and its implications for lithosphere coupling in southern Tibet. *Proc. Natl. Acad. Sci.* 115 (33), 8296–8300. doi:10.1073/pnas.1717258115

Li, Z., and Hou, Z. (2005). "Partial melting in the upper crust in southern Tibet: Evidence from active geothermal fluid system," in *Mineral deposit research: Meeting the global challenge* (Berlin, Heidelberg: Springer). doi:10.1007/3-540-27946-6317

Liang, C., and Song, X. (2006). A low velocity belt beneath northern and eastern Tibetan Plateau from Pn tomography. *Geophys. Res. Lett.* 33, L22306. doi:10.1029/2006GL027926

Liao, Z. (2017). *Thermal springs and geothermal energy in the qinghai-Tibetan plateau and the surroundings*. Springer, Berlin, Heidelber. doi:10.1007/978-981-10-3485-5

Liu, J., Shen, X. H., and Meng, K. (2009). Preliminary study on late Quaternary activity of faults in the Western margin of Gulu Basin. *Earthquake* 29 (3), 45–53. doi:10.3969/j.issn.10003274.2009.03.006

Liu, Z., Lin, W., and Zhang, M. (2014). Origin of geothermal fluid and contribution of mantle source in Nimu-Nagqu, Tibet. *Earth Sci. Front.* 21 (6), 356–371. doi:10.13745/j.esf.2014.06.034

Majorowicz, J., and Grasby, S. (2010). Heat flow, depth–temperature variations and stored thermal energy for enhanced geothermal systems in Canada. *J. Geophys. Eng.* 7 (3), 232–241. doi:10.1088/1742-2132/7/3/002

Muffler, P., and Cataldi, R. (1978). Methods for regional assessment of geothermal resources. *Geothermics* 7, 53–89. doi:10.1016/0375-6505(78)90002-0

Muñoz, G. (2014). Exploring for geothermal resources with electromagnetic methods. *Sur. Geo.* 35, 101–122. doi:10.1007/s10712-013-9236-0

Nelson, K. D., Zhao, W., Brown, L. D., Kuo, J., Che, J., Liu, X., et al. (1996). INDEPTH seismic teamPartially molten middle crust beneath southern Tibet: Synthesis of project INDEPTH results. *Science* 274, 1684–1688. doi:10.1126/science.274.5293.1684

Newman, G., Gasperikova, E., Hoversten, G., and Wannamaker, P. E. (2008). Three-dimensional magnetotelluric characterization of the Coso geothermal field. *Geothermics* 37, 369–399. doi:10.1016/j.geothermics.2008.02.006

Paolo, F., Ledo, J., Slazak, K., Martinez, D., Cabrera-Perez, I., and Pereze, N. (2020). La Palma island (Spain) geothermal system revealed by 3D magnetotelluric data inversion. *Sci. Rep.* 10, 18181. doi:10.1038/s41598-020-75001-z

Peacock, J. R., Thiel, S., Reid, P., and Heinson, G. (2012). Magnetotelluric monitoring of a fluid injection: Example from an enhanced geothermal system. *Geophys. Res. Lett.* 39, 1–5. doi:10.1029/2012gl053080

Pellerin, L., Johnston, J. M., and Hohmann, G. W. (1996). A numerical evaluation of electromagnetic methods in geothermal exploration. *Geophysics* 61, 121–130. doi:10.1190/1.1443931

Piña-Varas, P., Ledo, J., Queralt, P., Marcuello, A., Bellmunt, F., Hidalgo, R., et al. (2014). 3-D magnetotelluric exploration of Tenerife geothermal system (Canary islands, Spain), Surv. Geophys. 35:1045–1064Nonlinear conjugate gradients algorithm for 2-D magnetotelluric inversion. *Geophysics* 66, 174–187. doi:10.1190/1.1444893

Rybach, L. (2010). *Status and prospects of geothermal energy*. Bali, Indonesia: world geothermal congress.

Shen, M. (1992). *Evolution and model of Yangbajing hydrothermal system. Selected papers of international symposium on high-temperature geothermal development and utilization in Tibet*, Lhasa, 95–98.

Shi, D., Klemperer, S. L., Shi, J., Wu, Z., and Zhao, W. (2020). Localized foundering of Indian lower crust in the India–Tibet collision zone. *Proc. Natl. Acad. Sci.* 117, 24742–24747. doi:10.1073/pnas.2000015117

Siripunvaraporn, W. (2011). Three-dimensional magnetotelluric inversion: An introductory guide for developers and users. *Surv. Geophys.* 33 (1), 5–27. doi:10.1007/s10712-011-9122-6

Spycher, N., Peiffer, L., Sonnenthal, G. L., Saldi, G., Reed, M., and Kennedy, B. (2014). Integrated multicomponent solute geothermometry. *Geothermics* 51, 113–123. doi:10.1016/j.geothermics.2013.10.012

Su, J., Tan, H., and Chen, X. (2020). The groundwater deep circulation and large-scale geothermal deposition in response to the extension of the Yadong–Gulu rift, South Tibet, China. *J. Volcanol. Geotherm. Res.* 395 (4), 106836. doi:10.1016/j.jvolgeores.2020.106836

Tapponnier, P., Mercier, J. L., Armijo, R., Han, T., and Zhao, T. J. (1981). Field evidence for active normal faulting in Tibet. *Nature* 294, 410–414. doi:10.1038/294410a0

Tian, X. B., Chen, Y., Tseng, T., Klemperer, S., Thybo, H., Liu, Z., et al. (2015). Weakly coupled lithospheric extension in southern Tibet. *Ear. Plan. Sci. Lett.* 430, 171–177. doi:10.1016/j.epsl.2015.08.025

Unsworth, M. J., Jones, A., Wei, W., Marquis, G., Gokarn, S. G., and Spratt, J. E. (2005). Crustal rheology of the Himalaya and Southern Tibet inferred from magnetotelluric data. *Nature* 438 (7064), 78–81. doi:10.1038/nature04154

Ussher, G., Harvey, C., Johnstone, R., and Anderson, E. (2000). Understanding resistivities observed in geothermal systems, *Proceedings world geothermal congress*, Kyushu-Tohoku, Japan.

Wang, G., Wei, W., Ye, G., Jin, S., Jing, J., Zhang, L., et al. (2017). 3-D electrical structure across the Yadong-Gulu rift revealed by magnetotelluric data: New insights on the extension of the upper crust and the geometry of the underthrusting Indian lithospheric slab in southern Tibet. *Earth Plan. Sci. Let.* 474, 172–179. doi:10.1016/j.epsl.2017.06.027

Wang, R., Winberg, F., Zhu, D., Hou, Z. Q., and Yang, Z. M. (2022). The impact of a tear in the subducted Indian plate on the Miocene geology of the Himalayan-Tibetan orogen. *GSA Bull.* 134 (3-4), 681–690. doi:10.1130/b36023.1

Wang, S., Chevalier, M., Pan, J., Bai, M., Li, K., Li, H., et al. (2020). Quantification of the late Quaternary throw rates along the Yadong rift, southern Tibet. *Tectonophysics* 790, 228545. doi:10.1016/j.tecto.2020.228545

Wang, S., Lu, C., Nan, D., Hu, X., and Shao, J. (2017). Geothermal resources in Tibet of China: Current status and prospective development. *Environ. earth Sci.* 76, 239. doi:10.1007/s12665-017-6464-5

Wang, Y., and Guo, Q. (2010). *The yangbajing geothermal field and the Yangyi geothermal field: Two representative fields in Tibet, China*. Bali, Indonesia: Proceedings World Geothermal Congress, 25–29.

Wang, Y., Li, L., Wen, H., and Hao, Y. (2022). Geochemical evidence for the nonexistence of supercritical geothermal fluids at the Yangbajing geothermal field, southern Tibet. *J. Hydrology* 604, 127243. doi:10.1016/j.jhydrol.2021.127243

Wannamaker, P. E., Rose, P. E., Doerner, W. M., Berard, B. C., McCulloch, J., and Nurse, K. (2004). "Magnetotelluric surveying and monitoring at the coso geothermal area, California, in support of the enhanced geothermal systems concept: Survey parameters and initial results," in *proceedings, 29th workshop on geothermal reservoir Engineering* (United States: Stanford University).

Wright, P., Ward, S., Ross, H., and West, R. C. (1985). State of the art geophysical exploration for geothermal resources. *Geophysics* 50, 2666–2696. doi:10.1190/1.1441889

Wu, C. L., Tian, X. B., Xu, T., Liang, X., Chen, Y., Taylor, M., et al. (2019). Deformation of crust and upper mantle in central Tibet caused by the northward subduction and slab tearing of the Indian lithosphere: New evidence based on shear wave splitting measurements. *Earth Plan. Sci. Let.* 514, 75–83. doi:10.1016/j.epsl.2019.02.037

Wu, Z., Ye, P., Barosh, P., and Wu, Z. (2011). The October 6, 2008 Mw 6.3 magnitude Damxung earthquake, Yadong-Gulu rift, Tibet, and implications for present-day crustal deformation within Tibet. *J. Asian earth Sci.* 40, 943–957. doi:10.1016/j.jseaes.2010.05.003

Wu, Z., Zhao, X., Wu, Z., et al. (2006). Quaternary geology and faulting in the Damxung-Yangbajain basin, southern Tibet. *Jour. Geome.* 12 (3), 3005–3315.

Yang, X. (2011). Origin of high electrical conductivity in the lower continental crust: A review. *Surv. Geophys* 32, 875–903. doi:10.1007/s10712-011-9145-z

Yin, A., and Harrison, T. (2000). Geologic evolution of the Himalayan-Tibetan orogen. *Ann. Rev. Ear. Plan. Sci.* 28, 211–280. doi:10.1146/annurev.earth.28.1.211

Yu, X., Wei, Z., Wang, G., Ma, X., Zhang, T., Yang, H., et al. (2022). Hot spring gas geochemical characteristics and geological implications of the northern Yadong-Gulu Rift in the Tibetan Plateau. *Front. Earth Sci.* 10, 863559. doi:10.3389/feart.2022.863559

Zhang, J., Quay, P. D., and Wilbur, D. O. (1995). Carbon isotope fractionation during gas-water exchange and dissolution of CO2. *Geochim. Cosmochim. Acta* 59, 107–114. doi:10.1016/0016-7037(95)91550-d

Zhang, M., Lin, W., Liu, Z., Liu, Z., Hu, X., and Wang, G. (2014). Hydrogeochemical characteristics and genetic model of Gulu high-temperature geothermal system in Tibet. *Jour. Chengdu Univ. Tech. (Sci. Tech. Ed.* 41 (3), 382–392. doi:10.3969/j.issn.16719727.2014.03.15

Zhang, M., Zhang, Li., Zhao, W., Guo, Z., Xu, S., Sano, Y., et al. (2021). Metamorphic CO2 emissions from the southern Yadong-Gulu rift, Tibetan Plateau: Insights into deep carbon cycle in the India-Asia continental collision zone. *Chem. Geo.* 584, 120534. doi:10.1016/j.chemgeo.2021.120534

Zhao, J., Yuan, X., Liu, H., Kumar, P., Pei, S., Kind, R., et al. (2010). The boundary between the Indian and Asian tectonic plates below Tibet. *Natl. Acad. Sci.* 107 (25), 11229–11233. doi:10.1073/pnas.1001921107

Zhao, P., Xie, E., and Duoji, X. (2002). Geochemical characteristics and geological significance of geothermal gases in Tibet. *Acta petro. Sin.* 18 (4), 539–550.

Zhao, Y., Zhao, X., and Ma, Z., (2010). Chronology and significance of Gulu geothermal spring type cesium deposit in Xizang Province. *Acta Geol. Sin.* 84 (2), 211–220.

frontiers | Frontiers in Earth Science

TYPE Original Research
PUBLISHED 06 March 2023
DOI 10.3389/feart.2023.1140326

OPEN ACCESS

EDITED BY
Hu Wang,
Southwest Jiaotong University, China

REVIEWED BY
Wenjun Zheng,
School of Earth Sciences and Engineering, Sun Yat-sen University, China
Chuanyong Wu,
Institute of Disaster Prevention, China
Daoyang Yuan,
Lanzhou University, China
Jun Shen,
Institute of Disaster Prevention, China

*CORRESPONDENCE
Lichun Chen,
glutclc@glut.edu.cn

SPECIALTY SECTION
This article was submitted to Structural Geology and Tectonics, a section of the journal Frontiers in Earth Science

RECEIVED 08 January 2023
ACCEPTED 17 February 2023
PUBLISHED 06 March 2023

CITATION
Feng J, Chen L, Han M, Gao S, Li Y, Lu L and Chen S (2023), Multi-fault rupture behavior of the 1786 *M* $7^3/_4$ Kangding earthquake on the eastern margin of the Tibetan Plateau.
Front. Earth Sci. 11:1140326.
doi: 10.3389/feart.2023.1140326

Multi-fault rupture behavior of the 1786 *M* $7^3/_4$ Kangding earthquake on the eastern margin of the Tibetan Plateau

Jiahui Feng[1], Lichun Chen[2]*, Mingming Han[3], Shuaipo Gao[4], Yanbao Li[1], Lili Lu[1] and Shunyun Chen[1]

[1]State Key Laboratory of Earthquake Dynamics, Institute of Geology, China Earthquake Administration, Beijing, China, [2]College of Earth Sciences, Guilin University of Technology, Guilin, China, [3]Chengdu Center of China Geological Survey, Chengdu, China, [4]College of Earth Sciences and Engineering, Hebei University of Engineering, Handan, China

The 2022 Luding *Ms* 6.8 earthquake has drawn attention to the Xianshuihe fault zone. Historically, there was an *M* $7^3/_4$ earthquake in this region in 1786. Because the surface rupture of this historic earthquake was not obvious, there is still much debate over the extent of the surface rupture, which is critical for comprehending tectonic activity and assessing seismic risk for the Xianshuihe fault (XSHF). In particular, the seismogenic structure of this earthquake was connected by three active left-lateral strike-slip faults—the Anninghe fault (ANHF), Daliangshan fault (DLSF), and XSHF—where a large earthquake could cause multi-fault rupture. Given these criteria, we report the results of a series of trenches excavated in the vicinity of the epicenter at the northern section of the DLSF, the northern section of the ANHF, the Zheduotang section, and the Selaha section of the XSHF. We find that 1) three palaeoseismic events have been revealed on the northern section of the ANHF: BE1, ~1003 AD; BE2, 1000–1182 AD; and BE3, 1536 AD as *M* 7 earthquakes, and 2) two palaeoseismic events have occurred on the Selaha fault during the last 500 years. The first event corresponds to the AD 1725 Kangding *M* 7 earthquake, and the latest event may be the AD 1786 *M* $7^3/_4$ earthquake. 3) Three palaeoseismic events occurred on Zheduotang: ZD1, 1215 BC~315 AD; ZD2, 830 BC~705 AD; and ZD3, the 1955 AD Kangding *M* $7^1/_2$ earthquake. 4) The 1786 Kangding *M* $7^3/_4$ earthquake was probably a multi-fault rupture event, as evidenced by the trenching profile evidence, nearby offset geomorphic features, and historical earthquake data. Not only the Moxi fault, a seismogenic structure, but also the southern end of the Selaha fault to the north and the Shimian fault (DLSF) to the south simultaneously broke during this earthquake.

KEYWORDS

1786 Kangding earthquake, Xianshuihe fault, palaeoearthquake, multi-fault rupture, complex seismogenic structure

1 Introduction

Large earthquakes typically occur at the ends of faults or in the region where the fault strike changes (Gkarlaouni et al., 2008; Lozos et al., 2017). The Kangding–Shimian area's structural node is where the Longmenshan fault (LMSF), Xianshuihe fault (XSHF), Anninghe fault (ANHF), and Daliangshan fault (DLSF) all converge, making the area's structural features more complicated and

prone to earthquakes. The epicenter of the 5 September 2022, Luding *M* 6.8 earthquake was located near Moxi township, Kangding. Twenty-five individuals remain missing, and ninety-three people died in this earthquake. In 1786 AD, the Kangding *M* $7^3/_4$ earthquake also struck this region. Because the surface rupture of the earthquake has vanished since it occurred more than 200 years ago, there is still controversy about the distribution of the surface rupture. Some studies have suggested that the surface rupture of the 1786 Kangding *M* $7^3/_4$ earthquake was distributed in the Moxi–Selaha segment of the XSHF (Li, 1997; Wen et al., 2008). According to the most recent mapping data, the seismogenic structure of this earthquake is the southern section of the XSHF, and the surface rupture was located between Kangding and Tianwan (Chen et al., 2011, 2016), with a rupture length of approximately 80 km. Generally, it is thought that Kangding is the segmented boundary of the Moxi segment and the central segment (Selaha segment) of the XSHF (An, 2010). The beginning and end positions of an earthquake's surface rupture are determined by the segmentation boundary of the fault, which has an impact on how strain is accumulated and distributed on the fault as well as how large earthquakes rupture. Recent studies on multi-fault ruptures have altered the previous understanding of fault activity segmentation boundaries (Fletcher et al., 2014; Stirlinghv et al., 2017; Hamling et al., 2017; Chen et al., 2018). The three branches of the Huiyuansi–Kangding segment and the Moxi segment along the XSHF, as well as the ANHF, are seismogenic in their own right (Liang et al., 2020; Ma et al., 2022) and have also experienced *M*>7 earthquakes throughout history. However, some researchers believe that the

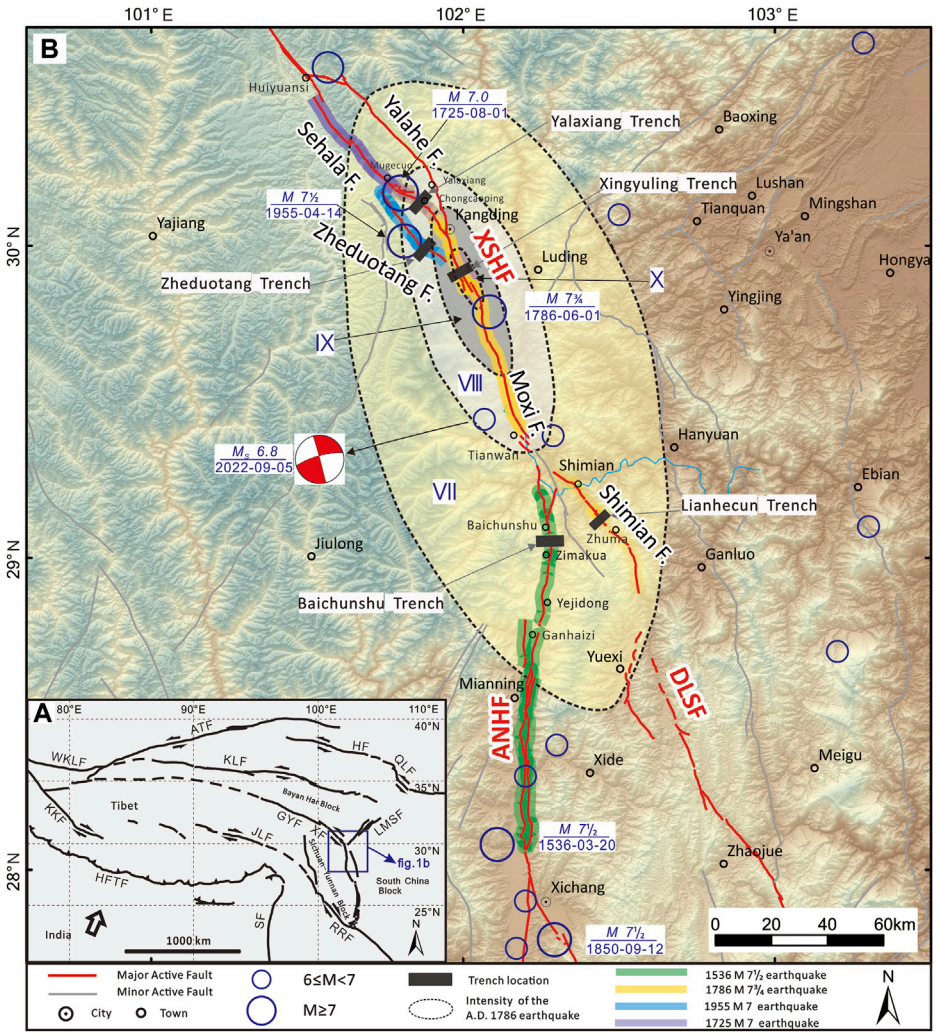

FIGURE 1
Regional tectonics and seismicity in south-eastern Tibet. **(A)** Geotectonics of the study area. **(B)** Characteristics of seismicity in the study area. The blue rectangle in Figures 1A indicates the study area located at the boundary of the Bayan Har block, Sichuan–Yunnan block, and South China block. The blue circles of different sizes indicate epicenters of earlier documented historical earthquakes (Department of Earthquake Disaster Prevention, 1995; Department of Earthquake Disaster Prevention, 1999). Dotted lines indicate the intensity map of the 1786 AD earthquake (Gu, 1983; Wang and Pei, 1998). The bands of different colors represent the surface rupture range of historical earthquakes: the rupture extent of the 1536 AD earthquake obtained from Wang et al. (2014) and Ran et al. (2008a); the rupture extent of the 1786 AD earthquake obtained from Wang and Pei (1998) and Chen et al. (2011); the rupture extent of the 1955 AD earthquake obtained from Zhou et al. (2001a); and the rupture extent of the 1725 AD earthquake obtained from Han et al. (2022). The Hillshade map is generated from the Advanced Spaceborne Thermal Emission and Reflection Radiometer (ASTER) Global Digital Elevation Model (ASTGTM) (90-m resolution). Abbreviations of the active faults: ATF, Altyn Tagh fault; HF, Haiyuan fault; XF/XSHF, Xianshuihe fault; JLF, Jiali fault; RRF, Red River fault; BLF, LMSF, Longmenshan fault; DLSF, Daliangshan fault; ANHF, Anninghe fault; and ZMHF, Zemuhe fault.

Huiyuansi–Kangding segment's three secondary faults are integrated into the deep crust and have a unified fault surface, which means that these three faults exhibit the tail effect of deep fracture dislocation on the surface (Zhou et al., 2001a). This structure appears to indicate that multiple faults could rupture simultaneously in the southern segment of the XSHF fault and the northern segment of the ANHF and DLSF. Based on previous trenching work, we have excavated several trenches in the northern segment of the DLSF, the northern segment of the ANHF, and the Zheduotang and Selaha segments of the XSHF. In addition to exploring the rupture range of the 1786 Kangding earthquake, we aim to expose and contrast the (previous) earthquake rupture events of these faults which can also provide new basic data for understanding and evaluating the future seismic risk in the Shimian–Kangding area.

2 Regional seismotectonic setting

The study area, located at the boundary of the Bayan Har block, the Sichuan–Yunnan block, and the South China block (Deng et al., 2002; Zhang et al., 2003), is connected by three active left-lateral strike-slip faults, the ANHF, DLSF, and XSHF (Figure 1B). The XSHF shows a NE-trending protruding arc in a plane shape, which can be roughly divided into three major geometric segments bordered by the Qianning Basin and Kangding County, known as the NW segment, middle segment, and SE segment (Long and Deng, 1986; Li, 1997; Wen, 2000; Wen et al., 2008; An, 2010).

The middle segment of the XSHF has a complicated geometric structure. This segment separates into three secondary faults—the Yalahe fault, the Selaha fault, and the Zheduotang fault—between the southern Huiyuansi Basin and southern Kangding. The three secondary faults have historically experienced earthquakes of $M \geq 7$ (Liang et al., 2020; Ma et al., 2022). The Selaha fault is the seismogenic structure for the 1725 Kangding M 7 earthquake, and the surface rupture of this earthquake can still be seen (Han et al., 2022; Long & Deng, 1986). The Yalahe fault may have been the source of the 1700 North Kangding M 7 earthquake (Liang et al., 2020). An M 7 earthquake struck the Zheduotang fault in 1955 (Zhou et al., 2001a; Wen et al., 2008).

The south-eastern portion of the XSHF (Moxi Segment) is distributed from Kangding to Shimian. The Moxi segment's surface morphology consists of a single structure with a straightforward form. The most widespread and damaging earthquake ever recorded in the XSHF's history was the South Kangding M $7^3/_4$ earthquake that struck the Moxi region in 1786 (Chen et al., 2011; Chen et al., 2016).

Although various researchers have obtained varied findings about the late Quaternary activity rate of each segment of the XSHF, the overall trend indicates that the southeast segment's late Quaternary activity rate is approximately 6–10 mm/a, and the center segment's late Quaternary activity rate is typically 3–8 mm/a (Qian et al., 1988; Zhao et al., 1990; Allen et al., 1991; Li, 1997; Zhou et al., 2001b; Xu et al., 2003; Wen et al., 2008; Chen, 2006).

The ANHF was divided into two segments by Mianning (Ran et al., 2008a). The results of the field investigation indicate that the left-strike slip rate of the northern segment of the ANHF is 3.6–4.0 mm/a, while the southern segment's slip rate since the Holocene is approximately 4.4–6.5 ± 1 mm/a (Wang et al., 2018; Xu et al., 2003), and the Xichang earthquake of magnitude M $7^1/_2$ occurred on the ANHF fault in 1536 AD (Ran et al., 2008b; Wang et al., 2014).

The DLSF is a structural belt with a total width of approximately 15 km, consisting of six secondary faults (He et al., 2008). The Gongyihai fault and the Shimian fault make up the northern segment (Institute of Geology, CEA, 2019). Since the late Pleistocene, the Gongyihai fault has been a weakly active fault according to the most recent geological and geomorphological surveys. High-precision geomorphological observations and satellite interpretation indicate that the late Quaternary left-strike rate of the Shimian fault is 1.5–3.3 mm/a, which is consistent with the fault's relatively intense late Quaternary activity (Sun et al., 2015). Although the DLSF lacks historical earthquake records, palaeoearthquake research has shown evidence of intense seismic activity, indicating that earthquakes of M 7 or above have occurred and will occur in the future (Gao et al., 2016; Sun et al., 2019; Feng et al., 2021).

3 Methods

Generally, earthquakes with a magnitude greater than M $6^3/_4$ will produce surface rupture (Deng et al., 1992). The surface rupture traces of large earthquakes in geological records can be revealed according to the palaeoearthquake research (Ran et al., 2012a; 2012b). Based on the comparative analysis of palaeoearthquakes in different locations, the rupture range of historical earthquakes can be found, and then, the rupture mode of faults can be clarified (Scharer et al., 2017; Onderdonk. et al., 2018; Yuan, 2018; Wang et al., 2018). In this regard, to explore the rupture range of the 1786 earthquake, we excavated four trenches in the vicinity of the 1786 earthquake epicenter in the northern section of the DLSF, the northern section of the ANHF, the Zheduotang section, and the Selaha section of the XSHF.

3.1 Trench excavation and identification of palaeoearthquakes

To investigate palaeoearthquakes along the strike-slip faults in the Sichuan–Yunnan area, fault troughs and sag-ponds are emerging as the best trench sites (Ran et al., 2012a). We have chosen four trenching sites that favor fine-grained deposits. During excavation, trenches were required to be 2.5 m deep and 2.5 m wide, and each wall was virtually vertically excavated and then meticulously cleaned, gridded in squares of 1×1 m, photographed, and printed for thorough field mapping. According to Ran et al. (2012a, 2012b), the main criteria for identifying strike-slip fault palaeoearthquake events with strike-slip faults can be summarized as follows: sedimentary sequence characteristics (such as sedimentary evolution and sedimentary interruption), the relationship between faults and strata, strata deformations (such as bending and dislocation), tension-filled wedges, and infilled and void fissures.

3.2 Radiocarbon dating

In all trenches, several radiocarbon samples were taken from both faulted and unfaulted strata. These samples came from organic

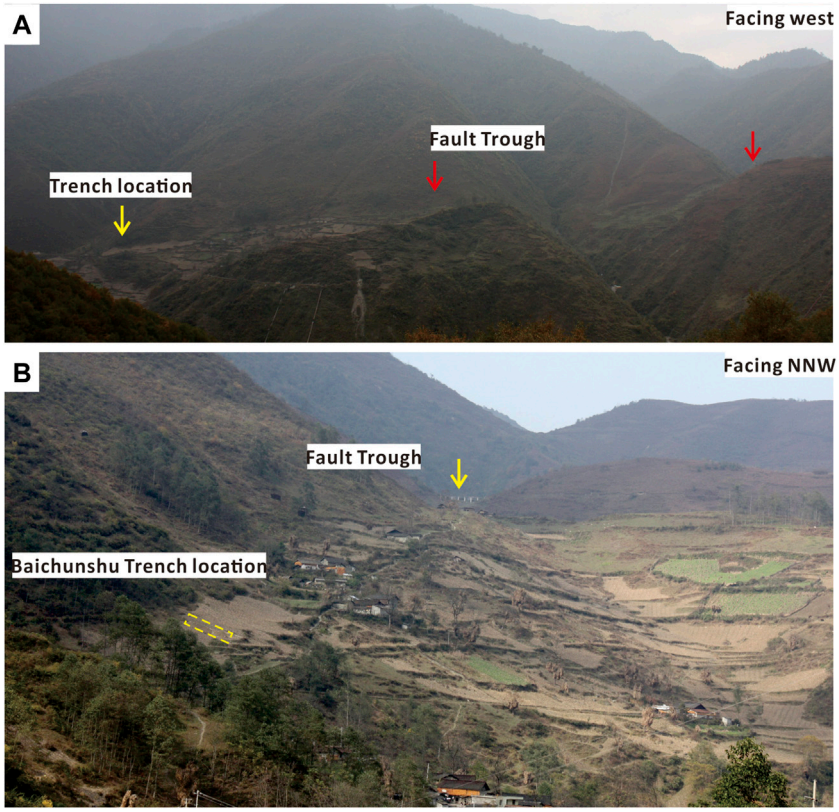

FIGURE 2
Fault geomorphology and trench layout in Baichunshu. **(A)** Field photo of the faulted landforms around trench. **(B)** Local enlarged photograph of **(A)**.

sediment, wood, and charcoal, which have all been advocated as excellent sources for determining the sedimentation age of stratigraphic units. All samples were sent to Beta Analytic, Inc., United States, for accelerometer mass spectrometer dating. Using the OxCal 4.4 technique procedure (Ramsey, 2009; Reimer et al., 2013), the sample ages were adjusted to two-sigma calendar ages (95.4% confidence interval).

4 Palaeoearthquake investigation

4.1 Baichunshu trench

Evident fault activity indications and micro landforms, including fault troughs, steep ridges, fault ponds, and abandoned gullies, were found along the northern section of the ANHF in the region from Ganhaizi to Shimian County. The linear image characteristics of fault activity in the late Quaternary are particularly obvious close to Baichunshu village, with a linear distribution of fault troughs and slope trough landforms (Figure 2). The trench was excavated at a slope trough approximately 1 km north of Baichunshu village, and the valley topography favors continuous deposition with fine-grain deposits carried by a hillside stream (Figure 2B). The trench profile reveals that the underlying materials are mostly clay materials of static water accumulation or faulted ponds, as opposed to the overlying materials, which are primarily sand gravels of deluvial facies (Figure 3). Based on the differences in composition, structure, color, and sedimentary facies, these clays and gravel layers are divided into five units, including six subunits (Table 1).

By analyzing the deformation evidence revealed by the Baichunshu trench, two faults can be identified. On the eastern wall, the fault events are clear. Unfortunately, the timing of palaeoseismic events in Table 1 cannot be well constrained due to the absence of sedimentary sequences. On the western wall, faulted events are also very clear (Figure 3). According to the relationship between stratigraphic characteristics and faulted deformation, three palaeoseismic events were revealed, namely, BE1, BE2, and BE3, from the oldest to youngest.

The BE1 event occurred before U3b and after U2c. The main evidence is as follows: ①F2-1 faulted layer U2-1 (Figure 3); ②sedimentary facies had changed after U2c; U3b, which is only distributed on the west side of the profile, is the hydrostatic sedimentary environment, with sag-pond sedimentary characteristics, while the U2c layer is deluvial facies with the continental sedimentary environment.

The BE2 event occurred after U3b and before U4a. The main evidence is as follows: ①sedimentary facies had changed after U3b; ②there are differences in the deformation degree—the dragging deformation of U3b is very strong, while the deformation of U4,

10.3389/feart.2023.1140326

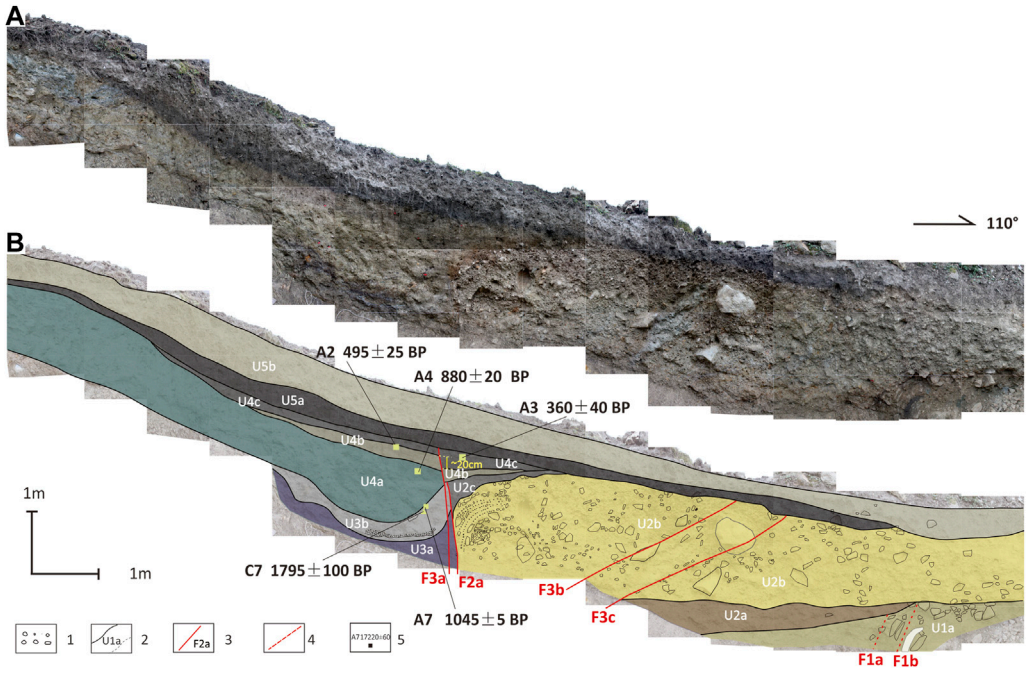

FIGURE 3
Photographic mosaic (upper) and interpretation log(lower) of the Baichunshu trench. **(A)** Photographic mosaic of the north wall of the trench; **(B)** interpretation log(lower) of the trench. 1) Gravel; 2) depositional unit sequence and stratigraphic boundary (dotted line indicates the unclear boundary); 3) fault trace; 4) speculate fault; and 5) location and dating of ^{14}C samples.

TABLE 1 Units and descriptions exposed by the Baichunshu trench.

Unit	Description
U1	The yellow–brown slightly gray gravel layer, the gravel particle size is large, ranging from 1 cm to 20 cm, the sorting is poor, and it is an alluvial accumulation
U2	A clay gravel layer containing siltier gravel, which is slope sediment. It can be divided into three sublayers, U2a is a brownish-yellow slope flood gravel layer, the gravel diameter is less, there is a certain rounding, and the boundary with the lower strata is clear, and it is stacked before the ridge; U2b is a mixture of bluish-gray gravel and clay, containing boulders; U2C is a brownish-red gravel-bearing clay layer
U3	Gray gravel-bearing clay layer with clear boundaries from the upper and lower strata. According to the gravel content, it can be divided into two sublayers, U3a is a gray gravel clay layer; U3b is a blue–gray carbon-containing silt layer and clay layer, and the top is partially laminated carbon chips and carbon mud, and the carbon AMS dating result obtained in this layer is 1045 ± 5 BP.
U4	Pale yellow clay layer, which can be divided into three sublayers according to color and sedimentary characteristics, U4a is an earthy yellow gravel-bearing fast clay layer, and the carbon-like AMS dating result is 880 ± 20 BP; U4b is a light earthy yellow clay layer, and the carbon-like AMS dating result is 495 ± 25 BP; U4c is an earthy yellow clay layer, and the carbon AMS dating result is 360 ± 40 BP.
U5	The surface clay layer, which has a clear stratigraphic boundary with the underlying stratigraphy, showing unintegrated contact, and the U5a layer is a gray–black clay layer; U5b is a surface tillage soil layer
U5	Gray–black topsoil layer rich in plant roots, containing a small amount of small gravel particles. Some large gravel particles are only visible near the fault at the northern end of the eastern wall

especially the upper part U4b and U4c, is weaker, and the dislocation of U4b is only 20 cm.

The BE3 event occurred between U4c and U5a, and the main evidence is that U5a was not faulted and deformed, while U4c was dislocated by F3-1.

At the 95.4% confidence interval (Table 4), the calendar ages of the three events from OxCal 4.4 are as follows: Event BE1, ~1003 AD; Event BE2, 1000–1182 AD; and Event BE3, after 1535 AD.

4.2 Yalaxiang trench

The Selaha fault along the northern Kangding faults is a sequence of moraine ridges, fluvioglacial accumulation platforms, and fluvioglacial terraces, yielding structural landforms such as linear troughs and fault ponds. On the south side of Chongcaoping, we excavated a trench in the fault trough, which spanned the entire fault depression. This trench's north wall collapsed during excavation, while the south wall was in good

10.3389/feart.2023.1140326

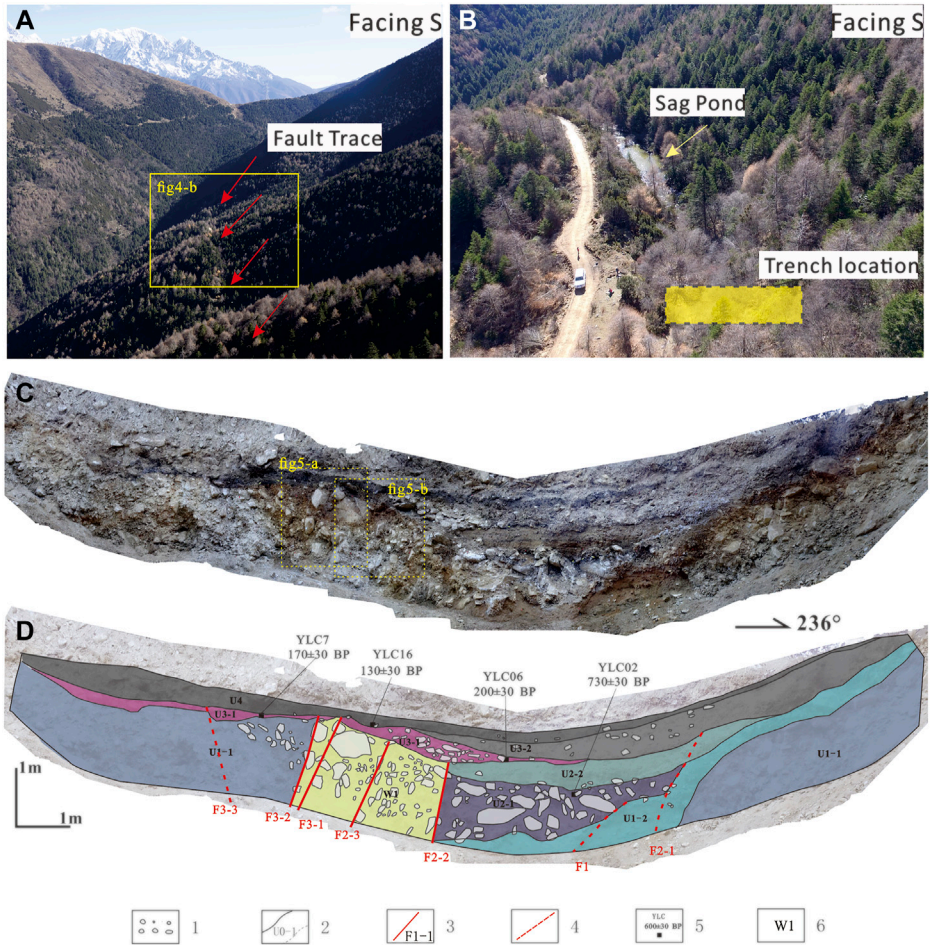

FIGURE 4
Fault traces and locations of trenches. Faulted landforms near Yalaxiang township **(A,B)**. **(C)** photographic mosaic of the south wall of the trench; **(D)** interpretation log(lower) of the trench. 1) Gravel; 2) depositional unit sequence and stratigraphic boundary (dotted line indicates the unclear boundary); 3) fault trace; 4) speculate fault; 5) location and dating of ^{14}C samples; and 6) structural wedge.

TABLE 2 Units and descriptions exposed by the Yalaxiang trench.

Unit	Description
U1	Clay-containing gravel layer, containing boulder can be divided into two sublayers according to the content of clay. U1a is an earthy yellow gravel layer, semiconsolidated, and formed by the accumulation of alluvial facies; U1-b is a dark-yellow clay layer with gravel and slope accumulation
U2	Fault pond sedimentation, both sides controlled by faults, the strata appear bowl-shaped, can be divided into two sublayers. U2a is a black organic soil layer, and the AMS dating result of a carbon chip at the top is 730 ± 30 BP. U2b is a fine gray–yellow sand layer with horizontal layers
U3	The clay layer, which can be divided into two sublayers. U3a is a black organic soil layer with a thin layer; AMS dating results were 200 ± 30 BP and 170 ± 30 BP, respectively; U3b is a gray gravel-bearing clay layer
U4	The light-yellow clay layer can be divided into three sublayers according to color and sedimentary characteristics, U4a is an earthy yellow gravel-bearing fast clay layer, and the carbon-like AMS dating result is 880 ± 20 BP. U4b is a light earthy yellow clay layer, and the carbon-like AMS dating result is 495 ± 25 BP. U4c is an earthy yellow clay layer, and the carbon AMS dating result is 360 ± 40 BP.
U5	The black clay layer, which contains a large amount of organic matter in the middle of the trough, and the MS dating result of 1carbon chip at the bottom is 130 ± 30 BP.

shape (Figure 4). The trench profile reveals that there are multistage fault pond sediments and alluvial–pluvial deposits on the eastern side, while the alluvial deposits along the slope dominate the western side. According to the sedimentary characteristics, it can be roughly divided into four sets of strata, including six sublayers (Table 2).

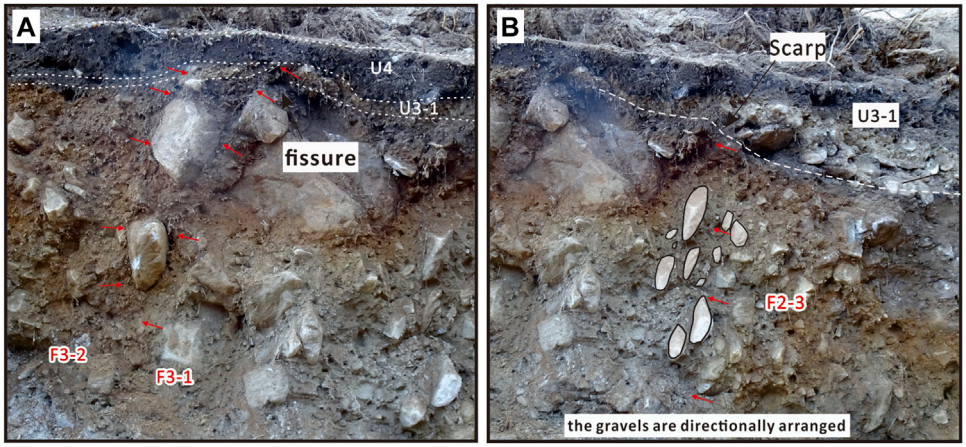

FIGURE 5
Close shots of the local topical partial trench wall and the details of the fault. **(A)** the fault trace of F3-2/F3-1. **(B)** the fault trace of F2-3.

Two palaeoseismic events, SL1 and SL2, can be identified by stratigraphic evidence according to the relationship between faulting and sedimentation in the sedimentary sequences of the fault depression, and the times of the two events were restricted to between U2-2 and U3-1 and U3-2 and U4-l, respectively.

The main evidence of event SL1 is as follows: ①the stratigraphic boundary is very clear: layer U2-2 is fine sand, while the bottom of U3 is an organic clay layer with gravel, which means that the sedimentary facies of the strata has changed; ② the topographic uplift on the eastern side of the trench is caused by fault F2-1/F2-2/F2-3, which faults layer U2-2. Layer U3-1 is a local gravel layer that formed quickly in front of the ridge (Figure 5B).

The main evidence for SL2 is as follows: ①clear stratigraphic and sedimentary boundaries; ②layer U3-1 is deformed and faulted along faults F3-2 and F3-1, and it is arched and faulted along fault F3-3 (Figure 5A), whereas layer U4 above it covers it firmly and without any deformation.

Four carbon debris samples were obtained and sent to Beta Laboratory for accelerated mass spectrometry (AMS) dating. At a 95.4% confidence interval (Table 4), the calendar ages of the two events from OxCal 4.4 are as follows: SL1, 1272–1720 AD; SL2, 1703–1929 AD.

4.3 Zheduotang trench

The Zheduotang fault delineates a string of ridges from Zheduoshan to Zheduotang village, creating fault ponds, fault troughs, and slope ridges. The surface rupture of the 1955 M $7^1/_2$ earthquake formed a 1.8 m reverse scarp on alluvial–diluvial terrace

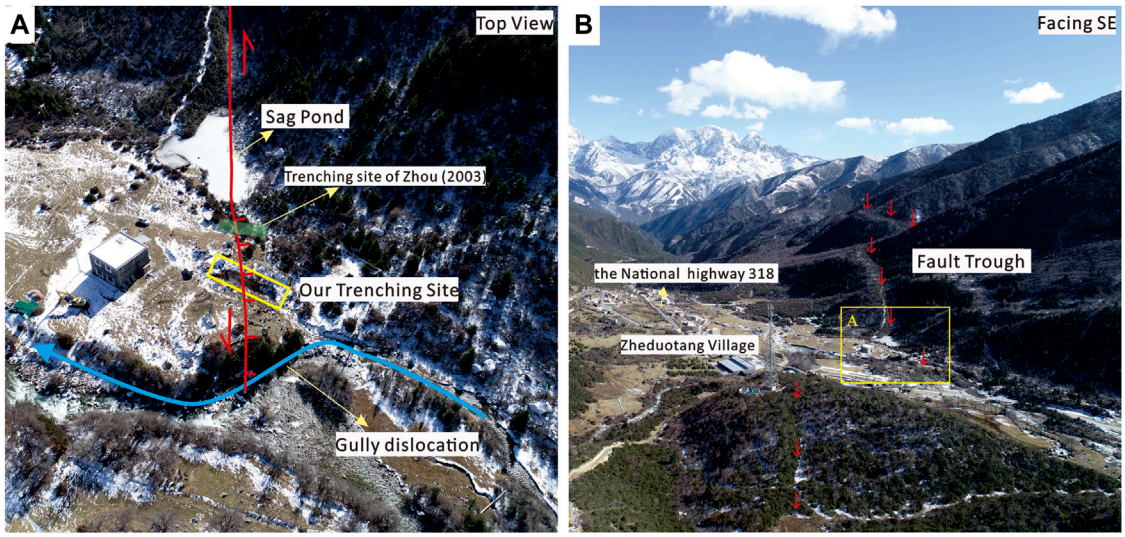

FIGURE 6
Fault field photographs of the fault traces near the Zheduotang Village. **(A)** Representative faulted landforms. **(B)** The location of Zheduotang trench.

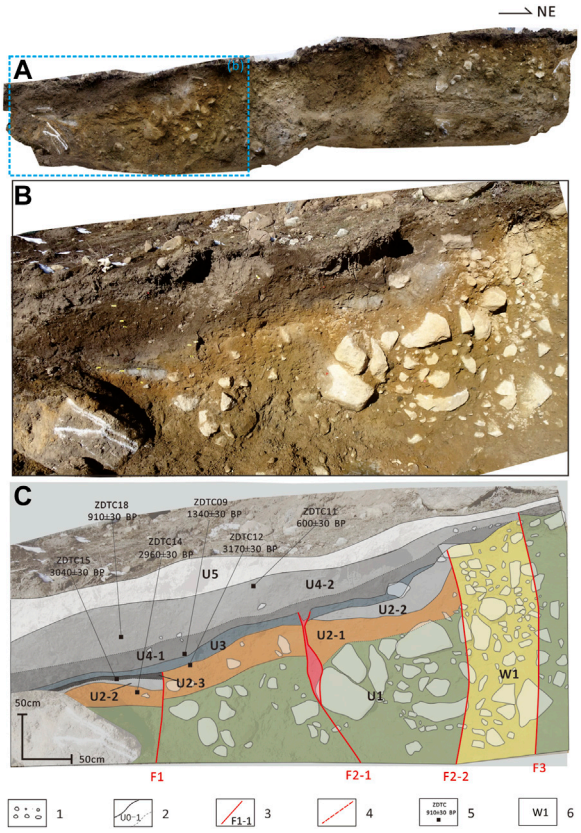

FIGURE 7
Photographic mosaic **(A–B)** and interpretation log **(C)** of the Zheduotang trench. a, photographic mosaic of the north wall of the trench; b, close shots of the local topical partial trench wall; and c, interpretation log(lower) of the trench. 1) Gravel; 2) depositional unit sequence and stratigraphic boundary (dotted line indicates the unclear boundary); 3) fault trace; 4) speculate fault; 5) location and dating of ^{14}C samples; and 6) structural wedge.

T1 along the fault, which is distributed on the right step near Zheduotang village. The Zheduotang trench crosses the fault scarp (Figure 6). On the western side of the trench, there is a sandy gravel layer of terrace alluvium and diluvium with a lenticular sand layer, while on the eastern side, there are deposits from many stages of fault depression (Figure 7). Because of gurgling and flooding in the low-lying section of the western wall, only a portion of the walls was kept. According to the sedimentary characteristics, the site can be divided into five sets of strata, including three sublayers. The strata are shown in Table 3.

There was a fault zone with a width of approximately 1 m that ruptured upward to the ground surface (Figures 7A, B), which should correspond to the 1955 *M* 7 earthquake. The strata in the sag-pond have experienced faulting, fold deformation, and fracture filling to varying degrees since the fault zone governs these processes. Based on this deformation evidence and depositional sequences, three events can be identified.

Event ZD1 occurred after U2-3 and before U3. The main evidence is as follows: ①the boundary of strata deposition is very clear; U2-3 is an organic layer rich in carbon debris, and there is a sedimentary phase change with U3, which does not include carbon debris; ②F1 faults layer U2 and is covered by layers U3.

Event ZD2 occurred after U3 and before U4-1. The main evidence is as follows: ①F2-1 faults U3, dragging it into the structural zone, and U4-1 fills the gap along the fracture (Figure 7C); ②along fault F2-2, which causes U2 and U3 bending deformation, the gravels are directionally arranged, and U4 covers it (Figure 7C).

Event ZD3 occurred after U4-2 and before U5. The gravels in F3 are directionally organized to the surface, with clear fault traces. A scarp can be observed on the surface, which should be associated with the 1955 AD earthquake.

Six carbon debris samples were obtained and sent to Beta Laboratory for accelerated mass spectrometry (AMS) dating. At a 95.4% confidence interval (Table 4), the calendar ages of the two events from OxCal 4.4 are as follows: ZD1, 1215 BC ~ 315 AD; ZD2, 830 BC ~ 705 AD. The latest event, ZD3, is after 1500 AD.

4.4 Lianhecun trench

From the Zhuma basin to the Huilong uplift, several faulted landforms, including the fault trough, water system, ridge

TABLE 3 Units and descriptions exposed by the Zheduotang trench.

Unit	Description
U1	The light-green pebbly clay is formed by piedmont alluvial–pluvial facies. It can be divided into three sublayers from top to bottom. The top is brown–yellow clay (U2a), containing a small amount of gravel; middle U2b grayish white mud layer, controlled by fault; The top is U2c black organic clay layer, in which a carbon fragment is collected, and the AMS dating result is 3010 ± 30 BP
U2	The light-green pebbly clay is formed by piedmont alluvial–pluvial facies. It can be divided into three sublayers from top to bottom. The top is brown–yellow clay (U2a), containing a small amount of gravel; middle U2b grayish white mud layer, controlled by fault; The top is U2c black organic clay layer, in which a carbon fragment is collected, and the AMS dating result is 3010 ± 30 BP
U3	A grayish green clay layer, with a clear boundary line with the underlying strata, accumulated along the ridge, a stable layer thickness of grayish black clay layer, mixed with small gravel blocks, which can be divided into two sublayers U4a and U4b according to the content of organic matter. AMS dating result of a carbon fragment at the bottom is 1340 ± 30 BP; U4b is a grayish black clay layer, containing a large amount of organic matter. Two carbon fragments were collected from this layer, and the AMS dating results are 600 ± 30 BP and 910 ± 30 BP, respectively. Now, it represents the development of soil layers and grass roots
U4	A grayish green clay layer, with a clear boundary line with the underlying strata, accumulated along the ridge, a stable layer thickness of grayish black clay layer, mixed with small gravel blocks, which can be divided into two sublayers U4a and U4b according to the content of organic matter. AMS dating result of a carbon fragment at the bottom is 1340 ± 30 BP; U4b is a grayish black clay layer, containing a large amount of organic matter. Two carbon fragments were collected from this layer, and the AMS dating results are 600 ± 30 BP and 910 ± 30 BP, respectively
U5	Surface layer; the development of soil layers and grass roots

TABLE 4 Radiocarbon samples and dating results for the four trenches.

Sample	Lab code	$^{13}C/^{12}C$ (o/oo)	Radiocarbon age (years BP±σ)	Calendar years (cal BP)	Description	Unit sampled
				2σ(95.4%)		
ZDTC11	548371	-25.1	600 ± 30	1295-1410AD	Charcoal	ZD/U4-2
ZDTC18	548375	-22.9	910 ± 30	1030-1205AD	Charcoal	ZD/U4-2
ZDTC09	548370	-24.0	1340 ± 30	640-715AD (83.4%)	Charcoal	ZD/U4-1
				740-770AD (12.0%)		
ZDTC15	548374	-23.2	3040 ± 30	1400-1215BC	Charcoal	ZD/U2-3
ZDTC14	548373	-22.9	2960 ± 30	1265-1055BC	Organic sediment	ZD/U2-1
ZDTC12	548372	-22.9	3170 ± 30	1505-1395BC	Charcoal	ZD/U2-1
YLC16	548379	-24.4	130 ± 30	1804-1950AD	Charcoal	SL/U4
YLC07	548378	-23.6	190 ± 30	1655-1705AD (36.7%)	Charcoal	SL/U3-1
				1719-1816AD (58.7%)		
YLC06	548377	-24.7	200 ± 30	1648-1687AD (36.7%)	Charcoal	SL/U3-1
				1732-1806AD (58.7%)		
YLC02	548376	-26.8	730 ± 30	1225-1234AD (1.7%)	Charcoal	SL/U2-3
				1240-1299AD (92.1%)		
				1371-1379AD (1.6%)		
A2	--	-21.8	495 ± 25	1407-1446 AD	Charcoal	BCS/U4b
A3	--	-22.9	360 ± 40	1450-1634 AD	Charcoal	BCS/U4c
A4	--	-23.2	880 ± 20	1055-1219 AD	Charcoal	BCS/U4a
A7	--	-24.3	1045 ± 5	988-1019 AD	Charcoal	BCS/U3
C7#	--	--	1700 ± 100	--	Charcoal	BCS*/U3
LH-C39	514443	-28.5	250 ± 30	1521-1578AD (22.5%)	Charcoal	LH/U5
				1625-1677AD (72.9%)		
LH-C40	52559	-24.6	230± 30	1524-1559AD (6.9%)	Charcoal	LH/U5
				1631-1685AD (88.2%)		
				1786-1790AD (0.3%)		
LH-C73	521562	-26.2	170 ± 30	1667-1689AD (7.3%)	Charcoal	LH/U6
				1721-1823AD (73.3%)		
				1831-1880AD (10.2%)		
				1917-1944AD (4.8%)		
LH-C61	521564	-24.4	390 ± 30	1441-1524AD (69.2%)	Charcoal	LH/U5
				1570-1630AD (26.2%)		
LH-C102	514433	-25.8	390 ± 30	1441-1524AD (69.2%)	Charcoal	LH/U5
				1570-1630AD (26.2%)		
LH-C109	521563	-24.8	170± 30	1667-1698AD (7.1%)	Charcoal	LH/U6
				1721-1823AD (73.2%)		
				1831-1880AD (10.2%)		
				1917-1944AD (4.9%)		

(Continued on following page)

TABLE 4 (*Continued*) Radiocarbon samples and dating results for the four trenches.

Sample	Lab code	$^{13}C/^{12}C$ (o/oo)	Radiocarbon age (years BP±σ)	Calendar years (cal BP) 2σ(95.4%)	Description	Unit sampled
LH-C104	514434	-26.4	140 ± 30	1677-1783AD (47.2%)	Charcoal	LH/U6
				1796-1891AD (43.9%)		
				1913-1934AD (4.3%)		

*BCS: Baichunshu trench; SL: Yalaxiang trench; ZD: Zheduotang trench; LH: Lianhecun trench; #C7 are the results of conventional^{14}C dating (tested by the Institute of Geology, China Earthquake Administration).

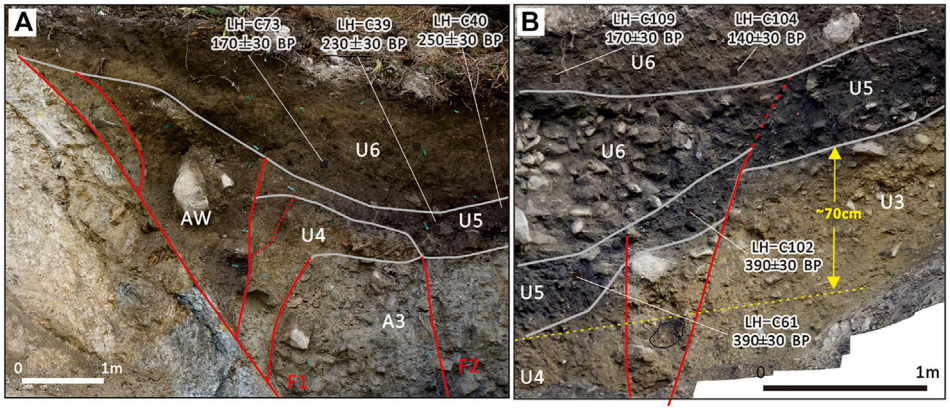

FIGURE 8
Close shots of the local topical partial trench wall and the details of the latest event in the Lianhecun trench. **(A)** Details of the south wall of Lianhecun TC1 (Feng et al., 2021); **(B)** details of the north wall of Lianhecun TC2; 70 cm indicates an apparent vertical dislocation.

dislocation, and minor fault depression, were formed along the Shimian fault. The fault trough and tiny fault depression are very visible at Lianhecun, where the left-lateral dislocation of the gully is approximately 107 m. Two trenches (Feng et al., 2021) were excavated across one of the small fault ponds. Four events were revealed: E1, 20925–116850 BC; E2, 15265 BC ~ 1785 BC; E3, 360 AD ~ 1475 AD; and E4, 1655 AD ~ 1815 AD.

The latest event that the trench showed is quite obvious. Between U5 and the primary fault zone F1 on the southern wall (Figure 8A), there is wedge-shaped filling (AW). The black soil in layer U5 was filled into the AW, and overlying layer U6 had not deformed. On the northern wall, there was a bottom gravel layer in U6 (Figure 8B), which indicates a change in the sedimentary environment. There were approximately 70 cm vertical dislocations along the fault. Seven samples of carbon debris from U4 and U5 were sent to the Beta Laboratory in the United States for AMS dating. The initial date was adjusted using the age correction program OxCal4.44 (Table 4), and the event occurred between 1655 and 1815 AD.

5 Discussion

As a result, the latest event of the northern segment of the Anninghe fault revealed by the Baichunshu trench occurred after 1535 AD The latest two events, SL1: 1272–1720 AD and SL2: 1703–1929 AD, in the Selaha fault were revealed by the Yalaxiang trench. The latest event of the Zheduotang fault occurred after 1500 AD by the Zheduotang trench. The latest event of the Shimian fault was exposed by the Lianhecun trench between 1655 and 1815 AD. Additionally, the Xingyulin trench found that the Moxi fault's most recent event occurred between 1280 and 1850 AD (Gao et al., 2021), while the Yalahe fault's most recent event may have been the 1700 AD earthquake (Liang et al., 2020) (Figure 9).

Since 1700 AD, four earthquakes of $M \geq 6.5$ have been recorded in the history of the area from Kangding to Shimian in the order of the 1725 AD M 7 Kangding earthquake, the 1748 AD M $6^1/_2$ earthquake in northwest Kangding, the 1786 AD M $7^3/_4$ earthquake in southern Kangding, and the 1955 AD M $7^1/_2$ Kangding earthquake (Department of Earthquake Disaster Prevention, 1995). Among them, the elapsed time of the 1955 AD M $7^1/_2$ Kangding earthquake is the shortest. This earthquake left a surface rupture zone of about 30 km along the Zheduotang fault (The Chengdu Seismic Brigade, 1972). According to prior knowledge and earthquake cases, an earthquake's magnitude that results in a surface rupture on the Chinese mainland is often greater than M $6^3/_4$ (Deng et al., 1992). There were only few kilometers of ambiguous surface rupture from the Luding M 6.8 earthquake in 2022 AD (Li et al., 2022; Han et al., 2023). It is concluded that the 1748 AD Kangding M $6^1/_2$ earthquake may not have

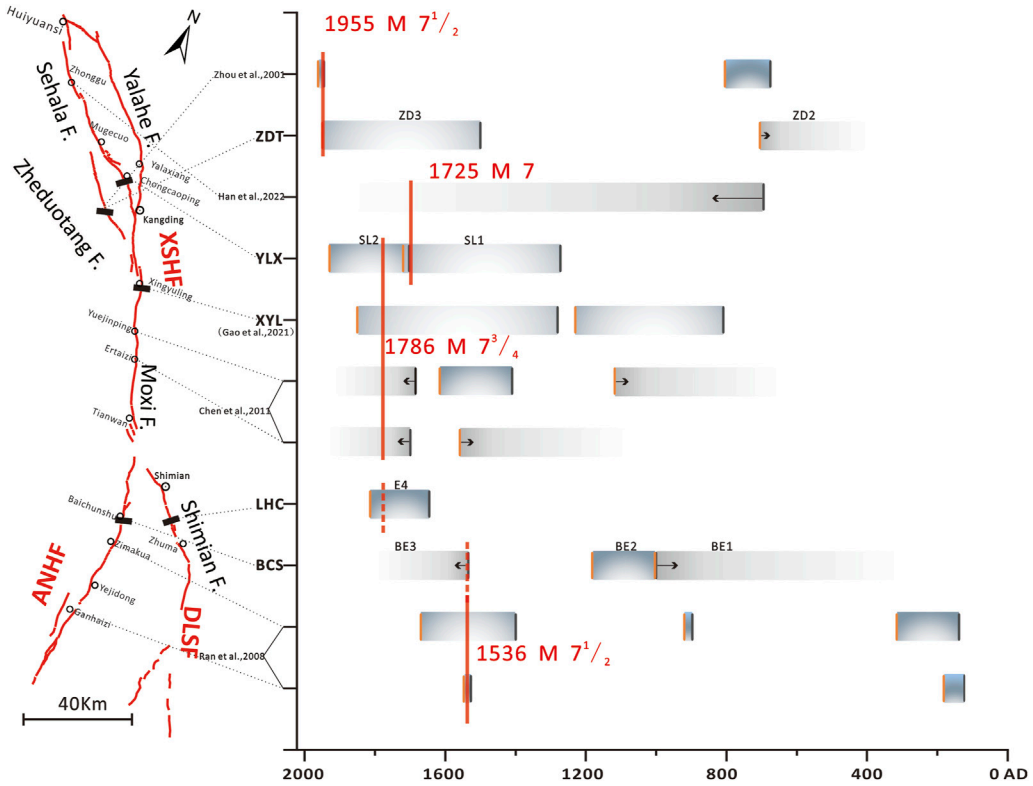

FIGURE 9
Palaeoseismic sequence from trenching at different sites and compared with historical record earthquakes. The gradient area represents the range of palaeoseismic events revealed by different trenches. The orange vertical line is the upper limit of the event, while the black vertical line is the lower limit of the event.

produced a surface rupture. A 100 m-long ground fissure was discovered on the moraine gravel platform at Chongcaoping, the epicenter of the AD 1725 Kangding *M* 7 earthquake, and the gravel there exhibited clear twisting marks (Wang, 1992; Li, 1997). It is possible that event SL1 revealed by the Yalaxiang trench, which was excavated 500 m south of Chongcaoping in the meizoseismal region of the 1725 earthquake, was the earthquake. However, the meizoseismal region of the 1786 AD earthquake extends from Kangding to Shimian (Department of Earthquake Disaster Prevention, 1995). The prior study results and the Xingyulin trench indicate that a surface rupture occurred during the earthquake in the Kangding–Moxi region (Gao et al., 2021). Some investigations have suggested that the northwest end may extend to the vicinity of Mugecuo, and the southeast end may reach the Tianwan area (Wang and Pei, 1998; Zhou et al., 2001b). Yalaxiang trench data show that the most recent incident SL2 closely matches the 1786 earthquake. According to the degree of bending deformation and elevation in the trench profile, the trench site should be located near the northernmost end of the surface rupture. In recent years, some new evidence has been obtained in the southeastward of the rupture, which shows that the rupture extends at least to the south of Tianwan (Chen et al., 2011, 2016). The results from the Lianhecun trench indicate that the most recent event in the Shimian fault occurred between 1655 and 1815 AD. Since 1500 AD, the historical earthquake data of $M \geq 7$ in this area have been complete (Huang and Li, 1994). Except for the 1786 Kangding earthquake, no unambiguous written records of earthquakes have been discovered in Shimian since the Ming and Qing Dynasties, according to historical earthquake records (Gu, 1983; Department of Earthquake Disaster Prevention, 1995; Sun, 2010). So, the 1786 earthquake should be considered the most recent seismic event on the Shimian fault, which is constrained by the Lianhecun trench.

By excavating the trench groups in Zimakua, Ganhaizi, and Dahaizi, Ran et al. (2008) proposed that the northern segment of the ANHF can be separated into two distinct subsections, namely, the Dahaizi–Ganhaizi section and the Zimakao–Yejidong section. In the northern part of the Zimakao–Yejidong section, three palaeoseismic events occurred: 280–550 B.P., 1030–1050 B.P., and 1634–1811 B.P. The three events disclosed by the Baichunshu trench correspond to the most recent three occurrences at the site of the Zimakua trench (Figure 9). Wang et al. (2014) examined palaeoseismic data from the southern and northern parts of the ANHF and determined that the 1536 Xichang M $7^1/_2$ earthquake ruptured the whole length. The latest event (after 1535 AD) revealed by the Baichunshu trench may correspond to the 1536 Xichang M $7^1/_2$ earthquake. However, due to the lack of historical records, it cannot be completely ruled out that the latest event revealed by the Baichunshu trench may also be the 1786 earthquake (Figure 9).

In summary, the latest event limited by the Baicunshu and Zheduotang trenches cannot rule out the 1786 AD earthquake. This earthquake ruptured the Shimian fault (the northern section of the DLSF) and the southern segment of the XSHF, with a total length of approximately 120 km from the northern end near the Yalaxiang trench to the southern end on the south side of the Lianhecun trench. Similar to

the *Ms* 8.0 2008 Wenchuan earthquake and the *Mw* 7.8 2016 Kaikōura earthquake (Tan et al., 2013; Hamling et al., 2017), this earthquake is also a complex earthquake with a multi-fault rupture.

According to the empirical relationship between the length of the surface rupture of the strike-slip fault type and the magnitude of earthquake occurrence,

$$M = 5.16(\pm 0.13) + 1.12(\pm 0.08)*\log(SRL),$$

where *M* is the magnitude of the earthquake, SRL is the surface rupture length, and the values in brackets are the error coefficients (Wells and Coppersmith, 1994). If the length is 120 km, the magnitude of the earthquake is approximately *M* $7^3/_4$, which is equivalent to the estimated result of historical earthquake intensity.

Furthermore, according to historical records, there was an aftershock of magnitude 6 or greater on June 2 after the major earthquake of magnitude *M* $7^3/_4$ on 1 June 1786 AD, and there may have been an earthquake of magnitude 7 or greater near Detuo on June 10 (Sun, 2010). It also reflects that the 1786 AD *M* $7^3/_4$ earthquake along the XSHF may have triggered the rupture of the Shimian fault, resulting in multi-fault rupture behavior.

6 Conclusion

Four trenches, excavated in the vicinity of the epicenter in the northern section of DLSF, the northern section of the ANHF, the Zheduotang fault, and the Salaha fault of the XSHF, revealed the depositional sequences and deformation evidence in the palaeoearthquakes. The major results are given as follows:

1) From trenching and ^{14}C ages, two palaeoseismic events have occurred on the northern section of the ANHF: BE1, ~1003AD; BE2, 1000–1182AD. We associate the most recent event BE3 with the historical records of 1536 AD *M* 7.
2) Two palaeoseismic events have occurred on the Selaha fault in the last 500 years, SL1, 1272–1720 AD; SL2, 1703–1929 AD. We associate two young events with the historical records of the 1725 AD Kangding *M* 7 earthquake and the 1786 AD Kangding *M* $7^3/_4$ earthquake.
3) Three palaeoseismic events have occurred on the Zheduotang: ZD1, 1215 BC ~ 315 AD; ZD2, 830 BC ~ 705 AD; and ZD3, 1955 AD Kangding *M* $7^1/_2$ earthquake.
4) The 1786 AD Kangding *M* $7^3/_4$ earthquake was probably a multi-fault event, based on the trenching profile evidence, the nearby offset geomorphic features, and the historical earthquake data. This earthquake's seismogenic fault is the Moxi fault, which triggered the southern end of the Selaha fault to the north and the Shimian fault (DLSF) to the south. The total rupture length is approximately 120 km.

Data availability statement

The original contributions presented in the study are included in the article/Supplementary Material; further inquiries can be directed to the corresponding author.

Author contributions

The study was designed by LC; the field work was carried out by MH, YL, SG, JF, LL, and LC; the writing and preparation of the original manuscript were carried out by JF; and the review and editing of the final manuscript were performed by LC, MH, and CS. All authors contributed to the article and approved the submitted version.

Funding

This work was supported financially by the National Natural Science Foundation of China (41872228, 41672207), the Second Tibetan Plateau Scientific Expedition and Research (2019QZKK0901), and the Basic Scientific Work of the Institute of Geology, China Earthquake Administration (IGCEA1418).

Acknowledgments

The authors thank Prof Ran Yongkang for meticulous guidance on the exploration and thesis research work. They also would like to thank Deng Jinhua for the careful revision of the paper format. The authors give great thanks to Wenjun Zheng, Chuanyong Wu, Daoyang Yuan and Jun Shen for their constructive suggestions to improve the article.

Conflict of interest

The authors declare that the research was conducted in the absence of any commercial or financial relationships that could be construed as a potential conflict of interest.

Publisher's note

References

Allen, C. R., Luo, Z. L., Qian, H., Wen, X. Z., Zhou, H. W., and Huang, W. S. (1991). Field study of a highly active fault zone: The Xianshuihe fault of southwestern China. *Geol. Soc. Am. Bull.* 103, 1178–1199. doi:10.1130/0016-7606(1991)103<1178:fsoaha>2.3.co;2

An, Y. F. (2010). *Study on the boundary characteristics of seismic rupture segments in Xianshuihe fault zone*. Ph.D. Thesis. China Earthquake Administration: Institute of Geology. (in Chinese with English Abstract).

Ch, G., Papadimitriou, E. E., Karakostas, V. G., Wen, X. Z., Jin, X. S., Kilas, A., et al. (2008). Implication of fault interaction to seismic hazard assessment in Sichuan-Yunnan provinces of southeastern China. *Earthq. Sci.* 21, 181–201. doi:10.1007/s11589-008-0009-7

Chen, G. H., Xu, X. W., Wen, X. Z., and Chen, Y. G. (2016). Late quaternary slip-rates and slip partitioning on the southeastern Xianshuihe fault system, eastern Tibetan plateau. *Acta Geol. sin.* 90, 537–554. doi:10.1111/1755-6724.12689

Chen, G. Y., Min, W., and Song, F. M. (2011). Preservation of co-seismic surface rupture in diffrrent geomorphological settings from the study of the 1786 Moxi earthquake (in Chinese with English Abstract). *Seismol. Geol.* 33 (4), 804–817.

Chen, G. Y. (2006). *Tectonic transformation and deformation demarcation of the active tectonic belt on the northeast boundary of the Sichuan-Yunnan block (in Chinese)*. Ph.D. Thesis. China Earthquake Administration: Institute of Geology.

Chen, L. C., Li, Y. B., and Gao, S. P. (2018). Fracture behavior of multiple faults and prediction of large earthquakes (in Chinese). 24: 24–24

China News Network (2022). *Sichuan Luding earthquake has caused 93 deaths and 25 missing*. Available at: https://www.chinanews.com.cn/sh/2022/09-12/9850488.shtml.

The Chengdu Seismic Brigade (1972). *A suggestion on that medium and long term earthquake prediction in Shimian-Kangding area (in Chinese)*.

Deng, Q. D., Yu, G. H., and Ye, W. H. (1992). *Study on relationship between earthquake surface rupture and earthquake magnitude (in Chinese)*. Beijing: Study on Active Faults, 247–264.

Deng, Q. D., Zhang, P. Z., Rang, Y. K., Yang, X. P., Min, W., and Chun, Q. Z. (2002). Basic characteristic of active tectonics in China (in Chinese with English Abstract)(. *Sci. Chinaseries D)* 32 (12), 1020–1030.

Department of Earthquake Disaster Prevention (1995). "State seismological bureau," in *Catalogue of historical strong earthquakes in China (23rd century B.C.to 1911)* (Beijing: Seismological Press), 1–514. (in Chinese).

Department of Earthquake Disaster Prevention (1999). "State seismological bureau," in *Catalogue of modern earthquakes in China (1912-1990)* (Beijing: Seismological Press), 1–637. (in Chinese).

Feng, J. H., Chen, L. C., Wang, H., Li, J., Han, M. M., Li, Y. B., et al. (2021). Paleoseismologic study on the Shimian fault in the northern section of daliangshan fault zone (in Chinese with English Abstract). *Seismol. Geol.* 43 (1), 53–71.

Fletcher, J. M., Teran, O. J., Rockwell, T. K., Oskin, M. E., Hudnut, K. W., Mueller, K. J., et al. (2014). Assembly of a large earthquake from a complex fault system: Surface rupture kinematics of the 4 april 2010 el mayor-cucapah (Mexico) *Mw* 7.2 earthquake geosphere. *Geosph. (Boulder).* 10, 797–827. doi:10.1130/ges00933.1

Gan, W. J., Zhang, P. Z., Shen, Z. K., Niu, Z. J., Wang, M., Wan, Y. G., et al. (2007). Present-day crustal motion within the Tibetan Plateau inferred from GPS measurements. *J. Geophys. Res. Solid Earth* 112 (B8), B08416. doi:10.1029/2005JB004120

Gao, W., He, H, L., Sun, H. Y., and Wei, Z. Y. (2016). Paleoearthquakes along puxiong fault of daliangshan fault of daliangshan fault zong in Chinese with English Abstract. *Seismol. Geol.* 38 (4), 797–816.

Gao, S. P., Chen, L. C., Liang, M. J., Wang, D., Li, Y. B., Han, M. M., et al. (2021). Rupture characteristics and seismic recurrence behaviors of Xianshuihe fault reveals by Xingyulin trences, south of kangding (in Chinese with English abstract). *Adv. Eng. Sci.* 53 (3), 53–61.

Gu, G. X. (1983). *The Catalogue of Chinese earthquake (from 1831 B.C. to 1969 A.D)*. Beijing: China Science and Technology Press, 1–300. (in Chinese).

Han, B. Q., Liu, Z. J., Chen, B., Li, Z. H., Yu, S., Zhang, Y., et al. (2023). Coseismic deformation and slip distribution of the 2022 luding Mw 6.6 earthquake revealed by InSAR observations. *Geomatics Inf. Sci. Wuhan Univ.* 48 (1), 36–46. doi:10.13203/j.whugis20220636

Hamling, I. J., Hreinsdóttir, S., Clark, K., Eliott, J., Liang, C., Fielding, E., et al. (2017). Complex multifault rupture during the 2016 M_w 7.8 Kaikōura earthquake, New Zealand. *Science* 356, eaam7194. doi:10.1126/science.aam7194

Han, M. M., Chen, L. C., Zeng, D., Li, Y. B., Liang, M. J., Gao, S. P., et al. (2022). Discussion on the latest surface ruptures near the Zhonggu village along the Selaha segmentof the Xianshuihe fault zone (in Chinese). *J. Geomechanics* 28 (6), 969–980. doi:10.12090/j.issn.1006-6616.20222824

He, H. L., Ikeda, Y., He, Y. L., Chen, J., Chen, C. Y., et al. (2008). Newly-generated Daliangshan fault zone-ShortCutting on the central section of xianshuihe-xiaojiang fault system. *Sci. China Ser. D Earth Sci.* 51 (9), 1248–1258. doi:10.1007/s11430-008-0094-4

Huang, W. Q., and Li, W. X. (1994). Study on completeness of seismic data in China's continent (2): The beginning year of basically complete seismic data in different regions. *Earthquake* 16 (4), 10 [in Chinese].

Institute of Geology, CEA (2019). *Map of the northern section of the Anning River active fault*, 1. Beijing: Seismological Press, 50000. (in Chinese).

Li, T. T. (1997). *The Xianshuihe fault zone and assessment of strong earthquake risk (in Chinese)*. Chengdu: Science and Technology Press of Sichuan, 1–315.

Li, Y., Zhao, D., Shan, X., Gao, Z., Huang, X., and Gong, W. (2022). Coseismic slip model of the 2022 Mw 6.7 Luding (Tibet) earthquake: Pre- and post-earthquake interactions with surrounding major faults. *Geophys. Res. Lett.* 49, e2022GL102043. doi:10.1029/2022GL102043

Liang, M. J., Chen, L. C., Ran, Y. K., Li, Y. B., Wan, D., Gao, S. P., et al. (2020). Late-quaternary activity of the Yalahe fault of the Xianshuihe fault zone, eastern maprgin of the Tibet plateau (in Chinese with English Abstract). *Seismol. Geol.* 42 (2), 514–525.

Long, D. X., and Deng, T. G. (1986). A preliminary study on segment feature of fault motion along Xianshuihe fault belt ((in Chinese with English Abstract)). *J. deismological Res.* 5 (9).

Lozos, J. C., Oglesby, D. D., Duan, B., and Wesnousky, S. G. (2017). The effects of double fault bends on rupture propagation: A geometrical parameter study. *Bull. Seismol. Soc. Am.* 101, 385–398. doi:10.1785/0120100029

Ma, J., Zhou, B. G., Wang, M. M., and An, L. K. (2022). Geological and geomorphic evidences for the Holocene activity of the NW zheduotang brance within the Xianshuihe fault system ((in Chinese with English Abstract)). *Seismol. Geol.* 42 (05), 1021–1038.

Mark, S. B., Nicola, L., Pilar, V., Andy, N., Jarg, P., Phillip, B. S., et al. (2017). The Mw7.8 2016 Kaikōura earthquake: Surface fault rupture and seismic hazard context. *Bull. N. Z. Soc. Earthq. Eng.* 50 (2), 73–83.

Onderdonk, S., McGill, S., and Rockwell, T. (2018). A 3700 yr paleoseismic record from the northern San Jacinto fault and implications for joint rupture of the San Jacinto and San Andreas faults. *Geosphere* 14 (6), 2447–2468. doi:10.1130/ges01687.1

Qian, H., Allen, C. R., Luo, Z. L., Wen, X. Z., Hou, H. W., and Huang, W. S. (1988). The active characteristics of Xianshuihe fault in Holocene ((in Chinese with English Abstract)). *Sci. China* 02, 11–20.

Ran, Y. K., Chen, L. C., Cheng, J. W., and Gong, H. L. (2008a). Late Quaternary surface deformation and rupture behavior of strong earthquake on the segment north of Mianning of the Anninghe Fault. *Sci. China (Ser D)* 51 (9), 1224–1237. doi:10.1007/s11430-008-0104-6

Ran, Y. K., Chen, J. W., Gong, H. L., and Chen, L. C. (2008b). Late Quaternary geomorphic deformation and displacement rates of the aninghe fault around zimakua (in Chinese with English Abstract). *Seismol. Geol.* 30 (1), 86–98.

Ran, Y. K., Wang, H., Li, Y. B., and Chen, L. C. (2012a). Key techiques and several cases analyisis in paleoseismic studies in mainland China (1): Trenching sites, layouts and paleoseismic indicators on active strike-slip faults (in Chinese with English abstract). *Seismol. Geol.* 34 (2), 14.

Ran, Y. K., Wang, H., Li, Y., and Chen, L. C. B. (2012b). Key techiques and several cases analyisis in paleoseismic studies in mainland China (5): nonvisibility,dieout of fault strands and identification of young paleoseismic events(in Chinese with English abstract). *Seismol. Geol.* 34 (2), 197–210.

Ramsey, C. B. (2009). Bayesian analysis of radiocarbon dates. *Radiocarbon* 51 (1), 337–360. doi:10.1017/s0033822200033865

Reimer, P. J., Bard, E., Bayliss, A., Beck, J. W., Blackwell, P. G., Ramsey, C. B., et al. (2013). IntCal13 and Marine13 radiocarbon age calibration curves 0-50,000 years cal BP. *Radiocarbon* 55 (4), 1869–1887. doi:10.2458/azu_js_rc.55.16947

Scharer, K., Ray, W., Glenn, B., Ashley, A., and Thomsa, F. (2017). Ground-rupturing earthquakes on the northern big bend of the san andreas fault California, 800 A.D. To present. *J. Geophys. Res. Solid Earth* 122, 2193–2218. doi:10.1002/2016jb013606

Stirlinghv, M. W., Litchfield, N., Villamor, P., Dissen, R., Nicol, A., Pettinga, J., et al. (2017). "The Mw7.8 2016 Kaikōura earthquake: Surface fault rupture and seismic hazard context," in *Bulletin of the New Zealand Society for Earthquake Engineering* 50, 73–84.

Sun, C. M. (2010). *A compilation of sichuan historical earthquakes editorial board (from 26 B.C. To 1949.9 A.D.)*. Chengdu: Sichuan People's Publitshing house, 13–15. (in Chinese).

Sun, H. Y., He, H. L., and Wei, Z. Y. (2015). Late quaternary activity of zhunma fault on the north segment of daliangshan fault zone (in Chinese with English Abstract). *Seismol. Geol.* 37 (2), 440–454.

Sun, H. Y., HeIkedaWei, H. L. Y. Z. Y., Chen, Y. R., Shi, F., Chen, C., Xu, Y., et al. (2019). Paleoearthquake history along the southern segment of the Daliangshan fault zone in the southeastern Tibetan Plateau. *Tectonics* 38 (4), 2208–2231. doi:10.1029/2018TC005009

Tan, X. B., Yuan, R. M., Xu, X. W., Chen, G. H., and Chang, C. P. (2013). Co-seismic rupture and displacement in the Xiaoyudong area produced by the 2008 Wenchuan earthquake, China, and its mechanism (in Chinese with English Abstract). *Seismol. Geol.* 35 (2), 14.

Wang, H., Liang, M. J., Gao, S. P., Ran, Y. K., Chen, L. C., et al. (2018). Reevaluation of coseismic surface ruptures produced by the 1850 M 7.5 Xichang earthquake on the southeastern margin of the Tibetan plateau and implications for rupture propagation at bends on strike-slip faults. *Bull. Seismol. Soc. Am.* 108 (1), 101–115. doi:10.1785/0120170202

Wang, H., Ran, Y. K., Chen, L. C., Liang, M. J., Gao, S. P., and Li, Y. B. (2018). Determination of slip rate on the southern segment of the Aninghe fault (in Chinese with English Abstract). *Seismol. Geol.* 040 (005), 967–979.

Wang, H., Ran, Y. K., Li, Y. B., Gomez, F., and Chen, L. C. (2014). A 3400-year-long paleoseismologic record of earthquakes on the southern segment of Anninghe fault on the southeastern margin of the Tibetan Plateau. *Tectonophysics* 268, 206–217. doi:10.1016/j.tecto.2014.04.040

Wang, X. M. (1992). Discussion on the characteristics and conditions of tectonic rupture of the Xiaojin earthquake (in Chinese). *Sichuan Earthq.* 4, 24–32.

Wang, X. M., and Pei, X. Y. (1998). Some new points of view on the 1786 earthquake (M = 73/4) occurring in the area between KangDing and Moxi, Luding, Sichuan Province (in Chinese). *Earthq. Res. China* 1, 110–117.

Wells, D. L., and Coppersmith, K. J. (1994). New empirical relationships among magnitude, rupture length, rupture width, rupture area, and surface displacement. *Bull. Seismol. Soc. Am.* 84 (4), 974–1002.

Wen, X. Z. (2000). Character of rupture segmentation of the xianshuihe-aninghe-zemuhe fault zone, wester Sichuan (in Chinese with English Abstract). *Seismol. Geol.* 22 (3), 239–249.

Wen, X. Z., Allen, C. R., and Luo, Z. L. (1989). Segmentation, geomrtric features,and their seismotectionic implications for the Holocene Xianshuihe fault zone (in Chinese). *Acta Seismol. sin.* 11 (4), 362–372.

Wen, X. Z., Fang, J., Yi, G. X., Deng, Y. W., and Long, F. (2008). The seismic gap of Aninghe fault in the west of Sichuan (in Chinese). *Sci. China Ser. D Earth Sci.* 22 (3), 239–249.

Xu, X. W., Wen, X. Z., and Zhen, R. Z. (2003). The latest tectonic deformation style and its dynamic source of the active blocks in the Sichuan-Yunnan region (in Chinese with English Abstract). *Sci. China (series D)*, 12–20.

Yuan, Z. D. (2018). *Long paleoseismic record on the wuzunxiaoer-xorkoli section of the central Altyn Tagh fault*. Ph.D. Thesis. China Earthquake Administration: Institute of Geology. (in Chinese with English Abstract).

Zhang, P. Z., Deng, Q. D., Zhang, G. M., Ma, J., Gan, W. J., Min, W., et al. (2003). China continental strong earthquake activities and active blocks (in Chinese). *Sci. China Ser. D. Earth Sci.* 33, 12–20.

Zhao, G. G., Liu, D. Q., and Wei, W. (1990). "The late Quaternary slip rate and segmentation of the Xianshuihe active fault zone," in Proceedings of the PRC-USA bilateral symposium on the Xianshuihe fault zone (Seismological Press Beijing), 41–57.

Zhou, R. J., He, Y. L., Yang, T., He, Q., and Li, X. G. (2001a). Slip rate strong earthquake rupture on the Moxi-Manning segment along the Xianshuihe-Aninghe fault zone (in Chinese). *Earthq. Res. Chian* 17 (03), 253–262.

Zhou, R. J., He, Y. L., Yang, T., He, Q., and Li, X. G. (2001b). Slip rate and strong earthquake rupture on the Moxi—Mianning segment along the xianshuihe-anninghe fault zone (in Chinese). *Earthq. Res. China* 17 (3), 25–34.

Frontiers in Earth Science

Investigates the processes operating within the major spheres of our planet

Advances our understanding across the earth sciences, providing a theoretical background for better use of our planet's resources and equipping us to face major environmental challenges.

Discover the latest Research Topics

See more →

Frontiers

Avenue du Tribunal-Fédéral 34
1005 Lausanne, Switzerland
frontiersin.org

Contact us

+41 (0)21 510 17 00
frontiersin.org/about/contact